Loss Quantification and Reduced Order Modeling of Rotating Detonation Combustor Performance

by

Riley T. Huff

A dissertation submitted in partial fulfillment
of the requirements for the degree of
Doctor of Philosophy
(Aerospace Engineering)
in the University of Michigan
2025

Doctoral Committee:

Associate Professor Mirko Gamba, Chair
Professor James Driscoll
Professor Venkat Raman
Professor Margaret Wooldridge

The views expressed in this document are those of the author and do not reflect the official policy or position of the Department of the Air Force, Department of Defense, or the U.S. Government.

Riley T. Huff
ryhuff@umich.edu
ORCID iD: 0000-0001-9541-7762

© Riley T. Huff 2025

DEDICATION

I would like to dedicate this dissertation first to my family. My parents and grandparents paved the way for any success I have had in life and I greatly appreciate the example they set and their encouragement along the way. Any achievements of mine are theirs as well. To my little brother, you're doing big things, making me proud, and giving me the motivation to keep improving myself. Also, I know that it is not a *competition*, but it looks like we are all tied now!

Finally, and most importantly, I would like to dedicate this entire research effort to my beautiful wife Alexa. I know that I have been mentally absent with research and writing throughout large portions of my time at Michigan, but your understanding and support is the only thing keeping me going during this process. Thank you for being there through thick and thin, I am excited to get back to "just us" time and I love you more than ever!

ACKNOWLEDGMENTS

I would first like to thank my lab mates for their support along the way. Josh and Alex, thank you for the mentorship and guidance throughout my initial time at Michigan and for helping me through all of my classes and preliminary exams without too many gray hairs. On that note, I also want to thank Jose and Will for the prelims study sessions! Jose, I also wanted to thank you for the thoughtful discussion on which style of hotdog is the best. Rahul, thanks for helping keep this whole dissertation in perspective and for all of our side quests! I'm sure one day we will figure out this whole hydrogen thing...

Finally, I would like to thank my advisor, Prof. Gamba. Thank you for encouraging me to step outside of my comfort zone and pushing me to understand my subject of interest at a much deeper level. Also, thank you for your guidance and the great example that you provided as my advisor. I don't know where my career will end up, but if it is in academia, you will have a big part in that!

Portions of this work are based on awards No. DOE FE0031228 and DE-FE0031773 with Dr. Mark Freeman as Program Monitor (DOE NETL/UTSR program).

TABLE OF CONTENTS

DEDICATION ii

ACKNOWLEDGMENTS iii

LIST OF FIGURES vii

LIST OF TABLES xv

LIST OF APPENDICES xvii

LIST OF ACRONYMS xviii

LIST OF SYMBOLS xx

ABSTRACT xxiii

CHAPTERS

1 Introduction 1

1.1 Fundamentals of Detonation Combustion 2
1.1.1 Chapman-Jouguet Theory of Detonations 2
1.1.2 Zel'dovich, von Nuemann and Döering Theory of Detonations 8
1.1.3 Summary of Key Characteristics of Detonation Waves 11
1.2 Applications of Detonation-Based Cycles 11
1.3 Detonation and RDC Performance Metrics and Loss Mechanisms 13
1.4 Reduced Order Modeling of Detonation-Based Cycles 16
1.5 Loss Parameter Estimation with Markov Chain Monte Carlo 19
1.6 Goals of this Research Effort 23

2 Loss Mechanisms Specific to Detonation Waves 25

2.1 Detonation Performance Metrics 26
2.2 Description of Loss Mechanisms 27
2.2.1 Incomplete Combustion, Deflagration Losses and Product Re-circulation 27
2.2.2 Lateral Relief 30
2.2.3 Heat Transfer 34
2.2.4 Friction 35
2.3 Description of Detonation Performance Models 36

2.3.1 Deflagration Loss Model . . . 37
2.3.2 Non-Ideal CJ Analysis . . . 40
2.3.3 Non-Ideal ZND Model . . . 41
2.4 Results . . . 42
2.4.1 Deflagration Loss Model . . . 43
2.4.2 Non-Ideal CJ and ZND Models . . . 55
2.4.3 Non-Ideal CJ Loss Model with Deflagration Losses . . . 68
2.4.4 Additional Thoughts on Weak Detonations . . . 71
2.5 Conclusion . . . 74

3 Loss Mechanisms Specific to Rotating Detonation Combustors . . . 76

3.1 RDC Performance Metrics . . . 76
3.2 Loss Mechanism Description . . . 77
3.2.1 Inlet Blockage . . . 77
3.2.2 Incomplete Combustion, Deflagration Losses and Product Gas Re-Circulation . . . 83
3.2.3 Non-Zero Azimuthal Velocity . . . 83
3.2.4 Post-Detonation Expansion, Heat Transfer and Friction in RDC Flowpath 90
3.3 Modeling of RDC Losses . . . 91
3.3.1 State to State Cycle Model . . . 92
3.3.2 Non-Zero Azimuthal Velocity Model . . . 97
3.3.3 Blockage and Effective Area Ratio Inlet Model . . . 110
3.4 Results . . . 121
3.4.1 State to State Cycle Model . . . 121
3.4.2 Non-Zero Azimuthal Velocity Model . . . 131
3.4.3 Blockage and Dynamic Inlet Model . . . 142
3.5 Conclusion . . . 145

4 Non-Ideal RDC Reduced Order Cycle Model Description and Parametric Study . . . 148

4.1 Summary of Coding Language Trade-offs . . . 149
4.2 Cycle Model Description . . . 150
4.2.1 Detonation and Inlet Fill Model . . . 153
4.2.2 Shock-Expansion Complex . . . 163
4.2.3 Inlet Mass Flow . . . 191
4.2.4 Cycle Model Summary . . . 199
4.3 Results . . . 206
4.3.1 Grid Convergence and Sensitivity Analysis . . . 207
4.3.2 Parametric Study . . . 217
4.3.3 Detonation and RDC Performance . . . 256
4.4 Conclusion . . . 257

5 Non-Ideal RDC Reduced Order Cycle Model Comparison to Experimental Data . . . 259

5.1 Experimental Data Set for Model Evaluation . . . 259
5.1.1 Pintle Inlet . . . 260
5.1.2 Axial Inlet . . . 261

5.2 Results . . . 262
5.2.1 Comparison with Experimental Data . . . 263
5.2.2 Comparison with Other Cycle Models . . . 269
5.3 Conclusion . . . 274

6 Is "Gain" Achievable in a Detonation-Based Cycle? . . . 276

6.1 Pressure Gain . . . 276
6.2 Additional Thrust Production . . . 279
6.3 Additional Work Extraction . . . 280
6.4 Reduced Entropy . . . 280
6.5 Compactness and Combustor Simplicity . . . 281
6.6 Application that may Benefit from Detonation Combustion . . . 282
6.7 Final Thoughts on the Feasibility of Detonation-Based Systems . . . 282

7 Future Work . . . 284

7.1 Model Evaluation Time Improvements . . . 284
7.2 Improvements to Model Accuracy . . . 285
7.3 Additional Model Closures . . . 288
7.4 Additional Model Validation . . . 288
7.5 Future Model Applications . . . 289
7.6 Conclusion . . . 289

8 Conclusions . . . 291

8.1 Detonation Specific Loss Mechanisms . . . 291
8.2 RDC Specific Losses . . . 292
8.3 Detonation and RDC Coupling . . . 292
8.4 Non-Ideal RDC Cycle Model . . . 293
8.5 Path Forward for RDCs . . . 295

APPENDICES . . . 296

BIBLIOGRAPHY . . . 312

LIST OF FIGURES

FIGURE

1.1 Rayleigh Line Plot . . . 3
1.2 Rankine-Hugoniot Curve . . . 4
1.3 Example of the expansion process within a detonation tube. . . . 5
1.4 Example of a detonation tube without a wall boundary condition. . . . 8
1.5 ZND Structure . . . 9
1.6 Example of the Mach number and thermicity profile through a stoichiometric hydrogen-air detonation, using the ZND model. In this example, the cutoff Mach number for the integration was selected to be 0.95. . . . 10
1.7 Computational Fluid Dynamics solution of an RDE . . . 13
1.8 Chart distinguishing differences in detonation and RDC cycle loss mechanisms. . . . 16
1.9 RDC Model Trade-space. . . . 17
1.10 Reduced Order RDC Model Trade-space Example. . . . 19
1.11 Example Markov Chain Monte Carlo Sampling. . . . 21
1.12 Example Delayed Rejection Adaptive Metropolis MCMC Sampling. . . . 23

2.1 Example of pre- and post-detonation deflagrative combustion. Detonation moving right to left, image color altered from [1]. . . . 28
2.2 Phase Averaged OH* Chemiluminescence Measurement through a Photo-Multiplier Tube. Binned according to location with respect to detonation wave.[2]. . . . 28
2.3 Example of Area Change Between Shock Wave and CJ Plane.[3] . . . 33
2.4 Fuel partitioning for the Deflagration Loss Model. χ_{NP} represents an intermediate state of non-parasitic fuel, which is further broken down into detonation and leaked, χ_{D} and χ_{L} respectively. . . . 38
2.5 Deflagration Loss Model. . . . 38
2.6 Maps of wave speed and pressure ratio relative to ideal values as a function of parasitic combustion fraction and leaked combustion fraction. Hydrogen/air at $\phi = 0.6$. . . . 40
2.7 Gain, G, at (3.2) versus the deflagration loss parameters. Normalized by the ideal G at $\xi_{\mathrm{P}}, \xi_{\mathrm{L}} = 0$. . . . 44
2.8 Gain, G, versus detonation fraction, χ_{D}. Solid lines of constant leaked fraction, ξ_{L}, and dashed lines of constant parasitic fraction, ξ_{P}. Line separated by loss parameter increments of $0.15 \in [0, 0.9]$. . . . 46
2.9 Estimated detonation fraction (a) and estimated "gain" at the CJ plane (b) versus inlet pressure drop normalized by plenum total pressure. . . . 47

2.10 Detonation work required (normalized by heat addition) versus entropy creation as a function of heat release partitioning. Entropy normalized by ideal deflagration at the same initial conditions. Dashes lines of constant parasitic fraction, ξ_{P}, and solid lines of constant leaked fraction, ξ_{L}. 49
2.11 Posterior Distribution of the Deflagration Loss Parameters for Run 667. 51
2.12 Comparison of deflagration loss model parameters to PMT measurement. Wave speed is shown as black contours, and the pressure ratio is shown as red contours. 53
2.13 Example effects of additional loss parameters. 54
2.14 Normalized Wave speed and Detonation Pressure Ratio versus Area Ratio using the CJ Solver. 55
2.15 ZND profiles as a function of the area change rate for a stoichiometric detonation. Static pressure (a), Mach number (b), and laboratory frame velocity (c). 56
2.16 ZND profiles at an area change rate, $\frac{dA}{dx} = 1\text{e-}5$, as a function of the velocity decrement for a stoichiometric detonation. 57
2.17 ZND profiles during the solution of the ZND iteration method. The red line assumes the ideal CJ wave speed without area change, the blue line represents the first wave speed that allows for the sonic condition for the given area expansion rate, and the black line shows each intermediate step. $\frac{dA}{dx} = 6e^{\text{-}4}$. 58
2.18 Comparison of ZND and CJ solver with area ratio. 59
2.19 Normalized Wavespeed (left) and Detonation Pressure Ratio (right) versus Normalized Heat Transfer. 61
2.20 Contour Plots of Normalized Wavespeed (black) and Detonation Pressure Ratio (blue) versus Area Change and Normalized Heat Transfer. 61
2.21 Velocity Decrement from Ideal CJ Wave speed versus Heat Transfer Coefficient. . . . 62
2.22 Wavespeed and Pressure Ratio from ZND model as a function of the heat transfer coefficient. 63
2.23 Normalized detonation performance as a function of the total frictional momentum loss. Wave speed (left) and pressure ratio (right). 64
2.24 Contours of normalized detonation performance as a function of total frictional momentum losses, area change, and heat transfer. Wave speed (black) and pressure ratio (blue). 64
2.25 Thermicity profiles from ZND solver with friction as a function of the coefficient of friction. 65
2.26 Final fuel content at the end of the ZND profile as a function of friction coefficient. . . 66
2.27 Sobol Indices for the Non-Ideal CJ Model. 67
2.28 Sobol Indices for the Non-Ideal CJ Model with Deflagration Losses. 69
2.29 Deflagration Loss Parameter Estimation with Non-Ideal Loss Mechanisms. Compared to the Base Model and PMT Measurements. 71
2.30 Heat release versus ideal as a function of velocity decrement and equivalence ratio. . . 73
2.31 $P - \nu$ Diagrams at Different Velocity Decrement Values. 74

3.1 Scaling of Pressure Gain through a modeled RDC with respect to inlet pressure recovery. Data taken from Kaemming et al. [4]. 78
3.2 Blockage fraction as a function of corrected inlet mass flux. Figure adapted from [5]. . 80
3.3 Example of Laboratory Frame Particle Paths within a RDC Flowpath.[6] 84

3.4 Azimuthal Velocity Components of Various Particles within RDC geometries. Standard RDC configuration (a), RDC with Extension (b), and RDC with Extension and Converging-Diverging Nozzle.[7] . . . 85
3.5 Inlet measurement of luminescent particles through RDC cycle. . . . 87
3.6 Azimuthal velocity profile for an experimental RDC run. Hydrogen-Air operating at 150 g/s air mass flow rate and $\phi = 0.6$. . . . 87
3.7 Fixed strength shock wave moving from right to left into quiescent flow (a) and flow with a non-zero incoming velocity (b). Pre-shock state is given by (1) and post-shock state is given by (2) . . . 89
3.8 Experimental Exit Plane PIV Results.[8] . . . 90
3.9 Example of the Change in Area from the CJ Plane to a Post-Expansion Location . . . 91
3.10 Fuel partitioning for State to State Model. Fuel fraction not consumed within cycle shown with gray background. . . . 93
3.11 State to State Model Diagram. . . . 95
3.12 Effects of non-zero incoming velocity on an ideal detonation wave. . . . 97
3.13 Example RDC flow field used in this model with inlet flow area shown with a dashed-dotted line. Unrolled representation of the RDC flow field process regions broken down by color based on the region of interest at the control volume exit, along with non-dimensional length scales. Control volume of interest shown by dashed, magenta lines. . . . 99
3.14 Example of the expansion angle, α, from the CJ plane, (3.2). . . . 102
3.15 Velocity component profiles (in laboratory frame) at the control volume exit. A positive azimuthal velocity, u, is defined by the direction of wave propagation, i.e. a negative velocity means the flow is moving towards the incoming detonation wave. . . . 102
3.16 Example of the modeled profiles at the control volume exit for an ideal, hydrogen air detonation-based on an experimental run. $P_0 = 2.14$, $P_{ch} = 1.256$, and $\phi = 0.6$. Pressure profile (a), azimuthal velocity profile (b), and swirl profile (c). . . . 106
3.17 Diagram of the model used in the MCMC sampling process. . . . 107
3.18 Flow Angle Diagram, with Angle Definition. . . . 109
3.19 Histogram of Flow Angles using a 20 Degrees Standard Deviation. . . . 109
3.20 Curve Fit Errors for Cold Flow Interpolation. . . . 115
3.21 Experimental Measurement Standard Deviations for Blockage Fraction and Effective Area Ratio versus Mass Flow Rate. . . . 116
3.22 Blockage Fraction versus one minus the Effective Area Ratio (left). Injector Pressure Losses versus one minus the Effective Area Ratio (right). . . . 117
3.23 Example of the randomly generated air profile. . . . 118
3.24 Example of Dynamic Inlet Model Pressure Profile . . . 120
3.25 T-s Diagram State to State Model with ξ_{NC}, $\xi_{\mathrm{CP}} = 0.0$. . . . 122
3.26 Post-expansion Treatment for the State to State Model. . . . 123
3.27 Specific impulse gain of RDC versus an ideal deflagration device as a function of the parasitic combustion fraction, ξ_{P}, and the leaked fuel fraction, ξ_{L}, at two inlet pressure drop fractions, $\xi_{\Delta P} = 0$ in solid and $\xi_{\Delta P} = 0.5$ in dotted styles. Assuming complete combustion of leaked fuel and the post-expansion pressure $P_{3.3}$. (ξ_{NC}, $\xi_{\mathrm{CP}} = 0.0$) . . . 125

3.28 Normalized specific impulse versus normalized wave speed and detonation fraction. Lines separated by deflagration loss parameter increments of $0.15 \in [0, 0.9]$. Assuming ξ_{NC}, $\xi_{\text{CP}} = 0.0$. 126
3.29 Normalized specific impulse versus combustion efficiency, η_c, with effects of each loss parameter isolated. Changes in non-commensal fraction, ξ_{NC}, at a fixed $\xi_{\Delta P},\ \xi_{\text{CP}} = 0$ (a). Changes in inlet pressure drop fraction, $\xi_{\Delta P}$, at a fixed $\xi_{\text{NC}} = 0.9,\ \xi_{\text{CP}} = 0$ (b). Changes in commensal pressure fraction, ξ_{CP}, at a fixed $\xi_{\Delta P} = 0,\ \xi_{\text{NC}} = 0.9$ (c). . . . 128
3.30 Normalized specific impulse versus commensal combustion pressure, $P_{3.4}$. 129
3.31 Normalized specific impulse versus normalized detonation work as a function of ξ_{P} and ξ_{L}. $\xi_{\Delta P}$, ξ_{CP}, ξ_{NC} = 0. 130
3.32 Decrement in ideal detonation properties at the Chapman-Jouguet plane with increasing incoming velocity. Hydrogen-air detonation at standard temperature and pressure, and $\phi = 1.0$. 133
3.33 Decrement in ideal detonation properties at the CJ plane with increasing incoming velocity for a non-ideal detonation with parasitic combustion. Stoichiometric hydrogen-air detonation at standard temperature and pressure, and $\xi_{\text{L}} = 0$. 134
3.34 Decrement in ideal detonation properties at the CJ plane with increasing incoming velocity for a non-ideal detonation with leaked fuel. Stoichiometric hydrogen-air detonation at standard temperature and pressure, and $\xi_{\text{P}} = 0$. 134
3.35 Modeled performance contours versus deflagration loss parameters. Fixed expansion angle, $\alpha = 45^\circ$ 135
3.36 Modeled performance contours versus parasitic deflagration fraction and expansion angle. Fixed leaked fuel fraction, $\xi_{\text{L}} = 0.0$ 136
3.37 Modeled performance contours versus leaked fuel fraction and expansion angle. Fixed parasitic deflagration fraction, $\xi_{\text{P}} = 0.0$ 136
3.38 Run 2848 Sampler Results. Posterior distribution of loss parameters (a), post-predictive distribution of model outputs (b). 138
3.39 Run 2848 Sampler Results ignoring the pressure ratio measurement. Posterior distribution of loss parameters (a), post-predictive distribution of model outputs (b). 139
3.40 u and v Velocity Distributions with a 20 Degree Flow Angle Standard Deviation. . . . 141
3.41 Normalized Axial Velocity versus Flow Angle Standard Deviation. 141
3.42 Blockage Fraction versus Fill Based Blockage: Air Examples 143
3.43 Mach Profile Typical of Dynamic Inlet Model: Full Profile 143
3.44 Mach Profile Typical of Dynamic Inlet Model: Zoomed on Un-choked Region 144
3.45 Example of High Backflow at Low Blockage Ratio 145

4.1 Unwrapped RDC Geometry used for the Cycle Model 151
4.2 RDC Flowpath for Cycle Model with all Regions Highlighted. 151
4.3 RDC Flowpath Locations of Interest 152
4.4 Block Diagram of Cycle Model 153
4.5 Detonation and Fill Regions Highlighted within Flowpath. 153
4.6 Block Diagram of the Detonation and Fill Model 154
4.7 Visual Representation of the Detonation Height Calculation 157
4.8 Diagram of Key Locations and Angle within the RDC Cycle Model 158
4.9 Diagram Visualizing the Virtual Origin Calculation 159

4.10 Examples of Applying the Virtual Origin Process to Particle Paths from Multiple CFD Results. Modified from Grunewald et al. (a)[9], Schwer et al. (b)[10] 160
4.11 Diagram of the Pre-Detonation Differential Area used in the Fill Height Model, Algorithm 15. 160
4.12 Isentropic Inlet Flow Profile as a Function of Pressure Ratio. 161
4.13 Velocity Profile from Fill Model (left). Time Integration of Velocity Profile to Calculate Fill Height (right). 162
4.14 Shock-Expansion Complex Region within Flowpath. 163
4.15 Zoomed in view of Shock-Expansion Complex. 163
4.16 Block Diagram of the Shock Complex Solver. 164
4.17 Basic Shock Complex Diagram. 166
4.18 Shock Complex Angle and State Definition. 167
4.19 Post Expansion Fan Velocity Vectors. 170
4.20 Example of Downstream Expansion Node Generation. 171
4.21 Example of using the Direct MOC Node Solution. 173
4.22 Post Expansion Velocity Interaction with Next Wave. 174
4.23 Shock Complex with Velocity Deflection. 175
4.24 Shock-Expansion Complex Regions of Interest with Post-Expansion Deflection and Further Expansion. 176
4.25 Example of a Channel Flow Object within the RDC Flowpath. 176
4.26 Diagram of the Channel Flow Object with Key Locations and Nomenclature. 177
4.27 Visual Representation of the Last Node Angle and Shocked Flow Angle. 180
4.28 Channel Flow Region Breakdown with Larger Last Node Angle (left) and with Larger Shock Angle (right). 181
4.29 Visual Representation of the Calculation of the Initial Area for the Channel Flow Object Informed by the Expansion Fan Nodes. 186
4.30 Visual Representation of the Calculation of the Initial Area for the Channel Flow Object not Informed by the Expansion Fan Nodes. 187
4.31 Visual Representation of the Calculation of the Final Area for the Channel Flow Object. Non-Shocked Channel Flows (left) and Shocked Channel Flows (right). 188
4.32 Diagram of the Final Mach and Area of the Shocked Channel Flow Objects. 191
4.33 Inlet Region within Flowpath. 191
4.34 Block Diagram of the Inlet Mass Flow Rate Solver. 192
4.35 Example Inlet Total Pressure Profile Generated from Expansion Fan Nodes. 194
4.36 Resultant Inlet Mach (left) and Mass Flux Profiles (right) from the Total Pressure Profile in Figure 4.35. 194
4.37 Diagram of the Upstream Most Expansion Fan Nodes used to Generate the Total Pressure Profile in Figure 4.35 (left). Diagram of the y-direction Velocity Component used to Calculate the y-direction Total Pressure (right). 196
4.38 Example of the Quadratic Fit Procedure for the Total Pressure Profile in Figure 4.35. . 197
4.39 Example of Inlet Model Differential Areas 199
4.40 Block Diagram of the Post-Processing Algorithm. 204
4.41 Post-Processing Regions within the Flowpath. 205
4.42 Example Result. Pintle Style Inlet, $\dot{m} = 300$ [g/s], $\xi_{\mathrm{P}} = 0, \xi_{\mathrm{L}} = 0$. 205
4.43 Grid Convergence Study: Minimum Number of Expansion Fan Mach Lines 209

4.44 Grid Convergence Study: Maximum Mach Line Deflection Angle 209
4.45 Grid Convergence Study: Actual Number of Expansion Fan Mach Lines 210
4.46 Grid Convergence Study: Number of Channel Flow Objects 211
4.47 Grid Convergence Study: Mass Flow Tolerance 212
4.48 Grid Convergence Study: Pressure Change Tolerance 212
4.49 Grid Convergence Study: Maximum Inlet Spacing for Mass Flow Calculation 214
4.50 Total Sobol Indices for the Cycle Model 216
4.51 Blockage (left) and Injector Pressure drop (right) versus Inlet Area Ratio 216
4.52 Mass Flow versus Equivalence Ratio Parametric Study: Mass Flow Error and Plenum Pressure. 218
4.53 Example of Inlet Mach versus Mass Flow Rate 219
4.54 Mass Flow versus Equivalence Ratio Parametric Study: Cycle Exit Condition 220
4.55 Mass Flow versus Equivalence Ratio Parametric Study: Wavspeed, Pressure Ratio, Blockage and Fill. 221
4.56 Mass Flow Rate, Fill and Blockage changes with Detonation Height 222
4.57 Plenum pressure (left) and Inlet Mass Flow (right) versus Specified Mass Flow 223
4.58 Mass Flow versus Equivalence Ratio Parametric Study: Net Thrust, Pressure Gain and Thrust Gain 224
4.59 Mass Flow versus Equivalence Ratio Parametric Study: Polytropic Rate Terms and Coefficient 225
4.60 Injector Area Ratio Parametric Study: Mass Flow Rate Error (left) and Plenum Pressure (right). 226
4.61 Injector Area Ratio Parametric Study: Blockage (left) and Fill Properties (right) 226
4.62 Injector Area Ratio Parametric Study: Net Thrust, Pressure Gain and Thrust Gain . . . 227
4.63 Injector Area Ratio Parametric Study: Polytropic Rate Terms and Coefficient 227
4.64 RDC Length Parametric Study: Net Thrust, Pressure Gain and Thrust Gain 228
4.65 RDC Length Parametric Study: Polytropic Rate Terms and Coefficient 229
4.66 Nozzle Swirl Probability Density versus RDC Length 230
4.67 Nozzle Swirl Probability Density 231
4.68 Nozzle Swirl versus RDC Length 231
4.69 Example of Flow with Multiple Shock Passes 232
4.70 Percent Exit Area and Percent Mass Flow Processed by Shock, with Net Thrust 233
4.71 Parasitic and Leaked Fuel Fractions Parametric Study: Mass Flow Rate Error (left) and Plenum Pressure (right). 234
4.72 Parasitic and Leaked Fuel Fractions Parametric Study: Cycle Exit Conditions. 235
4.73 Parasitic and Leaked Fuel Fractions Parametric Study: Wave speed, Pressure Ratio, Blockage and Fill Properties. 236
4.74 Parasitic and Leaked Fuel Fractions Parametric Study: Net Thrust, Pressure Gain and Thrust Gain. 237
4.75 Parasitic and Leaked Fuel Fractions Parametric Study: Polytropic Rate Terms and Coefficient. 237
4.76 Ambient Pressure Parametric Study: Mass Flow Rate Error (left) and Plenum Pressure (right). 238
4.77 Ambient Pressure Parametric Study: Wave speed, Pressure Ratio, Blockage and Fill Properties. 239

4.78 Blockage versus Inlet Pressure Ratio. 240
4.79 Ambient Pressure Parametric Study: Net Thrust, Pressure Gain and Thrust Gain. . . . 240
4.80 Ambient Pressure Parametric Study: Polytropic Rate Terms and Coefficient. 241
4.81 Discharge Coefficient Parametric Study: Mass Flow Rate Error (left) and Plenum Pressure (right). 242
4.82 Discharge Coefficient Parametric Study: Blockage. 243
4.83 Discharge Coefficient Parametric Study: Net Thrust, Pressure Gain and Thrust Gain. . 243
4.84 Blockage (left) and Pressure Gain (right) versus Inlet Diodicity. 244
4.85 RDC Flowfield as a Function of the Number of Detonation Waves. 245
4.86 Wave Number Parametric Study: Mass Flow Rate Error (left) and Plenum Pressure (right). 245
4.87 Wave Number Parametric Study: Fill Properties. 246
4.88 Wave Number Parametric Study: Net Thrust, Pressure Gain and Thrust Gain. 246
4.89 Wave Number Parametric Study: Polytropic Rate Terms and Coefficient 247
4.90 Percent of Thrust from Shocked Gas versus Number of Waves 247
4.91 Nozzle Velocity Profile versus Number of Waves 248
4.92 Averaged Velocities at Exit Plane versus Number of Waves 249
4.93 Nozzle Swirl versus Number of Waves. 249
4.94 Modeled Pressure Gain versus Inlet Mass Flux 250
4.95 Pressure Gain versus Inlet Pressure Drop. 251
4.96 Inlet Pressure Drop versus Inlet Mass Flux. 252
4.97 Percent of Sonic Forward Inlet Flow versus Blockage. 253
4.98 Polytropic Momentum Rate versus Energy Rate, ... 253
4.99 Specific Net Thrust versus Parasitic Combustion Fraction. 254
4.100 Polytropic Rate Terms versus Parasitic Combustion Fraction. 255
4.101 Specific Net Thrust (left) and Pressure Gain (right) versus Percent of Thrust Produced by Shocked Flow. 255
4.102 Pressure Gain as a function of wave speed and detonation pressure ratio. 256
4.103 Thrust Gain as a function of wave speed and detonation pressure ratio. 257

5.1 Flow Profile for Pintle and Axial Inlet Geometries 259
5.2 Scatter of the Loss Metric as a Function of Mass Flow Rate (a) and Plenum Pressure (b). 268
5.3 Model Evaluation: Times for all Test Points 271
5.4 Model Evaluation: Percent Errors for all Test Points 272
5.5 Model Evaluation: Loss Metrics for all Test Points 273
5.6 Model Evaluation: Times versus Losses for all Models 274

6.1 Modeled Pressure Gain versus Inlet Mass Flux with Experimental Results. 278

7.1 Example of the Post-Shock Channel Flow Modification 287

B.1 Inert Bounded Detonation Model from Sommers.[11] 305
B.2 Expected Behavior of a Singular Expansion Fan Based on Sommers.[11] 306
B.3 Actual Behavior of a Singular Expansion at Realistic Channel Pressures, P_{ch}. 306
B.4 Shock tube analogy for an inert bounded detonation wave.[3] 307

B.5 Example of an one-dimensional dual shock tube configuration (left) and the initial conditions from the inlet sub-model (right). 308
B.6 Example of an isentropic one-dimensional expansion fan complex. 309

LIST OF TABLES

TABLE

1.1 Differences in deflagration and detonation combustion. Deflagration is modeled as laminar, stoichiometric methane-air at standard pressure and temperature; the shock is modeled in air with an initial Mach number of 5.0. Data is adapted from [12]. . . . 2

2.1 Description of States used in Detonation Cycle Analysis 26
2.2 Summary of experimental operating conditions for select runs used to evaluate the Deflagration Loss Model. 43
2.3 Sobol's Sensitivity Indices for the loss parameters in the Deflagration Loss Model. . . 46
2.4 MCMC Sampling Results for the Deflagration Loss Model. 50
2.5 Table of thermodynamic property percent differences between the CJ solver and the ZND solver's final state. 59
2.6 Table of major species for an ideal hydrogen-air detonation using the GRI3.0 mechanism. 60
2.7 Deflagration Loss Model with Non-Ideal Effects 70

3.1 Summary of Measurement Uncertainty 115
3.2 Sobol's Sensitivity Indices for the loss parameters in the State to State Model. 131
3.3 Run 106 Initial Conditions 134
3.4 Table of run conditions for cases with particle tracking. 137
3.5 Sampling Most Probable Values and Errors Relative to Measured Quantities. * represents cases not matching pressure ratio, PR. 137
3.6 Specific thrust results for Runs 2848 and 2849 based on most probable loss parameters from Table 3.5. * represents fitting process without pressure ratio. 140

4.1 Summary of Shock-Expansion Complex States. 166
4.2 List of configuration variables. 200
4.3 Description of Model Exit Conditions. 206
4.4 Grid Sensitivity Input, Outputs and Maximum Resolution Values. 207

5.1 Experimental Dataset: Pintle Inlet. 261
5.2 Experimental Dataset: Axial Inlet. 262
5.3 Experimental Comparison: Mass flow and plenum total pressure. *: did not converge, -: measurement error 264
5.4 Experimental Comparison: Thrust and blockage. 265
5.5 Experimental Comparison: Mass flow and plenum total pressure. *: model non-convergence 266
5.6 Experimental Comparison Axial: Blockage. 267

5.7 Reduced Order RDC Cycle Models. * indicates which version was used. 269
5.8 Sample Dataset for Model Comparison Study. *: next closest point estimate 270

LIST OF APPENDICES

A Pressure Gain **296**

B Trials and Tribulations of Developing a RDC Cycle Model **304**

LIST OF ACRONYMS

AR Area Ratio

CEA Chemical Equilibrium with Applications

CF Channel Flow

CFD Computational Fluid Dynamics

CJ Chapman & Jouguet

CPU Central Processing Unit

DRAM Delayed Rejection Adaptive Metropolis

EAP Equivalent Available Pressure

EGR Exhaust Gas Re-circulation

ESS Effective Sample Size

FS Full Scale

GIL Global Interpreter Lock

ISP Specific Impulse

JIT Just-in-Time

LHV Lower Heating Value

MAP Maximum a Posteriori

MCMC Markov Chain Monte Carlo

MH Metropolis-Hastings

MOC Method of Characteristics

OD Outer Diameter

PDC Pulse Detonation Combustor

PDF Probability Density Function

PG Pressure Gain

PGC Pressure Gain Combustion

PIV Particle Image Velocimetry

PM Prandtl-Meyer

PMT Photo-multiplier Tube

PR Pressure Ratio

RDC Rotating Detonation Combustor

RH Rankine-Hugoniot

ROM Reduced Order Model

RPM Rotations per Minute

STP Standard Day Temperature and Pressure

T-s Temperature versus Entropy

UM University of Michigan

VBA Visual Basic for Applications

VN von Nuemann

ZND Zel'dovich, von Nuemann & Döering

LIST OF SYMBOLS

A: Area
A_{ch}: Detonation Channel Area
A_{eff}: Effective Area
A_{inj}: Inlet Throat Area
AR: Area Ratio
B: Blockage Fraction
BR: Blockage Ratio
BR$_{fill}$: Fill Based Blockage Ratio
cw: Channel Width
c_d: Discharge Coefficient
$c_{d,b}$: Reverse Discharge Coefficient
$c_{d,f}$: Forward Discharge Coefficient
c_f: Friction Coefficient
c_h: Heat Transfer Coefficient
c_p: Specific Heat at Constant Pressure
c_v: Specific Heat at Constant Volume
D: Wavespeed
d: Distance
D_H: Hydraulic Diameter
D_{lab}: Laboratory Wavespeed
F: Thrust (or Total Friction Loss)
F_g: Gross Thrust
F_{net}: Net Thrust
F_{sp}: Specific Thrust
G: Gain (Multiple Definitions)
g_0: Gravitational Constant
h: Enthalpy
HR: Heat Release
h_{det}: Detonation Height
h_{fill}: Fill Height
h_{rdc}: RDC Channel Length
ID: Inner Diameter
I_{sp}: Specific Impulse
k: Exponential Decay Constant
l_{ch}: Channel Length
$\mathcal{L}$: Likelihood, or Loss Metric
M: Mach Number

m: Slope
$\dot{m}$: Mass Flow Rate
$\dot{m}''$: Mass Flux
$\dot{m}_c$: Corrected Mass Flow Rate
$\dot{m}_c''$: Corrected Mass Flux
MW: Molecular Weight
N: Number of a Quantity
n: Polytropic Coefficient
$\mathcal{N}$: Normal Distribution
OD: Outer Diameter
P: Pressure
PG: Pressure Gain
PR: Pressure Ratio
$\mathcal{P}$: Probability
P_0: Plenum Total Pressure
P_{ch}: Channel Static Pressure
Q: Total Heat Rate
q: Specific Heating Rate
R: Gas Constant
s: Entropy
S_T: Total Sobol Index
u: Velocity (typically x-direction)
U: Total Velocity
$\mathcal{U}$: Uniform Distribution
V: Total Velocity
v: Velocity (typically y-direction)
T: Temperature
t: Time
tol: Tolerance
TR: Temperature Ratio
$x_{_{VO}}$: Virtual Origin x Location
Y: Mass Fraction
$y_{_{VO}}$: Virtual Origin y Location
α: Effective Area Ratio (or Detonation Tilt Angle)
β: Fill Angle
χ: Molar Fraction
δ: Diodicity (or Slip Angle)
η_c: Combustion Efficiency
γ: Ratio of Specific Heats
λ: Induction Length
ν: Specific Volume (or Prandtl-Meyer Function)
ϕ: Equivalence Ratio
ρ: Density
σ: Standard Deviation
$\dot{\sigma}$: Thermicity

Σ: Covariance Matrix
τ: Normalized Time or Frictional Loss
Θ: Parameter Set
θ: Oblique Shock Angle
ξ: Loss Fraction
ξ_{L}: Leaked Fuel Fraction
ξ_{P}: Parasitic Deflagration Fraction

ABSTRACT

Detonation combustion is a highly energy-dense mechanism by which chemical energy is converted into usable work. Numerous attempts have been made to utilize detonation combustion, yet the proposed higher performance has yet to be realized. This research focuses explicitly on the Rotating Detonation Combustors (RDC) application, which allows for a continuously propagating detonation wave, potentially producing a device-level pressure gain. Like many other applications, these devices incur different losses, which are not fully captured by an idealized analysis. Therefore, one goal of this research is to capture and quantify the loss mechanisms that affect the performance of detonation waves and RDC devices. Care must be taken not to assume that decreases in the performance of one is indicative of a loss in the other, though they are often influenced by one another.

This research characterized the loss mechanisms inherent to detonation combustion using reduced order models of different processes within the detonation wave. Showing that detonation performance is particularly susceptible to parasitic pre-detonation deflagrative burning. Across many detonation performance metrics, parasitic combustion accounts for 40-80% of the total losses, where the highest impact of parasitic combustion is seen in the pressure ratio across the detonation wave.

The same methodology was used to study loss mechanisms specific to the RDC. These results showed how the performance of the RDC is directly impacted by the losses incurred through the RDC inlet; however, the inlet performance is also influenced by the detonation, where one must make an appropriate trade-off between detonation and device performance. Through a state-based RDC cycle model, the combination of parasitic combustion and inlet pressure loss can significantly reduce RDC performance. Without losses, the specific impulse gained by the RDC device over a constant pressure analog was between 0% to +58%; however, including moderate inlet pressure losses, this dropped to -13% to +50%, showing a specific impulse degradation versus an ideal deflagrative device.

Using the lessons learned, a non-ideal reduced order cycle model was developed to integrate the different losses across detonations and RDC devices. This model was also developed to improve evaluation times for future use cases. Across a wide range of test conditions and parametric model evaluation, the new cycle model provided an accurate prediction of the operation of the RDC device using performance metrics such as thrust and inlet blockage. However, the model requires

some improvements to better capture conditions of low inlet mass flux, where the predicted performance and operating conditions differ from the experimental measurements by up to 200%. For moderate mass flow rates around 300 g/s, the model offers 2-6x improvements in predictive capability relative to current state-of-the-art models while also providing a 10-10000x improvement in model evaluation time.

Finally, this research provided a broader discussion on the performance of RDCs, specifically the pressure gain, and whether this metric is achievable within RDCs. The cycle model results did not predict any pressure gain and did not show a correlation between the detonation performance and the pressure gain metric; therefore, the author offered other metrics, such as thrust gain, or applications, such as rocket-style RDC motors, in which RDCs may show improvements.

CHAPTER 1

Introduction

Detonation combustion offers an intriguing physical process by which chemical energy is converted to usable work. By using a detonation process to combust fuel sources, a potential gain in combustion performance can be achieved. To this end, significant effort has been dedicated to the study of detonation-based combustion and the application thereof. This dissertation seeks to narrowly focus on the performance aspects of detonations, as well as a particular application of interest, Rotating Detonation Combustors (RDC). Many experimental RDCs have been built and studied over the last decade. However, the promised performance benefits have yet to be realized in a physical device. Due to the mismatch in theory and reality, this study aims to identify and quantify loss mechanisms specific to detonation combustion. The study focuses on the application of detonation combustion in air-breathing RDCs. Along with capturing these loss mechanisms, this research also develops and exercises a reduced order model (ROM) and key sub-models for RDCs to better understand how these loss mechanisms propagate through a detonation-based system.

The following sections will provide a more robust introduction to detonations and a few fundamental models used to study the physical processes inherent to detonation combustion and detonation-based cycles. This chapter will also examine some applications of detonation combustion, their history, and the performance metrics of interest associated with these devices. The majority of the detailed discussion will be included in the relevant chapters. Finally, the goals of this research will be outlined in detail, along with the motivation behind this effort.

As for the remaining chapters, this research will focus on the performance and modeling of detonation waves and RDC performance. Notably, these two metrics (detonation versus cycle performance) are not guaranteed to be correlated. In some instances that will be discussed later, the detonation performance runs counter to the performance of the RDC as a system. Besides simply quantifying the loss mechanisms, the primary outcome of this research is to develop and study a non-ideal reduced order model of air-breathing RDC devices. It is hoped that this model, the culmination of the prior research on loss mechanisms, provides new insights into the use of detonation combustion for air-breathing applications. Finally, this research will discuss the attainability of the theorized performance benefits of detonation combustion, with a specific focus on RDC.

Property	Deflagration	Normal Shock	Detonation
M_1	0.001	5.0	5-10
M_2	0.003	0.42	1.0
u_2/u_1	7.5	0.2	0.4-0.7
P_2/P_1	≈ 1.0	29	13-55
T_2/T_1	7.5	5.8	8-21
ρ_2/ρ_1	0.13	5.0	1.7-2.6

Table 1.1: Differences in deflagration and detonation combustion. Deflagration is modeled as laminar, stoichiometric methane-air at standard pressure and temperature; the shock is modeled in air with an initial Mach number of 5.0. Data is adapted from [12].

1.1 Fundamentals of Detonation Combustion

The detonation process is a well-studied phenomenon by which reactants are consumed in a supersonic combustion event. This event features a coupled shock wave followed by a short but intense combustion zone. Because a shock wave compresses and preheats the reactant mixture, the reactants are consumed at a higher pressure than their initial state. For this reason, detonation combustion and devices reliant on detonation combustion are classified under the pressure gain combustion (PGC) umbrella. Table 1.1, adapted from Turns, summarizes deflagration and detonation combustion differences.[12]

The properties of the detonation wave listed in Table 1.1 are given in the wave frame of reference at the Chapman-Jouguet (CJ) plane. More details on this specific point in the detonation process and the Galilean transform required to analyze a detonation wave in the laboratory frame are provided in the next section. The results of Table 1.1 suggest that the detonation wave has the potential for improved utilization of the chemical energy provided by the fuel compared to a similar deflagration-based cycle.

1.1.1 Chapman-Jouguet Theory of Detonations

The Chapman-Jouguet (CJ) theory of the detonation phenomena uses a control volume analysis of the detonation wave in its frame of reference. This assumes that the detonation wave is purely one-dimensional with no area change, steady (in the wave frame of reference), and adiabatic. The following set of equations provides the conservation laws (mass, momentum, and energy, respectively) for the CJ analysis:

$$\dot{m}'' = \rho_1 D = \rho_2 u_2 \tag{1.1}$$

$$P_1 + \rho_1 D^2 = P_2 + \rho_2 u_2^2 \tag{1.2}$$

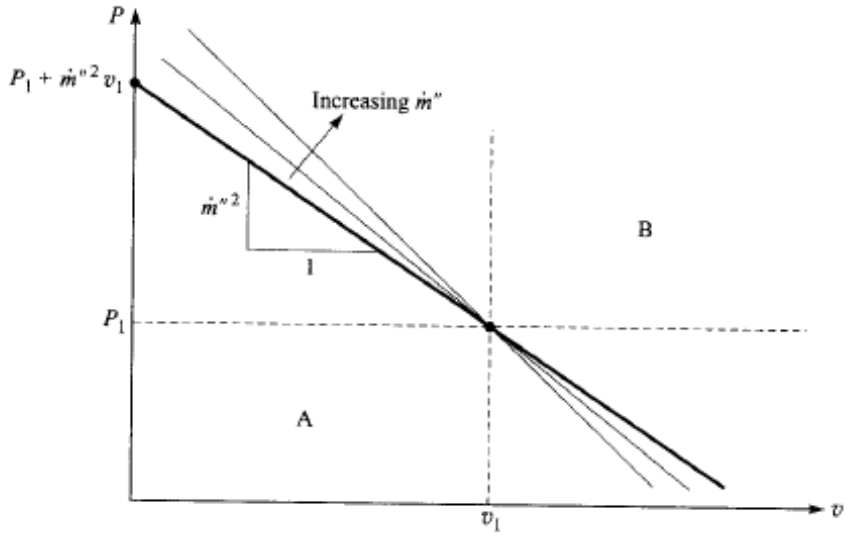


Figure 1.1: Plot of multiple Rayleigh lines for a given set of initial conditions. Figure from [12].

$$h_1 + \frac{D^2}{2} + q = h_2 + \frac{u_2^2}{2} \tag{1.3}$$

where D represents the wave speed (in this case, the speed of the reactants moving into the wave).

Assuming a calorically perfect gas (CPG) with constant specific heats, the energy equation can be reduced to:

$$c_p T_1 + \frac{D^2}{2} + q = c_p T_2 + \frac{u_2^2}{2} \tag{1.4}$$

Combining Equation 1.1 and Equation 1.2 yields the Rayleigh line:

$$\frac{P_2 - P_1}{1/\rho_2 - 1/\rho_1} = -\dot{m}''^2 \tag{1.5}$$

Figure 1.1 shows examples for the Rayleigh line on the pressure / specific volume plane, where increases in mass flux $\dot{m}''$ correspond to a steepening of the slope. This line represents a combination of the continuity and momentum conservation equations, along which the mass flux is constant. Note that regions A and B in Figure 1.1 are invalid as they require a negative mass flux.

When an ideal gas is assumed, the momentum and energy equations can be combined into a single equation. This representation is known as the Rankine-Hugoniot (RH) curve and is shown in Equation 1.6:

$$\frac{\gamma}{\gamma - 1}\left(\frac{P_2}{\rho_2} - \frac{P_1}{\rho_1}\right) - \frac{1}{2}\left(P_2 - P_1\right)\left(\frac{1}{\rho_1} + \frac{1}{\rho_2}\right) - q = 0 \tag{1.6}$$

Figure 1.2 shows an example of the RH curve for a given initial condition and heat addition,

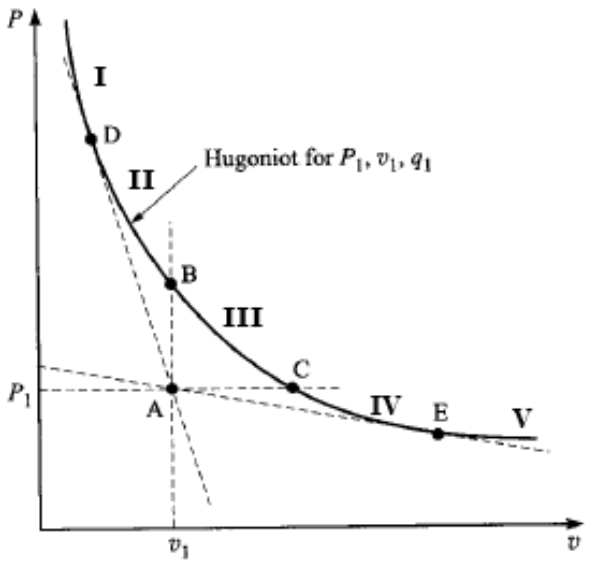


Figure 1.2: Plot of a Rankine-Hugoniot curve. Figure from [12].

q. It also contains two Rayleigh lines starting from the same initial conditions at point A. The line AC represents the zero mass flux condition. Line AE represents a choked deflagration line, where any point along the RH curve between points C and E is valid for deflagration combustion events. Line AB represents an infinite mass flux case, so any point along the RH curve from point B to C is invalid, as it would require a negative flux. For detonation combustion, line AD represents the ideal detonation process. This is the tangent point on the RH curve along the Rayleigh line from the initial conditions. This is a key characteristic of a detonation wave and will be revisited in a later section.

1.1.1.1 Derivation and Discussion of Detonation Work

When first introduced to the author, detonation waves were described as a coupled shock and combustion event, where the shock provides the activation energy to initiate the combustion, and the combustion event provides the energy to drive the shock wave. Although the initial part of this description matches well with the theory provided in the previous section, the latter portion requires some additional thought that is not discussed sufficiently in the literature. Recalling the summary in Table 1.1, we can see that in the wave frame of reference, a detonation provides increased pressure and temperature relative to a deflagration operating at the same initial conditions. This would appear to increase the available work for a detonation. However, one must recognize that the work extraction process must occur in the laboratory frame of reference (the frame of reference of the system using the detonation for work production). A discussion of this accounting has been

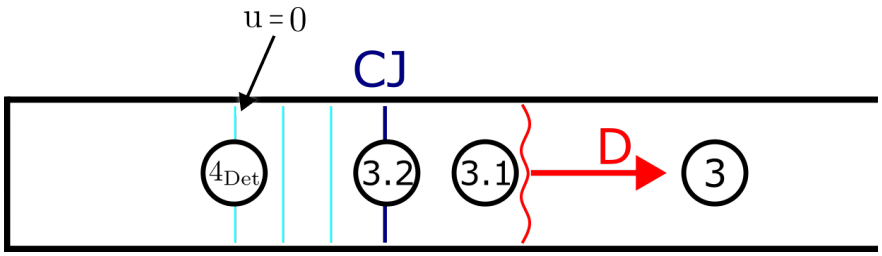


Figure 1.3: Example of the expansion process within a detonation tube.

provided by Dyer and Kaemming [13, 14, 15] for detonation tubes or pulse detonation combustors (PDCs), and by Nordeen et al.[16, 6] for RDCs. Langweiler [13] and Taylor [14] both analyzed the detonation process in a purely one-dimensional detonation tube configuration. In their analysis, a simple expansion fan accounted for the energy reduction from the CJ plane to a state of usable work. This expansion wave, in effect, provides identical reductions in the state properties from the CJ plane used in Dyer and Kaemming.

Dyer and Kaemming present a Mollier diagram for the PDC cycle to model integrated PDC systems for flight purposes. In their research, they introduce that using the CJ state as the point from which work may be extracted results in an available energy much higher than that of the energy available in the fuel source. Because of this, they propose that the state from which work may be extracted at the system level must not have more energy than that provided to the system. Yes, the conservation of energy holds, even in detonations. Dyer and Kaemming reduced the final temperature from the CJ temperature to the equivalent temperature at the same entropy state as the post-detonation products (at the CJ state). They did not offer a mechanism for this reduction, but further research provided additional historical examples.

In the PDC/detonation tube configuration, the detonation wave provides a non-zero velocity at the CJ plane in the direction of the detonation propagation. Those familiar with shock tubes will recognize that the boundary condition of these configurations will require a zero velocity condition at the wall. An example of the detonation tube is shown in Figure 1.3, where the work extraction for the system occurs at the post-expansion state, (4_{Det}).

To describe this process in terms of conservation equations, one can focus on the Galilean transform of the energy equation, Equation 1.4, from the wave frame to the laboratory frame of reference. Therefore, we can simply replace D and u_2 with u_1' and u_2', where the $'$ represents speed in the wave reference frame:

$$c_p T_1 + \frac{{u_1'}^2}{2} + q = c_p T_2 + \frac{{u_2'}^2}{2} \tag{1.7}$$

In the laboratory reference frame of reference, u_i' can be written as:

$$u_i' = D - u_i \tag{1.8}$$

where i represents state 1 or 2. Substituting Equation 1.8 into Equation 1.7 results in:

$$c_p T_1 + \frac{(D-u_1)^2}{2} + q = c_p T_2 + \frac{(D-u_2)^2}{2} \tag{1.9}$$

By further expanding, one derives:

$$c_p T_1 + \frac{D^2}{2} - Du_1 + \frac{u_1^2}{2} + q = c_p T_2 + \frac{D^2}{2} - Du_2 + \frac{u_2^2}{2} \tag{1.10}$$

The $\frac{D^2}{2}$ terms cancel out. Without loss of generality, we can also assume that the initial laboratory frame velocity, u_1, is zero, like in the detonation tube example, yielding:

$$c_p T_1 + q = c_p T_2 + \frac{u_2^2}{2} - Du_2 \tag{1.11}$$

The above results look like the familiar form of the energy equation but with an additional Du_2 term. This term will be referred to as the *detonation work term* and essentially represents the energy required to move the CJ plane at velocity, u_2, in a wave frame moving at speed, D. This detonation work term and the expansion fan required to match the detonation tube boundary condition account for the mechanism by which the combustion process *provides the energy to drive the shock wave*. Although not a direct loss mechanism, it decreases the available energy for work extraction by adequately accounting for the energy required to move the detonation reference frame. It is important to remember that this falls out of the fact that the detonation wave is unsteady in the laboratory frame, yet we extract work in this frame.

We can then relate the energy equation to the post-expansion state, $\textcircled{4_{\mathrm{Det}}}$ in Figure 1.3. We will also assume that the post-expansion state is at zero velocity, $u_4 = 0$, in the laboratory frame due to the detonation tube boundary condition, yielding:

$$c_p T_2 + \frac{u_2^2}{2} - Du_2 = c_p T_4 \tag{1.12}$$

Rearranging Equation 1.12 and knowing $h = c_P T$ for calorically perfect gases (CPG), we can breakdown the energy "gain" through a detonation as:

$$h_4 = h_{\mathrm{CJ}} + \frac{u_{\mathrm{CJ}}^2}{2} - D_{\mathrm{CJ}} u_{\mathrm{CJ}} \tag{1.13}$$

Equation 1.13 shows that the final enthalpy in the laboratory frame consists of the sensible enthalpy gain across the detonation, the kinetic energy gained from the induced velocity at the CJ point, and the detonation work term. The detonation work term reduces the enthalpy gained at the CJ plane in the wave frame to the final enthalpy available in the laboratory frame.

The relationship between D_{CJ} and u_{CJ} is of particular note. With a zero initial velocity condition ahead of the detonation wave (in the laboratory frame), it is known that the magnitude of the wave speed must be greater than the induced velocity $|D_{\mathrm{CJ}}| > |u_{\mathrm{CJ}}|$. This means that the detonation work term is always more significant than the kinetic energy gain term:

$$|D_{\mathrm{CJ}} u_{\mathrm{CJ}}| > \left| \frac{u_{\mathrm{CJ}}^2}{2} \right| \tag{1.14}$$

Essentially, the detonation work term cancels out all of the kinetic energy gained in a detonation tube and reduces the sensible enthalpy gained up to the CJ plane, exactly what Dyer and Kaemming captured in their PDC model.

The same analysis applies to the RDC configuration. An analogy has been drawn to the work analysis conducted in turbo-machinery, specifically the analysis of rothalpy, by Nordeen et al.[16, 6]. Making the same assumptions of zero velocity ahead of the detonation wave and after the post-expansion product gases, the same argument can be made about how this detonation work term affects the available energy within a RDC cycle. It should be noted that the boundary conditions within a RDC device vary drastically from those within a PDC cycle; therefore, this post-expansion state with zero velocity is simply a fictitious state within the complete RDC cycle that is useful for analysis only.

Taylor also presented an example of an analogous situation in 1950.[14] He discusses a one-dimensional detonation tube without the back wall boundary condition. A pressure boundary condition was applied in this case, and the expansion process proceeds to this specified pressure. Figure 1.4 shows an example of the wall-less detonation tube, stepping through the pressure profile at three different time steps of interest and showing the processes at the final time step.

At the initial time step, $t = 0$, the wall-less detonation tube is filled with reactants at the ambient pressure, P_{amb}. Next, the detonation is initiated at the left side of the tube and propagates towards the right. In the second time step, t_1, the detonation has moved a distance such that the expansion process progresses to the condition $u_4 = 0$. At this step, the post-expansion gases at the left side will present the same properties as that in the state $\textcircled{4_{\mathrm{Det}}}$ in Figure 1.3. However, this pressure is higher than the boundary pressure, so the expansion process proceeds further. The final time step, t_2, is at a point where the detonation wave is far enough downstream such that the entire expansion to the ambient pressure has been completed. At this point, the velocity at the end of the expansion wave is non-zero and in the direction opposite to that of the detonation wave propagation.

The last subplot in Figure 1.4 shows the processes within the detonation tube at this final time step. It can be seen that the point at which $u = 0$ can still be calculated based on the detonation work analysis presented above. However, this state becomes mostly irrelevant if we examine the system's performance. For example, if we were to calculate the thrust of this device, we would

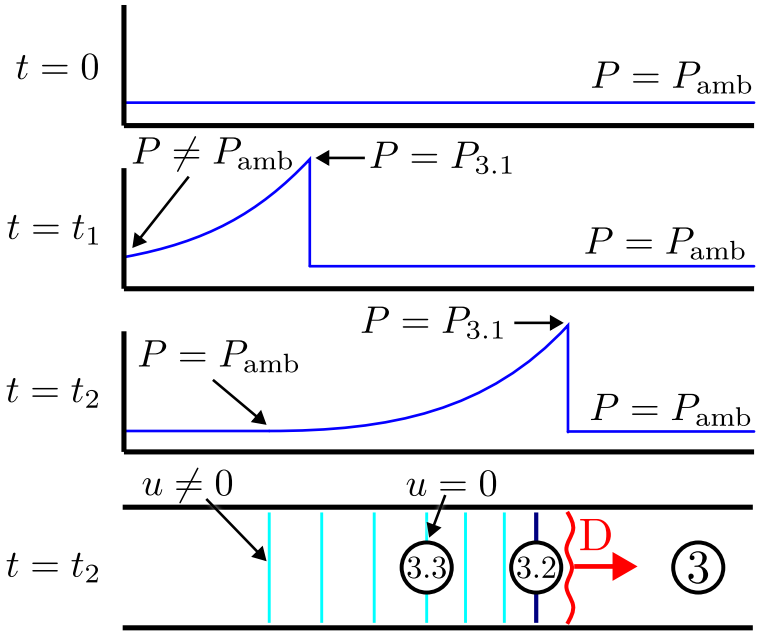


Figure 1.4: Example of a detonation tube without a wall boundary condition.

be more concerned with the post-expansion gases and the velocity magnitude at the end of the expansion.

The wall-less detonation tube serves only as an analogy to the detonation within the RDC cycle, as the RDC is a fully three-dimensional flow field. However, this analogy helps in understanding the processes within the RDC flowpath. It also explains the high post-detonation circumferential velocities seen in RDCs.[16, 6, 7, 9] It will also be useful in a later discussion of the effects of non-zero velocities ahead of the detonation wave.

1.1.2 Zel'dovich, von Nuemann and Döering Theory of Detonations

The Zel'dovich, von Nuemann and Döering (ZND) theory of the detonation phenomena extends the CJ theory, where the infinitesimally thin detonation assumption is removed. This methodology temporally or spatially marches through the one-dimensional flow within the detonation region, starting from a post-shock state to the sonic condition at the end of the detonation wave. The detonation can be separated into three distinct regions in this model, shown in Figure 1.5. These regions, not shown to scale, include the shock region from 1 to $1'$, the induction region from $1'$ to $1''$, and finally, the reaction region from $1''$ to 2. The induction region is where the chemical reaction begins, and the energy imparted on the gas mixture by the shock begins to break down the initial bonds. After this process, the combustion proceeds until the end of the reaction zone, which coincides with the sonic condition.

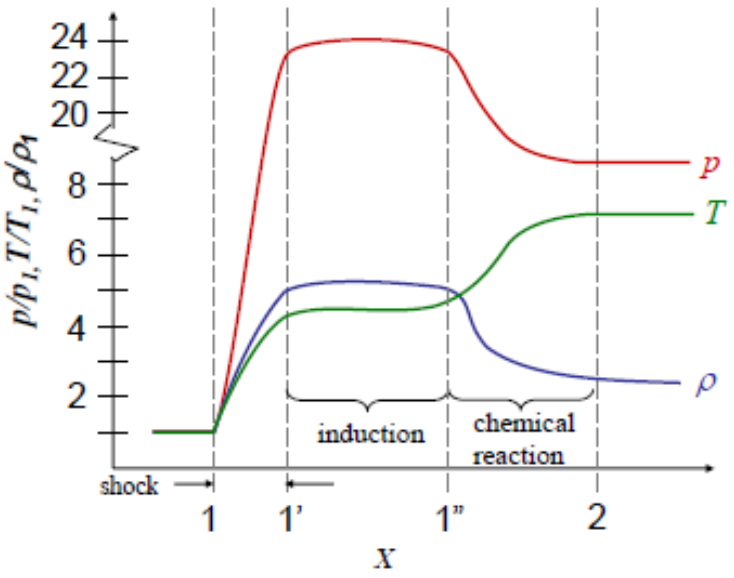


Figure 1.5: ZND structure. Figure from [17]

Figure 1.5 also plots the lines of pressure, temperature, and density through the detonation regions. This shows that the peak pressure within the detonation wave is just after the shock passes, known as the von Nuemann (VN) point. As the combustion begins, the pressure and density drop while the temperature and wave frame velocity increase.

The ZND model of the detonation wave now includes a crucial time component, accounting for chemical rate processes that must occur within the reaction zone. This model provides insights as to the thickness of the detonation wave based on finite-rate chemistry, whereas the CJ model assumes equilibrium combustion will occur. Both models offer a framework for capturing the physics of the detonation wave but at differing levels of fidelity.

In practice, the value of thermicity is used to sum the effects of the chemical reaction process into a single rate term. Equation 1.15 shows the formulation for the thermicity value, σ:

$$\dot{\sigma} \equiv \sum_{k=1}^{K} \left(\frac{\mathcal{W}}{\mathcal{W}_k} - \frac{h_k}{c_p T} \right) \frac{DY_k}{Dt} \tag{1.15}$$

Using a time-marching scheme, the rate of change in pressure can be written as a function of the current state, the thermicity, and the Mach number, where $\eta = 1 - M^2$.

$$\dot{P} = \frac{-\rho u^2 \dot{\sigma}}{\eta} \tag{1.16}$$

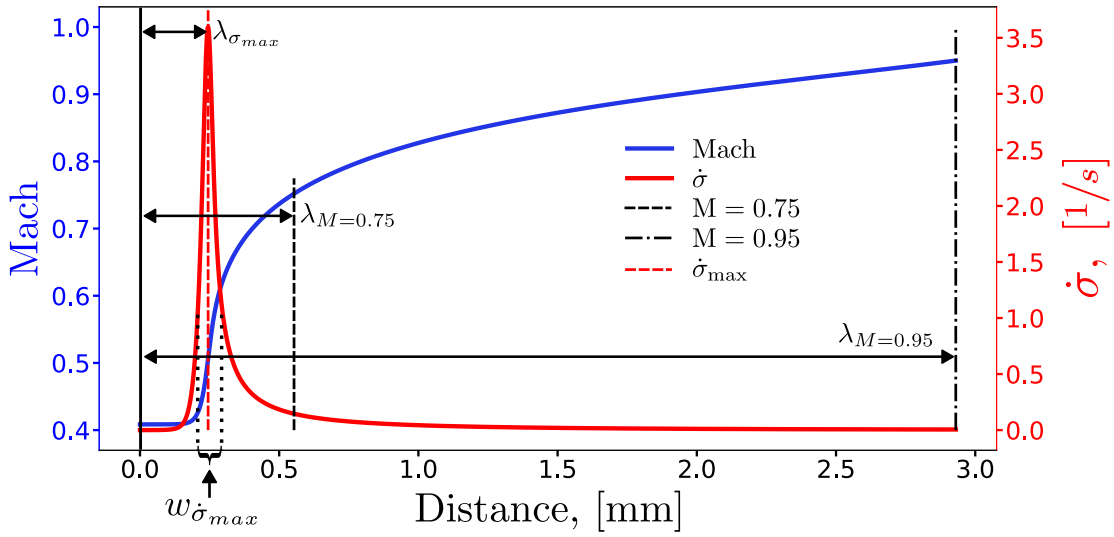


Figure 1.6: Example of the Mach number and thermicity profile through a stoichiometric hydrogen-air detonation, using the ZND model. In this example, the cutoff Mach number for the integration was selected to be 0.95.

The density rate of change can likewise be written as a function of the same parameters:

$$\dot{\rho} = \frac{-\rho\dot{\sigma}}{\eta} \tag{1.17}$$

where the rate of change of each species used in the thermicity calculation is determined using finite-rate chemistry. Computation models of chemical kinetics allow a simple methodology for implementing a ZND-style solver. At the same time, this research uses the *Python's Cantera* package that provides a gas object to calculate both the thermodynamic state and net production rates of each species.[18] These equations of motion were integrated from the post-shock state (von Neumann VN, state) until the sonic condition was met.

Figure 1.6 shows an example solution from the *Cantera*-based ZND solver, where the Mach number through the profile is shown in blue and the thermicity values are shown in red. This figure also shows the length scales of interest as they relate to the size of the detonation wave. Two key metrics are the induction length, discussed in Figure 1.5, and the length of detonation based on the distance to the sonic condition. These scales are indicative of the size of the detonation wave when calculated in a purely one-dimensional sense and provide insights when compared with application-specific length scales.

1.1.3 Summary of Key Characteristics of Detonation Waves

As will be discussed in Chapter 2, a detonation wave in a given application will not consistently achieve the ideal metric determined from the CJ or ZND models. Regardless of achieving these ideal metrics, we can evaluate the "validity" of a detonation wave versus a deflagration wave by examining a few key characteristics of detonation combustion.

Key aspects of the detonation phenomena include:

1. Supersonic combustion with a shock attached to a combustion region: This is, by definition, where the shock wave provides the activation energy required to initiate the combustion event, which in turn supports and drives the shock wave forward.

2. The flow is sonic at the CJ plane: this is the result of the CJ analysis, where the final state is sonic in the wave frame of reference.

3. At the CJ state, the Rayleigh line is tangent to the RH curve: this is shown in Figure 1.2 and is a key characteristic that falls out of the post-detonation sonic condition.

4. Increased pressure over a purely deflagrative combustion process: this was also shown in Figure 1.2 where the pressure decreases across a deflagration region.

5. With no pre-detonation velocity (in the lab frame), the detonation wave will induce a velocity (in the lab frame) at the CJ plane in its direction of motion: this point was discussed in Section 1.1.1.1 where this induced velocity represents a kinetic energy gained across the detonation front.

6. The last point also requires a detonation work term to maintain the rotating reference frame: this falls out of the analysis conducted after the CJ plane, which requires an expansion process to move the CJ plane in the laboratory frame of reference.

These characteristics will be revisited as we begin discussing loss mechanisms inherent to the detonation phenomena that may reduce performance relative to the predictions provided by the CJ or ZND analysis.

1.2 Applications of Detonation-Based Cycles

Multiple detonation-based applications are hoping to realize the potential benefits of detonation combustion in a usable manner, particularly in aerospace applications requiring thrust production or work extraction from the post-detonation combustion gases. The first example described here

is the detonation tube, which includes a more practical implementation known as the Pulsed Detonation Combustor (PDC). PDCs, first theorized by Hoffman in the 1940s and tested by Nicholls et al. in the 1950s, consist of a tube filled with a reactant mixture through which the detonation wave propagates.[19, 20] In the case of the detonation tube, both end-walls are solid, providing a fully enclosed combustion cycle. At the same time, the PDC device features an opened end that is exposed to atmospheric conditions. Like conventional piston engines, PDCs also feature a four-step cycle consisting of the intake, combustion, exhaust, and purge. The intake brings in a fresh reactant mixture, which is then ignited to produce a detonation wave that moves toward the exit of the PDC. As the exhaust gases exit, they produce thrust or usable work. A purge gas is typically required to prevent pre-combustion of the next injection of reactants. Through this described cycle, a PDC operates cyclically on the order of tens to hundreds of hertz.[20]

Some reasons PDCs may not realize the projected benefits proposed by the cycle analysis are as follows: First, PDCs are highly unsteady devices that only produce thrust over a fraction of the overall cycle.[21] They also likely require a purge gas buffer between the post-combustion products remaining in the tube and the fresh fill to avoid auto-ignition. This increases the fraction of the cycle that does not produce thrust. Because of this, the time-averaged thrust over the entire cycle will be significantly lower than the ideal predictions based on a one-dimensional analysis of the detonation.

The next issue revolves around the pre-detonation static pressure of the fresh reactants. Without valving at the exit of the PDC or an incredibly restrictive nozzle, it would be difficult, if not infeasible, to attain a static pressure inside the PDC much higher than the ambient conditions to which the exhaust side is exposed. So, even though the detonation wave provides a temporary pressure gain of 10-30 times the initial pressure at higher altitude applications (10 km altitude, or 25 kPa), the realized chamber pressure is still low. Lower chamber pressure, even post-shock, will result in higher entropy production and less net thrust. If a restrictive nozzle was implemented instead of an active valve, the pressure could be increased at the expense of a potential overfill of fresh reactants to reach the higher pressure. This would lead to higher overall plenum pressures and detrimental effects during the detonation and blowdown, for example, reflected shocks of higher strength due to the nozzle geometry.

The cyclical nature of the PDC, combined with the high impulse created by the detonation wave, also leads to challenges with integrating a PDC device with any aerospace flight system and/or downstream turbo-machinery.[22, 23] Though the PDC showed some benefits over a deflagration-based cycle during the combustion portion of the cycle, the combination of the purge/refill time, valving schemes and integration issues led to the development of the Rotating Detonation Combustor (RDC), seeking to eliminate this downsides.[24]

RDCs are geometrically simple devices but rely on complex physical processes by which a det-

onation wave is stabilized in an annular channel, running perpendicular to the bulk flow direction. Figure 1.7 shows a computation example of the RDC flowpath, where the bulk flow moves from bottom to top, and the detonation wave travels circumferentially around the RDC channel. RDCs eliminate the PDC's low frequency, high impulse cycle by tailoring the geometry and flow field to allow the detonation wave to operate continuously. In doing this, the RDC now provides a more "steady" exhaust gas profile in the cycle-averaged sense. This is not to say that RDCs are steady devices; quite the contrary. However, depending on the size, the donation wave rotates around the RDCs at thousands of Hertz, which is typically much faster than the time scales associated with the net thrust production or measurement and any turbomachinery used for work extraction. For example, the rotational speed of turbomachinery in typical gas turbine engines operates between 10-24 kRPM, translating to operation between 160-420 Hz. In contrast, a typical 6-inch RDC operating on hydrogen-air will operate around 3 kHz. In a sense, the high frequency of the RDC exhaust appears relatively steady to anything downstream. In this example, a given turbine blade would see 7-20 detonation cycles within a single rotation.

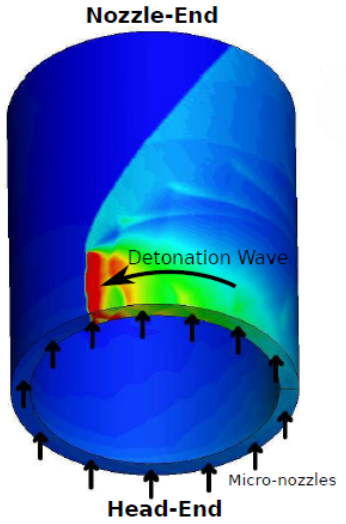


Figure 1.7: Computational fluid dynamics solution of an RDE. [10]

1.3 Detonation and RDC Performance Metrics and Loss Mechanisms

To justify changing a deflagration-based system to a detonation-based system, some form of benefit that detonation combustion can provide to the system is required. This section will discuss some performance and loss metrics for detonations and systems based on detonation combustion. It will

also introduce some potential downsides of using these performance definitions, which will be backed up by the results and discussion presented later in this thesis. This section will only briefly discuss each metric, saving most of the discussion for the respective sections in Chapter 2.

We must be careful to distinguish the differences in detonation performance and RDC performance. What qualifies as "good" detonation performance, based on any chosen metric, does not necessarily ensure "good" RDC cycle performance. This thesis will discuss this difference further in detail as each performance and loss metric is discussed. In the remainder of this section, we will describe performance metrics for both detonations and detonation-based systems.

For the detonation wave itself, wave speed and pressure ratio, typically normalized by their ideal CJ values, are used widely to establish the performance of a detonation wave with respect to the expected (ideal) value. We discussed in Section 1.1.1 that the detonation wave is a supersonic combustion event, and the pressure ratio across the wave is proportional to the speed of the wave. For one seeking to use a detonation-based system, the pressure ratio across the wave becomes a key metric of interest. This aspect of the pressure raise across the wave provides a motivation for classifying RDCs as Pressure Gain Combustion (PGC) devices.

Other metrics of detonation performance are centered on the percentage of fuel detonated by the passing wave. This can be considered a detonation-specific combustion efficiency, where ideally, 100% of the input fuel is consumed by the detonation wave. In real applications, large fractions of the fuel may be consumed ahead of the detonation wave or pass through the CJ plane without contributing to the heat release process within the detonation region.[25, 26]

Although the following detonation loss metrics arise from the particular application, they are still worth referencing with respect to the deviation from ideal. These include lateral relief, friction or other momentum losses, and heat transfer within the detonation region. Detonation models, such as the CJ or ZND methodology, assume adiabatic, one-dimensional, frictionless boundary conditions across the entire detonation waves; however, the boundary conditions in real applications may violate these assumptions. We will explore these factors later in Chapter 2. We now turn our attention to RDC-specific performance metrics.

The typical performance metric associated with RDCs is thrust (and specific impulse), frequently used for any air-breathing application. This can also include the pressure gain metric as defined in Equation 1.18,

$$PG = \frac{P_{t,8}}{P_{t,3}} - 1 \tag{1.18}$$

and the Equivalent Available Pressure (EAP) metric from Kaemming and Paxson, which are determined from the thrust produced by the device as measured in an experimental setting.[27] In Equation 1.18, $P_{t,8}$ is the total pressure at the RDC exit plane, and $P_{t,3}$ is the total plenum pressure before the RDC detonation channel.

EAP represents an equivalent total pressure at the RDC exit, providing the same measured thrust as an equivalent steady flow device. The metric allows for capturing a pressure gain across the device based on its thrust production to relate the thrust to a steady combustion device. EAP is frequently used in place of $P_{t,8}$ in the pressure gain equation. The goal of any device categorized as a pressure gain combustor is that the pressure gain metric is positive.

The following metrics that are useful for studying RDC devices center around the performance of the RDC inlet. Specifically, the fraction of the inlet that is blocked by the detonation wave and the pressure ratio across the inlet. As one might expect, these terms are intertwined, but both are useful in determining overall RDC performance. Because of the high-pressure region within the detonation wave, there exists a high probability that this region of the inlet is blocked to forward-flowing reactants. In some cases, it will produce a backflow of product gases. Inlet blockage is a key metric for studying the impacts of the detonation wave on the RDC inlet, which drives (and is driven) by the inlet pressure ratio.

The inlet pressure ratio, defined in Equation 1.19, relates the static pressure in the RDC channel to the total plenum pressure:

$$\Delta P_{inj} = \frac{P_{ch}}{P_0} \tag{1.19}$$

where P_{ch} is the static channel pressure in the RDC and P_0 is the RDC plenum pressure. A higher value means that the channel and plenum are at similar pressures, whereas a low value means the inlet is at a much lower pressure relative to the plenum, also referred to as a more "stiff" injector. This metric is directly tied to the overall RDC pressure gain metric.[28]

To provide additional clarity, Figure 1.8 shows a breakdown of key loss metrics associated with detonation and RDC performance. When colored, other than gray, the blocks in Figure 1.8 show metrics that are linked between the detonation and the RDC cycle. For example, the lateral relief metric associated with detonation performance is directly linked to the inlet performance of the RDC; simultaneously, the RDC flowpath configuration allows/modulates the lateral relief that the detonation wave experiences. It is important to distinguish between the two, as the detonation performance metrics and losses are not indicative of the RDC performance or losses. For this reason, this research will examine each separately, with detonation-specific performance and loss mechanisms discussed in Chapter 2 and RDC-specific performance and loss mechanisms discussed in Chapter 3.

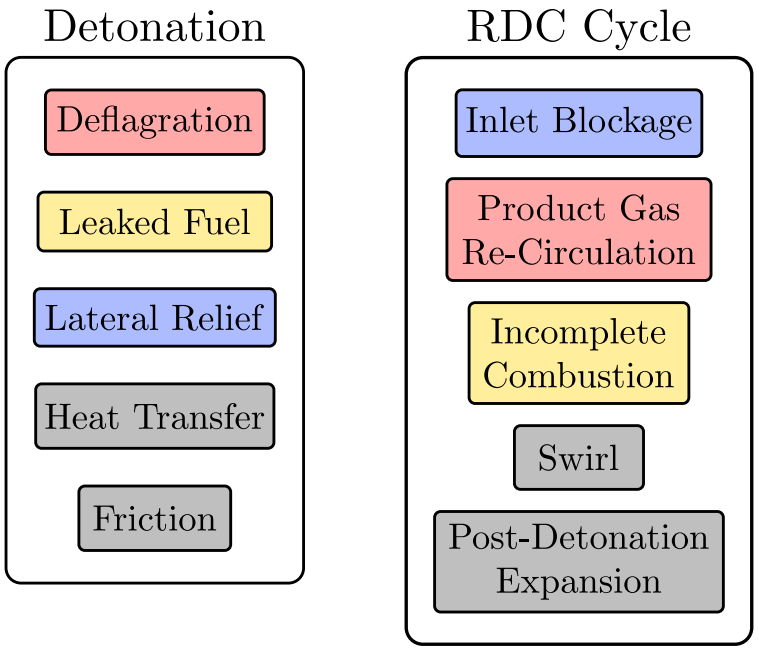


Figure 1.8: Chart distinguishing differences in detonation and RDC cycle loss mechanisms.

1.4 Reduced Order Modeling of Detonation-Based Cycles

Before we discuss the performance and loss mechanisms for both detonation waves and RDC devices, we will review the aspects and examples of reduced order models (ROM) used to study detonation waves and RDC devices as a whole. Reduced order loss models are beneficial in characterizing where potential losses occur within a RDC, which may lead to decreased performance versus an ideal analysis. These models hope to capture key physical processes within the cycle, which offer explanations of measured performance results while also assisting with the design and operability of new and existing RDC hardware.

In general, the modeling of RDC devices can scale from simple sub-models of the device to capture performance associated with those specific regions to full reduced order cycle models and, finally, to full computation fluid dynamics (CFD) models of RDCs. Figure 1.9 shows the trade-space in which these models reside, along with experimentation. The left subplot shows the trade-offs between the amount of data that can be collected versus the fidelity of the model. Here, fidelity refers to a perceived accuracy versus what is physically happening. Experimental testing undoubtedly provides the ”real” results; however, certain information contained within the experiment cannot be accurately or readily measured. CFD delivers what would be considered a high-fidelity model, with a large amount of data available for analysis. Reduced order models provide data availability that falls between experimental and CFD but is likely the lowest in fidelity.

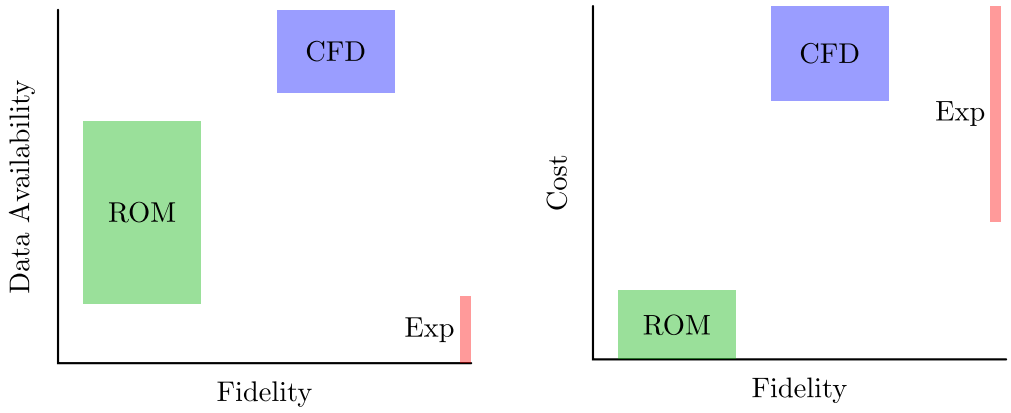


Figure 1.9: RDC Model Trade-space.

The other side of this argument is the cost required to obtain the data, shown in the right subplot of Figure 1.9. This cost metric can be measured as an actual price, such as the expenses required to set up an experimental facility or attain diagnostic equipment. The cost metric includes computational expenses like the physical computer/server, energy requirements, and the time required to solve the model. This subplot shows the niche where reduced order models provide an excellent modeling option. While perceived to be more accurate, experimentation and CFD require a significant cost, whereas reduced order models are simple enough to be run on a commercially available laptop CPU. For this reason, reduced order models are more suited to Monte Carlo based analysis methods, which require numerous model evaluations to construct a predicted output. Section 1.5 provides an example of a Monte Carlo based method used throughout this research, that is applied to estimate unknown parameters within a given model.

ROMs also provide the ability to create sub-models for processes that are known or thought to exist within the cycle of interest. An excellent analogy for CFD is the wall modeling in turbulent flows. In ROMs, instead of directly capturing the physical process at the cost of computational hours, a closure model is applied to capture enough of the physics or be sufficiently tuned to provide a relatively accurate simulation of the actual processes. Throughout this thesis, multiple loss processes inherent to both detonation waves and RDCs will be examined using smaller, loss-specific models. With this framework, including these sub-models into a full RDC cycle model becomes much more trivial. To summarize, the benefits/requirements of ROMs can be simplified down to:

1. Able to run on a commercially available CPU
2. Reasonable evaluation times to conduct Monte Carlo based studies
3. Provide reasonably accurate results when compared to experimental datasets

4. Allow for the addition of sub-models better suited to capture certain metrics of interest

Of particular interest for this study were the following reduced order RDC cycle models: the RDC Cycle Model from Kaemming et al.[29], the RDC Blowdown Model from Paxson[30] and the 2-D Method of Characteristic (MOC) RDC Cycle Model from Fievisohn[31]. Kaemming et al. published a state-based reduced order thermodynamic RDC model that separated the flow path into four distinct regions, each with different combustion processes.[29] These regions were paths that traveled solely through the detonation wave, paths that deflagrate before passing through the oblique shock, paths that detonated before passing through the oblique shock, and a mixed combination of the last two paths. The model also included inlet and exhaust flow sub-models to capture the complex interactions between the detonation wave and the plenum and exhaust. Lastly, their model also included additional loss mechanisms, such as exhaust flow distortion and lateral relief of the detonation wave. The model was then used to estimate the effects of each loss mechanism on the RDC-based cycle and compare it with a standard ramjet cycle. Their model predicted significant losses associated with overall engine dynamics, diodicity of the injector, exhaust distortion, and combustion efficiency.

The RDC Blowdown Model from Paxson was originally developed for rocket-style RDC devices but can be used to evaluate RDC cycle performance for air-breathing devices. This model uses a blowdown analogy from a PDC to generate an equivalent RDC cycle. It was shown to produce an accurate estimate of performance when compared to a 2-D CFD simulation, and can be used to properly size a RDC sub-system based on the requirements from a larger application.[30]

Finally, the 2-D MOC Model from Fievisohn features a complete method of characteristic solution for the RDC channel flow.[31] This model implements an inlet sub-model, which does not include backflowing product gases, used to initialize the flow path. It iterates on the flowpath's characteristic network to match a prescribed plenum total pressure and ambient exit pressure. It also included the ability to specify a variety of detonation sub-models, a key benefit of the reduced order model framework.

To provide additional motivation for this work, Figure 1.10 shows the same trade-space presented in Figure 1.9, but now specifically focusing on these ROMs, a simple state-based model also developed in this research, and the target regime for a new RDC cycle model. The left subplot again shows the trade-off between the data availability and the perceived fidelity of the model, where the models essentially become sorted by their complexity to implement, and the fidelity directly influences the data availability in capturing the processes within a RDC cycle. For this research, the cycle model targets a similar data availability that is provided by the RDC Cycle model from Kaemming et al.; however, it is also preferable to reduce the complexity of the model to save on computational cost.

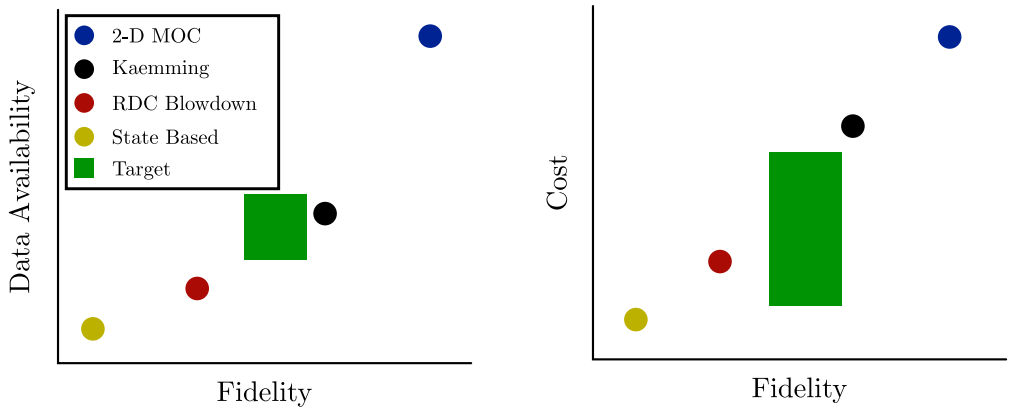


Figure 1.10: Reduced Order RDC Model Trade-space Example.

For the cost subplot, the model cost also scales directly with the complexity of each model. This subplot also shows the target region for the computational cost for the new cycle model, where the cost target is set based on the requirement for Monte Carlo based analysis processes. This cost metric is achieved through various methods, including the reduction in complexity with simplifying assumptions, selection of a proper coding language for the model, and optimizations revolving around model computational speed and convergence tolerance. All of these will be discussed in more detail in Chapter 4

1.5 Loss Parameter Estimation with Markov Chain Monte Carlo

This section will discuss the methods used in this research to estimate losses given a set of experimental data. The losses and their required experimental measurements were model-specific; however, the methodology for calculating them relied on Markov Chain Monte Carlo (MCMC). MCMC is a method for estimating the probability density function (PDF) of any unknown distribution, provided one can sample from that distribution. This technique offers a more efficient process for estimating PDFs relative to simple Monte Carlo by relying on a simple "hack" in Bayesian analysis.[32]

Bayes theorem, shown in Equation 1.20, provides a mathematical framework for how one should update their beliefs given a new set of information.

$$\mathcal{P}(\Theta|\mathrm{D}) = \frac{\mathcal{P}(\mathrm{D}|\Theta)\mathcal{P}(\Theta)}{\mathcal{P}(\mathrm{D})} \tag{1.20}$$

where $\Theta = [\theta_0 \dots \theta_i]$ is a set of the parameters of interest, D is the measured data, $\mathcal{P}(\mathrm{D}|\Theta)$ is the

likelihood of the measured data based on the given parameter set, $\mathcal{P}(\Theta)$ is the prior distribution, or the prior belief, of the parameters, and $\mathcal{P}(\mathrm{D})$ is the evidence or the probability distribution of all of the data. Typically, the evidence term is difficult, if not impossible, to calculate because one can rarely know the entirety of this distribution.

The genius of MCMC is in the way it evaluates the evidence term algorithmically. To better understand, we first must introduce the process for the Metropolis-Hastings method shown in Algorithm 1.[33, 34]

Algorithm 1 Metropolis-Hastings MCMC

Require: Initial State Vector $\Theta = [\theta_0 \dots \theta_i]$, Some Function $f(\Theta) = \mathcal{P}(\Theta|\mathrm{D})$

1: Initialize at a point in the state space, $\Theta^k = \Theta^0$
2: Propose a new sample in the state space, $\Theta^{k+1} \sim \mathcal{N}(\Theta^k, \mathrm{C})$
3: Evaluate function, f, at Θ^k and Θ^{k+1}
4: Compute acceptance ratio, $a(\Theta^k, \Theta^{k+1}) = min\left(1, \frac{f(\Theta^{k+1})}{f(\Theta^k)}\right)$
5: Draw random sample from a uniform distribution, $u \sim \mathcal{U}[0, 1]$
6: **if** $u \leq a$ **then**
7: Accept new sample, Θ^{k+1}, and move to new location
8: **else**
9: Reject Θ^{k+1} and re-propose new $\Theta^{k+1} \sim \mathcal{N}(\Theta^k, \mathrm{C})$
10: **end if**
11: Increment k
12: Repeat 2-11 for a given number of samples

If we provide the function f as the posterior distribution, we can relate it to Equation 1.20:

$$f(\Theta) = \mathcal{P}(\Theta|D) = \frac{\mathcal{P}(\mathrm{D}|\Theta)\mathcal{P}(\Theta)}{\mathcal{P}(\mathrm{D})} \tag{1.21}$$

MCMC fixes the data between samples; therefore, the evidence term cancels out during the evaluation of the acceptance ratio in step 4 of Algorithm 1. Because of this, we can simplify our function f:

$$f(\Theta) = \mathcal{P}(\Theta|\mathrm{D}) \propto \mathcal{P}(\mathrm{D}|\Theta)\mathcal{P}(\Theta) \tag{1.22}$$

Now, we only require two distributions: the likelihood of the data given the parameters and the prior distribution of the parameters. The likelihood can be any function that relates the "goodness" of fit of the data and parameters. In most cases, as in this research effort, the likelihood function invokes some external model, $\mathrm{M}(\Theta)$, which outputs the same set of data used in the estimation

process. To evaluate the goodness-of-fit, it is typical to use a simple multivariate normal distribution. This allows for the form of the likelihood function used throughout the parameter estimation conducted in this research effort, shown in Equation 1.23.

$$\mathcal{P}(\mathrm{D}|\Theta) = \frac{1}{\sqrt{(2\pi)^{\mathrm{N}}|\Sigma|}} \exp\left(-\frac{1}{2}(\mathrm{D}-\mathrm{M}(\Theta))^{\mathrm{T}}\Sigma^{-1}(\mathrm{D}-\mathrm{M}(\Theta))\right) \tag{1.23}$$

, where $\mathrm{M}(\Theta)$ is the model of interest as a function of parameters Θ, D is the experimental measurements, and Σ, is the covariance matrix that takes into account the uncertainty of the measurements. Notably, the data, D, can be of any dimensionality and does not need to be the same size as the parameter set, Θ. The prior, $\mathcal{P}(\Theta)$, can be any distribution, and so long as this distribution contains the optimal parameter within its bounds, the MCMC method will find such a solution.

An example of the Metropolis-Hastings sampling process for a two-dimensional parameter space is shown in Figure 1.11. Figure 1.11 (a) shows the initial proposal process, where the proposal covariance matrix, C, is a bivariate normal of a given variance around the current location. In this step, X^1 was accepted, and the next proposal now emanates from X^1. Figure 1.11 (b) shows an example of rejecting a proposal and re-proposing from the same location, where the move from X^1 to X^2 was rejected, but the move from X^1 to X^3 was accepted. Finally, Figure 1.11 (c) shows the posterior distribution of accepted points after a given number of samples. The resulting points are distributed according to the actual posterior distribution, shown in red. The output samples from the MCMC process can then be used in other Monte Carlo based models, or statistics can be computed from them, such as the expected value and variance of the parameters set.

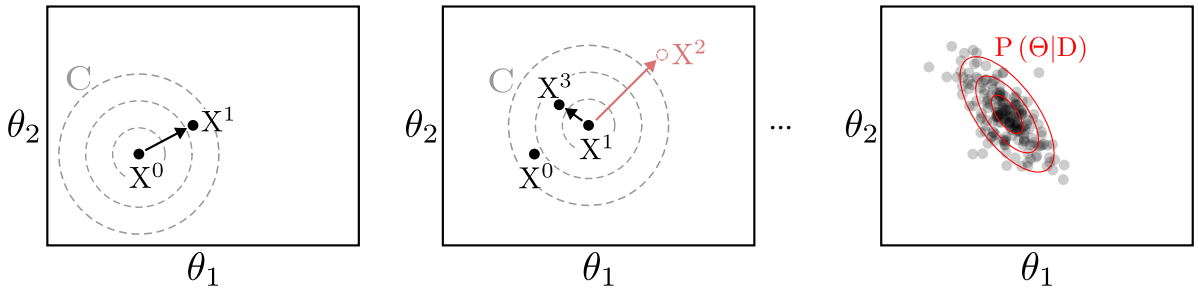


Figure 1.11: Example Markov Chain Monte Carlo Sampling.

With the final set of data points (shown as black dots in Figure 1.11 (c)), one can estimate the shape of the posterior distribution, generate random samples from the final set of points, or estimate the most likely parameter distribution in a learning process. The latter is done throughout this research; however, it is easy to conclude that once the parameter space has been learned sufficiently, one can sample this distribution in other external models.

There is one drawback to the Metropolis-Hastings MCMC algorithm. It starts with a fixed covariance matrix for the proposal distribution. It requires additional tuning to propose new points that are still within the distribution but without getting stuck in a high-probability location. An Adaptive Metropolis algorithm allows for adaptation of the proposal distribution as samples are generated, providing a much more efficient sampling algorithm than the Metropolis-Hastings MCMC method.[35] Delayed Rejection Adaptive Metropolis (DRAM) MCMC extends Adaptive Metropolis MCMC by continually adjusting the proposal covariance matrix based on the current samples in the distribution while also re-proposing a new point using a reduced magnitude covariance matrix if the initial proposal is rejected. The re-proposal process is then repeated until a sample is accepted, with the acceptance ratio calculated based on the recurrent formula provided by Haario et al.[36]. By doing this, the proposal distribution for new points auto-tunes to match the general shape of the distribution it tries to estimate while also delaying the rejection process at each point. This enables more efficient sampling compared to other Monte Carlo methods. The methodology for DRAM is shown in Algorithm 2.

Algorithm 2 Delayed Rejection Adaptive Metropolis MCMC

Require: Initial State Vector $\Theta = [\theta_0 \dots \theta_i]$, Some Function $f(\Theta) = \mathcal{P}(\Theta|\mathrm{D})$

1: Initialize at a point in the state space, $\Theta^k = \Theta^0$, and Proposal Covariance Matrix, $\mathrm{C}^k = \mathrm{C}^0$
2: Propose a new sample in the state space, $\Theta^{k+1} \sim \mathcal{N}(\Theta^k, \mathrm{C}^k)$
3: Evaluate function, f, at Θ^k and Θ^{k+1}
4: Compute acceptance ratio, $a(\Theta^k, \Theta^{k+1}) = min\left(1, \frac{f(\Theta^{k+1})}{f(\Theta^k)}\right)$
5: Draw random sample from a uniform distribution, $u \sim \mathcal{U}[0, 1]$
6: **if** $u \leq a$ **then**
7: Accept new sample, Θ^{k+1}, move to new location, update C^{k+1} based on Haario et al.[36]
8: **else**
9: Reject Θ^{k+1} and re-propose new $\Theta^{k+1} \sim \mathcal{N}(\Theta^k, s\mathrm{C}^k)$, where $s < 1$, go to Step 3
10: **end if**
11: Increment k
12: Repeat 2-11 for a given number of samples

Figure 1.12 shows an example of the DRAM process, where Figure 1.12 (a) shows the initial proposal process in which the proposed point is rejected. Figure 1.12 (b) shows the re-proposal process from a scaled-down covariance matrix. Figure 1.12 (c) shows the update process for the proposal covariance matrix for the next step. The process repeats for a given number of samples, and the resulting posterior distribution will match the results shown in Figure 1.11 (c), without the need for human-in-the-loop tuning, while also being more efficient computationally.

It is essential to recognize that the samples returned from MCMC represent random samples

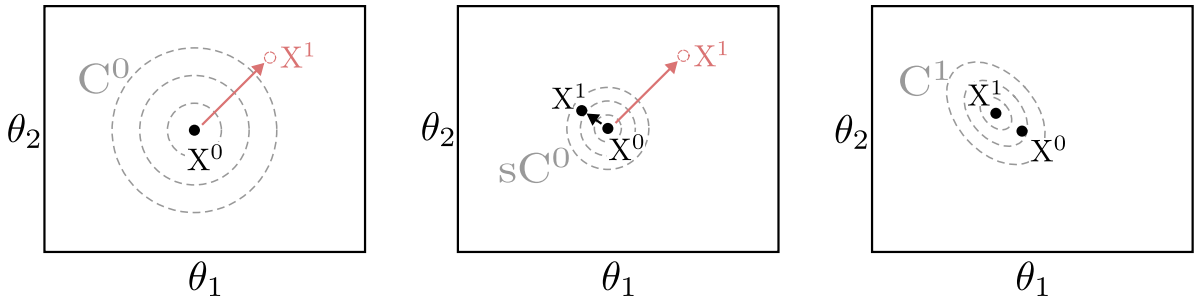


Figure 1.12: Example Delayed Rejection Adaptive Metropolis MCMC Sampling.

from the posterior distribution but not the exact posterior distribution. This is the trade-off in MCMC and using an exact update to Bayes theorem, which is not always possible analytically. In this project, the *Python* version of the MCMC package call *ParaMonte* was used for the sampling, post-processing, and initial figure generation.[37] This package allows for easy implementation of DRAM MCMC to any model. Also, it can take advantage of multiprocessing speed-ups without the need for a complete change to the analysis code.

Finally, trade-offs exist between using the Monte Carlo method in a given application and other options other than what has been discussed above. For example, the integration of simple functions can be calculated accurately using Monte Carlo sampling with a large enough number of samples. Still, it is much more efficient to use analytical integration if possible. A similar situation arises with MCMC with respect to optimization. Optimization is solving for the best possible answer to the question at hand; however, it returns a single value, and propagating uncertainty and measurement variance through the optimizer is difficult, if not impossible, for certain optimization schemes. MCMC, on the other hand, provides an estimate of the distribution of probable parameter values while also propagating measurement uncertainty and variance through the likelihood function in the Bayesian update. This property of MCMC parameter estimation is particularly well suited for analyzing RDC data sets, as there is typically high cycle-to-cycle variation in measured values.

1.6 Goals of this Research Effort

The initial goal of this research project includes identifying and quantifying the effect of multiple loss mechanisms. This consists of losses specific to the detonation wave, losses due to the applications of the detonation wave in a combustion system, and the relationship between the two. For each identified loss mechanism, a reduced order model will be constructed to examine the effects of that particular mechanism on the performance of the detonation wave or detonation-based sys-

tem. These models will also be helpful in the development of a full RDC cycle model, the final goal of this research effort.

The RDC cycle model is the culmination of the loss mechanism quantification and modeling, a deep study of the physical processes within the RDC cycle, and a modification (and hopefully improvement) over current state-of-the-art RDC cycle models. Aside from capturing the loss mechanisms, this model also seeks to be computationally efficient such that it can be used in Monte Carlo based analysis methods, as well as system-level models of air-breathing devices operating with a detonation-based combustion cycle. This sets a target model evaluation time of 100 ms, allowing 10 model evaluations per second.

Finally, this model seeks to provide physics-based closure models for many of the input parameters not typically known ahead of time. In doing so, the model would become fully closed and only require inputs such as operating conditions and device geometry. By relying on informed physics, the model methodology also seeks to eliminate curve fitting of historical data. This step may increase the model complexity but improves the fidelity of the model by capturing known physical processes in a reduced order. It also allows for additional flexibility when implementing future improvements to the model, as each sub-model will have a physical basis from which to start.

CHAPTER 2

Loss Mechanisms Specific to Detonation Waves

One must be careful not to associate detonation performance with the system-level performance of a device utilizing detonation combustion. For this reason, the two will be discussed in separate chapters, where this chapter focuses solely on loss mechanisms and performance metrics specifically related to the performance of the detonation wave. Along with discussing the existence of these loss mechanisms, this chapter also provides simple models to examine the effects of each loss on the detonation wave. Finally, the concluding remarks will give opinions on the most impactful loss mechanisms and offer potential remedies.

Before defining detonation performance and associated metric, one should review Table 2.1 for a list of state locations of interest within the detonation wave and the RDC cycle, the latter of which will be discussed fully in Chapter 3. This chapter will focus primarily on states $\textcircled{3_p}$-$\textcircled{3.3}$, which include the state just ahead of the detonation wave to a state just downstream of the post-detonation expansion that was introduced in Section 1.1.1.1.

Table 2.1: Description of States used in Detonation Cycle Analysis

State	Label	Description
Plenum	3	Plenum condition assuming premixed.
Post-Injector	$3'$	Inlet injection state after inlet pressure drop
Post-Parasitic Combustion	3_p	Pre-detonation state after parasitic combustion
von-Nuemann (VN)	3.1	Post-shock von-Nuemann condition accounting for leaked fuel
Chapman-Jouguet (CJ)	3.2	Post-detonation state accounting for leaked fuel
Post-Expansion	3.3	Post-detonation state after isentropic expansion accounting for detonation work
Post-Commensal	3.4	Post-expansion state after equilibration at a post-expansion pressure accounting for non-commensal fraction and commensal combustion pressure fraction
RDC Exhaust	4	State from which work may be extracted

2.1 Detonation Performance Metrics

To characterize the quality of a detonation wave, a few key performance metrics have been defined and used widely in the detonation field. The main two metrics of interest discussed in the literature are the wave speed and the wave pressure ratio, D and PR, respectively. Typically, these measured values are normalized by their ideal CJ value to ascertain how close to ideal is the detonation wave of interest, $\frac{D}{D_{\mathrm{CJ}}}$, and $\frac{PR}{PR_{\mathrm{CJ}}}$. Both of these metrics provide a methodology for comparing measured data to the ideal, one-dimensional CJ detonation properties.

Another metric that will be defined in more detail later is the fraction of fuel consumed in the detonation wave. Think of this term as a marker of combustion efficiency for the detonation wave itself. Ideally, 100% of the input fuel gets processed by the detonation wave; however, literature has shown this is not always the case in the RDC application.[1, 25, 2, 26] This metric will directly affect the prior two performance metrics negatively, with more details on this exact relationship between the metrics discussed in Section 2.3.1.

2.2 Description of Loss Mechanisms

This section discusses the known loss mechanisms affecting the performance of detonation waves. These losses include mechanisms that affect detonation waves in general and mechanisms that affect detonation waves due to their application in a system. For example, detonation waves are typically modeled as adiabatic combustion events; however, when using a detonation wave in a combustion device like PDCs/RDCs, the gases transfer some energy to the walls where the detonation resides. While the application causes this effect, it will still be included because of its impact on the performance of the detonation wave.

2.2.1 Incomplete Combustion, Deflagration Losses and Product Re-circulation

Incomplete combustion and deflagration losses within the detonation wave will lead to a decrease in performance, and are lumped together due to the similarity of the two on the performance of the detonation wave. In the same sense, product gas re-circulation, also known as exhaust gas re-circulation (EGR), causes a similar effect to deflagrative pre-burning. In all cases, one should seek to reduce or eliminate all three of these losses to improve detonation performance.

A deflagration loss is defined by combustion occurring outside of the detonation region. This includes deflagration before the detonation wave, termed parasitic combustion, and deflagration occurring after the wave has passed but without contributing to the heat release in the detonation region, termed commensal combustion. The latter occurs when a fraction of the fuel passes through the detonation wave unburnt. Because this unburnt fuel does not necessarily need to combust to degrade the detonation wave performance, another metric that captures this effect is defined as the leaked fuel fraction. Both of these losses reduce the fraction of fuel consumed within the detonation region, and both parasitic and commensal deflagration have been seen experimentally using OH* chemiluminescence by Chacon et al. and Feleo et al.[1, 25, 2, 26]

Chacon et al. imaged a racetrack style RDC, and Figure 2.1 shows a snapshot from a run, where the detonation wave is the brightest feature and is moving from the right to the left. A significant portion of deflagration combustion happens ahead of the detonation, and even large regions of combustion happen after the wave, suggesting that not all of the fuel was consumed by the detonation. These features break the standard assumptions in the theoretic models, leading to significant reductions in detonation wave performance.

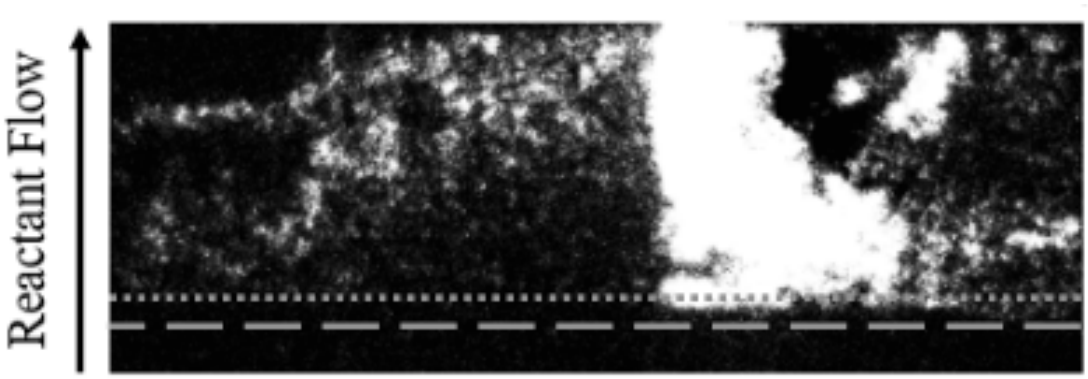


Figure 2.1: Example of pre- and post-detonation deflagrative combustion. Detonation moving right to left, image color altered from [1].

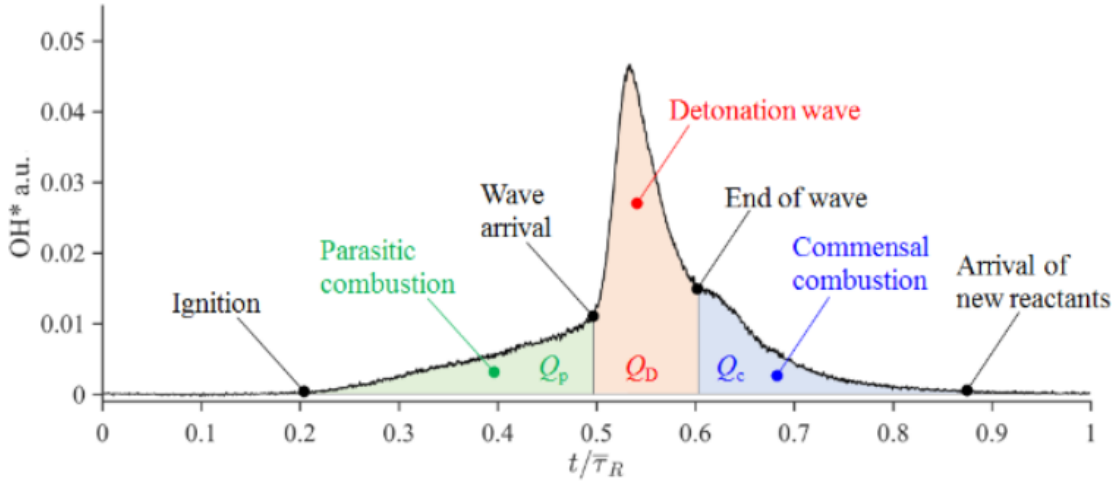


Figure 2.2: Phase Averaged OH* Chemiluminescence Measurement through a Photo-Multiplier Tube. Binned according to location with respect to detonation wave.[2].

When averaging the effects of the deflagration on the wave in a standard cylindrical RDC, Feleo et al. also showed that a significant portion of the heat release during a detonation cycle can occur before and after the detonation wave itself (see Figure 2.2).[2, 26] Initial estimates showed that nearly a quarter of the heat release occurred before the detonation wave arrived, which increases the speed of sound in this gas and drastically reduces the incoming Mach number of the wave. This would lead to a much lower pressure rise across the detonation and lower propagation speeds of the wave. To make matters worse, nearly a quarter of the heat release occurs behind the detonation wave, suggesting that a large portion of the fuel is not combusted by the wave. This means a large portion of the fuel is along for the ride through the detonation, not contributing to the heat release needed to propagate the wave. With these studies being conducted on different types of RDCs, it

also suggests that these effects may be RDC geometry agnostic.

The effects of deflagrative combustion losses on the performance of the detonation wave have been examined in detail by Strakey et al., Burr and Paulson, Barnouin et al., and Raman et al.[38, 39, 40, 41] Strakey et al. examined a variety of losses that reduced RDC performance. These losses included unburnt fuel and parasitic combustion ahead of the detonation wave. Their results provided insight into the effects of these losses on the performance of the detonation wave, showing a reduction in wave speed and detonation pressure ratio.

Burr and Paulson [39] examine the deflagration losses within a modeled RDC cycle, specifically looking at three loss parameters: parasitic combustion, leaked fuel, and commensal combustion post-detonation. This methodology also provided a means to estimate combustion efficiency for the cycle and compare it to RDC performance. They used specific impulse as the performance metric of interest and showed the effects of each loss parameter on the thrust production of the modeled cycle. Their results suggest that parasitic combustion was the most detrimental loss parameter, given that all of the fuel was consumed within the cycle. They also noted the lack of a strong correlation between the modeled specific impulse and the wave speed, suggesting the separation of detonation performance from RDC performance when comparing RDCs to conventional combustion devices.

Barnouin et al. isolated the effects of the deflagration loss terms on the performance of a detonation wave. For consistency with the model used in the research, these deflagration losses will be defined by parasitic deflagration fraction, ξ_{P}, and leaked fuel fraction, ξ_{L}. This effort showed a reduction in the wave speed and pressure ratio with increased loss fractions, where the parasitic combustion ahead of the wave had the most drastic effect. This was due to the combination of the reduction in fuel available for the detonation wave and the increased sound speed in the pre-detonation gases. This led to a much weaker shock wave, in terms of Mach number, resulting in a much lower pressure rise across the shock front.

Raman et al. conducted a review of numerous computational, reduced modeling, and experimental research on the effects of non-ideal processes on the performance of a detonation wave and RDC performance in general. They discuss multiple non-idealities observed in prior research, including product re-circulation and deflagrative combustion within the RDC cycle. With either effect, the performance of the detonation wave (in terms of wave speed and pressure ratio) was reduced. This meta-analysis eventually extended the non-ideal deflagration to RDC performance (thrust in this case). Similarly to the effects on detonation performance, increases in deflagrative combustion reduced the performance of RDC thrust production. Finally, they included an analysis of the impact of deflagration on the operability of the RDC, where, in certain situations, the deflagrative combustion can actually improve the operability of RDCs at the expense of some performance.

Stechmann et al. examined the effects of product re-circulation on the operation of RDCs. [42] Their results looked at the mixing of fuel and oxidizer as the flow paths are modulated by the pressure wave of the previous detonation wave. Along with the study on mixing, Stechmann et al. also focused their efforts on the effects of product re-circulation, specifically examining the auto-ignition times of the mixed reactants relative to the operation times of the RDC. At certain levels of product re-circulation and reactant temperature, they noticed that the auto-ignition time for the reactants dropped below the cycle time of the detonation wave. This leads to the potential for deflagrative combustion occurring in the reactants before the detonation wave arrives.

In a related effort, Fievisohn et al. examined the effect of product re-circulation on the performance of RDCs. They identified timescale thresholds for pockets of auto-ignition of the fresh reactant in a given RDC wave cycle.[43, 44]

Kaemming et al.[29, 4] examined the effects of multiple loss mechanisms, including tracking particle path lines through an ideal detonation wave cycle. A small fraction of particles do not pass through the detonation portion of the wave, therefore reducing the performance of the RDC with respect to ideal conditions. Strakey et al. conducted a computational study that provided insight into multiple loss mechanisms within an RDC.[38] This research showed the adverse effects of pre-detonation wave combustion on the performance of an RDC and examined the portion of unburnt fuel during RDC operation. This prior research led to the development of the Deflagrative Loss Model discussed in Section 2.3.1 of this research.

2.2.2 Lateral Relief

Lateral relief describes another loss mechanism that affects the detonation performance, but only due to the change in boundary conditions relative to the CJ analysis. In certain applications, such as RDCs, the detonation is bounded by a compressible gas layer instead of a solid wall. This allows the high-pressure detonation region to expand laterally into the gas boundary. This has been modeled using an inert boundary on one side of a planar detonation wave, where the consequence of lateral relief is a diminished post-detonation pressure and wave speed relative to the ideal, purely one-dimensional detonation.[11, 3, 45] This has also been studied in the RDC application by Kaemming et al. with similar results.[29]

The following sections will provide additional insight into the effects of lateral relief by modeling the process as simple area change within the detonation region. This will first be analyzed in a framework akin to the CJ analysis, then will be extended to the ZND methodology for further insights. Due to the configuration of RDCs, it is unlikely that this term can ever be eliminated, so it is crucial to understand its impact and how one might mitigate this process without causing any detrimental effects from other known losses.

2.2.2.1 From the CJ Perspective

We start with the one-dimensional conservation equations, like the CJ analysis (see Section 1.1.1); however, now we will not neglect the area terms. Equations 2.1-2.3 are the one-dimensional conservation equations with area change.

$$\rho_1 u_1 A_1 = \rho_2 u_2 A_2 \tag{2.1}$$

$$P_1 A_1 + \rho_1 u_1^2 A_1 = P_2 A_2 + \rho_2 u_2^2 A_2 \tag{2.2}$$

$$h_1 + \frac{u_1^2}{2} = h_2 + \frac{u_2^2}{2} \tag{2.3}$$

In the same manner as the constant area CJ derivation, we solve for the upstream velocity in Equation 2.1:

$$u_1 = \frac{\rho_2 u_2 A_2}{\rho_1 A_1} = \frac{\rho_2 u_2}{\rho_1} AR \tag{2.4}$$

where, $AR = \frac{A_2}{A_1}$ is the area ratio between state 2 and 1. Next, we divide equation 2.2 by A_1 to get it in terms of the area ratio, AR.

$$P_1 + \rho_1 u_1^2 = P_2 AR + \rho_2 u_2^2 AR \tag{2.5}$$

Now we will substitute Equation 2.4 into Equation 2.5 and simplify where possible, resulting in:

$$P_1 + \frac{\rho_2^2 u_2^2}{\rho_1} AR^2 = P_2 AR + \rho_2 u_2^2 AR \tag{2.6}$$

This results in the final equation for the momentum conservation with the mass conservation included in the definition. We similarly substitute Equation 2.4 into the energy equation, Equation 2.3, which results in:

$$h_1 + \frac{\rho_2^2 u_2^2}{2\rho_1^2} AR^2 = h_2 + \frac{u_2^2}{2} \tag{2.7}$$

We are now left with the final two conservation equations, Equation 2.6 and Equation 2.7. Instead of developing a solver for this system of equations, we will iterate on the temperature and density of state 2 with the *fsolve* function provided by the *Scipy* package in *Python*. With a proper initial guess, this solver performs in a similar, if not faster, method as the CEA implementation of the CJ detonation solver.[46]

The steps for this solver are described in Algorithm 3, where an initial guess of the post-detonation pressure and density, $P_{\mathrm{CJ}} = 15P_1$ and $\rho_{\mathrm{CJ}} = 1.5\rho_1$ are used to provide a close approximation. With these initial guesses, an estimated post-detonation enthalpy can be calculated with Equation 2.8. This enthalpy is used within the Gas Object to calculate the equilibrium composition at P_{CJ} and h_{CJ}. After this step, the residuals for the momentum equation and energy equation are calculated with Equation 2.9 and Equation 2.10, respectively. This iteration continues until convergence in the momentum and energy residual are below a certain tolerance. Finally, the state at the CJ plane with area change is returned for further processing.

$$h_{\mathrm{CJ}} = h_1 + 11.25R_u\frac{T_1}{MW_1} \tag{2.8}$$

$$R_{mom} = P_1 + \frac{\rho_2^2 u_2^2}{\rho_1}AR^2 - P_2AR - \rho_2 u_2^2 AR \tag{2.9}$$

$$R_{en} = h_1 + \frac{\rho_2^2 u_2^2}{2\rho_1^2}AR^2 - h_2 - \frac{u_2^2}{2} \tag{2.10}$$

Algorithm 3 CJ solver with Area Change

Require: Gas Object at Initial Conditions and Iteration Tolerance, tol
  Guess Pressure Ratio of 15 & Density Ratio of 1.5
  Estimate Final Enthalpy ▷ *Equation 2.8*
  while $|R_{mom}| > tol$ & $|R_{en}| > tol$ **do**
    Equilibrate Gas Object at Constant Enthalpy and Pressure
    Calculate Residuals R_{mom} & R_{en} ▷ *Equation 2.9 & Equation 2.10*
  end while
  return Gas Object at CJ Condition at A_2

2.2.2.2 From the ZND Perspective

Figure 2.3 shows an example of a non-zero distance between the shock and the CJ plane. In this example problem, the upper portion of the detonation wave is bound by an inert gas layer. Because of this, an area change can occur between the shock and the CJ plane. Depending on the rate of change of the area within the combustion region, the combustion process can be quenched as the gases expand. At certain area change rates, the CJ condition may not even be reached. This process is sure to occur within an RDC cycle as the downstream portion of the detonation wave is bounded by the post-combustion products, while the upstream portion is bounded by the oxidizer gases.

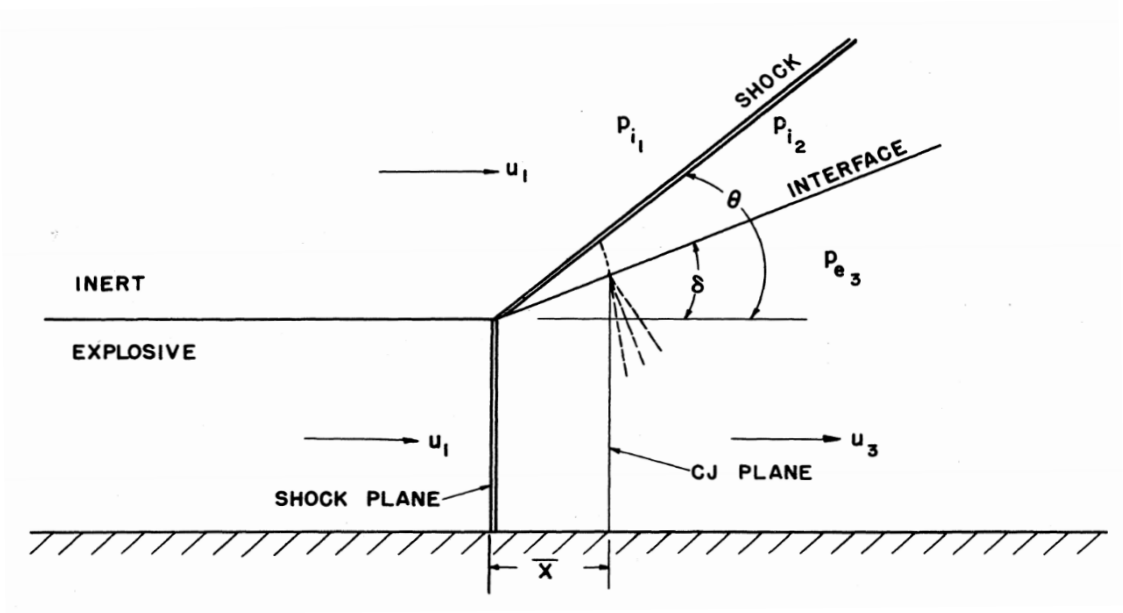


Figure 2.3: Example of Area Change Between Shock Wave and CJ Plane.[3]

The CJ analysis with area change makes one key assumption that may be violated when transitioning to the one-dimensional ZND analysis. This assumption revolves around the fact that the CJ solver assumes equilibrium combustion compositions at the CJ plane. For this reason, we turn our attention to the effects of area change on the detonation as modeled by the ZND method. The following system of equations were adapted from the Shock and Detonation Toolbox provided by CalTech, and are used to solve steady reacting flow with area changes.[47]

$$\frac{d\rho}{dx} = \frac{-\rho}{\eta}\left[\dot{\sigma}' - \frac{M^2}{A}\frac{dA}{dx}\right] \tag{2.11}$$

$$\frac{dP}{dx} = \frac{-\rho U^2}{\eta}\left[\dot{\sigma}' - \frac{1}{A}\frac{dA}{dx}\right] \tag{2.12}$$

$$\frac{dU}{dx} = \frac{U}{\eta}\left[\dot{\sigma}' - \frac{1}{A}\frac{dA}{dx}\right] \tag{2.13}$$

where, $\eta = 1 - M^2$ and $\dot{\sigma}' = \sum_k \sigma_k \frac{dY_k}{dx}$. The latter term is spacial thermicity, which is not in a format that is conducive to solving the ZND profile. The integration process uses *Cantera* to get net species production rates, which are in the time domain, and calculates the thermicity value as a temporal derivative. We can relate the form specified in the equations above to the standard, time-based species rate and thermicity calculation by applying the chain rule:

$$\frac{d()}{dx} = \frac{d()}{dt}\frac{dt}{dx} = \frac{d()}{dt}\frac{1}{U} \tag{2.14}$$

Applying Equation 2.14 to Equation 2.37, we are left with the familiar definition of the time rate of change in density from Section 1.1.2:

$$\frac{d\rho}{dt} = \frac{-\rho\dot{\sigma}}{\eta} \tag{2.15}$$

When applying this process to the thermicity calculation, we will apply the chain rule to each species' net production rates:

$$\frac{dY_k}{dx} = \frac{dY_k}{dt}\frac{dt}{dx} = \frac{dY_k}{dt}\frac{1}{U} \tag{2.16}$$

After substitution, the spacial thermicity term can be written as:

$$\dot{\sigma}' = \sum_k \frac{\sigma_k}{U}\frac{dY_k}{dt} = \frac{\dot{\sigma}}{U} \tag{2.17}$$

2.2.3 Heat Transfer

As mentioned earlier in this Chapter, heat transfer within any application based on detonation combustion is sure to exist.[48, 49, 50, 51] The post-detonation state is at elevated temperatures over that of a conventional combustor operating at the same conditions, and in the case of PDCs and RDCs, the boundary condition for the detonation wave is typically a metal wall with no form of boundary layer or film cooling. This allows for incredibly high heat transfer coefficients that heat the walls of the device but also remove energy from the flow. The latter of which is the focus of this section. Both the CJ and ZND analyses assume adiabatic flow; however, we will relax this assumption and examine how removing heat from the detonation wave affects its performance.

2.2.3.1 From the CJ Perspective

From the CJ analysis, we will keep the mass and momentum equations (Equations 1.1 and 1.2) as described in Section 1.1.1. However, we will update the energy equation to account for heat removal from the system. This is shown below in Equation 2.18.

$$h_1 + \frac{u_1^2}{2} + q_{out} = h_2 + \frac{u_2^2}{2} \tag{2.18}$$

where q_{out} represents the bulk heat removal rate from the detonation wave as it progresses to the CJ conditions. A slightly modified version of the solver in Algorithm 3 was used to calculate the CJ condition given an initial reactant mixture and a specified heat removed.

2.2.3.2 From the ZND Perspective

Because the ZND analysis includes the integration over a distance (or time) when solving, we get a temperature profile along the combustion wave post-shock (see Figure 1.5). This allows for the specification of a heat transfer coefficient between the detonation product gases and the wall as a function of the gas temperature. With this, we can capture the effects of removing heat from the combustion region on the performance of the detonation wave. More details on this process and the model used to study it are provided in Section 2.3.3

$$\frac{d\rho}{dx} = \frac{-\rho}{\eta}\left[\dot{\sigma}' + \frac{G}{\rho a_f^2}\frac{\bar{q}}{U}\right] \tag{2.19}$$

$$\frac{dP}{dx} = \frac{-\rho U^2}{\eta}\left[\dot{\sigma}' + \frac{G}{\rho a_f^2}\frac{\bar{q}}{U}\right] \tag{2.20}$$

$$\frac{dU}{dx} = \frac{U}{\eta}\left[\dot{\sigma}' + \frac{G}{\rho a_f^2}\frac{\bar{q}}{U}\right] \tag{2.21}$$

where G is the Gruneisen coefficient, and a_f is the frozen speed of sound for the gas, and the heat flux parameter, $\bar{q}$, is the heat transfer rate.

2.2.4 Friction

This section will discuss the frictional forces that may be acting on the detonation wave. Though we will specifically examine friction, any mechanism that results in a loss in momentum through the detonation process will produce similar effects. This is especially true in the first section, which discusses momentum losses, as modeled by friction, from the perspective of the CJ analysis.

2.2.4.1 From the CJ Perspective

Frictional forces require a distance of action, but the CJ model framework uses an infinitesimally thin detonation wave approximation. Hence, we will capture the effect of friction and other momentum loss mechanisms in a single momentum loss variable, F. Equation 2.22 shows an updated momentum conservation equation with the new momentum loss term.

$$P_1 + \frac{\rho_2^2 u_2^2}{\rho_1} AR^2 = P_2 AR + \rho_2 u_2^2 AR - F \tag{2.22}$$

where F represents a total momentum loss from frictional forces and the like. Using this form of the momentum equation changes the residual calculation in the momentum equation but is solved in the same method presented in Algorithm 3.

2.2.4.2 From the ZND Perspective

Using the ZND methodology, friction can be captured directly as we now have the appropriate length scale. Another benefit of the ZND framework is that it includes a time/space dependency. The density rate change rate can now be written as:

$$\frac{d\rho}{dx} = \frac{-\rho}{\eta}\left[\dot{\sigma}'\frac{G}{\rho a_f^2} + (G+1)\bar{\tau}\right] \tag{2.23}$$

The pressure rate of change is now:

$$\frac{dP}{dx} = \frac{-\rho U^2}{\eta}\left[\dot{\sigma}' + \frac{G}{\rho a_f^2}(G + \frac{1}{M^2})\bar{\tau}\right] \tag{2.24}$$

Finally, the velocity rate of change is:

$$\frac{dU}{dx} = \frac{U}{\eta}\left[\dot{\sigma}' + \frac{G}{\rho a_f^2}(G+1)\bar{\tau}\right] \tag{2.25}$$

where friction, $\bar{\tau}$, is written in terms of coefficient of friction:

$$\bar{\tau} = \frac{4}{D}\tau_w = \frac{2}{t_w}\frac{1}{2}\rho U^2 c_f = \frac{1}{t_w}\rho U^2 c_f \tag{2.26}$$

where c_f is the coefficient of friction. Because friction acts in the lab frame and we are solving the ZND profile in the wave frame, we need to perform a Galilean transform of the velocity term used in Equation 2.26:

$$\bar{\tau} = \frac{1}{t_w}\rho U'^2 c_f \tag{2.27}$$

where $U' = D_{\mathrm{CJ}} - U$, where U is in the wave frame and U' is in the lab frame.

2.3 Description of Detonation Performance Models

From Section 1.1, the assumptions typically employed to calculate the fundamental characteristic of a propagating detonation wave assume complete combustion, a one-dimensional flow field of constant cross-sectional area, and adiabatic, inviscid flow. Historical examples have proven that this is not the case in practical detonation-based systems (see Section 2.2). In this section, we will depart from these assumptions and examine the models used to quantify the impacts on the performance of detonation from these effects.

2.3.1 Deflagration Loss Model

The first set of losses will examine the assumption of complete combustion of the fuel provided within the detonation wave. These effects will be captured with a reduced order model termed the Deflagration Loss Model. Section 2.2.1 has provided numerous examples of incomplete combustion within the detonation wave and deflagrative combustion occurring outside of the detonation wave. For modeling purposes, we will reduce these effects into two losses: parasitic deflagrative combustion occurring before the detonation wave and fuel leaking through the detonation wave. These terms were used to define two loss parameters of interest: the parasitic fuel fraction, ξ_{P}, and the leaked fuel fraction, ξ_{L}.

The parasitic fuel fraction represents a molar fraction of the initial fuel that is allowed to combust in a deflagrative manner ahead of the detonation wave. Modeling of the parasitic deflagrative combustion assumes a constant-pressure combustion of the specified fuel fraction at the pre-detonation state (temperature, pressure, enthalpy). By using the fuel fraction representation of the loss parameter, we are left with a parameter that varies between zero and one, where one represents a complete deflagration event. We can also relate this parameter in terms of the mole fraction of the fuel consumed parasitically, with respect to the initial moles of the fuel with Equation 2.28:

$$\chi_{\mathrm{P}} = \xi_{\mathrm{P}} \tag{2.28}$$

The definition of the leaked fuel fraction, ξ_{L}, is slightly more complicated. This fraction represents the fractions of moles of fuel remaining after the parasitic combustion that leak through the detonation wave. It was defined in this manner to also vary between zero and one, where one represents all of the remaining fuel that leaks through the detonation. It can also be referenced to the initial number of moles of fuel with Equation 2.29:

$$\chi_{\mathrm{L}} = \xi_{\mathrm{L}}(1 - \xi_{\mathrm{P}}) \tag{2.29}$$

Finally, we can define the mole fraction of fuel consumed by the detonation wave, again normalized by the initial number of moles of fuel, with Equation 2.30

$$\chi_{\mathrm{D}} = (1 - \xi_{\mathrm{P}})(1 - \xi_{\mathrm{L}}) \tag{2.30}$$

where:

$$\chi_{\mathrm{P}} + \chi_{\mathrm{D}} + \chi_{\mathrm{L}} = 1 \tag{2.31}$$

Figure 2.4 provides an illustration of the breakdown in the three different processes, including an intermediate state, χ_{NP}, which simply refers to the moles of the fuel that are not consumed by

parasitic combustion.

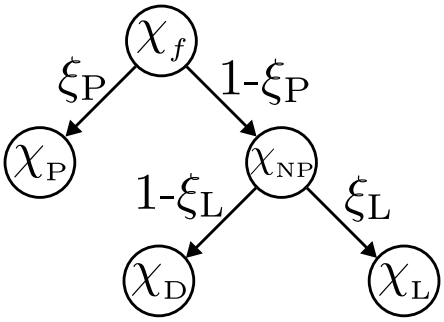


Figure 2.4: Fuel partitioning for the Deflagration Loss Model. χ_{NP} represents an intermediate state of non-parasitic fuel, which is further broken down into detonation and leaked, χ_D and χ_L respectively.

The goal of this model is to predict the effects of deflagration losses on both the detonation wave. Figure 2.5 shows a schematic of the model. It should be noted that from the perspective of the model, there is no difference in fuel being consumed in parasitic combustion or product gas re-circulation from the previous wave. This means that the parasitic fraction accounts for a combination of the two but cannot distinguish between them. In the same vein, the model is insensitive to what happens to the fuel that leaks through the detonation wave. This means the detonation only cares that the fuel leaked through the detonation, not if/how much was combusted after the wave. Both of these facts make comparison to measured data difficult because the measurements used for comparison are based on imaging of where combustion is seen and cannot account for product gas re-circulation or non-combusted leaked fuel.

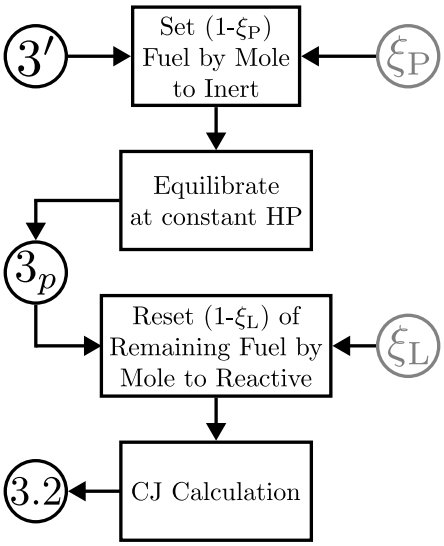


Figure 2.5: Deflagration Loss Model.

A custom implementation of the *Cantera* Solution object, implemented in *Python*, was used to calculate thermodynamic properties at each state, and the CJ solver uses a custom implementation following the methodology provided by Gordon et al.[18, 46] The process for setting the fuel to and from an inert species was done through the addition of non-reactive surrogates of each fuel in question to the reaction mechanism. Each surrogate mimics the thermodynamic properties of its base species without including it in any reaction paths. This allows for a simple method of calculating each step without having to manage multiple gas streams. The pseudo-code of the solution process is shown in Algorithm 4.

Algorithm 4 Deflagration Loss Model

Require: $\xi_{\mathrm{P}}, \xi_{\mathrm{L}} \in [0, 1]$

1: Initialize gas object at pre-detonation initial state: $(3')$
2: Set (1-ξ_{P}) fuel (by mole) to inert
3: Equilibrate at constant pressure/enthalpy, mimicking deflagration burning ahead of the wave: (3_p)
4: Reset (1-ξ_{L}) of remaining fuel (by mole) to reactive
5: CJ calculation, while accounting for detonative heat release lost by leaked fuel: (3.2)

From this model, two maps of detonation performance metrics of interest were created. Figure 2.6 shows an example of the detonation wave speed, relative to the ideal wave speed, plotted in black against the fraction of parasitic combustion on the x-axis and the fraction of leaked fuel on the y-axis. This map shows a similar drop in the speed of the detonation as either of these parameters are increased. In dashed gray, the pressure ratio across the detonation, relative to the ideal pressure ratio, is plotted against the same deflagration loss fractions. This map shows a much steeper drop-off in pressure ratio as the parasitic combustion increases but is less affected by a similar increase in the leaked fuel fraction. This is due to the fact that the pressure ratio across the detonation scales with the detonation Mach number, relative to the pre-shock state. Parasitic combustion has the effect of decreasing the detonation wave speed while simultaneously increasing the speed of sound of the pre-detonation gases.

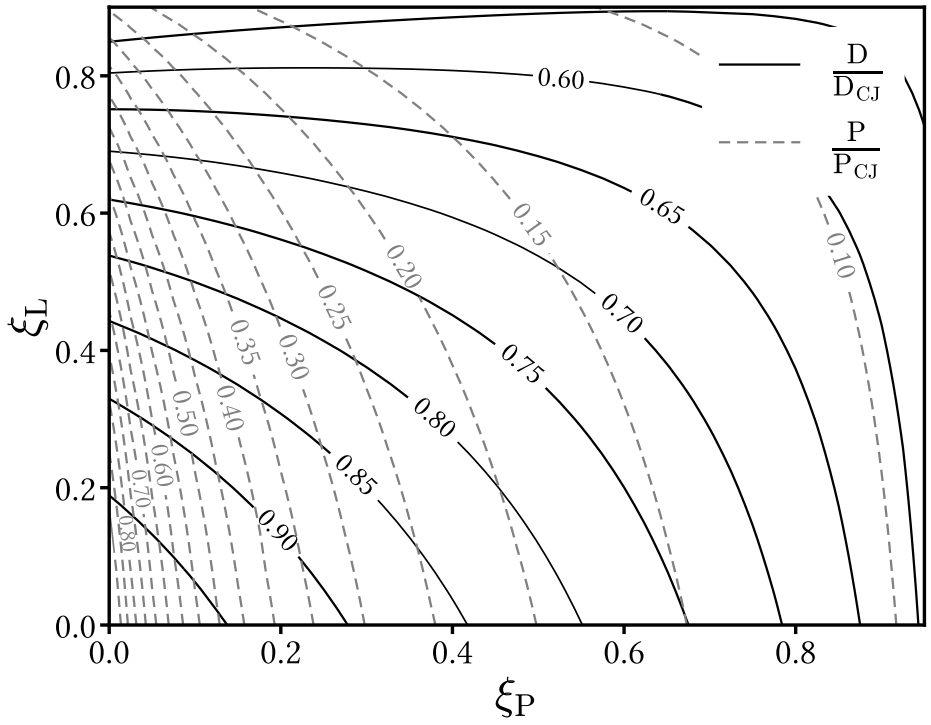


Figure 2.6: Maps of wave speed and pressure ratio relative to ideal values as a function of parasitic combustion fraction and leaked combustion fraction. Hydrogen/air at $\phi = 0.6$.

2.3.2 Non-Ideal CJ Analysis

The next set of potential loss parameters of interest revolves around the core assumptions of the standard CJ analysis. First, we will discuss the role of area change within the detonation region. This phenomenon is likely of no concern in the detonation tube or PDC context, where the walls bound the combustion event; however, this is not the case in RDCs. Because the boundaries of the detonation in a RDC consist of two layers of inert gases rather than solid walls, there exists the potential for area changes to occur within the combustion region due to what is colloquially termed lateral relief. This, in effect, reduces the potential pressure increase across the wave since the detonation wave, in the quasi-one-dimensional sense, due to the expansion occurring as the area increases.

Next, the effects of heat loss to the wall can be accounted for by assuming a known, or specified, heat removal rate, q_{out}. This term provides a simple method for capturing the heat transferred to the cooler walls from the detonation combustion region during operation, and in practice, would vary based on the combustion gas temperature, the wall temperature, and a heat transfer coefficient.

Finally, although likely a small contributor, frictional forces within the detonation region can produce a loss in momentum. This can be studied by specifying a term that accounts for any

momentum losses, F, including friction.

The effects of lateral relief, heat transfer, and frictional losses within the detonation region were modeled using Algorithm 5, with the momentum residual modified to account for frictional losses (Equation 2.32) and the energy residual equation modified to account for heat transfer, as shown in Equation 2.33

$$R_{mom} = P_1 + \frac{\rho_2^2 u_2^2}{\rho_1} AR^2 - P_2 AR - \rho_2 u_2^2 AR + F \tag{2.32}$$

$$R_{en} = h_1 + \frac{\rho_2^2 u_2^2}{2\rho_1^2} AR^2 - h_2 - \frac{u_2^2}{2} - q_{out} \tag{2.33}$$

Algorithm 5 Non-Ideal CJ Model

Require: AR, Q, F, Gas Object at Initial Conditions and Iteration Tolerance, tol

Guess Pressure Ratio of 15 & Density Ratio of 1.5

Estimate Final Enthalpy ▷ *Equation 2.8*

while $|R_{mom}| > tol$ & $|R_{en}| > tol$ **do**

Equilibrate Gas Object at Constant Enthalpy and Pressure

Calculate Residuals R_{mom} & R_{en} ▷ *Equation 2.32 & Equation 2.33*

end while

return Gas Object at CJ Condition at A_2

2.3.3 Non-Ideal ZND Model

The following system of equations were used to solve steady reacting flow with area changes, heat transfer, and friction. They contain all of the losses discussed in Section 2.4 and are written using the temporal thermicity value.

$$\frac{d\rho}{dx} = \frac{-\rho}{\eta}\left[\frac{\dot{\sigma}}{U} + \frac{G}{\rho a_f^2}\left[\frac{\bar{q}}{U} + (G+1)\bar{\tau}\right] - \frac{M^2}{A}\frac{dA}{dx}\right] \tag{2.34}$$

$$\frac{dP}{dx} = \frac{-\rho U^2}{\eta}\left[\frac{\dot{\sigma}}{U} + \frac{G}{\rho a_f^2}\left[\frac{\bar{q}}{U} + (G + \frac{1}{M^2})\bar{\tau}\right] - \frac{1}{A}\frac{dA}{dx}\right] \tag{2.35}$$

$$\frac{dU}{dx} = \frac{U}{\eta}\left[\frac{\dot{\sigma}}{U} + \frac{G}{\rho a_f^2}\left[\frac{\bar{q}}{U} + (G+1)\bar{\tau}\right] - \frac{1}{A}\frac{dA}{dx}\right] \tag{2.36}$$

where, in the instance of an adiabatic, inviscid, constant area solution, these equations reduce back to the rate-change equations used in the standard ZND solution method. For example, Equation

2.34 reduces to the spatial version of Equation 1.16 from Section 1.1.2:

$$\frac{d\rho}{dx} = \frac{-\rho\dot{\sigma}}{\eta U} \tag{2.37}$$

In the solver, the area change rate, $\frac{dA}{dx}$, is specified directly as a function of x and can be calculated ahead of time based on geometric constraints. Likewise, the coefficients, c_h and c_f, are also specified as input parameters to the model. The model integrates over a specified length, l, or until the sonic condition is reached. Algorithm 10 shows the pseudo-code for the non-ideal ZND model.

Algorithm 6 Non-Ideal ZND Solver

Require: $\frac{dA}{dx}, c_f, c_h$, Initial conditions: P_0, T_0, Gas Object, final integration length, l

Calculate CJ wave speed: D_{CJ}
Use wave speed to calculate post-shock state: $\mathbf{Y}_0$ ▷ *Equation 2.38*
while $M_i < 1.0$ & $x_i < l$ **do**
    Set gas object to new state, $\mathbf{Y}_i$
    Calculate re-used terms: $[\frac{1}{\rho_i}, U_i^2, a_i^2, M_i^2, \eta_i]$
    if $c_h \neq 0 \mid c_f \neq 0$ **then**
        Calculate $G_i, \bar{q}_i, \bar{\tau}_i$
    end if
    Calculate net production rates: $\left(\frac{dY_k}{dx}\right)_i$ ▷ *Equation 2.16*
    Calculate spacial thermicity: $\dot{\sigma}'$ ▷ *Equation 2.17*
    Calculate rate changes: $\frac{d\rho}{dx}, \frac{dP}{dx}, \frac{dU}{dx}$: ▷ *Equations 2.34 - 2.36*
    Integrator calculates next state: $\mathbf{Y}_{i+1}$
end while

The state vector for the non-ideal ZND model is shown in Equation 2.38:

$$\mathbf{Y} = [P, \rho, Y_0 \dots Y_k] \tag{2.38}$$

where the states include the pressure, density, and mass fraction of each species. This model framework allows for the study of a detonation wave from the ZND perspective but now accounts for loss mechanisms along the detonation profile.

2.4 Results

The following section provides the results from studying the non-ideal detonation models from Section 2.3. First, an evaluation of the effects of deflagration-based losses will be provided using

the Deflagration Loss Model. Next, the non-ideal CJ and ZND models will be examined to study the losses present within the detonation region. This section will conclude with a study combining both of the latter two models, followed by a review of the detonation characteristics as they apply to "weak" detonation waves.

2.4.1 Deflagration Loss Model

The following table provides a list of experimental run conditions and measurements used to evaluate the Deflagration Loss Model. These will be discussed later in this section.

Case	$\dot{m}$, [g/s]	ϕ	U, [m/s]	U/U_{CJ}, [%]	σ_U, [%]	$\frac{P_2}{P_1}$	$\left(\frac{P_2}{P_1}\right)_{CJ}$	σ_P, [%]
654	400	1.1	1564	78.4	3.07	2.3	15.1	6.07
656	130	0.9	1379	71.9	1.05	2.0	13.0	2.73
657	130	1.2	1463	72.1	3.2	1.9	12.5	3.01
658	130	1.4	1520	73.3	7.55	1.9	12.4	3.09
659	160	0.7	1325	74.9	1.19	2.3	17.3	3.4
660	150	0.9	1412	73.1	2.39	2.1	13.8	3.58
661	150	1.1	1469	72.9	4.03	2.1	13.3	3.66
662	150	1.4	1464	70.9	5.99	1.9	12.3	2.95
663	180	0.7	1343	76.0	1.25	2.5	18.9	4.83
664	180	0.9	1451	75.5	1.31	2.2	14.3	3.62
665	180	1.1	1508	75.2	3.76	2.1	13.4	3.76
666	180	1.3	1508	73.3	3.15	2.1	13.7	3.42
667	230	0.6	1387	79.2	1.28	2.1	16.1	5.02
668	230	0.9	1480	77.9	2.62	2.3	15.3	4.69
669	230	1.0	1536	77.6	2.6	2.3	14.8	5.03
670	290	0.6	1403	81.3	1.3	2.2	16.9	6.08
672	280	0.8	1465	77.6	3.02	2.4	16.1	5.34
675	290	1.0	1548	78.3	1.77	2.5	16.0	5.94
677	400	0.6	1399	82.3	1.59	3.4	26.4	8.7
681	400	1.0	1539	78.5	3.83	2.2	14.5	5.5
682	390	1.1	1542	76.9	4.37	2.7	17.4	7.9
686	230	1.3	1562	76.4	1.33	3.0	19.3	8.38

Table 2.2: Summary of experimental operating conditions for select runs used to evaluate the Deflagration Loss Model.

We have already seen how parasitic combustion and leaked fuel affect the performance of a detonation wave in terms of the wave speed and pressure ratio (see Figure 2.6). We will now dive deeper into analyzing these effects on other detonation performance metrics, defining a representative "gain" of a detonation wave in the process. This "gain" metric examines the change in the

available energy at the CJ plane, (3.2), as a function of the two loss parameters, ξ_{P}, and ξ_{L}. These results are shown in Figure 2.7, where the "gain" is determined by the energy available at the CJ plane, shown in Equation 2.39.

$$G = h_{t,3.2} - h_{t,3'} \tag{2.39}$$

where the total enthalpy is defined as:

$$h_{t,i} = h_{s,i} + \frac{u_i^2}{2} \tag{2.40}$$

where the velocity, u_i, is referenced in the laboratory frame. In this case, it is assumed $u_{3'} = 0$ and $u_{3.2}$ is the induced velocity at the CJ plane, which is non-zero. The "gain" plotted in Figure 2.7 is normalized by the ideal "gain" calculated at ξ_{P}, ξ_{L}= 0. All results produced for Figure 2.7 were conducted with a stoichiometric, premixed hydrogen-air detonation operating at an initial pressure of 2 atm and an initial temperature of 300 K. It is clear that both deflagration loss parameters have a significant impact on the available energy at the CJ plane, which comes as no surprise based on the results shown in Figure 2.6.

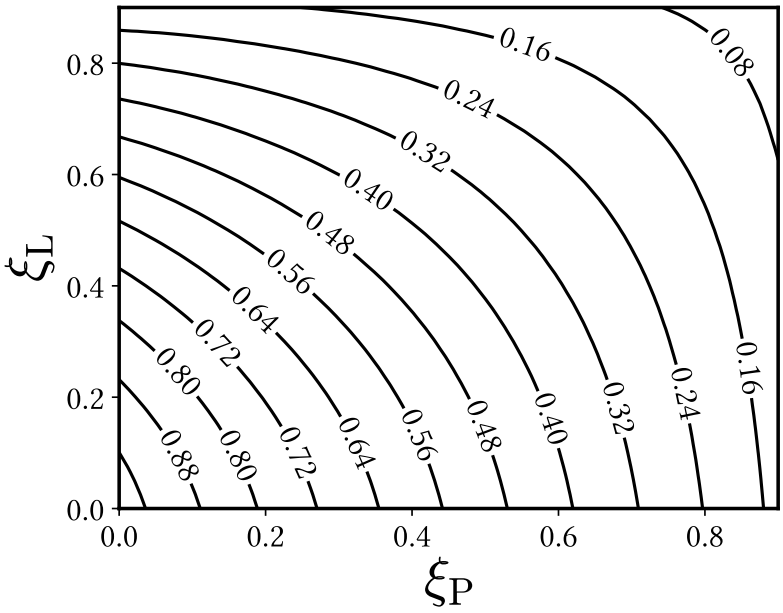


Figure 2.7: Gain, G, at (3.2) versus the deflagration loss parameters. Normalized by the ideal G at ξ_{P}, ξ_{L}= 0.

The contours of constant "gain" in Figure 2.7 appear to follow the contours of wave speed shown in black in Figure 2.6. Further analysis of the correlation coefficients between the "gain" and both the wave speed and pressure ratio showed a near-perfect correlation between the wave

speed and the "gain" as defined in this research, with a correlation coefficient of 0.96. The pressure ratio also had a relatively high correlation coefficient of 0.84. The main driver for the higher correlation in "gain" with the wave speed stems from the fact that higher wave speed inevitably produces a higher induced velocity at the CJ plane, $u_{3.2}$.

These results point to the need for reductions in the deflagration loss parameters if one wishes to improve the performance of the detonation wave, with a particular focus on improving the wave speed. However, the question remains whether the "gain" metric defined in Equation 2.39 is also critical to the performance of the RDC. More discussion on this front will be included in the next chapter, but now we will focus solely on the detonation wave performance.

Figure 2.8 shows a normalized "gain" at the CJ plane as a function of the fraction of fuel consumed in the detonation wave, χ_{D}, defined by Equation 2.30. The solid lines represent constant leaked fraction, ξ_{L}, which ranges from $[0, 0.9]$ in steps of 0.15, where the right most solid line represents $\xi_{\mathrm{L}} = 0.0$ and the left most solid line represents $\xi_{\mathrm{L}} = 0.9$. The dashed lines represent a constant parasitic fraction, ξ_{P}, with the same range and steps where the top dashed line represents $\xi_{\mathrm{P}} = 0.0$ and the bottom dashed line represents $\xi_{\mathrm{P}} = 0.9$. From this plot, it is clear that there is a high correlation between the "gain" and the fraction of fuel consumed in the detonation wave, where the correlation coefficient was calculated to be 0.99. As the detonation fraction approaches 0, so does the "gain" metric, which means that the model is approaching the ideal deflagration device with the same initial conditions.

An interesting takeaway from Figure 2.8 is the fact that at a high detonation fraction, in the range of 0.8, the "gain" can vary between approximately 0.7 and 0.9 of the ideal detonation "gain". This means that it is of increased importance where the heat addition is distributed. For example, parasitic combustion appears to be much worse than leaked fuel of the same magnitude for both the "gain" and the detonation pressure ratio. This result means that despite consuming a large fraction of fuel in the detonation if the rest of the fuel was consumed in a parasitic manner, the performance of the wave is worse than if that fuel had simply leaked through without contributing to the detonation heat release, a similar result as the detonation pressure ratio.

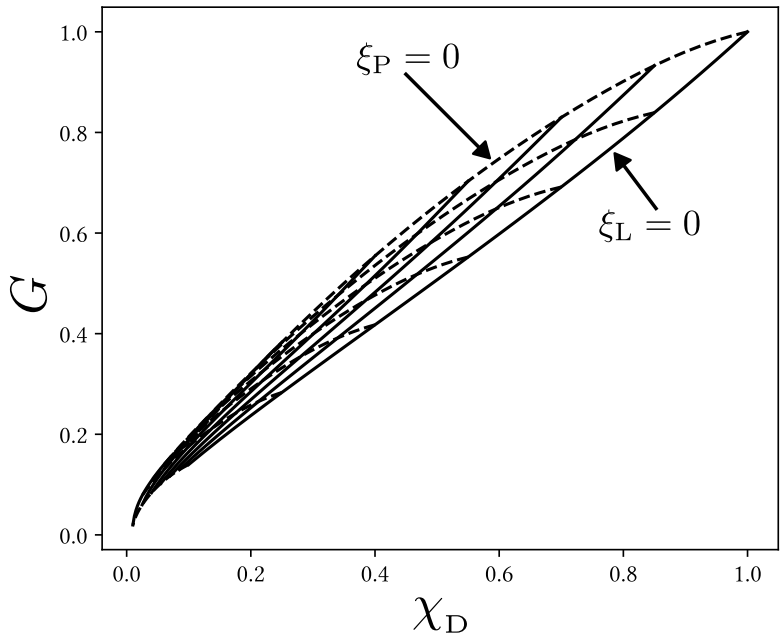


Figure 2.8: Gain, G, versus detonation fraction, χ_D. Solid lines of constant leaked fraction, ξ_L, and dashed lines of constant parasitic fraction, ξ_P. Line separated by loss parameter increments of $0.15 \in [0, 0.9]$.

To better capture the sensitivity of the "gain" metric across the detonation wave to each loss parameter in the Deflagration Loss model, a global sensitivity analysis was conducted using the Sobol Indices method.[52] Table 2.3 shows the total and first-order sensitivities, along with their associated 95% confidence interval. To generate these results, 6144 sets of loss parameters were drawn according to the Sobol methodology, and the secondary effects were neglected as the null value was contained within all 95% confidence intervals. As expected from the examination of Figure 2.6, the "gain" metric is most influenced by the parasitic fraction. This is likely due to the pre-heating of the pre-detonation reactants, which essentially reduces the Mach number, and therefore strength, of the detonation wave. The leaked fraction is also detrimental to the "gain"; however, it was slightly less impactful, echoing the sentiment that the parasitic combustion appears to be most impactful on detonation performance.

Sobol Index	ξ_P	ϵ_{ξ_P}	ξ_L	ϵ_{ξ_L}
S_T	0.64	0.06	0.44	0.05
S_1	0.56	0.07	0.36	0.06

Table 2.3: Sobol's Sensitivity Indices for the loss parameters in the Deflagration Loss Model.

Using the deflagration loss model and the experimental dataset shown in Table 2.2, the defla-

gration loss parameters were estimated for each case, and the following results of these values were compared to other measurements of interest. The loss parameters were estimated using the measured wave speed and pressure ratio (from high-speed pressure transducers within the RDC channel) and the MCMC framework discussed in Section 1.5. With the parasitic and leaked fuel fractions, the detonation fraction, χ_{D}, can be calculated with Equation 2.30. Figure 2.9 shows a visualization of the correlation between the estimated detonation performance and the bulk flow conditions within an experimental RDC.

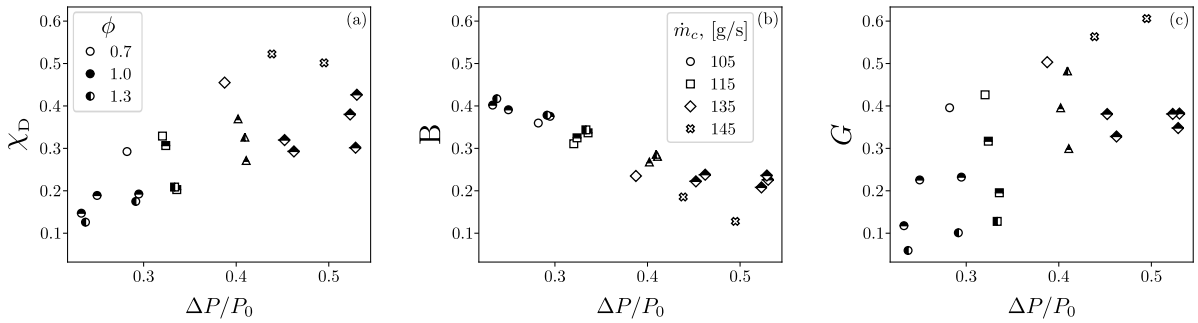


Figure 2.9: Estimated detonation fraction (a) and estimated "gain" at the CJ plane (b) versus inlet pressure drop normalized by plenum total pressure.

Figure 2.9 (a) shows the estimated detonation fraction as a function of the inlet pressure drop normalized by the plenum total pressure. This subplot is binned into three different equivalence ratio bands of lean, stoichiometric, and rich (shown by the marker fill style), as well as binning the corrected mass flow rate by marker shape, where the corrected mass flow rate is normalized by the total pressure and temperature of the plenum, Equation 2.41. At a given equivalence ratio, the detonation fraction appears to correlate directly with the inlet pressure drop, which is also a function of the corrected mass flow rate. At a certain mass flow rate/inlet pressure drop, this trend levels off. This is especially evident in the lean and stoichiometric conditions, unfilled and filled marker styles, respectively.

$$\dot{m}_{\mathrm{c}} = \dot{m}\frac{\sqrt{\frac{T_t}{T_{ref}}}}{\frac{P_t}{P_{ref}}} \tag{2.41}$$

Figure 2.9 (b) shows the calculated blockage fraction, B, as defined by Feleo et al., versus the inlet pressure drop.[5] As the inlet pressure drop increases, the inlet blockage decreases, indicating a "stiffer" inlet results in a much lower blockage fraction. This intuitively makes sense based on the argument that a higher inlet pressure drop would better resist the blockage caused by the detonation wave. The blockage fraction itself is not a great indicator of performance, so a comparison with the "gain" across the detonation wave is required. One note on the blockage fraction is that a lower

inlet blockage (stiffer inlet) results in a decrease in the parasitic combustion fraction. This indicates that a trade-off must be made between the inlet pressure drop and the parasitic combustion fraction to maximize performance across the cycle.

Figure 2.9 (c) shows the "gain" as a function of the normalized inlet pressure drop, where the gain is normalized by the ideal gain with no deflagration losses. This plot shows that the "gain" increases with increased inlet pressure drop and under leaner conditions. At a given mass flow rate, a leaner condition results in less pressure drop across the inlet due to the lower blockage from the fuel injection. This subplot raises the issue that in an experimental setting, the "gain" across the detonation wave is also inversely correlated with the inlet pressure drop. This result will be discussed again with the full State to State model in a later section, but in general, it is concerning, as the performance of the device is highly correlated with inlet pressure losses.[4]

To reduce inlet pressure losses, a lower corrected mass flow is required. However, based on experimental data, a lower corrected mass flow results in a higher blockage fraction and could even lead to inlet backflow. Based on these results, there appears to be an inverse correlation between the detonation performance and the inlet pressure drop. It should be noted that these performance estimates are focused strictly on the performance of the detonation wave; a more robust model is required to estimate the RDC performance.

The final aspect of this analysis includes a short discussion of detonation-based combustion as a lower entropy combustion method over deflagration. We will start with the knowledge that in the Deflagration Loss Model, the fuel is distributed to certain reaction bins, which means that the heat release is distributed in a certain way to produce a final CJ state, (3.2). A direct connection can be drawn to the work in RAM jet combustors, where tailoring the heat release distribution can result in an optimal performing device. We will examine a similar concept with the deflagration loss model by calculating the detonation work, as defined in Section 1.1.1.1, and the entropy production at the CJ state, (3.2), normalized by the entropy produced in an ideal deflagration combustor at the same initial conditions. These results are shown in Figure 2.10, where the heat release distribution is shown with contours of constant parasitic fraction in dashed lines and constant leaked fraction in solid lines.

$$q_{in} = \mathrm{LHV}_f Y_f \tag{2.42}$$

From this plot, we can glean two key takeaways: the entropy production decreases as a function of the leaked fuel fraction and the trade-off between entropy production and detonation work. First, the reason for the decreasing entropy production with increased leaked fuel fraction is solely due to the fact that the deflagration loss model does not provide a combustion path for leaked fuel, as it stops at the CJ plane. In this vein, the entropy production is minimized by not burning any of the fuel; therefore, it is argued that the entropy production across the detonation, on its own, may not

be a valid performance metric for characterizing RDC performance.

Moving to the second observation, at a given leaked fuel fraction, a reduction in entropy production (due to lower parasitic fraction) comes at the cost of a higher detonation work term; therefore, a reduction in available energy for work extraction. The issue arises that a higher performing detonation, in terms of wave speed and detonation fuel fraction, requires a higher detonation work to be sustained.

Another result of this analysis is the discussion surrounding performance evaluations in RDCs, where one can work to improve the detonation wave performance (wave speed, detonation fraction, pressure ratio, etc.); however, the benefits of RDC devices are only realized based on the work extraction that occurs downstream of the detonation wave and other cycle performance metrics like inlet pressure drop. This leads to the need for a RDC performance modeling framework based on the full RDC cycle, such as the State to State model discussed in Algorithm 9 in Section 3.3.1, to evaluate the actual benefits of RDCs and where shortcomings may be corrected to improve performance.

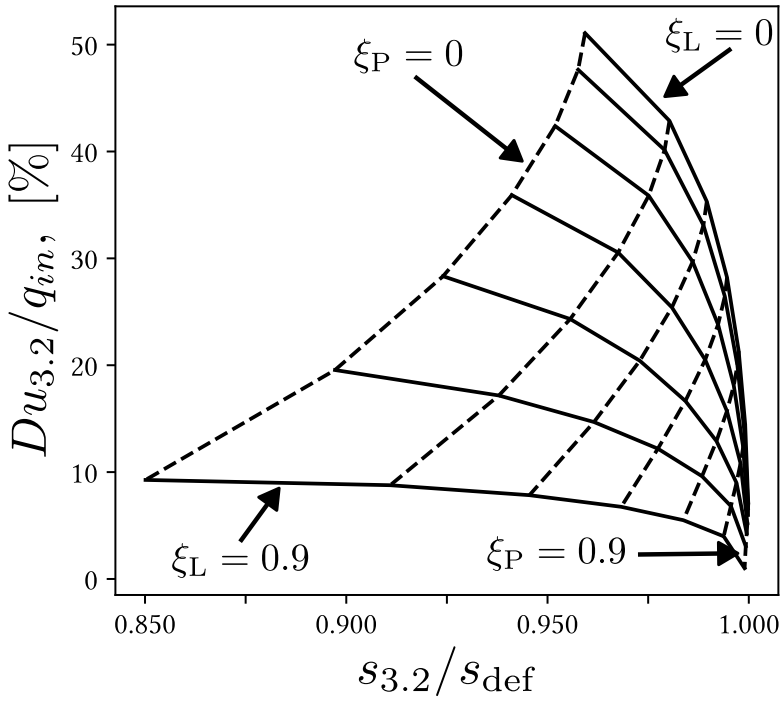


Figure 2.10: Detonation work required (normalized by heat addition) versus entropy creation as a function of heat release partitioning. Entropy normalized by ideal deflagration at the same initial conditions. Dashes lines of constant parasitic fraction, ξ_{P}, and solid lines of constant leaked fraction, ξ_{L}.

2.4.1.1 MCMC Results

The methods outlined in Section 1.5 were applied to the set of runs given in Table 2.2. For each run, the average value of wave speed and pressure ratio, along with their associated measurement variance, were used to learn the deflagration loss fractions by the MCMC sampling process. Table 2.4 shows the final results of the MCMC sampler, where the two listed deflagration fractions are the expected value (mean) from the posterior distribution. Finally, the effective sample size is shown as an indicator of sampler efficiency.

Run Number	ξ_P	ξ_L	ESS
654	0.48	0.18	23074
656	0.65	0.46	20974
657	0.68	0.54	27805
658	0.72	0.55	27847
659	0.55	0.35	36750
660	0.63	0.48	36086
662	0.67	0.47	41768
663	0.53	0.30	14062
664	0.58	0.27	20924
665	0.61	0.48	44535
666	0.64	0.42	32459
667	0.50	0.09	45244
668	0.52	0.23	21483
669	0.54	0.41	33182
670	0.45	0.05	15181
672	0.53	0.32	17999
675	0.52	0.39	32004
677	0.34	0.24	30767
681	0.50	0.24	28232
682	0.48	0.42	28090
686	0.32	0.52	25508

Table 2.4: MCMC Sampling Results for the Deflagration Loss Model.

Figure 2.11 shows an example of the posterior distribution of a selected run, with the marginal distributions for each parameter on the upper and right plots and a kernel density estimate of the posterior distribution piloted on the model parameter map in the center. The posterior seems to trace out a path along a constant wave speed line but spanning a wide range of pressure ratios. This is indicative of the measurement uncertainty and variance in both of these measurements. As the model is less certain of the pressure ratio, or more cycle-to-cycle variation occurs in the pressure ratio measurement, the posterior is also less certain in the parameters it samples. This is a key example of error propagation through MCMC parameter estimation and the usefulness of MCMC in general.

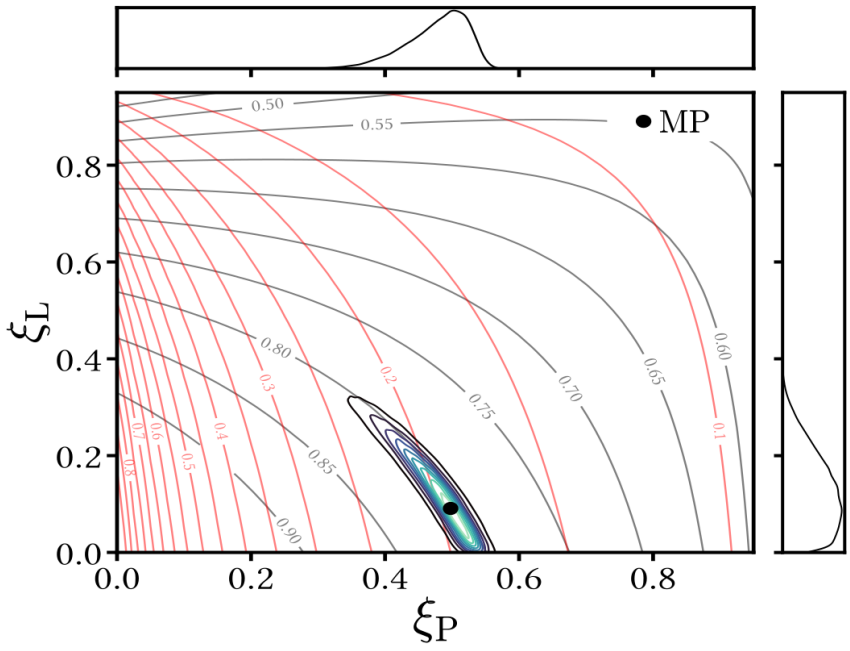


Figure 2.11: Posterior Distribution of the Deflagration Loss Parameters for Run 667.

Another important factor in the uncertainty in the value for ξ_L is the fact that the model does not allow for all combinations of measured values. In this example, the measured values of wave speed and pressure ratio are 1414 m/s and 2.1335, respectively, while the maximum a-posteriori, MAP, of the two quantities are 1412 m/s and 2.489. The map does not include the experimental measurement combination within its bounds, so the MCMC sampler finds the closest representation allowed for by the model. In this specific case, the measured pressure ratio was much lower than the minimum pressure ratio on the map, given the measured wave speed, suggesting other potential loss terms are missing from this model. With these concerns acknowledged, a comparison to experimental data was conducted to determine the validity of the model.

2.4.1.2 Comparison to Measured Deflagration

Experimentally, it is difficult to quantify the heat release distribution (in both space and time) over the cycle, but the OH* chemiluminescence emission can be used as a marker for the locations and, to an extent, the magnitude of the heat release. This approach was outlined by Feleo et al. [2], who conducted OH* emission measurements at a single fixed point in the RDC as a function of time using a photo-multiplier tube (PMT) and suitable collection optics and filters (see Figure 2.2 for an example). To relate the PMT data for each run to the deflagration loss fractions, the following methodology was used under the assumption that the PMT captures all of the heat release processes and that the fuel is completely consumed within this measurement window. The PMT data in

Figure 2.2 were broken down into three regions: parasitic combustion section, detonation section, and commensal combustion section. The area under the curves for each region in Figure 2.2 was used to determine the percentage and total heat release in these regions. The relationships between components of the PMT data and the deflagration loss parameters are shown below.

First, the total area under the OH* distribution in Figure 2.2 is set as the total heat release, inherently assuming 100% combustion efficiency. Thus:

$$\mathrm{Q_T} = \mathrm{Q_P} + \mathrm{Q_D} + \mathrm{Q_C} \tag{2.43}$$

Each term is normalized by the total heat release to obtain the fraction of heat release in each region:

$$\%\mathrm{Q_P} + \%\mathrm{Q_D} + \%\mathrm{Q_C} = 1 \tag{2.44}$$

The parasitic and leaked combustion parameters from the deflagration loss model are related to the measured quantities by the following equations:

$$\xi_\mathrm{P} = \frac{\mathrm{Q_P}}{\mathrm{Q_T}} = \%\mathrm{Q_P} \tag{2.45}$$

$$\xi_\mathrm{L} = \frac{\mathrm{Q_C}}{\mathrm{Q_T} - \mathrm{Q_P}} = \frac{\%\mathrm{Q_C}}{1 - \%\mathrm{Q_P}} \tag{2.46}$$

With these relationships developed, a comparison was made between the estimated deflagration loss fraction from the MCMC application and the measured PMT values from Feleo et al. converted into the deflagration loss fractions. Figure 2.12 compares the results for all the experimental cases listed in Table 2.2. In nearly all cases, parasitic combustion estimated with the deflagration loss model was much higher than the PMT data suggests, while the estimates for leaked fuel were only slightly lower than measured, in general. Inputting all PMT points into the deflagration loss model predicts higher wave speeds and pressure ratios than measured values, indicative of the difference between what the PMT is measuring and the actual deflagration losses.

From these initial results, it is clear that the deflagration loss model and the PMT data do not result in the same parameters. This could be mostly due to the fact that the PMT methodology may not properly capture EGR, while the parasitic combustion fraction accounts for both EGR and combustion of fresh reactants. The trend of the PMT data falling towards the lower end of the parasitic combustion parameter is indicative of this phenomenon. Another area where this comparison may be lacking is dependent on the location of the measurements from PMT data. The PMT will only measure the OH* emission where there is combustion, so the sensor may miss certain regions of combustion depending on its axial location. The assumption for this analysis was that the PMT was located in the fill region and captured the full cycle combustion, which

allowed for the conversion of the measured heat release distribution to the deflagration loss model parameters. This is most certainly not the case, as the combustion processes may occur both ahead of and aft of the axial location of the PMT sensor within the RDC.

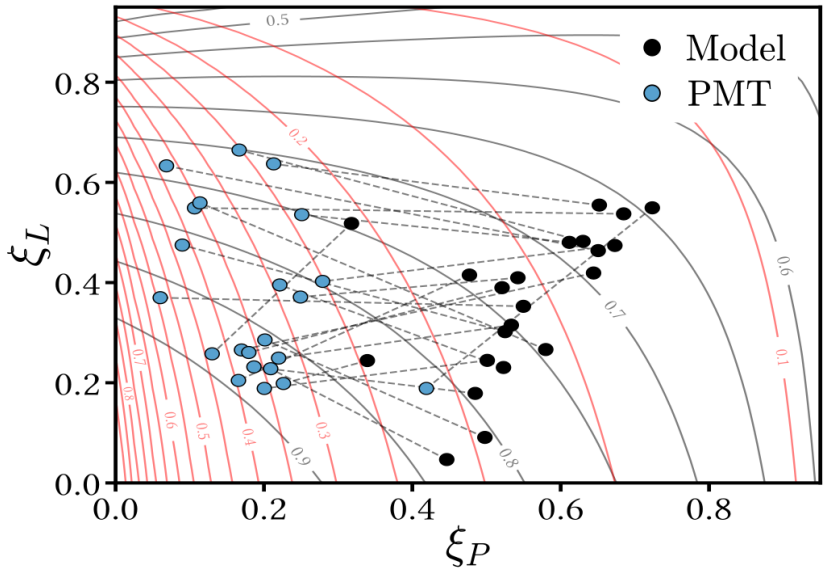


Figure 2.12: Comparison of deflagration loss model parameters to PMT measurement. Wave speed is shown as black contours, and the pressure ratio is shown as red contours.

To try to account for these issues, the simplest next step was to add a term that was separate from the commensal combustion fraction that accounts for leaked fuel that is not consumed within the PMT measurement location. This would be leaked fuel, which the PMT model does not account for but is captured in the detonation model. This is described as follows:

$$\mathrm{Q_T} = \mathrm{Q_P} + \mathrm{Q_D} + \mathrm{Q_C} + \mathrm{Q_L} \tag{2.47}$$

where the Q_L term is heat (fuel) that leaked through the detonation but was not combusted within the measurement window of the PMT. These terms are re-normalized to percentages with the following equation:

$$\%\mathrm{Q_P} + \%\mathrm{Q_D} + \%\mathrm{Q_C} + \%\mathrm{Q_L} = 1 \tag{2.48}$$

Equations 2.49-2.51 (below) shows the updated conversion from the measured heat release distribution from the PMT data to the model parameters, but now including the purely leaked fuel term. An increase in the purely leaked fuel will lead to an increase in the model leaked fuel parameter, ξ_L, and a slight decrease in the parasitic combustion parameter, ξ_P. The additional purely leaked parameter also acts as a proxy for combustion efficiency, as shown by Equation 2.51. In this analysis, it is not possible to validate the updated model with the PMT data and the purely

leaked parameter because the heat release profiles are calculated assuming complete combustion. Additional measurements would be needed to estimate the combustion efficiency of the RDC.

$$\xi_{\mathrm{P}} = \frac{\mathrm{Q_P}}{\mathrm{Q_T}} = \frac{\mathrm{Q_P}}{\mathrm{Q_P} + \mathrm{Q_D} + \mathrm{Q_C} + \mathrm{Q_L}} \tag{2.49}$$

$$\xi_{\mathrm{L}} = \frac{\mathrm{Q_C} + \mathrm{Q_L}}{\mathrm{Q_T} - \mathrm{Q_C}} = \frac{\mathrm{Q_C} + \mathrm{Q_L}}{\mathrm{Q_D} + \mathrm{Q_C} + \mathrm{Q_L}} \tag{2.50}$$

$$\eta_{\mathrm{c}} = \frac{\mathrm{Q_T} - \mathrm{Q_L}}{\mathrm{Q_T}} = \frac{\mathrm{Q_P} + \mathrm{Q_D} + \mathrm{Q_C}}{\mathrm{Q_T}} = 1 - \frac{\mathrm{Q_L}}{\mathrm{Q_T}} \tag{2.51}$$

In the same manner, an example re-circulation fraction, ξ_R parameter, can be introduced in an attempt to account for product gas re-circulation that would not be captured by the PMT. This results in a simple addition to the parasitic fraction calculated from the PMT data.

Figure 2.13 shows an example of the effects of the 10% purely leaked parameter for the PMT relations, as well as having $\xi_{\mathrm{R}} = 0.2$. Including the purely leaked fraction makes a slight trade between the parasitic fraction and the leaked parameter, where there is a much more drastic increase in the leaked fraction relative to the slight decrease in the parasitic fraction. The plot also shows an example of adding a re-circulation fraction that simply acts as a linear shift in the parasitic fraction. This is because the amount of flow re-circulation will change the calculated ξ_P for the PMT data but does not count towards the measured heat release profile.

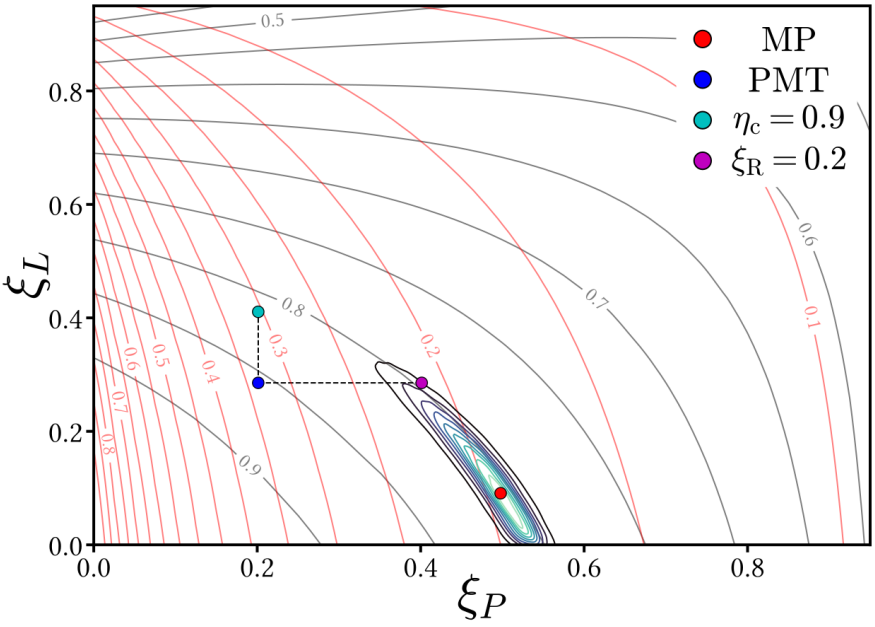


Figure 2.13: Example effects of additional loss parameters.

The search for additional parameters to gain a better model fit to the PMT measurements was

not exhaustive, as the model and the PMT data represent two different outputs. Despite the discrepancy between the measured values, this model and its results were critical to inform the modeling choices for the state-based RDC cycle model (Section 3.3.1), as well as the non-ideal RDC cycle model (Chapter 4).

2.4.2 Non-Ideal CJ and ZND Models

This section includes the results from both the non-ideal CJ model and the non-ideal ZND model. Because these two models produce similar results in most cases, it makes sense to study their outputs simultaneously. Each loss parameter will be examined on its own and in concert with other losses to determine the individual and compounding effects on detonation performance.

2.4.2.1 Lateral Relief

First, the lateral relief study will be examined by varying the area ratio from 1.0 to 2.0. Figure 2.14 shows the results of this process, where the calculated wave speed, normalized by ideal, is shown in the left subplot as a function of the area ratio for a hydrogen-air detonation at standard temperature and pressure. These results show a modest decrease in wave speed over the change in area ratios. However, when examining the change in the detonation pressure ratio, we see a much more drastic impact. These results are shown in the right subplot and predict a halving of the pressure ratio across the detonation when the CJ area is twice that of the initial area.

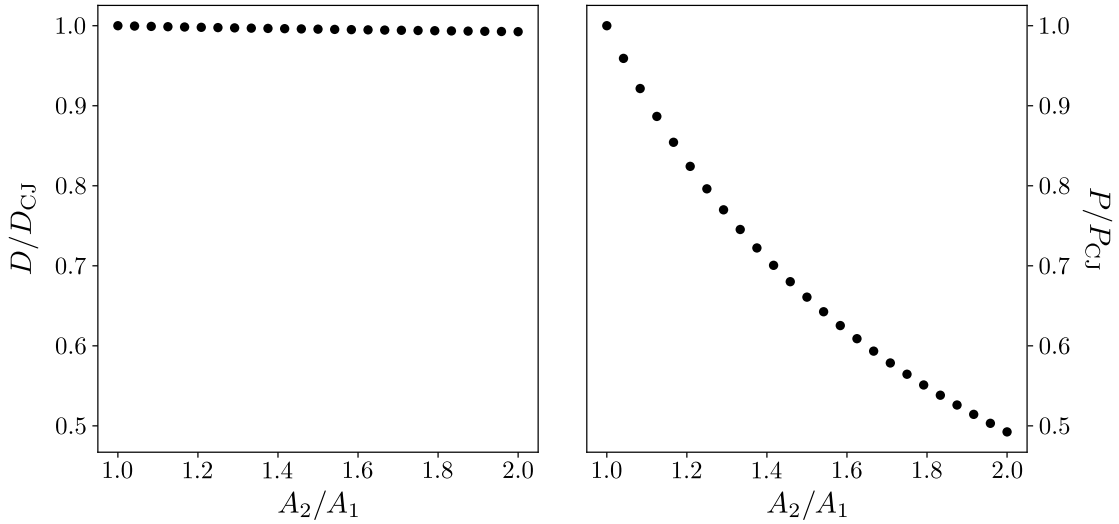


Figure 2.14: Normalized Wave speed and Detonation Pressure Ratio versus Area Ratio using the CJ Solver.

Although the non-ideal CJ framework provides a method to capture the effects of area changes

across the detonation wave, it assumes complete equilibrium between the two states. This assumption can easily be tested for validity through the use of the full time marching solution using a modified, non-ideal ZND analysis framework. Figure 2.15 shows the results as a constant area variation rate was specified between 0 and 0.001 m^2/m. It contains the pressure (a), Mach number (b), and laboratory frame velocity (c) profiles for each simulation.

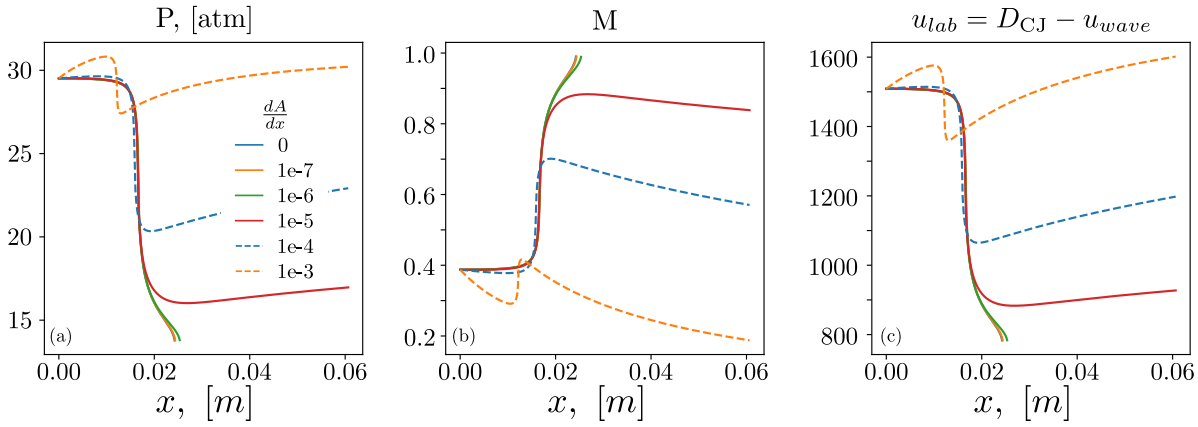


Figure 2.15: ZND profiles as a function of the area change rate for a stoichiometric detonation. Static pressure (a), Mach number (b), and laboratory frame velocity (c).

For small increases in area, $\frac{dA}{dx} \leq$ 1e-6, there is minimal change in these profiles. However, as the area change rate increases, we now notice that the Mach number never reaches $M = 1$, which is the definition of the CJ detonation. Also, as the area change rate increases, we notice an increase in pressure through the induction zone. This is due to the expansion in the area slowing the flow and returning some of the kinetic energy to potential energy (pressure).

Because the ZND solver requires a wave speed as the input condition to calculate the shock strength and post-shock state, we need to vary this parameter from the ideal CJ wave speed that is typically used. This was done for the results shown in Figure 2.16, where ΔU represents a decrease in wave speed from ideal. This sweep in initial velocities was conducted at an area change rate of 1e-5. The figure includes subplots of the pressure, temperature, density, Mach number, thermicity, and laboratory frame velocity across the profiles.

Figure 2.16 shows that as the wave speed is decreased, the maximum Mach number profile slowly increases as well, up to the point where the Mach number reaches the sonic condition. As the velocity decrement increases, the profile continues to reach the sonic condition; however, at a much later value, due to the decrease in the pressure and temperature jump across a weaker shock. This also comes with an increased induction length. In addition, the thermicity profile appears to be clipped before returning to the zero value associated with complete combustion, an aspect that will be reviewed in a later section.

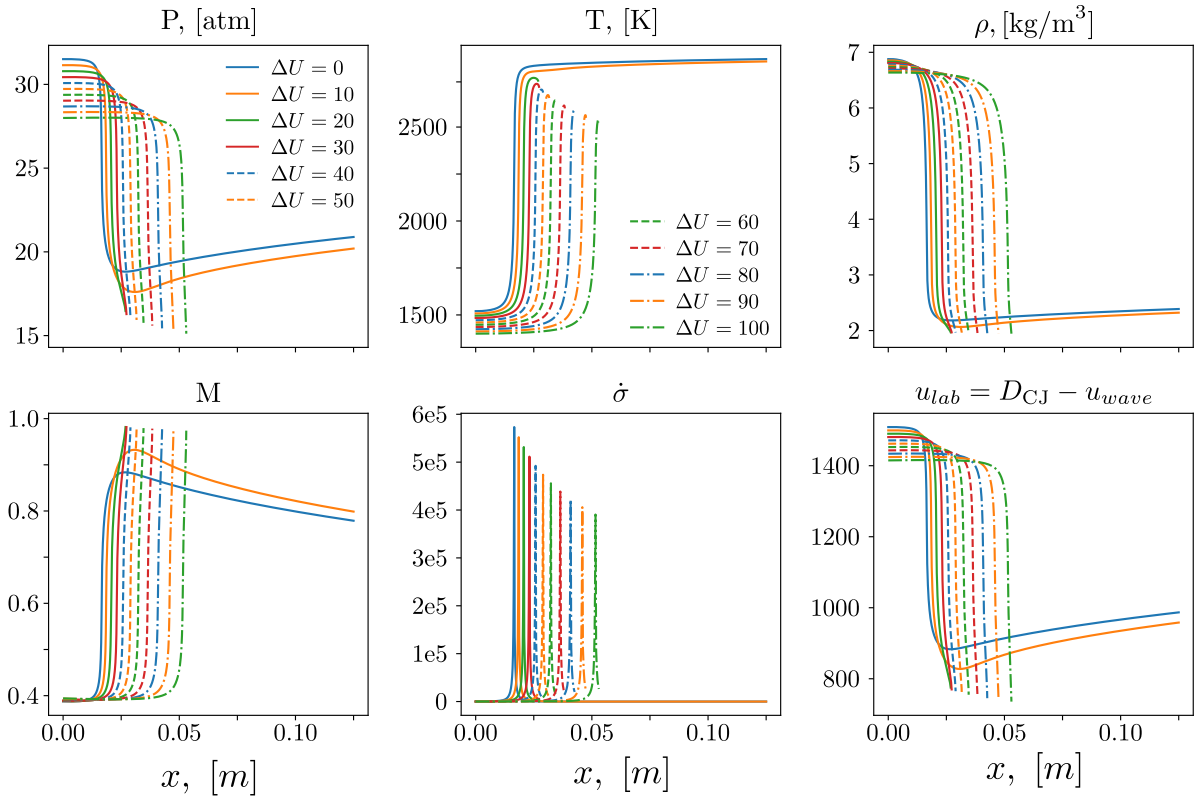


Figure 2.16: ZND profiles at an area change rate, $\frac{dA}{dx}$ = 1e-5, as a function of the velocity decrement for a stoichiometric detonation.

The question now is, what is the correct velocity decrement value? If probed using the non-ideal CJ solver from earlier in this section, the wave speed at a larger area change rate will not produce a significant enough reduction to allow for the CJ condition to be met using the ZND solver. More detail on this subject will be included at the end of this section; however, it led to the development of an iteration methodology used to determine the maximum wave speed that allows the ZND solver to reach the CJ condition, shown in Algorithm 7.

Now that we have defined the algorithm used to find the maximum wave speed, we will examine some of the results. Figure 2.17 shows the Mach number versus distance on the left subplot and the thermicity versus distance on the right subplot. The initial starting point of $\Delta U = 0$ is shown in the red line, the intermediate velocity decrements are shown in the light black lines, and the final velocity, which satisfies the CJ condition, is shown in blue. The final velocity decrement of 88.6 $[m/s]$ was calculated as the minimum velocity decrement to achieve the CJ condition. The final area change calculated across the ZND structure with this method was 1.039, which would result in an estimated wave speed decrement of less than 1 m/s. This indicates that the assumption of complete equilibrium in the CJ solver may not account for the finite rate effects present in the ZND methodology.

Algorithm 7 ZND with Area Change Solver

Require: $\frac{dA}{dx}$

1: Initialize solver at ideal CJ wave speed: $U_0 = D_{\text{CJ}}$
2: **while** $M_i \neq 1.0$ **do**
3: Integrate ZND profile
4: **if** $M_i < M_{i-1}$ **then**
5: Break (No convergence possible at $\frac{dA}{dx}$)
6: **end if**
7: Decrease initial velocity: U_{i+1}
8: **end while**

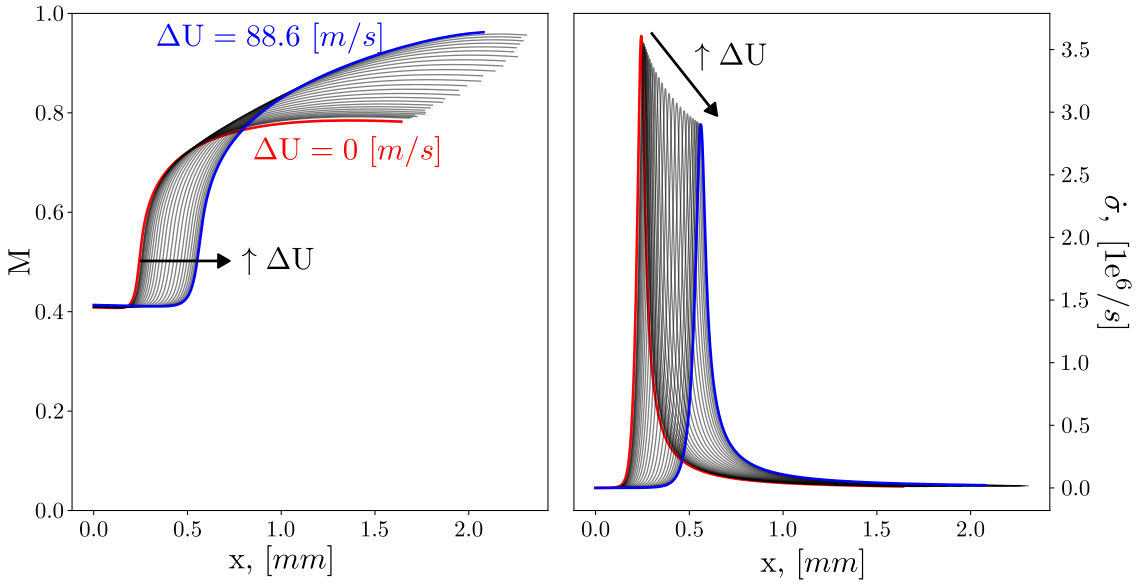


Figure 2.17: ZND profiles during the solution of the ZND iteration method. The red line assumes the ideal CJ wave speed without area change, the blue line represents the first wave speed that allows for the sonic condition for the given area expansion rate, and the black line shows each intermediate step. $\frac{dA}{dx} = 6e^{-4}$.

One interesting takeaway from this plot is the fact that the induction length based on the maximum thermicity has increased with the velocity decrement, at the same time the peak thermicity value has also decreased. Both of these results can be attributed to the lower temperature and pressure ratios provided by the weaker shock.

Comparison of ZND Iteration Method and CJ Solver with Area Change Now we have a method for solving for the wave speed of a detonation with area expansion in the reaction zone through the use of a ZND solver. The next step is to compare these results with the CJ solver and the area expansion discussed earlier in this section. Figure 2.18 shows the wave speed as a

function of the area ratio between the shock and the CJ plane for the CJ solver (orange) and the ZND solver using the wave speed maximization optimizer (blue). It is clear from these results that the CJ solver predicts minimal changes in wave speed as the area ratio is varied to a roughly 3.5% increase in area. The ZND solver, on the other hand, predicts a much steeper drop-off in wave speed, even at these lower area ratios. Note that the wave speed calculated for the ZND solver with no area change is about 5 m/s higher than that of the CJ solver.

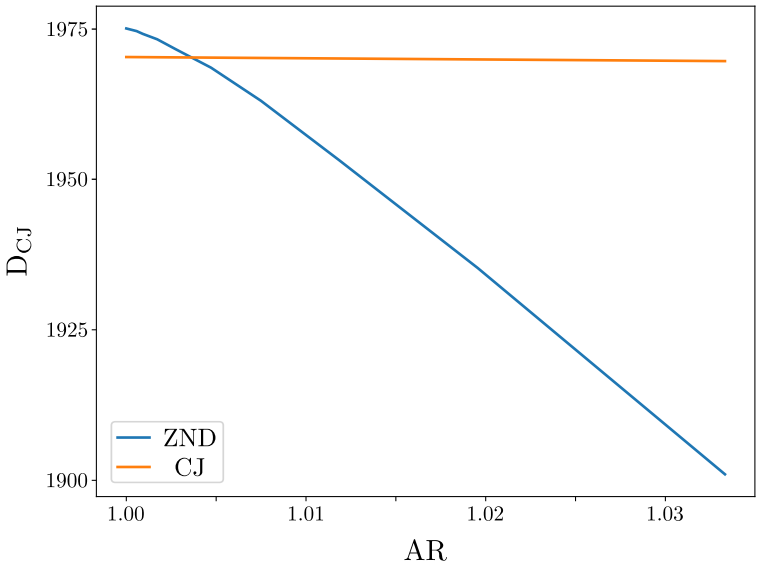


Figure 2.18: Comparison of ZND and CJ solver with area ratio.

This change is likely due to the use of finite-rate chemistry in the solver, as opposed to the equilibrium assumption used in the CJ calculation. Previous testing has shown that even for an ideal case, the final state of the ZND solver can have up to 3.6% difference in thermodynamic properties compared to the CJ solver. Table 2.5 shows the percent difference between the CJ state calculated from the CJ and ZND solvers using an ideal stoichiometric detonation in air for three different fuels and two different reaction mechanisms.

Fuel	Mech	P	T	ρ	h
H_2	GRI3.0	3.42	0.71	2.86	2.64
CH_4	GRI3.0	3.44	0.72	2.86	3.42
C_2H_6	GRI3.0	3.6	0.76	2.99	3.22
H_2	San Diego	-0.16	-0.02	-0.14	-0.12
CH_4	San Diego	-2.04	-0.25	-1.77	-1.98
C_2H_6	San Diego	-2.56	-0.3	-2.23	-2.23

Table 2.5: Table of thermodynamic property percent differences between the CJ solver and the ZND solver's final state.

This change in properties is shown in Table 2.5, was likely due to the larger changes in the concentrations of the major species between the two solvers, where some of the major species had percentage differences up to 94%. Table 2.6 shows the results for a hydrogen-air detonation using the GRI3.0 mechanism as a reference.

Species	X_{CJ}	X_{ZND}	% Difference
$N2$	0.632	0.635	0.47
$H2O$	0.295	0.293	0.68
$H2$	0.0314	0.0309	1.59
OH	0.0178	0.0201	12.9
$O2$	0.00782	0.0105	34.3
NO	0.00773	0.000465	94.0
H	0.00599	0.00677	13.0
O	0.00210	0.00272	29.5

Table 2.6: Table of major species for an ideal hydrogen-air detonation using the GRI3.0 mechanism.

From these results, we can see the drastic difference between the equilibrium assumption in the CJ solver and the result that finite-rate chemistry predicts. Although these results are likely specific to the reaction mechanism of choice, it is clear that the two do not produce the exact same CJ state. Notably, the reaction mechanisms in question are not directly calibrated for detonation combustion, which may prove to be a major factor in the previously discussed discrepancies.

2.4.2.2 Heat Transfer in the Detonation Region

Next, we examine the effects of heat transfer within the detonation region. This will initially focus on the modified CJ solver and then move to the ZND implementation.

CJ Solver Figure 2.19 shows plots of the normalized wave speed and detonation pressure ratio as a function of the heat removed from the detonation normalized by the ideal detonation heat release. These results were determined using Algorithm 3. The left subplot shows the wave speed, normalized by the ideal wave speed with no heat transfer, and the right subplot shows the pressure ratio across the detonation wave, normalized by the same ideal pressure ratio. A significant heat transfer value, on the order of 30% of the heat available in the fuel, can be removed with only a 10% reduction in the wave speed; however, this would produce a nearly 20% reduction in the pressure ratio across the wave. This result is similar to the parasitic combustion results in Section 2.4.1, where the wave speed was moderately affected, but the pressure ratio dropped significantly.

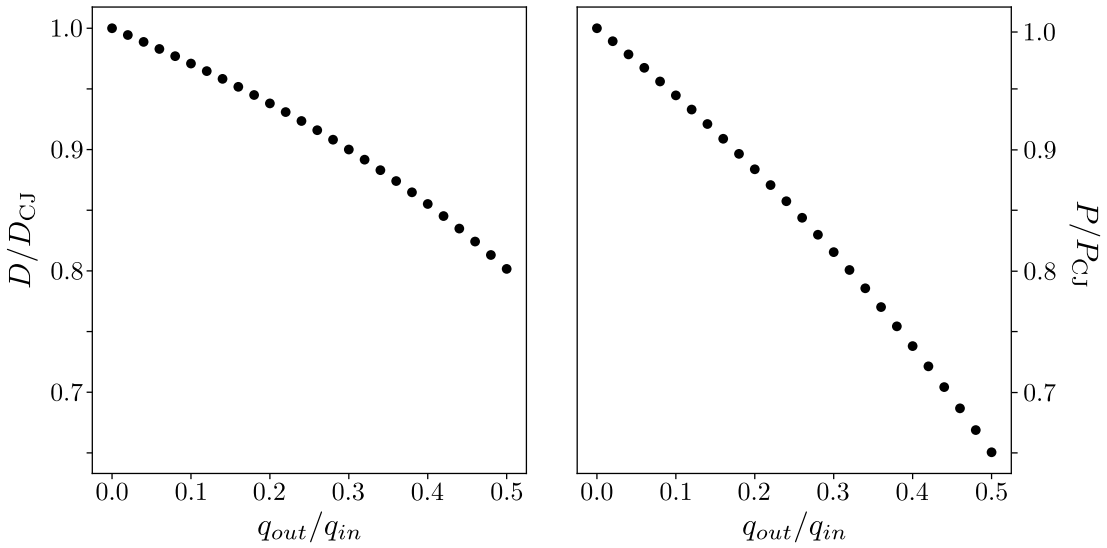


Figure 2.19: Normalized Wavespeed (left) and Detonation Pressure Ratio (right) versus Normalized Heat Transfer.

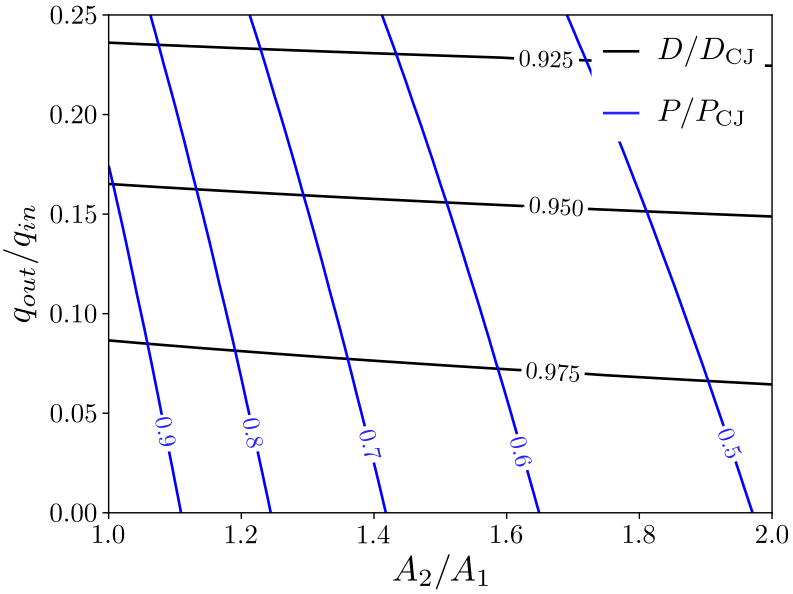


Figure 2.20: Contour Plots of Normalized Wavespeed (black) and Detonation Pressure Ratio (blue) versus Area Change and Normalized Heat Transfer.

If we pull in the CJ analysis results with area change from Section 2.4.2.1, we can study the effects of both area change and heat transfer within the detonation region. Figure 2.20 shows these results as contour plots of the normalized wave speed in black and the normalized pressure ratio in blue. In this example, the removed heat was studied only up to 25% of the heat content in the fuel.

In Figure 2.20, we can see that the changes in the area ratio produce less impact on the detonation wave speed compared to the heat transfer but a higher impact on the pressure ratio. Together, these loss mechanisms, even at low magnitudes, can produce significant losses in wave speed and pressure ratio compared to the expected performance of an ideal detonation wave.

ZND Solver Much like the results for the area change, when integrating the ZND profile with heat transfer, there exists a parameter space where the CJ condition will not be met. Because of this, the velocity decrement minimizer in Algorithm 7 was used to calculate the reduction in wave speed from the ideal that allows for the CJ condition to be met. This algorithm was modified to accept the heat transfer coefficient as an input rather than the area change rate. Unlike the results with only area change, the heat transfer coefficient was more troublesome to achieve convergence. Figure 2.21 shows an example sweep of the calculated velocity decrement from ideal required to attain the CJ condition. It is clear that the solver methodology does not produce a smooth and consistent result expected from the CJ analysis of heat transfer, and any coefficient above 0.05 could not converge within the velocity decrement bounds of [0, 1000] [m/s]. Therefore, the remaining analysis is best viewed from a qualitative perspective.

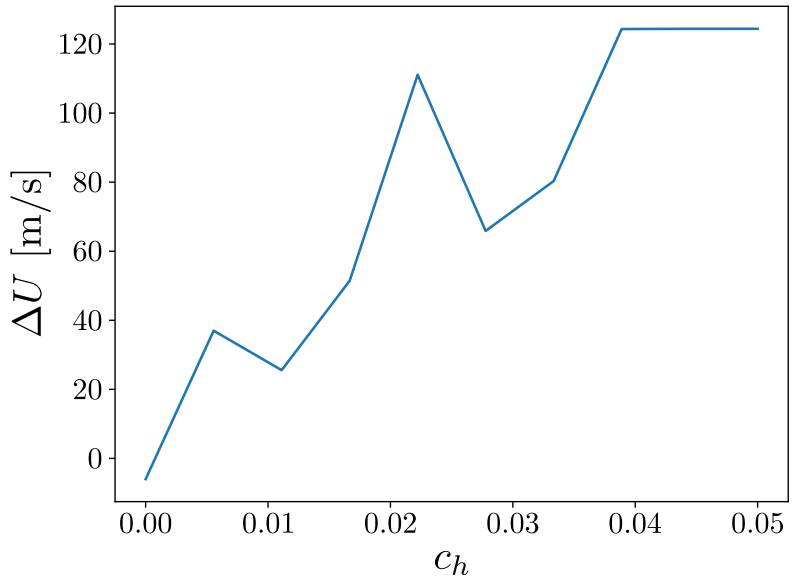


Figure 2.21: Velocity Decrement from Ideal CJ Wave speed versus Heat Transfer Coefficient.

Figure 2.22 shows the normalized wave speed and pressure ratio as a function of the heat transfer coefficient. In general, the wave speed and pressure ratio decrease at a similar rate with heat transfer. This differs slightly from the above results of the CJ analysis, where Figure 2.19 shows that the pressure ratio decreases faster. This is likely due to the difficulty in achieving a converged ZND result and the fact that the ZND model does not assume complete equilibrium at the CJ plane.

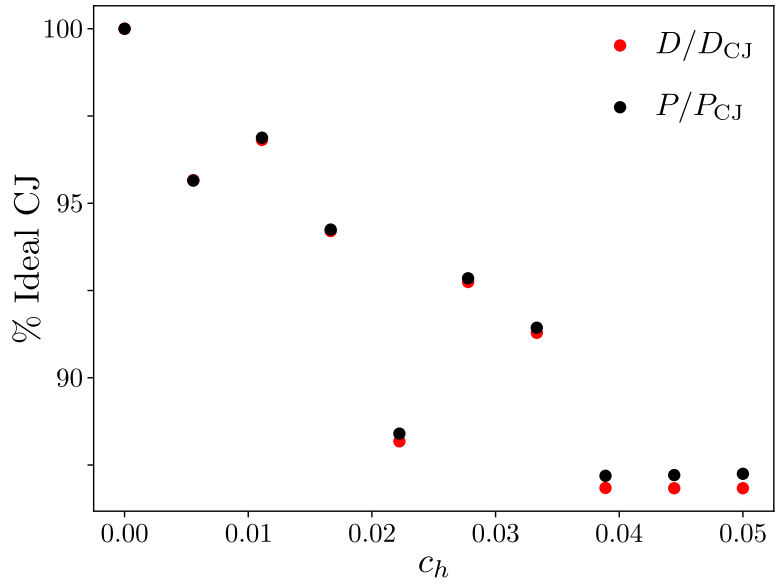


Figure 2.22: Wavespeed and Pressure Ratio from ZND model as a function of the heat transfer coefficient.

The previous results show how heat transfer within the detonation region can negatively affect the performance of the detonation wave. Like the other loss parameters, heat transfer from the detonation wave to the boundary will reduce both the wave speed and the pressure ratio across the detonation wave. In this case, heat transfer will almost equally decrease both metrics, something that is often seen experimentally (see Table 2.2).

2.4.2.3 Friction in the Detonation Region

This section discusses the results from the momentum loss sweep, which accounts for friction within the detonation region. For the CJ analysis, the total momentum loss term varied, while the ZND analysis varied the friction coefficient.

CJ Solver Figure 2.23 shows the normalized wave speed and pressure ratio across the detonation wave as a function of the momentum loss term, F. This plot shows a steady acceleration in the loss in both metrics as the momentum loss term increases. Both metrics decrease at roughly the same rate with the momentum losses.

Figure 2.24 shows the result for the CJ solver with a momentum loss combined with area change (left) and heat transfer (right). From these plots, we can see which terms are most detrimental across their specified parameter sweep. The left subplot shows that the momentum loss solely determines the wave speed (see Figure 2.14), while both the momentum losses and the area change provide a similar decrease in the pressure ratio.

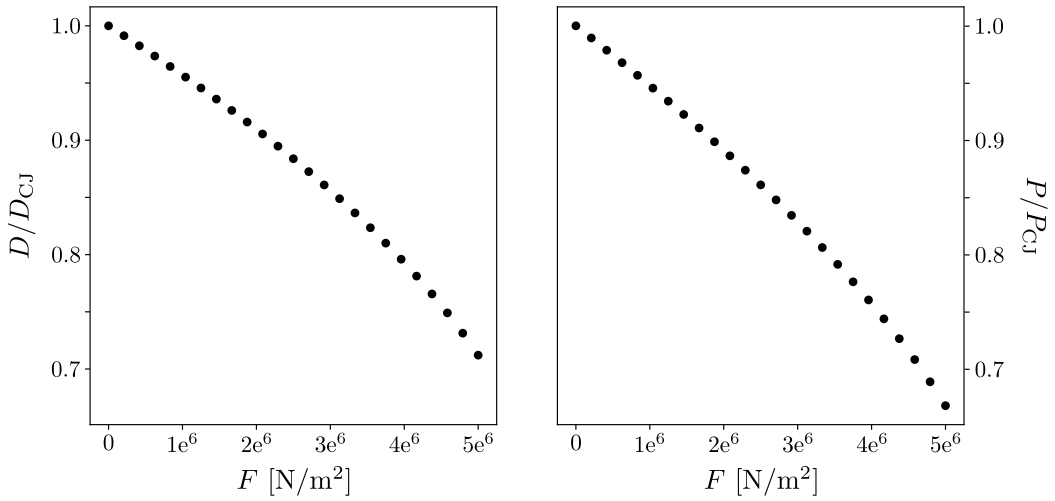


Figure 2.23: Normalized detonation performance as a function of the total frictional momentum loss. Wave speed (left) and pressure ratio (right).

Finally, the right subplot shows the relationship between the normalized performance metrics as a function of the momentum loss and heat transfer. This plot shows that across the parameter space, the heat transfer provides slightly less of a change in both performance metrics. Note that while the area ratio and heat transfer losses can be easily related to a given input metric, the momentum loss term bounds were arbitrarily set. With a more customized momentum loss term with physical bounds, these results could change to indicate that the momentum loss is not more detrimental to the detonation performance.

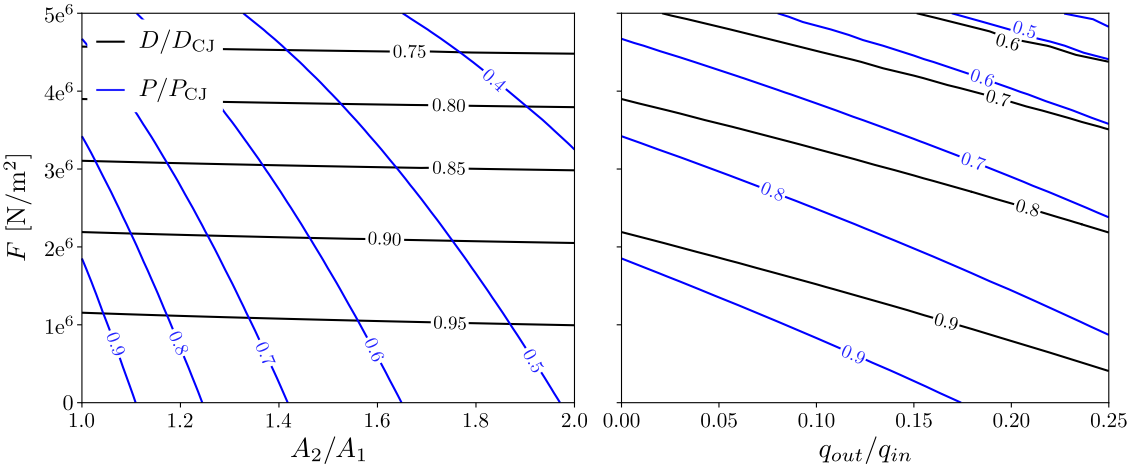


Figure 2.24: Contours of normalized detonation performance as a function of total frictional momentum losses, area change, and heat transfer. Wave speed (black) and pressure ratio (blue).

ZND with Friction Finally, we examine the ZND solve with a friction coefficient specified to

capture the momentum losses through the detonation wave. This solver used the same velocity decrementing scheme presented in Algorithm 7, and in general, produced similar results to the CJ solver (see Figure 2.23).

Figure 2.25 shows the thermicity across the detonation wave as a function of the friction coefficient. From this plot, we can see that as the friction increases, the thermicity profile does not return to the post-combustion value seen in the case with no skin friction. This is because the sonic condition is achieved before the reaction can complete.

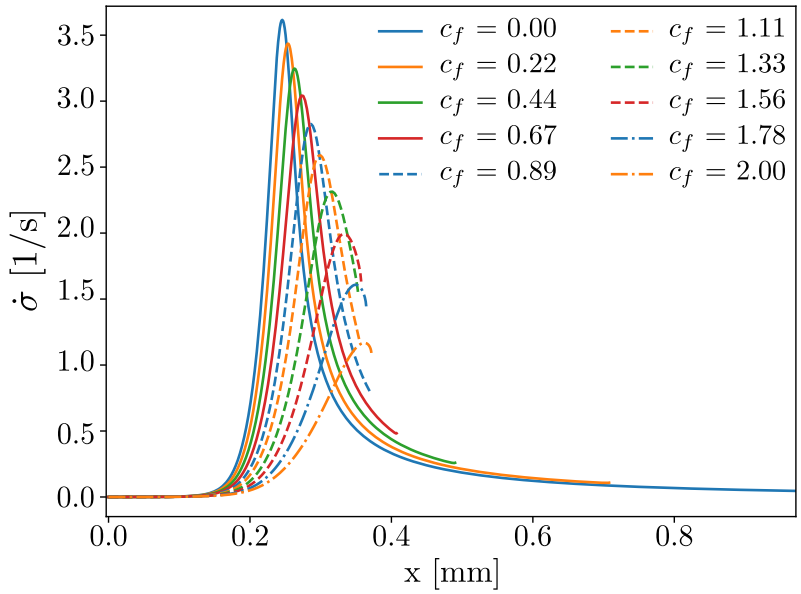


Figure 2.25: Thermicity profiles from ZND solver with friction as a function of the coefficient of friction.

To confirm that the CJ plane was reached before the fuel was completely consumed, the CJ chemical composition was analyzed. Figure 2.26 shows the mole fraction of hydrogen remaining at the CJ plane as a function of an increasing friction coefficient. This clearly shows that at a high enough value of friction, the combustion process is halted due to reaching the CJ plane prematurely, and the trend approaches the limit of the initial mole fraction of the reactants. This result does bring questions as to the validity of the velocity decrement algorithm used to solve these ZND profiles. A potential update to the methodology may result in solutions where the majority of the fuel is consumed regardless of the friction coefficient.

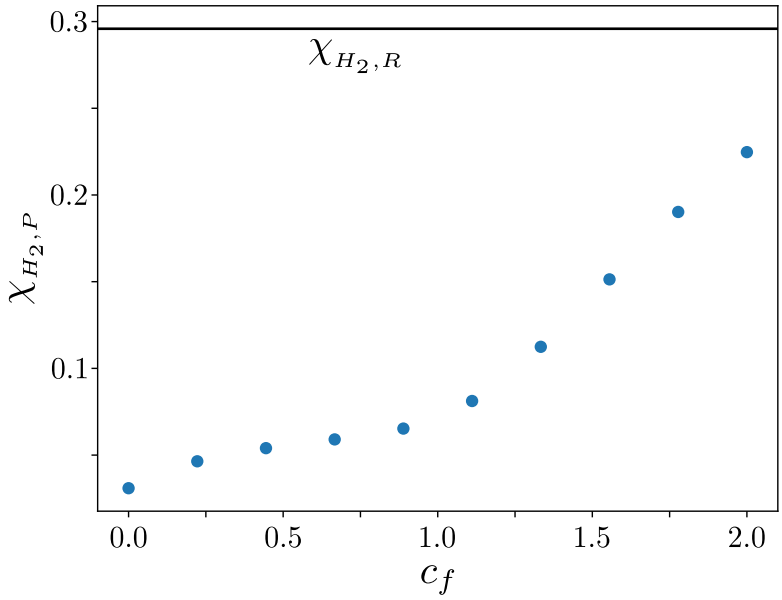


Figure 2.26: Final fuel content at the end of the ZND profile as a function of friction coefficient.

If the ZND solution indeed shows a valid trend, this would indicate a limiting frictional loss that still allows for a detonation wave by definition. This would also be another process by which the fuel may leak through the detonation wave. Regardless of the cause, if the CJ plane is reached before complete combustion, there will be a fraction of fuel that cannot contribute to the heat release within the detonation. Section 2.4.4 will provide some additional discussion on this front.

2.4.2.4 Non-Ideal CJ Model without Deflagration Losses

With each loss metric discussed, the next step was to evaluate the combination of all three losses. Algorithm 5 allows for the study of all three of the aforementioned loss mechanisms, and the high arching results of evaluating this model are discussed in this section. Because of the issue with convergence seen in some of the non-ideal ZND sweeps, this section will focus solely on the CJ model. Figure 2.27 shows the Sobol Indices for the CJ model with the three loss mechanisms discussed in this section. Each index is binned by the performance metric of interest: wave speed, pressure ratio, and the "gain" metric from Equation 2.39, moving from left to right. This plot shows how sensitive each performance metric is to each loss metric, where a higher sensitivity index indicates which loss metric produces the most change to the performance metric of interest. In this case, we can also deduce the directional change associated with the Sobol indices, as we know that all parameters have a detrimental effect.

The wave speed shows almost zero sensitivity to the area change, which was also evident from the results in Section 2.4.2.1, and is moderately sensitive to heat transfer. By a small margin, the

wave speed was most sensitive to the momentum removal from the frictional forces. The detonation pressure ratio is almost entirely determined by the area ratio, showing little dependence on the other two loss mechanisms. Finally, the gain metric, as defined by Equation 2.39, is predominately determined by the heat losses, with a moderate sensitivity to the momentum losses. This result makes sense as we have defined a gain metric based on energy gained across the detonation wave. As one removes energy through heat transfer in this example, there should be a direct reduction in gain across the wave. While momentum losses inevitably affect the energy gain metric, it is not the same extent.

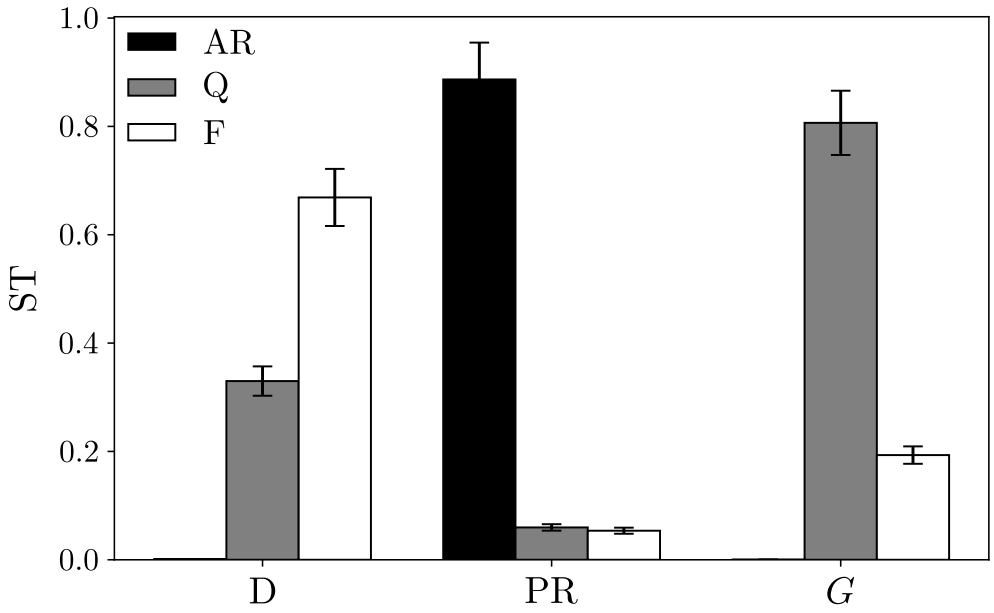


Figure 2.27: Sobol Indices for the Non-Ideal CJ Model.

Essentially, all loss mechanisms affect detonation performance to different degrees, where each is a key contributor to a given performance metric. This means that depending on which performance metric is of interest or which makes sense for a given application, optimization would be weighted to a different loss mechanism. The troubling result from this analysis is the fact that the detonation pressure ratio is particularly sensitive to the change in area. Because of the boundary conditions associated with the RDC, this would likely be a difficult metric to reduce. With the detonation pressure ratio decreasing, it will become more difficult to achieve an overall cycle pressure gain, something that will be discussed throughout this work. For a given detonation wave, the amount of lateral relief is completely dependent on the geometry of the RDC and bulk flow conditions. We will discuss the effect in more detail in the next chapter, but the inlet performance of the RDC is critical to overall performance. This is defined as the ratio of the channel static pressure to the total plenum pressure, and higher-performing systems typically fall in the direction

of a less "stiff" inlet. A less stiff inlet with a channel pressure near the plenum pressure will be more susceptible to detonation wave perturbations, allowing a higher level of lateral relief in the detonation region.

In addition, for a practical detonation-based system, heat transfer from the detonation wave to the walls of the device would be incredibly difficult. As this is the leading factor for changes in the gain metric, it becomes difficult to image a system that achieves an energy "gain" solely across the detonation wave that is near the theoretical values provided by the standard CJ analysis. This also raises questions as to the viability of the detonation energy gain metric as a useful performance metric for any system-level application of detonation combustion.

2.4.3 Non-Ideal CJ Loss Model with Deflagration Losses

With the individual loss mechanisms affected detonation performance discussed in the previous sections, a non-ideal CJ model with deflagration losses was constructed. Algorithm 8 provides the pseudo-code for the solver, which includes five loss metrics specific to the detonation wave.

Algorithm 8 Non-Ideal Deflagration Loss Model

Require: $\xi_{\mathrm{P}}, \xi_{\mathrm{L}}, AR, Q, F$, Gas objects
  Set $(1 - \xi_{\mathrm{P}})$ of fuel to inert
  Equilibrate at constant enthalpy and pressure
  if $\xi_{\mathrm{L}} \neq 0$ **then**
    Set $(1 - \xi_{\mathrm{L}})$ remaining fuel to inert
  end if
  Run non-ideal CJ model ▷ *Algorithm 5*
  return Pre-Detonation State, Post-Detonation State, D_{CJ}, u_{ind}

Figure 2.28 shows the resulting Sobol Indices for the Non-Ideal Deflagration Loss Model. With the inclusion of the deflagration losses, the secondary effect changes how the area ratio, heat transfer, and momentum losses affect each performance metric. Now, the decrement in wave speed is most sensitive to the parasitic combustion fraction, with moderate sensitivity to all other loss metrics aside from the area ratio. The detonation pressure ratio is now nearly entirely determined by the parasitic combustion fraction, with a small sensitivity to the area ratio. This result echoes the variations in the pressure ratio with small changes in the parasitic combustion fraction seen in Figure 2.6. Finally, the energy gain metric is now predominately a function of the parasitic combustion fraction and the heat loss metric.

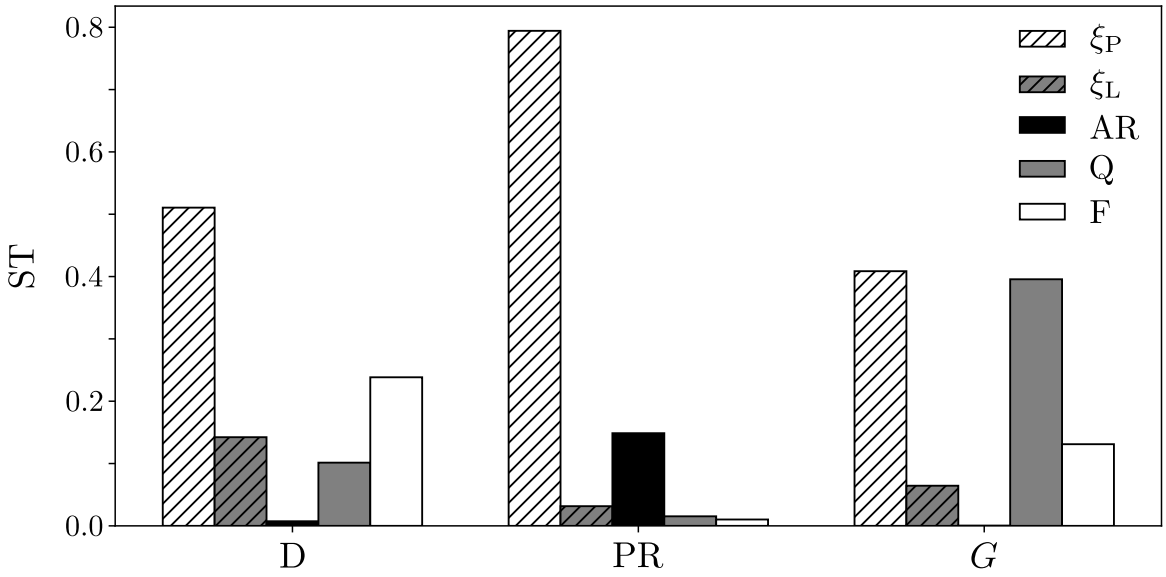


Figure 2.28: Sobol Indices for the Non-Ideal CJ Model with Deflagration Losses.

Across the board, the parasitic combustion fraction had the largest impact on the detonation performance metrics. This result was partially expected from the analysis done in Section 2.4.1, but the magnitude of the parasitic combustion effects was much higher than initial expectations. As a reminder, this term captures the effects of both pre-detonation deflagrative burning and product gas re-circulation. As one can imagine, there is a direct link between the stiffness of the RDC inlet and the propensity for product gas re-circulation and parasitic combustion. As the inlet becomes less stiff, the detonation wave is more impactful on the inlet flow, resulting in additional inlet blockage and a higher likelihood for the effects captured with the parasitic combustion fraction. See Figure 2.9 in Section 2.4.1 for an example of this relationship.

2.4.3.1 Parameter Estimation

Using the updated deflagration loss model with other non-idealities from Algorithm 8, another MCMC study was conducted to attempt to gather a better estimation of the parasitic and leaked fuel fraction. Recall from Section 2.4.1 that the base deflagration loss model over-predicted the measured PMT values by a significant margin. We have already discussed the issues with the PMT measurements not capturing the full effects of the deflagration loss parameters; however, it is also true that the base deflagration loss model can only attribute degradation in detonation performance to parasitic combustion and leaked fuel. With the addition of the non-ideal detonation effects, the model has other mechanisms for binning the different losses.

The MCMC sampler was conducted in a manner similar to that discussed in Section 2.4.1.1; however, only 1000 accepted samples were requested due to the extended evaluation time with

this version of the model. Table 2.7 shows the results of the MCMC sampling, showing the mean values for each parameter.

Run	ξ_{P}	ξ_{L}	AR	Q/Q_{in}	F/1000
654.0	0.3	0.24	1.52	0.04	16.37
656.0	0.42	0.41	1.49	0.01	14.57
657.0	0.38	0.27	1.35	0.0	0.0
658.0	0.35	0.26	1.56	0.02	18.15
659.0	0.31	0.5	1.44	0.02	25.95
660.0	0.36	0.37	1.49	0.02	23.03
662.0	0.37	0.3	1.53	0.04	14.9
663.0	0.34	0.44	1.46	0.03	24.49
664.0	0.4	0.34	1.47	0.02	13.46
665.0	0.33	0.3	1.55	0.01	19.6
666.0	0.34	0.3	1.52	0.01	18.26
667.0	0.42	0.41	1.46	0.04	9.88
668.0	0.34	0.31	1.52	0.04	17.14
669.0	0.35	0.28	1.54	0.01	13.07
670.0	0.41	0.39	1.5	0.01	15.88
672.0	0.36	0.35	1.49	0.02	16.09
675.0	0.3	0.25	1.52	0.04	16.76
677.0	0.31	0.42	1.44	0.04	22.87
681.0	0.3	0.25	1.54	0.04	19.16
682.0	0.34	0.27	1.48	0.05	5.46
686.0	0.27	0.32	1.5	0.01	16.37

Table 2.7: Deflagration Loss Model with Non-Ideal Effects

As expected, the additional loss mechanisms allow for convergence to deflagration loss fractions that were lower than those determined from the base deflagration loss model (see Table 2.4). With these results, Figure 2.29 shows the comparison of the estimated deflagration loss fractions. It shows the base model results in black, the PMT measurement values in blue, and the non-ideal deflagration loss model results in red. Across the board, the next loss mechanisms allow the model to better predict the values that the PMT is measuring. Now, the estimated deflagration losses fall much closer to their measured PMT value and are much lower in magnitude relative to the base model predictions. These new values are also much more in line with the expected deflagration loss parameters.

In general, the new model predicts larger changes in area ratio and momentum losses than it does in heat losses. Nearly every test point predicted the area ratio across the detonation falls around the 1.5 value, suggesting a large amount of lateral relief is expected for these test cases. This is also particularly interesting as the geometry of the RDC was held constant across the data set; however, the bulk flow conditions did vary. With this model change, the updated model also allows for a prediction as to the magnitude of the lateral relief, given the experimental measurements, showing the value of the MCMC sampling methodology.

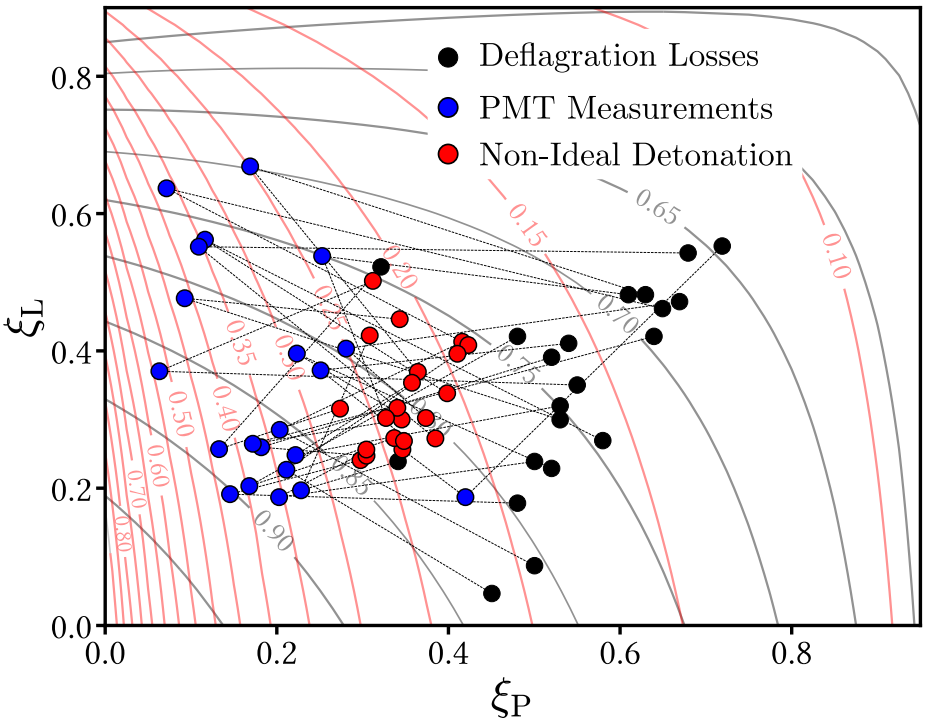


Figure 2.29: Deflagration Loss Parameter Estimation with Non-Ideal Loss Mechanisms. Compared to the Base Model and PMT Measurements.

2.4.4 Additional Thoughts on Weak Detonations

During the evaluation of the ZND solver with no ideal effects, there were parameter sets that caused the CJ plane to be reached before the full heat release could occur. An example is shown in Figure 2.25, where the thermicity profile never returns down to a non-reactive value. When inspecting the remaining fuel fraction in Figure 2.26, a large fraction of the fuel was still remaining, confirming the suspicions from the thermicity profiles. The same result was also observed for the variation in area across the ZND profile. To better resolve these findings, the following will examine this phenomenon in more detail.

We will first define a term that captures the heat release achieved at the CJ plane as the loss

parameters were swept. To do this, we will define the reactant enthalpy, h_1, and the fuel mass fraction of the reactants, Y_f, which is hydrogen for this example. We can then determine the ground state enthalpy for the products at the CJ plane, $h_2|_{(P_{std},T_{std},X)}$. From this, we can calculate the heat released during the reaction with the following:

$$HR = \frac{h_1 - h_2|_{(P_{std},T_{std},X)}}{Y_f} \tag{2.52}$$

Figure 2.30 shows the results of this comparison, where the ZND solver was initialized as a stoichiometric hydrogen-air detonation with no losses discussed in the previous sections; however, the initial wave speed was manually decreased from the ideal CJ wave speed. This was done to simulate any method by which the detonation wave would not be at the CJ wave speed. This plot shows the velocity decrement sweep in blue, an equivalence ratio sweep in orange, and a leaked fuel sweep in magenta. The sweep of the equivalence ratio involved decreasing the equivalence from 1.0 to 0.2, calculating the ideal CJ wave speed at the equivalence ratio. This was done to compare the amount of fuel contributing to the detonation propagation.

The sweep in the leaked fuel fraction was done by calculating the non-ideal wave speed using Algorithm 4 without any parasitic combustion fraction. After the wave speed was calculated to initialize the ZND solver, the leaked fuel was kept as an inert species for the remainder of the ZND marching scheme. For clarity's sake, one can think of the velocity-decrementing sweep in blue as having the wave speed as an input, while the heat release is the output. For the equivalence ratio and the leaked fuel sweep, the heat release is now the input, and the wave speed becomes the output. In addition, the heat release plotted on the y-axis is normalized by the ideal heat release.

It is clear that all of the profiles are a near-match, showing a decrease in one parameter corresponds to a decrease in the other. One key takeaway from this figure is that manually decreasing the wave speed (blue) provides the same output as specifying a leaked fuel fraction (magenta). That is, the decrement in wave speed captures the same physical effects as the leaked fuel fraction. The question remains as to the causal chain for these effects. On the one hand, the logic holds that if fuel is not combusted within the detonation region, then the performance will decrease. This can be calculated directly from the conservation equations by noting that the energy released would decrease. However, this result could suggest that any external process that reduces the wave speed (area change, friction, etc.) will result in a decrease in the maximum amount of fuel that can be consumed within the detonation wave.

It is likely that both of these aspects are at play, and if the model framework allows for it, the contributions of each can be dissected. For this research, however, this topic remains a question for future efforts.

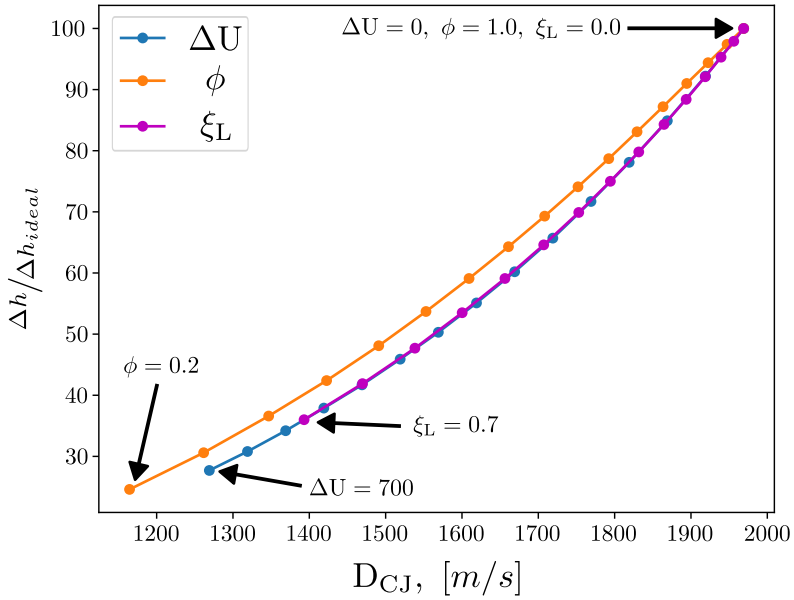


Figure 2.30: Heat release versus ideal as a function of velocity decrement and equivalence ratio.

The final area of interest that arose from the prior results is the discussion around a weak detonation wave. For reference, if a wave speed is seen near the product gas speed of sound, do we have a detonation wave of a simple deflagrative combustion wave? We have seen many non-ideal mechanisms that adversely affect the performance of the detonation wave, and the combination of all of the above could result in an exceptionally low wave speed. So, to determine whether or not a detonation is achieved in a practical device, we can return to some of the key characteristics of detonation waves discussed in Section 1.1.

By definition, the CJ plane is sonic with respect to the wave, and as the velocity of the wave decreases, it means that less fuel is required to burn before thermal choking begins. Here is the interesting takeaway: these velocity-decremented ZND solutions still meet the definitions for a CJ detonation, but at a reduced fuel consumption. We can prove this concept by examining the $P - \nu$ diagram for the velocity-decremented ZND profiles shown in Figure 2.31. The solid black line represents the shock Hugoniot for the initial conditions, assuming an average ratio of specific heats across the shock. Each ZND profile's Rayleigh line is plotted as a solid line, where the color in each sub-figure represents the velocity decrement in $[m/s]$. Along with the Rayleigh line, a new Rankine-Hugoniot (RH) line is plotted as a dashed line. These RH lines were constructed using the heat release value calculated with Equation 2.52 and the average ratio of specific heats through the ZND profile.

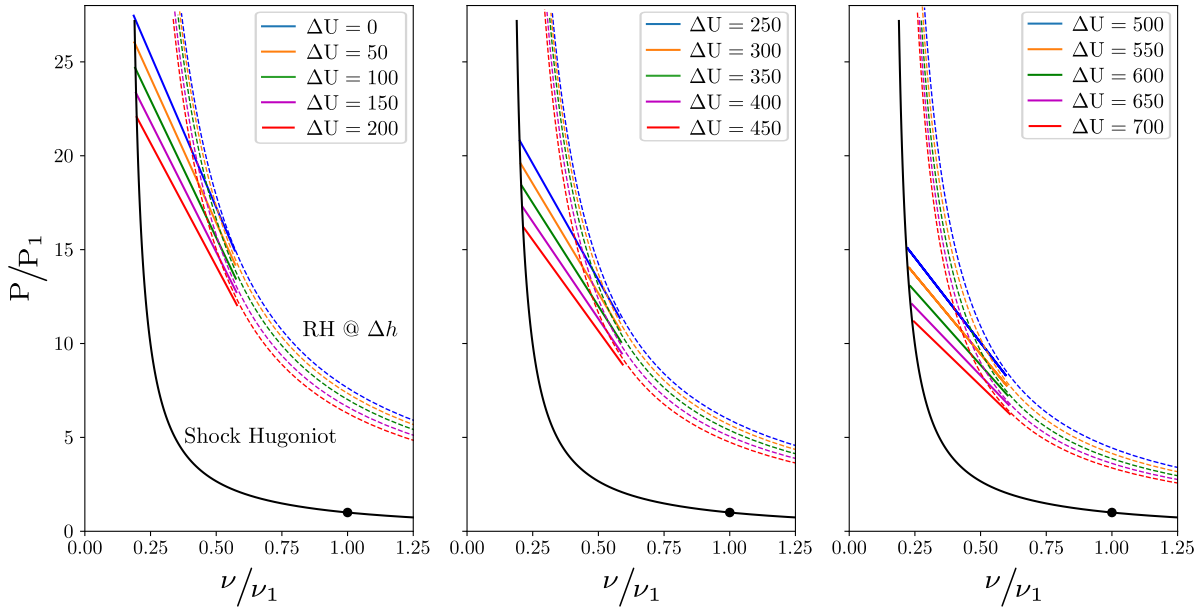


Figure 2.31: $P - \nu$ Diagrams at Different Velocity Decrement Values.

The first takeaway is that each ZND solution follows along the same shock Hugoniot but at different pressure and density ratios based on the speed of the shock. This comes as no surprise, but it is good to check for consistency in the solver. Next, and more importantly, each Rayleigh line is tangent to the associated RH line at the calculated heat release. This is another definition of a detonation wave, a shock coupled with heat release, resulting in thermal choking behind the wave at the CJ plane. Now, we have demonstrated, alongside the results from the Deflagration Loss Model, that a detonation wave moving at a reduced speed still meets all criteria for a CJ detonation; however, now it is at a lower heat release value or with a differing initial condition due to parasitic combustion. These results suggest that wave speed and pressure ratio alone and/or normalized by ideal are not adequate classification metrics for a detonation wave. We have shown in multiple models that all of the criteria for a detonation wave are met depending on the loss mechanism, but the performance decreases from what the ideal CJ analysis predicts.

2.5 Conclusion

This chapter was dedicated to the study of loss mechanisms specific to detonation waves. We introduced these mechanisms, along with some definitions of detonation performance. These loss metrics included deflagration combustion based losses, specifically focusing on parasitic combustion occurring before the wave and fuel that leaks through the detonation before contributing to the detonation heat release. These results show a decrease in performance as each loss metric was increased, where the parasitic combustion had the more significant impact.

Next, a study was conducted to examine other non-ideal effects impacting the detonation wave directly. These included area changes between the pre-detonation state and the CJ plane, which simulate lateral relief of the wave, momentum losses through effects like friction, and heat transfer out of the detonation wave to a given boundary conditions. In general, each metric produced a decrease in the detonation wave performance; however, the area ratio did not produce a significant change in the wave speed using a non-ideal CJ solution technique. Further examination of a non-ideal ZND solver showed that the area change would indeed produce a change in the wave speed but is only captured using the ZND solver with finite-rate chemistry.

The non-ideal CJ solver was then used in concert with the deflagration loss model to show the overall sensitivity of the detonation performance to each loss metric. Across the board, it appears that the parasitic combustion fraction produced the largest impacts on the performance of the detonation wave, while other loss metrics provided moderate impacts across different performance metrics.

Finally, this chapter provided a discussion on the classification of a weak detonation wave versus a similarly performing deflagrative combustion wave. With certain combinations of losses, the detonation wave will produce a performance output similar to that in a deflagration wave, but it will still exhibit the defining characteristics of a detonation. This result makes the determination of detonation combustion more difficult. Across this chapter, the performance of a non-ideal detonation wave was studied; however, additional modeling and analysis are required to determine if the loss in detonation performance has an impact on the performance of a device relying on detonation combustion. This system-level performance and associated loss mechanisms will be discussed in detail in the next chapter.

CHAPTER 3

Loss Mechanisms Specific to Rotating Detonation Combustors

The following chapter discusses the loss mechanism that affects the performance of RDCs. We will first introduce some performance metrics of interest that are affected by the loss mechanisms and that we seek to model. We will then describe each loss mechanism in detail, as well as provide examples of these mechanisms in literature. Next, a discussion of the models used to capture the effects of these losses will be provided, followed by the results of these models. Finally, a conclusion on the impact of these losses and mitigation strategies will be provided.

3.1 RDC Performance Metrics

Chapter 2 discussed the loss mechanism specific to the detonation wave, regardless of whether they were the result of the RDC flowpath characteristic, and how the performance of the detonation wave is affected. Performance decreases within the detonation wave itself and may or may not be perfectly correlated with the performance of the RDC system. It is important to note that the performance metrics for the detonation wave are not the same as those used to describe RDC performance; therefore, this section will give an overview of the performance metric of interest used in this analysis.

The first metric is the pressure gain, as defined by Kaemming and Paxson.[27] This quantity seeks to capture the cycle-averaged total pressure ratio between the exit plane of the RDC and the RDC inlet and is used as a marker to determine the additional thrust or work extraction available as a result of the detonation-based combustion cycle. On this front, thrust and specific impulse are also terms that are used to describe the performance of direct thrust-producing applications.

$$PG = \frac{P_{t,8}}{P_{t,3}} - 1 \tag{3.1}$$

where station 8 is at the RDC exit plane and station 3 is in the RDC oxidizer plenum.

Whether air-breathing or rocket style, RDC thrust (or specific impulse) provides a metric that is both measurable and specific to the application. It *can* also provide a metric for which other combustion-based cycles may be compared to RDCs. A great example of this is in rocket-style RDC, where thrust and specific impulse are both critical measurements for the final application and can be related to standard rocket motors. The specific impulse also directly relates to the next performance metric, combustion efficiency.

Although not a metric that would demonstrate a performance gain, it is a metric that measures how well the RDC is using the energy provided within the fuel of choice. It can be a comparison point when combined with other performance metrics, such as thrust, to project the performance of RDCs, given a more complete combustion process. In most cases, this metric is also specific to the RDC in question rather than an application, as poor combustion efficiency would be corrected before the RDC was ever used in that application.

Specific to air-breathing applications, inlet pressure losses are a critical metric in determining the performance of a system using a RDC. We have already touched on the fact that the performance of the detonation wave has an inverse correlation to this term (see Section 2.4), and because it is related to pressure gain, the inlet pressure drop is nearly perfectly correlated. Although the effects of the inlet pressure losses will be captured in other performance metrics, it is important to try to distinguish them from other losses. This will provide insights on how to mitigate inlet losses while not increasing the impact of other loss mechanisms.

Finally, we examine the potential for entropy production in the RDC combustion process. From the CJ analysis and the results in Section 2.4.1, combusting fuel in a detonative manner will reduce the entropy produced versus deflagration under the same initial conditions. The key aspect is the reduction of the combustion entropy. Within the rest of the RDC cycle, other forms of entropy production exist that could potentially outweigh any reduction from the combustion process. It should be noted that entropy production is difficult, if not impossible, to measure directly, so this metric is more suited to modeling the RDC cycle.

3.2 Loss Mechanism Description

The following sections provide a detailed description of each loss mechanism studied in this research effort. Additional historical information on each mechanism will also be provided.

3.2.1 Inlet Blockage

Inlet blockage is a phenomenon specific to RDC devices, especially air-breathing RDCs, as the oxidizer plenum is exposed directly to the combustion chamber. Due to the local pressure rise in

the detonation region, there exists the potential for back-flowing product gases and a large fraction of the inlet being blocked to forward flow.[53, 54, 55, 56, 57, 58, 59, 5] The effect is especially evident in RDCs operating with large inlet to channel area ratios, operating with low channel static pressure to plenum total pressure ratios, or operating at low plenum pressures relative to the expected post-detonation pressure. For the first two cases, convention would say the inlets are high performing due to the lower inlet pressure losses.[4] The detonation wave provides a continually propagating region of high-pressure post-combustion gases that blocks the inlet, which potentially limits the effective performance that these devices can achieve.[59] As we will discover throughout this chapter, inlet blockage and detonation performance are inversely correlated, which means that there is no method, outside of a valved inlet, to reduce inlet blockage and improve detonation performance. The remainder of this section will discuss historical examples of inlet-related studies, specifically focusing on the blockage and backflow aspects.

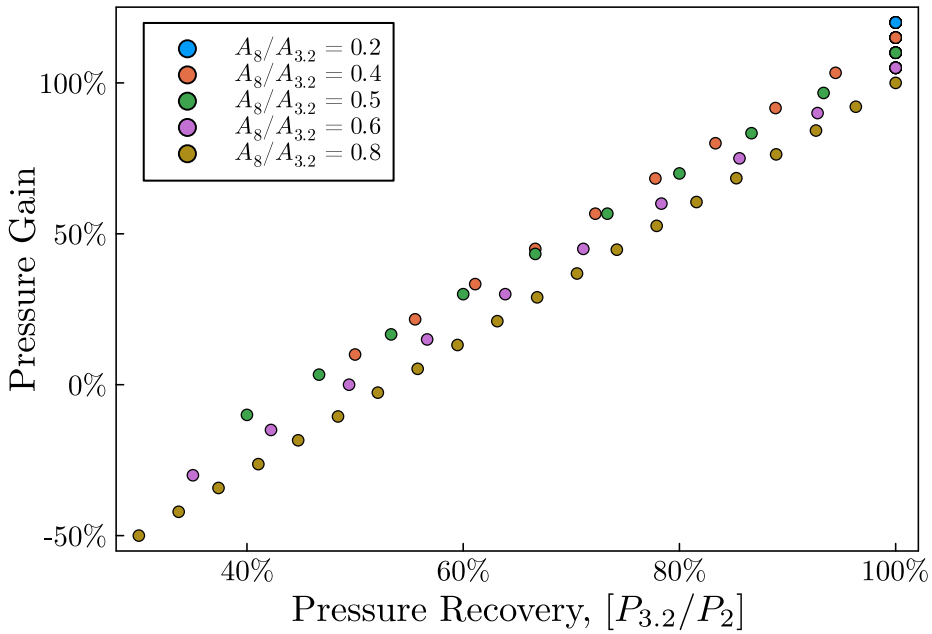


Figure 3.1: Scaling of Pressure Gain through a modeled RDC with respect to inlet pressure recovery. Data taken from Kaemming et al. [4].

The reason for inlet blockage being a critical loss metric comes from the work of Kaemming et al. who examined the effects of different loss mechanisms on the predicted pressure gain of a modeled RDC operating in a ramjet configuration.[4] Their results showed a highly linear correlation between the pressure recovery through the inlet of the RDC and the predicted pressure gain. Figure 3.1 shows a scatter plot of their data at five different nozzle to channel area ratios, $A_8/A_{3.2}$. Although the magnitudes of the pressure gain varied with the nozzle area ratio, the scaling with

respect to the pressure recovery was similar between all geometries, suggesting that if one seeks to improve the potential for pressure gain, the inlet pressure recovery is a key metric to address.

Through the use of a reduced order model, Bedick et al. examined the inlet dynamics associated with the blockage caused by the detonation wave. Their model determined that the inlet blockage based on the amount of time pressure behind the detonation wave was above the driving plenum pressure.[57] Therefore, their form of inlet blockage can be formulated according to the following definition of *blockage ratio* BR:

$$\mathrm{BR} = n_{\mathrm{waves}} \frac{t_{\mathrm{int}}}{\tau_{\mathrm{wave}}} \tag{3.2}$$

where t_{int} is the time in which the channel pressure is higher than the plenum pressure, τ_{wave} is the rotational time of the wave, and n_{waves} is the number of waves. Based on this metric, Bedick et al. also defined the effective area of the inlet based on the calculated blockage ratio according to

$$A_{\mathrm{eff}} = A_{\mathrm{min}}(1 - \mathrm{BR})$$

This methodology assumes a constant plenum pressure ahead of the inlet, which can then be used to compare with a measured pressure ratio in the channel. Deng et al. used this definition of blockage ratio, but also provided another formulation of blockage ratio.[60] Their version of blockage ratio was defined by assuming the injector is sonic when flowing in the forward direction, along with constant gas properties, and that the pressure rise in the plenum from cold flow to hot flow due to the detonation wave can be related to an area change. At a fixed mass flow rate, which is typically the case for experimental RDC testing, the sonic mass flow rate is simply a function of the pressure and area where $P_{0,Cold}A_{Cold} = P_{0,Hot}A_{Hot}$. With these assumptions, Deng et al. defines their plenum pressure-based blockage ratio as

$$BR_{sonic} = 1 - \frac{A_{Hot}}{A_{Cold}} = 1 - \frac{P_{0,Cold}}{P_{0,Hot}} \tag{3.3}$$

Feleo et al. [5] defined an inlet blockage parameter using a different approach. They refer to *inlet block fraction*, B, as a measure of the ratio between the mass flux through the device during fueled operation, relative to the corresponding mass flux under un-fueled operation (i.e., non-combustion operation) at the same inlet plenum pressure observed during fueled operation. By expressing this quantity in terms of a mass flux evaluated at the actual inlet throat (the geometric area of the inlet, A_{g}), the inlet blockage fraction can thus be defined as

$$B = 1 - \frac{\dot{m}''_{\mathrm{Hot}}}{\dot{m}''_{\mathrm{Cold}|P_{\mathrm{t},3}}} \tag{3.4}$$

This essentially quantifies the change in the inlet conditions caused by the presence of the det-

onation wave and represents the change in the effective flow area (A_{eff}) through the RDC inlet. A blockage fraction value of zero would indicate that the effective area has not changed (i.e., $A_{\text{eff}} = A_{\text{g}}$), while a value of one means that the inlet is impenetrable (i.e., $A_{\text{eff}} = 0$). During operation, the blockage fraction is observed to vary with the operating conditions and geometry over a wide range of possible values ($0 \leq B \leq 1$) [5].

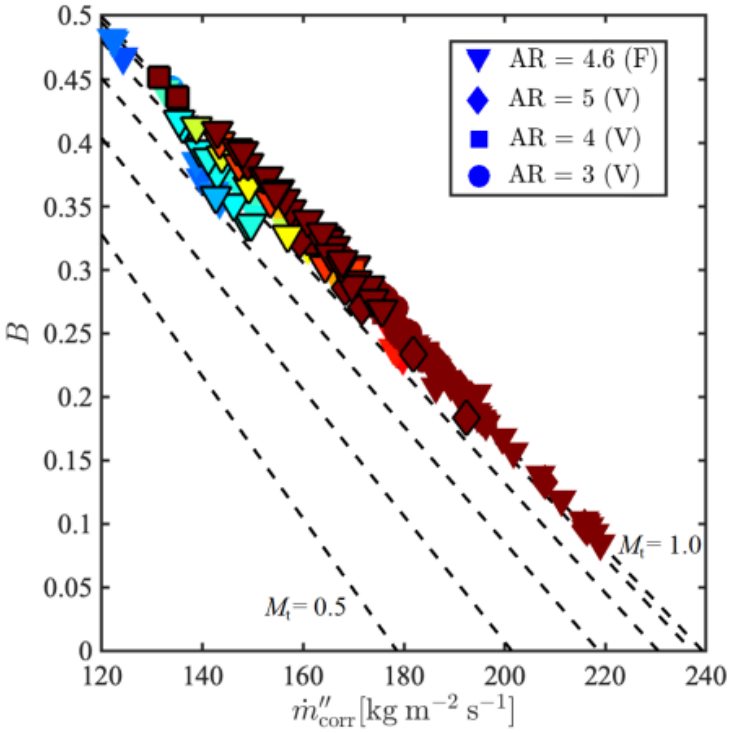


Figure 3.2: Blockage fraction as a function of corrected inlet mass flux. Figure adapted from [5].

Independently of the exact definition of inlet blockage, the concept is a useful metric to quantify the coupling between the detonation wave in the RDC channel and the plenum conditions upstream, where higher values of blockage reflect a plenum that is more significantly affected by the detonation wave. Figure 3.2 shows the blockage calculated for a set of operating conditions and inlet-to-channel area ratios (AR) as a function of the corrected mass flux through the unblocked portion of the inlet. It is important to note that the inlet air temperature and composition were assumed to be standard day temperatures and pure air, which could break down if there is significant backflow into the plenum at high blockage values. This figure also plots lines of constant Mach number (M_{t}) through the unblocked portion of the inlet throat (i.e., through the effective area $A_{\text{eff}} = (1 - B)A_{\text{g}}$). The results indicate a non-zero value of blockage fraction when operating in a detonative mode (independently of the exact characteristics of one or multiple competing

detonation and secondary waves), and these values nearly completely collapse along the $M_{\mathrm{t}} = 1$ inlet (throat) condition. This suggests that the Mach number in the unblocked portion of the RDC inlet is, under most conditions, sonic during operation. An exception could be at higher levels of blockage, where the trend deviates, but the inlet throat Mach number remains larger than about 0.7. Larger magnitudes of inlet blockage would likely be correlated with a higher likelihood of backflow into the air plenum, changing the air temperature and/or composition.

Another important finding associated with the unblocked region of the inlet being choked is the potential for a larger plenum to channel static pressure ratios, $P_0/P_{\mathrm{s,ch}}$, across the inlet. This increase pressure ratio is unfortunately directly at odds with the results from Kaemming et al.[4], where the higher performing RDC configuration, in terms of pressure gain, was achieved at a higher inlet pressure recovery (lower plenum to static pressure ratio). A sonic inlet, even for a fraction of the cycle, can produce a low pressure recovery in the RDC channel and at some conditions, it will produce super-sonic inflow for part or all of the inflowing region ahead of the detonation wave.

Schwer and Kailasanath saw similar results of inlet choking through the flowing region in a two-dimensional computational study of a RDC with a non-ideal inlet.[55] Their research compared the results of two non-ideal inlet models with the normally used ideal inlet, where an ideal inlet allows for no backflow into the plenum. The results were shown for all three models on an inlet consisting of fifty injection ports, with an effective area ratio between the channel flow area and the injectors of 0.2. One interesting finding of their results was the Mach number profile through the inlet injectors across the cycle, where the injectors ahead of the detonation wave are all sonic through their minimum area, resulting in under-expanded jets in the fill region of the RDC. Much like the results from Feleo et al., the Mach number profile through unblocked injectors appear to be sonic, or approaching sonic as the wave passes further away from the injector.

The Schwer and Kailasanath work also show the pressure perturbations from the detonation wave propagated back upstream into the air plenum for the non-ideal inlet cases. This is also shown in experimental measurements through the use of high-speed pressure measurements. Research conducted on the UM RDC on axial type air inlets of various geometries showed pressure perturbation from the detonation wave propagate back upstream into the plenum, despite operating a higher inlet mass fluxes that would choke the inlet.[58] This result suggests that the inlet must be un-choked during a portion of the cycle for any pressure perturbation to propagate back into the plenum. Based on this data-set, there appears to be a correlation between a detonation operation and the inlet being, on average, un-choked. Even if the forward flowing portion of the inlet is choked, if there is any blockage, the average inlet Mach number across the whole cycle will be less than one by definition.

From an average inlet flow perspective, the pressure recovery can be increased by operating the inlet at a lower corrected mass flux, essentially lowering the Mach number through the inlet.

However, from the perspective of a RDC, a less restrictive inlet can result in higher blockage [5] or higher inlet backflow, as shown in a numerical study conducted by Paxson and Miki.[59] Their research computationally examined the inlet backflow, and the resulting performance changes, in both a quasi-two-dimensional and three-dimensional RDC. They define an inlet diodicity metric to which the performance characteristics were compared. The inlet diodicity term, Equation 3.5, quantifies the amount of backflow into the plenum caused by the detonation wave. By allowing backflow in their simulation, they saw reductions in the potential for pressure gain, where the limiting condition they explored reduced performance to that of an ideal constant pressure combustor. These results echoed the results of Kaemming et al.[4] in that plenum dynamics are a large contributor to the overall reduction in RDC performance, at least from a modeling standpoint. One key trade-off of particular interest to this study is the relationship between the stiffness of the air inlet on an air-breathing RDC and the propensity for reverse flow through said inlet during detonation operation, which has consequences on operability and realized performance [59]. Here inlet stiffness is defined as the static to total pressure ratio between the RDC channel and the plenum, respectively.

$$\delta = 1 - \frac{A_{\mathrm{i,back}}}{A_{\mathrm{i,forward}}} \tag{3.5}$$

where, $A_{\mathrm{i,back}}$ is the effective backward-flowing area and $A_{\mathrm{i,forward}}$ is the effective forward-flowing area of the inlet. This term allowed for the exploration of inlets with asymmetric forward and backward flow characteristics, where an ideal inlet would be a perfect diode, $\delta = 1$, which allows no flow from the channel back into the plenum. As expected, the higher the diodicity of the inlet, the lower the percentage of backflow and the higher the pressure gain. The issue that now arises is that the pressure gain is dependent on the pressure recovery through the inlet, while simultaneously depending on the backflow through the inlet. A low backflow inlet might feature restrictive areas, high corrected fluxes, and/or restrictive geometric features that negatively affect forward-flowing characteristics. In any of these cases, the pressure gain now becomes a trade-off between backflow and pressure recovery, two terms that are inversely correlated.

The results from previous studies suggest that the pressure gain in the RDC operation is highly dependent on the flow characteristic of the inlet. On the one hand, the inlet should be operated in a less restrictive configuration to improve pressure recovery. On the other hand, this is likely to increase the responsiveness of the plenum to the detonation wave, also increasing the probability of inlet backflow and blockage.

3.2.2 Incomplete Combustion, Deflagration Losses and Product Gas Re-Circulation

The majority of the discussion on deflagration losses and product re-circulation effects was provided in Section 2.2.1. These effects directly impact the performance of the detonation wave, but are a factor caused by the RDC configuration. Like discussed in the previous section, the plenum of the RDC is directly exposed to the combustion channel. This, in concert with the high pressure, post-detonation gases, allows for backflow and mixing of product gases with the fresh incoming reactants. This elevates the temperature within the reactant mixture, elevating the potential for pre-detonation ignition. Product gas re-circulation, even without pre-ignition, will increase the speed of sound ahead of the detonation wave, resulting in reduced detonation performance. This reduction in performance will likely trickle downstream and reduce the overall cycle performance.

Even without product re-circulation from the backflow products, the fill region will be in contact with post-combustion gases for a large fraction of the cycle time. Kaemming et al. showed that this layer can also produce a mixing of the two streams and modeled any pre-ignition in this region based on a laminar flame speed argument.[29] Regardless of the cause of the product gas re-circulation and pre-ignition, these likely reduce the overall cycle performance and within an RDC cycle would be extremely difficult to eliminate completely.

One other key benefit proposed for RDC is the high energy density, due to the larger mass flux operation versus a deflagrative device.This theoretically allows the RDC to consume the same amount of fuel at a much more compact size, which is a great benefit for rocket-style RDCs. However, in an air-breathing configuration, the compact design can raise additional concerns. Aside from cooling the combustor walls with the higher heat loads, the compactness of the device can also affect the combustion efficiency. We have seen that there exists the potential for leaked fuel through the detonation wave in Chapter 2, now we shift our focus to what happens to this fuel after leaking through the detonation wave. With this high flux through the RDC channel, it is likely that some of this leaked fuel will exit the RDC channel before combusting, reducing the combustion efficiency and reducing the compactness benefit.

3.2.3 Non-Zero Azimuthal Velocity

The following section discusses the presence of non-zero azimuthal velocity within the RDC flowpath. This includes both in the inlet region ahead of the detonation wave and at the exit plane of the RDC. Due to the boundary conditions present in RDC flowpaths, this non-zero azimuthal velocity profile is likely self-exited by the detonation wave, and produces different losses depending on the location and magnitude of the azimuthal velocity. In the inlet region, this will primarily affect the detonation wave and inlet performance, whereas at the exit plane it will reduce the thrust of

the device. Each scenario will be examined in more detail in the following sections, along with examples of these phenomena in experimental and computational settings.

To introduce the concept of non-zero azimuthal velocity throughout the RDC flowpath, Figure 3.3 shows a computational result of the laboratory frame particle paths within an RDC device. This figure provides an example of both the non-zero azimuthal velocity in the inlet region, as well as the larger variations in azimuthal velocity at the exit plane. Another relevant aspect of Figure 3.3 is that depending on where the exit plane is defined, the magnitude and variance in the azimuthal velocity will also change drastically.

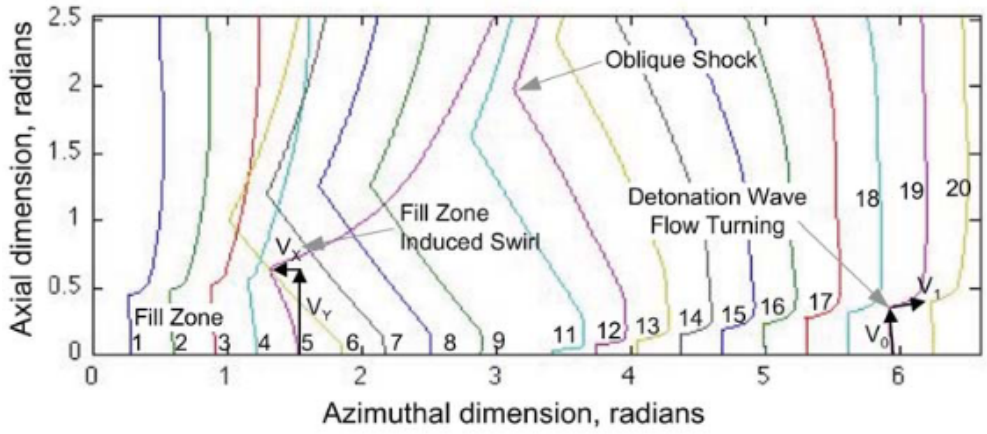


Figure 3.3: Example of Laboratory Frame Particle Paths within a RDC Flowpath.[6]

Figure 3.4 extends this example to a set of RDC simulations with additional hardware after the RDC exit plane. Moving from bottom to top shows the RDC alone (c), the RDC with an inner- and outer-body extension (b), and the RDC with the extension and a converging-diverging nozzle. This figure shows the development of the azimuthal velocity (swirl) as a function of the RDC length, which varies in magnitude and variance over the length of each configuration. Finally, Figure 3.4 (a) provide some insights on the required post RDC flow conditioning required to remove the larger perturbations in swirl generated by the detonation wave.

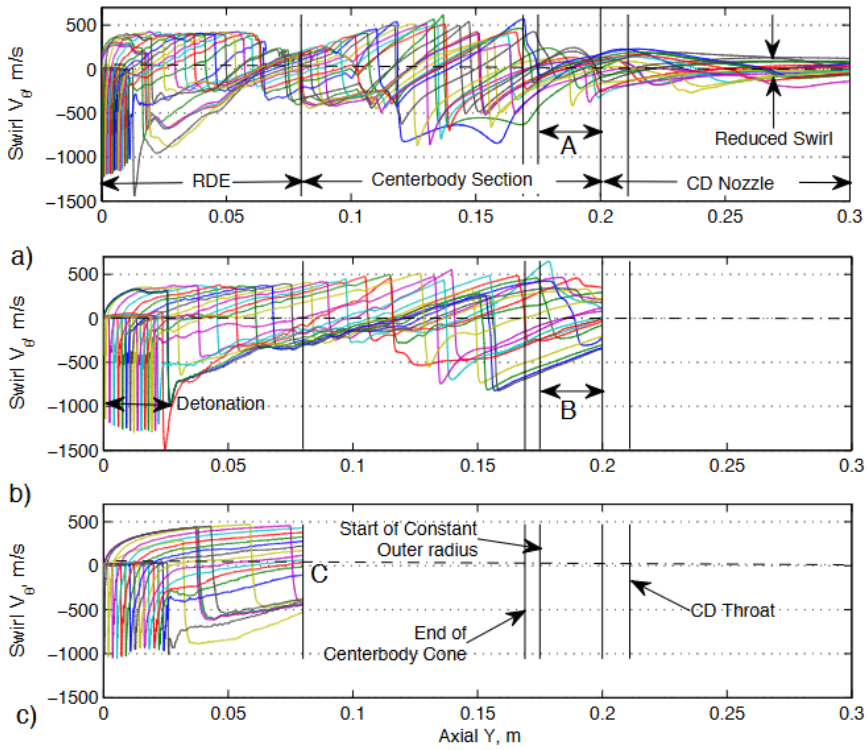


Figure 3.4: Azimuthal Velocity Components of Various Particles within RDC geometries. Standard RDC configuration (a), RDC with Extension (b), and RDC with Extension and Converging-Diverging Nozzle.[7]

3.2.3.1 Inlet Plane and Pre-Detonation

This section examines the fluid velocity profiles in the inlet region of the RDC, just ahead of the detonation wave. Typically, the inlet region fill velocity is thought to be purely axial with no azimuthal component. Several prior computational and experimental results have shown that this might not be the case.[16, 6, 61, 62] In 2-D computational study on RDCs, Nordeen et al. examined the paths of multiple particles as they propagate through the wave. These particles paths were initialized at various azimuthal locations around the RDC channel, allowing for the capture of the state diagram of the particles through a single cycle of the RDC (see Figure 3.3).[16, 6] For the present section, the most relevant finding from Nordeen et al. was the path-lines in the fill region of the RDC. Just after the wave passes, the particle paths of the fresh reactants are perfectly axial, which was shown as the y-direction in the study. This is the typical assumption of the inflow velocity of the fill region and depending on boundary conditions specified in the CFD simulation, and this may be enforced by any inlet sub-model. However, further downstream of the initial fill region, and hence a further distance from the previous passing wave, the particle paths begin to turn towards the incoming wave with the highest degree of turning (up to 20° off the axial direction)

directly ahead of the detonation wave. These results indicated that the assumption of purely axial inflow in the fill region of a RDC may need to be revisited.

On the experimental side, Andrus et al. studied a pre-mixed, hydrogen-air RDC operated at a stoichiometric condition and 0.38 kg/s.[61] Their research was primarily to study the effects of pre-mixed RDCs; however, the high speed video imaging captured luminescent particles during the run. These particles were not intentionally placed in the RDC, so there were only five particles that could be analyzed. Their analysis showed that the particles had a non-zero azimuthal velocity profile throughout the cycle, and specifically had azimuthal velocities ahead of the wave between 100-200 m/s in the direction opposite of the wave propagation. These results echoed what was seen in Nordeen et al. but in an experimental setting on a completely different geometry with higher azimuthal velocity magnitudes.

In recent years, other experimental particle imaging velocimetry (PIV) experiments have been conducted to include exhaust plane measurements conducted by Depperschmidt et al. and channel PIV measurements directly ahead of a nozzle section in Tobias et al.[63, 8] None of these studies examined velocities in the fill region of the RDC; however, they provide information on the velocity profile downstream of the combustion process, which has other effects on performance and is the subject of further investigation. These research efforts confirm the complex flow field in the RDC cycle with a non-zero azimuthal velocity profile throughout the locations examined. Another experimental PIV study in RDCs was conducted by Dunn et al. on a stoichiometric hydrogen-air RDC.[64] This research only presented a single time step of the PIV measurement and compared the results with the CFD particle paths. Due to the lack of available data in this study, no conclusions could be drawn about the flow field before the detonation wave.

Initial experimental particle tracking measurements were conducted at the University of Michigan, on the Pintle style injector configuration discussed by Duvall et al.[65] Though not classic PIV, these measurements were made with high speed imaging of luminescent particles that appeared within the flow field at the inlet region of each test. These particles appeared in the same manner as discussed in [61], but in a much larger number. Three cases were carried out at a mass flow rate of 150 g/s and equivalence ratios of [0.6, 0.8, 1.0]. Figure 3.5 shows an example of the particle paths captured during the steady segment of the leanest run, denoting the somewhat arbitrary regions of interest in relation to the wave's location in the cycle. The particle paths showed non-zero azimuthal velocity varying throughout the cycle, with a significant negative azimuthal velocity profile just ahead of the detonation wave. This indicated that there exist the potential for non-axial flow in the inlet region due to the complexities of the detonation process within the RDC cycle.

From the data shown in Figure 3.5, it was determined that the azimuthal velocity profile ahead of the wave was roughly -$158 \pm 26 m/s$, moving towards the next incoming detonation wave.

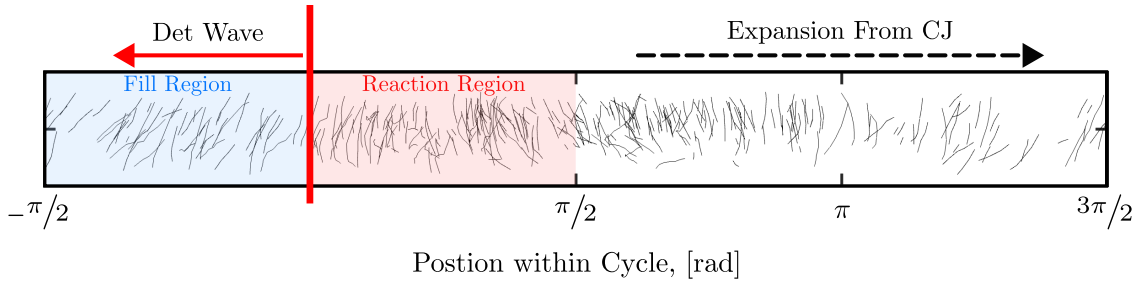


Figure 3.5: Inlet measurement of luminescent particles through RDC cycle.

Similar results were seen for the case operating at an equivalence ratio of 0.8, with a slightly lower magnitude of -82$\pm$40m/s. Unfortunately, the stoichiometric case exhibited strong, counter-propagating secondary waves, so the particle paths were highly non-uniform depending on the location of the secondary wave. These results are preliminary and additional testing is required to determine the validity of these measurements. However, this data represents a third instance, on a third unique geometry, with a significant non-zero azimuthal velocity flowing into the wave.

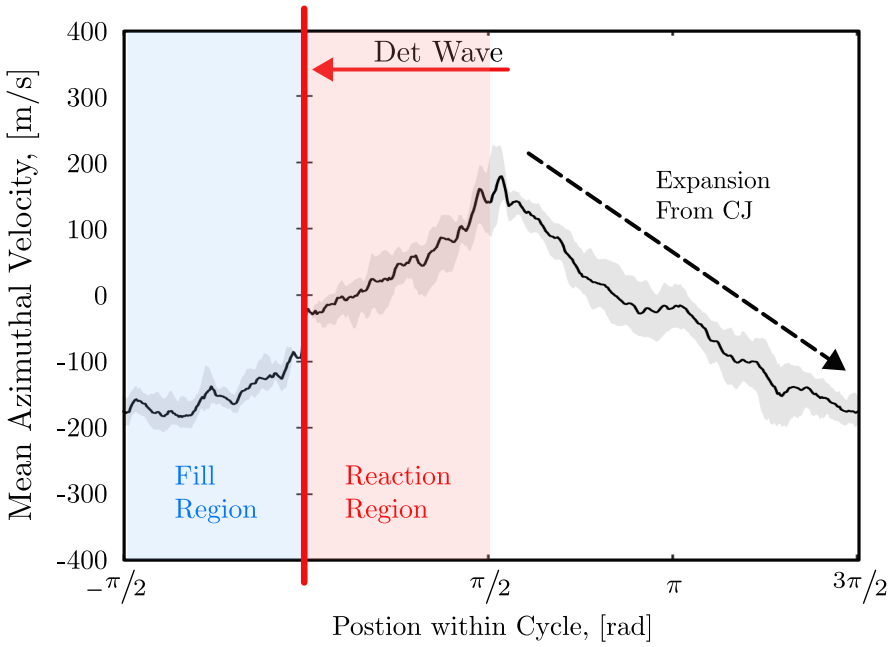


Figure 3.6: Azimuthal velocity profile for an experimental RDC run. Hydrogen-Air operating at 150 g/s air mass flow rate and $\phi = 0.6$.

To better illustrate the non-zero azimuthal profile, the particle paths were binned by azimuthal location and then averaged. Figure 3.6 shows the results of this process for the paths from Figure 3.5. The detonation wave is propagating from the right to left in this figure and shown with the solid red line. The same three region of interest from Figure 3.5 are also shown to give context

about the location, and implications, of the velocity profile of each region. First, the fill region is highlighted with light blue. In this region the velocity is negative, meaning moving in the opposite direction of the wave, with an average magnitude between 100-200 m/s. Next, the reaction region, red shaded, is shown directly after the detonation wave. In this region the velocity profile increases to a peak value nearly a quarter of the lap behind the leading edge of the detonation wave. It would be expected that the post-detonation azimuthal velocity was in the direction of the wave; however, in an ideal detonation the peak induced velocity would be located directly behind the leading shock at the Von-Nuemann condition, (3.1). The reason for the slowly increasing velocity profile is likely due to the size of the particles. Although an exact size of these particles was not known, they were likely too large to react to the sudden change in induced velocity post shock. For this reason, the induction region is labeled up to the peak velocity, even though this boundary may be somewhat arbitrary. Finally, the velocity profile reverts course, accelerating against the direction of wave propagation in the final region, without highlighting. This is attributed to the expansion process the must proceed the detonation wave which was discussed in Section 1.1.1.1 as the process from the CJ plane, (3.2), to the post-detonation expansion state, (3.3). This process has been discussed previously, and can also be seen clearly in the results from Watanabe et al. who show the laboratory frame velocity profile experimentally measured in a radial style RDC.[66]

3.2.3.2 Moving Shock Wave with Non-Zero Incoming Velocity

To assist with the analysis of the inlet plane non-zero azimuthal velocity profile, some prior knowledge about moving shock waves with incoming velocity profiles is required in order to understand the process of adapting this analysis to a detonation wave. A detailed explanation of the effects of non-zero incoming velocity on a moving shock wave of fixed strength is given by Anderson, but a summary of the analysis is provided below.[67] Figure 3.7 (a) shows an example of a standard moving shock wave, moving from right to left in the laboratory frame of reference (subscript l). In this example the medium through which the wave is propagating, (1), is initially at rest, $u_1 = 0$, which allows for the simple transform into the wave reference frame (subscript w). As the wave passes through the medium, the shock induces a velocity, $u_{\mathrm{i,l}}$, which pulls the post-shock fluid, (2), in the direction of the wave propagation (in the laboratory frame). In this analysis, W_* just references the wave's speed, while u_* is the velocity of the gas at each state.

The analysis was then extended to examine the effects of an incoming velocity profile ahead of the shock wave, shown in Figure 3.7 (b). For this example, the strength of the wave is fixed, which is shown as a constant wave velocity in the wave frame of reference, W_{w}. A non-zero incoming velocity, u_1, reduces the velocity of the shock wave in the laboratory frame, W_{l}, subsequently reducing the induced velocity in the laboratory frame, $u_{i,l}$. As explained by Anderson, because

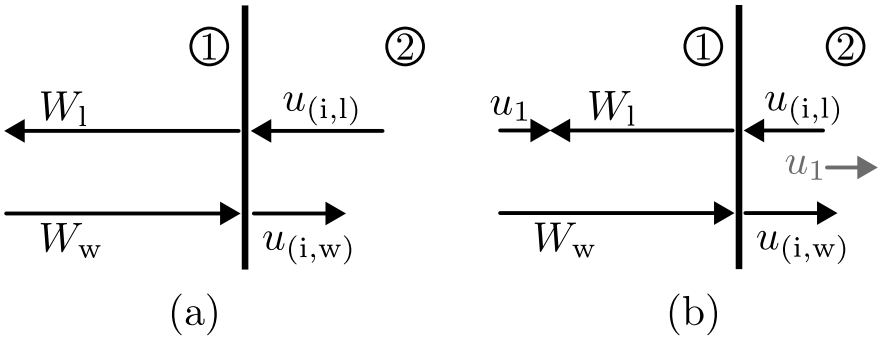


Figure 3.7: Fixed strength shock wave moving from right to left into quiescent flow (a) and flow with a non-zero incoming velocity (b). Pre-shock state is given by ① and post-shock state is given by ②

the shock is fixed strength (fixed incoming velocity in the wave frame, W_w) the non-zero initial velocity, u_1, is simply subtracted from the wave speed in the wave frame, W_w, producing the wave speed observed in the laboratory frame, W_l

When assuming the same static pressure ahead of both waves, and a shock of fixed strength, the static pressure behind the shock wave with incoming flow is also constant between the two cases. However, the state at the induced velocity of (b) is now less than that of (a), meaning a lower total pressure or total enthalpy. This represents a decrease in the usable work in the post shock state of (b). Viewed from an energy perspective, the post-shock state in (a) has a higher total enthalpy compared to the post-shock state in (b). A similar analysis can be applied to a detonation wave of fixed strength, which will be discussed in the Methodology section. In should be noted that because the static pressure (and temperature) ahead of the wave is assumed constant between cases but case (b) has a non-zero initial velocity, case (b) also has a higher upstream total pressure, or total enthalpy when frame from an energy perspective. This means the change in total pressure, or total enthalpy, *across* a wave of fixed strength is reduced more than the simple reduction in the total pressure, or total enthalpy, at the post-shock state.

3.2.3.3 Nozzle Plane Velocity Distribution

It was briefly discussed in Section 3.2.3.1, but like the inlet plane, the exit plane of the RDC is not at a constant axial velocity across the cycle. The non-zero azimuthal velocity effectively reduces the energy available for thrust production in the axial direction.[27] Experimental PIV studies have shown a large fraction of non-zero azimuthal velocity across the exit plane profile.[63, 8, 68] Not only does this effect make direct integration with turbomachinery problematic, it also results in a loss of thrust performance as the azimuthal velocity magnitude increases. These effects can also be seen in computational studies, in which particle tracking was conducted.[16, 6, 7, 9]

Figure 3.8 shows experimental results using PIV at the exit plane of a RDC.[8] The left subplot shows the distribution of the azimuthal velocity measurements, while the right subplots shows the axial distribution. From these, measurements, and the computation results shown in Figure 3.3, we can conclude that the exit plane azimuthal velocity profile of the RDC has highly variant probability densities. The swirl must be imparted by some exchange in momentum within the flow field, and an associate transfer in kinetic energy. Because this velocity is not acting in the direction of the thrust production, it acts as a direct loss in thrust performance of the RDC. Higher variations in the azimuthal velocity profile would incur a larger penalty in thrust, which would be depended on the location of the detonation wave relative to the exit plane (see Figure 3.4). Upon review of the previous historical data, it also appears that the azimuthal velocity profile is self excited by the detonation wave, the general RDC flowpath, or a combination of the two.

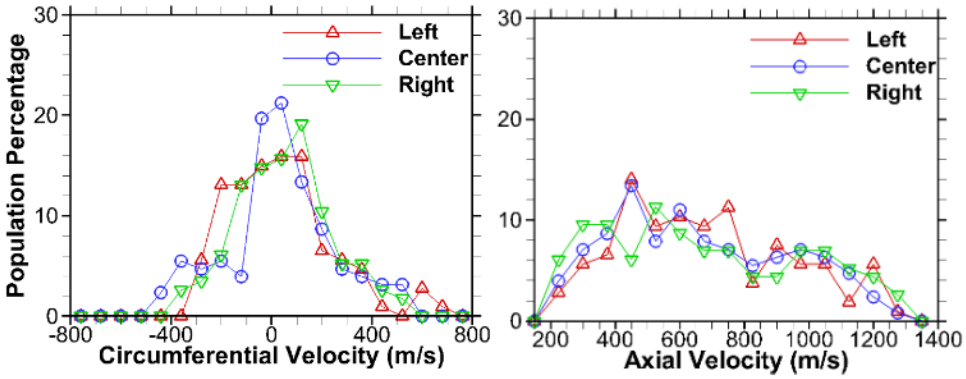


Figure 3.8: Experimental Exit Plane PIV Results.[8]

3.2.4 Post-Detonation Expansion, Heat Transfer and Friction in RDC Flowpath

This section focuses on the post-detonation heat transfer and friction effects within the RDC flowpath. Section 2.2.3 and Section 2.2.4 discussed how this effects the performance of the detonation wave, but now we shift focus to these effect the post-detonation gases. After the detonation wave (marked by the CJ plane), there is still substantial expansion within the cycle caused by the difference in the detonation area with respect to the remaining area of the RDC flowpath (see Section 1.1.1.1 and Section 3.2.3 from above). Figure 3.9 shows a simple example of the relationship between the area of the detonation products at the CJ plane defined by continuity (blue) and some post expansion area downstream of the detonation wave (cyan). This example is shown in the wave frame of reference, and is indicative of the how the boundary conditions of the RDC allow, or enforce, a large post-detonation expansion within the RDC channel. For this example, it is assumed

that the mass flow rate going into the device also goes through the detonation area, as well as the example post-expansion areas shown. Depending on the configuration of the RDC, the mass flow rate, and the wave speed of the detonation, these area ratios can be well above 10, resulting in expansion to atmospheric pressures, or below, within the RDC channel.

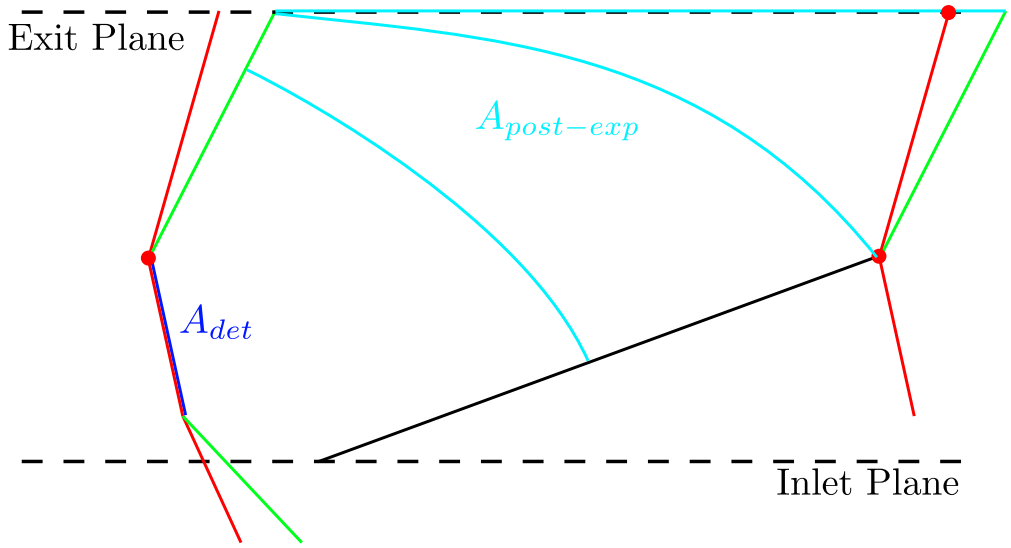


Figure 3.9: Example of the Change in Area from the CJ Plane to a Post-Expansion Location

Typically, this process is modeled as an isentropic expansion, either through a simple model or through the method of characteristic formation of choice.[31, 69, 39, 9] (Section 3.3.1) In reality, there will still be heat transfer and frictional forces effecting the post-detonation gases that require accounting. These effects can significantly reduce the gas temperature and the total pressure of the product gas exiting the RDC, resulting in a decrease in cycle performance. We can model these effects using a one-dimensional flow integrator that includes these loss mechanisms, referred to as a generalized one-dimensional flow solver, and developed by Hodges.[70] With this modeling methodology, we can include the area expansion, heat transfer, and friction as the post-detonation gases expand toward the RDC exit plane.

3.3 Modeling of RDC Losses

Now that the RDC loss mechanisms and physical processes have been described, the next step is to develop reduced order models that all for the study of each mechanism with regard to the performance of RDCs. These models include a state-based RDC cycle model with additional losses, a detailed model of the cause and effects of non-zero azimuthal swirl within the RDC flowpath, and finally, a model used to capture the effects of inlet blockage and its coupling with

the performance of the detonation wave.

3.3.1 State to State Cycle Model

As discussed in Section 2.4.1, the deflagration loss model only captures the performance impacts related to the detonation wave, so the following model, termed State to State model, was developed to determine the effects of these loss parameters on the RDC performance through a simple RDC cycle model. Along with the tracking of additional states through the detonation cycle, the State to State model also includes additional loss parameters that describe the distribution of the heat release across all processes occurring within the RDC cycle, along with RDC specific losses. The first loss parameter included is an inlet pressure loss fraction, $\xi_{\Delta P}$, which calculates a pressure drop across the inlet during operation. This value is defined $\in [0, 1]$, where the zero value represents no inlet losses ($P_{3'} = P_3$), and the value of one represents an inlet loss resulting in a channel pressure equal to the ambient ($P_{3'} = P_{amb}$). Having an inlet pressure fraction of one is not realizable in any real device, but the boundaries were set to normalize this loss parameter in a manor consistent with the other losses. It should be noted that this loss term captures a combination of the pressure losses through a non-ideal inlet, as well as the conversion of pressure to velocity through the fill region ahead of the detonation wave. This term can be related to the pre-detonation static channel pressure, $P_{3'}$, through the following relationship:

$$P_{3'} = (P_{amb} - P_3)\xi_{\Delta P} + P_3 \tag{3.6}$$

The next new parameter is the non-commensal combustion fraction, ξ_{NC}. This parameter captures the fraction of leaked fuel, post-expansion, that is not consumed before exiting the RDC. It also is bounded $\in [0, 1]$ like the parasitic and leaked fractions, where a higher value means that less of the leaked fuel burns post-expansion. By definition, if there is no leaked fuel, $\xi_{\mathrm{L}} = 0.0$, then this term becomes irrelevant to the model.

The final new parameter is the commensal combustion pressure fraction, ξ_{NC}. This term captures the average pressure at which the commensal combustion occurs. The parameter is also bounded $\in [0, 1]$, where a lower value indicates a higher combustion pressure. At $\xi_{\mathrm{CP}} = 0.0$, the commensal combustion occurs at the calculated post-expansion pressure, $P_{3.3}$, while $\xi_{\mathrm{CP}} = 1.0$ means that the commensal combustion occurs at the specified ambient conditions, P_{amb}. This term is useful in capturing the average channel pressure downstream of the detonation region, which is often much lower than any ideal pressure calculated through the detonation solver. The relationship between this parameter and the commensal combustion pressure is given below:

$$P_{3.4} = (P_{amb} - P_{3.3})\xi_{\mathrm{CP}} + P_{amb} \tag{3.7}$$

The inclusion of these two parameters follows the methodology of the deflagration loss model, where all parameters are bounded $\in [0, 1]$ and a lower value of a given parameter corresponds to a higher performance of detonation/RDC. Including the new loss parameters, specifically the non-commensal fraction, the partitioning of fuel is shown in Figure 3.10, with equations shown below:

$$\chi_0 = \chi_{\mathrm{P}} + \chi_{\mathrm{D}} + \chi_{\mathrm{C}} + \chi_{\mathrm{NC}} = 1 \tag{3.8}$$

where the leaked mole fraction from Equations 2.29 is further partitioned into a commensal mole fraction, χ_{C}, and the non-commensal mole fraction, χ_{NC}. The parasitic and detonation mole fractions remain the same as in Equation 2.28 and Equation 2.30, where the commensal and non-commensal mole fractions are given in Equation 3.9 and Equation 3.10, respectively.

$$\chi_{\mathrm{C}} = \xi_{\mathrm{L}}(1 - \xi_{\mathrm{P}})(1 - \xi_{\mathrm{NC}}) \tag{3.9}$$

$$\chi_{\mathrm{NC}} = \xi_{\mathrm{L}}\xi_{\mathrm{NC}}(1 - \xi_{\mathrm{P}}) \tag{3.10}$$

With this model formulation, a total combustion efficiency is also defined, shown with the substitution of Equation 3.10:

$$\eta_c = \frac{1 - \chi_{NC}}{\chi_0} = 1 - \xi_{\mathrm{L}}\xi_{\mathrm{NC}}(1 - \xi_{\mathrm{P}}) \tag{3.11}$$

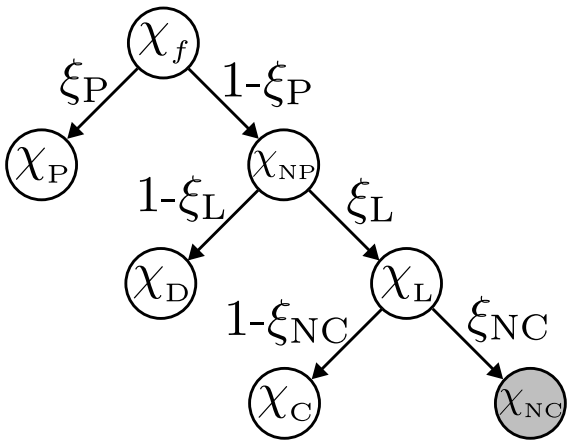


Figure 3.10: Fuel partitioning for State to State Model. Fuel fraction not consumed within cycle shown with gray background.

From this derivation, the combustion efficiency is always 100% if any of the following are true: all of the fuel is consumed parasitically, there is no leaked fuel, or there is no non-commensal fuel. The State to State model captures both the effects of the new loss parameters associated

with bulk flow quantities (inlet losses and RDC channel pressures) as well as properly accounting for detonation-specific process from the Deflagration Loss Model. This model also applies the detonation work correction (see Section 1.1.1.1) in calculating the post-expansion state, (3.3).

Algorithm 9 State to State Model

Require: $\xi_{\Delta P}, \xi_{\mathrm{P}}, \xi_{\mathrm{L}}, \xi_{\mathrm{CP}}, \xi_{\mathrm{NC}} \in [0, 1]$

Initial reactant mixture at plenum conditions: (3)

Apply inlet pressure drop from $\xi_{\Delta P}$(Equation 3.6): (3′)

Run Deflagration Loss Model assuming initial azimuthal velocity pre-detonation is zero ($u_{3_p} = 0$) with ξ_{P} and ξ_{L}: (3.2)

Isentropic expansion to match detonation work, assuming post-expansion azimuthal velocity is zero ($u_{3.3} = u_{3.4} = 0$): (3.3)

Reset (1-ξ_{NC}) moles of fuel to reactive

Set commensal combustion pressure based on ξ_{CP}(Equation 3.7)

Equilibrate remaining reactive fuel at constant commensal pressure/enthalpy: (3.4)

if No Additional Losses **then**

(3.4) = (4)

else

Calculate additional losses: (4)

end if

Calculate I_{SP} expanding (4) to P_{amb}

With the additional states and loss mechanisms included in the State to State model, it was used to examine the performance of both the detonation wave and a modeled RDC cycle. Algorithm 9 shows the steps used to calculate the states in the modeled cycle, as well as the specific thrust output used as one of the performance metrics of interest. Figure 3.11 shows a visual representation of these steps, where additional losses can be applied between (3.4) and (4). For example, a non-zero azimuthal velocity profile can be applied to the exit plane, which effectively reduces the axial velocity component that produces thrust (see Section 3.2.3.3), or an accounting for the oblique shock effects could also be applied here. For the results shown in this chapter, it is assumed that no other losses occur, so (4) is the same as (3.4). This produces the best-case thrust estimate, which will later be compared to the best case thrust achievable in an ideal deflagration device.

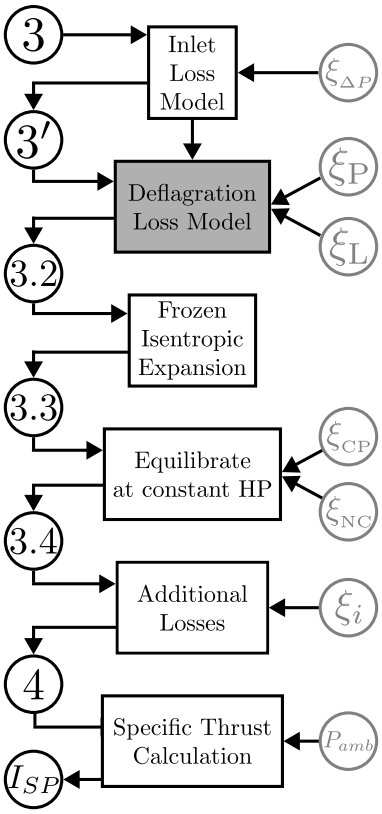


Figure 3.11: State to State Model Diagram.

The specific impulse will be calculated from the change in enthalpy between ④ and the ambient exhaust condition. This assumes isentropic expansion from ④ to an ambient pressure specified in the model, where all of the results in this analysis assume the exhaust pressure to be one atmosphere. Through the calculation of ④ in the State to State model, and Equation 3.12, a specific impulse can be predicted for the model. In the case of this research, the calculated specific thrust will always be normalized by the specific thrust of an ideal deflagration device with the same initial conditions. For this simple thrust model, it is assumed that all expansion from ④ occurs in the axial direction, and the nozzle geometry allows for perfect expansion. This provides the maximum estimated thrust performance of the RDC cycle.

$$I_{sp} = \frac{1}{g_0}\sqrt{2\left(h_4 - h|_{P_{amb},s_4}\right)} \tag{3.12}$$

If the gain of the detonation-based cycle is determined by pressure, PG in Equation 1.18, then the components of the pressure gain can be broken down into their contributing processes included in the State to State model. First, we will define pressure ratio terms that account for the process included in the State to State model. The inlet pressure ratio term, Equation 3.13, relates the static pressure in the channel, pre-detonation, to the total plenum pressure term in Equation 1.18. This

term captures viscous losses, mixing losses, total-to-static pressure conversion into velocity, and other additional processes which modulate the pre-detonation pressure.

$$PR_{inlet} = \frac{P_{3'}}{P_{t,3}} \tag{3.13}$$

Equation 3.14 relates the pre-detonation static pressure to the post-detonation static pressure at the CJ plane, (3.2). This term captures all of the effects included in the Deflagration Loss Model.

$$PR_{w} = \frac{P_{3.2}}{P_{3'}} \tag{3.14}$$

Equation 3.15 is the static pressure ratio of the expansion process from the CJ plane to the post-expansion state, (3.3). The need for this term was discussed previously; however, it is important to note that this pressure ratio scales proportionally to the detonation work term, $Du_{3.2}$.

$$PR_{exp} = \frac{P_{3.3}}{P_{3.2}} \tag{3.15}$$

Finally, Equation 3.16 captures any addition process from the post-expansion state to the final total pressure at the exit of the RDC.

$$PR_{i} = \frac{P_{t,8}}{P_{3.3}} \tag{3.16}$$

substituting these pressure ratios into Equation 1.18 yields:

$$PG \propto PR_{inlet} PR_{w} PR_{exp} PR_{i} - 1 \tag{3.17}$$

This relationship allows us to examine, in a rudimentary manner, the effects of the inlet losses, deflagration losses, post-detonation expansion requirements, and any additional loss on pressure gain across the device. It should be noted that both the inlet pressure ratio and the expansion pressure ratio are less than unity, $PR_{inlet} < 1.0$ and $PR_{exp} < 1.0$. Assuming no additional losses in the system, this means that to achieve a pressure gain across the device, the pressure losses across the inlet and the expansion process must be overcome by the gain across the detonation wave.

Unfortunately, increasing the gain across the detonation (from an energy or pressure perspective) has a negative consequence elsewhere. For example, an improved detonation pressure ratio will have a more severe effect on the RDC inlet flow field, potentially further reducing the inlet pressure ratio term. It would also increase the detonation work requirement as the post-detonation expansion process is proportional to the detonation wave speed.

3.3.2 Non-Zero Azimuthal Velocity Model

The following sections discuss the model implementations used to study the effects of non-zero azimuthal velocity within the RDC flowpath. The first model examines the effect in the inlet region, just ahead of the detonation wave using the conservation of angular momentum to establish a causal link between the phenomena and the detonation wave, and also predicts the magnitude of pre-detonation azimuthal velocity. Finally, a simple nozzle model will be shown that examines the change in thrust given an exit plane velocity profile with varying azimuthal components.

3.3.2.1 Inlet Plane and Pre-Detonation

Analyzing the possibility of non-zero velocity within a RDC fill region required the development of an RDC inlet model that quantifies and predicts the potential azimuthal velocity magnitude. This model and the methods used to determine its implication on RDC performing will be discussed below, but first, the methods for analyzing moving shock waves, Section 3.2.3.2, will be applied to a detonation wave to determine the differences in the pre- and post-detonation state as a non-zero incoming velocity is introduced. This model will be used to examine the ideal detonation wave, but also includes the deflagration loss model, which is discussed in Section 2.4.1, with additional losses and processes.

Section 3.2.3.2 discussed an example problem of a moving shock wave, of fixed strength, into a medium with and without an incoming velocity. This section will expand this analysis to an ideal detonation wave. Figure 3.12 shows an example of the typical ideal detonation process (a), along side an example of a detonation wave propagating into a non-zero incoming velocity, (b). The two states this initial analysis will focus on is the upstream, labeled ③ and the CJ condition, ③.2.

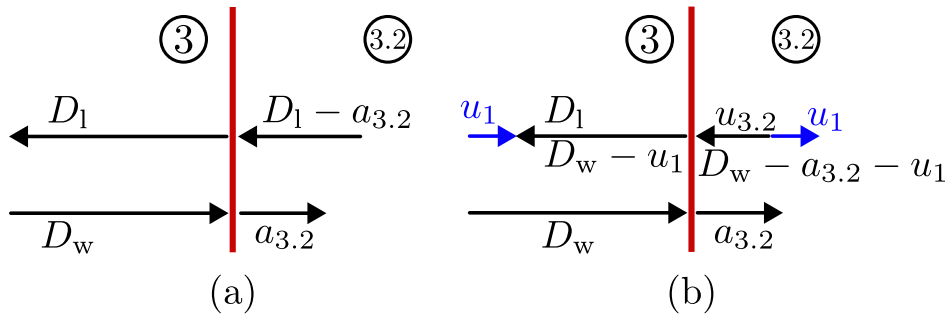


Figure 3.12: Effects of non-zero incoming velocity on an ideal detonation wave.

Much like the analysis for a moving shock wave, the effects of a non-zero incoming velocity on a detonation of fixed strength follow a similar process. Here, the detonation wave speed in the wave frame of reference, D_w, is constant between cases (a) and (b). This means that the wave speed observed in the laboratory, D_1, is reduced by the magnitude of the incoming velocity, u_1.

The CJ state, (3.2), in an ideal case, (a), has an induced velocity that is simply the wave speed in the laboratory frame, D_{l}, minus the speed of sound at (3.2), $a_{3.2}$ shown in Equation 3.18.

$$u_{3.2} = D_{\text{l}} - a_{3.2} \tag{3.18}$$

When accounting for a non-zero incoming velocity, case (b), both the laboratory wave speed, D_{l}, and the induced velocity, $u_{3.2}$, are reduced by the magnitude of the incoming velocity, u_1. This means that the speed of the wave, measured in the laboratory frame is lower, while also producing a lower induced velocity at the CJ state, (3.2). This reduction in the induced velocity at (3.2) in case (b) is a direct reduction in the potential gain through the detonation process, as described by Equation 1.13 in Section 1.1.1.1 and by Gamba.[71] Now that the initial impact on detonation performance has been describe, the remainder of this section will focus on the model implementation.

The model uses a control volume analysis of the RDC flowpath, beginning far upstream in the plenum region and concluding with an exit plane drawn at the midpoint of the detonation wave height. This analysis relies on the conservation of angular momentum at the exit plane to examine the processes near the inlet region of the RDC. The control volume in question is shown in Figure 3.13. The exit plane region can be broken down into 4 distinct regions:

- ZND Region for a fixed "strength" detonation
- Isentropic Expansion Region
- Constant Pressure Product Region
- Constant Pressure Fill Region

The ZND region refers to a fixed "strength" detonation wave as an input parameter. This is meant to mimic the analysis shown in Figure 3.12, where a non-zero incoming azimuthal velocity changes the wave speed in the laboratory frame, but the wave speed ("strength") is fixed in the wave frame. The regions are separated in a non-dimensional space that is normalized the distance by the flowpath circumference:

$$\bar{x} = \frac{x}{\pi \text{OD}} \tag{3.19}$$

where x represents the distance along the annulus flow path in physical space and $\bar{x} \in [0, 1]$ represents that distance normalized by the total annulus flowpath distance based on the outer diameter of the RDC in question. The following non-dimensional locations of interest are then defined as: $\bar{x}_{\text{ZND}}$, representing the end of the ZND reaction zone, $\bar{x}_{\text{Exp}}$, representing the end of an expansion region, and $\bar{x}_{\text{Fill}}$, representing the end of the constant pressure products zone and beginning of the

constant pressure inlet fill region. These regions, shown in Figure 3.13, are not scaled, with an exaggeration in size to show the breakdown more clearly.

To define these regions, a blockage fraction is required. In the case of the current model, this blockage fraction, $\mathrm{B_P}$ will be defined as the region behind the detonation shock front that has a higher pressure than the plenum, P_0. For this model, the blockage fraction is a measured value based on phase-averaged high-speed pressure transducers located in the detonation region and provides a similar measurement of inlet blockage to that described in Shepard et al. and Feleo et al.[72, 5]

Next, it is assumed that the fill region of the inlet recovers in a way such that a linear boundary forms between the post-expansion product and the fresh reactant fill. This assumption allows for the geometric determination of the length scales associated with the post-expansion products and the fill region, where:

$$\bar{x}_{\mathrm{Fill}} = 1 - \frac{1 - \mathrm{B_P}}{2} \tag{3.20}$$

where $\mathrm{B_P}$ determines the length between the shock front and the part of the Expansion region at which the pressure equals the plenum pressure, P_0. It should be noted that the expansion region extends slightly past the $\mathrm{B_P}$ line in Figure 3.13. This is due to the fact that the expansion in the RDC channel continues until the static channel pressure, P_{ch}, is reached. This means that the use of the blockage fraction does not directly define the end of the expansion region; therefore, an additional derivation is required to determine this length.

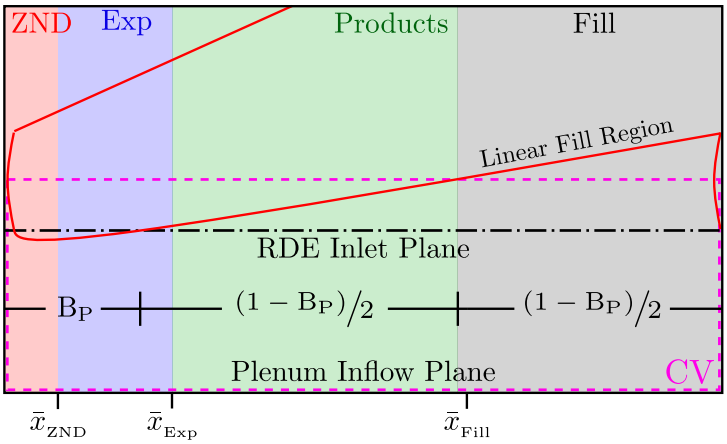


Figure 3.13: Example RDC flow field used in this model with inlet flow area shown with a dashed-dotted line. Unrolled representation of the RDC flow field process regions broken down by color based on the region of interest at the control volume exit, along with non-dimensional length scales. Control volume of interest shown by dashed, magenta lines.

The expansion process is modeled with a simple exponential decay from the CJ pressure to the

channel static pressure. It is determined based on the blockage, $\mathrm{B_P}$, as the characteristic length, along with the CJ pressure determined by the ZND solution end-point, P_{CJ}, and the measured plenum pressure, P_0. The modeling of the expansion as an exponential decay is similar to the method used by Kaemming et al. in their cycle model, except they use a time constant of the decay that is fit on a simulation of a 6" nominal OD RDC.[29] The goal with this model is to be able to examine any arbitrary RDC geometry in a reduced manor, which requires fitting a decay constant based on the flow conditions and RDC geometry, both assumed to be known inputs to the model. The exponential pressure decay rate is defined as:

$$\frac{dP}{dt} = -kP,\ P(t) = P_0 e^{-kt}$$

where the decay constant, k, governs the expansion process. Moving into non-dimensional space coordinates and substituting the known initial pressure leaves:

$$P(\bar{x}) = P_{\mathrm{CJ}} e^{-k\bar{x}} \tag{3.21}$$

where the above implementation provides the pressure as a function of non-dimensional space. Next, this equation is rearranged to solve for the decay constant, k, as a function of known quantities. First, the correct non-dimensional length must be calculated based on the non-dimensional distance between end of the ZND region and the blockage fraction, $\mathrm{B_P}$:

$$\bar{x}_{\mathrm{Exp}|P_0} = \mathrm{B_P} - \bar{x}_{\mathrm{ZND}} \tag{3.22}$$

where $\bar{x}_{\mathrm{ZND}}$ is the non-dimensional length of the ZND region and $\bar{x}_{\mathrm{Exp}|P_0}$ is the length of the expansion region up to the point of equality with the plenum pressure, P_0. With this information, the decay constant, in non-dimensional space, is simply:

$$k = \frac{-\ln(\frac{P_0}{P_{\mathrm{CJ}}})}{\bar{x}_{\mathrm{Exp}|P_0}} \tag{3.23}$$

where all values on the right hand side are measured quantities or outputs from the ZND solution. As one might have deduced, this treatment could mean that the expansion rate, which is a function of the blockage fraction, can be different for the same RDC geometry operating under different flow conditions. To date, no known methods exist for determining the exact blockage fraction a-priori, so the model must rely on experimental measurements or parametric sweeps of inputs.

Next, we give the derivation of the system of equations required to model the expansion process. The expansion modeling is conducted in the non-dimensional space defined above. First, the driver of the expansion process is the pressure change moving from the CJ plane to the static pressure within the channel. The pressure profile governing the expansion is modeled as an exponential

decay process:

$$\frac{dP}{d\bar{x}} = -kP_i \tag{3.24}$$

where k is determined by Equation 3.23 and P_i is the pressure at the current step. The velocity change rate in an isentropic expansion is governed by the following:

$$\frac{d|\mathbf{u}|}{d\bar{x}} = \sqrt{-2\frac{dh}{d\bar{x}}} \tag{3.25}$$

where $\frac{d|\mathbf{u}|}{d\bar{x}}$ represents the change in the magnitude of the velocity vector, given a change in enthalpy, $\frac{dh}{d\bar{x}}$. However, a simplification can be made based on the definition of the change in enthalpy in an isentropic expansion being a function of the density and pressure change rate:

$$\frac{dh}{d\bar{x}} = \frac{1}{\rho_i}\frac{dP}{d\bar{x}} \tag{3.26}$$

where the density, ρ_i, at the given step is determined through the use of a *Cantera* gas object using the GRI3.0 mechanism.[18, 73] Finally, this is reduced to the following equation used to calculate the velocity magnitude rate of change:

$$\frac{d|\mathbf{u}|}{d\bar{x}} = \sqrt{\frac{-2}{\rho_i}\frac{dP}{d\bar{x}}} = \sqrt{\frac{2kP}{\rho_i}} \tag{3.27}$$

Using 3.27 in the integration process results in changes in velocity based on the non-dimensional space; however, the analysis requires a dimensional velocity along the control volume exit. Equation 3.27 can be used to find the dimensional velocity profile through the use of the chain rule:

$$\frac{d|\mathbf{u}|}{dx} = \frac{d|\mathbf{u}|}{d\bar{x}}\frac{d\bar{x}}{dx} \tag{3.28}$$

where $\frac{d\bar{x}}{dx} = \frac{1}{\pi OD}$ based on Equation 3.19. This substitution results in:

$$\frac{d|\mathbf{u}|}{dx} = \sqrt{\frac{-2}{\rho_i}\frac{dP}{d\bar{x}}}\frac{1}{\pi OD} = \sqrt{\frac{2kP}{\rho_i}}\frac{1}{\pi OD} \tag{3.29}$$

An expansion angle is also included in the model since the expansion to static pressure within the RDC flowpath is not purely azimuthal. For reference, u represents the azimuthal velocity component, while v represents the axial velocity component. This angle, α, along with the associate vector components are shown in Figure 3.14, and can either be estimated based on the RDC geometry and wave fill height, or included in the parameter estimation process. It is assumed that this expansion flow angle is constant during the expansion process and is native only to the control vol-

ume exit plane of the expansion region. Included in this assumption is that the expansion process occurring in the combustion region of the ZND solution contributes to purely azimuthal-velocity changes, i.e. no change in axial velocity. The equations for each velocity component's rate of change in the expansion region are given below:

$$\frac{du}{dx} = \cos(\alpha)\frac{d|\mathbf{u}|}{dx} \tag{3.30}$$

$$\frac{dv}{dx} = \sin(\alpha)\frac{d|\mathbf{u}|}{dx} \tag{3.31}$$

As will be discussed later, this model will assume that the axial velocity profile along the control volume exit plane is relatively constant. The axial velocity profile will still be calculated to provide an estimated thrust; however, in the case of the control volume modeling, a non-zero expansion angle is included to reduce the contribution of the expansion process to the azimuthal direction. This methodology attempts to capture expansion effects in the azimuthal direction, knowing that the expansion will not be fully azimuthal.

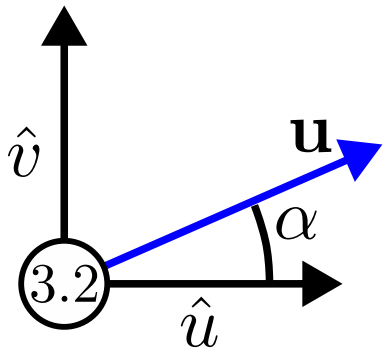


Figure 3.14: Example of the expansion angle, α, from the CJ plane, (3.2).

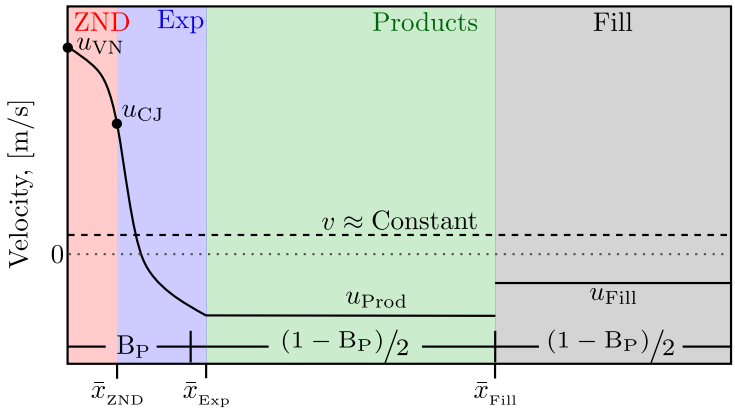


Figure 3.15: Velocity component profiles (in laboratory frame) at the control volume exit. A positive azimuthal velocity, u, is defined by the direction of wave propagation, i.e. a negative velocity means the flow is moving towards the incoming detonation wave.

To solve the for the expansion profiles, Equations 3.24, 3.29, 3.30 and 3.31 are then integrated until the channel static pressure, P_{ch} is reached. Figure 3.15 shows an example case of the velocity profiles calculated along the exit plane of the proposed control volume, showing the azimuthal velocity, u, as solid lines, and the axial velocity, v, shown with dashed lines. Of particular interest is the azimuthal velocity profile, which shows a negative velocity component in the Expansion, post-expansion Product, and Fill regions. The discussion of where the negative azimuthal fill

velocity comes from will be discussed later in this section. The changes in azimuthal velocity in the ZND region are assumed constant based on fixing the "strength" of the detonation wave; however, the azimuthal velocity profile in the Expansion region will be governed by the expansion angle, α, where higher expansion angles will result in lower changes in azimuthal velocity.

The proposed inlet model has defined a control volume such that the inlet to the control volume is located far enough upstream from the detonation wave that we can assume that there is no inlet angular momentum. There are no next torques on the RDC device or other external forces; therefore the exit angular momentum must be zero as well. Because the flow field at the exit of the control volume is much more complex than the inlet, a derivation of the conservation of angular momentum in a control volume must be conducted beginning from first principles. Below shows this derivation of the process, starting from the same derivation discussed by Shepherd and Karahara[69], but then deviating with a few key assumptions that result in the version used in this model. Conservation of angular momentum in a control volume is defined as:

$$M = \frac{\partial}{\partial t}\int_{\Omega} \mathbf{r} \times \rho\mathbf{u}\mathrm{d}V + \int_{\partial\Omega} (\mathbf{r} \times \rho\mathbf{u})\mathbf{n} \cdot \mathbf{u}\mathrm{d}S$$

The net angular momentum, referred to as swirl, in the plenum region, well upstream of the RDC, is assumed to be zero in the RDC control volume inlet; therefore, it is required that the exit plane net swirl is also zero. The domain is periodic, so averaging over the cycle allows for the following reduction:

$$0 = \frac{1}{\mathrm{T}}\int_{0}^{\mathrm{T}} \int_{\delta\Omega} (\mathbf{r} \times \rho\mathbf{u})\mathbf{n} \cdot \mathrm{d}S\mathrm{d}t$$

Transforming into the steady, wave reference frame:

$$0 = \int_{\mathrm{A}} r\rho uv dS$$

where r is the radial distance and each velocity component is broken out, u is the azimuthal velocity, and v is the axial velocity. Assuming no variation in the radial direction and a fixed area plane, the conservation of angular momentum can further reduce to:

$$0 = \frac{1}{2\pi}\int_{0}^{2\pi} \rho(\theta', z)u(\theta', z)v(\theta', z)\mathrm{d}\theta'$$

Because the analysis is conducted at the same axial height, the dependence on the axial location can be removed, leaving:

$$0 = \int_{0}^{2\pi} \rho(\theta')u(\theta')v(\theta')d\theta'$$

Next, the equations are transformed from the physical space θ' to the non-dimensional distance, $\bar{x}$, defined in Equation 3.19. Leaving the following equation of swirl conservation in the azimuthal direction in terms of the non-dimensional distance.

$$\int_0^1 \rho(\bar{x})u(\bar{x})v(\bar{x})d\bar{x} = 0$$

Due to the complexity of the axial flow across the control volume exit, it will be assumed that the fluctuations in the axial velocity along this profile are negligible. This argument has partial support when examining the particle path profile in certain CFD solutions along a plane drawn at the mid-point of the detonation wave.[10, 74, 75] In these computational studies, the axial velocity component appears to be relatively constant, and drawing tangent lines to the particle paths at the mid-point of the detonation resulted in an average estimated flow angle (in the wave frame) of 10.4° with a standard deviation of only $\pm 1.69^\circ$. The discussion from the previous section mentions the calculation of the axial velocity change through the expansions; however, this modeled axial velocity would be along a particle path that intersects the detonation wave directly at the mid-point, which cannot be used as a surrogate for other particle paths because of the complexities with the back-flowing region of the RDC. This means that the velocity profile along the exit plane of the proposed control volume is the result of particle paths passing through diffident axial locations of the detonation wave. For example, the velocity profiles closer to the Fill region will have propagated through the lower portion of the detonation wave and likely achieved a relatively high axial velocity backwards through the inlet. A more complex inlet model is required to accurately capture this effect. With the assumption of constant axial velocity along the exit plane, the conservation of angular momentum reduces to:

$$\int_0^1 \rho(\bar{x})u(\bar{x})d\bar{x} = 0 \tag{3.32}$$

where the azimuthal velocity profile is calculated based on the model assumptions discussed previously. Using the four regions shown in Figure 3.13, the integral can be separated, leaving the following:

$$\int_0^{\bar{x}_{ZND}} \rho(\bar{x})u(\bar{x})d\bar{x} + \int_{\bar{x}_{ZND}}^{\bar{x}_{Exp}} \rho(\bar{x})u(\bar{x})d\bar{x} + \int_{\bar{x}_{Exp}}^{\bar{x}_{Fill}} \rho(\bar{x})u(\bar{x})d\bar{x} + \int_{\bar{x}_{Fill}}^{1} \rho(\bar{x})u(\bar{x})d\bar{x} = 0$$

The ZND region and the Exp region are integrated across their respective profiles using a Simpson's Rule integrator in the model, while the other two regions can be reduced down to simple algebraic expressions by assuming uniform composition, pressure and velocity in each region. For the post-expansion Product region, this reduces down to:

$$\int_{\bar{x}_{Exp}}^{\bar{x}_{Fill}} \rho(\bar{x})u(\bar{x})d\bar{x} = \rho_{_{Prod}} u_{_{Prod}}(\bar{x}_{Fill} - \bar{x}_{Exp})$$

And for the reactant Fill region:

$$\int_{\bar{x}_{Fill}}^{1} \rho(\bar{x})u(\bar{x})d\bar{x} = \rho_{_{Fill}} u_{_{Fill}}(1 - \bar{x}_{Fill})$$

In this case, $\rho_{_{Fill}}$ is the density of the pre-detonation reactants and $u_{_{Fill}}$ is the azimuthal velocity of the Fill region, and must be calculated in order to conserve swirl at the exit plane of the control volume. This equation is shown below:

$$u_{_{Fill}} = \frac{-\left(\int\limits_{ZND} \rho u d\bar{x} + \int\limits_{Exp} \rho u d\bar{x} + \rho_{_{Prod}} u_{_{Prod}}(\bar{x}_{Fill} - \bar{x}_{Exp})\right)}{\rho_{_{Fill}}(1 - \bar{x}_{Fill})}$$

With this result, the azimuthal velocity in the fill region required to maintain a net swirl condition of zero can be calculated. The model is then iterated using the calculated $u_{_{Fill}}$ as an input, where the non-zero incoming fill velocity must be propagated back through the model, adjusting the laboratory frame wave speed, and therefore the azimuthal velocity profile across the control volume exit plane. Refer to Figure 3.12 for an example of what happens when the "strength" of the detonation wave is fixed, but now a non-zero incoming flow is introduced.

Now that the model has been properly introduced, a quick example of the model outputs was examined for an ideal hydrogen-air detonation operating at an equivalence ratio of 0.6. Figure 3.16 shows the pressure (a), azimuthal velocity in the laboratory frame (b), and the swirl profile (c), where a positive velocity is defined as moving in the same direction as the detonation wave. The most interesting features highlighted on these graphs are the azimuthal velocity, u, and the swirl term, ρuv, which contains the constant axial velocity component, v, only to maintain the proper units. Figure 3.16 (b) shows that the initial azimuthal velocity starts in the same direction as the wave propagation, due to the high induced velocity behind the shock wave. The ZND process then brings the flow to the CJ condition, effective slowing the particle in the lab frame. Examining the expansion process, the velocity at the end of the expansion process is relatively large in the direction opposite to the wave propagation direction. This is due to the fact that the boundary condition in the RDC is not a zero-velocity wall, but a static pressure boundary, allowing for expansion past the zero-velocity point that would exist in a detonation tube.[14] After iteration over the calculated azimuthal fill velocity, the model predicted a negative azimuthal velocity in the fill region, with a magnitude of -41 m/s.

From closer examination of Figure 3.16 (c), it is clear that the detonation wave produces a high positive swirl value due to the high density and high induced velocity throughout the ZND

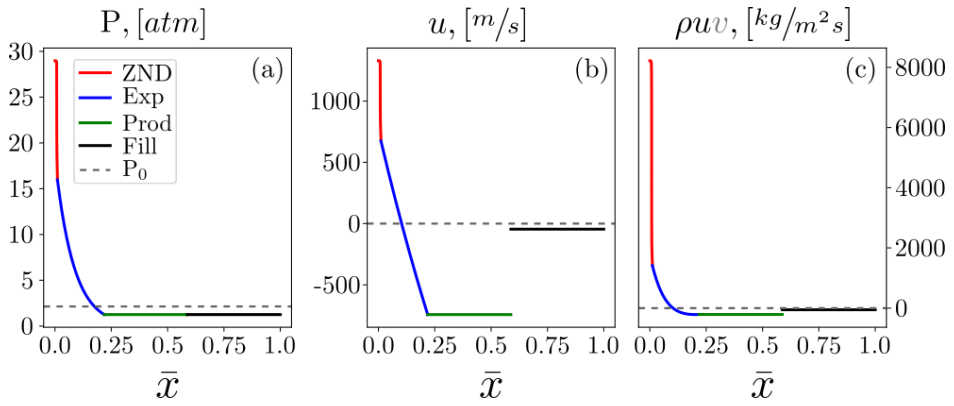


Figure 3.16: Example of the modeled profiles at the control volume exit for an ideal, hydrogen air detonation-based on an experimental run. $P_0 = 2.14$, $P_{ch} = 1.256$, and $\phi = 0.6$. Pressure profile (a), azimuthal velocity profile (b), and swirl profile (c).

region. Despite the shorter length of the ZND region, it still has a large positive contribution to the net swirl. The expansion process also has a significant contribution to the swirl in the positive direction, but because the expansion wave both decreases in azimuthal velocity and density, the magnitude in slightly lower than the ZND swirl contribution. This is up to the point at which the azimuthal velocity changes direction and the expansion region begins contributing negatively to the total swirl. However, this is at an even lower density relative to the beginning of the expansion region, netting an overall positive swirl contribution through the expansion process for this example. Post-expansion, the products are assumed to have a constant azimuthal velocity and density and to contribute negatively to the total swirl. The total swirl contributions from the ZND, Expansion and Product region leave a positive net swirl component, requiring the fill region to counter the remain positive swirl value. The increased density over the constant-pressure product region means that the azimuthal velocity magnitude is lower than the Product region azimuthal velocity; however, this still results in a negative velocity in the laboratory frame, which differs significantly from the assumptions typically used in RDC modeling of the inlet region. This treatment of the azimuthal velocity profile produces profiles similar to those shown in Figure 3.6 outside of the ZND region, which is likely caused by the larger than optimal particle sizes in the experimental setting not being able to fully resolve the high velocity gradients in this region.

The previous example looked at a sample problem with an ideal detonation, and the following describes the final implementation of the model, along with how each process is accounted for including the Deflagration Loss fraction from Section 2.2.1 The final model takes as inputs the deflagration loss parameters, ξ_{P} $and \xi_{\mathrm{L}}$, and the expansion region angle, α. The model iterates over the Fill region azimuthal velocity until converged, and uses the final solution to determine the laboratory wave speed, detonation pressure ratio, and induced azimuthal fill velocity. The

goal of this analysis is to capture the effects of non-zero azimuthal fill velocity and deflagration combustion on the potential performance of a given RDC.

The modeling process starts with a gas mixture of the appropriate reactants at the total pressure, P_0, and the total temperature, T_0 in advance of the detonation wave, along with the outer diameter of the RDC for conversion to non-dimensional space, and the blockage fraction, $\mathrm{B_P}$. The channel static pressure, P_{ch}, is also assumed to be a known/measured value and is representative of the static pressure in the Fill region. It is assumed that these states are known from measurements and specified flow conditions, and a constant state vector is defined, $\mathbf{X_0}$:

$$\mathbf{X_0} = [\mathrm{OD}, \text{fuel}, \phi, P_0, T_0, P_{ch}, \mathrm{B_P}] \tag{3.33}$$

where these values are RDC and flow dependent. This state vector will be used for both exercising the model and in a parameter estimation effort.

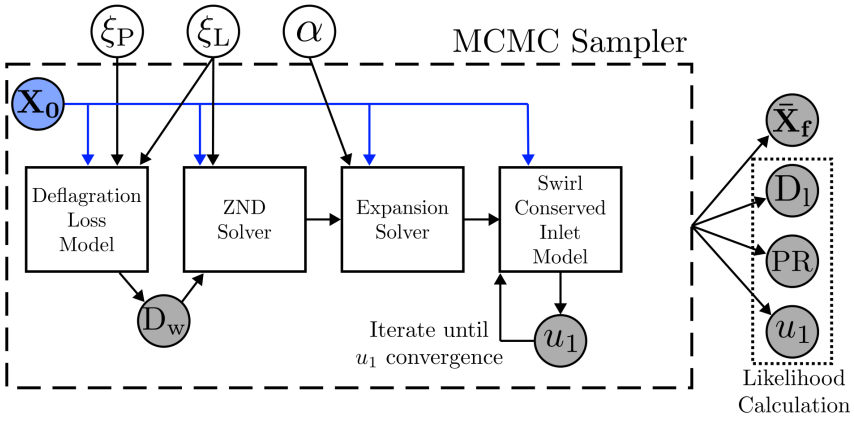


Figure 3.17: Diagram of the model used in the MCMC sampling process.

Figure 3.17 shows a model diagram, specifically highlighting the steps used in the parameter estimation process. With the initial state vector, $\mathbf{X_0}$, and the deflagration loss parameters, the deflagration loss model calculates a detonation wave speed in the wave frame, D_w. This wave speed, along with the initial state vector, are then used as inputs for the ZND solver. The ZND solver outputs a point-wise solution along the detonation processes starting from the shock wave and ending at the CJ plane. The final state of the ZND solution, along with the calculated, normalized distances, are passed to the Expansion solver. This solver also accounts for the constant expansion angle, α, input. Next, the state profiles from the ZND and Expansion solver are passed to the angular momentum conservation equations to calculate an azimuthal fill velocity. This last step is then iterated to account for the non-zero azimuthal fill velocity until convergence. Finally, the model produces a set of outputs that includes: a state vector along the control volume exit, $\bar{\mathbf{X}}_\mathbf{f}$, the laboratory wave speed, D_l, the CJ pressure ratio, PR and the calculated inlet azimuthal velocity,

u_1. For clarity, these steps are shown in detail in Algorithm 10.

Algorithm 10 Non-Zero Swirl Model

Require: ξ_{P}, $\xi_{\mathrm{L}} \in [0, 1]$ and $\alpha \in [0°, 90°]$

With $\mathbf{X_0}$, ξ_{P}, and ξ_{L}: Calculate wave speed in wave frame, D_{w}, with Deflagration Loss Model.

With $\mathbf{X_0}$, ξ_{L}, and D_{w}: Calculate ZND profile with Non-Ideal ZND Solver.

With $\mathbf{X_0}$, α, and ZND profile: Calculate expansion profile with Expansion Solver.

With $\mathbf{X_0}$ and expansion profile: Calculate initial guess of azimuthal fill velocity, u_1, with Swirl Conserved Inlet Model

while $u_{1,in} \neq u_{1,out}$ **do**

Iterate over Swirl Conserved Inlet Model with previous $u_{1,out}$ serving as new $u_{1,in}$

end while

Output state profile along control volume exit, $\bar{\mathbf{X}}_{\mathbf{f}}$, laboratory wave speed, D_{l}, detonation pressure ratio, PR, and converged induced azimuthal fill velocity, u_1.

In the case of the Markov Chain Monte Carlo (MCMC) sampling process, the model fixes the initial state vector, $\mathbf{X_0}$, while sampling over the deflagration loss parameters and the expansion angle [ξ_{P}, ξ_{L}, α]. The wave speed, pressure ratio, and azimuthal fill velocity [D_{l}, PR, u_1] are then used to evaluate the likelihood of the input parameters given the experimentally measured values of each output. This process seeks to learn the parameters that best fit the measurements, while also accounting for the error and uncertainty of each measurement. This parameter estimation process builds on the approach described in Section 1.5, which provided a detailed description of the sampling process.

3.3.2.2 Exit Plane

Assuming an isentropic flow with an ideal gas, the change in velocity based on a change in pressure can be calculated from Equation 3.34. We can use this as the baseline velocity achievable from a given post-detonation state. In the following example, we can simply assume that we get a velocity magnitude of 1250 m/s from the modeled expansion process. Following the examples from Section 3.2.3.3, we will specify a distribution in the azimuthal velocity component by drawing flow angles from a normal distribution of mean zero and a range of variances. Figure 3.18 shows a visual representation of the flow angle, which is defined off the axial direction and varies $\in [-90, 90]$ degrees. With these flow angles, the individual components of the velocity vector are calculated with Equation 3.35.

$$V = \sqrt{h_4 - h_(P, s_4)} \tag{3.34}$$

$$u = V\cos(\theta),\ v = V\sin(\theta) \tag{3.35}$$

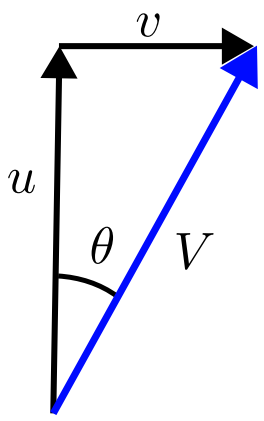


Figure 3.18: Flow Angle Diagram, with Angle Definition.

$$\theta \sim \mathcal{N}[0, \sigma_\theta] \tag{3.36}$$

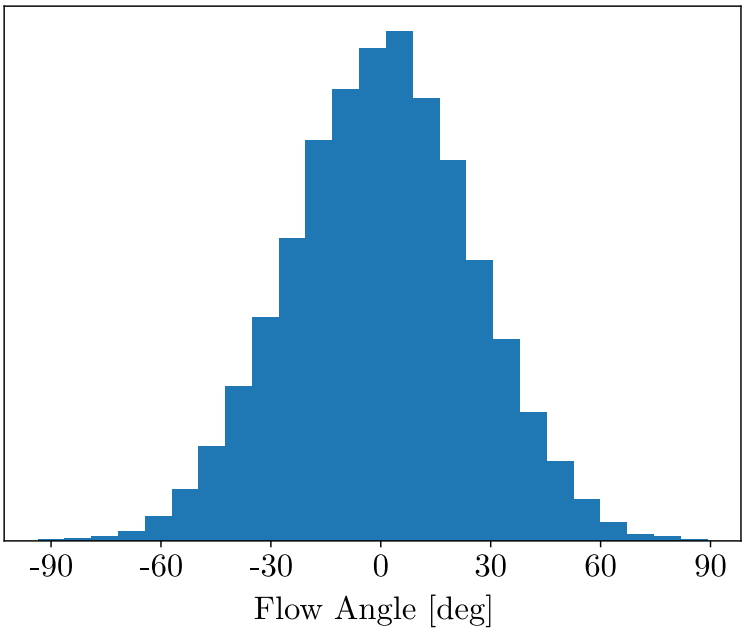


Figure 3.19: Histogram of Flow Angles using a 20 Degrees Standard Deviation.

Figure 3.19 shows an example of the flow angle distributions given an angle variation of 20 degrees. From this distribution, an axial velocity profile can be generated, allowing for the calculation of the expected value of the axial velocity, which corresponds to the specific thrust of the

device. Finally, this value can be compared to the total velocity magnitude, V, to measure the degradation in the mean axial velocity as a function of the expansion angle distribution.

3.3.3 Blockage and Effective Area Ratio Inlet Model

The following will describe and develop the effective area ratio parameter used, in concert with the blockage fraction, B, from Feleo et al., to evaluate the impacts of the passing detonation wave on the RDC inlet. First, we assume isentropic flow between the RDC plenum and the inlet throat, along with assuming no changes in the gas composition between the cold and hot flow conditions. We start with the definition of the steady, uniform mass flow rate through an area (taken to be the geometric area of the inlet), which can be expressed as:

$$\dot{m} = c_{\mathrm{d}} \frac{A_{\mathrm{g}} P_0}{\sqrt{T_0}} \sqrt{\frac{\gamma}{R}} M_{\mathrm{g}} \left(1 + \frac{\gamma - 1}{2} M_{\mathrm{g}}^2 \right)^{-\frac{(\gamma+1)}{2(\gamma-1)}} \tag{3.37}$$

This form of the mass flow function has a dependency on the total pressure and temperature, which change between fueled and un-fueled operation of the RDC. We can then introduce the corrected mass flow rate defined as:

$$\dot{m}_{\mathrm{c}} = \dot{m} \frac{\sqrt{\Theta}}{\Delta} \tag{3.38}$$

with

$$\Theta = \frac{T}{T_{\mathrm{ref}}}$$

and

$$\Delta = \frac{P}{P_{\mathrm{ref}}}$$

where P_{ref} and T_{ref} correspond to standard day conditions of 1 atm and 298.15 K, respectively. When cast in this form, the change in plenum total conditions can be properly accounted; thus,

$$\dot{m}_{\mathrm{c}} = A_{\mathrm{g}} c_{\mathrm{d}} \frac{P_0}{\Delta} \sqrt{\frac{\Theta}{T_0}} \sqrt{\frac{\gamma}{R}} M_{\mathrm{t}} \left(1 + \frac{\gamma - 1}{2} M_{\mathrm{t}}^2 \right)^{-\frac{(\gamma+1)}{2(\gamma-1)}} \tag{3.39}$$

The effective flow area is defined by:

$$A_{\mathrm{e}} = A_{\mathrm{g}} c_{\mathrm{d}} \tag{3.40}$$

with c_{d} defined as the discharge coefficient through the inlet. Substituting into the effective area definition and assuming a fixed (frozen) gas composition, the corrected mass flow rate becomes a

function of effective area and Mach number at the inlet throat only; i.e.,

$$\dot{m}_{\mathrm{c}} = A_{\mathrm{e}} \frac{P_{\mathrm{ref}}}{\sqrt{T_{\mathrm{ref}}}} \sqrt{\frac{\gamma}{R}} M_{\mathrm{t}} \left(1 + \frac{\gamma - 1}{2} M_{\mathrm{t}}^2\right)^{-\frac{(\gamma+1)}{2(\gamma-1)}} \tag{3.41}$$

The ratio of the corrected mass flow rates for fueled and un-fueled operation can then be taken to remove like terms and get a ratio of the effective areas between the two modes of operation:

$$\frac{\dot{m}_{\mathrm{c,H}}}{\dot{m}_{\mathrm{c,C}}} = \frac{A_{\mathrm{e,H}}}{A_{\mathrm{e,C}}} \frac{M_{\mathrm{t,H}}}{M_{\mathrm{t,C}}} \left(\frac{1 + \frac{\gamma-1}{2} M_{\mathrm{t,H}}^2}{1 + \frac{\gamma-1}{2} M_{\mathrm{t,C}}^2}\right)^{-\frac{(\gamma+1)}{2(\gamma-1)}} \tag{3.42}$$

where the subscript H refers to the conditions during operation and C represents the cold-flow conditions. The quantity of interest is the effective area ratio, α, is defined as:

$$\alpha = \frac{A_{\mathrm{e,H}}}{A_{\mathrm{e,C}}} \tag{3.43}$$

which represents the change in the effective area ratio as the RDC operates.

After substituting Equation 3.43 into Equation 3.42 and solving for α we are left with:

$$\alpha = \frac{\dot{m}_{\mathrm{c,H}}}{\dot{m}_{\mathrm{c,C}}} \frac{M_{\mathrm{t,C}}}{M_{\mathrm{t,H}}} \left(\frac{1 + \frac{\gamma-1}{2} M_{\mathrm{t,C}}^2}{1 + \frac{\gamma-1}{2} M_{\mathrm{t,H}}^2}\right)^{-\frac{(\gamma+1)}{2(\gamma-1)}} \tag{3.44}$$

Equation 3.44 now allows us to calculate the effective area change in terms of corrected mass flow and Mach number for the cold flow and hot flow. By assuming isentropic flow from the plenum to the inlet throat, the Mach number can be calculated from the pressure ratio between the plenum total and throat static, with the caveat that the Mach number at the throat can be at most sonic. This was accomplished with the isentropic flow equation evaluated between the plenum and the inlet throat:

$$M_{\mathrm{t}} = \sqrt{\frac{2}{\gamma - 1} \left[\left(\frac{P_0}{P_{\mathrm{t}}}\right)^{\frac{\gamma-1}{\gamma}} - 1\right]} \tag{3.45}$$

Given a measure of the plenum-to-inlet throat pressure ratio, P_0/P_{t}, the Mach number at the throat can be evaluated for each condition, leaving the effective area ratio as a function of the corrected mass flow rate and the pressure ratio only. In order to calculate this quantity only the nominal mass flow rate, the total plenum pressure and temperature, and the static pressure at the inlet throat are needed. This methodology allows for the calculation of effective area changes without the need for cold-flow calibration data, which is required for the method presented by Feleo et al. [5].

Equation 3.45 is written in a steady and uniform flow form; however, the detonation wave

creates a non-uniform flow field in the inlet plane. Though we can assume a quasi-steady process by time averaging over many laps, we are still left with a non-uniform profile across the inlet flow area. So we will need to provide an averaging method to calculate the Hot flow Mach number, specifically the Hot flow inlet static pressure. In the experimental setting, this is done using the phase-averaged high-speed pressure measurements, which effectively provides the static pressure across the inlet flow area. The area averaged inlet static pressure can then be defined as:

$$P_{\mathrm{t}} \equiv \bar{P}^{A}_{inj} = \frac{1}{A_{inj}} \int P(A) dA \tag{3.46}$$

Equation 3.45 still assumes that the gas properties remain constant from cold to hot flow (constant γ) and the total temperature of the plenum also remains constant. These assumptions almost certainty break down as the inlet blockage increases because of the higher potential and magnitude of the product gas backflow.

Finally, the relationship between the effective area ratio and the blockage fraction from Feleo et al. [5] is shown below:

$$1 - \alpha = \frac{A_{\mathrm{e,C}} - A_{\mathrm{e,H}}}{A_{\mathrm{e,C}}} \tag{3.47}$$

This formulation is arranged in a form that determines the percent change in the effective area from the cold flow to the hot flow conditions.

In practice, the blockage fraction defined by Feleo et al. uses the measured mass flow rate instead of a mass flux based on the geometric inlet area:

$$B = 1 - \frac{\dot{m}''_{Hot}}{\dot{m}''_{Cold|P_{0,Hot}}} = 1 - \frac{\dot{m}_{Hot}}{\dot{m}_{Cold|P_{0,Hot}}} \tag{3.48}$$

where $\dot{m}_{Hot}$ is calculated at the metering orifice and $\dot{m}_{Cold|P_{0,Hot}}$ is calculated by curve fit on a calibration dataset.

Under the same assumption of an isentropic inlet used in the derivation of the effective area ratio, the mass flow rate equation (Equation 3.37) can be substituted into the blockage fraction. After simplifying, this yields:

$$B = 1 - \frac{A_{e,H}}{A_{e,C}} \left(\frac{M_H (1 + \frac{\gamma-1}{2} M_H^2)}{M_C (1 + \frac{\gamma-1}{2} M_C^2)} \right)^{\frac{-(\gamma+1)}{2(\gamma-1)}} \tag{3.49}$$

In this sense, the blockage fraction does not reduce to a simple area ratio, unless under certain inlet Mach number conditions. It is a relationship of the area ratio caused by the blockage and a change in some inlet average Mach number.

3.3.3.1 Uncertainty Quantification for Blockage Fraction and Effective Area Ratio

For the uncertainty analysis of the two blockage fraction definitions, a Monte Carlo based uncertainty propagation was conducted for the effective area ratio, while standard uncertainty propagation technique were used to examine the blockage fraction. The following assumes uncorrelated uncertainties in the measurement and only examines the bias (systematic error) of the sensors and not the random uncertainty, which can simply be assumed as a constant between the two methods, given the same data set.

The effective area ratio can be reduced to the following dependencies for error analysis. Each term is assumed to be a time-averaged quantity, using the stable portion of the run as a single averaged point. Written in terms of the random variables in the definition of the effective area ratio:

$$\alpha \propto \frac{P_{0,C}}{P_{0,H}} \sqrt{\frac{T_{0,H}}{T_{0,C}}} \left(\frac{P_{0,C} P_H}{P_C P_{0,H}} \right)^{\frac{-(\gamma+1)}{2\gamma}} \frac{\psi(P_{0,C}, P_C)}{\psi(P_{0,H}, P_H)} \tag{3.50}$$

where:

$$\psi(P_{0,i}, P_i) \equiv \sqrt{\left(\frac{P_{0,i}}{P_i} \right)^{\frac{\gamma-1}{\gamma}} - 1}$$

therefore the uncertainty in the effective area ratio can be related as:

$$\sigma_\alpha^2 = \sum_{i=0}^{N} \left(\frac{d\alpha}{dx_i} \sigma_{x_i} \right)^2 \tag{3.51}$$

where i represents the random variables in Equation 3.50.

Rather than taking a complex partial derivative through Equation 3.50, a simple Monte Carlo uncertainty propagation was carried out using 20,000 samples, where each input variable was assumed to be normally distributed around a measured mean value with the standard deviation based on the systemic uncertainty of the sensor (see Table 3.1).

It should be noted that this discussion of the uncertainty in the measurement of the effective area ratio does not account for any discrepancy in the location of the static pressure measurement at the geometric throat. The methodology will therefore assume that the static pressure measurement is exactly at the geometric throat. Because of this fact, the uncertainty quantities of the effective area ratio that are calculated with this method are a best-case scenario.

The uncertainty analysis of the blockage fraction requires a more detailed analysis than the effective area ratio due to the need to calculate a cold-flow equivalent mass flow rate, given the measured plenum total pressure during the hot-flow portion of the run. This calculation is broken down into two techniques depending on the measured plenum pressure, one for an un-choked inlet and one for a choked inlet for the cold-flow equivalence mass flow rate.

In the un-choked region of the cold flow equivalent mass flow rate calculation: if the plenum pressure is at a calibration point, the uncertainty in the mass flow rate should remain the same as the measured uncertainty. If the plenum pressure is not at a calibration point, then a linear interpolation is conducted to estimate the cold-flow equivalent mass flow rate, along with the uncertainty. The cold-flow equivalent mass flow rate is estimated by the following:

$$\dot{\bar{m}}_C = \dot{\bar{m}}_0 + (\dot{\bar{m}}_1 - \dot{\bar{m}}_0)\,\frac{\bar{P}_{0,H} - \bar{P}_{0,0}}{\bar{P}_{0,1} - \bar{P}_{0,0}} \tag{3.52}$$

where $\dot{\bar{m}}_C$ is the estimated mass flow rate given the measured hot flow plenum pressure, $P_{0,H}$. Subscripts 0 and 1 refer to the calibrations points directly below and above the measured hot flow plenum pressure.

Because the interpolation process is linear, the standard, correlated uncertainty propagation can be applied:

$$\begin{aligned}\sigma^2_{\dot{m}_C} = &(\frac{d\dot{m}_C}{d\dot{m}_0}\sigma_{\dot{m}_0})^2 + (\frac{d\dot{m}_C}{d\dot{m}_1}\sigma_{\dot{m}_1})^2 + \\ &(\frac{d\dot{m}_C}{dP_{0,0}}\sigma_{P_{0,0}})^2 + (\frac{d\dot{m}_C}{dP_{0,1}}\sigma_{P_{0,1}})^2\end{aligned} \tag{3.53}$$

It should be noted that this formulation of the error propagation ignores the fact that the mass flow rate is not linear with plenum pressure while the inlet is un-choked. So, this only represents the propagation of the uncertainty from the systematic measurement uncertainty. Also, because of the assumption that the individual sensor uncertainties are independent, the mass flow rate and the plenum pressure uncertainties are also assumed to be uncorrelated. This assumption is valid since the uncertainty in the mass flow rate is only correlated with the orifice pressure measurement, which is independent from the uncertainty in the plenum pressure measurement.

For the choked cold-flow equivalent, a choked flow line is generated based on the calibration points that are certain to be choked. This yields an estimated slope, intercept, and flow area, based on the data and its associated uncertainty. Hot-flow pressures within the choked region are then propagated through the choked flow line:

$$\dot{m}_{choked} = m_{fit} P_{0,choked} + b_{fit} \tag{3.54}$$

where m and b are the slope and intercept of the curve fit. The uncertainty of the choked cold flow equivalent mass flow is given by:

$$\sigma_{\dot{m}} = \sqrt{(P_0\sigma_m)^2 + (m\sigma_{P_0})^2 + \sigma_b^2} \tag{3.55}$$

Figure 3.20 shows an example of the calibration process and the uncertainty propagation. The points in black represent the calibration points, while the red and blue points are the estimated

values outside of the calibration dataset, un-choked and choked, respectively.

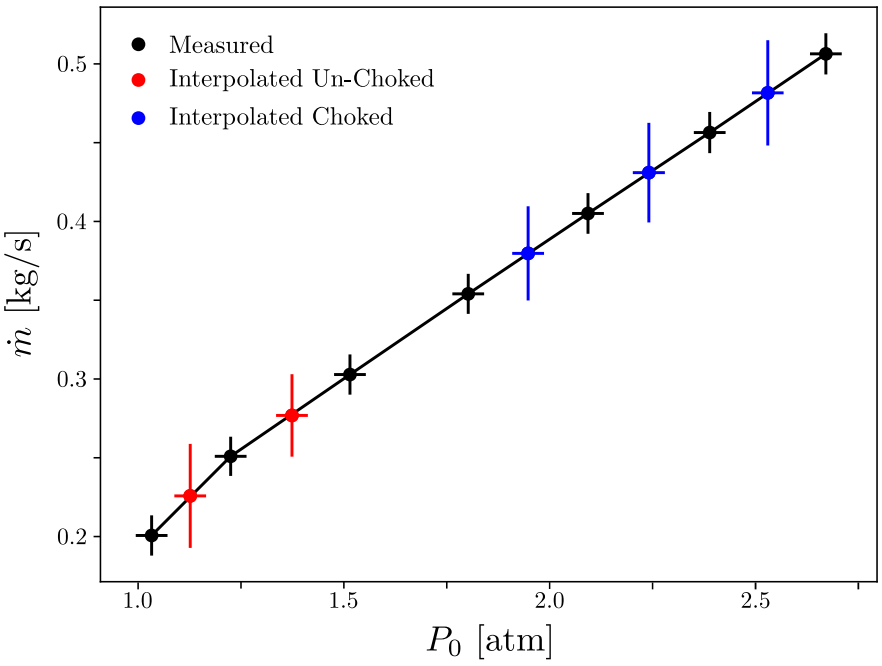


Figure 3.20: Curve Fit Errors for Cold Flow Interpolation.

Now the uncertainty in the blockage fraction, based on the systematic error, is given by:

$$\sigma_B = \sqrt{\left(\frac{\sigma_{\dot{m}_H}}{\dot{m}_C}\right)^2 + \left(\frac{\dot{m}_H}{\dot{m}_C^2}\sigma_{\dot{m}_C}\right)^2} \tag{3.56}$$

where $\sigma_{\dot{m}_C}$ is determined by either Equation 3.53 if the cold flow equivalent is un-choked, Equation 3.55 if the cold flow equivalent is choked, or the nominal mass flow uncertainty if at a calibration point.

Table 3.1 shows the published instrument uncertainty for the measurement locations of interest used in the calculation of the blockage fraction and the effective area ratio.

Measurement	Full Scale	Sensor Uncertainty
$P_{0,orifice}$	500 [psi]	0.25% FS
$P_{0,plenum}$	200 [psi]	0.25% FS
P_s	30 [psi]	0.25% FS
T	1260 [°C]	max(0.75%, 2.2 [°C])

Table 3.1: Summary of Measurement Uncertainty

Using the uncertainty analysis discussed above, with sensor errors in Table 3.1, Figure 3.21

shows the uncertainty of the measured value on a set of runs with varying mass flow rate. This figure shows that at low corrected mass flow rates, the effective area ratio has a much larger uncertainty; however, outside of the low flow rate condition, the effective area ratio provides a more accurate measurement methodology.

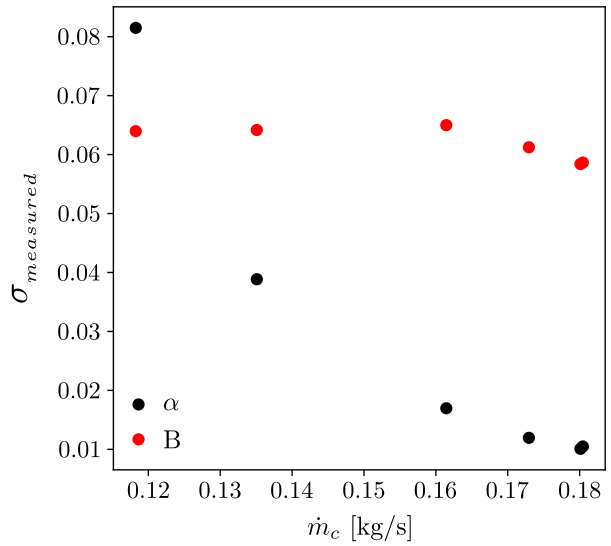


Figure 3.21: Experimental Measurement Standard Deviations for Blockage Fraction and Effective Area Ratio versus Mass Flow Rate.

Finally, a study was performed to examine the difference in the measured blockage fraction and effective area ratio across a much larger set of experimental data. Figure 3.22 shows the effective area ratio plotted against the blockage fraction (a) and the inlet pressure recovery (b). This plot shows that, when accounting for measurement error, the blockage fraction and effective area ratio are essentially measuring the same value. This means that we can use one in place of the other, depending on which value is more readily calculable. Figure 3.22 (b) shows that pressure recovery scales well with the effective area ratio, where the highest effective areas correspond to a stiffer inlet. As a refresher, the inlet stiffness is defined as the ratio between the channel static pressure and the total pressure of the plenum. As with the large majority of analysis on the injector, the inlet blockage, regardless of definition, is correlated directly with the stiffness of the inlet.

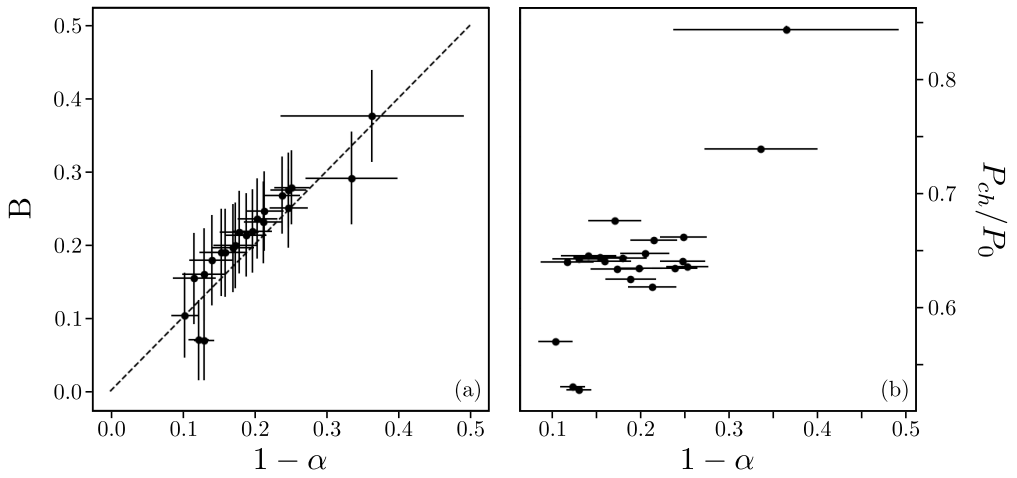


Figure 3.22: Blockage Fraction versus one minus the Effective Area Ratio (left). Injector Pressure Losses versus one minus the Effective Area Ratio (right).

3.3.3.2 Dynamic Inlet Model

With the knowledge of the two blockage measurement methods, a simple dynamic inlet model was used to provide additional insight as to what these blockage fractions are actually measuring. The model itself generates an arbitrary pressure profile across the inlet in a manor similar to the analysis in Bedick et al. Initially, an arbitrary pressure profile was used, assuming air as both the driving plenum gas and as the gas within the RDC channel. The pressure profile is generated assuming a isentropic, exponential decay from a peak pressure down to a given channel pressure. This expansion process provides the channel pressure against which the inlet is driving. In cases where the channel pressure profile is greater than the plenum pressure, the inlet allows for backwards flow, otherwise the inlet is flowing in the forward directions. Parametric pressure profile were generated by specifying a range of the following values: plenum total pressure, peak pressure (simulating the detonation wave), channel static pressure, and a location where the pressure profile equals the plenum pressure, BR. With the arbitrary pressure profiles, the blockage fraction, B, and the effective area ratio, α, can be calculated and compared to the specified blockage ratio BR.

Figure 3.23 shows an example of the pressure profile (subplot (a)) and the associated Mach number profile determined from the pressure profile. The vertical, dashed black line represents the location where the pressure profile equals the plenum pressure, BR, while the dashed blue line represents the point at which all backward-flowing gases have been replenished through the plenum. This location is another blockage metric that captures when the inlet begins to fill the fresh reactants and will be denoted as BR_{fill}. The details of the determination of the Mach profile will be given later in this section, but Figure 3.23 (b) shows an example of the profile, where the Mach number is correlated with the mass flow rate through the inlet.

$$\mathrm{BR}_{fill} = \frac{x_{fill}}{\pi OD} \tag{3.57}$$

Figure 3.23 also shows the different flow regions, as shown by the shading of the Mach profile plot. These regions show where backflow is present, where the backward flow is re-filling, and finally, where the forward flow begins. This highlights the differences in the blockage ratio, BR, and the location were fill resumes, BR_{fill}

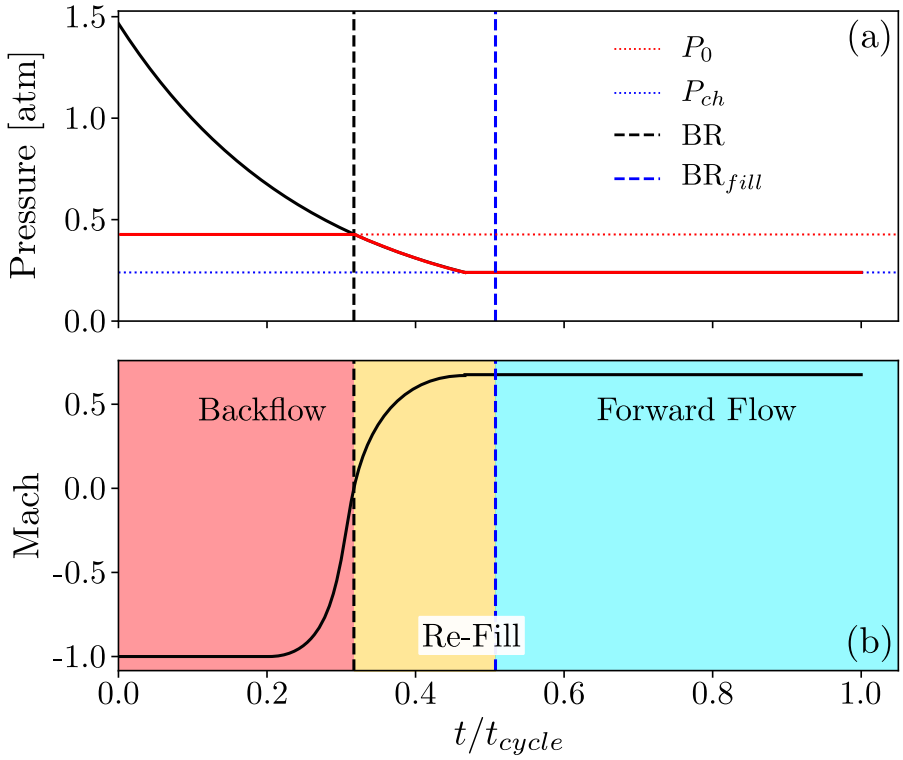


Figure 3.23: Example of the randomly generated air profile.

The process for generating the Mach number profile from the modeled pressure profile starts with a set of initial states for the air profile generation:

$$\mathbf{X}_0 = [A_{inj}, P_0, P_{peak}, P_{ch}, \mathrm{BR}]$$

This set was used to generate a profile of across the injector and does not provide any predictive characteristic. As mentioned earlier the pressure decay was modeled as an isentropic exponential decay process, where the equation for the pressure as a function of a non-dimensional space is given by:

$$P(\bar{x}) = P_{peak} exp(-k\bar{x}) \tag{3.58}$$

where $\bar{x}$ is a non-dimensional distance, $\frac{x}{\pi OD}$, such that it aligns with the definition of the blockage fraction.

This equation can then be rearranged solve for the decay constant, k. given a specified blockage ratio, plenum pressure, and peak pressure, where the initial pressure of the expansion process is the peak pressure, P_{peak}.

$$k = \frac{-ln(\frac{P_0}{P_{peak}})}{\mathrm{BR}} \tag{3.59}$$

Using the newly determined decay constant, the expansion process is modeled out to the point at which the pressure profile reaches the specified channel pressure. Upon reaching this pressure, the remaining flow area is assumed to be a region of constant static pressure flowing in the forward direction. An example of the pressure profile is seen in Figure 3.23 (a)

The next step is to relate the pressure profile to a mass flux profile through the inlet as a function of the non-dimensional distance $\bar{x}$. Using the pressure ratio profile, and assuming a isentropic inlet (with a constant c_d in both directions) the Mach number profile can be determined using the following equation:

$$M_i = \sqrt{\frac{2}{\gamma+1}\left[\left(\frac{P_{0,i}}{P_{s,i}}\right)^{\frac{\gamma-1}{\gamma}}\right]} \tag{3.60}$$

where the Mach number for each differential area is based on the total driving pressure, injector static pressure, and the ratio of specific heats at each point along the profile. In the backward flowing portion of the inlet, the driving ($P_{0,i}$) pressure is assumed to be that of the pressure profile, while the static pressure ($P_{s,i}$) is assumed to be the specified plenum pressure. The opposite is true for the forward flowing region, where the static pressure is assumed to be that of the pressure profile. An example Mach profile is shown in Figure 3.23 (b). A mass flux profile can then be generated using the Mach profile and the mass flow function:

$$\dot{m}_i'' = P_{0,i}\sqrt{\frac{\gamma}{RT_0}}M_i\left(1+\frac{\gamma-1}{2}M_i^2\right)^{\frac{-(\gamma+1)}{2(\gamma-1)}} \tag{3.61}$$

where the total temperature and gas properties are assumed to be constant and that of air.

To solve for the mass flow rate across the inlet, numerical integration was conducted on the mass flux profile:

$$\dot{m} = \int \dot{m}'' dA \tag{3.62}$$

yielding the nominal mass flow rate through the inlet, given the set of initial conditions.

In addition, the area averaged pressure (Equation 3.46) and the Mach number based on this quantity will be calculated, along with an area averaged Mach number. It should be noted that the area-averaged Mach number and the Mach number based on the area-averaged pressure are not measuring the same quantity but are useful when analyzing the effective area ratio, α, as this is defined as equivalent to the area average pressure. The area average Mach number is given by:

$$\bar{M} = \frac{1}{A}\int M(A)dA \tag{3.63}$$

while the Mach number based on the area averaged pressure, Equation 3.46, is given by:

$$\bar{M}|_{\bar{P}^A} = \sqrt{\frac{2}{\gamma - 1}\left[\left(\frac{P_0}{\bar{P}^A}\right)^{\frac{\gamma-1}{\gamma}} - 1\right]} \tag{3.64}$$

where it is important to note that this is the Mach number that is used in the calculation of the effective area ratio.

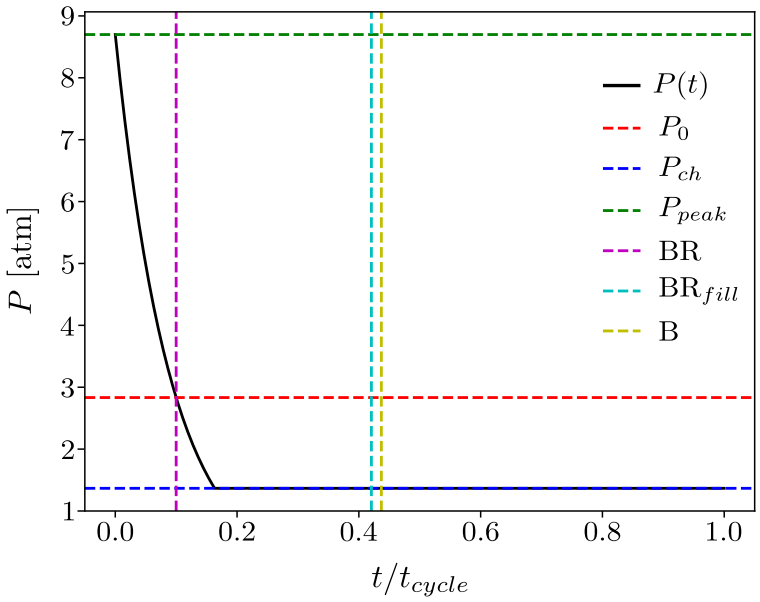


Figure 3.24: Example of Dynamic Inlet Model Pressure Profile

3.3.3.3 Extension to Detonations

A simple extension of the dynamic inlet model can be made to account for real detonation effects. In this case, the input parameters change to include the fuel and equivalence ratio, and rely on the detonation calculation to get the peak pressure instead of directly specifying it. There are two options for the detonation solver, using the CJ pressure ratio or calculating the full ZND profile. The former uses the exact processes discussed in the previous section, where the CJ pressure is

substituted in as the peak pressure, while the latter models the expansion starting from the CJ plane, accounting for the induction zone length. In either method, the expansion process is modeled as an exponential, isentropic expansion, but now using the post-detonation gas properties. To this end, the calculations of the Mach and mass flux profiles used the product gas composition in the backwards flowing portion of the inlet, while the forward flowing portion still used the properties of air. By modeling the detonation, there is now a high correlation of the peak pressure to the channel pressure, which is used as the pre-detonation state. The goal with this is to more accurately capture the effects of the detonation wave on the injector of the RDC.

3.4 Results

The following sections will discuss the results from the RDC loss models discussed in the previous section. This will begin with an in depth review of the State to State model with included loss mechanisms. Next, the non-zero velocity models will be evaluated, both at the inlet plane and the exit plane. Finally, we finish on a discussion of inlet blockage and it's relationship to RDC performance.

3.4.1 State to State Cycle Model

The follow results were constructed using the State to State model, shown in Figure 3.11 and Algorithm 9. The input conditions for the model were stoichiometric, hydrogen-air, operating at a premixed inlet condition of 2 atm and 300 K. It is assumed that the exhaust pressure is that of standard day sea level, 1 atm. The loss parameters varied between $[0, 0.9]$ except for the pressure drop fraction which was varied between $[0, 0.5]$. For reference, based on these specific initial conditions a $\xi_{\Delta P} = 0.5$ value results in an inlet pressure drop of 0.5 atm.

Figure 3.25 shows an example of a T-s diagram for the State to State model, incrementally adding loss parameters. Figure 3.25 (a) represents the ideal detonation, which accounts for the loss in available energy due to the post-detonation expansion process. Along with the ideal detonation, an ideal deflagration is shown with a dashed line, starting from the same initial conditions, which is also the case when ξ_{P} = 1.0. From this subplot, it is clear that the ideal detonation results in a final state with less entropy production, at a similar final combustion temperature; therefore, at a higher isobar. A dotted black line is also drawn around the final state of the ideal deflagration cycle (un-filled marker). This is a constant specific impulse line, where the final states above the line result in a high specific impulse compared to the ideal deflagration when isentropically expanding to the same final pressure. In Figure 3.25 (a), it is clear that the ideal detonation should produce thrust more efficiently than the ideal deflagration due to the significant reduction in entropy

production between the two cycles at a similar total heat release. This version can be thought of as the ”standard” model of RDC and other pressure gain cycles, where the expectation is a higher post-combustion pressure than the equivalent deflagration-based cycle.

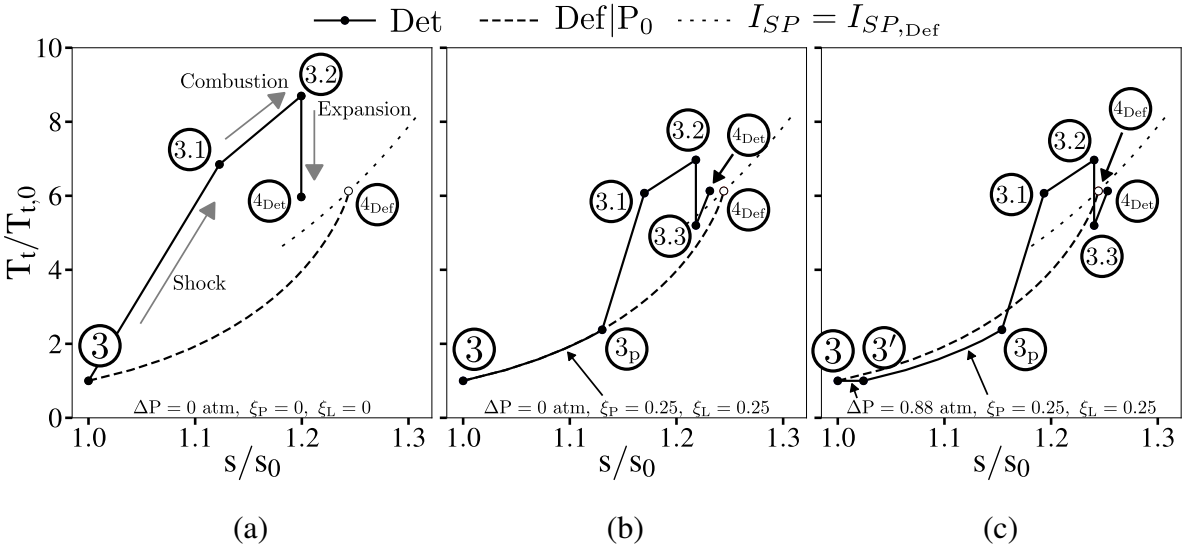


Figure 3.25: T-s Diagram State to State Model with ξ_{NC}, ξ_{CP}= 0.0.

.

As loss parameters are added, specifically the deflagration loss parameters, ξ_{P} and ξ_{L}, the detonation cycle begins to approach the same end state as the ideal deflagration. Figure 3.25 (b) shows an example of this with relatively moderate values of the deflagration loss parameters, ξ_{P}, ξ_{L} = 0.25. The distinction between the post-expansion state, (3.3), and the equilibrium exhaust state, (3.4) equals (4), is clearly shown. Because it is assumed that the fuel is fully consumed at (4), the resulting final state for the detonation in Figure 3.25 (b) still falls above the line of constant specific impulse. In this example, the entropy production of the non-ideal detonation is approaching that of the ideal deflagration device due to the larger entropy production caused by the parasitic combustion occurring before the wave. This results in a decrease in the post-detonation pressure, based on the final state isobar.

Finally, Figure 3.25 (c) shows the T-s diagram for a detonation with the same deflagration loss parameters as Figure 3.25 (b), but now with an inlet pressure loss of ΔP = 0.88 atm. This value was obtained from an experimental case with similar total conditions of the plenum and corresponds to a pressure drop fraction of $\xi_{\Delta P}$ = 0.74. Because of the high inlet pressure loss, the parasitic combustion is occurring at a much lower static pressure, resulting in a further increase in the entropy production due to the parasitic combustion. With this combination of parameters, even assuming complete combustion at the post-expansion pressure (ξ_{NC}, ξ_{CP} = 0.0), the non-ideal

detonation cycle results in a final state that is less efficient from an entropy production point of view, as well as producing less thrust than the ideal deflagration. These results show that there exist combinations of loss parameters that would result in a RDC producing much less thrust than expected, even if the combustion efficiency is 100%.

Figure 3.26 is shown below to clarify the treatment process of the post-expansion state. As was discussed in the Model Description section, the state model includes a non-commensal fuel fraction, ξ_{NC}, and a commensal pressure fraction, ξ_{CP}. The gray box outlines the potential final state, (4), based on these two parameters. The non-commensal fraction determines the amount of heat released from (3.3) to (4), where a higher non-commensal fraction means less heat release, resulting in a final state, (4), much closer to the post-expansion state, (3.3). The commensal pressure fraction, ξ_{CP}, determined the pressure at which commensal combustion occurs, where lower values correspond to combustion pressures near the post-expansion pressure at (3.3) and higher values are combustion pressures near the ambient condition, P_{amb}.

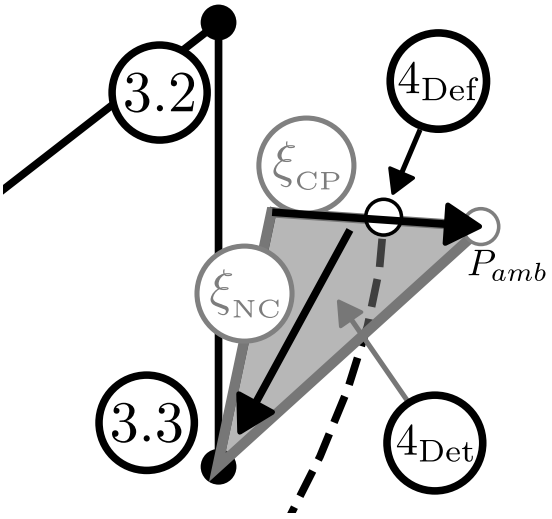


Figure 3.26: Post-expansion Treatment for the State to State Model.

When accounting for the detonation work, $Du_{3.2}$, the energy "gain" equation is now referenced to the equilibrated post-expansion state, (4). This is shown below:

$$G_4 = h_{t,4} - h_{t,3'} \tag{3.65}$$

With this definition, the gain reduces to zero for all combinations of loss parameters. This is solely due to the decrease in energy available from the detonation work term. Because of this result, it appears that defining a RDC "gain" based on the energy available is an improper definition. To combat this, the analysis shifts focus to the thrust production, or specific impulse in the case of this

section, because a better definition of "gain" is available in a detonation-based cycle.

First, the "gain" in the specific impulse over an ideal deflagration device is defined in Equation 3.66. Where $I_{SP,Def,ideal}$ is calculated assuming complete combustion at the total conditions of the plenum, and also assumes no losses through an inlet of the arbitrary deflagrative combustion. The calculated $I_{SP,Det}$ from the model is then normalized by the ideal deflagration specific impulse to provide a "gain" in thrust efficiency from the RDC.

$$I_{SP,norm} = \frac{I_{SP,Det}}{I_{SP,Def,ideal}} \tag{3.66}$$

An example of the specific thrust gain is shown in Figure 3.27, where the two loss parameters of interest, ξ_{P} and ξ_{L}, are compared at two different inlet pressure drops. For this figure, the other loss parameters are set to zero, which allows for the comparison of these results with the deflagration loss model in Figure 2.6 at the case of zero pressure drop, shown in solid lines. At the zero inlet pressure drop condition, all combinations of deflagration loss parameters resulted in a normalized specific impulse greater than 1.0. This means that the modeled cycle would result in a more efficient thrust production, relative to an ideal deflagration at the same plenum conditions. When accounting for losses in the deflagration device, these values of normalized specific thrust would improve, indicating a potential performance benefit.

At an inlet pressure drop fraction of $\xi_{\Delta P}$ = 0.5, the resultant lines of constant normalized specific impulse shift toward the bottom left of the figure. This results in cases where the modeled specific impulse is less than that of the ideal deflagration device at the same initial conditions. The combination of the inlet pressure losses with the parasitic fraction is particularly harmful due to the larger fraction of fuel being consumed at a lower static pressure, a result echoed in Figure 3.25.

Compared to the results in the base deflagration loss model results shown in Figure 2.6, it appears that the contours of normalized specific impulse from Figure 3.27 follow closely to the contours of detonation pressure ratio shown by the dashed gray lines in Figure 2.6. This result may suggest that the detonation pressure ratio is a better indicator of the RDC performance than the wave speed, regardless of the inlet pressure losses included in Figure 3.27. A deeper discussion on the pressure ratio effect on the RDC performance will be included later in this section, but first we will examine the RDC performance as a function of the wave speed and detonation fraction, χ_{D}.

Figure 3.28 shows the normalized specific thrust as a function of the normalized wave speed, $\frac{D}{D_{\mathrm{CJ}}}$, in subplot (a) and the detonation fraction, χ_{D}, in subplot (b). These plots are shown with a non-commensal fraction, ξ_{NC} = 0, which by default enforces the commensal combustion pressure to also be zero. Two inlet pressure drops are shown on the subplots, where the black lines denote zero pressure drop, and the gray lines represent a pressure drop fraction of $\xi_{\Delta P}$ = 0.5. Like Figure 2.8, lines of constant parasitic fraction, ξ_{P}, are shown in a solid style, and the lines of constant

leaked fraction, ξ_{L}, are shown in a dashed style.

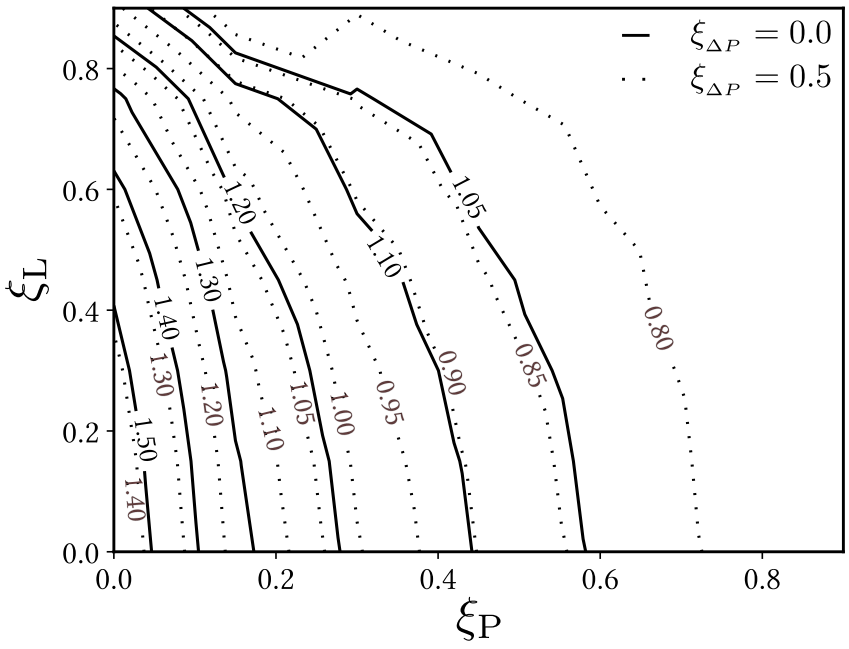


Figure 3.27: Specific impulse gain of RDC versus an ideal deflagration device as a function of the parasitic combustion fraction, ξ_{P}, and the leaked fuel fraction, ξ_{L}, at two inlet pressure drop fractions, $\xi_{\Delta P}$= 0 in solid and $\xi_{\Delta P}$= 0.5 in dotted styles. Assuming complete combustion of leaked fuel and the post-expansion pressure $P_{3.3}$. (ξ_{NC}, ξ_{CP}= 0.0)

Figure 3.28 (a) examines the normalized specific impulse as a function of the wave speed, relative to the ideal CJ speed. This figure shows the effects of the deflagration loss parameters on both the detonation wave and the RDC performance. The wave speed follows similar contours with increases in either loss parameter. The most interesting aspect of this plot is the low correlation between wave speed and the prediction of specific impulse. Looking at the contours with no pressure drop (black lines), at a wave speed of 80% of the CJ speed, the normalized specific impulse can vary widely between 105-150% of the ideal deflagration. This result suggests that wave speed, and detonation performance in general, may not be the best marker for successful RDC performance. Although these values indicate an improved performance of the ideal deflagration cycle, as additional losses are accounted for, the performance starts to dip below the deflagration specific impulse. For example, Figure 3.28 (a) also shows the contours of the deflagration loss parameters, but now at an inlet pressure drop fraction of $\xi_{\Delta P}$ = 0.5. With added inlet losses, the contour shifts downward, resulting in combinations of deflagration loss parameters with worse thrust performance relative to the ideal deflagration cycle. This result ignores the non-commensal fraction, ξ_{NC}, and the commensal pressure fraction, ξ_{CP}, so with these losses included the expected performance would decrease further.

Figure 3.28 (b) shows the same contours of deflagration loss parameters and the inlet pressure drop as Figure 3.28 (a), but now plots the detonation fraction on the horizontal axis. With zero inlet pressure drop (black lines), the performance converges to the deflagration cycle as the detonation fraction, χ_{D}, approaches zero. This result was expected based on the model methodology, especially when other losses are neglected. Similarly to Figure 3.28 (a), a moderately high detonation fraction does not necessarily indicate improved RDC performance. For example, at a detonation fraction of 80%, the normalized specific thrust can vary between 130-155% of the ideal deflagration cycle. Though this band is slightly tighter than the wave speed variation, it also provides evidence that the performance of the detonation wave is not solely linked to the the performance of the RDC cycle.

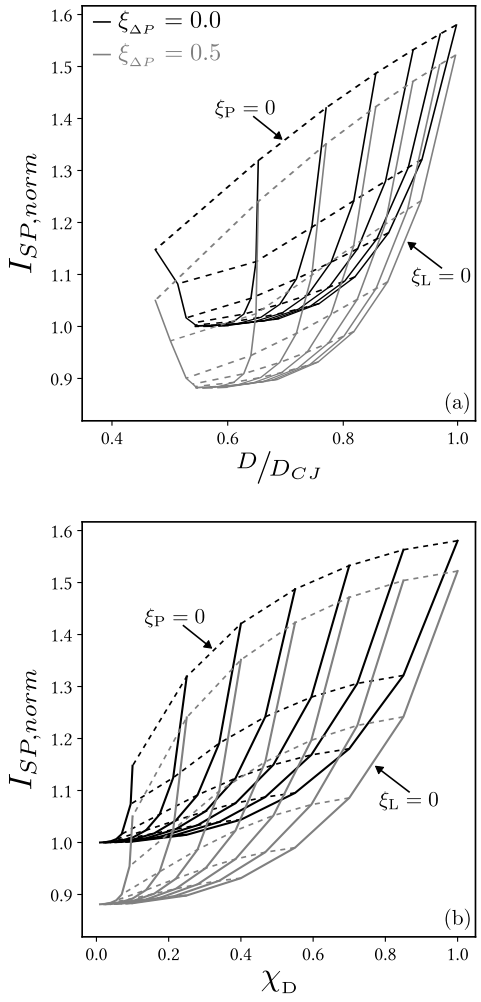


Figure 3.28: Normalized specific impulse versus normalized wave speed and detonation fraction. Lines separated by deflagration loss parameter increments of $0.15 \in [0, 0.9]$. Assuming ξ_{NC}, ξ_{CP}= 0.0.

The previous analysis of the State to State model focused only on three of the five loss parameters. Now, the examination of the non-commensal fraction, ξ_{NC}, and the commensal combustion pressure fraction, ξ_{CP}, is carried out on a manner similar to that shown in Figure 3.28. Figure 3.29 shows the contours of the two deflagration loss parameters, ξ_{P} and ξ_{L}, but now plotting the normalized specific impulse on the left axes and the estimated combustion efficiency, defined by Equation 3.11, on the bottom axes. Each subplot shows a different combination of loss parameters and their effects on the combustion efficiency and specific impulse of the modeled cycle. Figure 3.29 (a) fixed the inlet pressure drop and commensal combustion pressure fractions to zero and shows two different magnitudes of the non-commensal fraction. Because $\xi_{\mathrm{NC}} = 0$ means the combustion efficiency is 100% (see Equation 3.11), the figure uses the next step in the non-commensal fraction, $\xi_{\mathrm{NC}} = 0.15$, as the starting point, this is shown with the black contours. The right most solid line represents the zero leaked fraction case, which also indicated a 100% combustion efficiency (see again Equation 3.11). Along this line, as the parasitic combustion fraction increase (moving from top to bottom) the combustion efficiency remains at 100%; however, the normalized specific impulse decreases. This is yet another example of the difficulties in relating the performance of the detonation wave to the performance of the cycle.

Next, the non-commensal fraction was increased to the maximum value used in the parametric sweep, $\xi_{\mathrm{NC}} = 0.9$, shown by the gray contours. This increase in non-commensal fraction drastically reduces the estimated combustion efficiency. At this value of non-commensal fraction, high values of parasitic fraction or leaked fraction results in an estimated specific thrust less than that of the ideal deflagration cycle. The geometry of the RDC, specifically the length, will likely have an impact on the non-commensal fraction, and hence the combustion efficiency of the RDC. One of the promises of RDCs is the compact geometry; however, if the fuel is not able to be consumed before exiting the device, then the performance increases may not even achieve the same performance of a deflagration based combustor design with similar initial conditions. The exploration of these trade-offs is left for a future effort.

Figure 3.29 (b) takes the $\xi_{\mathrm{NC}} = 0.9$ contour from Figure 3.29 (a), now shown in black, and applies the inlet pressure drop fraction of $\xi_{\Delta P} = 0.5$ to the model (shown in gray). This subplot also fixed the commensal combustion pressure fraction at zero. The addition of the inlet pressure drop did not change the combustion efficiency, as one would expect; however, it does reduce the specific impulse performance in a manner similar to the results shown in Figure 3.28. This once again echoes the fact that the performance of the RDC is also heavily dependent on the geometry, and specifically the inlet losses.[4, 59]

Finally, the same contour of $\xi_{\mathrm{NC}} = 0.9$ from Figure 3.29 (a) is shown in Figure 3.29 (c) in black, but now the commensal combustion pressure fraction is increased from 0 to 0.9. This subplot also fixed the inlet pressure drop fraction to zero. Recall that the fraction in the commensal combustion

pressure indicates the average pressure at which commensal combustion occurs, ranging from the post-expansion pressure, $P_{3.4}$, at $\xi_{\mathrm{CP}} = 0$ to the ambient pressure, $\xi_{\mathrm{CP}} = 1$. As the commensal combustion pressure decreases (gray contours), performance decreases dramatically, mainly due to the fact that the thrust production occurs through an isentropic expansion from ④, and the lower the initial pressure at ④, the less expansion can occur. Regardless of the available energy at ④ if the exit pressure is too low, it is likely that the detonation cycle would not perform as well as the ideal deflagration, even without other loss parameters.

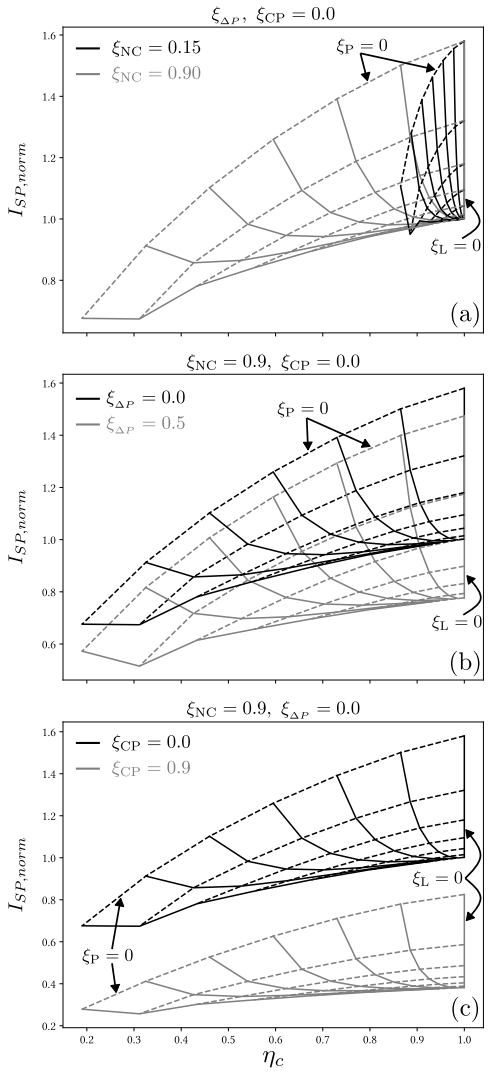


Figure 3.29: Normalized specific impulse versus combustion efficiency, η_c, with effects of each loss parameter isolated. Changes in non-commensal fraction, ξ_{NC}, at a fixed $\xi_{\Delta P},\ \xi_{\mathrm{CP}} = 0$ (a). Changes in inlet pressure drop fraction, $\xi_{\Delta P}$, at a fixed $\xi_{\mathrm{NC}} = 0.9,\ \xi_{\mathrm{CP}} = 0$ (b). Changes in commensal pressure fraction, ξ_{CP}, at a fixed $\xi_{\Delta P} = 0,\ \xi_{\mathrm{NC}} = 0.9$ (c).

Figure 3.30 shows an example of the detrimental effects of the commensal combustion pres-

sure fraction. This is shown by the normalized specific impulse versus the commensal combustion pressure, $P_{3.4}$, which also indicates P_4 based on the assumption of no additional losses occurring after the equilibration process. As the commensal combustion pressure decreases, so does the specific impulse. Despite having no additional losses, at a commensal combustion fraction high enough, the performance of the RDC cycle are predicted to be similar to that of the ideal deflagration. It should be noted that in the current implementation of the model reducing the commensal combustion pressure does not effect the velocity profile through the channel. This means that the commensal combustion pressure fraction acts as a pressure loss term. In reality, the static pressure change for which this parameters is trying to capture would lead to a change in the velocity profile. However, not all the velocity changes that occur from the post-expansion state, (3.3), to the equilibrated post-commensal state, (3.4), are in the axial direction. In a RDC, there exist azimuthal velocity profiles with non-insignificant magnitudes.[76, 66] In this version of the State to State model, the commensal combustion fraction can be thought of as treating the expansion from (3.3) to (3.4) (due to the change in static pressure) as a purely azimuthal expansion process; therefore, it does not contribute to the axial velocity component, and hence the specific impulse. An improved model with proper treatment of the expansion process from (3.3) to (3.4) is left for future efforts.

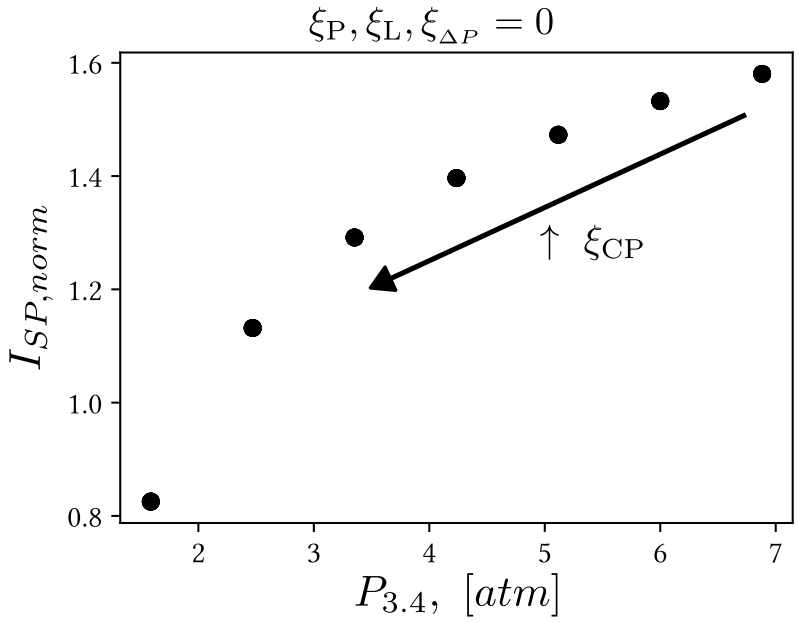


Figure 3.30: Normalized specific impulse versus commensal combustion pressure, $P_{3.4}$.

Figure 3.31 shows the normalized detonation work versus the modeled specific impulse, normalized by the ideal deflagration specific impulse. This plot shows fixed contours of ξ_{P} and ξ_{L}, while maintaining zero losses elsewhere. Much like Figure 2.10, this plot shows that as the perfor-

mance of the RDC improves with lower loss fractions, so does the amount of energy required to maintain the wave frame of reference.

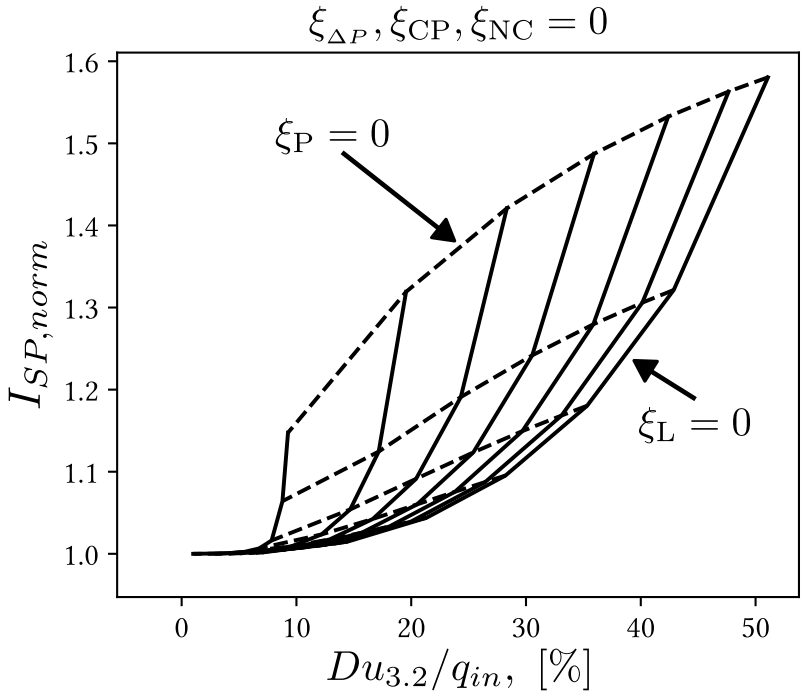


Figure 3.31: Normalized specific impulse versus normalized detonation work as a function of ξ_{P} and ξ_{L}. $\xi_{\Delta P}$, ξ_{CP}, ξ_{NC} = 0.

In a final examination of the State to State model, the Sobol sensitivity indices were calculated for the five input loss parameters, with respect to the output specific impulse. These results are shown in Table 3.2 below. From the sensitivity parameters, it is evident that the most impactful parameter on specific impulse production is the commensal combustion pressure. This term, which acts as an average post-detonation combustion pressure, effectively reduces the pressure from which the gases can expand to product thrust. In reducing this post-detonation pressure, the thrust is decreased regardless of the energy input (combustion efficiency).

The next two most sensitive parameters are the parasitic combustion fraction and the inlet pressure drop fraction. Both of these parameters had a similar impact on the thrust production from the cycle, where the inlet pressure drop fraction acts as a direct decrease on the pressure throughout the cycle. The inlet pressure drop has been seen to correlate directly with thrust production in RDCs, so this result comes as no surprise.[4, 77] The parasitic combustion fraction, similarly to the Deflagration Loss model, has a much more detrimental impact on thrust production than the leaked fuel fraction, where in the full cycle model the difference between the two are much more stark. This is due to the State to State model capturing what happened to the leaked fuel, post-detonation, where the Deflagration Loss model does not.

Parameter	S_T	ϵ_{S_T}	S_1	ϵ_{S_1}
$\xi_{\Delta P}$	0.25	0.02	0.25	0.04
ξ_P	0.29	0.03	0.22	0.06
ξ_L	0.12	0.02	0.06	0.03
ξ_{CP}	0.42	0.04	0.4	0.06
ξ_{NC}	0.01	0.00	0.00	0.01

Table 3.2: Sobol's Sensitivity Indices for the loss parameters in the State to State Model.

In general, the most important aspects for improved RDC performance appear to be increasing channel static pressure, reducing inlet pressure losses (through geometric or flow means) and reduce the parasitic combustion (provide the fuel is fully consumed elsewhere). One note of interest is the fact that the parasitic combustion fraction is the only loss mechanisms of the three that affects the performance of the wave. The other two are cycle specific losses that are less effected by the detonation wave performance, which provides another reason for framing RDC performance according to the desired use case, rather than to wave speed or detonation stability. For example, if detonation performance, in terms of wave speed, is improved with a much more restrictive inlet, then the cycle performance may decrease despite the improvement in the detonation wave.

3.4.2 Non-Zero Azimuthal Velocity Model

The following section discusses the results from the non-zero azimuthal velocity models described in Section 3.2.3. This will initially focus on the inlet region, but then move to performance impacts due to exit plane swirl.

3.4.2.1 Inlet Plane and Pre-Detonation

The following section will discuss the impacts of a non-zero incoming velocity on the potential performance of a detonation wave. First, an ideal detonation will be analyzed, similar to the example in Figure 3.12, to examine the best-case scenario. Then the same analysis will be applied to non-ideal detonation, accounting for parasitic deflagration and leaked fuel. Finally, analysis of the full non-zero swirl model from Algorithm 10 is applied across a parametric sweep of the loss parameters to determine the relationship between the expected performance of the RDC as a function of each parameter.

First, we examine the performance of an ideal detonation wave, defined from the pre-detonation state to the CJ plane, as a function of an arbitrarily specified azimuthal fill velocity. A stoichiometric, hydrogen-air detonation was used for this analysis with standard day initial temperature and

pressure. Following the process discussed in the Section 3.2.3.1, Figure 3.32 shows the effects of a non-zero incoming velocity of the state ahead of the wave, and the CJ state, (3.2), behind the wave. This figure shows a change in the properties at the CJ plane as a function of incoming velocity, normalized by the zero incoming velocity cases, subscript i. First, the wave speed in the laboratory frame, D_{l}, is reduced in magnitude directly by the incoming velocity magnitude because the detonation wave speed is fixed in the wave reference frame. Similarly, the laboratory frame induced velocity, $u_{3.2}$, is also reduced directly by the incoming velocity magnitude.

The pressure ratio and temperature ratios were then compared. Equation 3.67 shows an example of the definition of these ratios, specifically the pressure ratio. These terms compare the laboratory frame total quantity ratio across the wave with the ideal case with no incoming velocity, subscript i. The total pressure and temperature ahead of the wave are assumed to be constant as the velocity is increased, allowing for the cancellation of the pre-detonation total quantities and also reducing the static quantities of the pre-detonation state. Increasing the incoming velocity reduces both static quantities in the CJ plane while also reducing the induced velocity, resulting in a decreased total quantity in the CJ plane relative to the case of zero incoming velocity.

$$\frac{PR}{PR_i} = \frac{\frac{P_{0,3.2}}{P_{0,3}}}{\left(\frac{P_{0,3.2}}{P_{0,3}}\right)_i} = \frac{P_{0,3.2}}{\left(P_{0,3.2}\right)_i} \tag{3.67}$$

Figure 3.32 shows a slight drop-off in the total temperature achieved at the CJ condition, with respect to ideal. However, there is a much steeper drop-off in the total pressure. Without accounting for any other losses, a slight increase in the incoming flow velocity can have significant reductions in the total pressure gain through the detonation cycle. For example, the incoming velocity profile shown in Figure 3.6 would result in an approximately 25% decrease in the theoretical pressure gain of the cycle, just due to the incoming velocity alone.

With the effect of incoming velocity on the post-detonation state of an ideal detonation covered in the previous section, the focus is shifted to non-ideal detonation effects. First, the effects of parasitic deflagration on the same four parameters shown in Figure 3.32 are reproduced, along with a sweep at multiple values of parasitic fraction, ξ_{P}. These results are shown in Figure 3.33 where the condition of $\xi_{\text{P}} = 0.0$ has the same values as in Figure 3.32. The value through which the normalization is performed is the ideal detonation with no losses and no incoming azimuthal velocity. This analysis was also conducted using a stoichiometric hydrogen-air detonation at a standard day initial temperature and pressure. Similarly to the results from Figure 2.6, parasitic combustion reduces the wave speed by a slight margin, but has a much more drastic effect on the pressure ratio compared to ideal. A small initial fraction of parasitic combustion ($\xi_{\text{P}}= 0.1$), even without incoming velocity, can reduce the total pressure ratio by 50%. As the parasitic fraction increases, the effects from the incoming velocity are diminished; however, the combination of

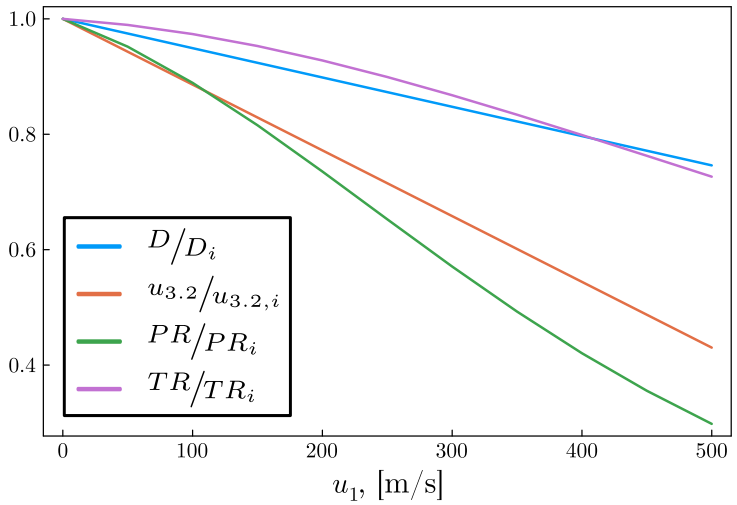


Figure 3.32: Decrement in ideal detonation properties at the Chapman-Jouguet plane with increasing incoming velocity. Hydrogen-air detonation at standard temperature and pressure, and $\phi = 1.0$.

parasitic combustion and incoming velocity can reduce the total pressure ratio by nearly 80% for small values of each ($\xi_P > 0.2$ & $u_1 \geq 100$ m/s). The effects on the total temperature ratio are similar to the cases of the total pressure ratio with increased parasitic combustion. This is due to the higher pre-detonation temperature because of the deflagration combustion.

Next, the effects of leaked fuel fraction were examined along with changes in the incoming velocity. Figure 3.34 shows the changes in the four parameters of interest, with each trace representing an increase in leaked fuel fraction, ξ_L. From these results, it is clear that on its own, leaked fuel does not have the same drastic effects on performance compared to parasitic combustion; however, the combination of leaked fuel and incoming velocity still have a significant effect on the performance. Even at moderate leaked fuel fractions and azimuthal velocities, the wave speed remains above 80% of the ideal CJ speed; however, the total pressure ratio is reduced by a much larger percentage. For example, a leaked fuel fraction of $\xi_P = 0.3$ and an azimuthal velocity of $u_1 = 250$ m/s resulted in a wave speed 80% of the CJ speed, but the total pressure ratio was only 55% of the ideal pressure ratio. This is a significant reduction in the "gain" across the detonation, despite what would be considered a relatively high wave speed.

Using the axial velocity solution from the expansion process, Equation 3.31, a specific thrust value can be calculated with respect to the input loss parameters using the model from Algorithm 10. The following analysis will parametrically examine the effects of each parameter on the expected performance of the detonation wave and the RDC. For reference, detonation performance included the laboratory wave speed, the total pressure at the CJ plane and the induced velocity at the CJ plane. Both of the last two terms directly effect the gain across the detonation.[71] The

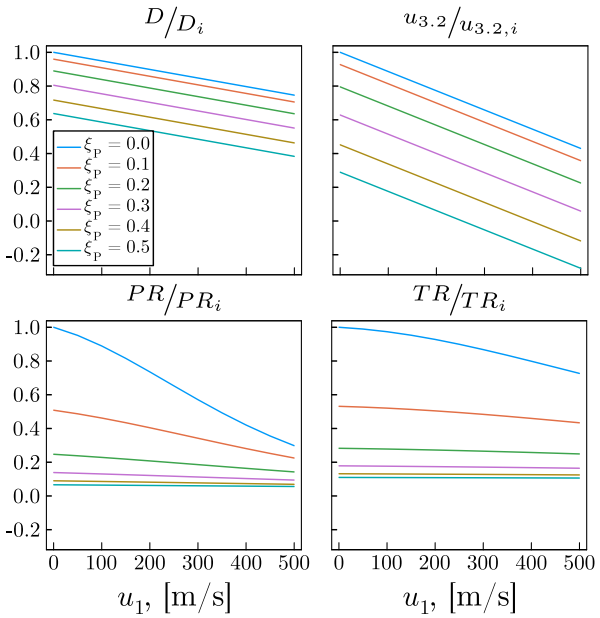


Figure 3.33: Decrement in ideal detonation properties at the CJ plane with increasing incoming velocity for a non-ideal detonation with parasitic combustion. Stoichiometric hydrogen-air detonation at standard temperature and pressure, and $\xi_L = 0$.

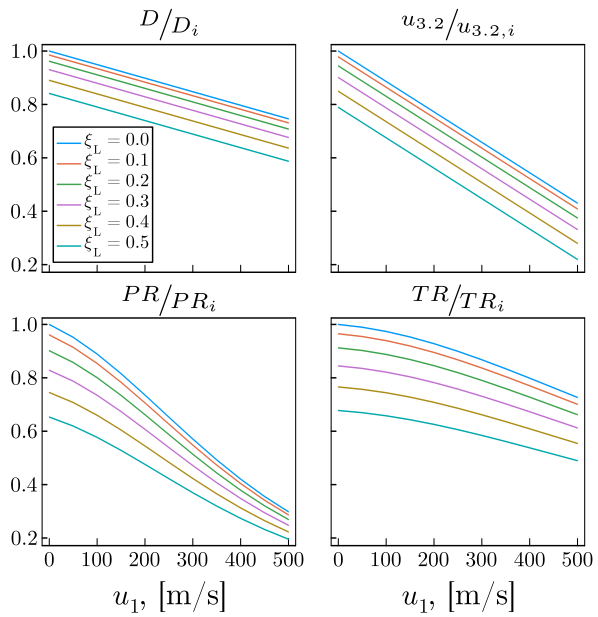


Figure 3.34: Decrement in ideal detonation properties at the CJ plane with increasing incoming velocity for a non-ideal detonation with leaked fuel. Stoichiometric hydrogen-air detonation at standard temperature and pressure, and $\xi_P = 0$.

RDC performance metric of interest is the modeled specific thrust, which will be assumed to be the axial velocity, v, predicted at the end of the expansion region, and can be related to thrust by, $F = \dot{m}v$. The following results were constructed using same the geometry from Section 3.2.3, using a stoichiometric hydrogen-air reactant composition. Table 3.3 shows the measured values that were used as the geometric and flow property inputs for exercising the model. With this data, a parametric study was conducted for each loss parameter, with the deflagration loss parameters varying between [0.0-0.5], and the expansion angle varying between [0-90°].

$\dot{m}, [g/s]$	ϕ	$P_0, [atm]$	$P_{ch}, [atm]$	PR_i	$D_{\mathrm{CJ},i}, [m/s]$	$u_{3.2,i}, [m/s]$	$\mathrm{B_P}$
301	1.02	2.34	1.33	21.89	1986.3	882.6	0.27

Table 3.3: Run 106 Initial Conditions

Figure 3.35 shows contour plots of the effects of the deflagration loss parameters on the laboratory wave speed, total pressure at the CJ plane, and the induced velocity at the CJ plane, all relative to the ideal case with no losses. Also, the specific thrust, or axial velocity post-expansion, is shown as a marker of the thrust performance of the RDC given each loss parameter. The contours in Fig-

ure 3.35 are shown for a fixed expansion angle, $\alpha = 45°$. In general, both loss parameters reduce the wave speed and induced velocities in a similar manor; however, the parasitic combustion appears to effect the pressure ratio and axial velocity to a greater degree. Specifically, a 10% parasitic deflagration loss results in a 50% reduction in the total pressure ratio, resulting in a significant loss in the "gain" across the wave. Closer examination of the induced velocity at the CJ plane shows negative values at high leaked fuel fraction and no parasitic deflagration. This is caused because the calculated induced azimuthal inlet fill velocity was greater than the induced velocity of the detonation wave at the CJ plane. Therefore, the laboratory frame induced velocity at the CJ plane is moving opposite of the wave direction.

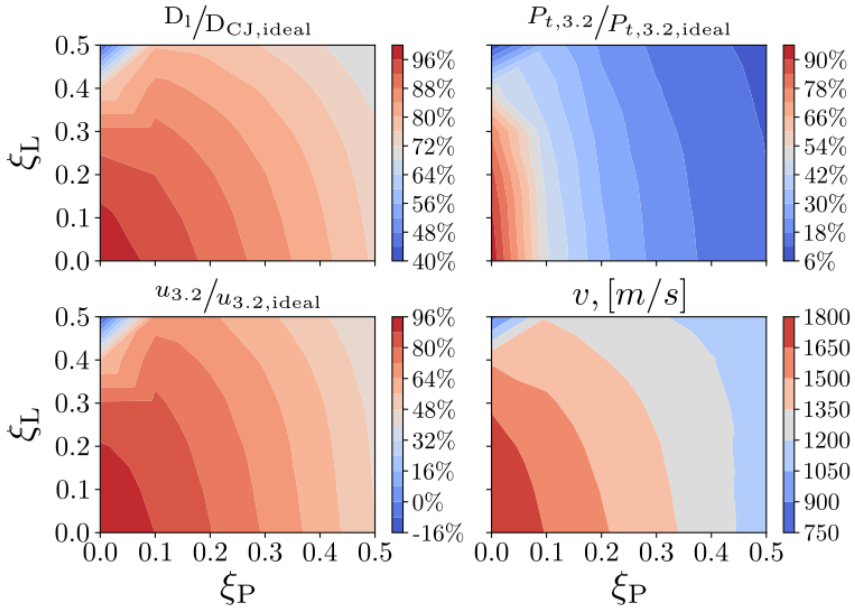


Figure 3.35: Modeled performance contours versus deflagration loss parameters. Fixed expansion angle, $\alpha = 45°$

Next, Figure 3.36 shows the same RDC performance predictions, now plotted against the parasitic deflagration fraction and the expansion angle, fixing the leaked fraction, $\xi_L = 0.0$. Because the expansion angle dictates the predicted azimuthal fill velocity, it has negative impacts on the detonation wave performance (wave speed, CJ total pressure, and CJ induced velocity) despite not directly affecting the detonation wave as modeled. Compared to Figure 3.35, it appears that the expansion angle has a similar effect on the detonation wave performance as the leaked fraction, ξ_L. The main difference is the predicted specific thrust values associated with the RDC performance. As expected, a higher expansion angle results in a higher specific thrust, due to the larger contribution to the axial direction in the expansion process from the CJ plane. The predicted maximum velocity, approximately 2800 m/s, assumed purely axial expansion from the CJ plane, with no other

loss parameters. It is unlikely that this value could be achieved based on the azimuthal expansion process required discussed in Section 1.1.1.1. For reference, with the same initial conditions, an ideal deflagration results in a specific thrust value of approximately 1200 m/s, when expanded to the same standard day atmospheric conditions. When comparing the modeled specific thrust to the results from the ideal deflagration, there exists a minimum expansion angle required to produce the same thrust, even without other losses. This is shown by the transition from the light blue contour to the gray, where at a given parasitic fraction any value of the expansion angle below the gray contour would produce less thrust than the ideal deflagration. As the parasitic fraction increases, this minimum expansion angle also increases.

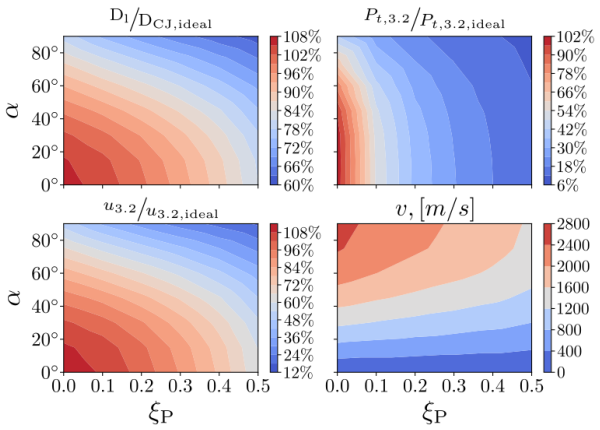


Figure 3.36: Modeled performance contours versus parasitic deflagration fraction and expansion angle. Fixed leaked fuel fraction, $\xi_L = 0.0$

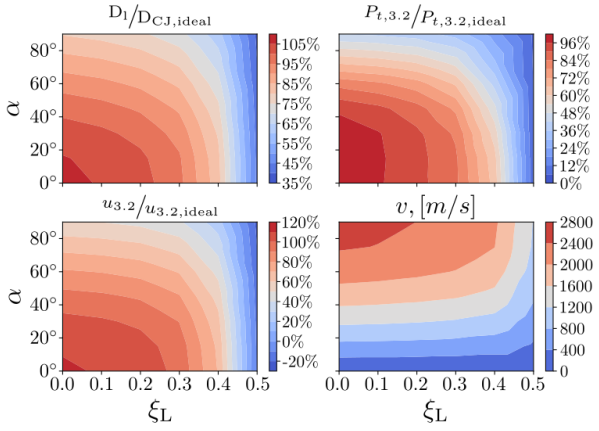


Figure 3.37: Modeled performance contours versus leaked fuel fraction and expansion angle. Fixed parasitic deflagration fraction, $\xi_P = 0.0$

Finally, Figure 3.37 shows the results for the leaked fuel fraction, ξ_L, and the expansion angle, α, with the parasitic fraction fixed, $\xi_P = 0.0$. The results echo the fact that the expansion angle and leaked fuel fraction have a similar impact on the detonation wave performance at lower leaked fuel fractions. At higher fractions, the leaked fuel becomes more dominant in terms of reducing performance. For the specific thrust, the effects of the leaked fuel have an impact similar to that of the parasitic combustion fraction from Figure 3.36. This is due to the assumption of the model of a frozen chemistry expansion process in the expansion region. With this assumption, any leaked fuel is not combusted before exiting the RDC; therefore, the total heat release is reduced. Figure 3.36 was created with no leaked fuel fraction, so despite the fact that the parasitic deflagration reduces detonation performance more than leaked fuel, the parasitic deflagration does at least consume all of the fuel. A more detailed expansion model is required to better estimate the specific thrust with the leaked fuel fraction, allowing the leaked fuel to combust along the expansion process, which almost certainly occurs within the RDC in an experimental setting.[1, 25, 2, 26]

Using the experimental data discussed in Section 3.2.3, parameter estimation was conducted to predict deflagration losses and the expansion angle in the manor shown in Figure 3.17. Table 3.4 shows the initial conditions for each case, together with the measured values and their uncertainties. MCMC sampling was conducted using the Delayed Rejection Adaptive Metropolis (DRAM) implementation through the use of the *Paramonte* sampling package.[37] The sampling requested 2500 accepted points, initialized at a random location for each case. The input parameters for the model were treated as uniformly distributed with the following bounds: deflagration loss parameters $\xi_{\mathrm{P}}, \xi_{\mathrm{L}} \in [0, 1]$ and expansion angle $\alpha \in [0°, 90°]$.

Run	$\dot{m}, [g/s]$	$P_0, [atm]$	$P_{ch}, [atm]$	ϕ	$u_1, [m/s]$	$D_{\mathrm{l}}, [m/s]$	PR
2848	148	1.43	1.17	0.56	-158 $\pm$ 26	1193 $\pm$ 220	1.62 $\pm$ 0.15
2849	148	1.47	1.21	0.80	-82 $\pm$ 40	1253 $\pm$ 150	1.78 $\pm$ 0.23

Table 3.4: Table of run conditions for cases with particle tracking.

After sampling the request amount of points, the *Paramonte* program systematically reduces the samples to remove auto-correlation between the points. The result of this process leaves a set of independent, identically distributed samples that follow the posterior distribution of the probability of the input parameters based on the given data. Table 3.5 shows the results of the sampling process, including the number of i.i.d samples for each case. Also included are the most probable input parameters, the model outputs for the most probable input parameters, and the percent error in the predicted outputs relative to the measured values. Initial inspection of these results shows that the most probable point for each case resulted in a large discrepancy between the model output and the measured values. For example, the error in the pressure ratio, PR, for each case was large, with the modeled output predicting a much higher pressure ratio. Table 3.5 also shows the same two cases, but now the pressure ratio was not included in the sampling process. The discussion of the pressure ratio mismatch will be discussed later, but first, the focus will shift to the posterior distributions of these cases.

Run	Samples	ξ_{P}	ξ_{L}	α	$D_{\mathrm{l},pred}$	PR_{pred}	$u_{1,pred}$	$e_{D_{\mathrm{l}}}$	e_{PR}	e_{u_1}
2848	2497	0.58	0.01	64.6	1182	2.48	-156	0.9	53.1	1.3
2848*	2500	0.47	0.16	65.4	1194	-	-158	0.1	-	≈ 0
2849	2498	0.54	0.45	5.3	1254	2.09	-82	0.1	17.4	≈ 0
2849*	2499	0.46	0.52	26.9	1253	-	-82	≈ 0	-	≈ 0

Table 3.5: Sampling Most Probable Values and Errors Relative to Measured Quantities. * represents cases not matching pressure ratio, PR.

Figure 3.38 shows the sampling results for Run 2848, with the pressure ratio term included in the fitting process. Figure 3.38 (a) plots the posterior distributions of the input parameters,

conditioned on the data, with the most probable value highlighted with a black point. This point is also summarized in Table 3.5. Due to the low measured wave speed and pressure ratio, the sampling process produces a posterior distribution with high parasitic combustion. These results are in line with the results from Section 2.4.1, where the pressure ratio is drastically reduced with even low fractions of parasitic deflagration ahead of the wave. Closer examination of the predicted expansion angle shows a large magnitude (relative to the azimuthal direction), indicating a smaller azimuthal expansion profile, which means that the majority of the expansion process is predicted to be in the axial direction. This large expansion angle is good in terms of the thrust prediction from this model.

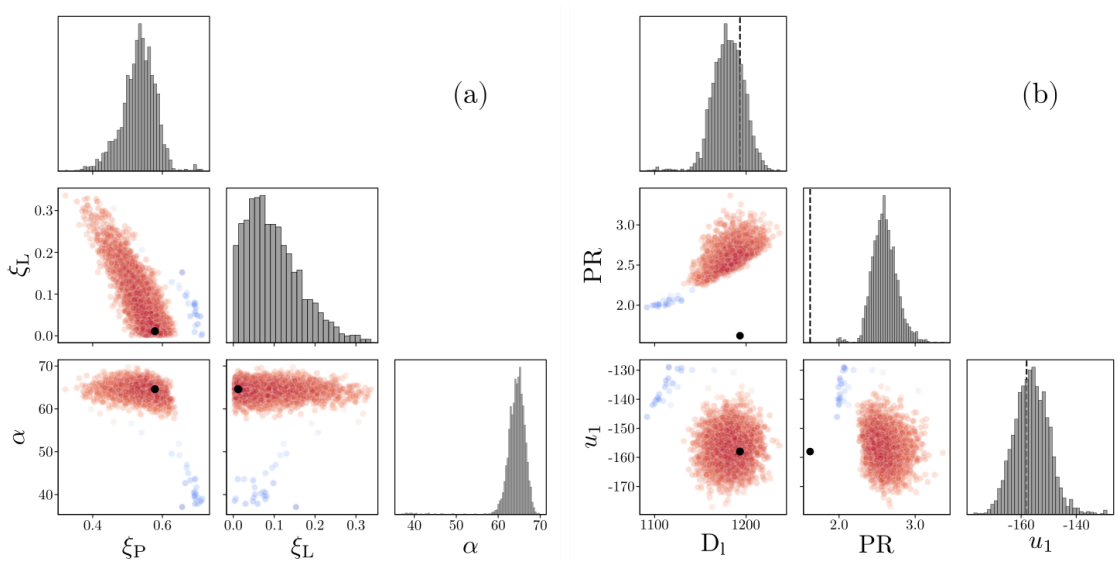


Figure 3.38: Run 2848 Sampler Results. Posterior distribution of loss parameters (a), post-predictive distribution of model outputs (b).

Examining the post-predictive distributions of the samples in Figure 3.38 (b), it is clear that the predicted pressure ratio is significantly higher than the measured pressure ratio. It is unclear at the moment if the measured pressure ratio is accurately captured, as the location of the sensor, relative to the wave, is not known for this experimental run. The opposite holds for the laboratory frame wave speed and the induced azimuthal fill velocity. Both of these distribution match closely with the measured values, indicating that the model fit the data well for these two terms.

As mentioned in this section, the pressure ratio predicted by the most probable input parameters for both cases deviated significantly from the measured value. Note that the pressure ratio measurement assumed that the high-speed probe is measuring directly in the detonation wave. With the validity of this assumption now in question, a second effort was conducted sampling the same two cases, but now ignoring the pressure ratio term as an output value in the fitting process. Now, the sampler fits the input parameters based on the wave speed, D_l, and the measured azimuthal

velocity of the inlet, u_1, only. An example of these results are shown below in Figure 3.39 for run 2848.

Figure 3.39 (a) shows the posterior distributions of the loss parameters, where the distributions are highly biased compared to those shown in Figure 3.38 (a). Of particular interest are the posterior distributions of the deflagration loss parameters, where the most probable point for the conditional distributions are significantly different from the marginal distribution for each parameter. For example, the parasitic loss parameter, ξ_{P}, has a marginal distribution with a most probable point near 0.2, while the conditional distribution predicts a value of 0.47 as the most probable value. This result is likely due to the high probability density of the expansion angle, α, around the value of 65°.

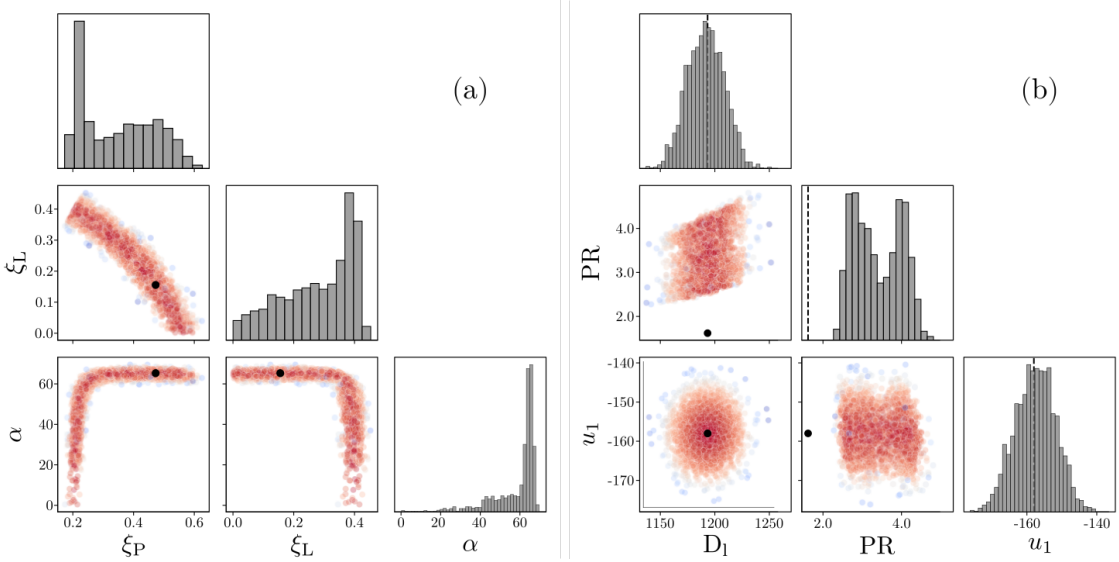


Figure 3.39: Run 2848 Sampler Results ignoring the pressure ratio measurement. Posterior distribution of loss parameters (a), post-predictive distribution of model outputs (b).

In general, the sampling process without the pressure ratio term matched the measured laboratory wave speed and induced azimuthal velocity. This resulted in similar loss parameters, which can be seen in Table 3.5. Despite removing the pressure ratio from the fitting process, the sample results in Figure 3.39 (b) predict a nearly identical pressure ratio as in the case where the pressure ratio was included. It is suspected that these results indicate that the measured pressure ratio may be lower than the actual pressure ratio. More data is required to confirm the suspicion; however, with improved measurements of the pressure ratio across the wave, these results predict a pressure ratio that one might hope to measure based on the current implementation of the model. It should be noted that it is unlikely that the model is capturing all of the necessary processes to predict an accurate pressure ratio, but it does provide more evidence that the pressure ratio measurement may not be as accurate as one would hope. An accurate measurement of the pressure ratio is required

to capture the "gain" across the detonation wave, and these results indicate that this value might be higher than what was measured, indicating that performance may not be as bad as the initial measurement would predict, at least according to the model methodology.

Using the results from the sampling process, Table 3.5, an estimated specific thrust can be calculated based on the most probable loss parameters. Table 3.6 shows the results of the predicted axial thrust, v_{pred}, compared to the specific thrust of an ideal deflagration, v_{defl}, starting at the same plenum conditions and expanding to standard day pressure. Run 2848, with and without the pressure ratio fitting, predicted higher specific thrust than an ideal deflagration. However, run 2849 had a much worse performance than the ideal deflagration for both sampling cases. This was a result of the smaller expansion angle predicted for Run 2849, combined with the higher deflagration loss parameters.

Run	$v_{pred}, [m/s]$	$v_{defl}, [m/s]$	% Defl.
2848	677	668	1.3
2848*	748	668	12.1
2849	100	781	-87.3
2849*	328	781	-58.0

Table 3.6: Specific thrust results for Runs 2848 and 2849 based on most probable loss parameters from Table 3.5. * represents fitting process without pressure ratio.

3.4.2.2 Exit Plane

This section will provide a brief discussion of the effects of the non-zero azimuthal velocity on the RDC performance, In this case, thrust will be used as a metric, which can also be normalized by the mass flow rate to give a specific thrust metric. The follow analysis examines the how a variation in the flow direction can change the thrust production due to a fraction of the flow not being aligned with the thrust producing direction.

We will assume that a post-combustion state can provide the enthalpy required to expand to a velocity of 1250 m/s. This perfectly expanded gas will then be subjected to a flow direction distribution of differing variance. See Figure 3.18 for an example of the flow direction distribution. Figure 3.40 shows the results from subjecting the ideally expanded flow to a flow angle distribution with a standard deviation of $\pm$ 20 degrees. The subplot (a) shows the axial velocity distribution, where subplot (b) shows the azimuthal velocity distribution which matches the normal distribution form provided by the flow angle distribution. This figure shows how a variation in the flow angle can reduce the expected axial velocity component, resulting in a direct loss in thrust performance.

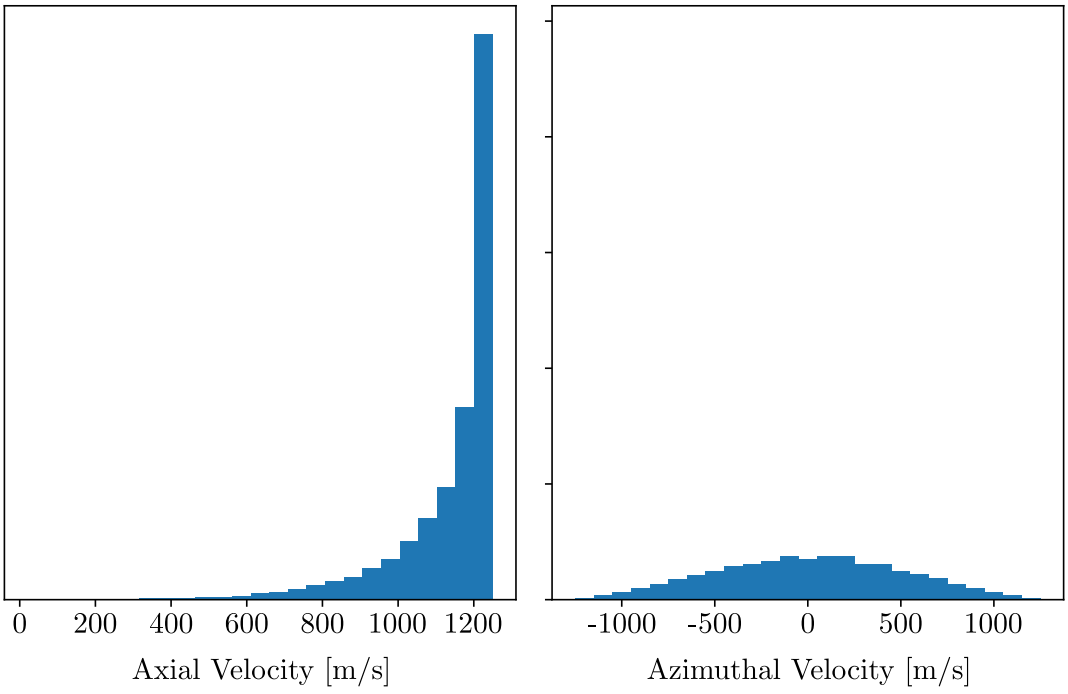


Figure 3.40: u and v Velocity Distributions with a 20 Degree Flow Angle Standard Deviation.

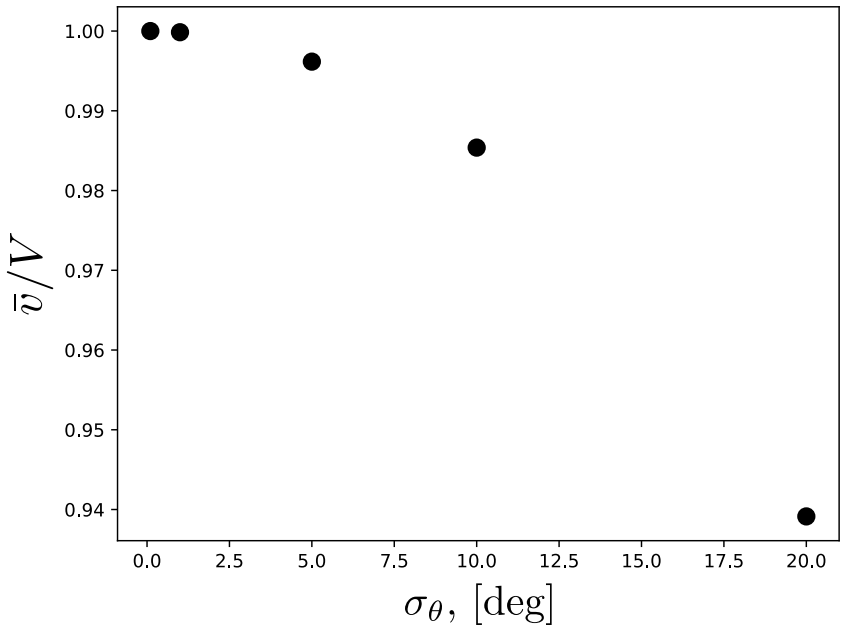


Figure 3.41: Normalized Axial Velocity versus Flow Angle Standard Deviation.

To extend this analysis, Figure 3.41 shows the average axial velocity, normalized by the ideal expansion velocity, V, as a function of the standard deviation in the flow angle. As expected, as

the variance in the flow angle increases, so does the loss in the mean axial velocity. At the highest variance, the thrust losses are approaching 10% of the thrust from the perfectly axially expanded flow. Although this loss is not large in magnitude, the variance in the flow profile is something inherent to the operation of a RDC. This means that depending on the variation in the nozzle exit flow, a noticeable percentage of the expected performance is lost to azimuthal velocity, regardless of any other loss mechanism.

3.4.3 Blockage and Dynamic Inlet Model

The following section discusses the results from the parametric study of the dynamic inlet model. This section focuses only on an example conducted using air as both the forward and reverse-flowing gas; however, these results can be extended to the detonation model. We have already discussed that the effective area ratio, α, provides a similar measurement as the blockage fraction, BR, so we will only include the blockage fraction in the following analysis, but understand the similarity between the two.

First, Figure 3.42 shows the entirety of the test points, plotting the fill-based blockage ratio, BR_{fill} as a function of the mass-based blockage fraction, B. The points are colored by the specified value of the blockage ratio defined by Bedick et al. BR.[57] From this figure, we can see that across nearly all cases, the fill-based blockage and the blockage fraction capture the same value. This result is likely due to this implementation of the inlet model, which predicts choked reverse, or forward, flow for the majority of the cycle.

Figure 3.43 shows a typical example of the inlet Mach profile from the dynamic inlet model, where the inlet profile is choked for nearly all of the injector area. Figure 3.44 shows a zoomed in view of the Mach profile, showing that there is a transition region of sub-critical flow. However, this region is so small relative to the full profile that its contributions to the overall mass flow rate are negligible.

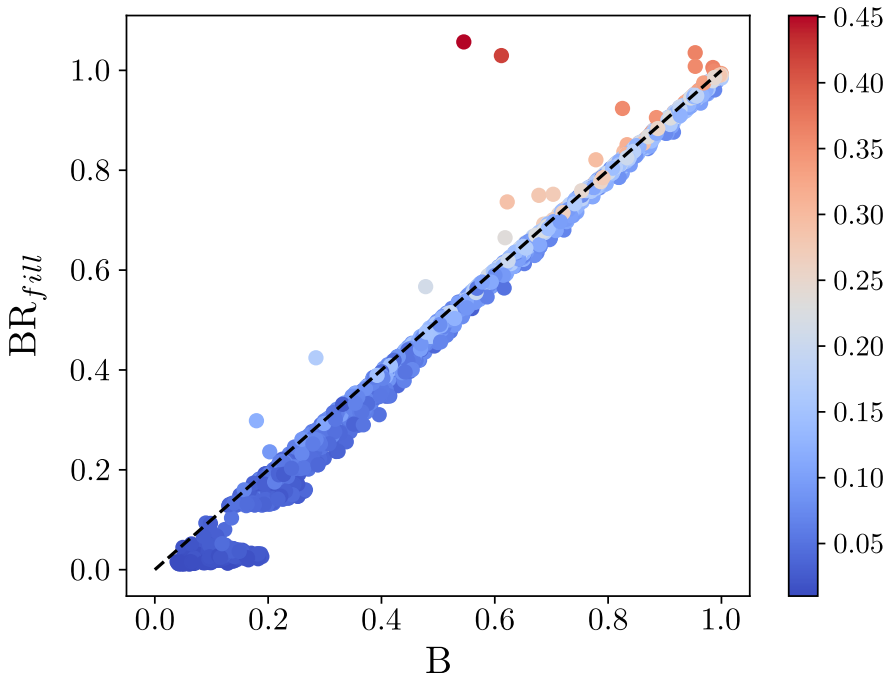


Figure 3.42: Blockage Fraction versus Fill Based Blockage: Air Examples

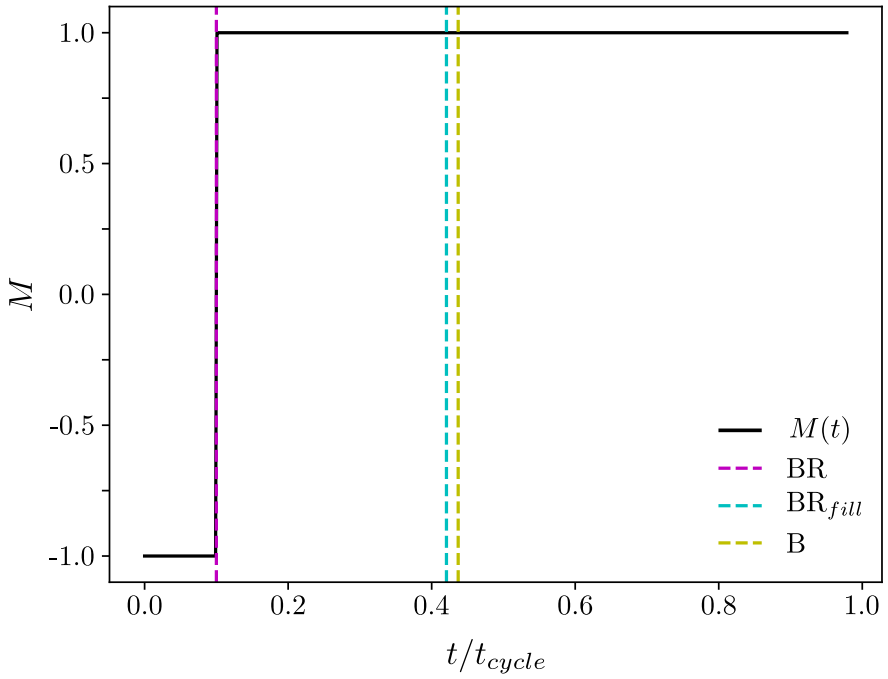


Figure 3.43: Mach Profile Typical of Dynamic Inlet Model: Full Profile

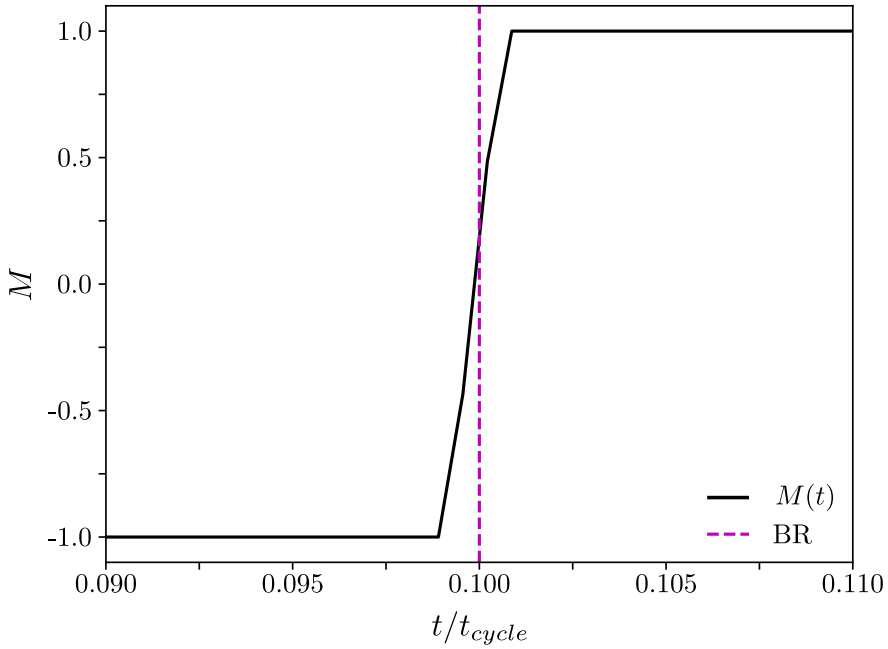


Figure 3.44: Mach Profile Typical of Dynamic Inlet Model: Zoomed on Un-choked Region

This result is interesting because it matches the blockage fraction, B, so well. As discussed by Feleo et al., the blockage fraction does not determine the inlet flow profile, so any arbitrary profile can match a given blockage value.[5] From these results, it appears that assuming a choked forward flowing region is not a poor assumption given the propensity for this result across the dynamic inlet model and the nearly identical values in the blockage fraction and fill-based blockage.

Finally, another situation of interest was discovered using the dynamic inlet model. This is best shown in Figure 3.45, where the maximum pressure is high relative to the plenum pressure (15x the channel pressure in this example), but the blockage ratio, BR, is low (5% in this example). Using the Bedick et al. definition of inlet blockage would describe the inlet as mostly forward flowing; however, this is not the case when examining the blockage fraction or the fill-based blockage. These terms show that over 30% of the inlet is blocked to the forward flow.

This example is representative of a RDC operating at a low mass flow rate condition, where the plenum and channel pressures are nearly matched. At this condition, with an ideal detonation, the detonation pressure ratio is over 13 times higher than the plenum pressure. At this condition, a significant amount of backflow is achieved despite the small area of back-flowing gases. This backflow must be re-introduced through the injector, but the plenum-to-channel pressure ratio is low, leading to an extended delay in the re-fill process, eventually resulting in a large fraction of the inlet being blocked to forward flow. This re-injection process is important to capture with any RDC inlet model, and the dynamic inlet model discussed in the chapter provides this and matches well with other definitions of blockage.

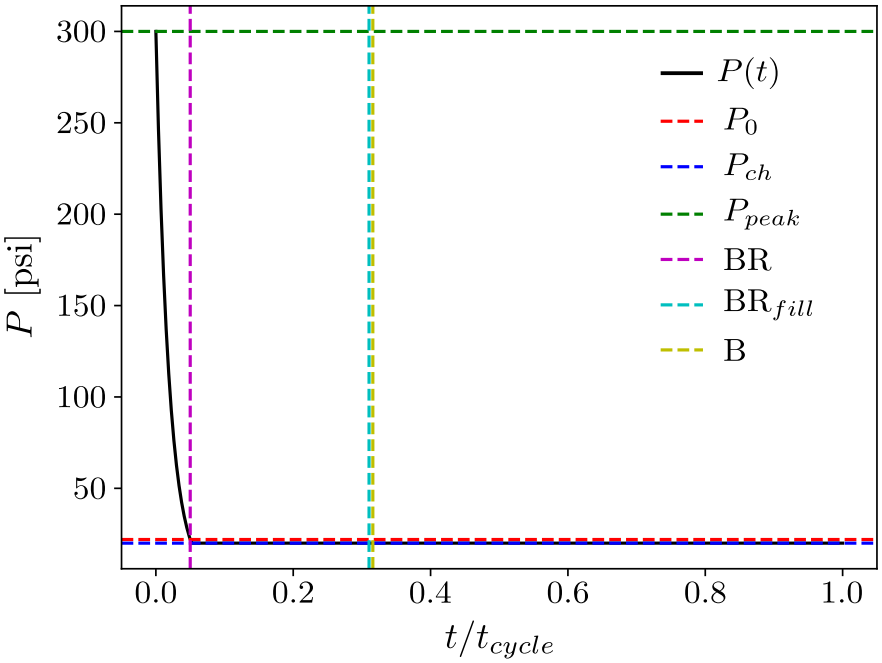


Figure 3.45: Example of High Backflow at Low Blockage Ratio

Inlet blockage is an extremely important metric when studying the operation and performance of the RDC device. The local pressure gain across the detonation wave provides a high-pressure region that directly affects the RDC injector. Depending on the overall bulk flow conditions, this high pressure zone leads to inlet blockage and significant backflow of post-detonation product gases. It is important to robustly model the inlet of the RDC and close coupling with the detonation wave in order to model the RDC more accurately as a whole system, which will be done in Chapter 4.

3.5 Conclusion

This chapter examined different loss mechanisms and processes specific to the RDC device. This was done through the study of multiple models, either dedicated to a certain aspect of RDC operation, or as a state-based cycle model. The State to State model presented in this work allowed for the variation in detonation performance, with the inclusion of losses seen within RDC devices. From this simple model, we could observe the scaling for a specific impulse metric as different losses are included. From this model, we have seen that the specific impulse for a RDC can provide an improvement over a conventional deflagration-based system, even with losses within the detonation wave. However, when we include RDC processes, specifically the inlet pressure ratio, we find that the RDC may be short of an equivalent deflagrative system.

One particular combination of losses that is detrimental to the performance of RDCs is inlet pressure loss combined with parasitic combustion. As the fluid moves through the RDC inlet, the static channel to the plenum total pressure must drop by some fraction. This means that the pre-detonation state is occurring at a static pressure lower than that being supplied by the plenum. As the stiffness of the inlet increases, so does the inlet pressure drop. When parasitic burning occurs at this reduced pressure, it provides a compounding effect that increases overall entropy production, leading to a reduction in performance.

We have also seen in Chapter 2 that the stiffness of the inlet is correlated with the parasitic combustion fraction. This is because as the inlet becomes less stiff, i.e., lower pressure drop, the detonation wave provides an increased impact on the inlet. This allows for increased inlet blockage and the potential for backward-flowing product gases. These product gases increase the temperature, and hence the speed of sound, of the pre-detonation state at best. This would result in a lower Mach number for the shock wave that leads to the detonation, reducing the overall detonation performance in terms of wave speed and pressure rate. At worst, the backward-flowing products will increase the likelihood of parasitic combustion ahead of the wave, resulting in reductions in performance.

The issue becomes the trade-space between inlet losses and detonation performance. A high-performance detonation wave, especially in terms of pressure ratio, will undoubtedly have a more significant impact on the inlet. Inlet stiffness could be increased through a reduction in inlet flow area; however, this will result in inlet losses that also reduce performance. Because of this coupling between the detonation and the inlet, a situation may arise where one would seek to reduce the performance of the detonation in order to preserve the performance of the inlet. As both experiment and modeling have shown, the inlet performance provides a nearly linear scaling factor on the pressure gain performance of the RDC.

Inlet and detonation performance trade-offs are not the only issues discovered in this section. We must also consider the effects of the non-zero azimuthal velocity profile that the detonation wave necessarily excites. Essentially, the detonation wave, being an unsteady phenomenon, progressing circumferentially around the RDC channel induces a wide variation in the azimuthal velocity profile across the RDC. This directly reduces the RDC's ability to convert the fuel gain across the detonation wave into device-level performance, such as thrust.

Finally, to maintain the detonation progression, some fraction of the energy gained across the detonation wave is lost to the system (see Section 1.1.1.1). This is inherent to detonation waves and, along with the RDC geometric configuration, the cause of the non-zero azimuthal velocity perturbations. This term also scales with the detonation performance, where the higher the wave speed, the larger the detonation work requirement. This raised the question as to the usefulness of a detonation-based system, and the detonation itself is producing the adverse effects on the inlet and

with the non-zero azimuthal velocity, while also requiring an energy return path proportional to its performance just to sustain itself. This topic and additional discussion on the ”gain” achievable with RDCs is included later in Chapter 6, but with the information gathered from the last two chapters, a new reduced order RDC cycle model was developed to better study RDC performance.

CHAPTER 4

Non-Ideal RDC Reduced Order Cycle Model Description and Parametric Study

This chapter will discuss the culmination of previous reduced order modeling efforts and RDC loss quantification. A non-ideal reduced order cycle model for RDC performance was developed in an effort to better quantify losses inherent to the RDC flowpath. This model contains many of the loss metrics, both detonation-specific and RDC-specific, discussed throughout the previous two chapters. Although it does not capture all potential loss mechanisms, it does capture the ones seen to produce the largest impact on RDC performance. This also leaves room for future efforts in developing additional loss sub-models to be used within the full cycle.

The goal of this model is to be as computationally efficient as possible while still maintaining a relatively accurate prediction of RDC performance. These two aspects occasionally run counter to one another, and in such cases, the model leans towards simplicity and efficiency over accuracy. This will be evident during the discussion of the model framework as well as the assumptions used within aspects of the model.

When quantifying the success of this model:

- The model must be computationally efficient, targeting less than 100 ms for a full cycle evaluation, and should be developed knowing it will be used for Monte Carlo based systems.
- The RDC is typically just one part of a larger system, so the model needs to be easily integrated into other models
- Needs to be able to relate detonation performance to RDC performance, specifically RDC inlets.
- This model should reduce inputs, providing closure models for typically unknown parameters based on known RDC physics.

- Although not a direct requirement, it is hoped that this model is provided in a manner that makes it simple to use for others.

This chapter will outline the model framework, along with the necessary sub-models, in full detail. After discussing the modeling procedure, this chapter will discuss a large parametric study used to exercise the model and provide bulk trends. The results of the model will then be analyzed, including a study of grid convergence on the model configuration parameters and an overall model parameter sensitivity. Finally, this chapter will conclude with a discussion of the overall viability of this cycle model, evaluations of the model structure, and physics-based methodology, and touch on the novelty of the cycle model.

4.1 Summary of Coding Language Trade-offs

A key objective for this cycle model is the execution speed of the cycle model. Aside from simplifying the model as much as possible, another key aspect of this is the selection of a proper coding language for the model. This section discusses some of the languages of interest, their trade-offs, and a summary of the language selected for this work.

Python provides an excellent option for this model because of its widespread use, great package management system, ease of use for beginners, and being free and open source. Due to being an interpreted garbage-collected language, Python is extremely slow in certain applications; however, there are options to improve the speed of code written in Python.

First, one can write a Fortran/C/C++ back-end for the performance critical parts of the code. Python will pass variables to the performant code, providing significant speed-ups. However, one issue with this is the need not only to learn a new language but also to be well versed in memory management. One would also need to generate simple, easy-to-use operations by hand due to the lack of base code functionality.

Next comes the just-in-time (JIT) compilation of Python functions. The Numba package provides wrappers that will compile a function as it is first executed. The benefit of this tool is that one simply writes their function in pure Python, which allows the compiler to improve function performance without the need to use a more complex language on the back end. Many of the models discussed in previous chapters were improved with the use of the Numba JIT compiler. To date, this tool lacks some very important functionality that makes it prohibitive to use for this cycle model. For one, the compiler works well for simple cases; however, it struggles as the functions become more complex. In some cases, the compilation takes 10-100x the time of a pure Python version of the function. This affects only the first call of the function, but unless the user is rapidly iterating within the same thread, the benefit of using the JIT compiler now becomes a detriment.

The current JIT compiler also cannot compile class objects (except for the most simple implementations). This becomes a deal-breaker when using the chemical kinetics and equilibrium solver in Cantera.

Next, new experimental languages are in development that would offer the performance of C but with the simplicity of coding in a simple language like Python. Mojo is a compiled, memory-safe programming language that offers these features. It uses the state-of-the-art MLIR compiler framework to provide efficient and performant compiled code while also using Python's coding style. This makes it an excellent choice for those familiar with Python and for this project; however, there are a few critical downsides at the moment. First, the language is brand new and still in development, so certain code can become inoperable with a change in the code base, which occurs rapidly at this stage in development. Next, this language looks like Python and can communicate with Python when required, but it is not callable from Python. This means that it cannot be the back-end for a Python function.

Finally, Rust is a relatively new programming language based on LLVM compiler technology. Rust can provide C-like speeds, is a memory-safe compiled language, and has an incredibly helpful precompile checker. This makes it much easier for someone with Python experience to learn. It also offers a great package management system, with a package called PyO3 that provides interoperability with Python. This package allows for the use of Python in Rust and exposes compiled Rust code to Python. There is one caveat: any Rust code that uses a Python object still requires the acquisition of the Python Global Interpreter Lock (GIL), meaning that the function requires some overhead for this process and is limited by the Python speeds for these scenarios.

After careful consideration of the trade-offs between each method listed above, it was determined that using Rust as the back-end provided the simplest method for improving the performance of the cycle model while still allowing the use of Python's Cantera package for chemical kinetics and equilibrium calculations. Ideally, a Rust-based chemical equilibrium package would be available to eliminate the Python GIL altogether, but until this package exists, this methodology provides a simple, performant base for the cycle model.

4.2 Cycle Model Description

The following sections discuss the RDC cycle model developed in this project. It will discuss the relevant, physics-based sub-models required to execute the full cycle, as well as how they are integrated into the full cycle model. This model uses a two-dimensional representation of the RDC device. Figure 4.1 shows a standard RDC layout on the left and a two-dimensional representation on the right. This modeling choice comes with the assumption that any radial variation in the flow field within the RDC is negligible. With the two-dimensional representation, the x-direction is

defined as the direction in which the detonation wave propagates, and the y-direction is the bulk flow direction from the inlet to the exit. Any area changes in the radial direction are captured as a function of the y-direction only.

Figure 4.1 also shows that the circumference of the RDC, based on the outer diameter of the channel, will serve as the extent of the cycle in the x-direction in the two-dimensional representation. It also shows the fill height, h_{fill}, a key dimension used to locate where the detonation wave resides within the RDC.

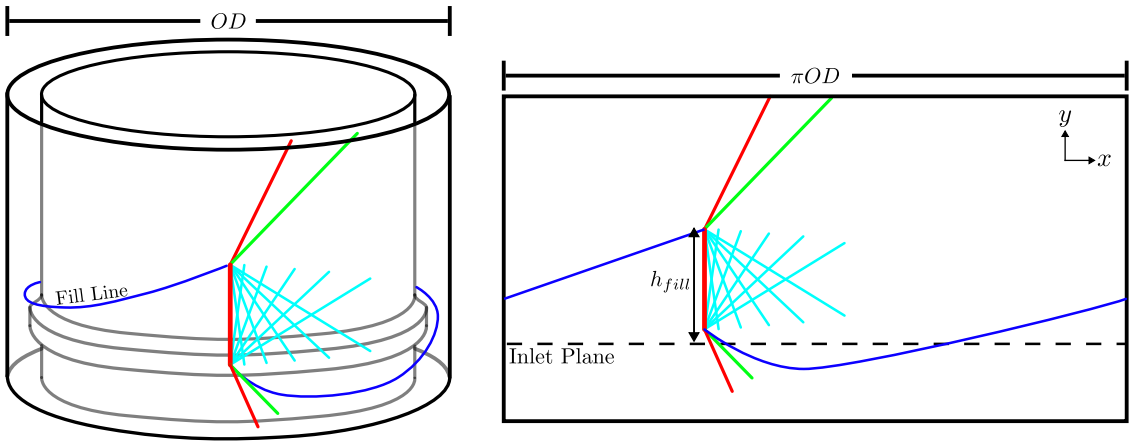


Figure 4.1: Unwrapped RDC Geometry used for the Cycle Model

With the unwrapped version of the RDC flowpath for the model, Figure 4.2 shows the regions that are captured by the various sub-models. Of particular interest are the inlet model and the post-expansion region, which provide the key link between the detonation wave and the remainder of the flowpath.

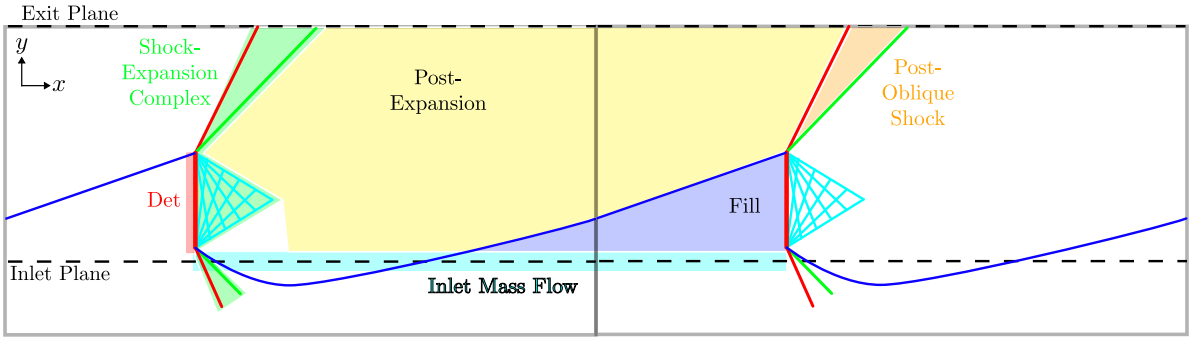


Figure 4.2: RDC Flowpath for Cycle Model with all Regions Highlighted.

Before introducing all the procedures for the cycle model, Figure 4.3 provides a diagram of some of the key locations within the RDC flowpath that are relevant to the model. The plenum plane is a constant area location within the oxidizer plenum of the RDC. This location also serves

as the datum point in the y-direction when discussing other locations. For example, the next location is the inlet plane. This is defined as the location of the minimum area within the inlet region of the RDC (blue and green). Next is the location of constant area within the RDC channel. The model assumes that the outer and inner diameters of the RDC are constant from this point to the RDC exit plane (shown in red). We also define the channel width in the region of constant area for use within the cycle model: $cw = \frac{1}{2}(OD - ID)$.

Figure 4.3 also labels certain distances in the y-direction that are used throughout the model. These include the distance from the plenum to the channel, y_{ch}, the distance from the plenum to the minimum inlet area, y_{inlet}, and finally, the distance from the minimum inlet area to the exit of the RDC, h_{RDC}.

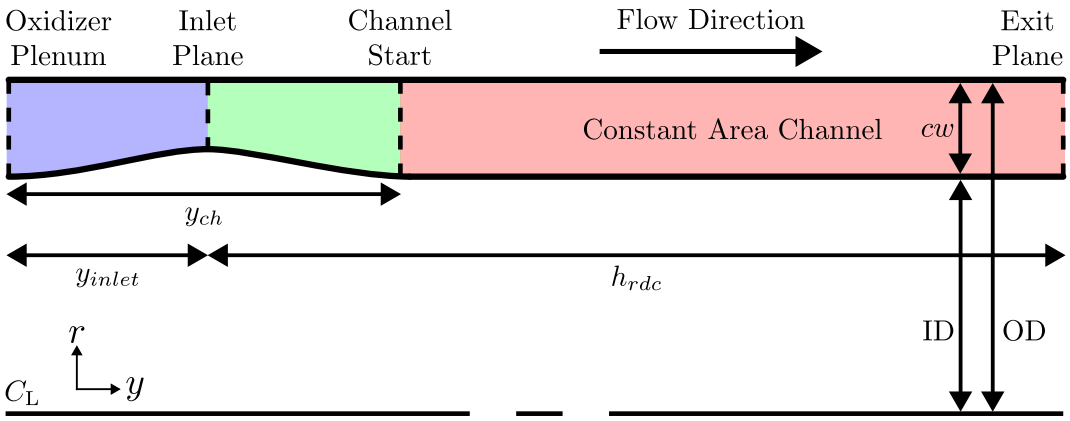


Figure 4.3: RDC Flowpath Locations of Interest

Finally, Figure 4.4 shows a block diagram of the cycle model. This includes the input variables and the main iteration methodology for the model. At a high level, the model iterates over the plenum pressure to match a specified mass flow rate. The model takes the flow conditions, RDC geometry, and deflagration loss parameters as input. Then, it calculates an initial guess for the channel static pressure term and the plenum pressure. The main model can be broken down into a non-ideal detonation calculation, a shock-expansion complex solver, and an inlet mass flow solver. So long as the difference between the inlet mass flow rate and the specified value is not within tolerance, the model will update the plenum pressure on the basis of the difference. Once convergence is achieved, the model then post-processes the results. Each sub-model within this diagram will be discussed in more detail in the following sections. Where applicable, the color scheme presented in Figure 4.4 will be maintained for each sub-model. Following the discussion of the sub-models, a final description of the full cycle model, including the pseudo-code, will be presented.

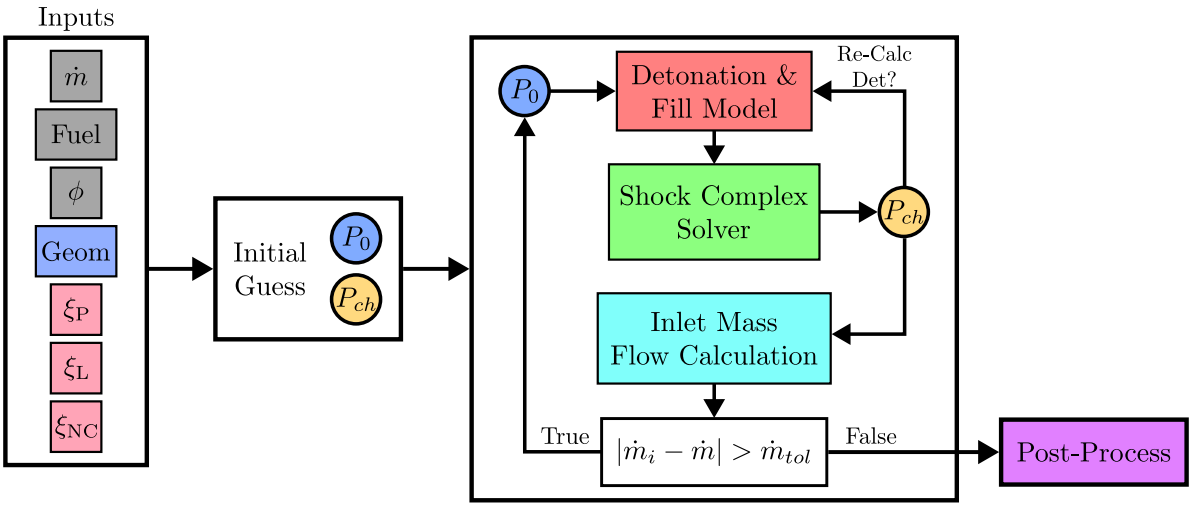


Figure 4.4: Block Diagram of Cycle Model

4.2.1 Detonation and Inlet Fill Model

The following section discusses the detonation and fill sub-model used within the full cycle model. Figure 4.5 shows the region of interest for this model, as it relates to the full cycle flowpath shown in Figure 4.2.

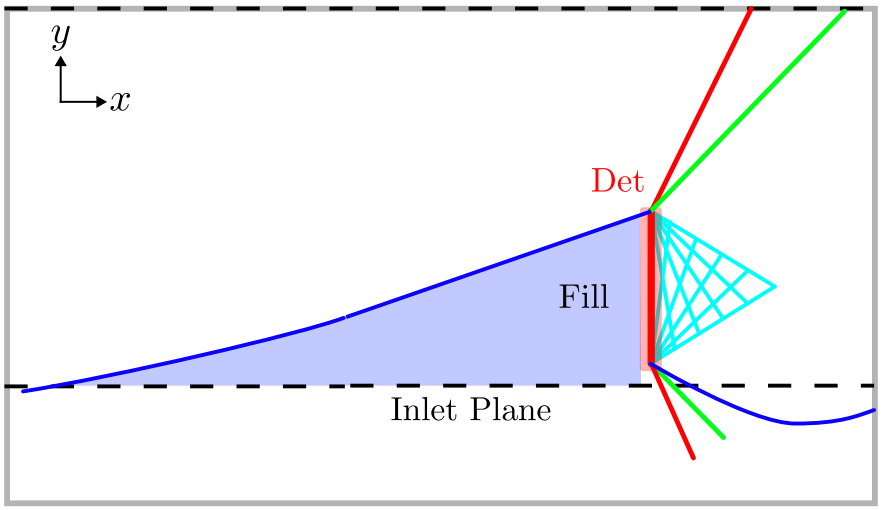


Figure 4.5: Detonation and Fill Regions Highlighted within Flowpath.

Figure 4.6 shows the block diagram for the detonation and fill model. This model takes as inputs the static channel pressure, P_{ch}, and the plenum pressure, P_0, as well as the deflagration loss parameters. First, the pre-detonation state is calculated based on the current channel pressure. Then, if this pressure has deviated by a specific amount, the non-ideal detonation model will be

recalculated. This was done to improve the calculation times when the static pressure converges, but the full model has not converged. Finally, the model will update the fill profile and properties just ahead of the detonation wave before returning these results to the shock-expansion solver.

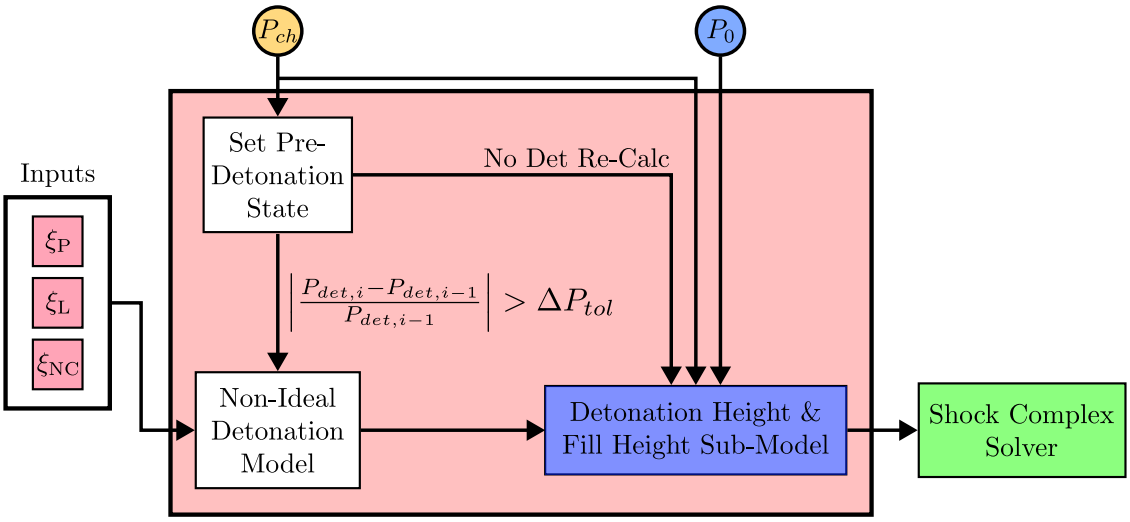


Figure 4.6: Block Diagram of the Detonation and Fill Model

The modeling of the detonation wave within the RDC cycle deck uses a modified, non-ideal CJ solver, which was chosen over a similar, non-ideal ZND solver to improve the efficiency of the cycle model. This sub-model relies heavily on the modified Cantera gas object and, therefore, requires the most communication time with the Python interpreter.

The detonation state calculation uses the CJ model from Section 3.3.1. This sub-model uses the following loss parameters: ξ_P, ξ_L, ξ_{NC}, which account for parasitic combustion and product re-circulation in the pre-detonation reactants, leaked fuel passing through the detonation wave, and the post-detonation combustion of a fraction of any leaked fuel, respectively. The detonation calculation is also grouped into the inlet fill update due to their dependence on one another. Algorithm 11 provides the pseudo-code for the process used to model the detonation wave, its impact on the RDC inlet, and vice-versa.

The detonation and fill sub-model begins with the input deflagration loss fractions and the current channel static pressure, P_{ch}. It will be discussed further in later sections, but whenever this channel pressure variable is updated, the detonation and fill sub-model will also be updated. This static pressure is compared with the ambient channel pressure, and a pre-detonation pressure is set, P_{det}. With this pressure, the pre-detonation state is updated with Algorithm 12, setting up the initial condition for the non-ideal CJ detonation model, Algorithm 13. If these initial conditions do not change by a given amount, the detonation calculation is skipped to save computational effort. Otherwise, the detonation properties are updated, and, if necessary, the post-expansion state

is equilibrated, and its properties are updated. Finally, the detonation and fill model updates the remainder of the inlet fill properties with Algorithm 14.

Algorithm 11 Detonation and Inlet Fill Model

Require: $\xi_{\mathrm{P}}, \xi_{\mathrm{L}}, \xi_{\mathrm{NC}} \in [0,1], P_{ch,i}, \Delta P_{tol}$

if $P_{ch,i} < P_{amb}$ **then**

$P_{det,i} = P_{amb}$

else

$P_{det,i} = P_{ch,i}$

end if

Calculate Pre-Detonation State: T_{ch} ▷ *Algorithm 12*

if $\left|\dfrac{P_{det,i} - P_{det,i-1}}{P_{det,i-1}}\right| > \Delta P_{tol}$ **then**

*Re-calculate non-ideal detonation ▷ *Algorithm 13*

*Update post-detonation properties: $D_{\mathrm{CJ}}, P_{\mathrm{CJ}}, T_{\mathrm{CJ}}$

if ξ_{NC}& ξ_{L}!= 0 **then**

*Equilibrate post-exp state

*Update post-expansion properties

end if

end if

Update Detonation Height: h_{det} ▷ *Equation 4.1*

Update fill properties ▷ *Algorithm 14*

* = *Requires Python Global Interpreter Lock*

Algorithm 12 calculates the pre-detonation state for the model. Given the RDC flowpath geometry, a pre-detonation pressure, P_{det} and plenum total pressure, P_0, this model first calculates a Mach number profile through the RDC inlet, assuming isentropic flow (outside of potential shock waves within the inlet). After this profile is constructed, the channel static temperature, T_{ch}, is also calculated. Finally, vectors of the inlet velocity and position are returned to the model for further calculations.

Algorithm 12 Pre-Detonation State Update Model

Require: $P_0, T_0, P_{det,i}$, RDC Geometry

Assuming isentropic flowpath solve the Mach profile through inlet region: $M(y)$

Check if normal shock is present in the post-injector region

Calculate static temperature in channel region: T_{ch}

return Vectors of position and velocity through flowpath starting at the injector, y_{inj}: $\overrightarrow{y}$, $\overrightarrow{v}$

Algorithm 13 shows the updated version of the non-ideal detonation model. This model requires the deflagration loss parameters and the pre-detonation static pressure and temperature used to set the pre-detonation state object. After initialization of the pre-detonation state, the deflagration loss model from Section 2.3.1 is used to calculate the detonation wave speed, pressure, and temperature. Provide there is leaked fuel, $\xi_{\mathrm{L}} \neq 0$, and the non-commensal combustion fraction is not one, the post-detonation state has a fraction of fuel reset to reactive for the post-expansion state equilibrium calculation.

Algorithm 13 Modified Deflagration Loss Model

Require: $\xi_{\mathrm{P}}, \xi_{\mathrm{L}}, \xi_{\mathrm{NC}} \in [0, 1], P_{ch}, T_{ch}$

*Initialize reactant mixture at P_{ch}, T_{ch}: (3′)

*Run Deflagration Loss Model ξ_{P} and ξ_{L}: (3.2) ▷ *Algorithm 4*

*Reset $(1 - \xi_{\mathrm{NC}})$ moles of leaked fuel to reactive

* = *Requires Python Global Interpreter Lock*

After the detonation properties are calculated with Algorithm 13, the height of the detonation wave can then be calculated based on a continuity argument. Equation 4.1 shows the continuity re-written to calculate the detonation height based on the assumption that all of the mass flow entering the device.

$$h_{Det} = \frac{\dot{m}}{\rho_{\mathrm{P}} D_{\mathrm{CJ}} cw} \tag{4.1}$$

where ρ_{P} is the pre-detonation density and cw is the channel width of the RDC. Figure 4.7 shows a visual representation of the calculation of the detonation height, Equation 4.1. For this model, it is assumed that the channel width is constant across the detonation wave. In reality, this may not be the case as the detonation moves closer to the inlet or exit plane of the RDC. It is reasonable to include this information in the model, as the RDC flow profile is already specified; however, it was determined that the fidelity gained from this operation would not outweigh the performance benefits of the simpler approach.

After the calculation of the detonation height, the detonation and fill model uses Algorithm 14 to update the properties associated with the fill process of fresh reactants. First, the fill time, t_{fill}, is calculated using the cycle time, t_{cycle}, and blockage ratio, BR. The cycle time is based on the laboratory wave speed in the x-direction of Figure 4.1, which will update each iteration. The blockage ratio is calculated using the details discussed in the inlet sub-model discussed in Section 4.2.3. With this cycle time, the fill height and fill velocity can be calculated using Algorithm 15. When the fill velocity updates, so too does the detonation tilt angle, α, and the laboratory wave speed in the x-direction, D_{lab}. This, in turn, updates the cycle time once more. Instead of

iteratively converging on the cycle and fill time within Algorithm 14, the model simply updates these variables for the next call of this algorithm. In doing so, an additional loop within the full model is removed, while convergence on the overall cycle is still achieved.

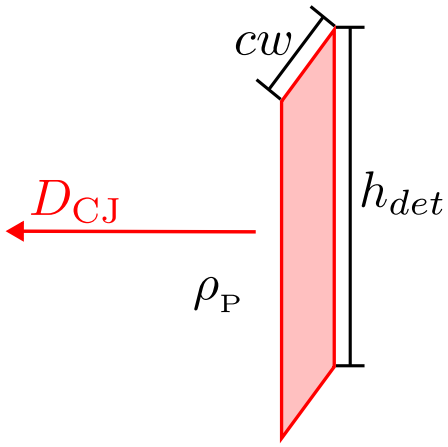


Figure 4.7: Visual Representation of the Detonation Height Calculation

Algorithm 14 next checks the fill height in relationship to the location of the constant area channel portion of the RDC (see Figure 4.3). If the fill height is too low, it will adjust appropriately, forcing the detonation to be fully within the constant area region. Though this is not completely accurate, it ensures a consistent cycle convergence, and the output results indicate that the fill height could not be achieved. In some cases, the initial conditions for the cycle result in this situation; however, further iteration will resolve this issue, and the fill height will not need to be updated in later iterations. If the fill height is too low in the converged solution, the cycle will be classified as a failed cycle. It should be noted that the fill model assumes air as the working fluid. If one were to include the addition of fuel injection, product re-circulation, and/or parasitic combustion, then the calculated fill profile would change. Specifically the fill height and fill velocity. This implementation is saved for future versions of the model.

Algorithm 14 Fill Model

Require: $t_{cycle} = \pi OD/D_{lab}, BR, D_{\text{CJ}}, h_{det}, \delta$

Update fill time: $t_{fill} = t_{cycle}(1 - BR)$

Run fill height calculator: h_{fill}, v_{fill} ▷ *Algorithm 15*

Update detonation angle: $\alpha = \sin^{-1}\left(\frac{v_{fill}}{D_{\text{CJ}}}\right)$

Update Laboratory Frame Wavespeed: $D_{lab} = \sqrt{D_{\text{CJ}}^2 - v_{fill}^2}$

Update Cycle Time: $t_{cycle} = \frac{\pi OD}{D_{lab}}$

if $h_{fill} < y_{ch} + h_{det}\cos(\alpha)$ **then**

$h_{fill} = y_{ch} + h_{det}\cos(\alpha)$

end if

Update Lower Detonation Location: $y_{det,0} = h_{fill} - h_{det}\cos(\alpha)$

Update Upper Detonation Location: $x_{det,1} = -h_{det}\sin(\alpha)$

Update Fill Angle: $\beta = \tan^{-1}\left(\frac{h_{fill} - y_{inj}}{\pi OD(1 - BR) + x_{det,1}}\right)$

Update Virtual Origin Point w/ new fill angle, β: x_{VO}, y_{VO} ▷ *Algorithm 16*

With the fill height established, the next step is to determine the locations of the upper and lower portions of the detonation wave in the laboratory frame. For clarity, the upper part of the detonation in Figure 4.1 is the side closest to the exit plane of the RDC, and it will be referenced as the downstream location (downstream of the inlet plane and initial injection of reactant). The lower portion of the detonation in Figure 4.1 will be referred to as the upstream location, as it is closest to the inlet and reactant injection plane. Finally, the fill angle. β, can be calculated based on the fill height, RDC circumference, blockage ratio, and previously calculated detonation locations. Figure 4.8 shows a diagram of the aforementioned angles and locations calculated in Algorithm 14.

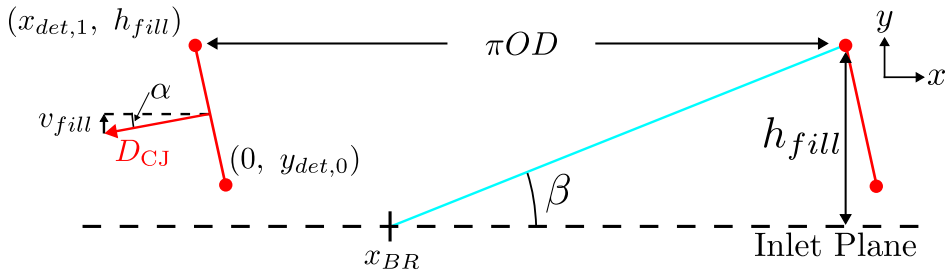


Figure 4.8: Diagram of Key Locations and Angle within the RDC Cycle Model

Finally, Algorithm 14 calculates the virtual origin point. This point, shown in Figure 4.10, is defined as the intersection of the slip line, at angle δ, and the fill line, at angle β. The virtual origin serves as a location from which all final particle paths (solid black lines in Figure 4.9) originate for

the post-expansion processes discussed in Section 4.2.2.6. This assumes that after the detonation and expansion fan (see Section 4.2.2.4), all fluid particles follow a path that can be traced back to this virtual origin. The virtual origin point methodology and the subsequent application thereof serve to directly couple the detonation region with the exit plane without the need for more complex solutions like the 2-D method of characteristics. An additional discussion of the processes behind this linkage is included in a later section.

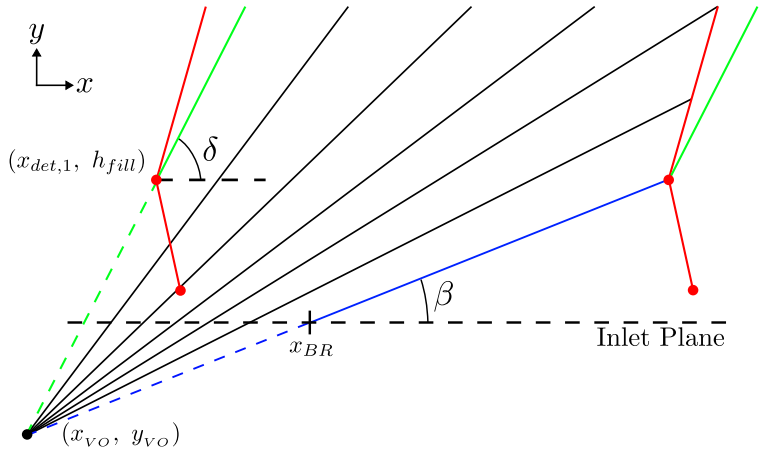


Figure 4.9: Diagram Visualizing the Virtual Origin Calculation

Figure 4.10 shows two examples of applying the virtual origin methodology to particle paths from CFD results.[10, 9] There are minor deviations from the virtual origin method compared to the calculated particle paths; however, the generally good agreement between the two provides confidence that the use of the virtual origin method does not deviation too far away from the physical processes happening within the RDC channel. This is especially true as the particle paths move further from the detonation wave, which is fortunate as this is the exact region where the particle flowpath is needed.

Algorithm 15 lists the steps required to calculate the fill height and the fill velocity. This sub-model assumes that reactant injection in a small differential area just ahead of the detonation wave is steady and fully developed. Figure 4.11 shows an example of the location of the differential area in question. It also assumes that the flow in this region is isentropic, except for potential shock waves within the inlet required to match a given pressure ratio. Future versions of this model may include a more *lossy* injection process, which more closely matches experimental RDCs.

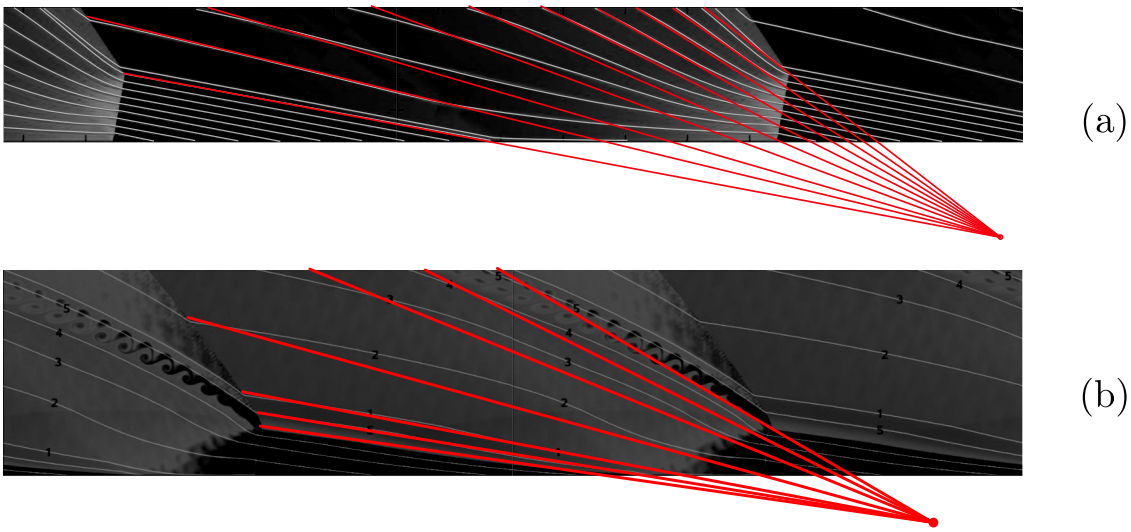


Figure 4.10: Examples of Applying the Virtual Origin Process to Particle Paths from Multiple CFD Results. Modified from Grunewald et al. (a)[9], Schwer et al. (b)[10]

Algorithm 15 Fill Height Calculation

Require: Vectors of position and velocity: $\overrightarrow{y}, \overrightarrow{v}$

By linear interpolation, generate velocity as a function of position: $v_{fill}(y)$

Integrate velocity profile in time $\in [0.0, t_{fill}]$: Δy_{file}

Calculate fill height: $h_{fill} = y_{inj} + \Delta y_{fill}$

return Fill height and final fill velocity: h_{fill}, v_{fill}

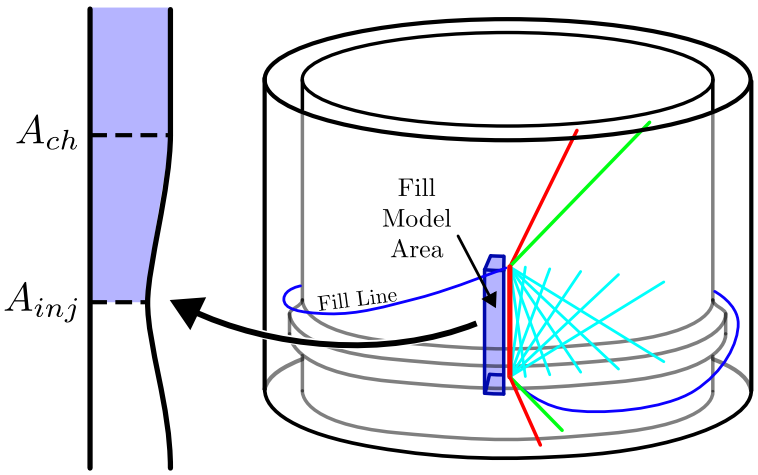


Figure 4.11: Diagram of the Pre-Detonation Differential Area used in the Fill Height Model, Algorithm 15.

Given the inlet flowpath of the RDC, the total plenum pressure, P_0, and the channel static pressure, P_{ch}, a Mach number profile can be calculated from the inlet. Figure 4.12 shows the region breakdown for an isentropic inlet, where the flow can be sub-sonic throughout the inlet, super-sonic with shock waves, or purely super-sonic through the RDC inlet. If the flow has a standing normal shock wave, a shock locating algorithm is called to find the location (and area) of the shock wave. Next, the normal shock relations are applied to calculate the post-shock state, after which the remainder of the Mach number profile is generated post-shock until the constant area channel location. Finally, the flow continues to the constant area channel portion of the RDC.

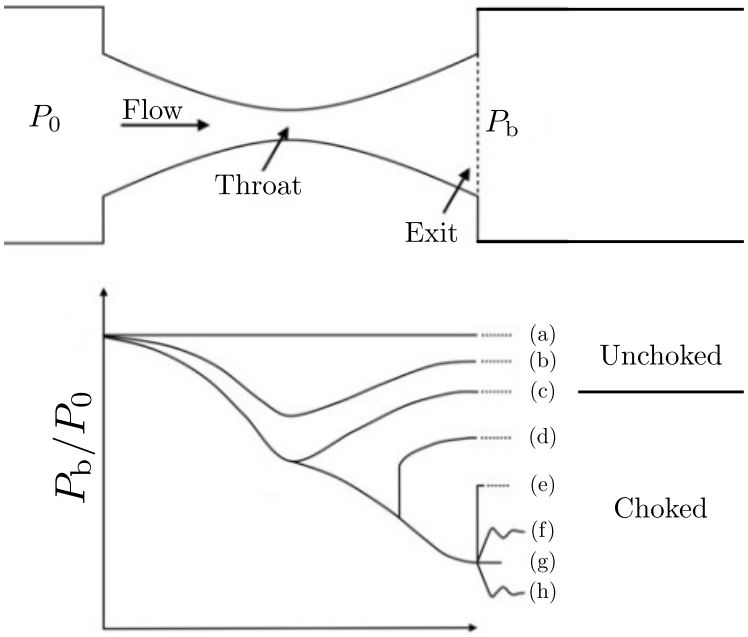


Figure 4.12: Isentropic Inlet Flow Profile as a Function of Pressure Ratio.

A velocity profile was also calculated with the full Mach profile. This velocity profile is then integrated in time, from 0 to t_{fill}, to determine the distance the fill will travel before the next wave. Figure 4.13 shows an example of the velocity profile in the case where there is a shock in the inlet region (left), along with the distance traveled by the particles (right). At the fill time, t_{fill}, the position of the particle is returned as the fill height. Because Algorithm 15 starts from the inlet plane of the RDC, this location is added to the calculated fill height to correctly position the fill height within the RDC flowpath.

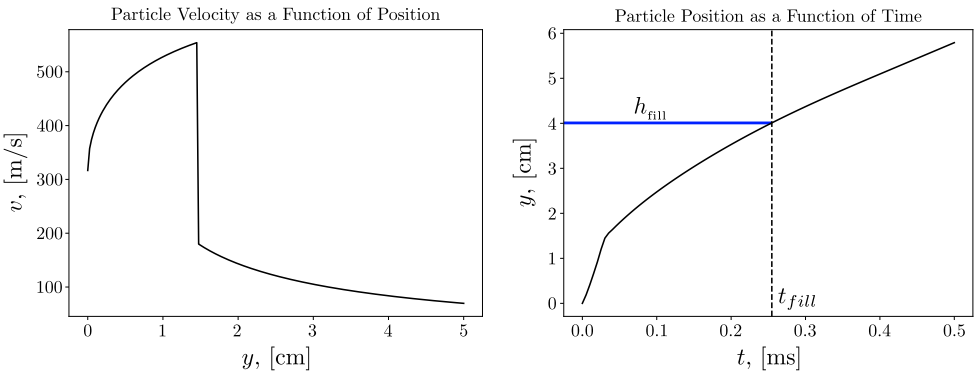


Figure 4.13: Velocity Profile from Fill Model (left). Time Integration of Velocity Profile to Calculate Fill Height (right).

Algorithm 16 provides the utility function used to determine the intersection of two lines, given the point and slope of each line. This algorithm is used frequently throughout the cycle model.

Algorithm 16 Get Intersection Point of Two Lines

Require: $x_1, y_1, m_1, x_2, y_2, m_2$, where m is the line's slope

if $m_1 = m_2$ **then**
  Raise Error
else
  if m_1 & m_2 are both finite **then**
    $x = \frac{y_2 - y_1 + m_1 x_1 - m_2 x_2}{m_1 - m_2}$
    $y = y_2 + m_2(x - x_2)$
  else
    if m_1 is finite **then**
      $x = x_1$
      $y = y_2 + m_2(x_1 - x_2)$
    else
      $x = x_2$
      $y = y_1 + m_1(x_2 - x_1)$
    end if
  end if
end if

4.2.2 Shock-Expansion Complex

This section discusses the methodology behind the shock and expansion sub-model. Figure 4.14 shows the regions of interest for the shock-expansion model. This includes the shock-expansion complex, highlighted in green, and the post-expansion region before the RDC exit. This post-expansion region includes both shocked and un-shocked flow, which is used to update the input conditions for the next iteration of the shock-expansion complex model.

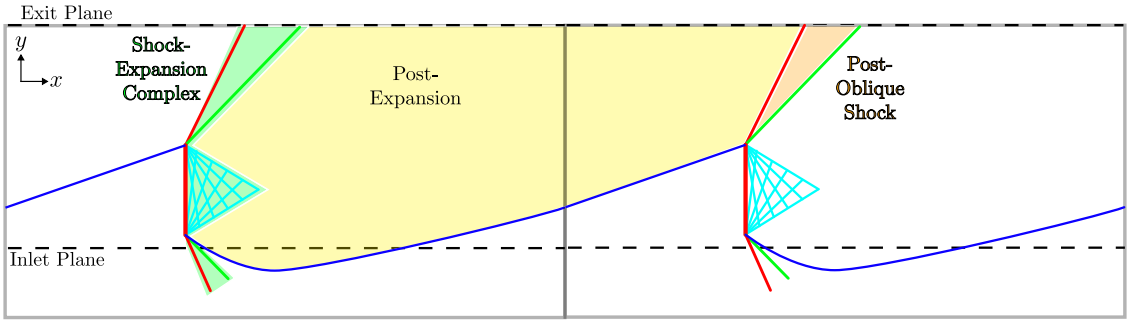


Figure 4.14: Shock-Expansion Complex Region within Flowpath.

Figure 4.15 shows a zoomed-in view of the Shock-Expansion complex. This includes upper and lower shock complexes, which will be discussed in detail in a later section, and the main expansion fan complex, which is solved using a simple method of characteristic network. It also shows the post-expansion region from the previous wave entering the current wave. This region acts as an input condition to solve the downstream shock complex.

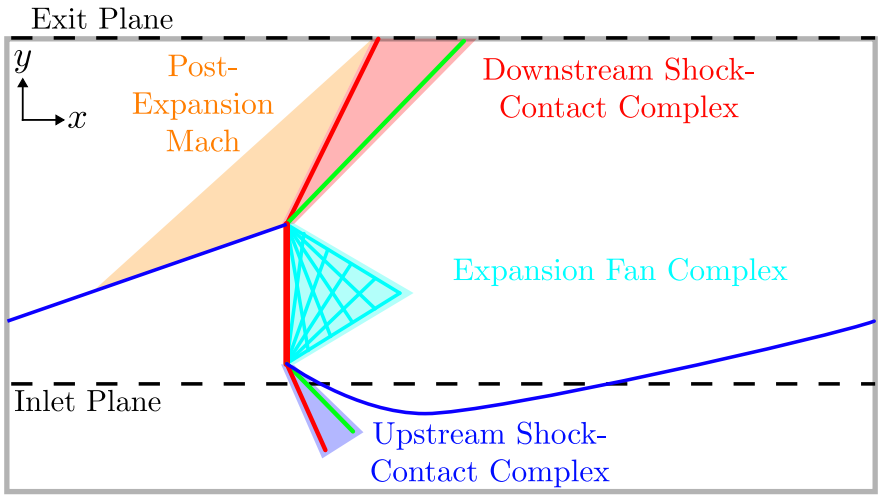


Figure 4.15: Zoomed in view of Shock-Expansion Complex.

Figure 4.16 shows the block diagram for the full shock-expansion complex model. This model takes numerous inputs from the overall model level, from the non-ideal detonation model, and

from the fill properties just ahead of the detonation wave. These inputs are color-coded based on which sub-model updates which variable. For example, the fill angle, β, is updated in the "Update Fill Props" sub-function. The model also takes the channel pressure and the plenum pressure, where it will update the channel pressure based on the solution of the post-expansion sub-model. This model closure for the channel pressure provides a physics-based methodology to calculate the channel pressure without the need for further iteration.

At a high level, the Shock-Expansion complex solver will determine the properties of the upstream and downstream shock complexes. Then, it will generate and solve the expansion fan complex emanating from the upstream and downstream shock-contact complexes. This model also uses the mass flow calculator to calculate an updated blockage ratio generated by the expansion fan region before updating the fill properties based on the new blockage. Then, the model will process the post-expansion region, which will update the next iteration input conditions. Before testing for convergence in the post-expansion Mach number, the detonation and fill sub-model will be called to update the detonation wave, if needed. The final converged results are then returned to the inlet mass flow model to check for the convergence of the main model loop.

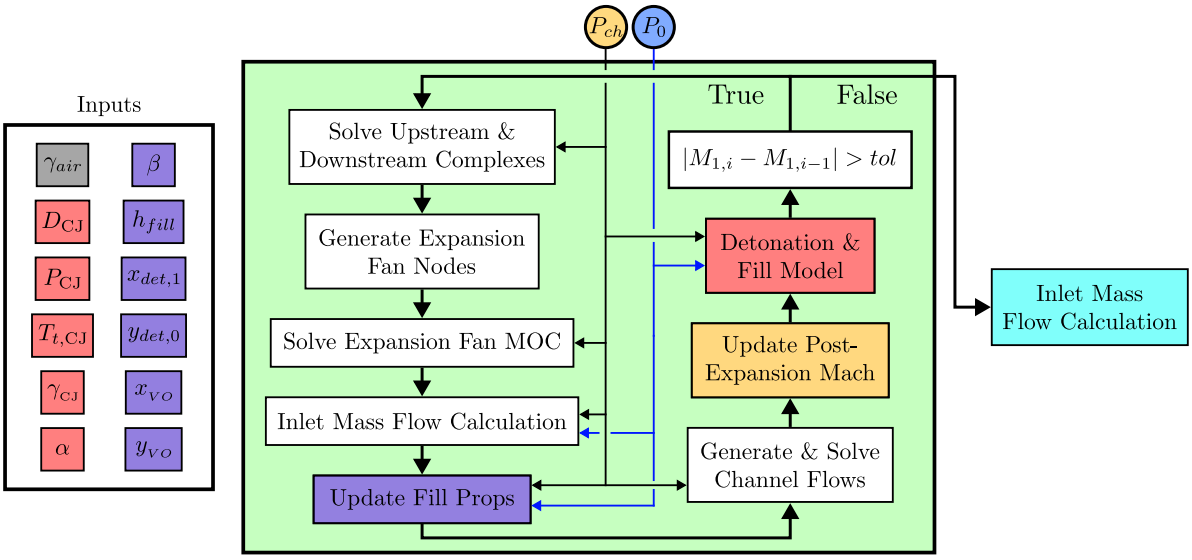


Figure 4.16: Block Diagram of the Shock Complex Solver.

The remainder of this section discusses the Shock-Expansion complex sub-model, which is used to generate the oblique shock/expansion fan complex that models the post-detonation gases as they progress through the flow field. To model this process, coupled oblique shock waves and expansion fans are generated from the upstream and downstream portion of the detonation wave. It should be noted that this analysis is conducted purely in the wave frame of reference, which is adjusted to account for the detonation tilt angle, α. The results are then translated back to the

standard flowpath frame by rotating by the tilt angle.

Algorithm 17 shows the full sub-model process that iteratively solves the shock-expansion complex model until a convergence of the post-expansion Mach number is achieved. Initially, a downstream Mach number is guessed, and the initial shock-expansion complexes are generated and solved. Next, an isentropic, irrotational method of characteristic solver is used to model an expansion fan, post-detonation. From this expansion fan, two additional calculations are made. First, the inlet mass flow rate is calculated by using the farthest upstream expansion fan nodes, which were generated by the MOC solution of the expansion fan. Second, a set of Channel Flow objects can be constructed from the furthest downstream expansion fan nodes. These objects provide a closure method to directly link the detonation wave to the exhaust plane and solve the one-dimensional flow, with losses, along the RDC channel from the expansion fan results to either the RDC exit or the next incoming oblique shock wave. Next, the solutions to the Channel Flow objects are used to update the incoming Mach number for the downstream shock-contact complex for the next iteration. Finally, the detonation and fill calculations are re-run to capture any changes in the blockage ratio from the inlet mass flow model. Each piece of this model will be discussed in more detail throughout the remainder of this section, except for the inlet model, which will have its own dedicated section.

Algorithm 17 Shock Complex Solver

Require: P_{ch}, γ_{air}, P_{CJ}, $T_{t,\text{CJ}}$, γ_{CJ}, β, α

Guess initial post-expansion Mach: $M_{1,0}$

while $|M_{1,i} - M_{1,i-1}| > tol$ **do**

- Solve up and downstream shock complexes ▷ *Algorithm 22*
- Generate up and downstream expansion nodes ▷ *Algorithm 19*
- Solve expansion fan with MOC ▷ *Algorithm 20*
- Calculate inlet mass flow rate ▷ *Algorithm 35*
- Update fill properties ▷ *Algorithm 14*
- Generate and solve Channel Flow objects ▷ *Algorithm 23*
- Update post-expansion Mach for next iteration: $M_{1,i+1}$ ▷ *Algorithm 34*
- Update detonation ▷ *Algorithm 11*

end while

Figure 4.17 shows an example of the shock-expansion fan complex in the wave frame of reference rotating by the detonation tilt angle to have the detonation wave travel purely in the x'-direction. Each side of the complex is solved individually and features a coupled oblique shock wave and expansion fan emanating from the upstream and downstream portion of the detonation wave. These expansion fans then generate Mach lines for use in solving the expansion fan com-

plex. These expansion fan nodes are later used to capture the pressure profile for the inlet mass flow model and the starting point for the post-expansion processes.

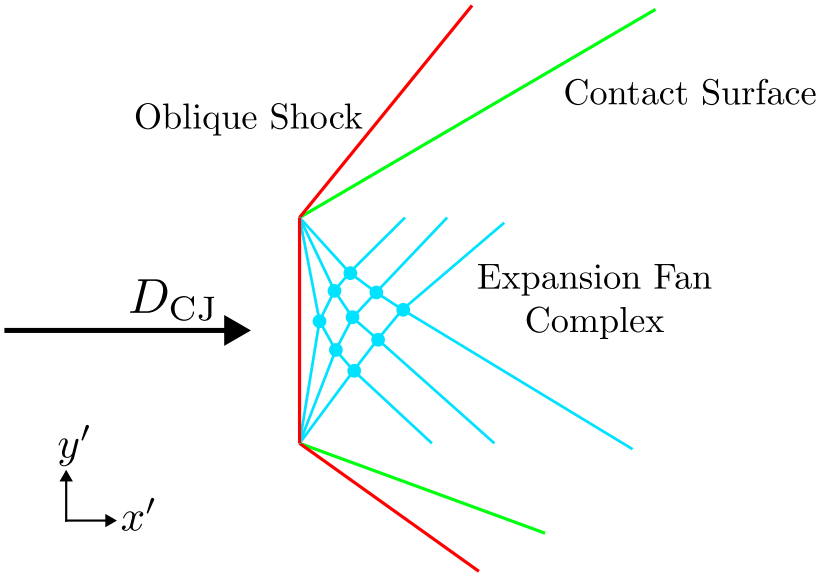


Figure 4.17: Basic Shock Complex Diagram.

Figure 4.18 shows the angles and state locations involved in the upper shock-expansion complex, and Table 4.1 shows a description of the states. For the angles shown in Figure 4.18, the oblique shock angle, θ, and the deflection angle, δ, are shown relative to the velocity vector of the incoming flow, D_{CJ}. Because this is solved in the wave frame of reference, we can define the x'-direction as the direction of the wave propagation and will define all angles off of this datum.

State	Description
1	Post-Expansion Product Gases - Pre-Oblique Shock
2	Post-Expansion Product Gases - Post-Oblique Shock
3	Post-Expansion Product Gases
4	Post-Detonation Product Gases - at CJ State

Table 4.1: Summary of Shock-Expansion Complex States.

Figure 4.18 provides more clarity that the deflection angle, δ, is a shared parameter that couples the oblique shock and the expansion fan. By definition, the velocity direction and static pressure are equal along this contact surface. With this information and a set of initial conditions, the entire shock-contact complex can be solved based on an iterative method.

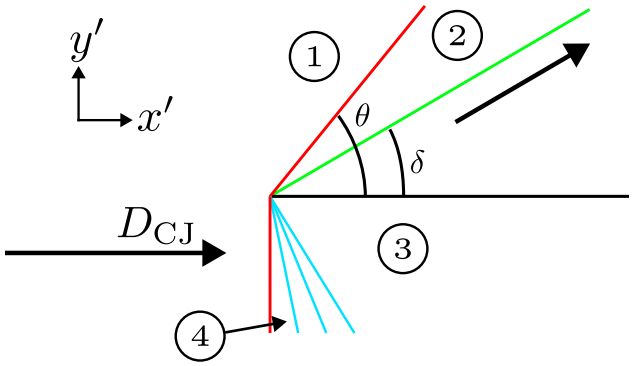


Figure 4.18: Shock Complex Angle and State Definition.

4.2.2.1 Oblique Shock Relations

This short section describes the relationships used to solve the oblique shock portion of the shock-contact complex. First, the equation that relates the angle of oblique shock, the deflection angle, and the initial Mach number is shown in Equation 4.2. This equation is used to determine the shock angle, θ, with a given initial Mach number, M_1, and the deflection angle, δ. To calculate the shock angle, a Brent method optimizer was used to iteratively solve the shock angle.

$$\tan(\delta) = 2\cot(\theta)\frac{M_1^2\sin^2(\theta) - 1}{M_1^2(\gamma + \cos(2\theta)) + 2} \tag{4.2}$$

With the said shock angle, θ, and the initial conditions, the pressure ratio across the oblique shock can be calculated with Equation 4.3.

$$\frac{P_2}{P_1} = \frac{2\gamma}{\gamma+1}M_1^2\sin^2(\theta) - \frac{\gamma-1}{\gamma+1} \tag{4.3}$$

Finally, some limiting is required to ensure that the oblique shock wave is physically possible for the set of initial conditions. First, the maximum shock angle, θ_{max}, is calculated for the initial condition set using Equation 4.4.

$$\sin^2(\theta_{max}) = \frac{1}{\gamma M_1^2}\left(\frac{\gamma+1}{4}M_1^2 - 1 + \sqrt{(\gamma+1)\left(1 + \frac{\gamma-1}{2}M_1^2 + \frac{\gamma+1}{16}M_1^4\right)}\right) \tag{4.4}$$

If the shock deflection angle is ever greater than δ_{max}, a detached shock will form. For the simplicity of the model, initial conditions will be adjusted to avoid this situation where possible. If this cannot be achieved, then the model exits with a detached shock error.

4.2.2.2 Expansion Fan Relations

The other half of the shock-expansion complex is the expansion fan. This is assumed to be an isentropic expansion from the CJ plane (see Figure 4.18). The pressure ratio across the expansion fan can be calculated with Equation 4.5.

$$\frac{P_2}{P_1} = \left(\frac{1 + \frac{\gamma-1}{2} M_1^2}{1 + \frac{\gamma-1}{2} M_2^2} \right)^{\frac{\gamma}{\gamma-1}} \tag{4.5}$$

where the initial Mach number, M_1, for this expansion fan, is always 1, by definition of the CJ condition. The Mach number is related to the deflection angle by Equation 4.6.

$$\delta = \nu(M_2) - \nu(M_1) \tag{4.6}$$

where the deflection angle, δ, depends on the change in the Prandtl-Meyer (PM) function (Equation 4.7) between the two Mach numbers.

$$\nu(M) = \sqrt{\frac{\gamma+1}{\gamma-1}} \arctan\left(\sqrt{\frac{\gamma-1}{\gamma+1}(M^2-1)} \right) - \arctan\left(\sqrt{M^2-1} \right) \tag{4.7}$$

Because the CJ plane is sonic in the wave frame, $\nu(M_1)$ is always zero by definition. Therefore, the deflection angle, δ, can be solved directly with the post-expansion Mach number, M_2, and vice-versa.

4.2.2.3 Relating the Two

As shown in Figure 4.18, the deflection angle for the oblique shock is the same as the deflection angle of the PM expansion fan. With this information, an iterative solver was constructed to determine the deflection angle required to match P_2 and P_3.

The following set of equations is used during the solution process presented in Algorithm 18. These include the proper substitution of the states in Table 4.1. First, the post-expansion pressure, P_3, is calculated from Equation 4.8.

$$P_3 = P_4 \left(\frac{2}{\gamma_4 + 1} + \frac{\gamma_4 - 1}{\gamma_4 + 1} M_3^2 \right)^{\frac{-\gamma_4}{\gamma_4 - 1}} \tag{4.8}$$

Equation 4.9 shows the Mach number as an inversion of the PM function (Equation 4.7) given δ_i. This was also solved using Brent's method optimizer.

$$M_3 = \nu^{-1}(\delta_i) \tag{4.9}$$

With the deflection angle, δ, the shock angle, θ, can be calculated with Equation 4.2, which is numerically solved again using Brent's method. Finally, the post-shock pressure, P_2, is calculated from Equation 4.10.

$$P_2 = P_1 \left(\frac{2\gamma_1}{\gamma_1 + 1} M_1^2 \sin^2(\theta_i) - \frac{\gamma_1 - 1}{\gamma_1 + 1} \right) \tag{4.10}$$

The summary of the steps used to calculate the Shock-Expansion Complex is shown in Algorithm 18.

Algorithm 18 Shock-Expansion Complex

Require: $M_1, \gamma_1, P_1, \gamma_4, P_4 = P_{\text{CJ}}, tol$
  Guess δ_0
  while $P_2 \neq P_3$ **do**
    Calculate Post-Expansion Pressure: P_3 ▷ *Equation 4.8*
    Calculate Oblique Shock Angle: θ ▷ *Equation 4.2*
    Calculate Post-Shock Pressure: P_2 ▷ *Equations 4.9-4.10*
    Update δ_{i+1}
    if $\delta_{i+1} > \delta_{max}$ & $|P_2 - P_3| > tol$ **then**
      Detached Shock, Modify Initial Conditions, and Re-Solve
    end if
  end while

4.2.2.4 Expansion Fan Complex MOC

The prior discussion of the Shock-Expansion Complex only solves for the boundary conditions around the expansion fan region of the flow field. To determine the remainder of the flow field within the Shock-Expansion Complex, an irrotational, isentropic, two-dimensional method of characteristic for compressible flow was used. Figure 4.19 shows an example of the nodes generated by the MOC expansion fan solver. The layer of nodes along the final mach line from the top expansion fan are shown in red, while the nodes from the final mach line from the bottom expansion fan are shown in dark blue. The dark blue nodes are used to inform both the post-expansion model and the inlet model, whereas the red nodes are only used in the post-expansion model.

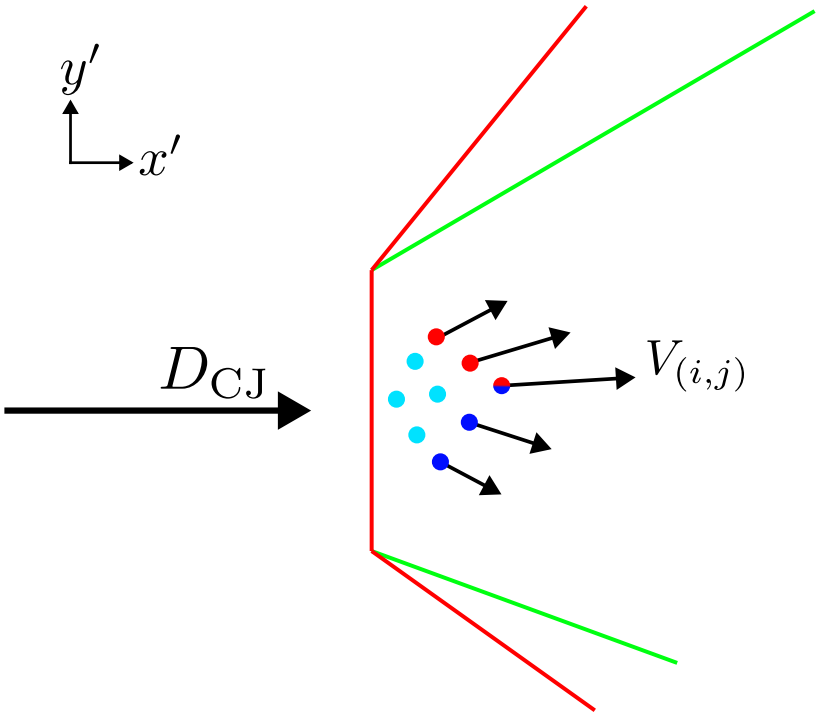


Figure 4.19: Post Expansion Fan Velocity Vectors.

Algorithm 19 shows the procedures for generating the set of initial expansion fan nodes at the upstream and downstream portion of the detonation wave. This algorithm starts with the solutions of the upstream and downstream shock-expansion complexes. With this information, the next step is to generate a series of deflection angles that inform the properties along the initial expansion fan nodes. This was done using an exponential spacing that would provide much more resolution near the detonation wave and space out more as the expansion fan moved further from the detonation. This configuration provided the most stable expansion fan solver, as the processes (and node solutions) nearest the detonation wave saw the highest gradients in property change. The gradually increasing spacing of the deflection angles provided a good balance of accuracy and sub-model evaluation time. This sub-model also ensures that the maximum deflection angle, $\Delta\nu_{max}$, along this series is preserved.

Algorithm 19 Expansion Node Generation

Require: $N_{exp}, \alpha, \Delta\nu_{max}$

Solve shock complex: δ ▷ *Algorithm 22*

Exponentially generate deflection angles: $\overrightarrow{\nu}$

Re-space deflection angles to not exceed a spacing of $\Delta\nu_{max}$

Calculate Mach number profile across expansion: $\overrightarrow{M}$

Calculate velocity magnitude assuming isentropic through expansion nodes: $\overrightarrow{\mathbf{V}}$

Calculate velocity components (accounting for α): $\overrightarrow{u}, \overrightarrow{v}$

Generate vector of nodes at proper location: $\overrightarrow{Node}$

Figure 4.20 shows an example of how these deflection angles are used to generate the initial nodes. The right sub-figure shows a zoomed-in view of the expansion fan from the downstream portion of the complex. For each deflection angle in the series, $\overrightarrow{\nu}$, the flow is turned slightly more across an infinitesimally small corner until the final expansion angle, δ, is achieved. When zoomed back out, these small corners vanish, and the Mach angles emanate from the same location on the detonation wave.

Along each small deflection, the Mach number and velocity can be calculated. With the deflection angle and these properties, the velocity components are also calculated, allowing for the initialization of the expansion fan nodes on each side of the detonation wave. When initializing the nodes, the angle of the detonation wave, α, is taken into account, allowing the expansion fan complex to be solved in the proper reference frame for the flowpath.

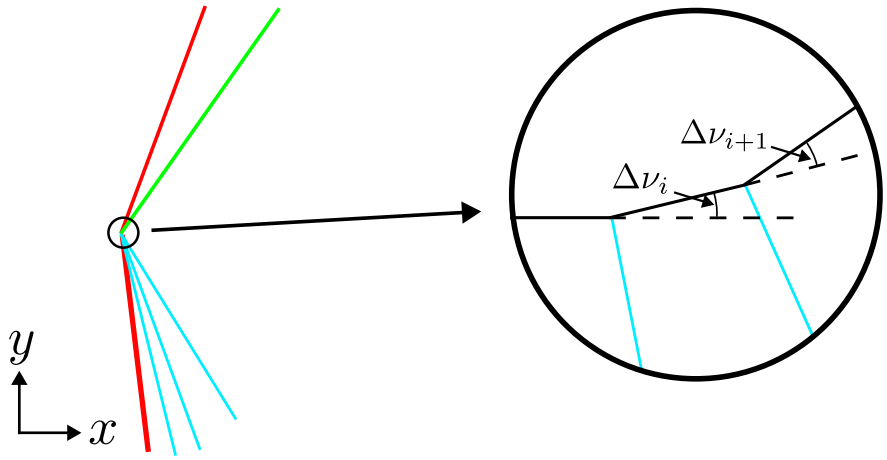


Figure 4.20: Example of Downstream Expansion Node Generation.

With the upstream and downstream initial expansion fan nodes, $\overrightarrow{Node}_{up}$, $\overrightarrow{Node}_{down}$, the full expansion fan profile is then solved using Algorithm 20. This algorithm loops over the initial

nodes and solves the full expansion fan complex at each Mach line intersection with Algorithm 21. After solving the expansion fan complex, the furthest upstream nodes are used later in the inlet mass flow model.

Algorithm 20 Expansion Fan Solver

Require: $\overrightarrow{Node}_{up},\ \overrightarrow{Node}_{down}$
  Initialize empty 2-D expansion node vector: $\overrightarrow{Node}_{exp}$
  for $i \in [0, len(\overrightarrow{Node}_{down})]$ **do**
    Initialize empty expansion node vector: $\overrightarrow{Node}_i$
    for $j \in [0, len(\overrightarrow{Node}_{up})]$ **do**
      if $i = 0$ & $j = 0$ **then**
        $Node_i \leftarrow MOC(\overrightarrow{Node}_{down,0}, \overrightarrow{Node}_{up,0})$
      else if $i = 0$ **then**
        $Node_i \leftarrow MOC(\overrightarrow{Node}_{i,j-1}, \overrightarrow{Node}_{up,j})$
      else if $j = 0$ **then**
        $Node_i \leftarrow MOC(\overrightarrow{Node}_{down,i}, \overrightarrow{Node}_{exp,i-1,0})$
      else
        $Node_i \leftarrow MOC(\overrightarrow{Node}_{i,j-1}, \overrightarrow{Node}_{exp,i-1,j})$
      end if
      Push $Node_i$ into end of $\overrightarrow{Node}_i$
    end for
    Push $\overrightarrow{Node}_i$ into end of $\overrightarrow{Node}_{exp}$
  end for

Algorithm 21 shows the solution process for the isentropic, irrotational, two-dimensional method of characteristic (modified from Zucrow and Hoffman).[83] Figure 4.21 shows an example of how nodes are used to calculate the location and properties of the next node. This methodology is incredibly simple and efficient, as only four variables need to be solved at each node intersection. It is also reduced in complexity by directly projecting the Mach lines from the input nodes versus the standard implementation that iteratively finds the node location using average properties.

Algorithm 21 Direct Irrotational MOC Solver

Require: $Node^-,\ Node^+$
  Calculate characteristic intersection: x, y ▷ *Algorithm 16*
  Calculate properties from input nodes ▷ *Equations 4.11-4.13*
  Solve for velocity components: u, v ▷ *Equations 4.14-4.15*
  return New node: $Node$

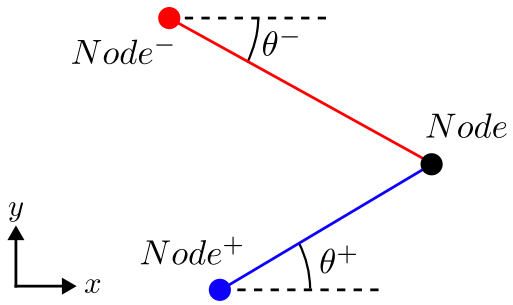


Figure 4.21: Example of using the Direct MOC Node Solution.

The following equations are included for reference.

$$Q^{\pm} = u_{\pm}^2 - a_{\pm}^2 \tag{4.11}$$

$$R^{\pm} = 2u_{\pm}v_{\pm} - Q^{\pm}\lambda^{\pm} \tag{4.12}$$

$$T^{\pm} = Q^{\pm}u_{\pm} + R^{\pm}v_{\pm} \tag{4.13}$$

$$v = \frac{T^- - \frac{Q^-}{Q^+}T^+}{R^- - \frac{Q^-}{Q^+}R^+} \tag{4.14}$$

$$u = \frac{T^+ - R^+v}{Q^+} \tag{4.15}$$

4.2.2.5 Non-Uniform Shock-Expansion Complex

Extending the particle trajectories from the expansion fan nodes to the next wave complex results in a non-uniform flow profile ahead of the oblique shock. This can be clearly seen in Figure 4.22. Instead of resorting to additional MOC calculations up to the downstream oblique shock, the process was simplified by using the Channel Flow Objects and assuming there is an average Mach number and average gas properties ahead of the downstream oblique shock that can be calculated based on particles whose trajectories intersect with the next oblique shock. It is also assumed that the average flow angle into the downstream oblique shock is constrained to align with the fill line angle, β. Figure 4.22 also shows how the fill angle, β, influences the flow moving into the downstream oblique shock.

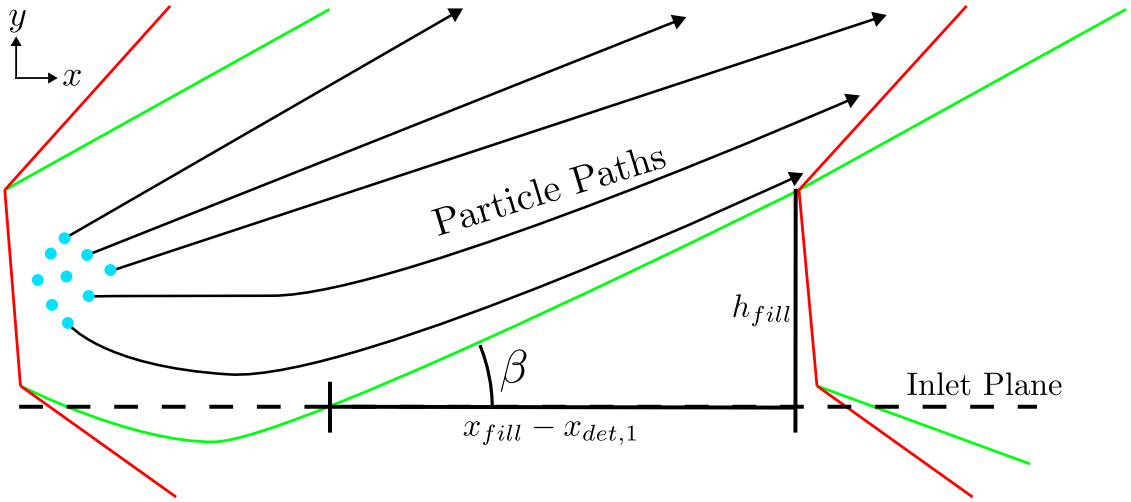


Figure 4.22: Post Expansion Velocity Interaction with Next Wave.

Figure 4.23 shows an updated view of the downstream oblique shock wave with the change in the approaching velocity vector. Here, the velocity magnitude, $V_{1'}$, and an offset angle from the nominal wave direction, β', are defined. $V_{1'}$ is defined as the sum of the nominal CJ wave speed and any additional velocity obtained from the expansion process. The flow deflection angle, defined in Equation 4.16, is corrected for the detonation tilt angle since this analysis is still carried out in the wave frame.

$$\beta' = \beta - \alpha \tag{4.16}$$

The expansion fan angle calculation remains the same; however, the oblique shock solver must now account for the updated velocity and relative flow angle. This requires the definition of two new angles, shown in Figure 4.23. The first is the relative deflection angle, δ', which is the deflection angle with respect to the incoming velocity vector, $V_{1'}$. Next is the relative shock angle, θ', which is used to calculate the state change across the oblique shock. The calculation of the expansion side of the complex remains the same as it is still emanating from the CJ plane.

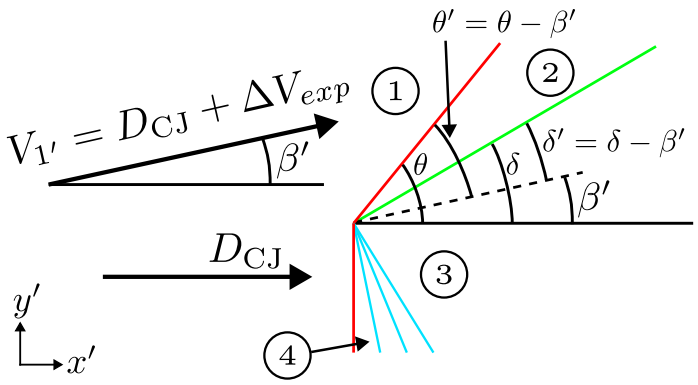


Figure 4.23: Shock Complex with Velocity Deflection.

With the accounting for the effects of the post-expansion velocity on the oblique shock, the solver updates are included in Algorithm 22

Algorithm 22 Shock-Expansion Complex with β Deflection

Require: $M_1, \gamma_1, P_1, \gamma_4, P_4 = P_{CJ}, tol, \beta$

$M_{1',0} \leftarrow M_{1,CJ}$

while $|M_{1',i+1} - M_{1',i}| > tol$ **do**

Solve complex at $M_{1',i}$ ▷ *Algorithm 18*

Get $M_{1'}$ from Channel Flow solutions ▷ *Algorithm 34*

end while

Figure 4.24 shows a final diagram of the shock-expansion complex with the fill line angle accounting. This figure also breaks down the flow region of interest for the complex. At the upstream end of the detonation, the pre-oblique shock flow is that of air (blue), moving at the same speed and direction as the CJ wave speed. The interior uses the pre-detonation state (red) that informs the inner expansion fan complex using the CJ state. Finally, the downstream portion is at the post-expansion state, flowing at the corrected flow angle (orange). The next section will discuss in more detail how this state (in orange) is calculated.

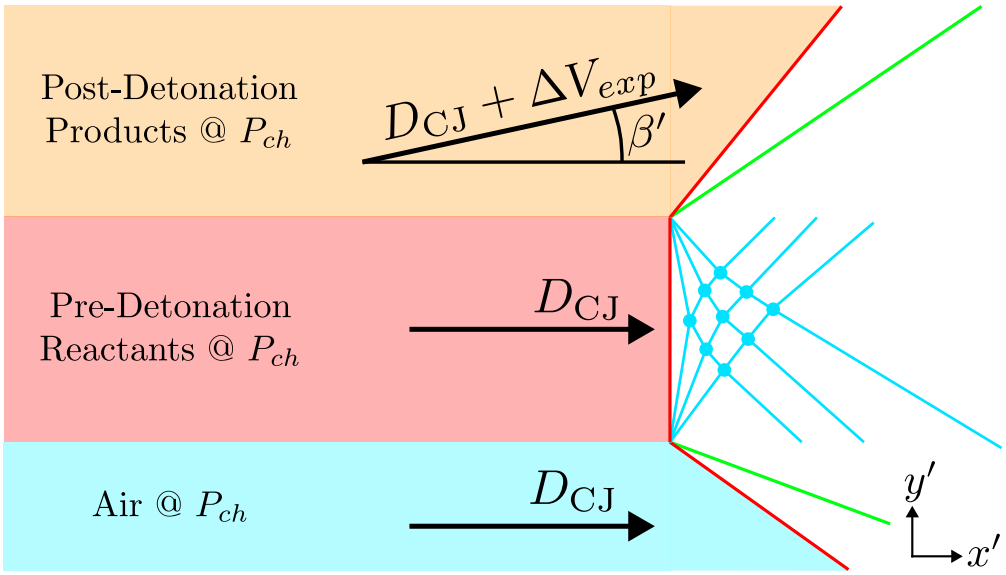


Figure 4.24: Shock-Expansion Complex Regions of Interest with Post-Expansion Deflection and Further Expansion.

4.2.2.6 Post-Expansion Fan Processes

As mentioned in the previous section, the post-expansion fan processes are captured with what is termed the Channel Flow object. This object provides a closure to solve the remainder of the flow field and simply conducts a one-dimensional flow integration procedure through the RDC channel from the end of the expansion fan complex to either the exit of the RDC or to the next oblique shock. Figure 4.25 shows where these objects reside within the larger cycle flowpath.

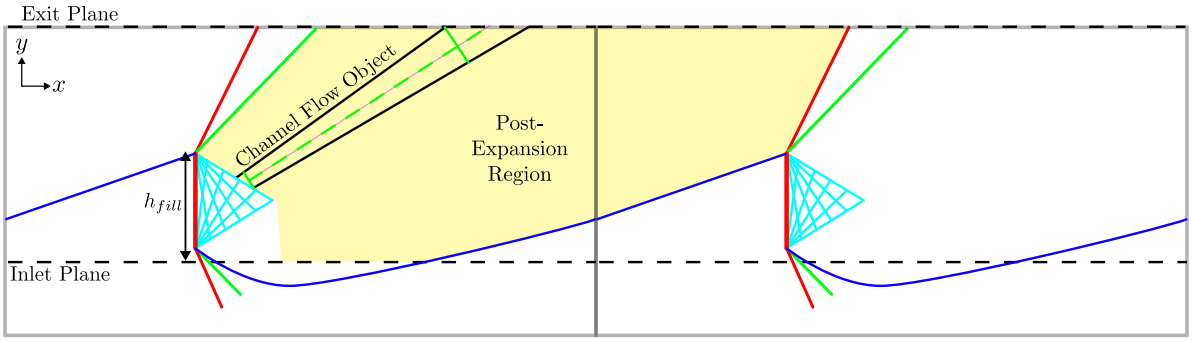


Figure 4.25: Example of a Channel Flow Object within the RDC Flowpath.

Figure 4.26 shows an example of what the Channel Flow object would look like, labeling the inlet and exit of the Channel Flow object, 1 and 2, respectively. These are constructed using lines projected from the virtual origin at angles θ_1 and θ_2, where we ensure $\theta_1 > \theta_2$. The spacing of these angles is a control variable for the cycle model.

The main task in initializing these objects is the determination of the Channel Flow inlet and exit areas, the details of which are discussed later in this section. With the one-dimensional flow assumption, the Channel Flow object also specifies the direction of flow as an average of the two bounding angles $\bar{\theta}$.

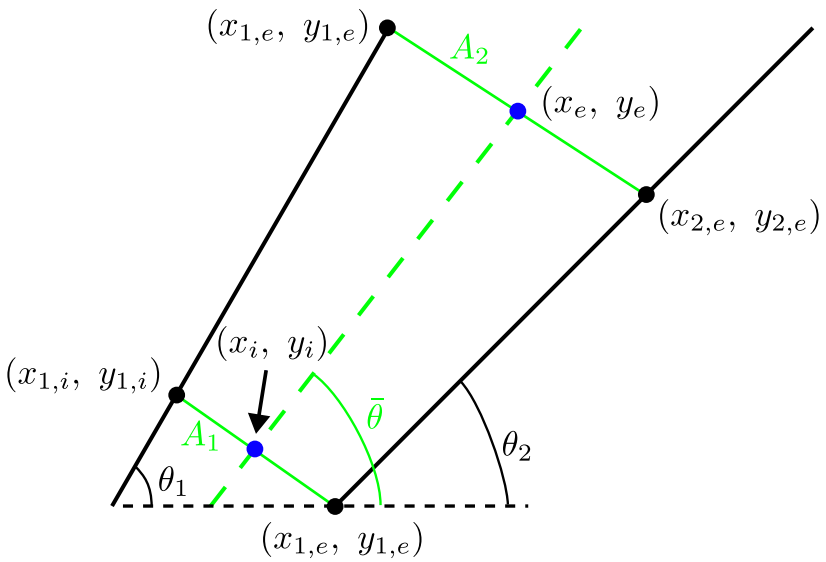


Figure 4.26: Diagram of the Channel Flow Object with Key Locations and Nomenclature.

Algorithm 23 provides the methodology for setting up these objects from the nodes of the expansion fan complex. It begins by calculating the angles of the lines from the virtual origin to the last expansion fan node and the location of the shock intersection with the RDC exit plane. Depending on these angles, one of two methods is used to set up the Channel Flow objects where between 1/3 and 2/3 of them will be informed directly by the expansion fan nodes. After initializing the objects, they will each be integrated using the non-ideal one-dimensional flow solver, Algorithm 33. In the case where the final static pressure of a Channel Flow object falls below the specified ambient pressure, the flow will be polytropically compressed to match the ambient pressure, and the final Mach number will also be updated. At the end of this solution step, the static channel pressure term, P_{ch}, is updated based on the final static pressure in the Channel Flow object nearest the RDC inlet plane.

Algorithm 23 Channel Flow Object Solver

Require: $\overrightarrow{Node}_{exp}, N_{CF}, \dot{m}$

Get last row of expansion nodes: $\overrightarrow{Node}_{last} \leftarrow \overrightarrow{Node}_{exp,last}$

Calculate angle from virtual origin to last expansion node: θ_l ▷ *Equation 4.20*

Calculate angle from virtual origin to next shock exit plane location: θ_S ▷ *Equation 4.21*

if $\theta_l < \theta_S$ **then**

$N_{Node,NS} + N_{Node,S} = \frac{2}{3} N_{CF}$

Split nodes into non-shocked and shocked: $N_{Node,NS}, N_{Node,S}$

Generate non-shocked node Channel Flows: $\dot{m}_{Node,NS}$ ▷ *Algorithm 25*

Generate shocked node Channel Flows: $\dot{m}_{Node,S}$ ▷ *Algorithm 26*

Calculate node and non-node mass flow splits: $\dot{m}_S = \dot{m} - \dot{m}_{Node,NS} - \dot{m}_{Node,S}$

Generate non-node, shocked Channel Flows ▷ *Algorithm 27*

else

$N_{Node,NS} = N_{NS} = N_S = \frac{1}{3} N_{CF}$

Generate non-shocked node Channel Flows: $\dot{m}_{Node,NS}$ ▷ *Algorithm 25*

Calculate node and non-node mass flow splits: $\dot{m}_{NS} + \dot{m}_S = \dot{m} - \dot{m}_{Node,NS}$

Generate non-shocked, non-node Channel Flows ▷ *Algorithm 28*

Generate shocked, non-node Channel Flows ▷ *Algorithm 27*

end if

for all Channel Flow Objects **do**

Integrate along flowpath ▷ *Algorithm 33*

Calculate final pressure and Mach: $P_{final,i}, M_{final,i}$

if $P_{final,i} < P_{amb}$ **then**

Polytropically compress to match P_{amb}: M_2 ▷ *Algorithm 24*

$P_{final,i} \leftarrow P_{amb}$ & $M_{final,i} \leftarrow M_2$

end if

end for

Set channel static pressure: $P_{ch} \leftarrow P_{final,last}$

Algorithm 24 shows the steps used to calculate the polytropic compression from the exit state of the Channel Flow object to a state that matches the same mass flow rate but at the limiting pressure. This model provides yet another closure method for capturing unspecified losses within the flowpath that are required for the model to converge and conserve the exit mass flow rate. The polytropic process iteratively solves for a momentum and energy rate term, $\dot{w}$ and $\dot{q}$, respectively. These terms are also included in the polytropic coefficient calculation, which led to the requirement of an iterative solution method.

Algorithm 24 Polytropic Compression

Require: $P_1, \dot{m}, M_1, A_1, T_{t,1}, P_2, A_2, \gamma, R, tol$

Guess work and energy terms: $\dot{w}, \dot{q}$

while $|R_{mom}| + |R_{en}| > tol$ **do**

if $\dot{q} = 0$ **then**

$n \leftarrow \gamma$

else if $\dot{w} = 0$ **then**

$n \leftarrow \infty$

else

$n \leftarrow (1 - \gamma)\frac{\dot{q}}{\dot{w}} + \gamma$

end if

Recalculate final density: ρ_2 ▷ *Equation 4.17*

Recalculate final temperature: $T_2 = \frac{P_{amb}}{R\rho_2}$

Recalculate final velocity: $u_2 = \frac{\dot{m}}{A_2\rho_2}$ ▷ *Application of mass conservation*

Calculate Momentum and Energy Residuals: R_{mom}, R_{en} ▷ *Equations 4.18 - 4.19*

end while

return Final state and M_2

Equation 4.17 shows the containing function for the post-polytropic process density. In this case, the ambient pressure, P_{amb}, specified for the model was used for the post-polytropic process pressure.

$$\rho_2 = \rho_1 \left(\frac{P_{amb}}{P_1} \right)^{\frac{1}{n}} \tag{4.17}$$

where n is the polytropic coefficient.

The residual equations used for the polytropic compression algorithm are shown below, where the momentum residual contains the continuity equation within.

$$R_{mom} = (P_1 + \rho_1 u_1^2)A_1 - P_{amb}A_2 - \rho_2 u_2^2 - \dot{w} \tag{4.18}$$

$$R_{en} = c_p T_1 + \frac{u_1^2}{2} - c_p T_2 - \frac{u_2^2}{2} + \dot{q} \tag{4.19}$$

Returning to the discussion of the initialization of the Channel Flow objects, Equation 4.20 and Equation 4.21 show how the angles of interest are calculated in Algorithm 23. This includes the angle of the line from the virtual origin to the last expansion fan node, θ_l, and the angle of the line from the virtual origin to the shock-exit plane intersection, θ_S.

$$\theta_l = \tan^{-1}\left(\frac{y_l - y_{VO}}{x_l - x_{VO}}\right) \tag{4.20}$$

$$\theta_S = \tan^{-1}\left(\frac{h_{RDC} - y_{VO}}{x_S - x_{VO}}\right) \tag{4.21}$$

where x_S is the location where the next shock wave intersects the exit plane of the RDC. Figure 4.27 shows an example of these angles as they relate to the rest of the RDC flowpath.

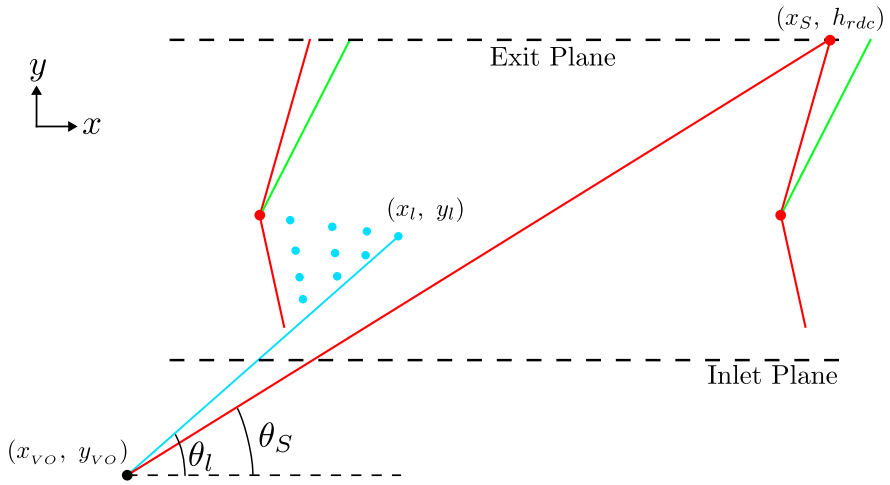


Figure 4.27: Visual Representation of the Last Node Angle and Shocked Flow Angle.

Algorithm 23 breaks down the Channel Flow object into different regions shown in Figure 4.28. If the angle to the last node is greater than to the shock-exit location, then regions mirror those shown on the left sub-plot. Otherwise, they will follow the layout in the right sub-plot. In the case where the angle to the last node is greater, the three regions of Channel Flow objects are as follows.

1. A region informed by the expansion fan nodes, and exiting the RDC before the oblique shock: $\overrightarrow{Node}_{NS}$, non-shocked node region in blue

2. A region not informed by the expansion fan nodes, and exiting the RDC before the oblique shock: NS, non-shocked non-node region in magenta

3. A region not informed by the expansion fan nodes, but will be processed by the oblique shock before exiting the RDC: S, shocked non-node region in red

In the case where the angle to the last node is less than the angle to the shock-exit location, the non-shocked non-node region in magenta is consumed by the non-shocked node region in blue.

The shocked non-node region in red is now cut by the last node line, and the shocked node region, $\overrightarrow{Node_S}$, in orange, is inserted. This region is informed by the expansion fan nodes but is now processed by the oblique shock before exiting the RDC.

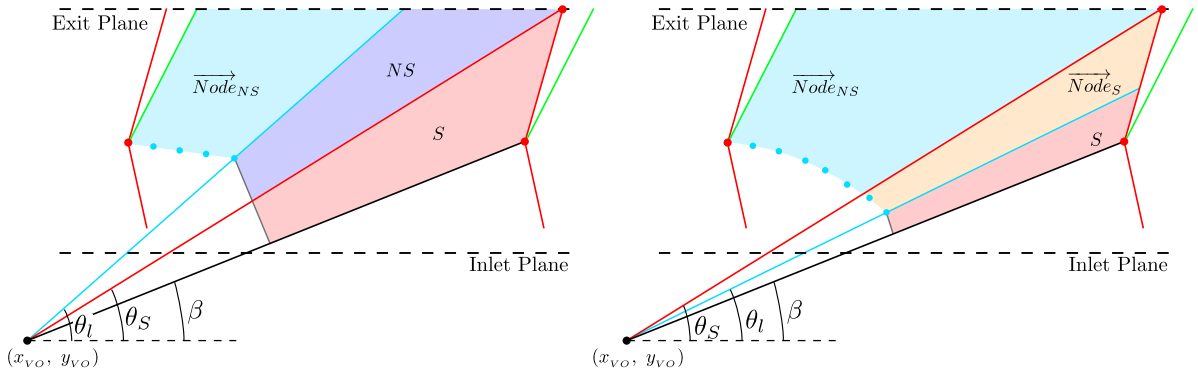


Figure 4.28: Channel Flow Region Breakdown with Larger Last Node Angle (left) and with Larger Shock Angle (right).

Algorithm 25 shows the pseudo-code for generating the Channel Flow objects informed by the expansion fan nodes but not processed by the oblique shock. Algorithm 26 shows the process for setting up the Channel Flow objects that are both informed by the expansion fan nodes and are processed by the oblique shock.

Algorithm 25 Non-Shocked Node Channel Flow Generation

Require: $\overrightarrow{Node}_{last},\ N_{Node,NS},\ \theta_l, \theta_S, \delta$

if $\theta_l < \theta_S$ **then**

$\theta_f \leftarrow \theta_S$

else

$\theta_f \leftarrow \theta_l$

end if

$\Delta\theta \leftarrow \frac{\theta_f - \delta}{N_{Node,NS}}$

for $i \in [0, N_{Node,NS}]$ **do**

$\theta_1 \leftarrow \delta + i\Delta\theta,\ \theta_2 \leftarrow \delta + (i+1)\Delta\theta,\ \bar{\theta} \leftarrow \frac{\theta_1 + \theta_2}{2}$

Find nodes between line 1 and 2

if No nodes **then**

Use previous iteration properties

else

Get average node properties: $M, \bar{V}, P, T, \rho$

end if

Get initial Channel Flow area: A_1 ▷ *Algorithm 29*

Calculate $\dot{m}_i$

Get Channel Flow exit area: A_2 ▷ *Algorithm 31*

Calculate $\frac{dA}{dx}$ & $\frac{dT_t}{dx}$

Generate Channel Flow object

end for

$\dot{m}_{Node,NS} \leftarrow \sum_{i=0}^{N_{Node,NS}} \dot{m}_i$

return $\dot{m}_{Node,NS}$

Algorithm 26 Shocked Node Channel Flow Generation

Require: $\overrightarrow{Node}_{last},\ N_{Node,S}, \theta_l, \theta_S$

$\Delta\theta \leftarrow \frac{\theta_l - \theta_S}{N_{Node,S}}$

for $i \in [0, N_{Node,S}]$ **do**

$\theta_1 \leftarrow \theta_S + i\Delta\theta,\ \theta_2 \leftarrow \theta_S + (i+1)\Delta\theta,\ \bar{\theta} \leftarrow \frac{\theta_1+\theta_2}{2}$

Find nodes between lines 1 and 2

if No nodes **then**

Use previous iteration properties

else

Get average node properties: $M, \bar{V}, P, T, \rho$

end if

Get initial Channel Flow area: A_1 ▷ *Algorithm 29*

Calculate $\dot{m}_i$

Get Channel Flow exit area: A_2 ▷ *Algorithm 32*

Calculate $\frac{dA}{dx}$ & $\frac{dT_t}{dx}$

Generate Channel Flow object

end for

$\dot{m}_{Node,S} \leftarrow \sum_{i=0}^{N_{Node,S}} \dot{m}_i$

return $\dot{m}_{Node,S}$

For the Channel Flow objects not informed by the expansion fan nodes, the total mass flow is conserved by enforcing that each new object is initialized based on the remainder of the mass flow rate outside of the expansion fan Channel Flow Objects. Algorithm 27 shows the pseudo-code for the initialization of the Channel Flow object for non-informed objects that are processed by the shock. The key difference between this method and the expansion fan informed method is the initial Mach number for the objects. This was solved using Equation 4.22, under the constraint of the mass flow rate of the objects. By enforcing continuity throughout the full collection of Channel Flow objects at their initial point, mass flow is also conserved at the exit plane of the RDC. This effectively removes an iteration loop from the main algorithm by providing a physics-based sub-model in its place.

Algorithm 27 Shocked Non-Node Channel Flow Generation

Require: $N_S, \theta_l, \theta_S, \dot{m}_S, \beta$

if $\theta_l < \theta_S$ **then**

$\theta_i \leftarrow \theta_l$

else

$\theta_i \leftarrow \theta_S$

end if

$\dot{m}_i \leftarrow \frac{\dot{m}_S}{N_S},\ \Delta\theta \leftarrow \frac{\beta - \theta_i}{N_S}$

for $i \in [0, N_S]$ **do**

$\theta_1 \leftarrow \theta_i + i\Delta\theta,\ \theta_2 \leftarrow \theta_i + (i+1)\Delta\theta,\ \bar{\theta} \leftarrow \frac{\theta_1 + \theta_2}{2}$

Get initial Channel Flow area: A_1 ▷ *Algorithm 30*

Get average node properties: M ▷ *Equation 4.22*

Get Channel Flow exit area: A_2 ▷ *Algorithm 32*

Calculate $\frac{dA}{dx}$ & $\frac{dT_t}{dx}$

Generate Channel Flow object

end for

Equation 4.22 is used to determine the initial Mach number for the non-informed Channel Flow objects. This equation was iteratively solved based on the isentropic mass flow function, where the Channel Flow object's initial mass flow rate is conserved.

$$M_1\left(1 + \frac{\gamma - 1}{2}M_1^2\right)^{-\frac{\gamma+1}{2(\gamma-)}} = \frac{\dot{m}_1}{A_1 P_{t,1}}\sqrt{\frac{RT_{t,1}}{\gamma}} \tag{4.22}$$

Finally, Algorithm 28 provides the methodology for initializing Channel Flow objects that are not informed by the expansion fan nodes and are not processed by the oblique shock.

Algorithm 28 Non-Shocked Non-Node Channel Flow Generation

Require: $N_{NS}, \theta_l, \theta_S, \dot{m}_{NS}$

$\dot{m}_i \leftarrow \frac{\dot{m}_{NS}}{N_{NS}},\ \Delta\theta \leftarrow \frac{\theta_S - \theta_l}{N_{NS}}$

for $i \in [0, N_{NS}]$ **do**

$\theta_1 \leftarrow \theta_l + i\Delta\theta,\ \theta_2 \leftarrow \theta_l + (i+1)\Delta\theta,\ \bar{\theta} \leftarrow \frac{\theta_1 + \theta_2}{2}$

Get initial Channel Flow area: A_1 ▷ *Algorithm 30*

Get average node properties: M ▷ *Equation 4.22*

Get Channel Flow exit area: A_2 ▷ *Algorithm 31*

Calculate $\frac{dA}{dx}$ & $\frac{dT_t}{dx}$

Generate Channel Flow object

end for

During the initialization of the Channel Flow objects, aside from the mass flow rate and Mach number, both the initial and final areas must be calculated. Algorithm 29 shows the methodology for calculating the initial area of a Channel Flow object that is informed by the expansion fan nodes. The main assumption with this algorithm is that the downstream portion of the initial area starts at the fill height location. Doing this allowed for a more uniform Channel Flow object distribution while also trying to maximally capture the flow path between the expansion fan nodes and the exit plane or oblique shock.

Algorithm 29 Initial Channel Flow Area: Node

Require: $h_{fill}, \theta_1, \theta_2, cw, x_{_{VO}}, y_{_{VO}}$, where $\theta_1 > \theta_2$

$\bar{\theta} \leftarrow \frac{\theta_1+\theta_2}{2}$, $m_\perp \leftarrow$ -1/ $\tan\left(\bar{\theta}\right)$

Locate point 1 at intersection of h_{fill} and line 1 from virtual origin: $x_{1,i}$ ▷ *Algorithm 16*

Locate point 2 at intersection of $\perp$ line and line 2: $(x_{2,i}, y_{2,i})$ ▷ *Algorithm 16*

return $cw * d$, where d is the distance between point 1 and 2 ▷ *Equation 4.23*

Equation 4.23 is frequently used in the calculation of the initial and final Channel Flow object area and is provided for reference.

$$d = \sqrt{\Delta x^2 + \Delta y^2} \tag{4.23}$$

For the initial area in non-informed Channel Flow objects, the assumption is that the first Channel Flow object starts at the final expansion fan node. Subsequent Channel Flow objects are then initialized from the upstream point of the previous Channel Flow object. Algorithm 30 provides the pseudo-code for this process.

Algorithm 30 Initial Channel Flow Area: No Node

Require: Last expansion node: $x_{_{LN}}, y_{_{LN}}$, last initial area node $x_{last}, y_{last}, x_{_{VO}}, y_{_{VO}}, \theta_1, \theta_2, cw$
where $\theta_1 > \theta_2$

$\bar{\theta} \leftarrow \frac{\theta_1+\theta_2}{2}$, $m_\perp \leftarrow \frac{-1}{\tan(\bar{\theta})}$

if First non-node initial area **then**

$x_1 \leftarrow x_{_{LN}}, y_1 \leftarrow y_{_{LN}}$

else

$x_1 \leftarrow x_{last}, y_1 \leftarrow y_{last}$

end if

Get intersection of line 2 from VO and $\perp$ line from (x_1, y_1): (x_2, y_2) ▷ *Algorithm 16*

$x_{last} \leftarrow x_2, y_{last} \leftarrow y_2$

return $cw * d$, where d is the distance between point 1 and 2 ▷ *Equation 4.23*

Figure 4.29 shows the procedure for calculating the initial area for Channel Flows that are informed by the expansion fan nodes. Each area starts at the intersection of the fill height and the first boundary line at θ_1. Next, a line perpendicular to the average flow angle is extended from the initial point to a point where it intersects the second boundary line at θ_2. The incoming flow properties are calculated as an average from all of the nodes that fall between the two boundaries. This process repeats until the final Channel Flow object that captures an expansion fan node is initialized.

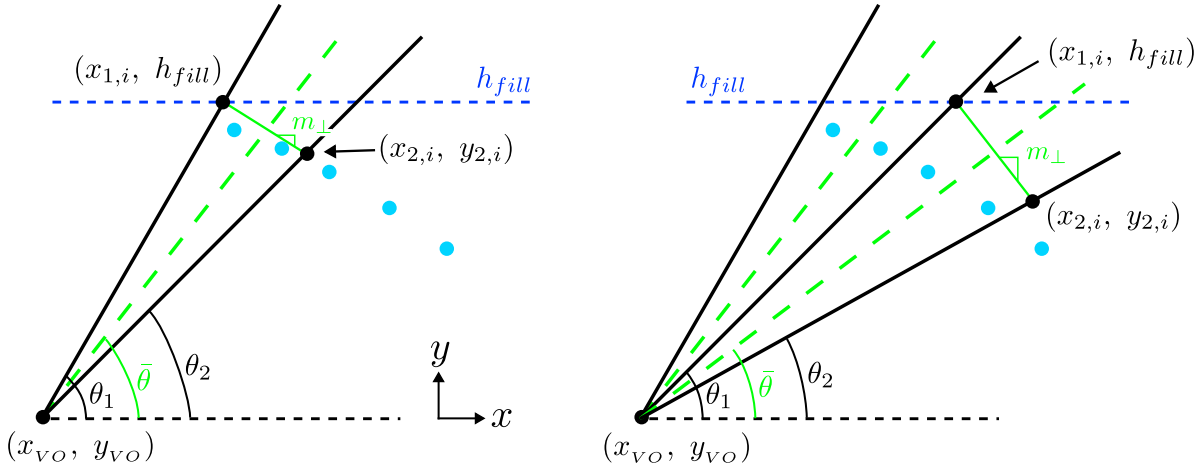


Figure 4.29: Visual Representation of the Calculation of the Initial Area for the Channel Flow Object Informed by the Expansion Fan Nodes.

Figure 4.30 shows the procedures for setting up the initial area in regions that do not contain the expansion fan nodes. The first Channel Flow object uses the last node location as the upper boundary. The line perpendicular to the mean flow direction is then extended, and its intersection with the lower boundary is determined. The inflow properties are determined based on assuming that the non-node mass flow rate is equally distributed amongst the non-node Channel Flow objects. The lower location of the inflow area is used as the initial location of the next Channel Flow inlet area, shown in the right subplot. This process repeats for the remainder of the non-node informed Channel Flow objects.

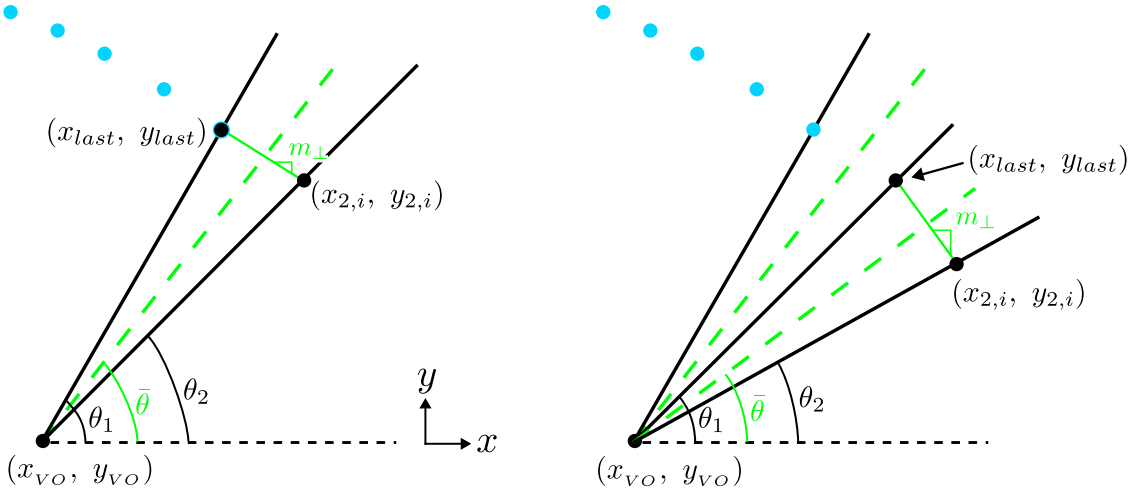


Figure 4.30: Visual Representation of the Calculation of the Initial Area for the Channel Flow Object not Informed by the Expansion Fan Nodes.

There are also two methodologies that can be used to calculate the exit area of the Channel Flow objects, depending on whether the object interacts with the oblique shock wave or not. Algorithm 31 shows the procedure for objects that exit the RDC without the oblique shock interaction, while Algorithm 32 provides the procedure for objects that interact with the oblique shock.

Algorithm 31 Final Channel Flow Area: Exit

Require: $h_{RDC}, \theta_1, \theta_2, cw, x_{VO}, y_{VO}$, where $\theta_1 > \theta_2$

$\bar{\theta} \leftarrow \frac{\theta_1+\theta_2}{2}$, $m_\perp \leftarrow \frac{-1}{\tan(\bar{\theta})}$

Locate point 1 at the intersection of RDC exit and line 1: $x_{1,e}$ ▷ *Algorithm 16*

Locate point 2 at intersection of $\perp$ line and line 2: $(x_{2,e}, y_{2,e})$ ▷ *Algorithm 16*

return $cw * d$, where d is the distance between point 1 and 2 ▷ *Equation 4.23*

Algorithm 32 Final Channel Flow Area: Shock

Require: Shock angle: $\Theta, x_{VO}, y_{VO}, x_{det,1}, OD, h_{fill}, cw, \theta_1, \theta_2$, where $\theta_1 > \theta_2$

$\bar{\theta} \leftarrow \frac{\theta_1+\theta_2}{2}$, $m_\perp \leftarrow \frac{-1}{\tan(\bar{\theta})}$

Get intersection of next shock at $(x_{det,1} + \pi OD, h_{fill})$ and line 2: (x_2, y_2) ▷ *Algorithm 16*

Get intersection of line 1 and $\perp$ line from (x_2, y_2): (x_1, y_1) ▷ *Algorithm 16*

return $cw * d$, where d is the distance between point 1 and 2 ▷ *Equation 4.23*

Figure 4.31 shows the diagrams for the two different calculations of the exit flow area. For non-shocked Channel Flow objects, the left subplot is used. This starts with finding the intersection of the upper boundary line and the exit plane of the RDC. In a similar manner as the inlet flow

regions, a line perpendicular to the average flow direction is extended until it intersects the lower boundary line. This process repeats for all Channel Flow objects that are not processed by the oblique shock.

For Channel Flow objects that are processed by the oblique shock, the right subplot of Figure 4.31 is used. In this case, the first step is to find the location where the lower boundary line intersects the next oblique shock. From this point, the line perpendicular to the average flow direction is projected until it intersects the upper boundary line. This process is repeated for the remainder of the Channel Flow objects that are processed by the oblique shock.

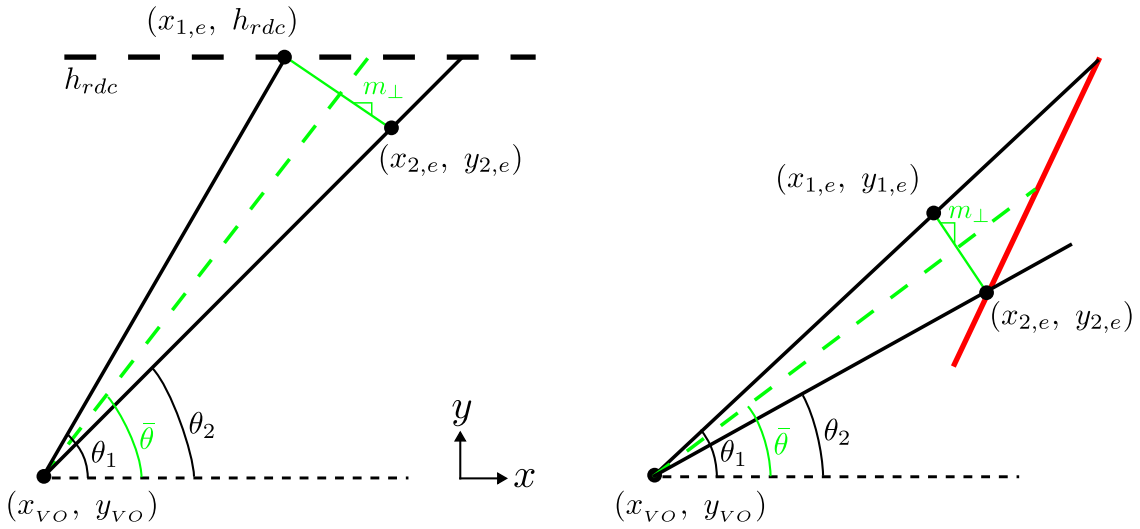


Figure 4.31: Visual Representation of the Calculation of the Final Area for the Channel Flow Object. Non-Shocked Channel Flows (left) and Shocked Channel Flows (right).

After the Channel Flow objects are constructed, the next step is to integrate these flowpaths from their initial conditions to the exit. This was done using a generalized one-dimensional flow integrator described in Hodges.[70] This non-ideal solver optionally includes a friction coefficient, f, heat removal, Q_{tot} and area change from $A_1 \rightarrow A_2$. The area will be assumed to vary linearly along the flowpath. The integrator requires the total temperature as a function of the distance along the path, $T_t(x)$, and the rate of change $\frac{dT_t}{dx}(x)$. The total temperature change from the beginning to the end of the flow path region is calculated based on the total heat transferred.

$$Q_{tot} = \dot{m} c_p \Delta T_t \tag{4.24}$$

$$T_{t,2} = T_{t,1} + \frac{Q_{tot}}{\dot{m} c_p} \tag{4.25}$$

where Q_{tot} is positive going into the product gas.

$$\frac{dT_t}{dx} = \frac{\Delta T_t}{\Delta x} = \frac{Q_{tot}}{\dot{m} c_p l} \tag{4.26}$$

where $\Delta x = l$. This results in the equation representing the variation in total temperature along the Channel Flow object:

$$\frac{dT_t}{dx}(x) = \frac{Q_{tot}}{\dot{m} c_p l} x \tag{4.27}$$

The integration methodology marches in space and calculates the rate change in the Mach number squared:

$$\frac{dM^2}{dx} = \frac{M^2 \psi(M^2) G(x, M^2)}{1 - M^2} \tag{4.28}$$

where $\psi(M^2)$ is defined in Equation 4.29.

$$\psi(M^2) = 1 + \frac{\gamma - 1}{2} M^2 \tag{4.29}$$

Ignoring mass addition, the total potential function, G, can be written as the sum of the potential functions for area change, friction, and heat transfer, shown in Equation 4.30.

$$G(x, M^2) = \frac{-2}{A}\frac{dA}{dx} + \gamma M^2 \frac{4f}{D_H} + (1 + \gamma M^2)\frac{1}{T_t}\frac{dT_t}{dx} \tag{4.30}$$

where D_H is the hydraulic diameter.

$$D_H = \frac{4A}{P} \tag{4.31}$$

where A is the area and P is the perimeter.

This process is repeated for each Channel Flow object when either a friction coefficient or a heat transfer rate is specified. Otherwise, the model used a single-step isentropic process that modeled the area change only. Algorithm 33 shows the pseudo-code used for the Channel Flow solver.

Of particular note, when trying to minimize input parameters, the polytropic compression algorithm, Algorithm 24, can be used instead of the general one-dimensional solver. This effectively provides a closure for the Channel Flow solution, eliminating the need for a costly integration process and removing unknown input parameters.

Algorithm 33 Channel Flow One-dimensional Flow Solver

Require: $x_0, A_0, T_{t,0}, P_{t,0}, l, \dot{m}_i, \Delta x, \frac{dA}{dx}, \dot{q}, f$

for all Channel Flow objects **do**

if $f = 0 \& \dot{q} = 0$ **then**

Isentropic flow with area change

else

Calculate potential function for temperature: $\frac{dT}{dx}$

Integrate Channel Flow object using Equation 4.28 from 0 to l

end if

Post-process to get Channel Flow exit state

end for

After each Channel Flow object is solved by either integration or the polytropic compression algorithm, the next step is to update the post-expansion gas properties that are entering the oblique shock. Algorithm 34 shows the steps involved in this update, requiring all of the Channel Flow objects that are processed by the shock.

Algorithm 34 Post-expansion Flow Update

Require: List of Channel Flow solutions

Initialize total flow area into shock: A_{tot}

Initialize average incoming Mach: $\bar{M}$

for all Channel flow results **do**

if Channel flow passes through shock **then**

A_{tot} += A_i

$\bar{M}$ += $M_i A_i$

end if

end for

return Area average Mach: $\bar{M}^A \leftarrow \frac{\bar{M}}{A_{tot}}$

The total area of the exits of these Channel Flow objects is then calculated. Finally, an area-average Mach number is calculated and returned for the next iteration of the downstream shock complex solver, Algorithm 17. Figure 4.32 shows an example of the shocked Channel Flow exit regions. For reference, Figure 4.32 is the post-expansion region, shown in orange in Figure 4.15.

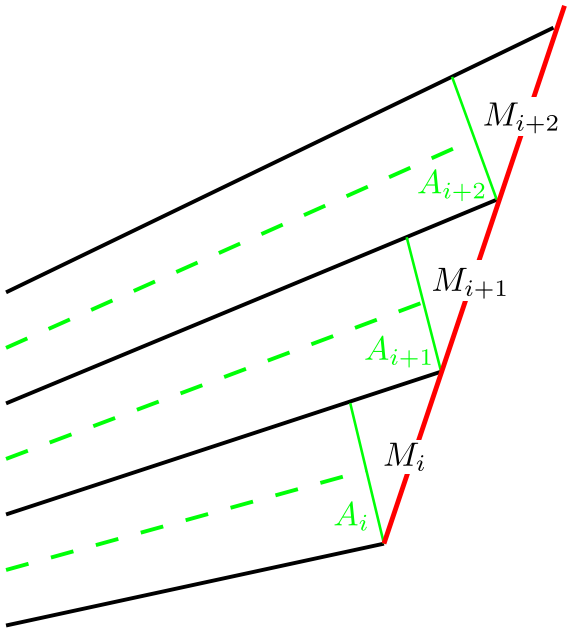


Figure 4.32: Diagram of the Final Mach and Area of the Shocked Channel Flow Objects.

4.2.3 Inlet Mass Flow

The inlet mass flow model is based on a modified version of the processes discussed in Section 3.3.3. It is now informed by the post-detonation expansion fan and uses the full inlet profile in determining Mach numbers and mass flow rates through individual differential areas dividing the inlet plane. This model closure provides a robust, physics-based method for linking the inlet plane of the RDC to the detonation region, subsequently linking the inlet performance to the performance of the detonation wave.

The details of this model will be discussed further in this section, but Figure 4.33 shows the region of interest for the inlet model. This region includes the flowpath profile from the plenum to the RDC channel, which stretches from the previous wave to the current wave.

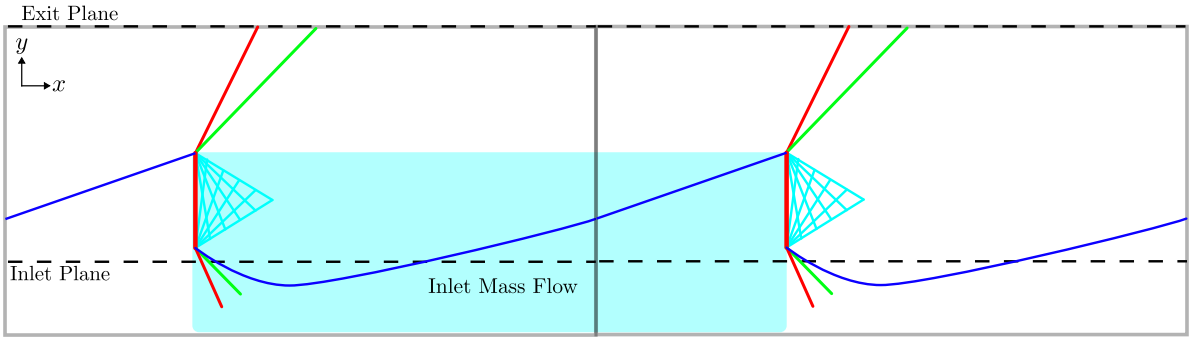


Figure 4.33: Inlet Region within Flowpath.

Figure 4.34 shows the block diagram for the inlet mass flow model. This sub-model requires the flowpath geometry and the channel and plenum pressure. It also requires information from the expansion nodes calculated in the Shock-Expansion Complex model.

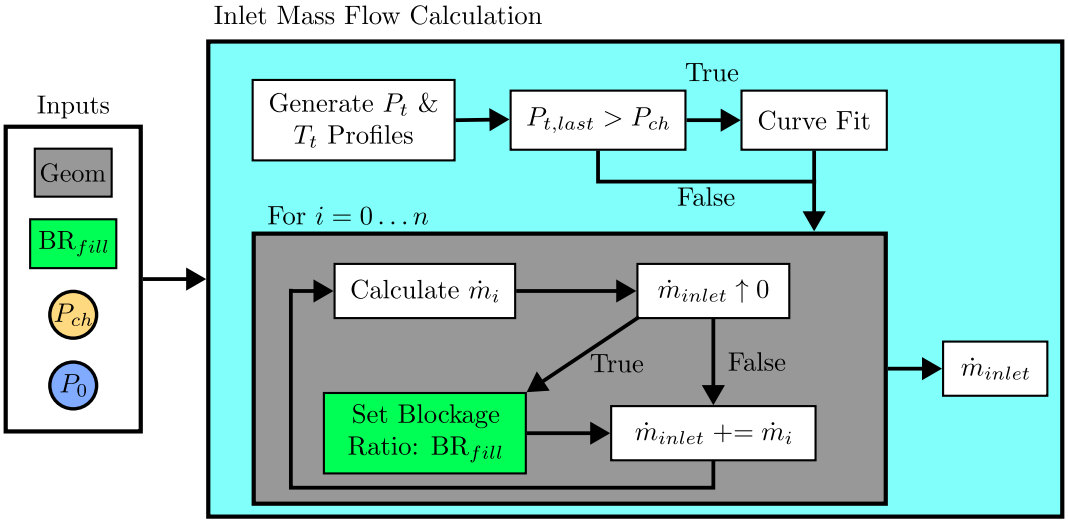


Figure 4.34: Block Diagram of the Inlet Mass Flow Rate Solver.

The inlet model uses the furthest upstream expansion fan nodes to generate a total pressure profile that the inlet experiences as the detonation wave passes. For this model, it is assumed that the inlet acts isentropically and is divided into multiple differential areas with average flow properties. After the total pressure profile is generated, the next step is to set up the remainder of the total pressure profile across the full inlet because the expansion fan region is only a small fraction of the RDC circumference. Next, the mass flow rate through each differential area is calculated and summed up to provide a total inlet mass flow rate. Finally, the blockage ratio is calculated based on the location where the backward-flowing products are re-expelled through the inlet.

Algorithm 35 Inlet Mass Flow Model

Require: $\overrightarrow{Node}_{exp}, OD, A_{inj}$

Generate total pressure and temperature profile: $\overrightarrow{x}, \overrightarrow{P_t}, \overrightarrow{T_t}, \Delta x$ ▷ *Algorithm 36*

Zero inlet mass flow and blockage location: $\dot{m}_{inlet} \leftarrow 0, x_{fill} \leftarrow 0$

if $P_{t,last} > P_{ch}$ **then**

Curve fit from $P_{t,last} \rightarrow P_{ch}$: x_{const} ▷ *Algorithm 37*

else

$x_{const} \leftarrow x_{Node,last}$

end if

Append constant property region to $\overrightarrow{x}$ $x_i \in [x_{const}, \pi OD] \propto \Delta x,\ \overrightarrow{P_t}, \overrightarrow{T_t}$

for $i \in len(\overrightarrow{x})$ **do**

Get differential area: $\Delta A_i \leftarrow \pi OD(x_{i+1} - x_i)/A_{inj}$

Calculate mass flow rate: $\dot{m}_i$ ▷ *Algorithm 38*

$\dot{m}_{inlet}$ += $\dot{m}_i$

if Forward product re-injection complete **then**

Set blockage location: $x_{fill} \leftarrow x_i$

end if

end for

Update blockage: $\mathrm{BR}_{fill} \leftarrow \frac{x_{fill}}{\pi OD}$

Set inlet mass flow rate: $\dot{m}_{inlet}$

Figure 4.35 shows an example of the final total pressure profile generated from the expansion fan nodes. It also shows the total plenum pressure, which is used to determine the flow direction, the static channel pressure, and the blockage ratio for this iteration. Figure 4.36 shows the associated Mach number profile through the inlet on the left sub-plot, which is broken down into the respective region of flow. Note that the backflow regions (negative Mach number highlighted in red) are associated with the region where the pressure profile from the expansion nodes is greater than the total pressure of the plenum. Also, with the conditions shown in this figure, a large fraction of the forward-flowing region is sonic. The right sub-plot shows the mass flux profile through the inlet, based on the flow properties and Mach numbers within each region. It is clear that the region where the detonation resides has a significantly higher mass flux as a result of the high post-detonation pressure. As the pressure decays through the expansion fan, the backward-flowing flux decreases.

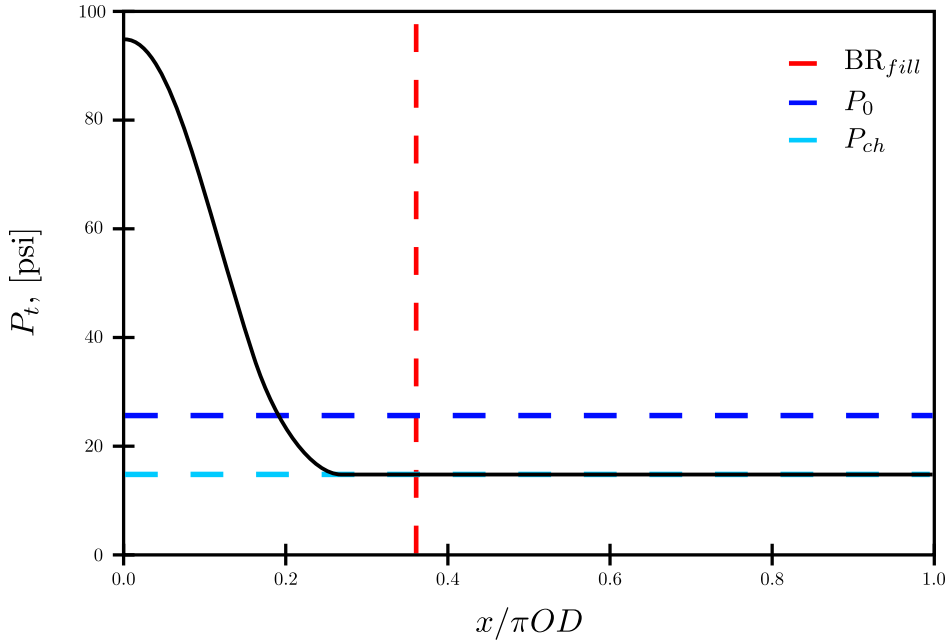


Figure 4.35: Example Inlet Total Pressure Profile Generated from Expansion Fan Nodes.

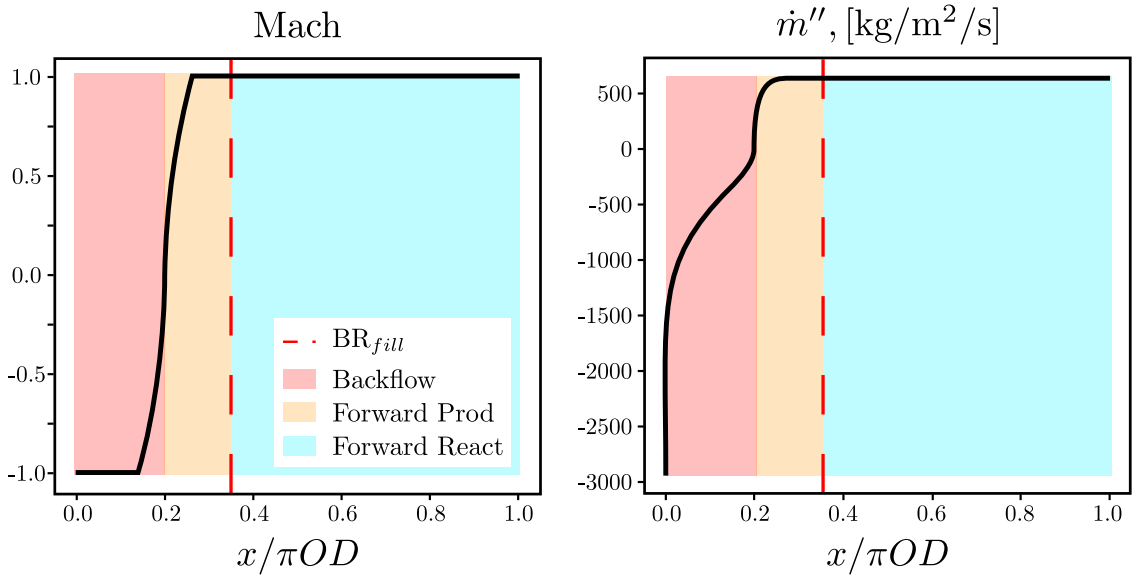


Figure 4.36: Resultant Inlet Mach (left) and Mass Flux Profiles (right) from the Total Pressure Profile in Figure 4.35.

Algorithm 36 shows the steps involved in generating the total property profiles from the expansion fan nodes. This methodology relies on using only the y-direction velocity component in defining total properties. At each node, the static properties are calculated; then, if the node has a negative y-direction velocity component, the associated y-direction Mach number is used to

calculate the total properties. Otherwise, the static properties are used as totals.

Algorithm 36 Generate Node Total Pressure and Temperature Profile

Require: $\overrightarrow{Node}_{exp}$
  Initialize empty vector for x location, total pressure, and total temperature: $\overrightarrow{x}, \overrightarrow{P_t}, \overrightarrow{T_t}$
  for all Bottom nodes in $\overrightarrow{Node}_{exp}$ **do**
    Get x location of node: x_i
    Get y-direction velocity component: v_i
    Get static pressure and temperature of node: P_i, T_i
    if $v_i < 0$ **then**
      Get the speed of sound of node: a_i
      $M_{y,i} \leftarrow |\frac{v_i}{a_i}|$
    else
      $M_{y,i} \leftarrow 0$
    end if
    $\psi_i \leftarrow 1 + \frac{\gamma-1}{2} M_{y,i}^2$
    $P_{t,i} \leftarrow P_i \psi_i^{\gamma/\gamma-1}$, $T_{t,i} \leftarrow T_i \psi_i$
    Append results to $\overrightarrow{x}, \overrightarrow{P_t}, \overrightarrow{T_t}$
  end for
  Check spacing and update according to $\Delta x_{inlet,max}$
  Interpolate P_t & T_t values at added x locations
  return $\overrightarrow{x}, \overrightarrow{P_t}, \overrightarrow{T_t}$

Figure 4.37 shows an example of how the expansion fan nodes are used to generate the total pressure profile. This figure shows the expansion fan node on the left subplot and the calculated total pressure profile on the right subplot. Because the inlet model is only concerned with the axial flow direction, the total pressure is simply defined based on the static pressure at the node and the associated y-direction velocity component. In cases where the velocity in the y-direction is positive (moving away from the inlet plane), the static pressure at those nodes was used. This generates a smooth curve in the total pressure profile while accounting for the fact that a positive axial velocity should reduce the impact on the inlet.

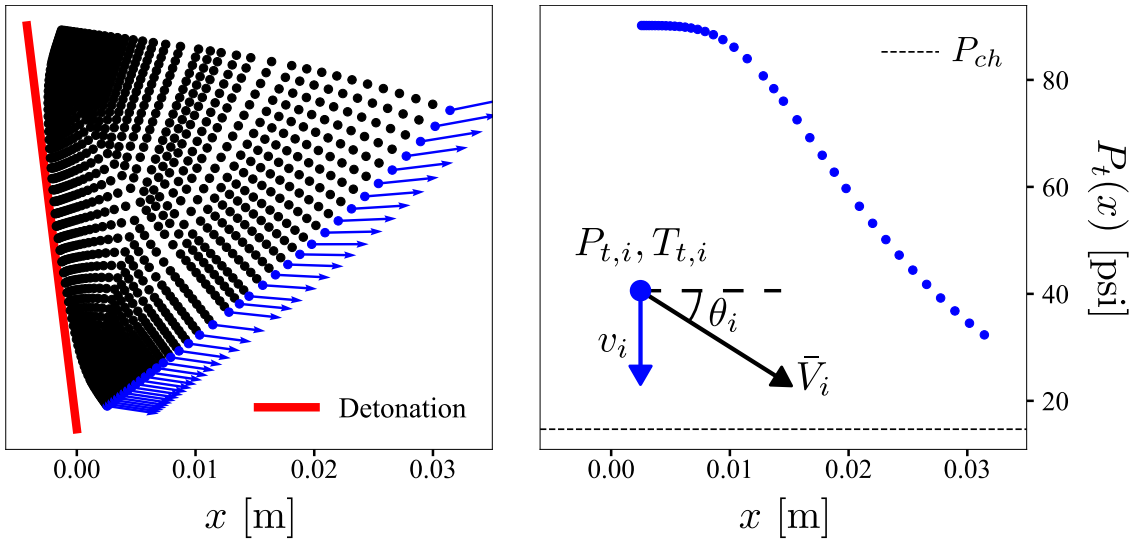


Figure 4.37: Diagram of the Upstream Most Expansion Fan Nodes used to Generate the Total Pressure Profile in Figure 4.35 (left). Diagram of the y-direction Velocity Component used to Calculate the y-direction Total Pressure (right).

In cases where the final expansion fan node has a higher pressure than the channel pressure, P_{ch}, a quadratic fit process is used to fill the gap. Figure 4.38 shows an example of fitting a quadratic equation to the total pressure profile generated from the expansion fan nodes. The quadratic fit line has four boundary conditions and four independent variables that require solving. The boundary conditions are the location of the final node, x_n, the total pressure at the final node, $P_{t,n}$, the slope at this point, $P' = dP_t/dx$, and the fact that the minimum pressure is the channel pressure with a slope at the channel pressure of zero. The unknowns are the three coefficients of the quadratic equation, a, b, c, and the location at which the quadratic reaches the channel pressure value, x_{const}. This methodology is described in more detail in Algorithm 37.

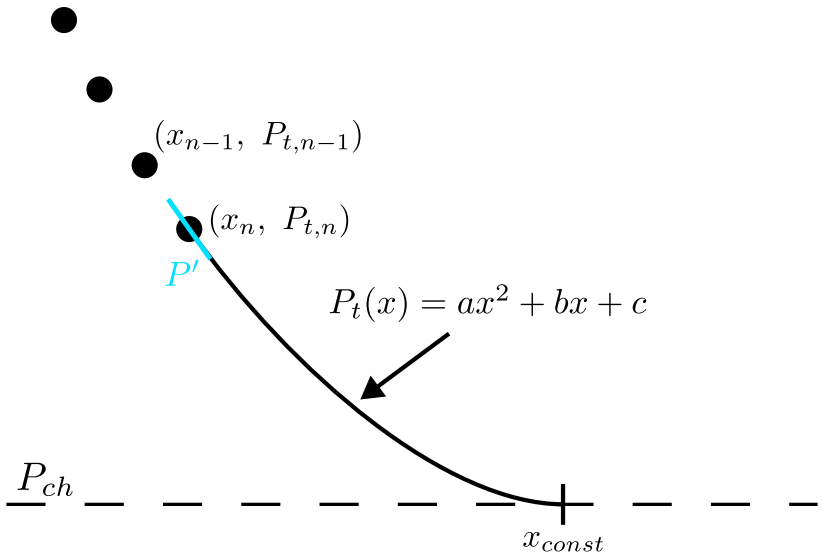


Figure 4.38: Example of the Quadratic Fit Procedure for the Total Pressure Profile in Figure 4.35.

Algorithm 37 Pressure Profile Fit Process

Require: $\overrightarrow{x}, \overrightarrow{P_t}$

Get spacing of final two x locations: $\Delta x \leftarrow x_n - x_{n-1}$

Get rate of change in total pressure: $P' \leftarrow \left(P_{t,n} - P_{t,n-1}\right)/\Delta x$

$a = P'^2/\left(4(P_{t,n} - P_{ch})\right)$

$b = \left(-P'(P'x_n - 2P_{t,n} + 2P_{ch})\right)/\left(2(P_{t,n} - P_{ch})\right)$

$c = \left(P'^2 x_n^2 - 4P'P_{t,n}x_n + 4P'P_{ch}x_n + 4P_{t,n}^2 - 4P_{t,n}P_{ch}\right)/\left(4(P_{t,n} - P_{ch})\right)$

$x_{const} = \left(P'x_n - 2P_{t,n} + 2P_{ch}\right)/P'$

Generate linearly spaced $x \in [x_n, x_{const}] \propto \Delta x$: $\overrightarrow{x}_{fit}$

for $x_i \in \overrightarrow{x}_{fit}$ **do**

$P_{t,i} = ax_i^2 + bx + c$

Append x_i to $\overrightarrow{x}$ & $P_{t,i}$ to $\overrightarrow{P_t}$

end for

return x_{const}, $\overrightarrow{x}, \overrightarrow{P_t}$

Finally, Algorithm 38 provides the pseudo-code for calculation of the mass flow rate through each differential area (see Figure 4.39 for an example). This algorithm determines the direction of flow, the associated gas composition, and the correct static/total pressure used to calculate the mass flow rate. In the case of backward-flowing product gases, the total pressure is that provided by the expansion fan node profile, and the static pressure is the total plenum pressure, P_0. In the case of forward-flowing products or fresh reactants, the total pressure is the total plenum pressure,

and the static pressure is that provided by the expansion fan node profile. After the correct gas compositions and pressure are determined, the algorithm calculates the Mach number through the inlet. This Mach number is finally used to calculate the mass flow rate through the differential area.

Algorithm 38 Differential Area Mass Flow Calculation

Require: $P_i, A_{inj}, A_{plen}, A_{ch}$

if Backflow Products **then**

$\gamma_i \leftarrow \gamma_{3.2}, A_i \leftarrow A_{plen}, P_{t,i} \leftarrow P_i, P_{s,i} \leftarrow P_0$

else if Forward Products **then**

$\gamma_i \leftarrow \gamma_{3.2}, A_i \leftarrow A_{ch}, P_{t,i} \leftarrow P_0, P_{s,i} \leftarrow P_i$

else

$\gamma_i \leftarrow \gamma_{air}, A_i \leftarrow A_{ch}, P_{t,i} \leftarrow P_0, P_{s,i} \leftarrow P_i$

end if

Calculate sub-sonic pressure: $P_{s,sub}$

if $P_{s,i} < P_{s,sub}$ **then**

$M_i = 1$

else

$M_{ch} = \sqrt{\frac{2}{\gamma_i - 1}[(P_{t,i}/P_{s,i})^{(\gamma_i - 1)/\gamma_i} - 1]}$

Calculate critical area: A^*

Calculate Mach from area ratio: $M_i \leftarrow f(A_{inj}/A^*, \gamma_i)$

end if

$\dot{m}_i \leftarrow P_{t,i} A_i \sqrt{\frac{\gamma_i}{R_i T_{t,i}}} M_i \left(1 + \frac{\gamma_i - 1}{2} M_i^2\right)^{-(\gamma_i + 1)/2(\gamma_i - 1)}$

return $\dot{m}_i$

Figure 4.39 shows an example of the differential areas constructed across the RDC inlet for the inlet mass flow model. The colors correspond to the regions of product backflow in red, forward-flowing products in yellow, and forward-flowing reactants in cyan. These differential areas are applied in the same manner as the injector fill model, Algorithm 14, but are now applied across the RDC inlet. The key difference is that this implementation does not require a full Mach number profile through the differential area, only the Mach number at the inlet plane.

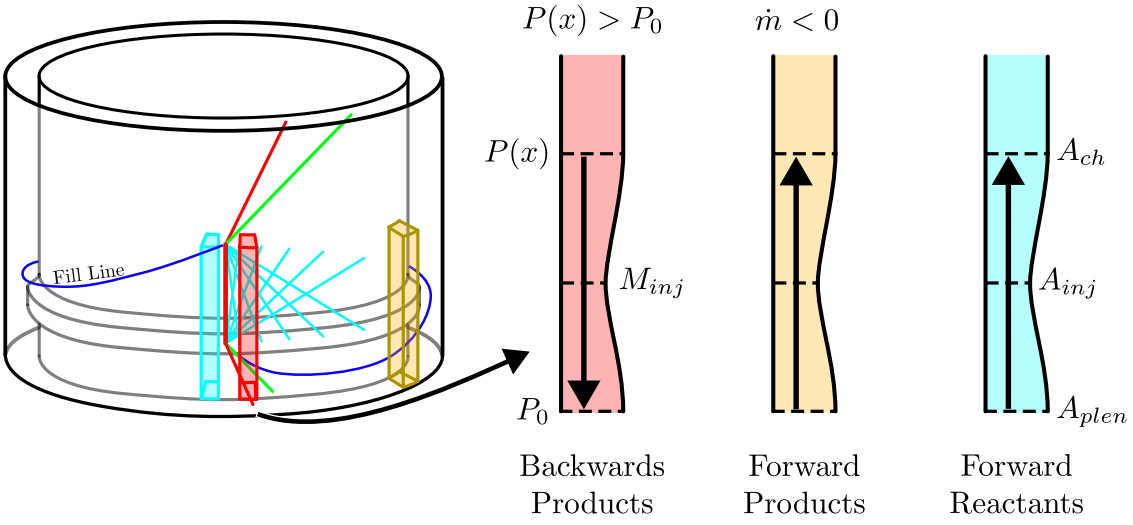


Figure 4.39: Example of Inlet Model Differential Areas

4.2.4 Cycle Model Summary

Algorithm 39 pseudo-code for the entire RDC Cycle Model. This shows the iteration and convergence criterion for the cycle model, along with the use of the various sub-models. The model takes as inputs a target mass flow rate, $\dot{m}$, the RDC geometry of interest, and an object containing configuration data for the model, shown in Table 4.2.

The solver starts by initializing an estimated rate of change in the plenum pressure given a change in mass flow rate, which is used during the plenum pressure update at the end of the main loop. This was done assuming an unblocked, choked inlet using air as the oxidizer. A similar procedure is used to obtain an initial estimate of the total pressure of the plenum, P_0, before estimating the channel static pressure P_{ch}. The main iteration loop for the cycle model matches the calculated inlet mass flow rate with the specified value. Within each loop, the model will run the detonation and fill sub-model to update the detonation properties and fill profile; see Section 4.2.1 for additional details. Next, the shock complex sub-model will execute and return a calculated inlet mass flow rate; for more details, see Section 4.2.2 and Section 4.2.3, respectively.

The difference between the calculated inlet mass flow rate and the specified is used to inform the update in the total plenum pressure for the next loop. The solver will check the magnitude of the mass flow rate difference and update the relaxation factor accordingly. It also checks the magnitude of the change in total pressure from iteration to iteration. If the total pressure change is below the threshold, the model will break from execution. This exit condition does not necessarily mean that the model failed to converge on a representative solution, only that the changes in total pressure are so small that the mass flow rate calculated in the next iteration will not change meaningfully.

Finally, if the maximum number of iterations has been reached, the model will also break from

execution. This exit condition also does not mean that the model did not produce a representative solution. In certain cases, the mass flow rate will converge in a slow enough manner that, given additional iterations, the solution will converge. After breaking from the main iteration loop, the data from the final iteration will be post-processed and returned as a separate data structure for further analysis.

Variable	Description	Default Value
$\dot{m}$	Target mass flow rate	300 [g/s]
$T_{t,0}$	Plenum total temperature	298.15 [K]
P_{amb}	Ambient pressure	1 [atm]
$c_{d,f}$	Forward RDC inlet discharge coefficient	1
$c_{d,b}$	Backward RDC inlet discharge coefficient	1
N_{waves}	Number of detonation waves	1
ξ_{P}	Parasitic deflagration fraction	0
ξ_{L}	Leaked fuel fraction	0
ξ_{NC}	Non-commensal fuel fraction	0
$h_{fill,0}$	Initial guess at the fill height	0.0254 [m]
$v_{fill,0}$	Initial guess at the fill velocity	300.0 [m/s]
$\mathrm{BR}_{fill,0}$	Initial guess at the fill based inlet blockage ratio	0.2
$P_{0,relax}$	Total plenum pressure relaxation factor during iterative solution	0.5
N_{exp}	Minimum number of upper/lower expansion nodes	25
P_{tol}	Tolerance in pressure based iterative solvers	50 [Pa]
$\dot{m}_{tol}$	Tolerance in mass flow rate based iterative solvers	0.5 [g/s]
N_{fill}	Number of points used in the inlet fill model	200
$\Delta\nu_{max}$	Maximum deflection angle in shock-expansion fan model	1 [deg]
h_{RK}	Default spacing for integration methods	1 [mm]
N_{CF}	Number of Channel Flow objects per region, total = $3N_{CF}$	10
N_{iters}	Number of iterations of the cycle model main loop	20
ΔP_{tol}	Percent change in pre-detonation pressure	2.0%
$\Delta x_{inlet,max}$	Maximum x spacing along the inlet plane for mass flow solver	1 [mm]

Table 4.2: List of configuration variables.

Algorithm 39 RDC Cycle Model

Require: Target Mass Flow: $\dot{m}, \dot{m}_{tol}, P_{tol}, P_{0,relax}, N_{iters}$, RDC geometry

$\frac{dP_0}{d\dot{m}} \leftarrow \left[A_{inlet} c_{d,f} \sqrt{\frac{\gamma_{air}}{R_{air} T_{t,0}}} \left(\frac{\gamma_{air}+1}{2} \right)^{(\gamma_{air}+1/2(\gamma_{air}-1))} \right]^{-1}$

$P_0 \leftarrow \frac{\dot{m}}{0.8 c_{d,f} A_{inlet}} \sqrt{\frac{R_{air} T_t}{\gamma_{air}}} \left(\frac{\gamma_{air}+1}{2} \right)^{(\gamma_{air}+1)/2(\gamma_{air}-1)}$

if $P_0 < P_{amb}$ **then**

  $P_0 \leftarrow 1.5 P_{amb}$

end if

$P_{ch} \leftarrow 0.7 P_0$

while $|\dot{m}_i - \dot{m}| > \dot{m}_{tol}$ **do**

  *Detonation and Fill Model ▷ *Algorithm 11*

  Solve Shock Complex: $\dot{m}_{inlet}$ ▷ *Algorithm 17*

  $\Delta\dot{m} \leftarrow \dot{m} - \dot{m}_{inlet}$

  $\Delta P_0 \leftarrow \frac{dP_0}{d\dot{m}} \Delta\dot{m} P_{0,relax}$

  if $|\Delta\dot{m}| < 2.5\dot{m}_{tol}$ **then**

    Reduce relaxation factor for next iteration: $P_{0,relax} \leftarrow 0.1$

  else if $|\Delta\dot{m}| < 5\dot{m}_{tol}$ **then**

    Reduce relaxation factor for next iteration: $P_{0,relax} \leftarrow 0.25$

  end if

  if $|\Delta P_0| < P_{tol}$ [Pa] **then**

    return Partially successful, inlet mass flow did not match

  end if

  if $i > N_{iters}$ **then**

    return Unsuccessful

  end if

  Update P_0

end while

Post-process ▷ *Algorithm 40*

return Data structure containing cycle model results

* = *Requires Python Global Interpreter Lock*

The post-processing methods are shown in Algorithm 40. This takes an error-free, converged model and first calculates whether the detonation height and fill height would allow for the detonation to be contained within the fill region. Next, it calculates other metrics related to inlet blockage, such as the blockage fraction from Feleo et al.[5]. Next, the exit plane properties will be examined, returning the thrust and pressure gain metrics. This will also include the angular momentum at the

exit plane to verify conservation. Finally, other parameters of interest are calculated. For example, the ideal deflagrative thrust is calculated using the modeled plenum pressure.

Algorithm 40 RDC Cycle Model Post-Processing

Require: Error-free, converged cycle

Check lower Detonation location

Calculate cold flow mass flow rate and blockage: $\dot{m}_{cold} \rightarrow \mathrm{B}$ ▷ *Algorithm 38*

Nozzle flow calculations: $\dot{m}$, F_g, EAP, PG ▷ *Algorithm 41*

Calculate Exit Swirl: $S = \frac{1}{A_{exit}} \sum_{i=0}^{k} \rho_i u_i v_i A_{e,i}$

Calculate Ideal Thrust ▷ *Algorithm 42*

Because the computations along the exit profile are more complex, Algorithm 41 shows the pseudo-code for all of the exit plane related metrics, which also requires an error-free, converged cycle result, and all of the Channel Flow objects. This algorithm iterates through all of the Channel Flow objects, calculating metrics of interest, like the mass flow, thrust, axial flow properties, etc.

Algorithm 41 RDC Cycle Model Nozzle Post-Processing

Require: Error-free, converged cycle with Channel Flow objects

$\dot{m} \leftarrow 0, F_g \leftarrow 0$

for all Unshocked Channel Flows **do**

Calculate Nozzle Differential Exit Area

Add CF mass flow: $\dot{m}$ += $\dot{m}_i$

Get Axial Properties: M_y, v, $P_{t,y}$

Update thrust: F_g += $F_{g,i}$

EAP: M_i, $T_{e,i}$, $V_{e,i}$, $v_{e,i}$, EAP_v += $\dot{m}_i v_{e,i}$, $T_{t,e}$ += $\dot{m} T_{e,i}$

Get the polytropic rate terms from Algorithm 24

end for

Get total shocked exit area

for all Shocked Channel Flows **do**

Get Differential Area

Add CF mass flow: $\dot{m}$ += $\dot{m}_i$

Calculate Pre-Shock State

Oblique Shock Jump Calculation

Get Axial Properties: M_y, v, $P_{t,y}$

Update thrust: F_g += $F_{g,i}$

EAP: M_i, $T_{e,i}$, $V_{e,i}$, $v_{e,i}$, EAP_v += $\dot{m}_i v_{e,i}$, $T_{t,e}$ += $\dot{m} T_{e,i}$

Get the polytropic rate terms from Algorithm 24

end for

Calculate net thrust: F_{net}

Calculate ISP: $I_{sp} = \frac{F}{g_0 \dot{m}_f}$

Calculate Ideal EAP, Experimental EAP, PG

Get Mass Averaged Polytropic Rate Terms

Algorithm 42 provides the methodology behind the ideal deflagrative thrust calculation. This model uses the calculated plenum pressure from the model to determine the net thrust that would be produced by a deflagration-based combustion at the same plenum conditions. It uses the isentropic expansion velocity difference from the plenum pressure, post-combustion state, to the specified ambient pressure. It also assumes a perfect expansion profile and no pressure losses through the combustion process.

Algorithm 42 Ideal Deflagrative Thrust

Require: P_0, T_0, P_{amb}, Gas Object

Set Gas Object mixture to reactants

Set Gas pressure and temperature to plenum: P_0, T_0

Equilibrate Gas object at plenum conditions: Constant enthalpy and pressure

Get pre-expansion enthalpy: $h_1 = c_{p,1}T_1$

Get pre-expansion entropy: s_1

Set Gas mixture to ambient pressure at constant entropy

Get post-expansion enthalpy: $h_2 = c_{p,2}T_2$

Calculate Isentropic expansion velocity: $v_{e,ideal} = \sqrt{2.0(h_1 - h_2)}$

Calculate thrust: $F_{ideal} = v_{e,ideal}\dot{m}$

return F_{ideal}

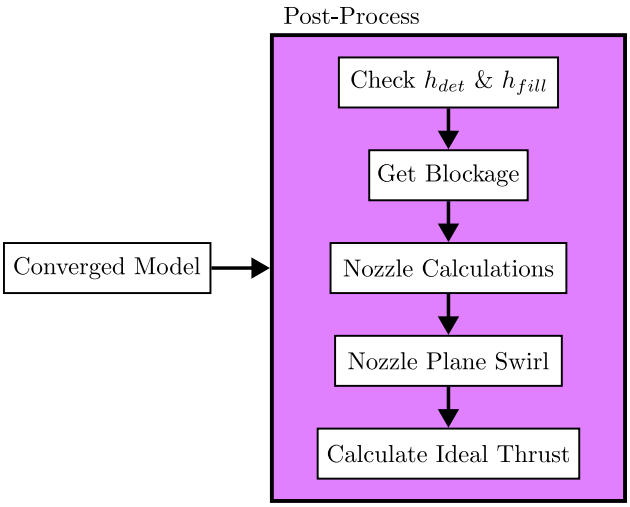


Figure 4.40: Block Diagram of the Post-Processing Algorithm.

For reference, Figure 4.41 shows the nozzle exit plane and the Channel Flow object region used to post-process the cycle model results.

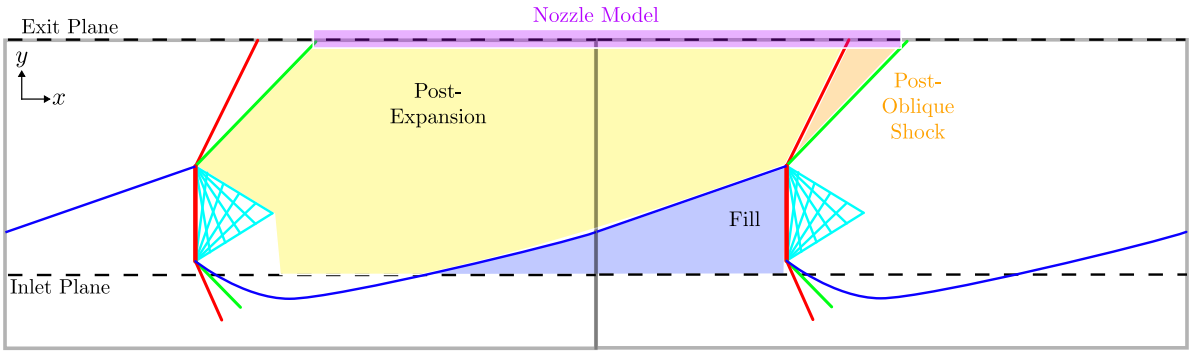


Figure 4.41: Post-Processing Regions within the Flowpath.

Finally, Figure 4.42 shows an example of the solved one-wave profile for the Pintle style inlet. This test case was conducted under a stoichiometric 300 g/s mass flow condition, with no detonation losses. The figure shows the locations of the upper and lower points of the detonation wave and their location with respect to the inlet plane. The downstream shock and slip lines are also plotted at each wave, while the Channel Flow objects between the waves are shown in black. This figure also shows the virtual origin point that extends from the fill and leftmost contact surface. This point falls slightly before the inlet plane and before the detonation wave, which was typical for all test points. For reference, the expansion fan node network, highlighted in cyan, is also shown to note the scale of the expansion fan versus the remainder of the flowpath.

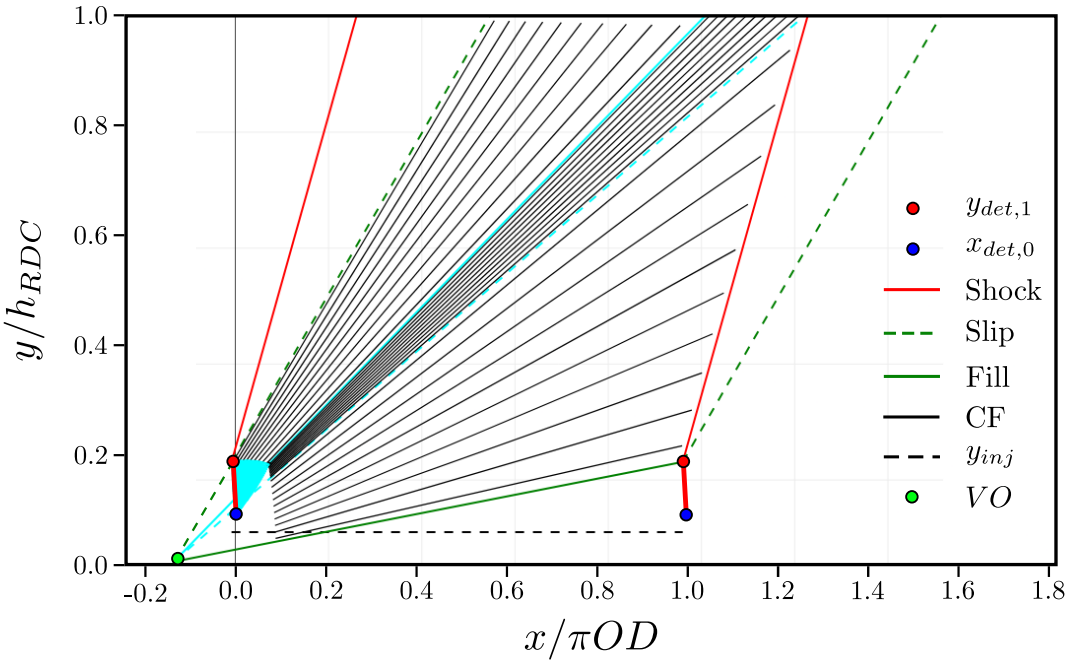


Figure 4.42: Example Result. Pintle Style Inlet, $\dot{m} = 300$ [g/s], $\xi_{\mathrm{P}} = 0, \xi_{\mathrm{L}} = 0$.

As mentioned above, post-processing requires an error-free, converged cycle. Table 4.3 provides a list of different methods by which the model exits the main iteration loop. This includes a brief description of the exit condition and whether the model exited with a terminal condition. The terminal condition means there was an error in the solution, and the post-processing will not occur.

Program Value	Description	Terminal
Success	Successfully matched required mass flow	False
Iter	Did not match mass flow in maximum iterations	False
Ptol	Changes in P_0 are below tolerance	False
Ydet0	Detonation height is larger than fill can provide	False
DetachedShock	Shock complex results in detached shock	True
Blowout	Detonation is larger than channel	True

Table 4.3: Description of Model Exit Conditions.

The two terminal conditions for the model include a detached shock detection, as the current version of the model does not implement a methodology for handling this situation. Within the model, certain steps can be taken to try to mitigate this error, such as lowering the pressure or increasing a Mach number; however, these are usually reserved for the first few iterations as a way to mitigate the errors caused by a poor initial guess. In subsequent iterations, this condition typically does not resolve, and the model has to break the solution process with a terminal status.

The next terminal condition was not encountered during the testing and evaluation of the model but is included as a reference. This case is for when the detonation wave would not be contained within the RDC channel. Future iterations of the model might remove this as a terminal condition, instead opting to split the detonation wave into multiple waves, which may alleviate this exit status.

The non-terminal conditions are straightforward, except for the detonation height error. This is calculated after the cycle exit and indicates that the configuration could not produce a fill height sufficient to contain the detonation wave. This does not exist as a terminal condition because it can also appear initially due to a poor initial guess. Future efforts will seek to apply other handling methods and potentially additional sub-models to remove this error. For this research, these points were simply classified as inoperable; however, the operability aspect of RDC devices was not the focus of this effort.

4.3 Results

The following sections will discuss the initial model evaluation, including a grid sensitivity study, a parameter sensitivity study, and a parametric evaluation of the model with respect to a number

of inputs and outputs. The discussion of the model comparison with experimental data and other similar cycle models is saved for the next chapter, so this section will only discuss larger trends in how input values affect the output of the model.

4.3.1 Grid Convergence and Sensitivity Analysis

This section is dedicated to a grid sensitivity study of the model with respect to certain configuration parameters and output metrics. The goal is to establish configuration parameters that produce reasonably accurate results while also maintaining short evaluation times. Because we do not have a ground truth value for any of the output values of interest, we will simply run the model at an arbitrarily high resolution for all configuration parameters of interest. This produces what will be termed the maximum resolution output, which we will use as the ground truth value as we look at model convergence. Table 4.4 shows the input configuration parameters of interest, with their respective maximum resolution values, and the model output metrics of interest, with their "ground truth" values.

Input Parameter	Max Resolution
$\Delta\nu_{max}$	0.1 [deg]
ΔP_{tol}	0.1 %
$\Delta x_{inlet,max}$	1e^{-4} [m]
h_{RK}	1e^{-4} [m]
$\dot{m}_{tol}$	1e^{-4} [kg/s]
N_{CF}	100
N_{exp}	1000
N_{fill}	1000
N_{iters}	10000
P_{tol}	0.1 [Pa]

Outputs	Max Resolution Value
Thrust	340.8 [N]
P_0	30.92 [psi]
BR	0.208
$\dot{m}$	0.3 [kg/s]
Inlet Choke %	100 %
PG	-0.256
n	1.564

Table 4.4: Grid Sensitivity Input, Outputs and Maximum Resolution Values.

Unless noted within a given section, the methodology for the grid sensitivity study was to fix all configuration parameters to their maximum resolution value while only varying a single parameter of interest at a time. The output results for each sweep were then compared to the maximum resolution value as a percent error. Although all parameter sweeps were performed, only the following subset produced meaningful results.

- Minimum number of expansion fan Mach lines, N_{exp}

- Maximum Mach angle spacing, $\Delta\nu_{max}$
- Total pressure tolerance breach value, P_{tol}
- Target mass flow rate tolerance, $\dot{m}_{tol}$
- Number of Channel Flow solution objects, N_{CF}
- Inlet total pressure spacing, $\Delta x_{inlet,max}$

Finally, along with tracking the output values, this section will capture the cycle evaluation time as a function of changes in each configuration parameter. This will allow for a visual representation of the trade-off between model accuracy, with respect to itself at a high resolution, and the time required to solve the cycle model. For each time presented in this section, only 1 trial was conducted, so the timing results should simply be used to show trends, and not a exact time measurements of the model.

4.3.1.1 Minimum Number of Expansion Fan Mach Lines and Max Mach Line Spacing

This section examines the model performance changes with regard to the expansion fan solution process. Figure 4.43 shows the convergence map and timing characteristic of the cycle model as the minimum number of expansion fan Mach lines was changed. Across all outputs, except for the polytropic coefficient, the model converges to a zero-percent error value with an increase in the number of Mach lines. The polytropic coefficient does not show signs of good convergence with the maximum resolution value; however, the overall percentage error was less than 1%, indicating little change with the number of Mach lines. In addition, the thrust and pressure gain metrics saw a greater improvement as the number of Mach lines increased above 20.

It should also be noted that the model will adjust the final number of expansion fan Mach lines based on the spacing. Because the sweeps were conducted with high resolution for all parameters outside of the current one being studied, this means that the maximum Mach angle spacing parameter, $\Delta\nu_{max}$, will increase the number of Mach lines over the specified minimums in the study.

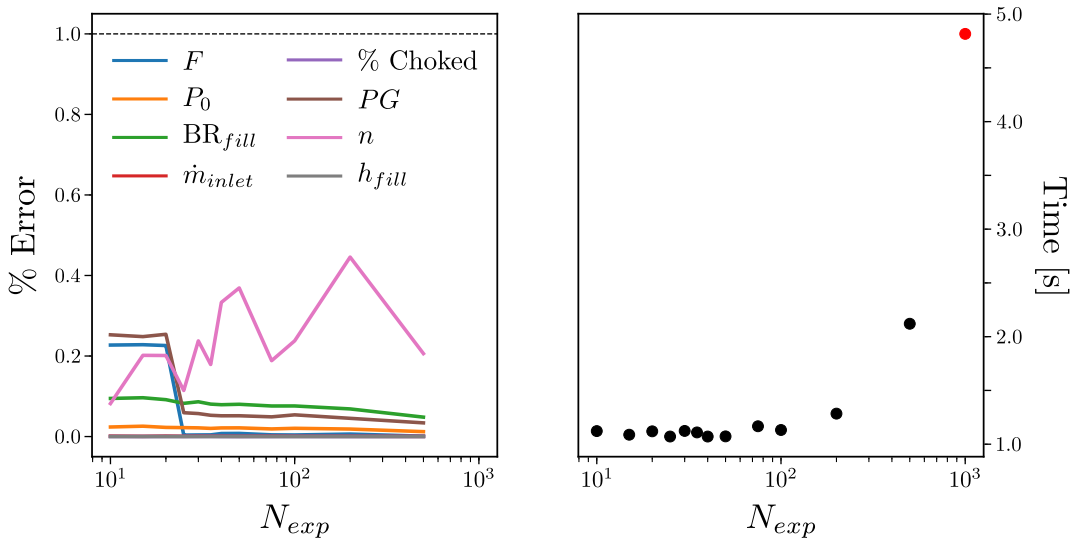


Figure 4.43: Grid Convergence Study: Minimum Number of Expansion Fan Mach Lines

A similar argument can be made for the expansion fan Mach angle spacing term. This parameter shows nearly constant percent errors across all output parameters, likely due to the minimum number of Mach lines at maximum resolution always producing a spacing less than the specified maximum spacing.

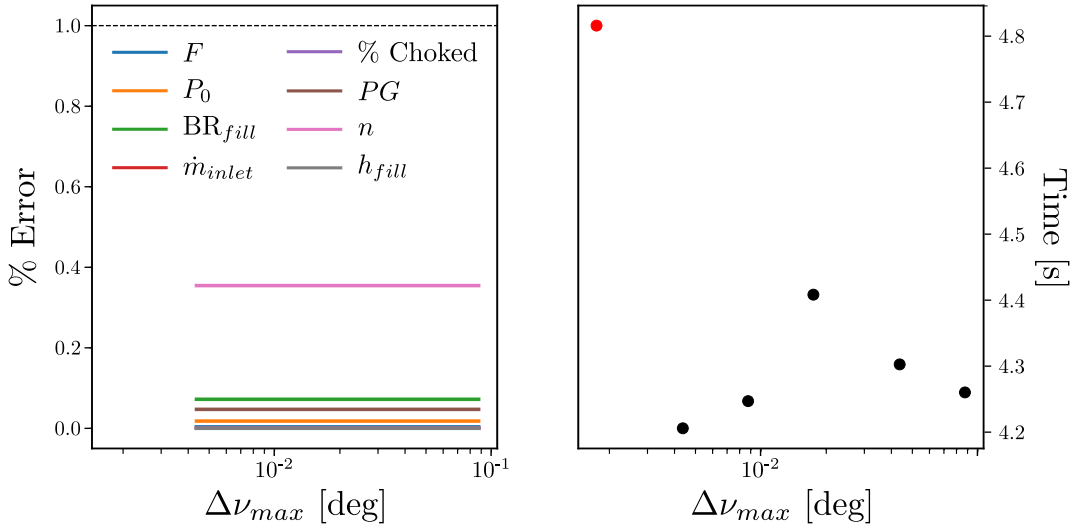


Figure 4.44: Grid Convergence Study: Maximum Mach Line Deflection Angle

Because these two terms likely impact the results of the individual sweeps, another sweep was conducted by simply examining the final number of Mach lines as opposed to each parameter individually. This was done by resetting the Mach angle tolerance back to the default 1-degree condition (see Table 4.2) and sweeping the input number of expansion fan Mach lines from 10 to

500. Figure 4.45 shows the results for the output convergence (a), the model evaluation time (b), and the requested versus actual number of Mach lines (c). This shows the expected convergence in the output parameter, aside from the polytropic coefficient. As the total number of final expansion fan Mach lines decreased, so did the model evaluation time. Finally, this figure shows the input versus the actual number of Mach lines, where at the higher number of requested Mach lines, there is a linear trend, suggesting that the input number of Mach lines is being used directly. At the lower number of requested Mach lines, the Mach angle spacing term is inserting additional points to ensure the maximum deflection angle is not above 1 degree.

From these improved results, it appears that as one approaches roughly 100 actual Mach lines, the error in all output terms decreases below the 1% mark, while also keeping the total cycle time to a reasonable value of approximately 364 ms.

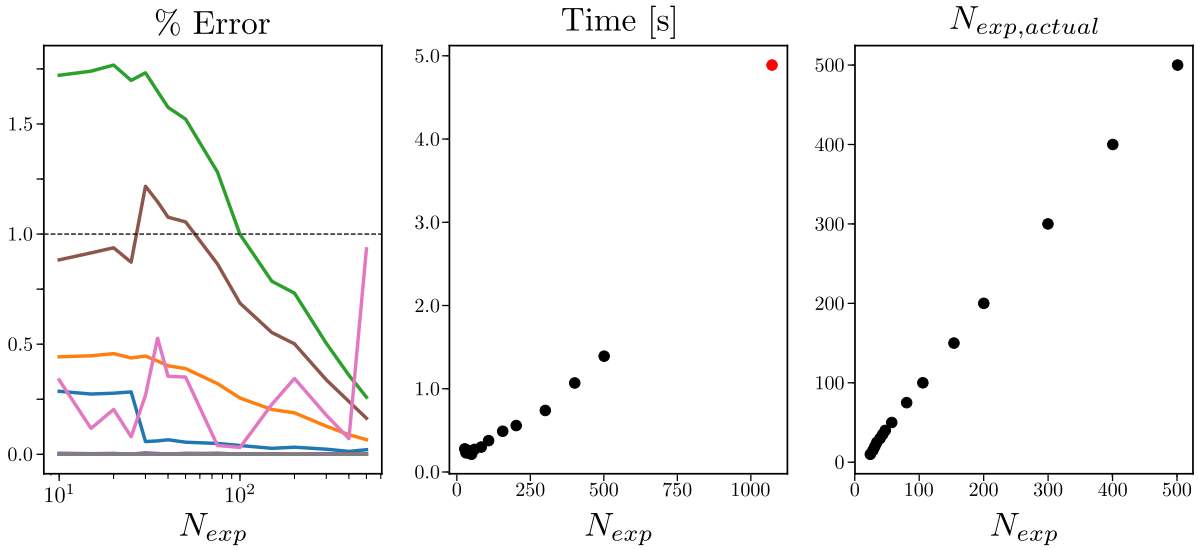


Figure 4.45: Grid Convergence Study: Actual Number of Expansion Fan Mach Lines

4.3.1.2 Number of Channel Flow Objects

This section discusses the results of the grid sensitivity study with respect to the number of Channel Flow objects (see Algorithm 23). Figure 4.46 shows the convergence of the output values (a) and the cycle evaluation times (b) as a function of the number of Channel Flow solution objects. These results show a steady convergence in all other output parameters, where the 1% threshold was reached with between 20 and 30 objects. From a timing perspective, a ten-fold increase in the number of solution objects resulted in an approximately 10% increase in the model evaluation time, showing another variable of interest that can be optimized to reduce cycle time while still maintaining relatively accurate outputs.

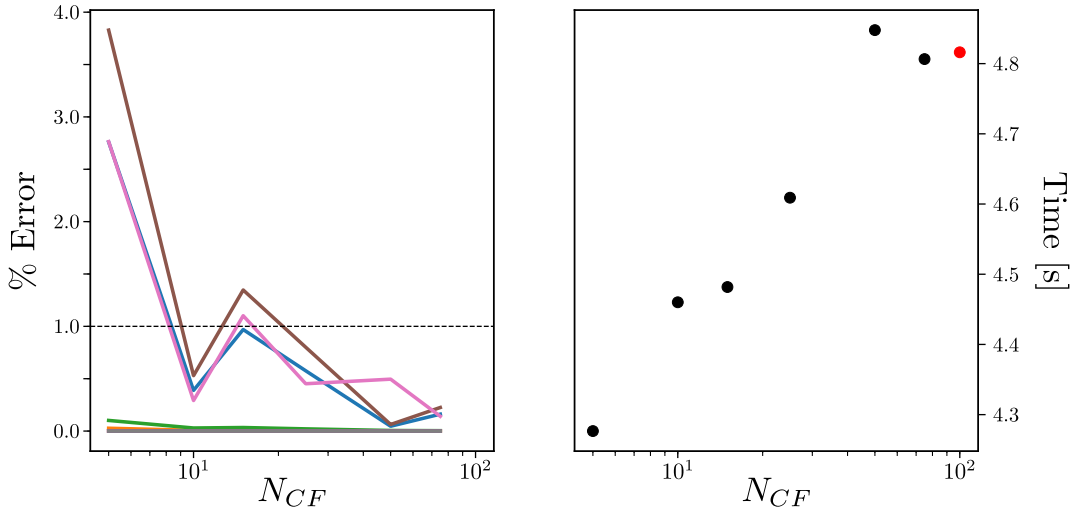


Figure 4.46: Grid Convergence Study: Number of Channel Flow Objects

4.3.1.3 Tolerance Changes

The following discussions surround the variation in the model tolerances. These include the mass flow rate and total pressure tolerance parameters, which directly affect when the model exits the main solution loop. The first and most obvious change was to study the model outputs as a function of the mass flow tolerance, shown in Figure 4.47. As the mass flow rate tolerance was tightened (moving from right to left on the x-axes), the model converged towards accurate values across all outputs, but at the expense of increased evaluation times. At a tolerance of 1 [g/s] (the default value), the model output error drops below the 1% threshold, but the total evaluation time triples. This was caused by the model requiring additional loops to converge with a tolerance less than or equal to 1 [g/s]. At higher tolerance values, the model could execute each sub-function and exit before any additional main evaluation loops were required. This suggests that even at tighter tolerances, a better initial guess at other parameters, specifically the plenum pressure, P_0, will allow the cycle to converge to the proper mass flow rate without the need for numerous iterations of the main loop. This is a difficult undertaking as terms such as inlet blockage cannot be well predicted ahead of time, which directly impacts the calculation of the inlet mass flow rate (see Algorithm 35).

Of particular interest, the model output thrust was not significantly impacted by the convergence in the mass flow rate. Despite greater percent errors in the mass flow rate at larger tolerances, the thrust value remained relatively unchanged and well within the target 1%. This could suggest that if thrust is the main output of interest for the model, this tolerance can be set so that the model only evaluates the main loop a single time, which more closely resembles the State to State model from Algorithm 9 that directly evaluates the model within an iterative portion.

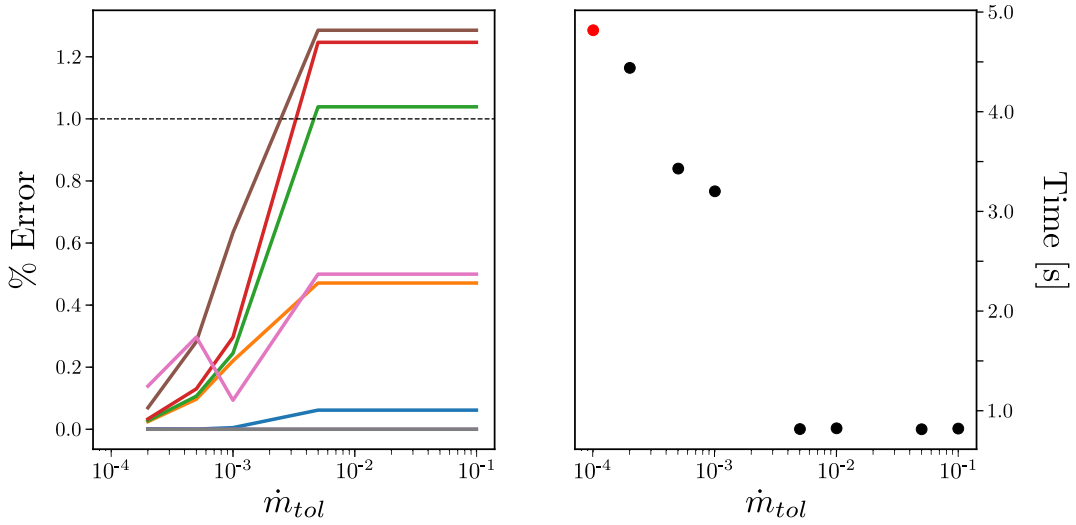


Figure 4.47: Grid Convergence Study: Mass Flow Tolerance

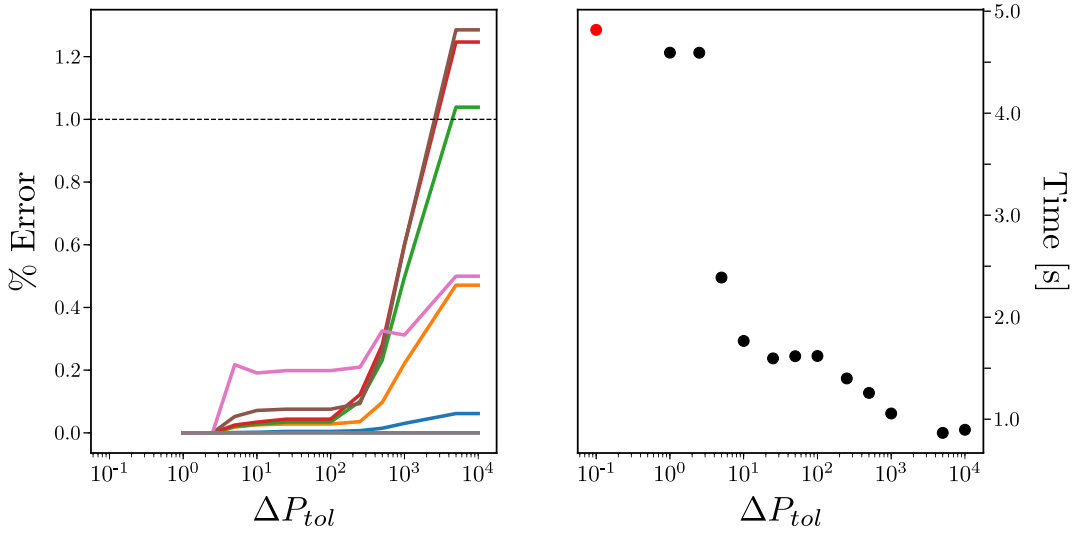


Figure 4.48: Grid Convergence Study: Pressure Change Tolerance

On the topic of the total plenum pressure, the next convergence evaluation was performed by varying the total pressure change threshold value. This parameter determines whether the update in pressure from the current iteration to the next is large enough so that it sufficiently modulates the inlet mass flow rate for the next loop. This is a subjective tolerance, as there are many non-linear competing variables that affect the inlet mass flow; however, it is useful when trying to optimize the model for overall evaluation time.

Figure 4.48 shows the results of the study, and, much like the sweep in the mass flow rate tolerance, the total pressure update tolerance produced a steady decrease in output error and increased

in evaluation time as the tolerance was tightened. Also, like the mass flow tolerance study, a pressure tolerance above 50000 Pa (0.73 psi) caused the model to exit the evaluation after the first loop with the same low error condition in the output thrust value.

Both of these parameters produce similar results across the board, and both are valuable in their ability to link accuracy with evaluation time in a more robust way. This opens up the possibility for parameter optimization techniques that specifically target these highly effective parameters, depending on the particular application of the model.

4.3.1.4 Other Parameters of Interest

Finally, this section will provide a discussion of other configuration parameters that were studied for grid convergence and produced a meaningful change in the convergence. The first is the maximum inlet spacing used in the calculation of the mass flow rate. Nominally, the inlet spacing is based on the spacing of the expansion fan nodes closest to the inlet plane (see Figure 4.37); however, this parameter will insert x values across the inlet plane to better resolve the mass flow calculation. At each new location added to the inlet profile, a linear interpolation in the total pressure and temperature was done. In essence, this variable simply trades off interpolation errors from adding new points with averaging errors for each inlet differential area.

This parameter also seeks to provide additional resolution within the region that transitions from choked product backflow to forward reactant flow. Figure 4.49 shows these results, where the output variable of interest most affected was the blockage ratio. The improved inlet spacing allowed for a more accurate determination of the exact location of the fresh reactant fill, thereby improving the inlet blockage calculation. However, decreasing the spacing along the inlet did increase the evaluation time by nearly 20% across the entire sweep.

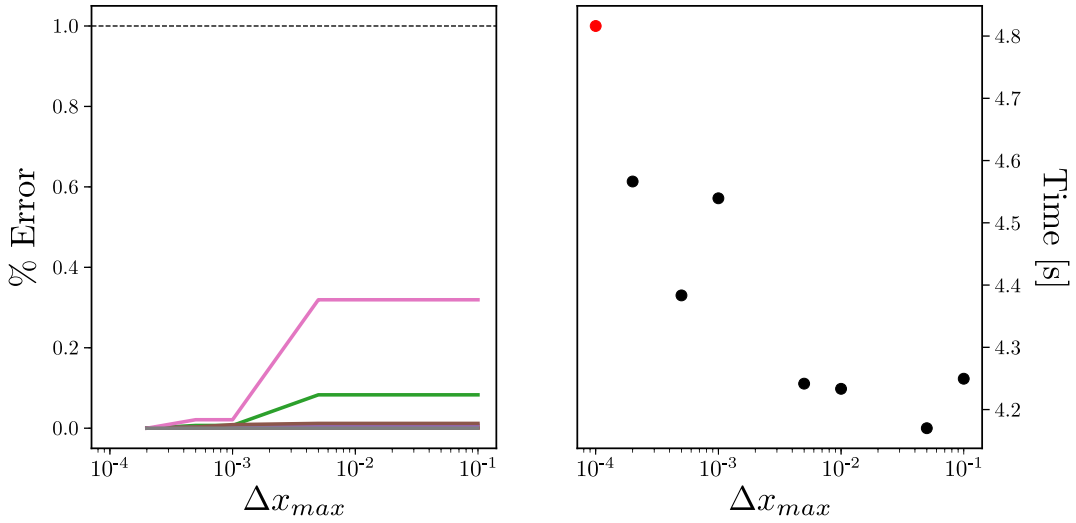


Figure 4.49: Grid Convergence Study: Maximum Inlet Spacing for Mass Flow Calculation

Of note is that the inlet spacing parameter provides a good target for future improvement, specifically being more specific about where the increased resolution is required. For example, in most of the forward-flowing reactant regions of the inlet, the total and static pressures are constant. This means that reduced grid spacing is not required in the constant property region, whereas additional resolution within the regions of the larger pressure ratio and property gradients is more likely to provide improved results. A similar concept has been applied successfully in full computation solvers for RDC devices.[78]

Next, none of the following produced a measurable change in model execution time or output accuracy versus the maximum-resolution case:

- Runge-Kutta (RK) integration spacing, h_{RK}
- Percent change in static pressure required for a detonation re-calculation, ΔP_{tol}
- Number of points along the inlet fill profile, N_{fill}

For the RK integration, all of the Channel Flow objects for this study did not use the friction or heat transfer coefficient due to the closure methodology provided by the polytropic compression algorithm, Algorithm 24. This results in a direct isentropic solution along the path that does not require integration. Therefore, this portion of the code was never called. A more detailed discussion on the validity of ignoring friction and heat transfer for the one-dimensional integration is provided in Section 4.3.2, but with the polytropic compression algorithm, Algorithm 24, a similar process can be achieved without the one-dimensional flow integration requirements. This could mean a potential elimination of this sub-function within the code to improve cycle evaluation times while still predicting known losses.

A similar argument can be made for the channel static pressure. Across all test cases, this value is limited to the ambient pressure (see Algorithm 23). Because of this, as soon as the static pressure, P_{ch}, is set to ambient, no additional changes to it occur in subsequent iterations, which means that future detonation calculations are not required. This leads to another path to improve the solver speed by simply imposing the static pressure on the ambient on the initialization of the solver.

Finally, because of the detonation relocation process that provides iteration stability when solving for the fill height and detonation location, the fill height is insensitive to the number of fill points for this particular configuration. As will be discussed in Section 4.3.2, this may not be the case at low mass flow rates, where the fill profile will become more sensitive.

4.3.1.5 Sensitivity Study

The final evaluation in this section examines the sensitivity of the model outputs as a function of the following inputs: deflagration loss fractions, mass flow rate, equivalence ratio, channel length, and injector area ratio. All of these data points were evaluated using the axial inlet configuration. Figure 4.50 shows the Sobol Indices for the net thrust, pressure gain, and inlet blockage as a function of each input parameter.

For the modeled net thrust, the mass flow rate provides the most impact on the thrust, which is due to the direct relationship between the thrust metric and the mass flow of the system. A similar conclusion can be made for the equivalence ratio since the chemical energy input into the system should also directly impact the output thrust. Aside from these two input parameters, the parasitic combustion fraction, the channel length, and, to a lesser extent, the injector area ratio all impact the thrust metric. The effects of channel length and injector area ratio will be discussed in more detail in the following sections.

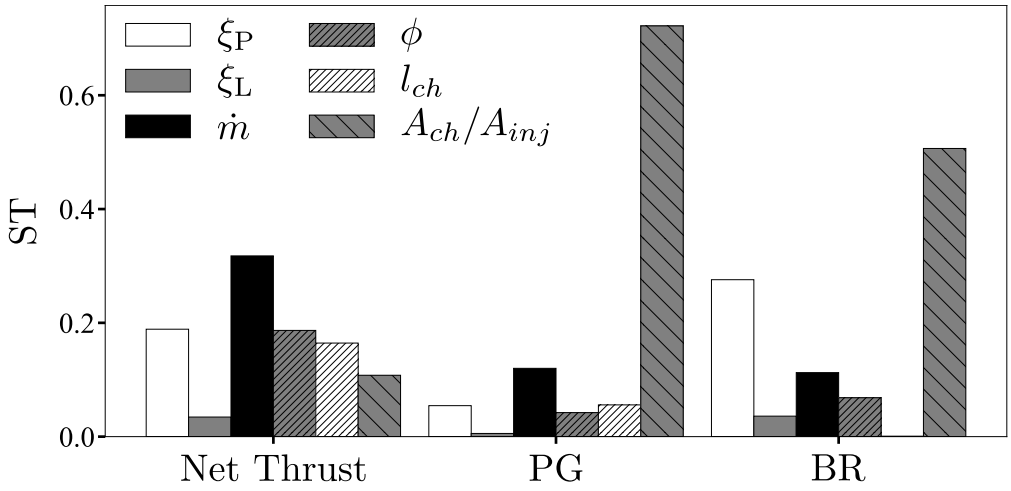


Figure 4.50: Total Sobol Indices for the Cycle Model

From these results, it appears that the pressure gain metric and the inlet blockage are mainly determined by the injector area ratio. This is an expected result, as the inlet dynamics play a crucial role in the performance and operability of RDCs. Figure 4.51 is provided to explain these results in more detail, showing the blockage (a) and the inlet pressure drop (b) as a function of the inlet area ratio. The blockage and injector pressure drop are known to be correlated, where the larger the inlet pressure drop (i.e., stiffer inlet), the lower the expected inlet blockage. Therefore, as the injector area decreases in relation to the channel area, the injector should provide a stiffer inlet at a given mass flow rate. This results in a reduction in the inlet blockage; however, a larger pressure drop also results in a much lower pressure gain. For this reason, the injector area ratio has the greatest impact on these two performance metrics.

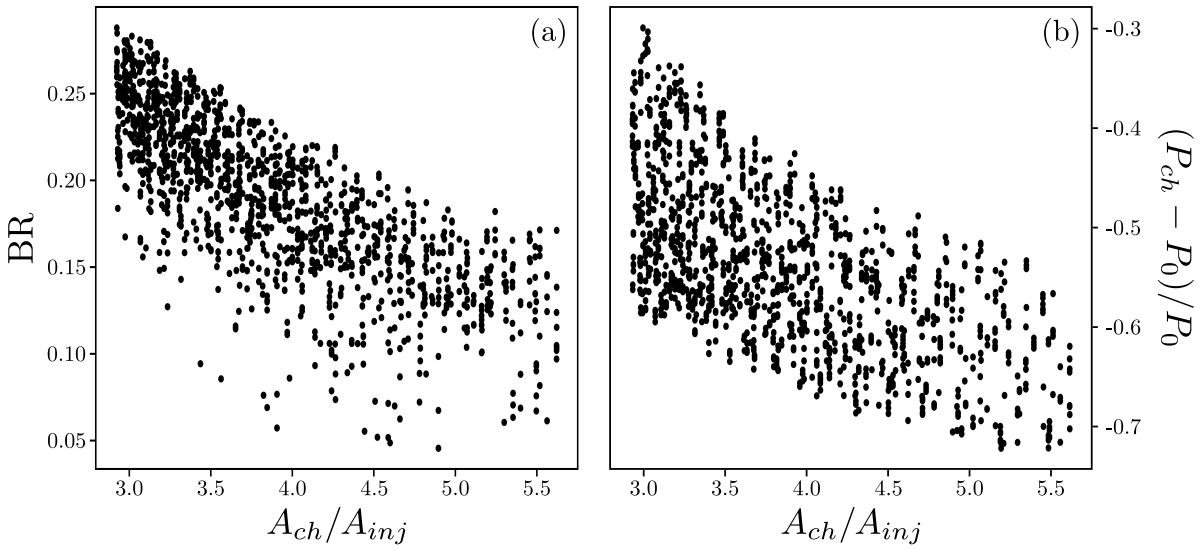


Figure 4.51: Blockage (left) and Injector Pressure drop (right) versus Inlet Area Ratio

4.3.2 Parametric Study

The following analysis covers the parametric study of particular input parameters for the cycle model. For some parameters, it made the most sense to include another parameter in the sweep, such as the mass flow rate and the equivalence ratio. These two parameter sections will contain contour plots of the model outputs, while other one-parameter sections will contain scatter plots of the results. In general, the sections are arranged in the following order. First, we will review the mass flow rate convergence and plenum pressure output from the model. Where contour plots are used, the mass flow convergence will be under-laid on the result of interest for the given contour. Next, the model exit condition will be presented, again showing regions where the data may not be valid. We will then move to detonation and inlet performance, which will be in terms of laboratory wave speed, detonation pressure ratio, inlet blockage, and detonation and fill heights. Next, the RDC performance metrics of net thrust, pressure gain based on net thrust, and a thrust gain metric will be examined. Finally, the polytropic rate terms, along with the overall polytropic coefficient, will be presented. For certain sections, the study did not produce meaningful changes in outputs, which were removed from the analysis. Also, certain aspects of the broader study warranted additional investigation, which will also be included in the section of interest.

4.3.2.1 Mass Flow Rate and Equivalence Ratio

The following section examines the change in predicted RDC performance with variations in mass flow rate and equivalence ratio. For this parametric sweep, the mass flow rate was varied in [0.1, 1.0] kg/s, while the equivalence ratio wave varied in [0.5, 1.2]. Figure 4.52 (a) shows the contours of the error in the final inlet mass flow rate achieved by the model versus the specified value. These contours serve to denote areas of good convergence, where the red locations indicate a model mass flow higher than the specified, and the blue indicates a lower model mass flow rate. As will become increasingly evident as the analysis of the cycle model unfolds, the model struggles to converge at mass flow rates below 200 g/s. This is likely due to the model enforcing a choked inlet in the forward-flowing regions, even at low plenum pressures.

For convenience, the mass flow rate error contours are all set as the background for other performance contours. For example, Figure 4.52 (b) plots the contours of the final plenum pressure across the parametric sweep, where the contours of the parameter of interest are overlaid on top of the mass flow rate error. This helps remind the reader of areas where model performance metrics may need to be taken with a grain of salt.

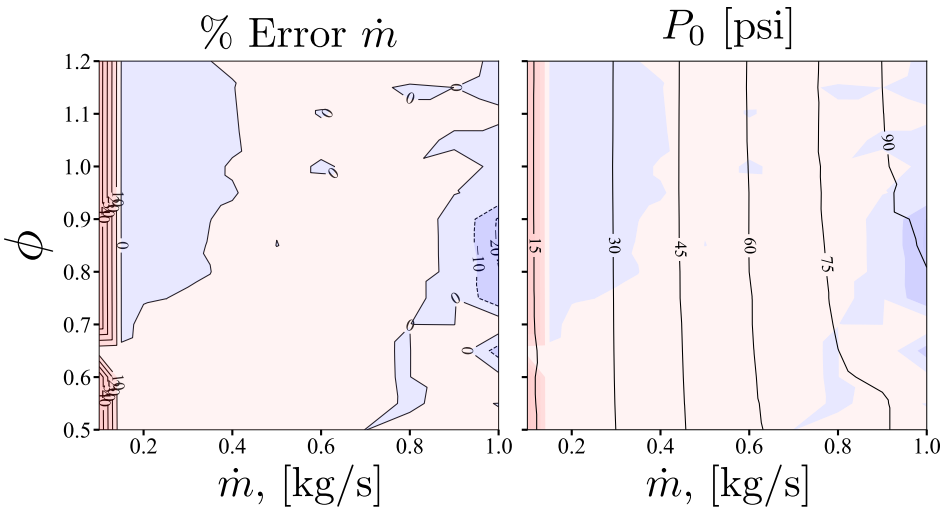


Figure 4.52: Mass Flow versus Equivalence Ratio Parametric Study: Mass Flow Error and Plenum Pressure.

Figure 4.53 shows the inlet Mach profiles as a function of the mass flow rate for a stoichiometric mixture. This figure also included the calculated fill-based blockage ratio at each flow rate as a reference. As we examine the Mach number profiles, we can see that even at mass flow rates of 150 g/s, the forward-flowing Mach number is always sonic. As the mass flow rate further decreases to 100 g/s, the inlet finally unchokes in the forward fill region. This region is still at a relatively high Mach number; however, it is likely leading to the inability to converge on the target mass flow rate. Some tuning could provide more resolution when this occurs, but that is saved for future iterations of the cycle model.

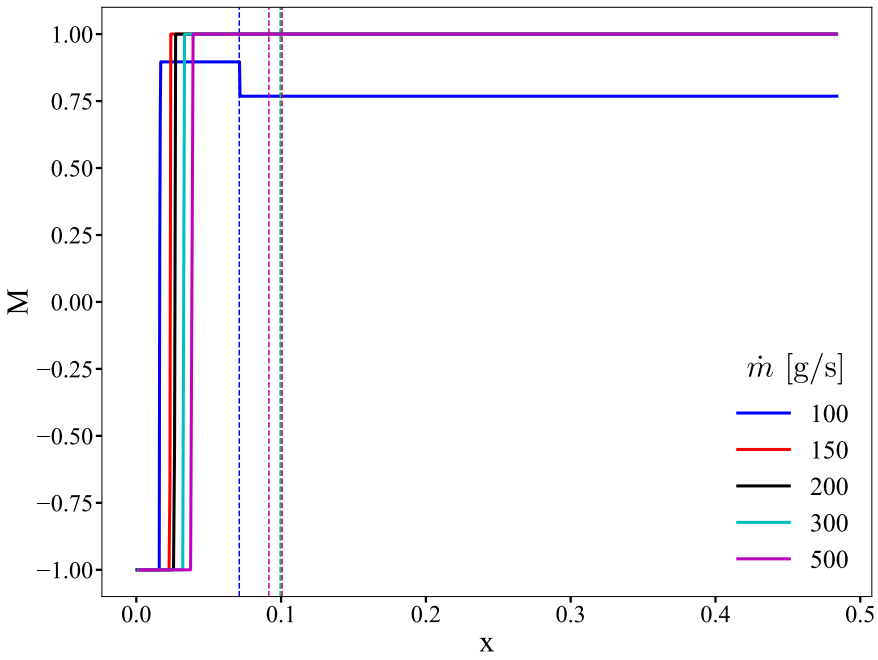


Figure 4.53: Example of Inlet Mach versus Mass Flow Rate

Despite the shortcomings of the model at low mass flow rates, we will continue our analysis to examine how changes in mass flow rate and equivalence ratio affect the model output parameters. Returning to Figure 4.52 (b), we can see that, in general, the total plenum pressure is proportional to the requested mass flow rate. This is especially true at near-stoichiometric conditions; however, at the leaner end of the range, the trend deviates from a one-to-one proportionality. Under lean conditions, the pressure ratio of the wave is much lower than under stoichiometric conditions, leading to less inlet blockage and allowing a higher inlet mass flow rate given the same plenum pressure. Figure 4.55 will provide additional support for this argument, but next, we will shift our attention to the model exit condition.

Figure 4.54 shows the same parametric sweep in mass flow rate and equivalence ratio, except now the model exit condition is plotted for each combination of input parameters. These exit conditions are defined in detail in Table 4.3. In general, the model exits with a $P_{0,tol}$ condition, indicating that the model has reached a stable plenum pressure but has not achieved an inlet mass flow rate within the specified tolerance. This condition typically results in a low mass flow error, which can be seen clearly with the under-laid mass flow rate error contour.

At higher mass flow rates and near-stoichiometric conditions, the model exits with a $Y_{det,0}$ condition. This is an error state that appears when the detonation height is greater than the fill height. In this case, the model predicts that the detonation wave is unsustainable with the given inputs, and operation would not be achievable.

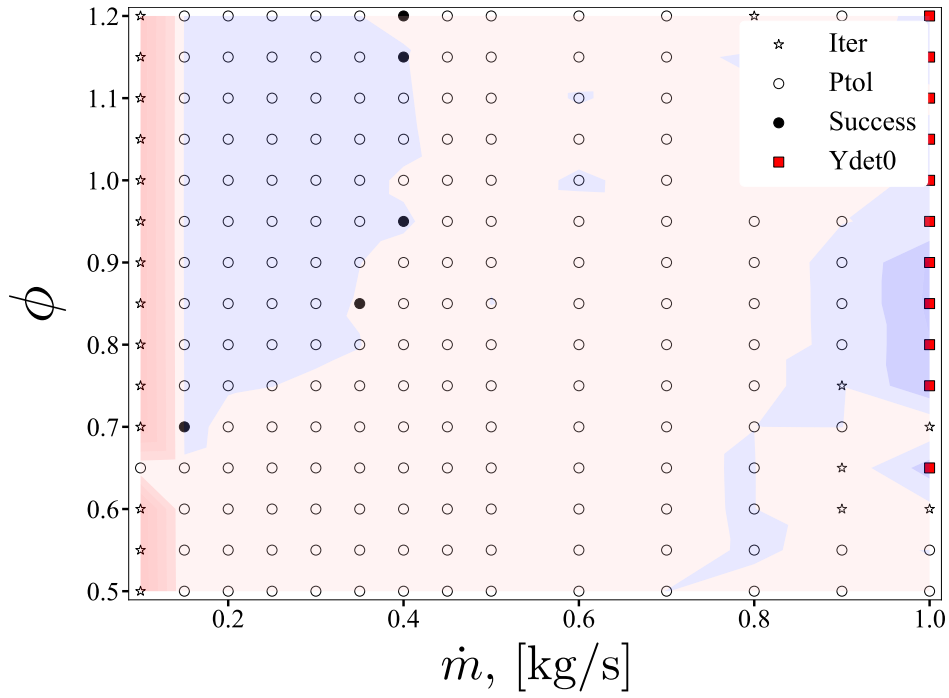


Figure 4.54: Mass Flow versus Equivalence Ratio Parametric Study: Cycle Exit Condition

Figure 4.55 shows the key characteristic of the detonation wave as a function of the parametric study values. This includes the lab frame wave speed (a), the detonation pressure ratio from the pre-detonation state to the CJ state (b), the blockage ratio, defined by the location of forward-flowing reactants (c), and the fill and detonation heights (d).

The wave speed and pressure ratio scale nearly perfectly with the equivalence ratio. This was expected as these cases were conducted assuming an ideal detonation wave. Also following an expected trend is the estimated blockage ratio (c). This was discussed earlier, but higher mass flow rates (i.e., higher plenum pressure) and lower equivalence ratios led to a reduction in blockage ratio.

Due to the poor convergence, we will ignore the blockage contours at the lower mass flow rate conditions, as the target mass flow rate was well outside of the model value. On the same note, the blockage ratios at high mass flow rates and near-stoichiometric may need to be ignored as well. These cases correspond to the locations with a fill height less than that of the detonation height.

Finally, the differences in the fill and detonation heights are shown in (d), which tracks exactly with the fill height error exit condition. This subplot shows that the equivalence ratio has a much larger impact on the fill height at higher mass flow rates than at moderate mass flow rates. It is expected that at high mass flow rates and stoichiometric conditions, there is simply not enough time or inlet flow area to allow for the full fill required to sustain the detonation wave. This may be mitigated with a lower-performing detonation wave, a larger RDC outer diameter, and potentially

a larger overall inlet flow area (ignoring potential trade-offs with inlet blockage).

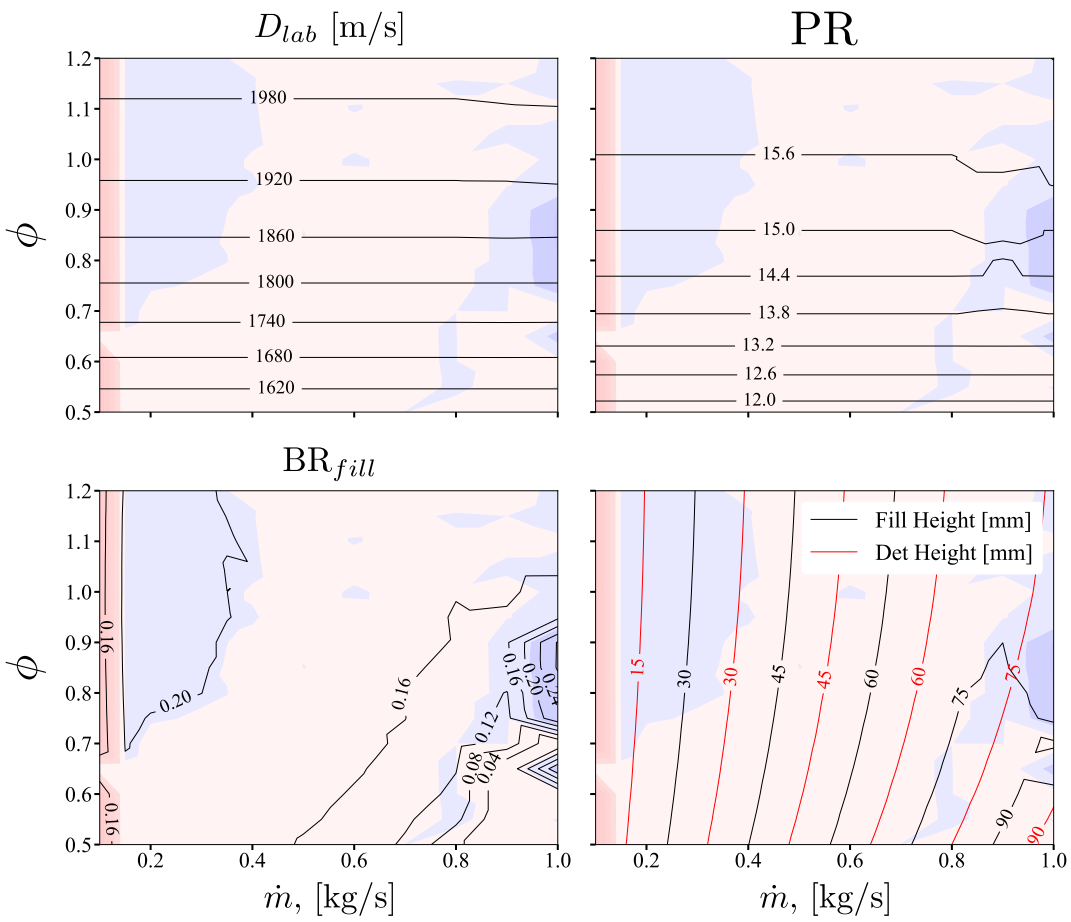


Figure 4.55: Mass Flow versus Equivalence Ratio Parametric Study: Wavspeed, Pressure Ratio, Blockage and Fill.

On the topic of inlet blockage, Figure 4.56 shows the relationships between the blockage location, x_{BR}, the detonation height, h_{det}, and expansion fan size, l_{exp}. Figure 4.56 (a) shows the height of detonation as a function of the mass flow rate. As described in Section 4.2.1, the detonation height is calculated assuming that all the reactant mass flow passes through the detonation wave; because of this, Equation 4.1 enforces a linear relationship between the two.

Figure 4.56 (b) shows the length of the expansion as a function of the height of the detonation, where the length of the expansion scales linearly with the height of the detonation. This subplot shows that as the mass flow rate target is reduced, so is the length of the expansion fan. At some point, the short expansion length begins to reduce the blockage ratio despite the lower plenum pressure.

Figure 4.56 (c) shows the location of the blockage as a function of the length of the expansion fan, defined from the detonation wave to the final expansion node. Although no correlation is

initially apparent due to all the other competing factors that impact the blockage, we can see that at the lowest mass flow rate, the expansion fan length is incredibly short. This means that despite the lower plenum pressure, the expansion process takes place at a much shorter distance, which in turn reduces the blockage ratio.

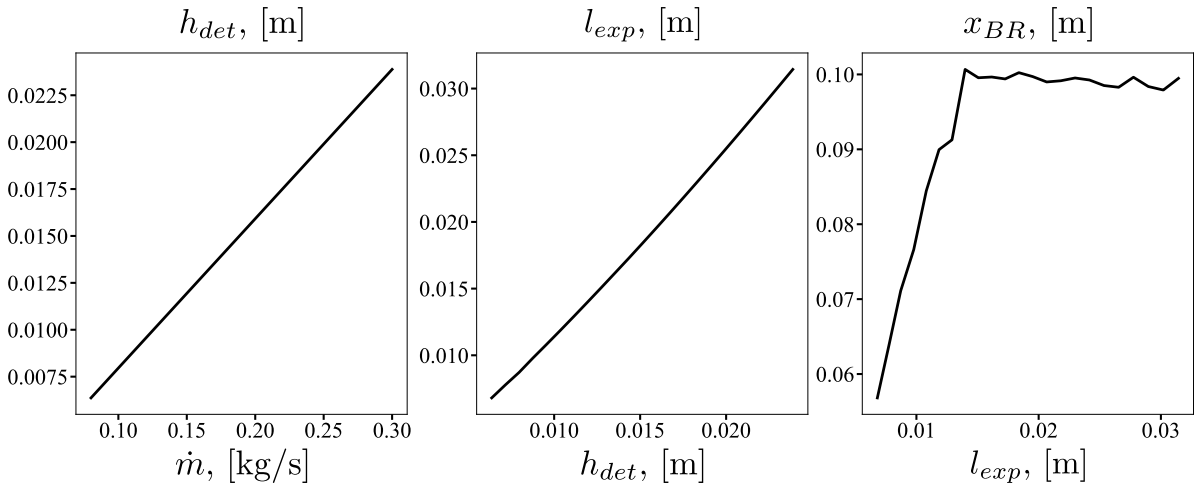


Figure 4.56: Mass Flow Rate, Fill and Blockage changes with Detonation Height

When referencing the traces from Figure 4.57, the reason behind the changes in blockage ratio becomes more evident. Figure 4.57 (a) shows the modeled plenum pressure as a function of the target mass flow rate. This plot shows a linear region where the unblocked area is fully choked. As the mass flow rate continues to decrease, the trend levels off to a near-constant plenum pressure. This is also reflected in Figure 4.57 (b), which plots the calculated inlet mass flow rate as a function of the target mass flow rate. At low mass flow conditions, the model cannot achieve good convergence with the target mass flow rate, and the plenum pressure is stabilized near the ambient pressure condition. This means that the model cannot adjust the plenum pressure any further, yet the inlet mass flow rate is still over-predicted, a major area for future improvement of the cycle model.

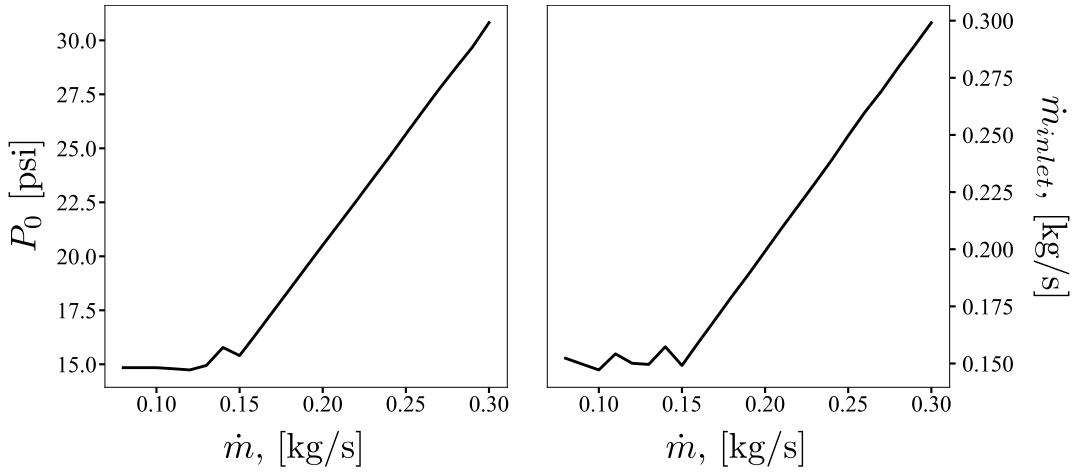


Figure 4.57: Plenum pressure (left) and Inlet Mass Flow (right) versus Specified Mass Flow

We now turn our attention to the predicted RDC performance from the model as a function of the mass flow rate and equivalence ratio. This included a discussion of the cycle net thrust, pressure gain based on the modeled thrust, and a thrust "gain" metric, all shown in Figure 4.58. The thrust gain metric, Equation 4.32, is defined as the calculated thrust normalized by the ideal deflagrative thrust at the same plenum conditions, mass flow rate, and fuel flow rate. This deflagrative thrust assumes complete combustion and a perfect isentropic expansion to the ambient pressure.

$$F_{gain} = \frac{F_{model}}{F_{defl}|_{P_0,\dot{m},\dot{m}_f}} - 1 \tag{4.32}$$

where F_{model} is the predicted thrust from the RDC cycle model and $F_{defl}|_{P_0,\dot{m},\dot{m}_f}$ is the equivalent, ideal deflagrative thrust produced by a constant pressure combustor. Because the plenum pressure, mass flow rate, and fuel flow rate are fixed between the two thrust values, this can also be thought of as a ratio between the specific impulses. Where:

$$I_{sp} = \frac{F}{g_0 \dot{m}_f} \tag{4.33}$$

Returning our attention to Figure 4.58 (a), we can see the expected trend that at a given equivalence ratio, the gross thrust increases with an increase in mass flow rate. This continues up to the larger mass flow rates, where we begin to see a slight drop in thrust. This trend will be discussed in further detail later in this section. We also see the predicted thrust improves as we move towards a stoichiometric mixture.

Figure 4.58 (b) shows the pressure gain metric based on the gross thrust value, using the methodology provided by Kaemming and Paxson.[27] These results predict that the thrust-based pressure gain was achieved at lower mass flow rates but turns negative at moderate mass flow rates around

300 g/s. Similar results can be seen in Figure 4.58 (c) with the thrust gain metric; however, the break-even point has shifted slightly towards a higher mass flow rate.

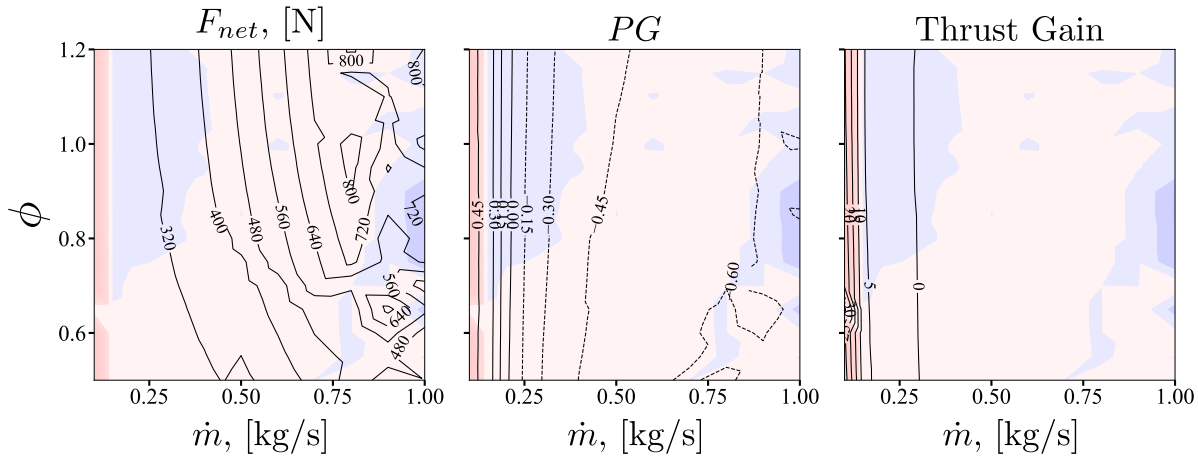


Figure 4.58: Mass Flow versus Equivalence Ratio Parametric Study: Net Thrust, Pressure Gain and Thrust Gain

Although not performance metrics, the predicted mass-averaged polytropic rate terms and the polytropic coefficient are shown in Figure 4.59. These were mass flow averaged based on Equation 4.34, using the results from each Channel Flow object within the RDC flowpath.

$$\bar{x}_{\dot{m}} = \frac{1}{\dot{m}} \sum_{i=0}^{k} x_i \dot{m}_i \tag{4.34}$$

where x is the value of interest.

As discussed in Section 4.2.2.6, the polytropic compression required to match the channel pressure was calculated with Algorithm 24 at the end of each Channel Flow object. The work and heat rates, $\dot{w}, \dot{q}$, and the associated polytropic coefficient, n, essentially act as a loss mechanism mimicking momentum losses due to friction and heat losses due to heat transfer. For reference, when this value is greater than the ratio of specific heats, γ, both momentum and heat are transferred out of the system, which was the case for all model runs.

Figure 4.59 (a) shows the momentum transfer rate, where positive values are out of the system. As expected, this value increases with mass flow rate but peaks around 800 g/s. These contours also match well with the thrust values in Figure 4.58 (a).

Figure 4.59 (b) shows the heat transfer rates where negative values are out of the system. These values also increase with mass flow rate and are larger in magnitude around stoichiometric, which was expected because the temperatures would be much higher in this region, and the higher mass flows should result in higher heat transfer values.

Figure 4.59 (c) shows the polytropic coefficients and the reason for the low pressure gain and thrust gain values at higher mass flow rates. At these high flow rates, the polytropic coefficients also increase, meaning that additional work and heat extraction are occurring. Because of this, any performance gain through the detonation wave is canceled out by the polytropic losses occurring post-detonation. This serves as another data point showing that detonation and RDC performance are not one and the same, and careful analysis of the RDC performance as a system must be done to provide an argument for any gain from a detonation-based system.

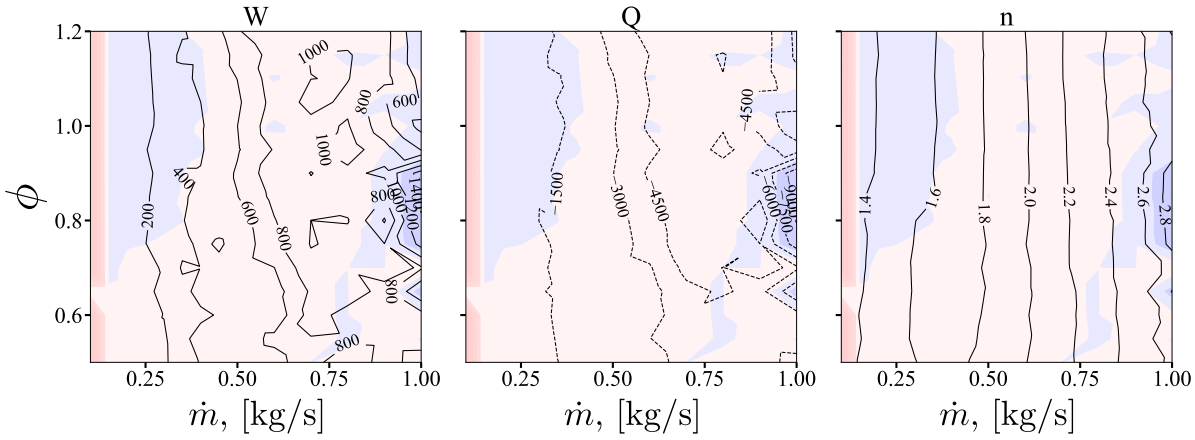


Figure 4.59: Mass Flow versus Equivalence Ratio Parametric Study: Polytropic Rate Terms and Coefficient

Due to the better convergence at a mass flow rate of 300 g/s, the remainder of the analysis will be conducted at this mass flow rate as other parameters of interest are varied.

4.3.2.2 Injector Area Ratio

This section will examine the effects of varying the inlet area ratio of the axial style inlet. All data points in this section were performed at a mass flow rate of 300 g/s and a stoichiometric mixture, using the default configuration values described in Table 4.2.

Figure 4.60 shows the mass flow convergence error and plenum pressure as a function of the area ratio. For all cases, the exit condition was that of the total plenum pressure tolerance criteria. This is reflected in the mass flow rate error; however, all of these were within 1% of the target. As the injector area tightens with respect to the channel, the plenum pressure required to drive the target mass flow rate increases. This is a nearly linear increase, indicating that we are within the region of chocked forward flow for all cases, and further examination of the Mach number profiles confirmed this.

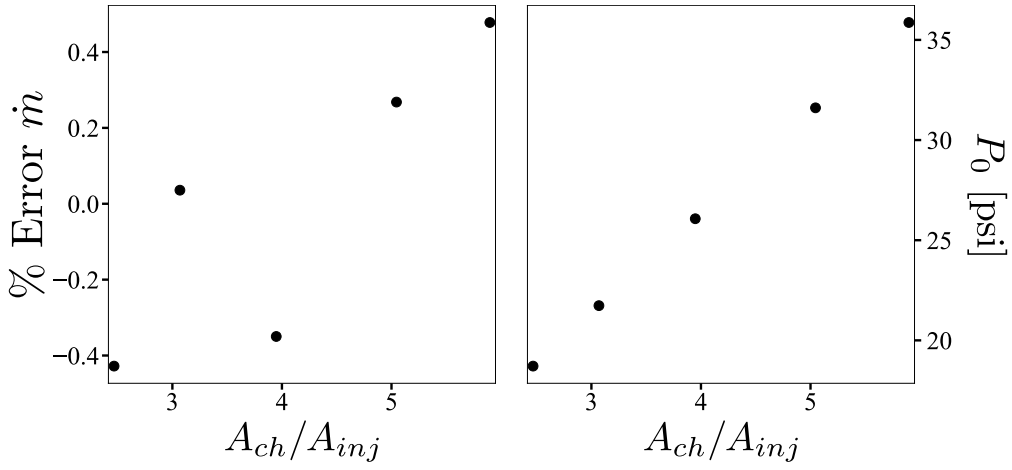


Figure 4.60: Injector Area Ratio Parametric Study: Mass Flow Rate Error (left) and Plenum Pressure (right).

For the detonation performance metrics, the wave speed and pressure ratio remained constant across all cases, with the only change being in the fill properties. The blockage fraction increased as the injector area approached the channel area, which is expected due to the combination of the plenum becoming more exposed to the detonation wave and the total pressure of the plenum dropping. By definition, the detonation height remains constant, but the fill height increases with a more restrictive inlet. This is due solely to the fact that the blockage ratio is also decreasing, allowing for a longer fill time for the fully choked forward-flowing reactants. It will be discussed later in the model improvement section, but the fill height to detonation height ratio is approaching 2x in these cases. This mismatch in heights may offer a path forward for improving the loss metric prediction of the model by attempting to match these more closely.

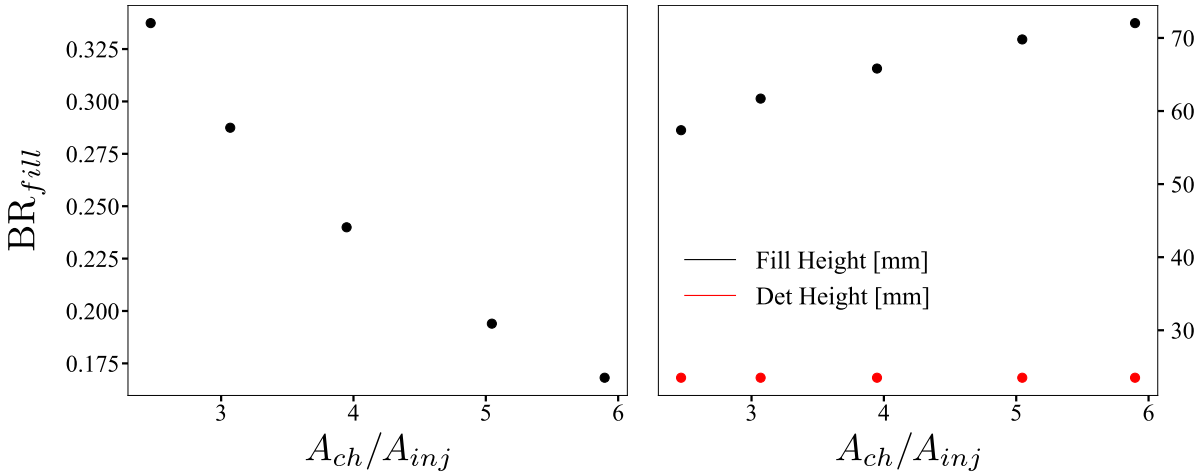


Figure 4.61: Injector Area Ratio Parametric Study: Blockage (left) and Fill Properties (right)

Moving on to the RDC performance, all metrics improve drastically with a less restrictive inlet, a recurring trend discussed by Kaemming et al., Paxson and Miki, and in Section 3.2.1.[29, 59] In this example sweep, there is also a break-even point in area ratio for both the pressure gain and thrust gain metrics; however, these do not occur at the same point.

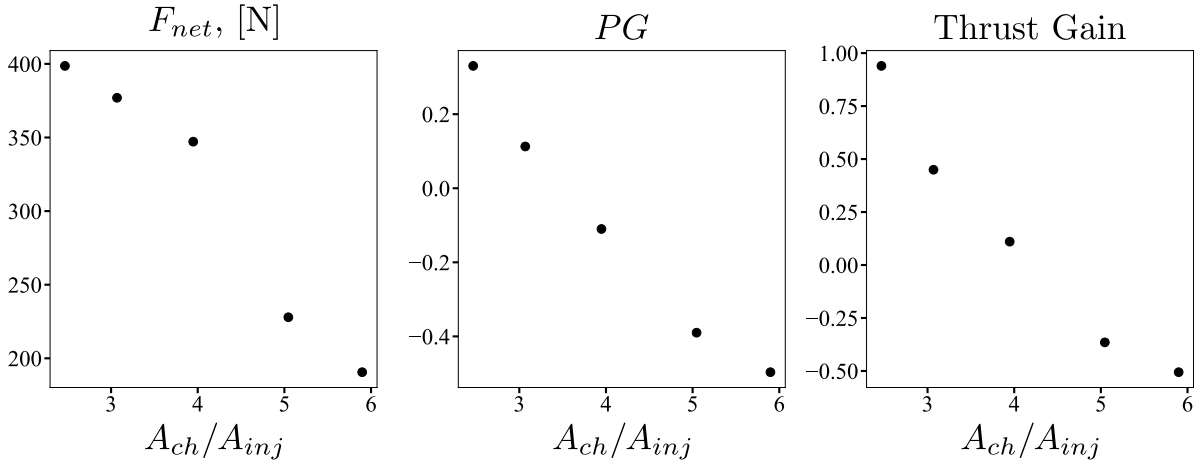


Figure 4.62: Injector Area Ratio Parametric Study: Net Thrust, Pressure Gain and Thrust Gain

Finally, an examination of the polytropic rate terms and coefficient shows a nearly constant magnitude across all values. This is expected as many of the flow properties are held constant for this area ratio sweep, and the resulting detonation properties were also relatively constant.

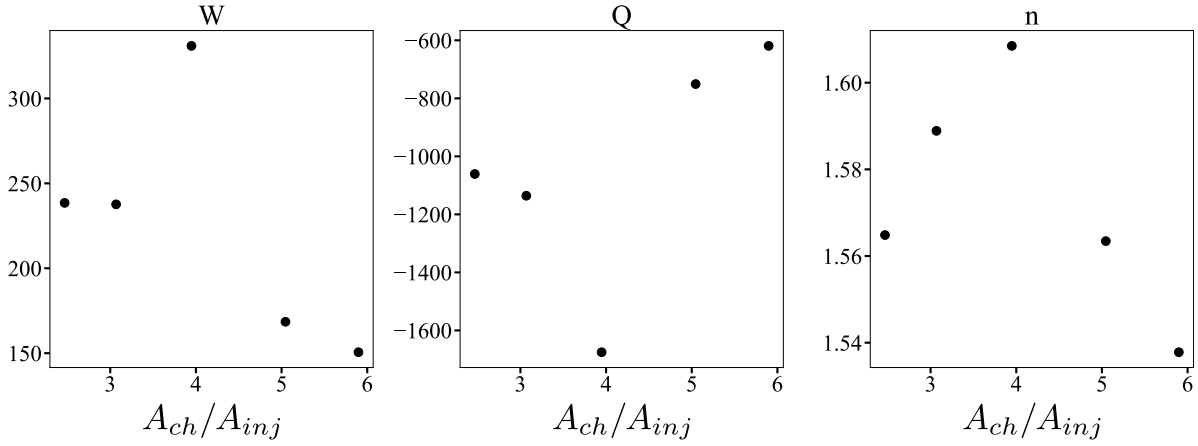


Figure 4.63: Injector Area Ratio Parametric Study: Polytropic Rate Terms and Coefficient

Like many prior studies, the cycle model indicates that a less restrictive inlet is preferable; however, it does not make any determination as to the operability of the device under the less restrictive inlet condition. The model does not include loss parameter dependencies of terms like the inlet blockage. Previous results show that higher inlet blockage levels may allow for additional

product re-circulation and parasitic combustion (see Section 2.4.1). A more closed-loop update to the model is required to capture these dependencies, which is saved for future model iterations.

4.3.2.3 RDC Channel Length

The following section discusses the modeled performance variation as a function of the length of the RDC channel. For these cases, the default configuration was used with the Pintle style injector at a stoichiometric 300 g/s flow rate.

Across the full parameter sweep in centerbody extensions, the mass flow rate error, plenum pressure and exit condition did not vary. The same invariance to channel length was seen for the wave speed, pressure ratio, blockage, and fill heights. For this reason, these figures have been removed.

The real impacts on channel lengths are shown in Figure 4.64, where the model predicts thrust, pressure gain, and thrust gain were more significantly affected by the changing length. The plots universally show that a longer channel is preferable. More discussion of why this may not be the case in a physical RDC will be provided later in this section.

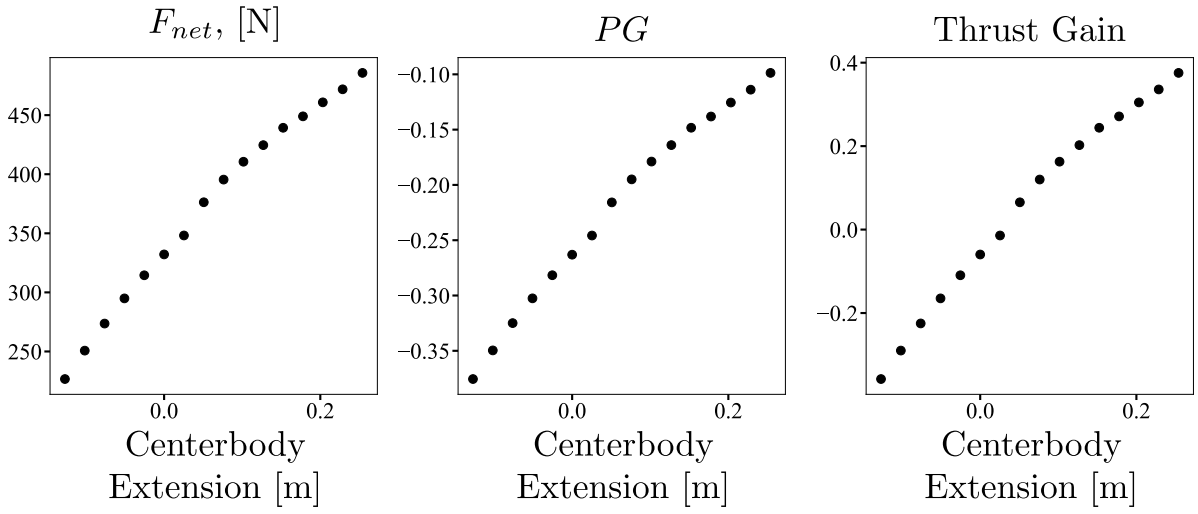


Figure 4.64: RDC Length Parametric Study: Net Thrust, Pressure Gain and Thrust Gain

Next, the examination of the polytropic rate terms and coefficient also shows an improvement in the expected losses with an increase in channel length. This result informs the RDC performance metrics predicted in Figure 4.64.

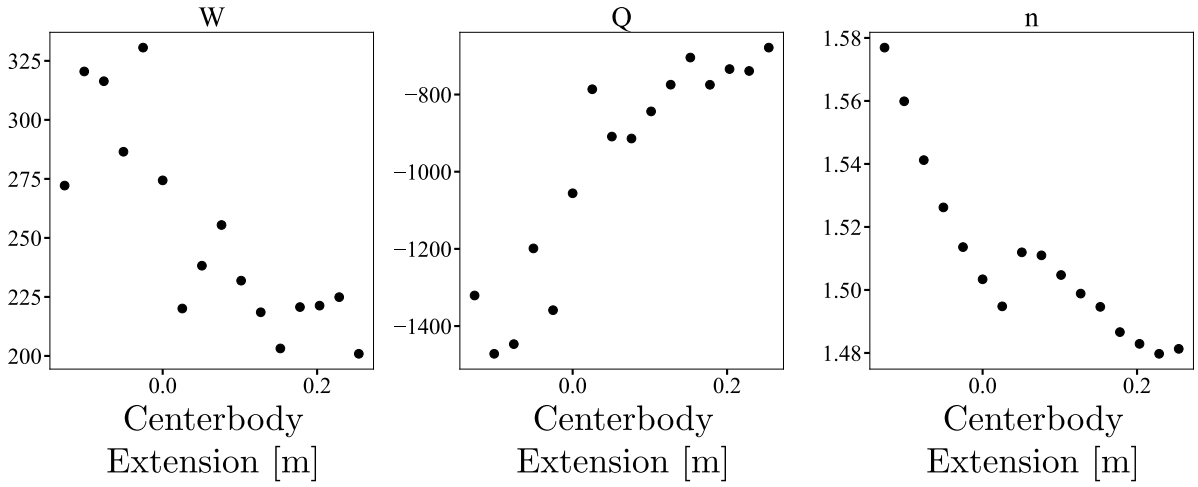


Figure 4.65: RDC Length Parametric Study: Polytropic Rate Terms and Coefficient

Figure 4.66 shows the PDFs for the axial and azimuthal velocity profiles at the exit plane as a function of the center-body extension. The plots on the left show the azimuthal velocities, while the plots on the right show the axial velocity. The upper plots were area-averaged, while the lower plots were mass-averaged. Regardless of the averaging methodology, the azimuthal velocity PDF for the shorter RDC channels fell more closely to the zero mark, while the longer RDC channel lengths produced larger negative velocity components at a much higher rate. From this result, one would expect the longer RDC channel to have a reduced thrust due to the increased energy lost to the larger azimuthal velocities. This was not the case, but a later examination into how the post-expansion flow is processed by the oblique shock will provide additional insights into this result.

Shifting attention to the axial velocity components, the PDFs for these cases become much more condensed with a longer RDC channel, and the expected values all appear to be near each other. This shows that despite the wide swings in azimuthal velocity across the channel length sweep, the axial exit velocities were relatively unchanged. These results will be confirmed later in this section.

Figure 4.67 shows the averaged nozzle velocities as a function of the center-body extension length. The x-component, y-component, and velocity magnitudes were all mass and area-averaged according to the exit plane conditions for each Channel Flow object. In general, the axial velocity component is relatively constant across the full sweep of the RDC channel lengths, but the average azimuthal velocity decreases rapidly with increasing channel length. This is accompanied by an increase in the magnitude of the average exit velocity. From this plot, Figure 4.64 and Figure 4.65, we can see that the decreases in thrust as the RDC is shortened are most likely due to the increase in the polytropic coefficient, leading to additional losses at the shortest RDC length. However,

these results also show that the magnitude of the azimuthal velocity decreases overall across the cycle.

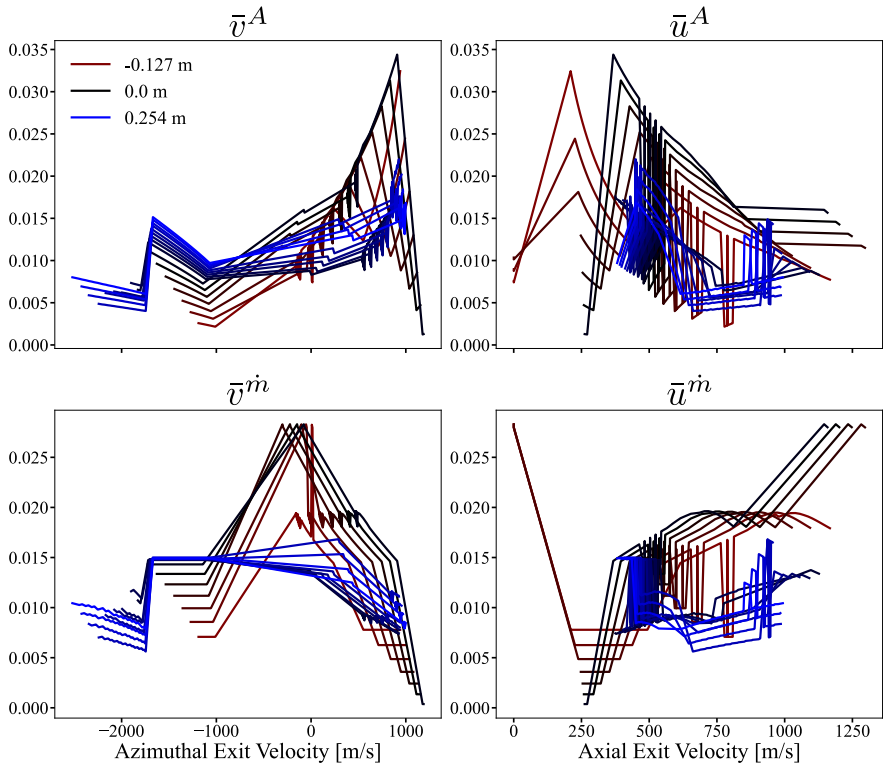


Figure 4.66: Nozzle Swirl Probability Density versus RDC Length

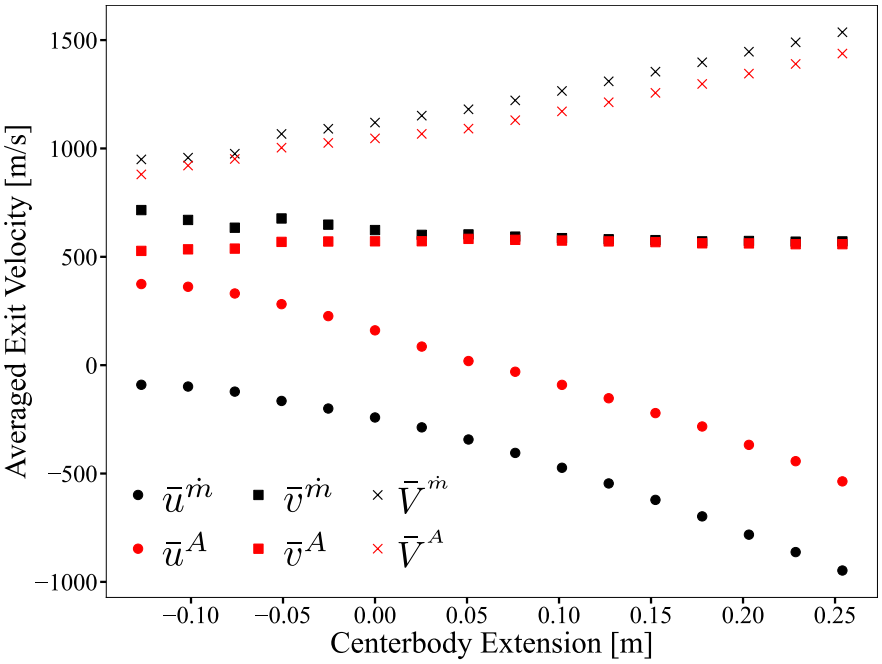


Figure 4.67: Nozzle Swirl Probability Density

To check if the model conserves angular momentum at the exit, Figure 4.68 was generated for each RDC channel length. Across all cases, the exit swirl was not conserved. Despite the longer channels, the high negative azimuthal velocities produced a further deviation in the exit plane swirl. These results show room for improvement in the model, and a future effort will provide methods to better conserve the angular momentum across the RDC.

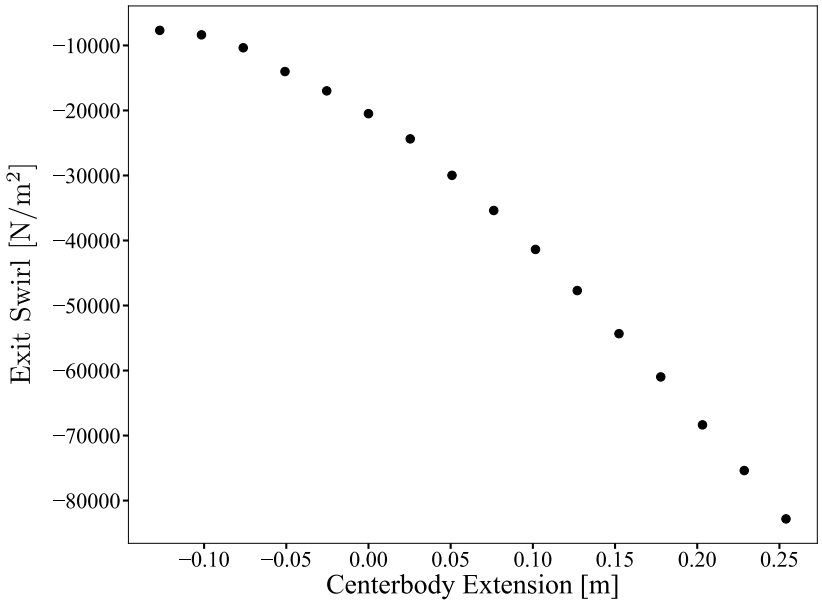


Figure 4.68: Nozzle Swirl versus RDC Length

To examine why the total angular momentum increases in magnitude with a change in channel length, we can define a term that relates the channel length, l_{ch}, to the distance between the detonation waves within the channel, w_{wave}. This is defined as the aspect ratio, $AR_{channel}$, and is shown in Equation 4.35.

$$AR_{channel} = \frac{l_{ch}}{w_{wave}} \tag{4.35}$$

Although not showing variations in channel length specifically, Figure 4.69 shows an example case with multiple detonation waves. Due to the decrease in the distance between the waves, the aspect ratio increases. As the aspect ratio increases, the fraction of the flow that is processed by the shock increases. In the case of Figure 4.69, all of the flow is now processed by the shock wave. Changes in channel length also impact the aspect ratio but to a much lesser extent.

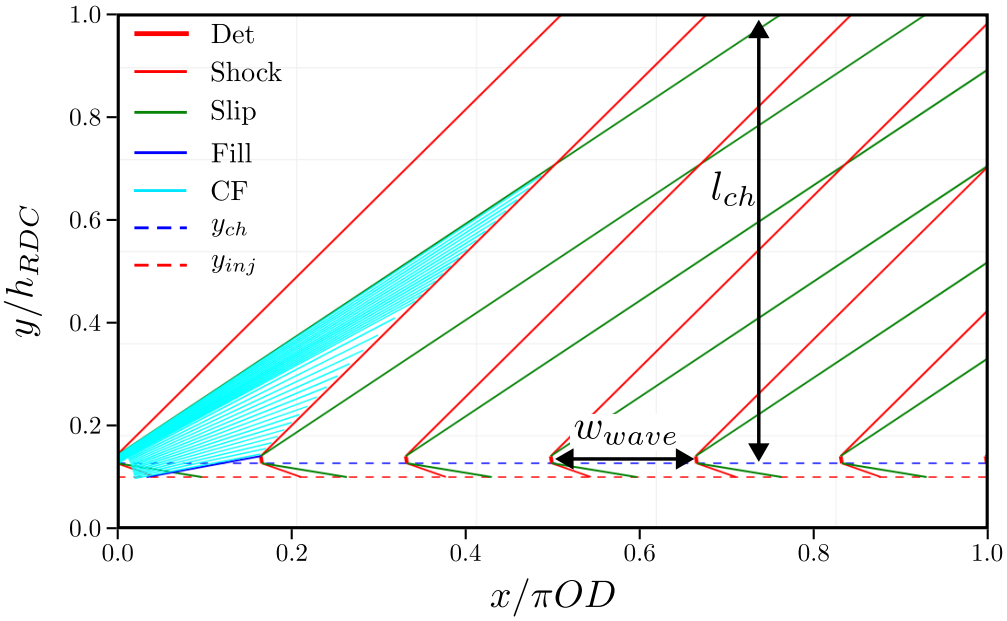


Figure 4.69: Example of Flow with Multiple Shock Passes

The change in aspect ratio can explain the divergence in angular momentum shown in Figure 4.68 due to an increase in the fraction of the flow that is processed by the oblique shock, as the oblique shock effectively pulls the flow in the direction of wave propagation. In this case, the angular momentum is increasing in the negative direction, which is the same direction as the wave propagation.

The effects of increasing the fraction of the flow process by the shock are not only limited to the exit angular momentum; it also has a direct impact on the predicted thrust. Figure 4.70 shows the fraction of the exit area (a) and the mass flow rate (b) that consists of the flow that passes through the oblique shock. This shows a linear trend in the fraction of shocked flow (by area) as

the channel length increases, where the shocked flow accounts for over half of the exit flow area at the longest channel. When examining the percentage of the mass flow rate processed by the shock, this begins to approach 80% at the longest channel. Figure 4.70 (c) shows the predicted thrust from the model and the high correlation between the percentage of flow that is shocked, regardless of the definition, and the estimated thrust. This suggests that whether or not the flow is shocked will have a significant impact on the predicted thrust.

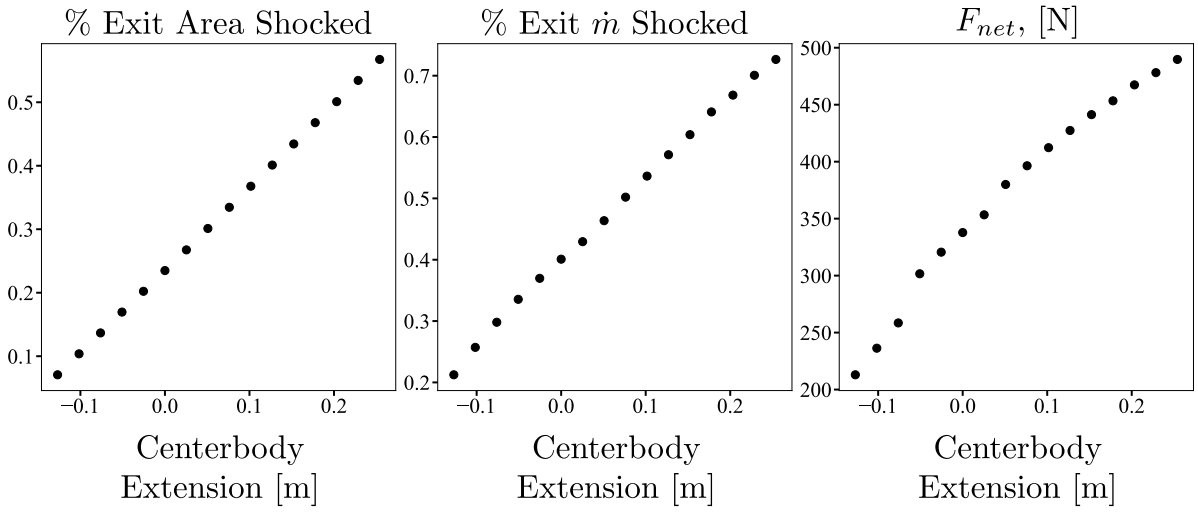


Figure 4.70: Percent Exit Area and Percent Mass Flow Processed by Shock, with Net Thrust

The change in the predicted thrust from the model was not expected based on experimental efforts examining variable RDC lengths.[79, 80] For this reason, it is likely that the model will require improvements in post-shock processing to better match experimental thrust data and potentially help conserve angular momentum at the exit plane.

4.3.2.4 Deflagration Losses

The following section will examine the model output performance as a function of the deflagration loss parameters. This section will examine only the effects of parasitic combustion and leaked fuel fraction, with the effects of combustion efficiency ignored. These cases were performed using the Pintle style injector at a stoichiometric 300 g/s flow rate and with the default configuration elsewhere.

Figure 4.72 shows the mass flow rate error and plenum pressure from the model. At higher deflagration losses, the mass flow error increases drastically, which is due to a convergence error in the model, which will be discussed later. For the plenum pressure, an increase in the deflagration loss fraction results in a decrease in plenum pressure. This is due to the decreased detonation

pressure ratio and inlet blockage, and the trend in plenum pressure follows an inverse correlation with the detonation pressure ratio shown in Figure 2.6.

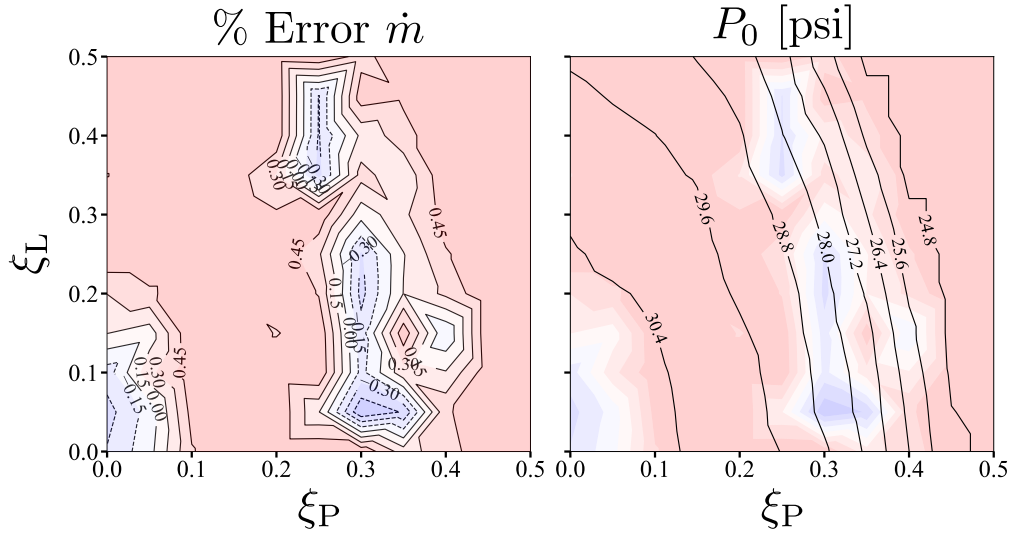


Figure 4.71: Parasitic and Leaked Fuel Fractions Parametric Study: Mass Flow Rate Error (left) and Plenum Pressure (right).

Figure 4.73 shows the model exit conditions as a function of the parasitic combustion fraction, ξ_{P}, and the leaked fuel fraction, ξ_{L}, only. The cases with a high parasitic fraction result in the Ydet0 exit condition, meaning the lower portion of the detonation is below the injector minimum area location. This essentially means that the detonation is too "large" for the given flow conditions. Recall that the height of the detonation is based on the wave speed and upstream density, and as the parasitic fraction increases, both terms decrease, leading to a larger detonation area requirement (see Equation 4.1). The other aspect of this argument is based on the fill height calculation, which is a function of the fill conditions, blockage, and wave speed. As the fraction of leaked fuel increases, the speed of the wave decreases, allowing a longer fill time and reduced blockage (see Figure 4.73). Due to this, at $\xi_{\mathrm{P}} = 0.3$ and higher leaked fuel fractions, the model does not exit with a Ydet0 condition, reverting to a pressure tolerance exit condition.

Figure 4.73 shows the lab wave speed (a), the detonation pressure ratio (b), the blockage ratio (c), and the fill properties (d). Subplots (a) and (b) should look familiar as the wave speed and pressure ratios match the trends shown in Figure 2.6 for the deflagration losses fractions. The blockage ratio, shown in (c), scales with the detonation pressure ratio, which reduces the backflow effects as the pressure ratio decreases. Of particular interest is the region where blockage trends towards zero. This exact part of the map corresponds to the region where the mass flow error begins to spike. In this region, the detonation pressure ratio becomes small enough that inlet blockage is minimal; however, operability concerns may arise here, which may also be indicative

of the detonation height error condition present in this region. More work is required on this front, along with a feedback mechanism to relate the deflagration losses to the blockage within the inlet.

Finally, the fill and detonation heights, shown in (d), track with the wave speed and pressure ratio as the deflagration losses are varied. As mentioned earlier, the detonation height is a function of the wave speed and upstream density, where the effects of increased parasitic combustion drive the detonation height increase despite an associated decrease in the wave speed. This decreased wave speed, however, does allow for a much longer fill time, and hence a larger fill height. This subplot also shows the boundary where the detonation height is larger than the fill height (lower right corner).

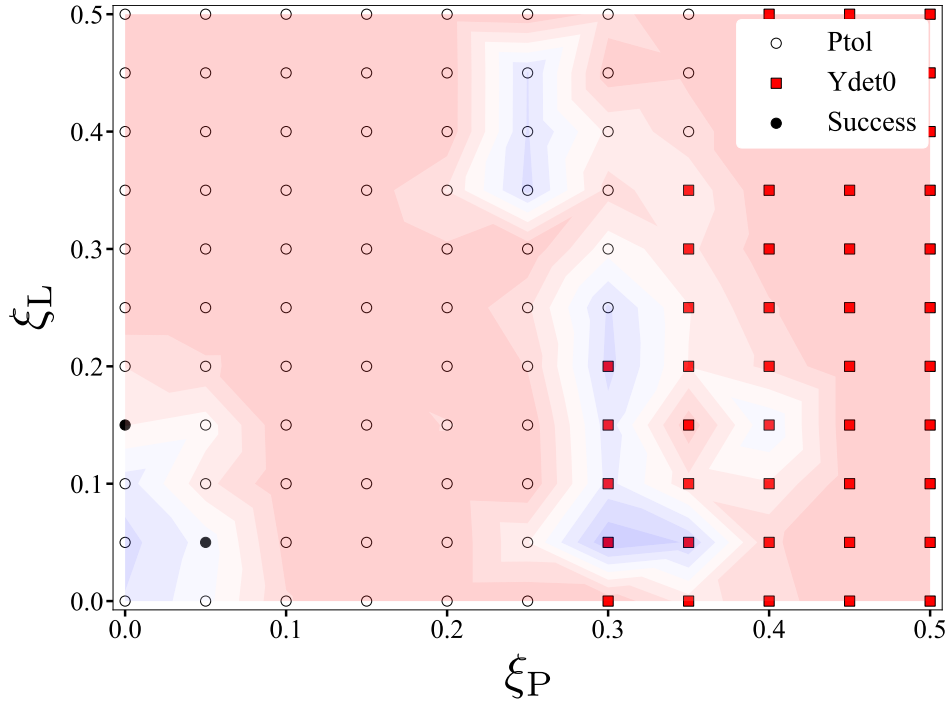


Figure 4.72: Parasitic and Leaked Fuel Fractions Parametric Study: Cycle Exit Conditions.

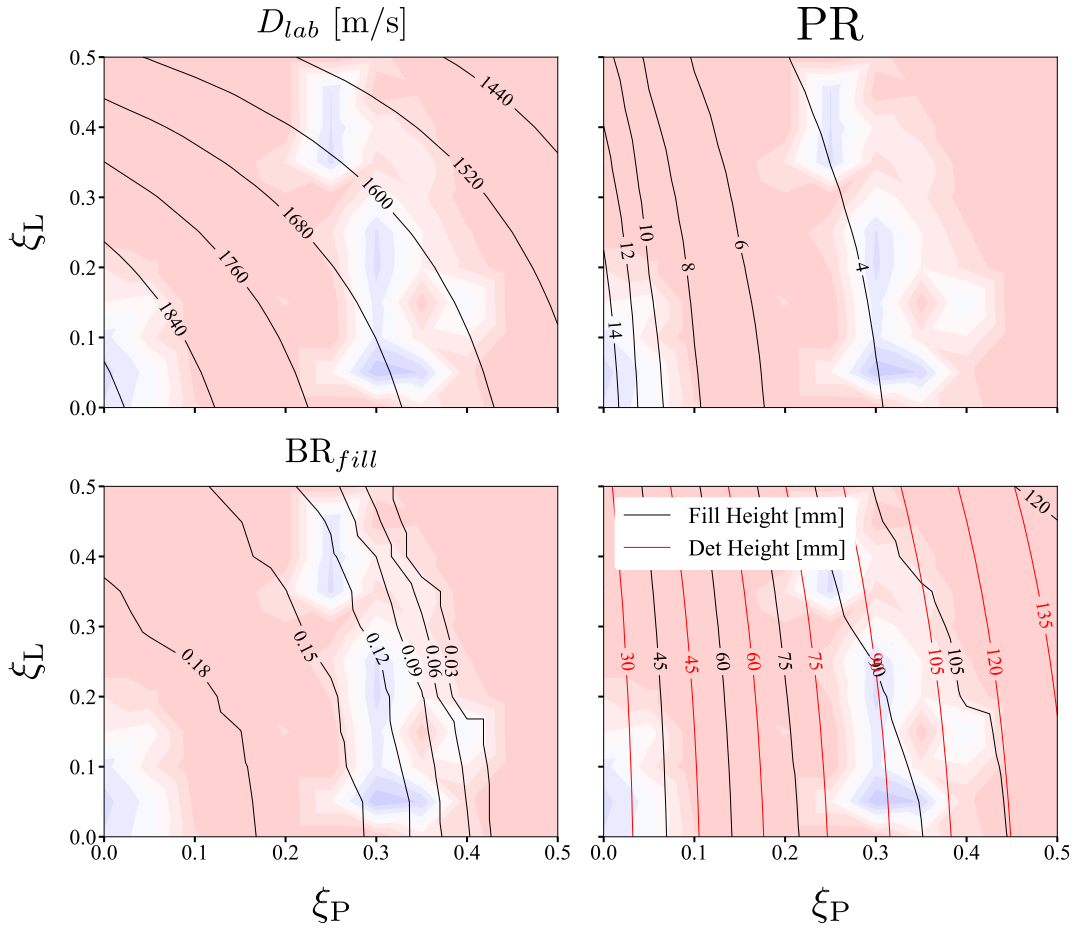


Figure 4.73: Parasitic and Leaked Fuel Fractions Parametric Study: Wave speed, Pressure Ratio, Blockage and Fill Properties.

The deflagration fractions are extremely detrimental to the performance of the modeled cycle. It is worth noting that in terms of which parameter is worse, the model predicts that parasitic combustion has a much more drastic impact on the thrust and pressure gain metrics. These results also follow the contours of the detonation pressure ratio, suggesting that it is crucial to achieve a high detonation pressure ratio despite how this may affect the inlet blockage. It must be stressed again that the model does not currently provide mechanisms that would link inlet blockage to these loss fractions, so the results may differ when better accounting for how the blockage effects trickle downstream to the detonation wave.

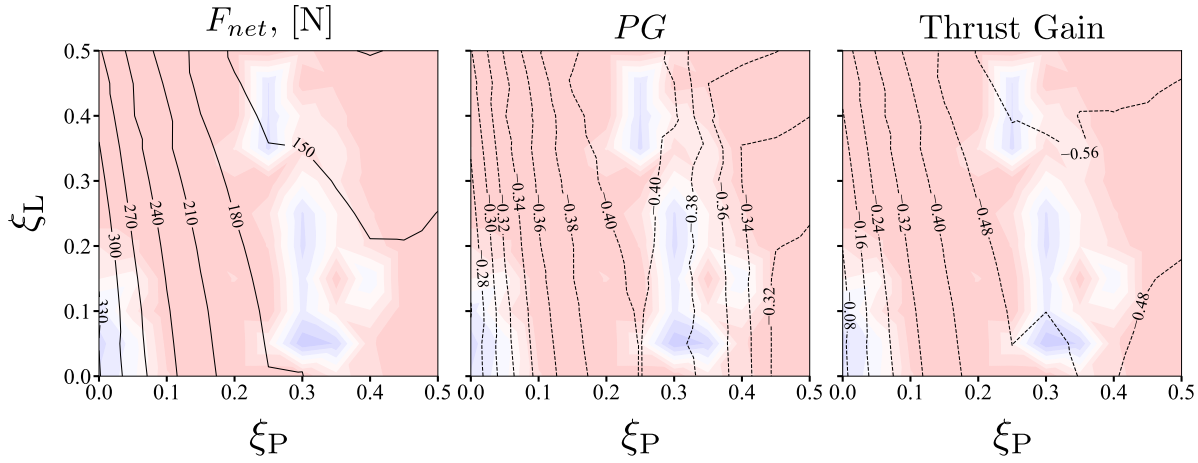


Figure 4.74: Parasitic and Leaked Fuel Fractions Parametric Study: Net Thrust, Pressure Gain and Thrust Gain.

The final examination of the deflagration losses looks at the polytropic rate terms and coefficient. These contours are shown in Figure 4.75. Both the work and heat rate terms have respective peak values at the lowest levels of deflagration loss fractions. This was expected based on previous results, as the higher detonation performance would incur the largest work and heat extraction rates. Although the work extraction rate remains approximately the same magnitude across the parametric sweep, the heat extraction rate is more highly correlated with the parasitic loss fraction. This is likely due to the drastic reduction in the detonation pressure ratio as the parasitic fraction increases. The same trend is evident in the polytropic coefficient, which is nearly perfectly correlated with the parasitic fraction.

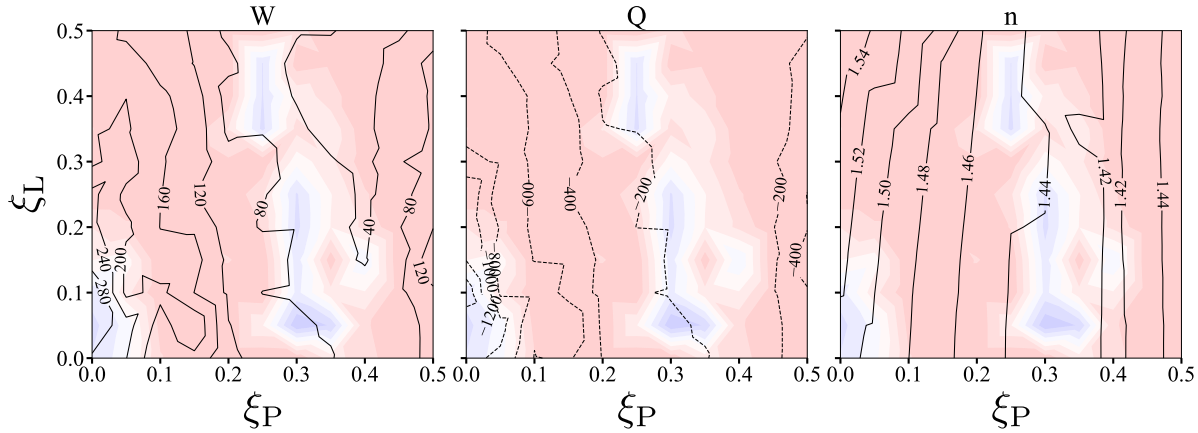


Figure 4.75: Parasitic and Leaked Fuel Fractions Parametric Study: Polytropic Rate Terms and Coefficient.

4.3.2.5 Ambient Back-Pressure

The following section discusses the variation in predicted performance as a function of the ambient back pressure on the RDC. The cases were tested using a 300 g/s stoichiometric mixture in the Pintle style geometry. Figure 4.76 shows the mass flow rate error and plenum pressure only as all cases converged to the Ptol exit conditions. All mass flow rates converged to within 1% of the specified value. As expected, the plenum pressure required to drive the target mass flow was reduced nearly linearly with the ambient pressure.

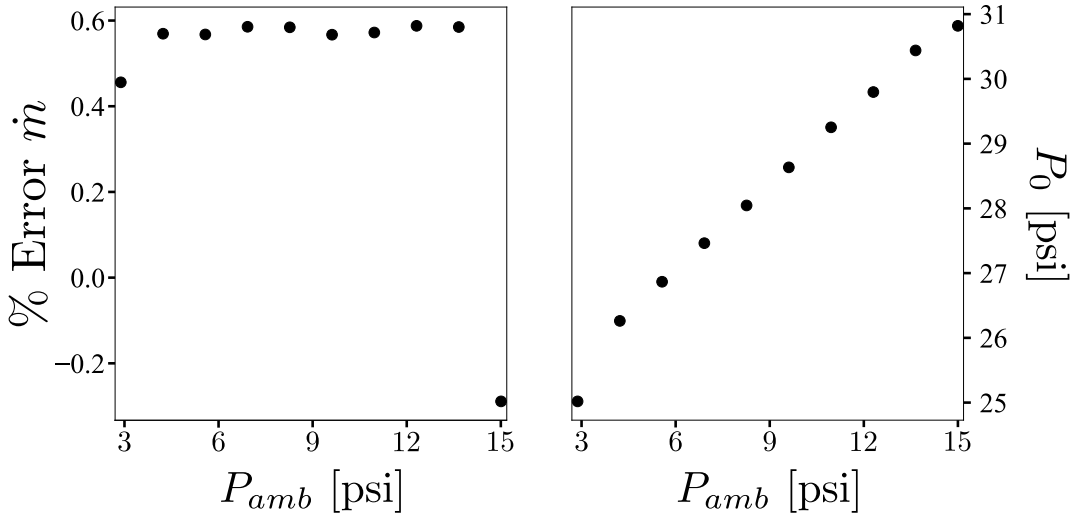


Figure 4.76: Ambient Pressure Parametric Study: Mass Flow Rate Error (left) and Plenum Pressure (right).

The wave speed and pressure ratio were also reduced at lower ambient pressure, but all changes in pressure ratio can be attributed directly to the decrease in wave speed since all cases were ideal detonations. As the ambient pressure decreased, the fill and detonation heights remained relatively constant. The biggest change with ambient back pressure was the blockage ratio. This decreased as the back pressure decreased, which was expected; however, the magnitude of the change was larger than expected.

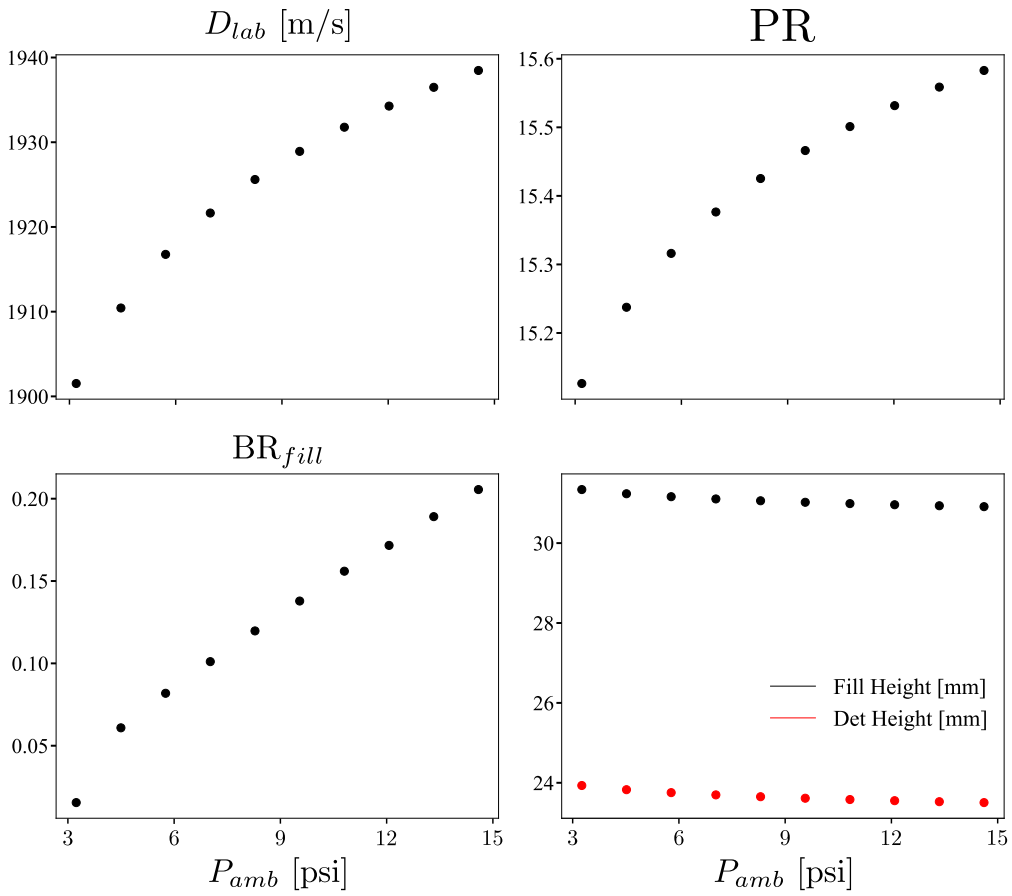


Figure 4.77: Ambient Pressure Parametric Study: Wave speed, Pressure Ratio, Blockage and Fill Properties.

Figure 4.78 provides some context on why the blockage ratio decreases so drastically as the back pressure is reduced. This comes down to changes in the stiffness of the injector, defined as the ratio between the channel static pressure and the total plenum pressure. As the injector becomes more stiff, it is more resistant to the backflow of post-detonation products, reducing the inlet blockage. This corresponds to a decrease in the plenum pressure as the blockage decreases; however, there is still a minimum plenum pressure required to drive the mass flow, even with zero blockage.

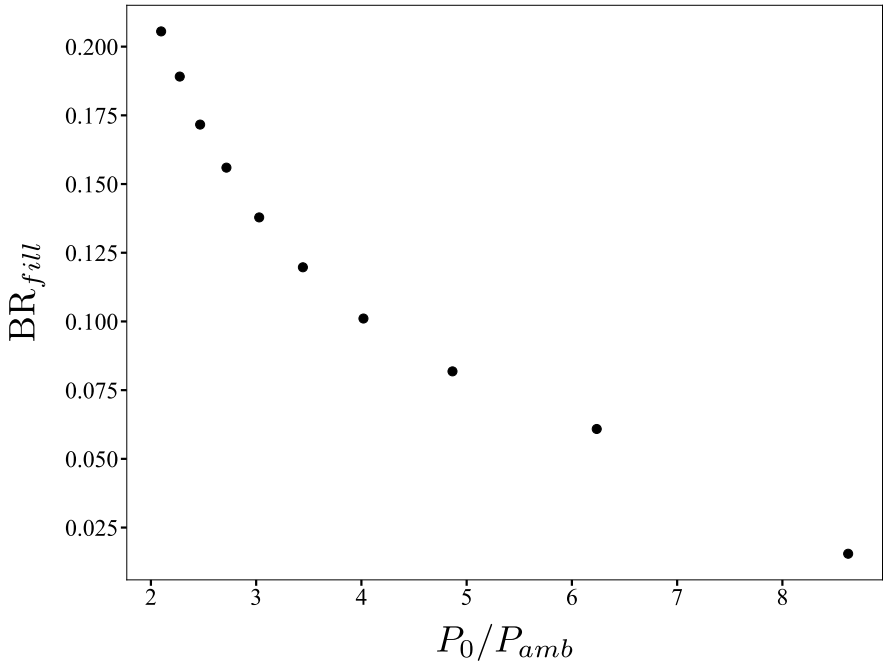


Figure 4.78: Blockage versus Inlet Pressure Ratio.

Figure 4.79 shows the relationship between the RDC performance and changes in ambient back pressure. An initial decrease in the back pressure results in a slightly less performant RDC; however, further decreases in the ambient pressure allow for a large improvement in RDC performance, specifically thrust production. The initial dip in performance is theorized to be mainly due to a slight decrease in the detonation wave performance, specifically the pressure ratio, without a significant reduction in inlet blockage. As the ambient pressure is reduced further, the blockage asymptotically approaches zero, counteracting any reduction in detonation performance.

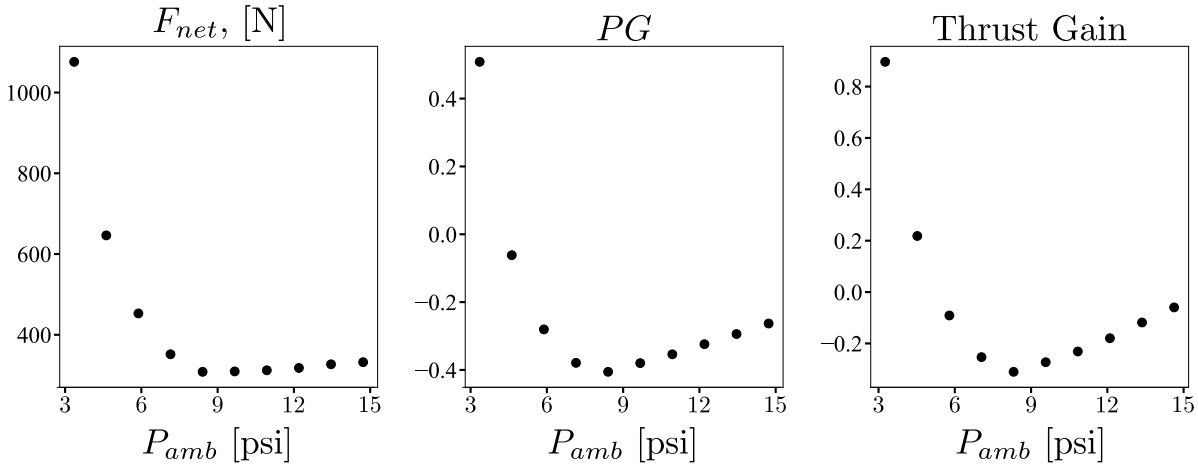


Figure 4.79: Ambient Pressure Parametric Study: Net Thrust, Pressure Gain and Thrust Gain.

Figure 4.80 shows the momentum rate term, the energy rate term, and the polytropic coefficients as a function of the ambient pressure. At moderate pressures, the polytropic coefficient is relatively constant before a large jump at the lowest pressures. This result is not the whole story. Looking at the work and energy rate terms provides more detail on the situation. As the pressure begins to decrease, the heat transfer rate term remains relatively constant while the momentum rate term increases by nearly 2x. This increase in lost momentum correlates well with the loss in thrust performance within this range. As the pressure further decreases, the momentum term drops to nearly half of the value at the largest back-pressure. This comes with a large increase in the energy transfer; however, this also corresponds to a rapid increase in the thrust. This could suggest that heat losses are less detrimental to thrust as opposed to momentum losses that produce a more drastic decrease in thrust.

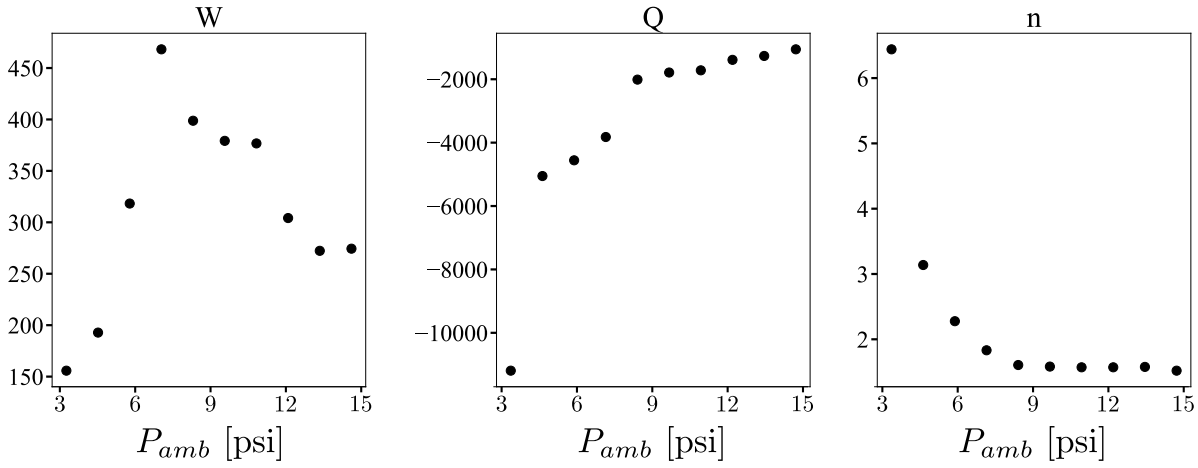


Figure 4.80: Ambient Pressure Parametric Study: Polytropic Rate Terms and Coefficient.

4.3.2.6 Discharge Coefficient and Diodicity

This section is dedicated to modeling geometric changes that alter the discharge coefficient on the injector, both in the forward and reverse direction. The idea behind this study was discussed in Paxson and revolves around the premise that higher RDC performance may be achieved if the reverse flow from the post-detonation products is reduced.[59] The following examines varying the forward and reverse discharge coefficient of the Pintle style injector using the default model configuration.

Figure 4.81 shows the mass flow rate error and plenum pressure as a function of the forward and reverse discharge coefficients. The errors in the mass flow rate were all below 1%, and the exit condition for all runs was the plenum pressure tolerance condition, which is why this figure is not included. The total plenum pressure scales as expected, where a decrease in the forward-flow discharge coefficient should produce a higher plenum pressure requirement to achieve the target

mass flow rate.

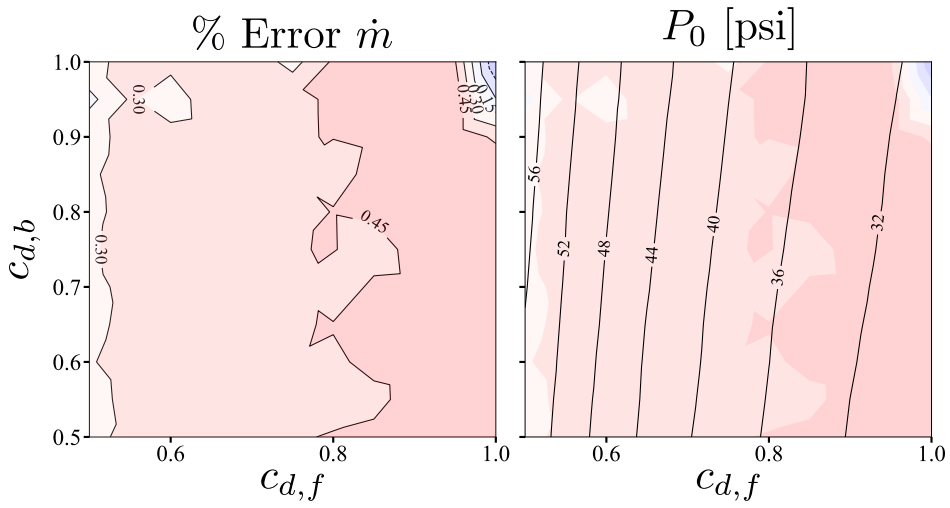


Figure 4.81: Discharge Coefficient Parametric Study: Mass Flow Rate Error (left) and Plenum Pressure (right).

The wave speed, pressure ratio, detonation height, and fill height were predicted to be constant throughout the test sweep; therefore, we will focus solely on the inlet blockage (shown in Figure 4.82). For a given forward discharge coefficient, as the reverse discharge coefficient decreases, so does the inlet blockage. This was an expected result and provides more support for the theory that having a high forward discharge coefficient but a small reverse discharge coefficient will provide some benefit to the RDE cycle. Although not initially expected, the trend of blockage decreasing as the forward discharge coefficient is completely explained by the increase in plenum pressure. This reduces the blockage fraction but will have additional negative impacts on the inlet performance, especially with respect to the inlet pressure losses.

As it relates to the RDC performance, however, the changes in the inlet discharge coefficient do not provide the expected increase in thrust. This can be seen in Figure 4.83 (a), where the thrust is nearly constant across the whole parameter sweep. The pressure gain and thrust gain are both highly correlated with the forward discharge coefficient but not with the reverse discharge coefficient, lending more credence to the previous statement that the negative impacts of the inlet pressure losses are more indicative of overall RDC performance.

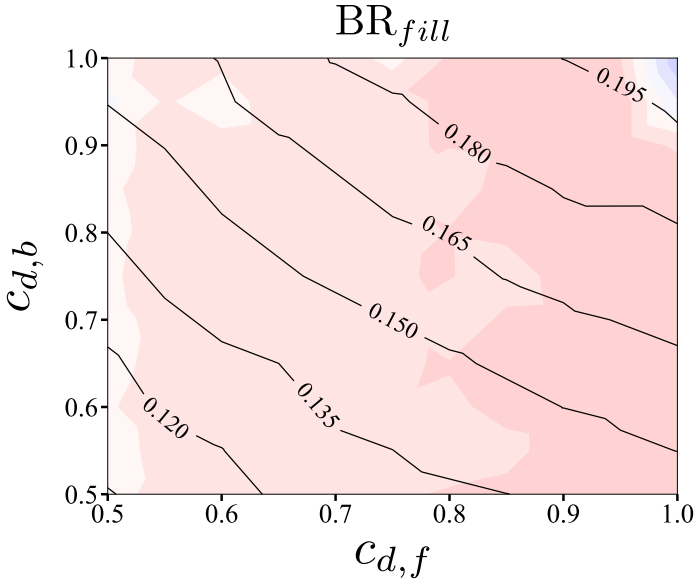


Figure 4.82: Discharge Coefficient Parametric Study: Blockage.

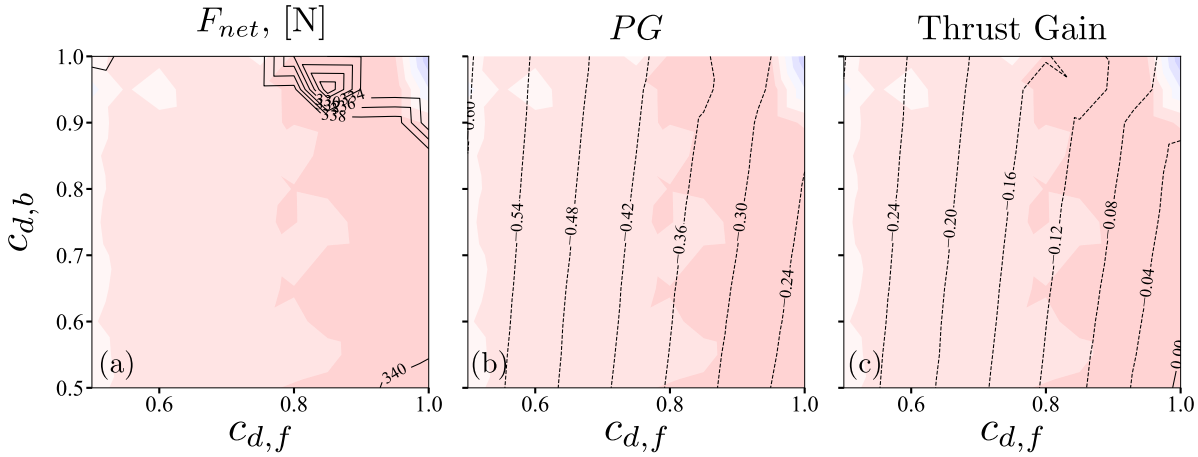


Figure 4.83: Discharge Coefficient Parametric Study: Net Thrust, Pressure Gain and Thrust Gain.

Across the full parameter sweep, the work extraction rate, the heat extraction rate, and the polytropic coefficient are all nearly invariant to the changes in the discharge coefficient. Figure 4.84 shows the calculated diodicity plotted against the blockage ratio (a) and the pressure gain (b) for the parameter sweep, where the diodicity is defined by Paxson (Equation 3.5).[59] The markers are color-coded based on the forward discharge coefficient, and the reverse discharge coefficient decreases moving from left to right. As discussed previously, the blockage ratio is not directly a function of the inlet diodicity unless the forward discharge coefficient is fixed. This is due to the increase in the plenum pressure as the forward discharge coefficient decreases. As for the pressure gain, this metric is relatively constant as a function of diodicity and more a function of the forward-

flowing discharge coefficient. Again, as the forward discharge coefficient decreases, the plenum pressure must rise. This increases the denominator of the pressure gain equation, Equation 3.1, and overall reduces the overall cycle pressure gain.

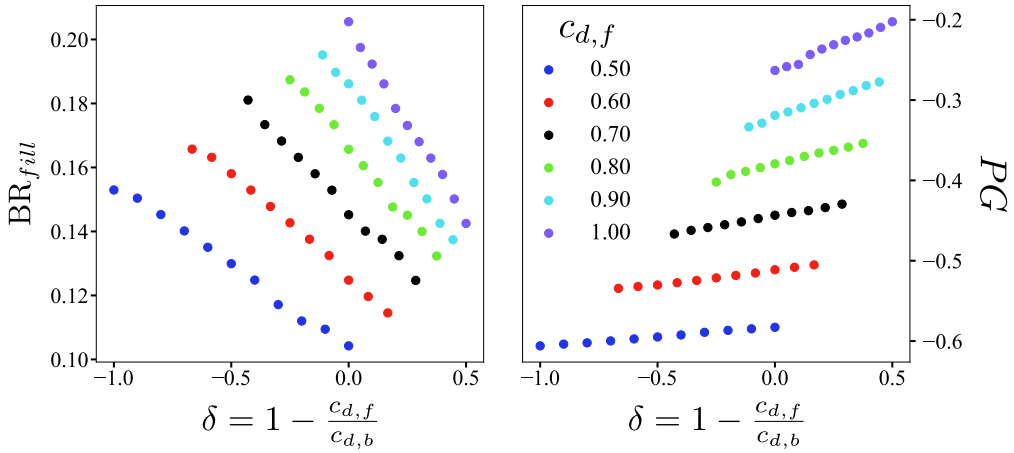


Figure 4.84: Blockage (left) and Pressure Gain (right) versus Inlet Diodicity.

4.3.2.7 Number of Waves

Increasing the number of waves is done by dividing the circumference and mass flow rate by the number of waves. Then, the same solution procedures are used to solve a smaller portion of the flow path. As discussed earlier, the effects of additional shock processing are not included in this version of the model (see Figure 4.69). Figure 4.85 shows an example of the flow field as the number of waves increases from one to four. It becomes clear that as the number of waves increases, the fraction of post-detonation products that are processed by the shock increases. At a certain number of waves, all of the post-detonation products are processed by the wave (four-wave example), and the location where the slip line intersects the shock occurs before the exit of the RDC. The model simply assumes that all of this flow exits the RDC without interacting with the next oblique shock; therefore, caution should be taken when interpreting the high wave number cases. In addition, this model places no restriction on the size of the detonation wave, which may allow the detonation heights to be smaller than those of a single detonation cell under the same initial conditions.

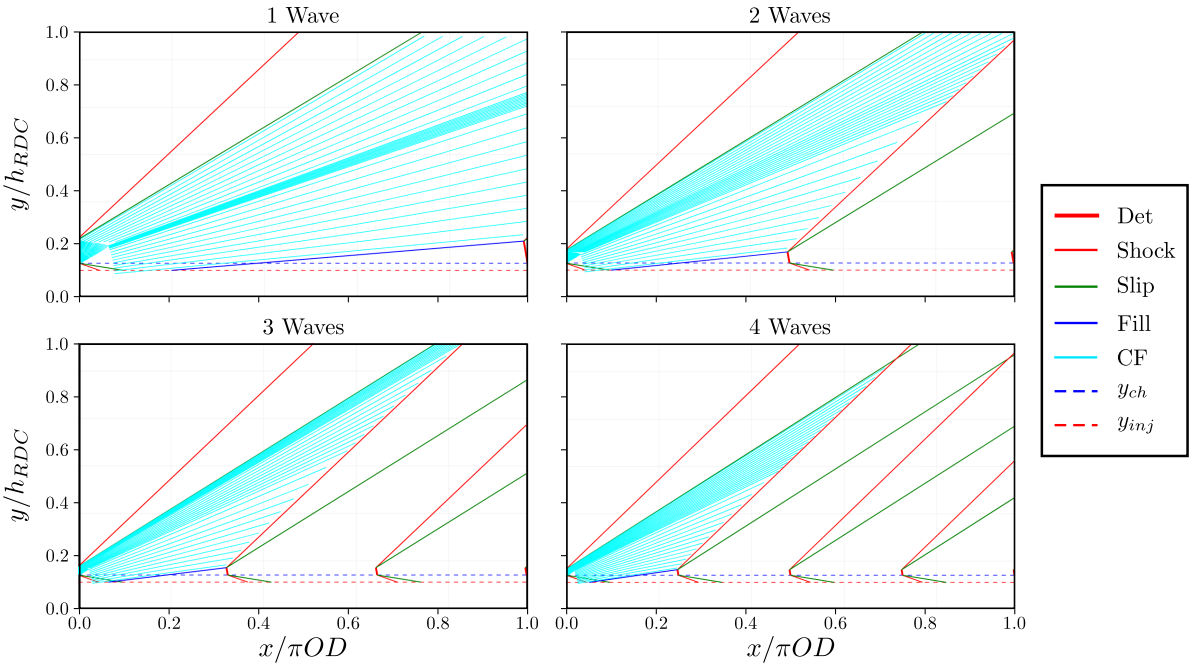


Figure 4.85: RDC Flowfield as a Function of the Number of Detonation Waves.

With the description of potential shortcomings of this section complete, we move on to examine the effects of changing wave numbers using the Pintle geometry and a 300 g/s stoichiometric mixture. Across the board, the mass flow rate error and the plenum pressure were determined to be constant and within the error of 0.4% (see Figure 4.86).

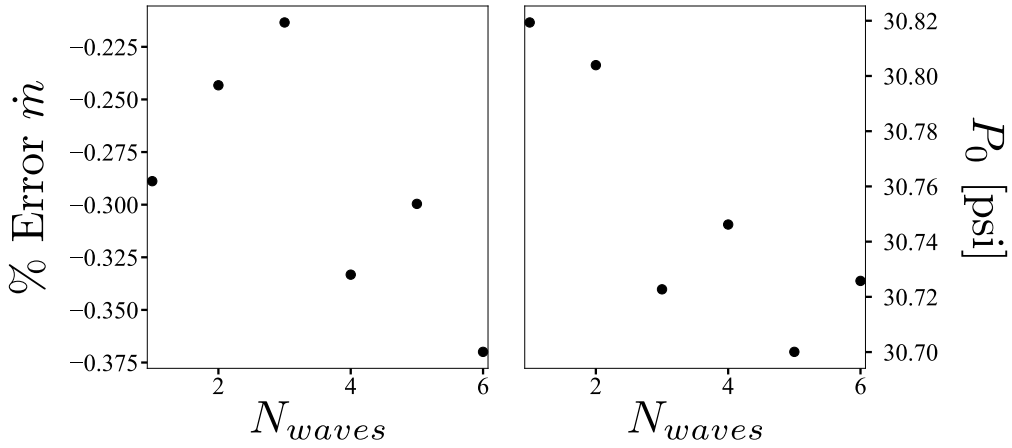


Figure 4.86: Wave Number Parametric Study: Mass Flow Rate Error (left) and Plenum Pressure (right).

In a similar manner, all of the detonation properties were also calculated to be constant, including the inlet blockage. The only change in the number of waves was the height of the fill

and detonation, shown in Figure 4.87. These values were simply decreased by the inverse of the number of waves from the single-wave value.

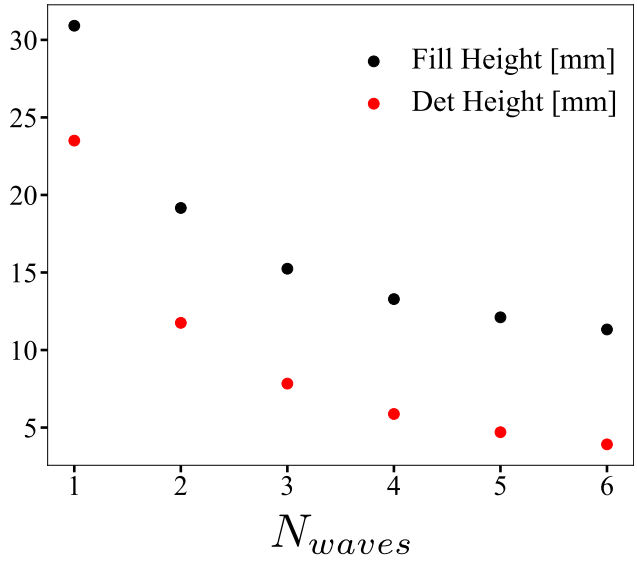


Figure 4.87: Wave Number Parametric Study: Fill Properties.

For the RDC performance metrics, all terms increased with an increase in the number of waves. This is likely not indicative of actual RDC performance due to the discussion of proper processing of all of the post-detonation products with additional shocks. The particular area of interest is the transition from one to two waves. In this region, the performance metrics are constant, and both of these points do not have the additional consideration of a second shock event (see Figure 4.85). If this is truly the trend with wave number, it suggests that there is no improvement in performance predicted with a change in wave number. This is an area that requires additional research that is saved for future efforts.

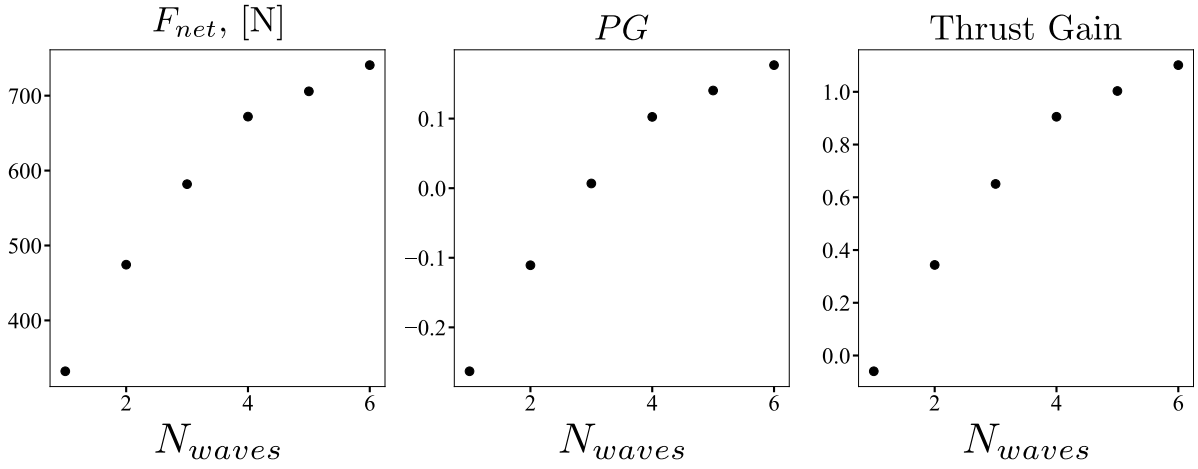


Figure 4.88: Wave Number Parametric Study: Net Thrust, Pressure Gain and Thrust Gain.

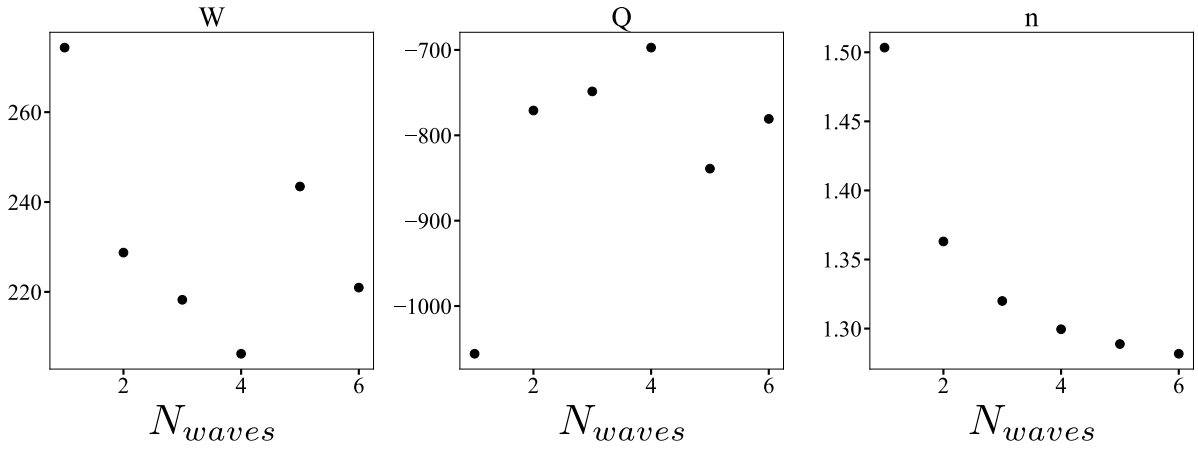


Figure 4.89: Wave Number Parametric Study: Polytropic Rate Terms and Coefficient

An area of discussion with respect to thrust performance revolves around the fraction of the flow that is processed by the shock. We saw in Figure 4.70 that the thrust may be well predicted by the fraction of the mass flow rate that is processed by the shock. We have also seen in Figure 4.88 that the higher number of waves corresponded to an improved thrust performance. Figure 4.90 combines these results to examine the percentage of the mass flow that is processed by the shock as a function of the number of waves. This plot shows that after the jump from three to four waves, the shock processes all of the mass flow, which is also evident in Figure 4.85. Due to the model lacking certain post-shock processing, including accounting for re-shock potential, these results may indicate that the thrust may be over-predicted when a large percentage of the mass flow is shocked.

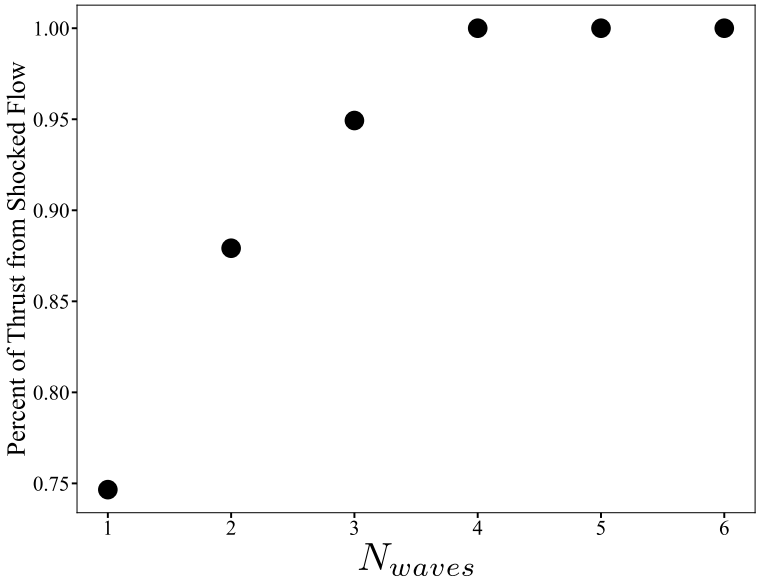


Figure 4.90: Percent of Thrust from Shocked Gas versus Number of Waves

Aside from the potential over-prediction in thrust due to the re-shock potential, we can examine other reasons why having additional flow processed by the shock wave may be beneficial. Figure 4.91 shows the velocity vectors along the exit plane as the number of waves was varied. The red arrows represent shocked flow, while the black arrows represent un-shocked flow. From this figure, we can see how the number of waves affects the amount of post-detonation gases that are processed by the oblique shock. At a wave count of 4, all of the post-detonation gases are processed by the oblique shock, effectively aligning all of the exit flow towards the direction of wave propagation. This appears to lead to a situation where the angular momentum will not be conserved, a detail that we will return to later in this section.

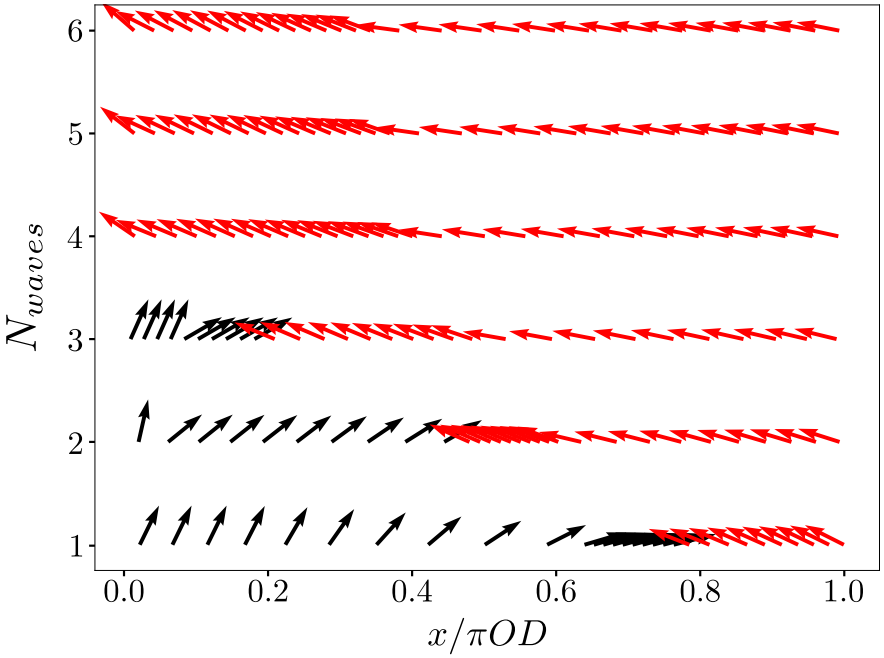


Figure 4.91: Nozzle Velocity Profile versus Number of Waves

Figure 4.92 provides the results of the mass and area averaging the axial, azimuthal, and total velocity at the exit plane. This figure shows a trend similar to that in Figure 4.67 where the averaged azimuthal velocity, by either method, lies mainly in the negative direction, which is defined as in the direction of wave motion. As the number of waves increases, this azimuthal velocity increases, mirroring the results shown in Figure 4.91. The average axial velocity also increases, which is a driving factor in the improved thrust output as the wave number increases. Essentially, the oblique shock wave provides some flow turning to the post-expansion gases, which better aligns the velocity vectors in the axial direction. This is in addition to the fact that the shock will provide an increase in the pressure and temperature of the gases before the exit of the RDC, providing an additional increase in the calculated thrust.

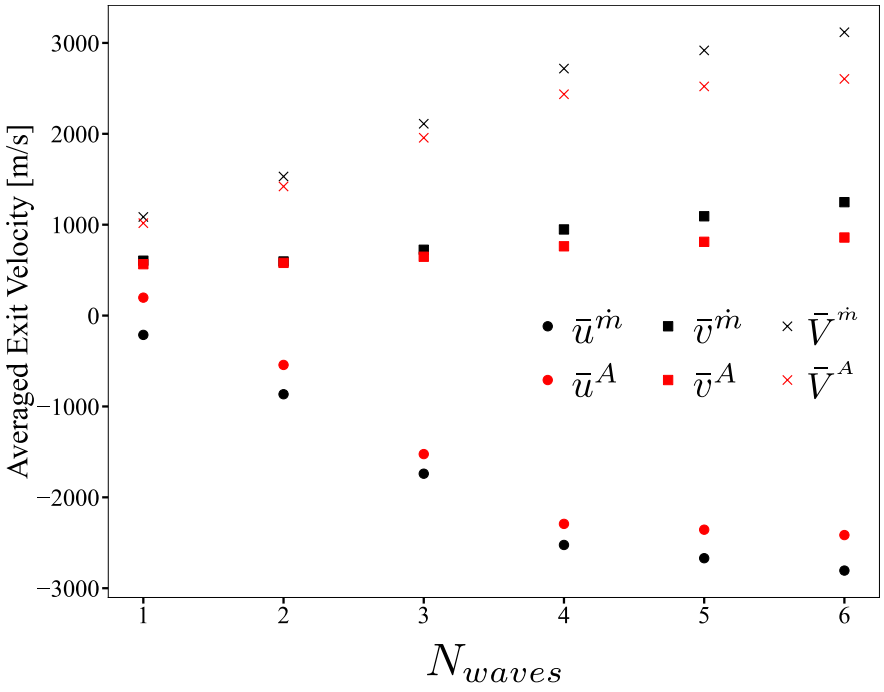


Figure 4.92: Averaged Velocities at Exit Plane versus Number of Waves

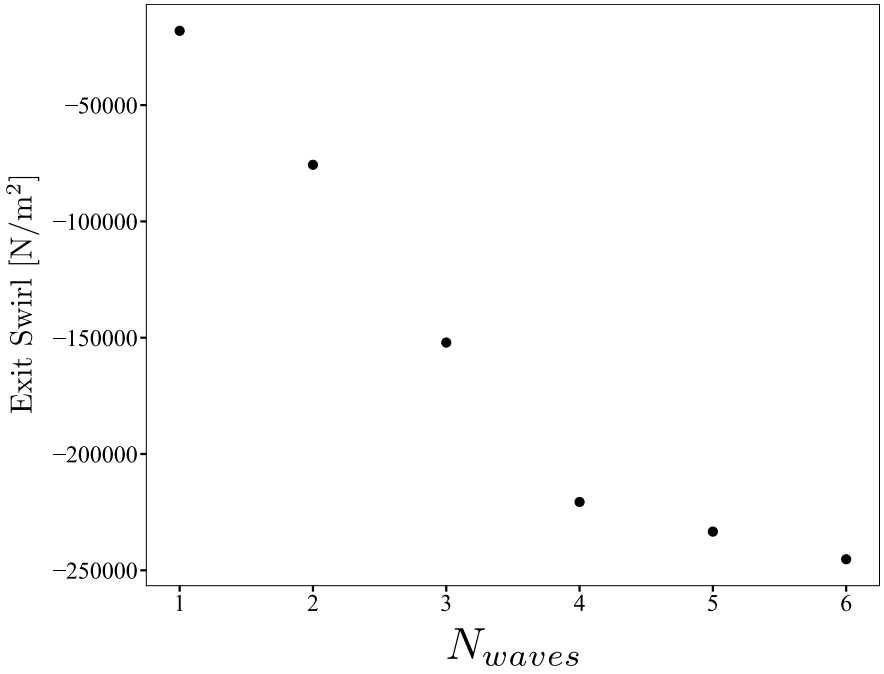


Figure 4.93: Nozzle Swirl versus Number of Waves.

Returning to concerns with the conservation of angular momentum, Figure 4.93 plots the total calculated swirl at the exit plane across the wave number sweep. As expected, this result shows

that the net angular momentum is not conserved by default for the cycle model. Additional model considerations, such as those presented in Section 3.3.2.1, may be required to ensure the conservation of angular momentum is maintained across the RDC. These updates are saved for future work.

4.3.2.8 Other Results from Parametric Study

As parametric and sensitivity analysis was performed, additional points of interest appeared. Figure 4.94 is a prime example of the analysis that falls out of the parametric study. This figure shows the calculated pressure gain, based on the net thrust, as a function of the inlet mass flux. The mass flux is calculated based on the inlet mass flow rate at the inlet minimum area. Across a wide range of deflagrative losses, target mass flow rate, and equivalence ratios, the model consistently predicts a pressure gain of less than 0. This is not a definitive result that RDC devices cannot produce a positive pressure gain; it is just that this model, including the specified losses, does not predict a positive pressure gain for the device geometries and operating conditions tested.

As reflected by experimental research efforts, this trend points to a lower mass flux condition being more apt to produce a pressure gain across the RDC. However, this result also opens the door for additional concerns about the viability of pressure gain within an RDC cycle. These concerns and other potential performance metrics will be discussed in more detail in Chapter 6

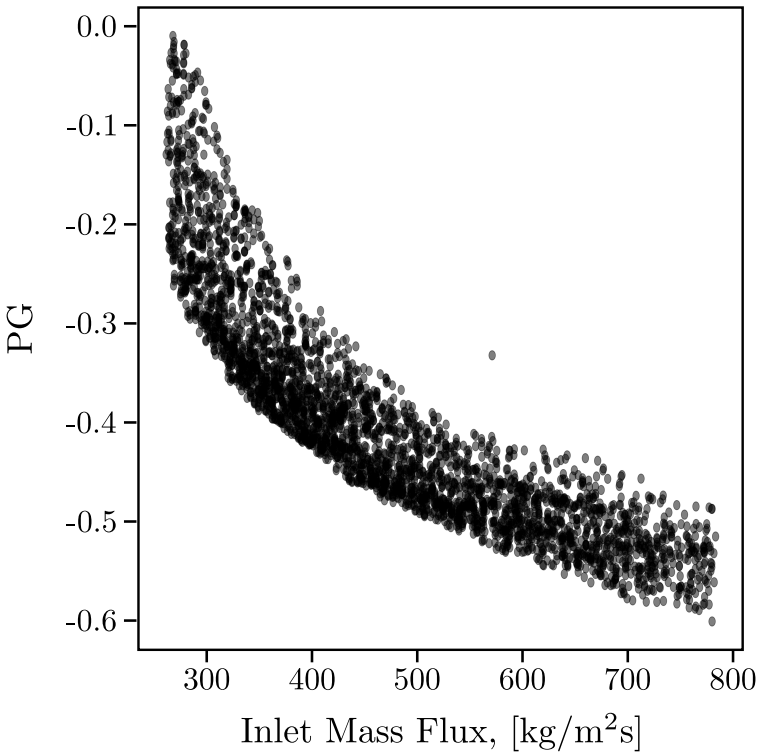


Figure 4.94: Modeled Pressure Gain versus Inlet Mass Flux

Figure 4.95 plots the pressure gain metric versus the channel static to plenum total pressure ratio. This figure echoes experimental results, where the larger the inlet pressure drop, by this definition, is nearly perfectly correlated with the device performance. Regardless of the performance of the detonation wave and any other operating conditions, the pressure gain metric appears to be solely determined by the injector pressure drop based on these model results and prior experimentation.

$$\Delta P_{inj} = \frac{P_{ch} - P_0}{P_0} \tag{4.36}$$

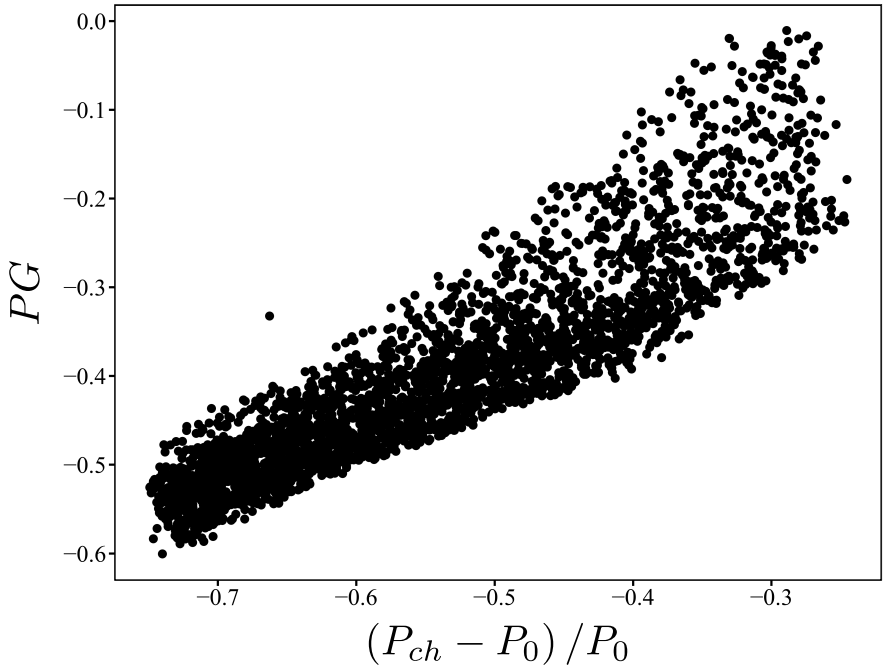


Figure 4.95: Pressure Gain versus Inlet Pressure Drop.

The main issue with the RDC pressure gain being determined by the channel-to-plenum pressure ratio is the fact that the inlet pressure ratio is a direct function of the mass flow rate being pushed through the device. Figure 4.96 shows the injector pressure drop as a function of the mass flux across the injector plane. This profile is determined by the geometry of the inlet and the mass flow rate through the device. Although high mass-flux operation is a potential benefit of RDC devices, if it comes at the cost of reduced performance, then it may become too detrimental to operate at the highest fluxes.

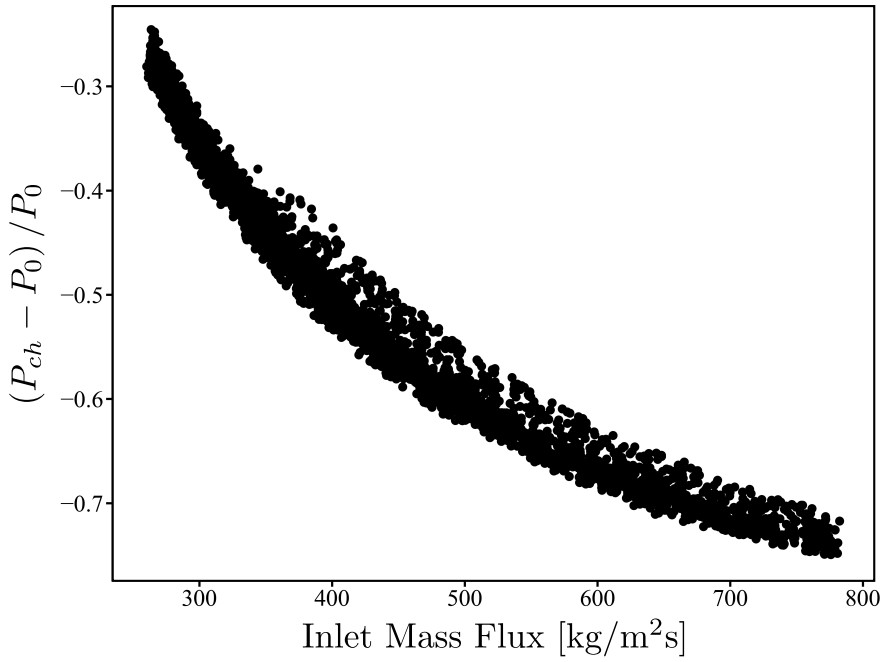


Figure 4.96: Inlet Pressure Drop versus Inlet Mass Flux.

Another inlet performance effect discovered through the evaluation of the cycle model is shown in Figure 4.97. This figure plots the percentage of the forward reactant flow that is choked across the inlet plane versus the calculated blockage. Aside from a few outlier points, this figure shows that the model predicts that the inlet is nearly always completely choked until the blockage value drops below 10%. However, across all test cases, between 90-100% of the forward-flowing inlet is choked, which was also predicted by the blockage study presented by Feleo et al.[5]

The next area of interest revolves around the polytropic rate terms. Figure 4.98 shows the mass averaged values for each rate term across all Channel Flow objects within the RDC channel. Keep in mind that these values are determined by the polytropic compression algorithm, Algorithm 24, to achieve the target channel pressure while conserving mass, momentum, and energy. Across all parameters swept in the evaluation of the model, these terms are nearly perfectly correlated, meaning that when one loss occurs, it is always associated with the other. Across these values, the average value of the polytropic coefficient was determined to be 2.44, which was roughly double the actual ratio of specific heats, which was 1.24 on average. From these results, we may be able to provide a more simple model of the RDC channel by simply specifying the polytropic coefficient to be twice the ratio of specific heats to save on additional computations. This modification would be saved for future efforts.

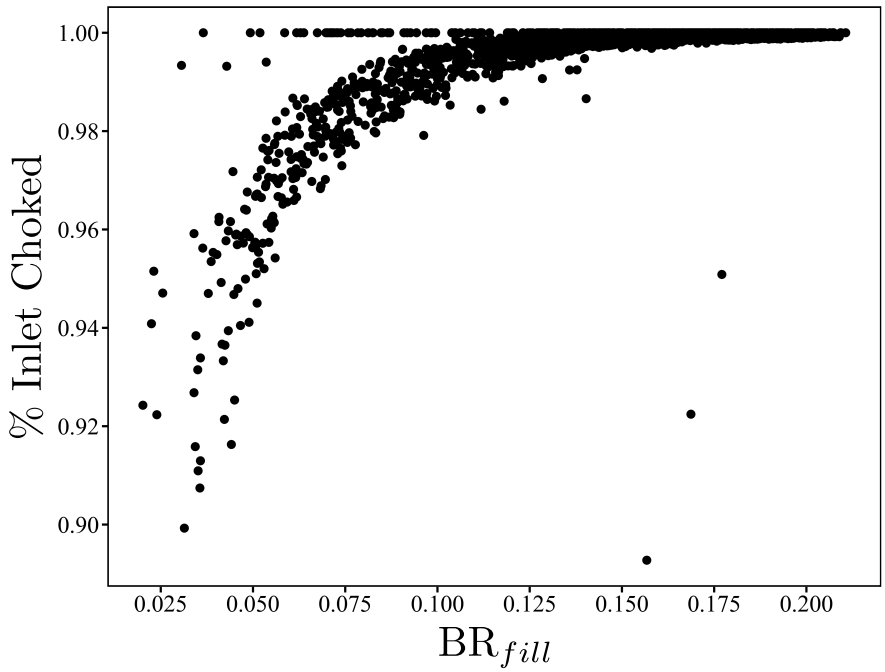


Figure 4.97: Percent of Sonic Forward Inlet Flow versus Blockage.

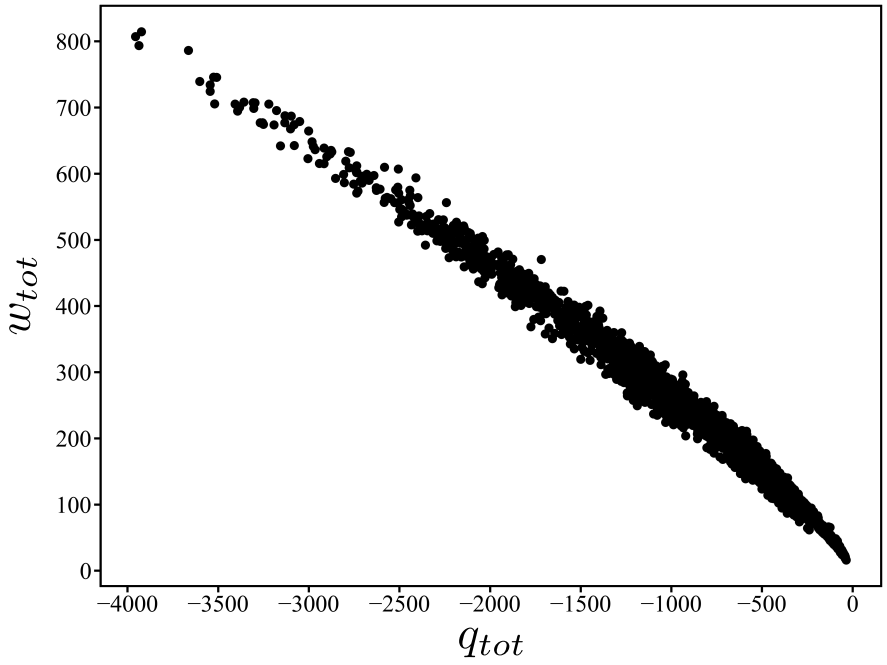


Figure 4.98: Polytropic Momentum Rate versus Energy Rate,

Next, additional trends associated with the parasitic combustion fraction are presented. Figure 4.99 shows the mass flow rate specific thrust as a function of the parasitic combustion fraction at all test points. While there are other contributing factors, this result shows that performance can be

reasonably estimated by parasitic combustion, where a higher value always resulted in a decrease in the performance of the device, a trend seen throughout this research.

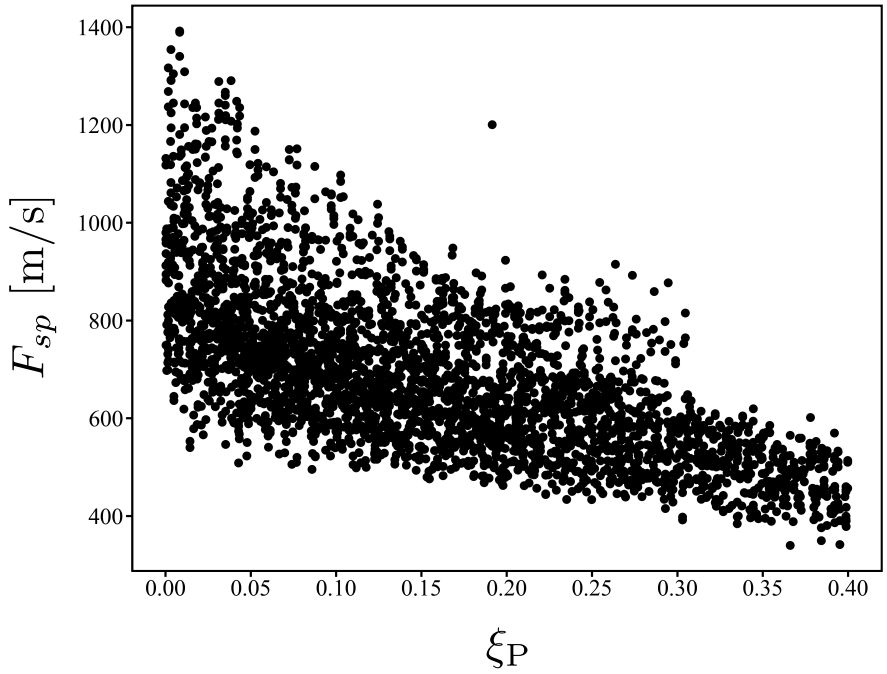


Figure 4.99: Specific Net Thrust versus Parasitic Combustion Fraction.

We can also examine the polytropic rate terms as a function of the parasitic combustion fraction, shown in Figure 4.100. These results show that at a higher parasitic combustion fraction, the rate terms asymptotically approach zero. This suggests that regardless of the performance of the detonation wave, there will be additional losses present within the cycle to allow the model to close. So, despite having a low parasitic combustion fraction, the improved performance of the detonation wave resulted in additional losses through the polytropic compression.

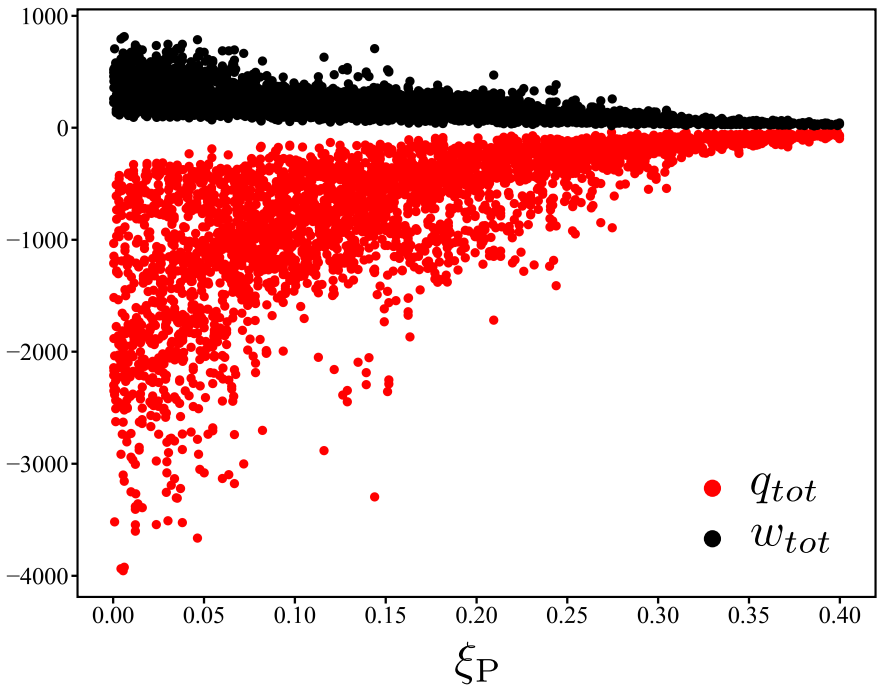


Figure 4.100: Polytropic Rate Terms versus Parasitic Combustion Fraction.

Finally, we will examine the RDC performance predictions as a function of the percentage of thrust generated by the shocked flow. This is shown in Figure 4.101, where both the specific thrust and the pressure gain increase, on average, as more flow is processed by the oblique shock. This was discussed earlier as a potential area for improvement for the model, as improper post-shock handling is likely leading to an over-prediction in RDC performance.

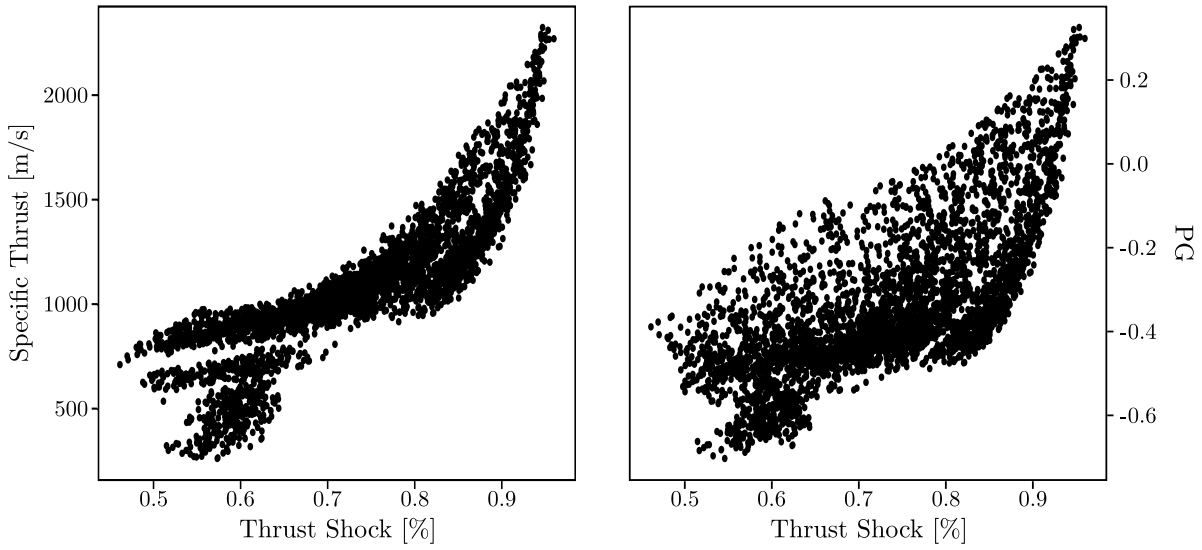


Figure 4.101: Specific Net Thrust (left) and Pressure Gain (right) versus Percent of Thrust Produced by Shocked Flow.

4.3.3 Detonation and RDC Performance

One final aspect of the parametric study was to examine the relationship between the detonation wave performance and the RDC system level performance. The following results were based on the data points from all parametric sweeps and those used in the sensitivity analysis. This was done to provide a wide range of operating conditions and RDC geometries.

The first RDC performance metric of interest was the pressure gain across the device. Figure 4.102 shows the pressure gain as a function of the laboratory wave speed (left) and the detonation pressure ratio (right). Across either detonation performance metric, the pressure gain at the RDC level remained uncorrelated. This means that according to the model, the performance of the detonation wave is not predictive of the performance of the RDC at the device level.

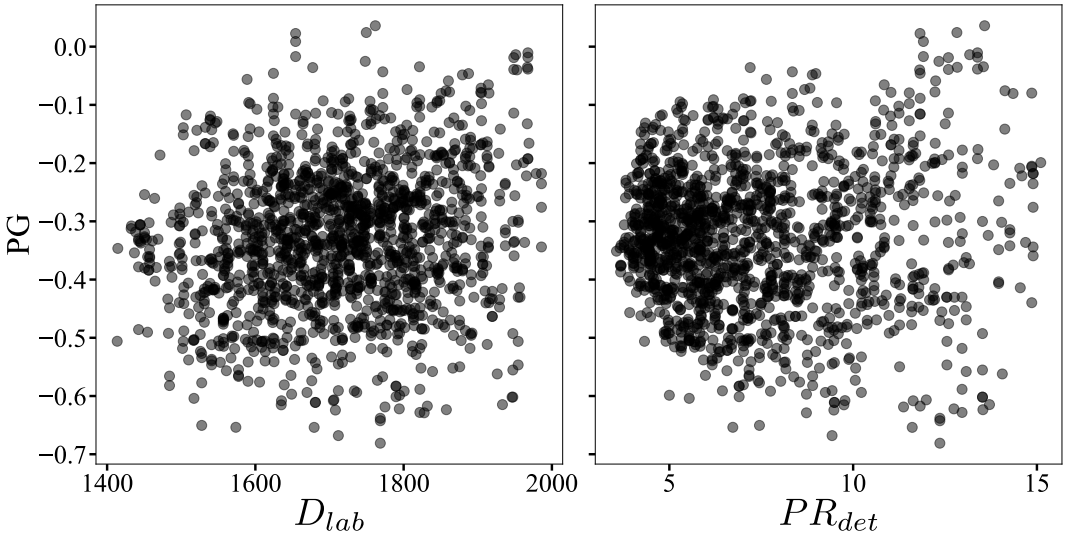


Figure 4.102: Pressure Gain as a function of wave speed and detonation pressure ratio.

The model did not show a correlation between the detonation performance and pressure gain across the device, so the question of whether any RDC level performance metric is correlated with detonation performance arose. Figure 4.103 shows that the thrust gain metric, Equation 4.32, is moderately correlated with both the wave speed (left) and the detonation pressure ratio (right). The thrust gain metric appears to be more correlated with the wave speed; however, across the wide sweep in input conditions, rarely was this metric predicted to be positive. Once again, this is not a definitive conclusion that RDC devices cannot produce a higher thrust than an equivalent deflagrative device; it is just that the model, under these input conditions, did not predict a performance increase.

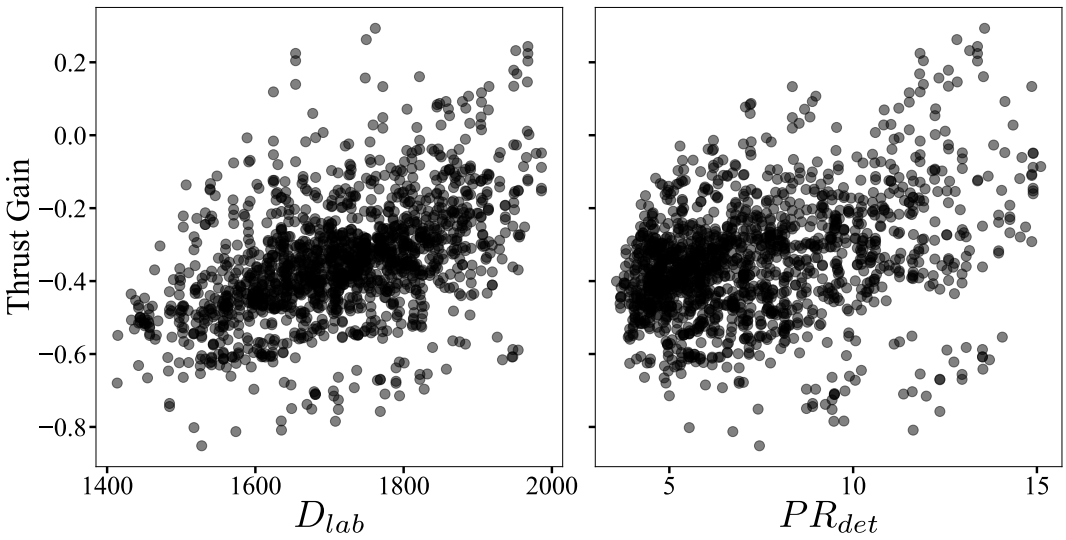


Figure 4.103: Thrust Gain as a function of wave speed and detonation pressure ratio.

4.4 Conclusion

At a high level, the presented cycle model provides the trends expected by historical data, as well as trends discovered by other sub-models. These results have shown that expected performance is affected by each input variable and how performance is correlated with different loss mechanisms throughout the flow field within an RDC. The most impactful predictor of pressure gain lies within the performance of the inlet, which is shown to be directly affected by the detonation wave. This chapter also showed a few examples of where detonation performance is not indicative of RDC-level performance metrics, specifically pressure gain. Other potentially more useful metrics, such as a thrust gain, did show some correlation with the detonation level performance metrics; however, these results still showed the majority of operating conditions would not produce this gain. These results do not lead to a definitive conclusion that the RDC device would not offer a system-level performance improvement; only this implementation of the model rarely predicts these benefits. The other aspects of RDC performance improvements, including integration within a larger system, were not studied in this research but may provide a path forward for future use cases.

Through the use of physics-based sub-model processes and the capture of unknown parameters with closure models, the present cycle model provides a more informed look at the workings within the RDC cycle but without the computational cost associated with full-scale CFD. However, this model still has some areas for improvement, which will be discussed in detail in Chapter 7. The next step for evaluating the model comes in the form of validation with an experimental dataset. This will be done in the next chapter, along with a comparison with other similar models.

Finally, a discussion on the predicted pressure gain results is in order. Other cycle models,

such as the one presented by Kaemming et al., show that a modeled positive pressure gain is the norm, where few cases fall below this value (see Figure 3.1).[4] The results presented in Figure 4.102 showed the exact opposite, where nearly every case falls below the zero value. This result is likely due to two factors. The first and most obvious is that the present model captures additional loss mechanisms that are not present in other models. The second and potentially most important reason is that the present cycle model allows product gas backflow within the inlet model. Because of this, inlet blockage becomes a much bigger driver in overall RDC performance, a novel result that is not captured by other models but is known to exist experimentally.[5]

CHAPTER 5

Non-Ideal RDC Reduced Order Cycle Model Comparison to Experimental Data

The following chapter is dedicated to the evaluation of the presented cycle model with respect to an experimental dataset. The model will be evaluated on multiple metrics, including predicted bulk flow conditions and overall device performance. After a comparison with experimental data, the model will also be evaluated with respect to other reduced order cycle models, both in terms of accuracy and model run times. Finally, this chapter will present a final conclusion on the viability of the presented model and the path forward.

5.1 Experimental Data Set for Model Evaluation

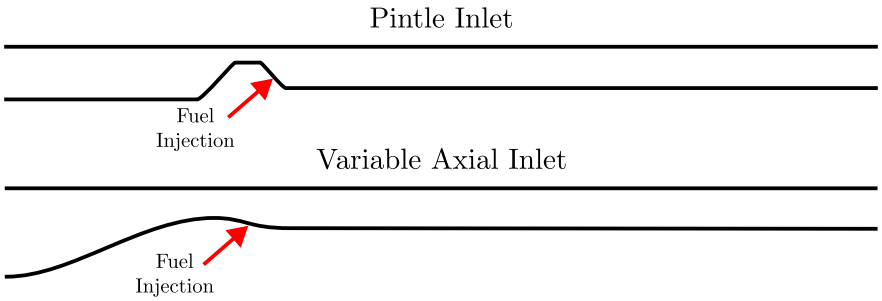


Figure 5.1: Flow Profile for Pintle and Axial Inlet Geometries

The experimental dataset for the model evaluation process was broken down into two different geometries. Figure 5.1 shows the two profiles of interest: the Pintle style injector and the variable axial inlet. The Pintle geometry consists of a more squared inlet profile, with a fixed area ratio of 4.6 between the RDC channel and the inlet throat. The variable axial inlet, features a more streamlined inlet profile and allows for the variation of the injector area while maintain self-similarity.[72] Both injector style introduce fuel downstream of the inlet minimum area, so while the effects of

fuel injection are not included in this cycle model, it may perform relatively well in terms of the inlet profile.

The dataset is binned across a few mass flow rates and equivalence ratios, with two different injector areas on the axial inlet. The mass flow rate was binned according to: $\dot{m} \in [150, 300, 500] \pm 15$ g/s, and the equivalence ratio was binned according to: $\phi \in [0.6, 0.8, 1.0] \pm 0.05$ as reasonably possible. The following sections will provide additional information regarding the dataset and provide the experimental data tables for future reference.

5.1.1 Pintle Inlet

Across the experimental data available for the Pintle style injector, Table 5.1 contains the set which fell within the previously described bins of mass flow rate and equivalence ratio. This set of test cases also featured the nozzle-less configuration because the current model lacks a variable area nozzle model. Where present, the dataset included a thrust measurement value for comparison; however, there may be questions as to the validity of these measurements as they were made before a series of corrective actions were taken at UM.[81] Nevertheless, these values provide a good starting point to determine the overall accuracy of the cycle model.

Run	$\dot{m}$ [g/s]	ϕ	P_0 [psi]	Thrust [N]	Run	$\dot{m}$ [g/s]	ϕ	P_0 [psi]	Thrust [N]
P0	143.7	1.0	20.3	165.0	P26	294.9	0.6	29.6	-
P1	149.4	0.6	21.4	-	P27	291.8	0.6	21.7	-
P2	155.4	0.6	20.8	-	P28	303.9	0.6	29.4	-
P3	164.3	0.6	21.7	-	P29	301.6	0.6	29.0	-
P4	156.3	0.6	20.7	-	P30	304.4	0.6	29.6	-
P5	155.4	0.7	21.2	-	P31	298.1	0.6	29.9	-
P6	135.7	0.6	19.3	91.9	P32	302.4	0.6	30.4	-
P7	151.3	0.8	20.7	-	P33	300.0	0.6	30.4	-
P8	145.5	0.9	21.0	-	P34	301.5	0.6	30.6	-
P9	144.1	0.9	21.0	-	P35	301.2	0.6	30.7	-
P10	141.0	0.9	20.3	-	P36	293.0	0.6	30.0	-
P11	163.3	0.9	21.9	-	P37	286.8	0.6	29.8	-
P12	136.0	0.9	19.2	126.9	P38	286.7	0.6	29.8	243.1
P13	300.9	1.0	35.0	-	P39	287.3	0.6	29.9	249.1
P14	289.2	1.0	32.4	-	P40	286.3	0.6	29.5	249.6
P15	289.1	1.0	32.1	-	P41	303.8	0.8	32.9	-
P16	287.8	1.0	32.5	386.3	P42	302.4	0.8	33.4	-
P17	288.6	1.0	32.1	398.3	P43	293.5	0.8	31.5	-
P18	288.6	1.0	32.2	385.8	P44	293.1	0.7	31.4	-
P19	289.3	1.0	32.5	373.1	P45	507.6	1.0	29.9	-
P20	289.0	1.0	32.5	371.1	P46	493.6	1.0	29.7	-
P21	285.1	1.0	32.3	-	P47	506.6	1.0	30.5	-
P22	286.2	1.0	32.4	363.5	P48	503.5	1.0	30.4	-
P23	306.2	0.6	31.5	-	P49	486.8	0.9	54.0	862.2
P24	294.1	0.6	29.5	-	P50	512.3	0.6	46.3	-
P25	298.2	0.6	29.6	-	P51	510.7	0.6	47.2	-

Table 5.1: Experimental Dataset: Pintle Inlet.

5.1.2 Axial Inlet

Next, we examine the experimental data for the variable axial inlet geometry. This dataset was much smaller because of the few test points without a nozzle configuration falling within the bin boundaries. In addition, this set of data lacks an experimental thrust measurement; however, it allows for the study of a changing inlet geometry, specifically the impact of inlet blockage. Table

5.2 shows the dataset, with the inclusion of the different area ratios that were tested.

Run	A_{ch}/A_{inj}	$\dot{m}$ [g/s]	ϕ	P_0 [psi]
A0	3.95	152.6	1.0	18.4
A1	3.95	293.7	1.0	25.3
A2	3.95	303.9	0.6	25.1
A3	3.95	306.6	0.6	25.2
A4	3.95	305.2	0.8	26.0
A5	3.95	506.4	0.9	44.3
A6	3.95	493.7	1.0	44.0
A7	3.95	493.3	1.0	41.6
A8	3.95	494.1	1.0	40.7
A9	3.95	495.6	0.6	37.5
A10	3.95	496.9	0.6	38.0
A11	3.95	496.2	0.6	38.6
A12	3.95	495.6	0.6	38.5
A13	3.95	494.9	0.6	38.8
A14	3.07	498.1	0.5	33.6
A15	3.07	504.5	0.5	33.8
A16	3.07	506.5	0.8	34.3

Table 5.2: Experimental Dataset: Axial Inlet.

5.2 Results

This section will discuss the results of the model evaluation with respect to both the experimental datasets and other similar models. First, a discussion of the model accuracy versus the experimental data will be presented, followed up with an evaluation with respect to three other reduced order models. Across all models, an ideal detonation wave was used as the input condition, which means that no additional losses due to deflagration or lateral relief were included.

For model timing evaluations, all cycle models were evaluated on a single-tread basis using an Intel i7-12700H mobile CPU. Due to CPU clock speed and architecture differences across potential users of this model, the times should be used as a qualitative metric to get trends of expected evaluation times. It should also be noted that these models were evaluated in their native programming language, which will have significant impacts on the cycle evaluation timing for each model.

5.2.1 Comparison with Experimental Data

The comparison of the experimental data sets will also be broken down by injector geometry, where each section will feature a more in-depth analysis of the performance metrics that are more relevant to the given geometry. For example, the thrust comparison will only be conducted for the Pintle style inlet due to the lack of thrust measurement for the axial flow configuration.

5.2.1.1 Pintle Inlet

Table 5.3 shows the comparison of the model results with the experimental dataset in Table 5.1. The model was solved using an ideal detonation wave with no heat or friction losses outside of those predicted by the polytropic compression algorithm. The subscript, e, refers to experimental measurements, and the subscript, m, refers to model results. This table focuses on the mass flow rate and total plenum pressure for each case. In general, all cases converged on the experimental mass flow rate to the specified tolerance. For cases with a mass flow rate around 300 g/s, the total plenum pressure was predicted within 10% error; however, at low mass flow rates, the errors grew much larger. This can be attributed to poorly capturing the sub-critical inlet mass flow rates. The model tends to enforce a choked inlet condition for the inlet mass flow model, even at low pressure ratios. This is likely not the case at the lower mass flow rates and inlet blockage at lower flow rates, meaning that the model would over-predict the forward-flowing reactant mass flow rate at a given pressure. Future improvements to the model will focus on revising the inlet model to close the gap between the measurements and model results.

At higher mass flow rates, we must be careful to fully analyze the experimental data set. For example, runs P45-P48 all show an abnormally low experimental plenum pressure. Ignoring these cases, the model does a much better job of predicting the plenum pressure at high mass flow rates; however, it still deviates outside of the 10% error bounds for some cases.

Run	$\dot{m}_e$	$\dot{m}_m$	% $\dot{m}$	$P_{0,e}$	$P_{0,m}$	% P_0	Run	$\dot{m}_e$	$\dot{m}_m$	% $\dot{m}$	$P_{0,e}$	$P_{0,m}$	% P_0
P0*	144	145	1.1	20.3	15.3	-24.4	P26	295	297	0.6	29.6	31.1	5.1
P1*	150	151	1.1	21.4	15.7	-26.6	P27	292	294	0.6	21.7	30.9	42.4
P2*	155	157	1.1	20.8	16.3	-21.7	P28	304	306	0.6	29.4	31.9	8.5
P3*	164	166	1.0	21.7	17.3	-20.5	P29	302	303	0.5	29.0	31.6	9.0
P4*	156	158	1.1	20.7	16.4	-21.1	P30	304	306	0.6	29.6	31.9	7.7
P5*	155	157	1.1	21.2	16.4	-22.6	P31	298	300	0.6	29.9	30.9	3.3
P6*	136	132	-3.0	19.3	14.9	-22.9	P32	302	304	0.5	30.4	31.3	3.0
P7*	151	153	1.1	20.7	16.1	-22.4	P33	300	302	0.6	30.4	31.1	2.2
P8*	146	147	1.2	21.0	15.5	-26.2	P34	302	303	0.6	30.6	31.3	2.0
P9*	144	146	1.1	21.0	15.3	-26.8	P35	301	303	0.6	30.7	31.2	1.8
P10*	141	143	1.2	20.3	15.0	-26.1	P36	293	295	0.6	30.0	30.5	1.6
P11*	163	165	1.0	21.9	17.3	-20.7	P37	287	289	0.6	29.8	29.9	0.3
P12*	136	132	-2.7	19.2	14.9	-22.6	P38	287	288	0.6	29.8	29.8	0.1
P13	301	303	0.5	35.0	31.8	-9.1	P39	287	289	0.6	29.9	29.9	-0.2
P14	289	291	0.6	32.4	30.6	-5.5	P40	286	288	0.6	29.5	29.8	0.7
P15	289	291	0.6	32.1	30.6	-4.7	P41	304	306	0.5	32.9	32.0	-2.8
P16	288	290	0.6	32.5	30.5	-6.3	P42	302	304	0.6	33.4	31.8	-4.8
P17	289	290	0.6	32.1	30.5	-5.0	P43	294	295	0.6	31.5	30.9	-1.8
P18	289	290	0.6	32.2	30.6	-5.1	P44	293	295	0.6	31.4	30.7	-2.2
P19	289	291	0.6	32.5	30.8	-5.4	P45-	508	509	0.3	29.9	54.1	81.0
P20	289	291	0.5	32.5	30.7	-5.5	P46-	494	495	0.3	29.7	52.5	77.1
P21	285	287	0.6	32.3	30.3	-6.1	P47-	507	506	-0.1	30.5	55.2	80.8
P22	286	288	0.5	32.4	30.4	-6.0	P48-	504	503	-0.1	30.4	55.0	80.7
P23	306	308	0.5	31.5	31.7	0.9	P49	487	489	0.4	54.0	50.8	-5.8
P24	294	296	0.6	29.5	31.0	5.0	P50	512	514	0.3	46.3	52.7	13.8
P25	298	300	0.6	29.6	31.3	6.0	P51	511	512	0.3	47.2	53.3	13.0

Table 5.3: Experimental Comparison: Mass flow and plenum total pressure.
*: did not converge, -: measurement error

Next, we will examine the experimental thrust and blockage measurements, shown in Table 5.4. The experimental thrust value shown is a net thrust measurement; however, as discussed before, these values may not be truly indicative of the actual RDC performance due to issues with the experimental setup. In cases with a blockage measurement, this was calculated using the method presented by Feleo et al., where the mass flow rate during operation was compared with the cold flow mass flow rate at the same plenum pressure.[5] For the model results, the thrust value was

the modeled net thrust, accounting for plenum inflow conditions, while the blockage ratio was calculated based on the location at which the reactants begin forward flow through the inlet.

In general, the model does a subpar job of predicting the performance of RDC at lower mass flow rates. This has been a continuous trend across all the analyses at low mass flow rates but is particularly poor here. The thrust was highly over-predicted, and the blockage was severely under-predicted at the low flow rate conditions. As we move to more moderate mass flow rates, both the blockage and thrust estimates from the model more closely follow the experimental measurement, where the thrust fell within $\pm$ 20% of the experimental value. At the highest flow rate condition, the thrust was predicted to be half of that of the experimental measurement; however, care should be taken to recognize that the higher mass flow rates were likely more susceptible to measuring a higher thrust value due to additional seal pressurization issues with the test setup.

Run	F_e	F_m	$\% F$	BR_e	BR_m	$\% BR$
P0*	165.0	300.5	82.2	-	0.201	-
P4*	-	291.6	-	0.343	0.186	-45.6
P5*	-	295.8	-	0.368	0.191	-48.0
P6*	91.9	300.5	227.0	-	0.193	-
P12*	126.9	304.9	140.2	-	0.2	-
P15	-	328.2	-	0.237	0.198	-16.3
P16	386.3	327.4	-15.3	-	0.199	-
P17	398.3	325.5	-18.3	-	0.198	-
P18	385.8	327.9	-15.0	-	0.2	-
P19	373.1	330.0	-11.5	-	0.202	-
P20	371.1	327.9	-11.6	-	0.201	-
P22	363.5	330.6	-9.0	-	0.203	-
P37	-	294.3	-	0.185	0.185	0.1
P38	243.1	291.3	19.8	-	0.183	-
P39	249.1	291.5	17.1	-	0.184	-
P40	249.6	291.2	16.6	-	0.184	-
P49	862.2	457.5	-46.9	-	0.19	-

Table 5.4: Experimental Comparison: Thrust and blockage.

In general, the model does a good job of predicting the bulk flow and cycle performance at a moderate flow rate condition. However, the model struggles to predict either at the lower mass flow rates. This has been discussed in detail multiple times and is a key point of improvement for future models.

5.2.1.2 Axial Inlet

For the axial inlet, the model does better in predicting the bulk flow conditions. These results are shown in Table 5.5. Even at the lowest mass flow rate used in this dataset, the model better predicts the plenum pressure relative to the Pintle inlet results. It still under-predicts the plenum pressure required to drive the mass flow rate, likely due to the aforementioned struggles with sub-critical flow within the inlet profile.

Run	A_{ch}/A_{inj}	$\dot{m}_e$	$\dot{m}_m$	% $\dot{m}$	$P_{0,e}$	$P_{0,m}$	% P_0
A0*	3.95	152.6	150.4	-1.4	18.44	16.05	-12.9
A1	3.95	293.7	292.5	-0.4	25.31	24.18	-4.4
A2	3.95	303.9	303.2	-0.2	25.05	23.83	-4.9
A3	3.95	306.6	305.7	-0.3	25.16	24.01	-4.6
A4	3.95	305.2	304.4	-0.3	25.95	24.32	-6.3
A5	3.95	506.4	505.8	-0.1	44.26	40.31	-8.9
A6	3.95	493.7	493.0	-0.1	44.0	39.34	-10.6
A7	3.95	493.3	492.5	-0.2	41.6	39.3	-5.5
A8	3.95	494.1	493.4	-0.1	40.66	39.37	-3.2
A9	3.95	495.6	494.6	-0.2	37.49	38.36	2.3
A10	3.95	496.9	496.0	-0.2	38.03	38.45	1.1
A11	3.95	496.2	495.2	-0.2	38.55	38.39	-0.4
A12	3.95	495.6	494.6	-0.2	38.49	38.33	-0.4
A13	3.95	494.9	494.1	-0.2	38.81	38.28	-1.4
A14	3.07	498.1	497.1	-0.2	33.58	33.12	-1.4
A15	3.07	504.5	503.5	-0.2	33.78	33.33	-1.3
A16	3.07	506.5	505.6	-0.2	34.25	33.59	-1.9

Table 5.5: Experimental Comparison: Mass flow and plenum total pressure.
*: model non-convergence

On the performance side, the only metric of interest available for analysis on the axial injector was the inlet blockage. At moderate flow rates, around 300 g/s, the model predicts blockage to within 10% for most cases. At larger mass flow rates for the more restrictive inlet and all cases with the more open inlet, the model over-predicts the blockage. This could be explained partially by the use of the ideal detonation assumption when running the model cases. It is likely that there are deflagration losses present, which may better align the over-predictions in blockage.

Run	A_{ch}/A_{inj}	BR_e	BR_m	$\%\ BR$
A2	3.95	0.224	0.242	8.1
A3	3.95	0.221	0.242	9.5
A4	3.95	0.248	0.254	2.4
A5	3.95	0.277	0.253	-8.9
A6	3.95	0.291	0.254	-12.9
A7	3.95	0.251	0.254	1.0
A8	3.95	0.232	0.254	9.1
A9	3.95	0.162	0.232	42.9
A10	3.95	0.173	0.232	34.1
A11	3.95	0.185	0.232	25.0
A12	3.95	0.185	0.232	25.1
A13	3.95	0.193	0.231	19.7
A14	3.07	0.263	0.299	13.7
A15	3.07	0.258	0.295	14.4
A16	3.07	0.265	0.298	12.1

Table 5.6: Experimental Comparison Axial: Blockage.

5.2.1.3 Summary of Experimental Comparison

Finally, a few loss metrics were defined to capture model errors in the mass flow rate, plenum pressure, thrust, and blockage. Equation 5.1 shows a linear loss metric, which adds the percent errors for each metric together, while Equation 5.2 shows the other loss metric based on the root mean square errors of the percent difference. For each metric, if the experimental data did not include either the thrust value or the blockage value, the loss metric was ignored as it would skew the data towards a better performing model.

$$\mathcal{L}_{Lin} = \sum_{i=0}^{k} \left| \frac{x_i - \mathbf{x}}{\mathbf{x}} \right| \tag{5.1}$$

$$\mathcal{L}_{RMS} = \left(\frac{1}{k} \sum_{i=0}^{k} \left(\frac{x_i - \mathbf{x}}{\mathbf{x}} \right)^2 \right)^{\frac{1}{2}} \tag{5.2}$$

where x_i represents the modeled value in [mass flow rate, plenum pressure, thrust, blockage], and $\mathbf{x}$ represents the experimental data. The reason for including both the mass flow rate and the plenum pressure in the loss metric is twofold. First, for the present model, this term can capture non-convergence by accounting for the mass flow rate difference from the specified value. The

second reason will become more evident in the comparison with other models, but is due to the method of convergence. For example, the present model iterates to a target mass flow rate, allowing the plenum pressure to flow. Other models may use the plenum pressure as the target variable, allowing the mass flow rate to float. Including both in the loss metrics allows for differences in iteration variables without skewing the results.

With these loss metrics, Figure 5.2 was created, showing the loss metrics as a function of the mass flow rate (a) and the plenum pressure (b). As expected from previous discussions, the model does a poor job at low mass flow rates and low plenum pressure. As the mass flow increases, and similarly, the plenum pressure, the model does a much better job across the board. This loss metric will be of more use when comparing different models, which will be discussed in the next section.

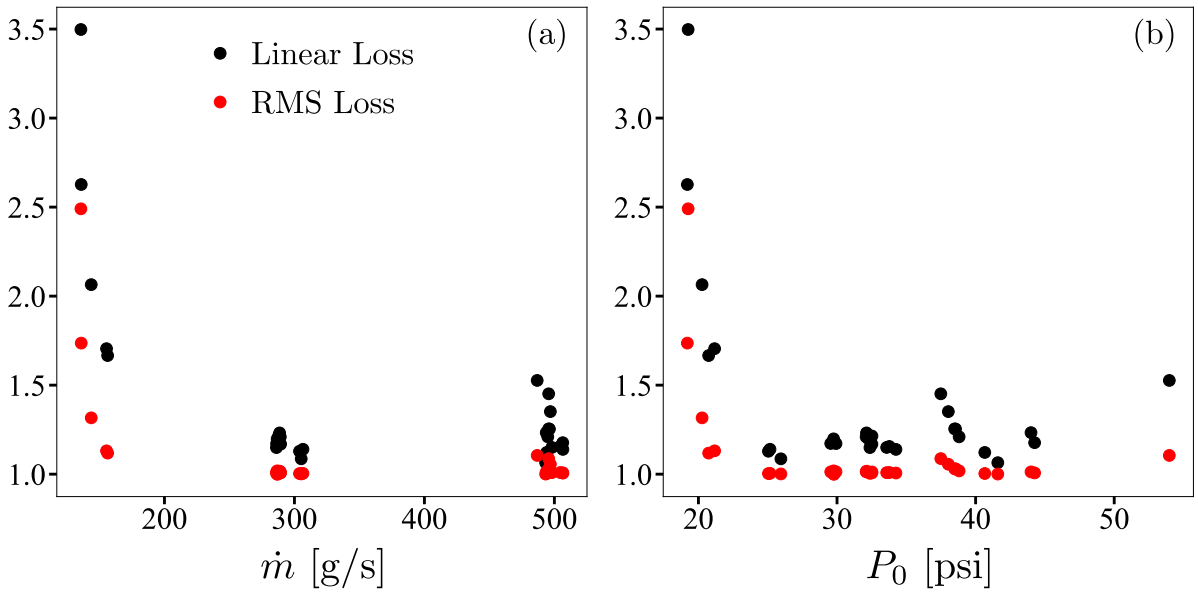


Figure 5.2: Scatter of the Loss Metric as a Function of Mass Flow Rate (a) and Plenum Pressure (b).

In terms of the predictive performance of the model, it is generally in agreement with experimental data at moderate mass flow rates (to within 10%) across a few different geometric configurations. It does a slightly worse job at predicting performance at higher mass flow rates and has the highest discrepancy at low mass flow rates. Many of these results could be improved with a better inlet model that handles sub-critical flows in a more accurate manner. Also, the inclusion of non-ideal detonation effects may move the model results closer to reality.

5.2.2 Comparison with Other Cycle Models

The following results show how the present cycle model performs versus three other reduced order cycle models. This is both in terms of accuracy with respect to experimental data and with regard to the model evaluation time. The following models, shown in Table 5.7, were used as comparison points: the RDC Cycle Model from Kaemming et al.[29], the RDC Blowdown Model from Paxson[30] and the 2-D MOC Model from Fievisohn[31]. Each model was exercised on the dataset shown in Table 5.8 to assess predictive performance and model evaluation time. Where possible, an additional number of model evaluations was conducted at each test point to gather information on the variability of the model evaluation time.

Model Name	Author	Year	Programming Language	Target Metric
Present	Huff	2024	Rust + Python	Inlet Mass Flow
RDC Model	Kaemming	2017	*VBA/Matlab/Mojo	Plenum Pressure
RDC Blowdown Model	Paxson	2021	VBA/*Matlab	Plenum Pressure
2-D MOC Model	Fievisohn	2017	Python	Plenum Pressure

Table 5.7: Reduced Order RDC Cycle Models. * indicates which version was used.

For the RDC Cycle Model, results were collected using an Excel spreadsheet formulation of the model, relying on the VBA programming language, in the origin author's evaluation condition. This effectively increases model evaluation times by over 100x when compared to other programming languages, which will be discussed in detail later. The model was evaluated with the standard input configuration, where the measured air and fuel plenum pressures were the input provided from experimental data. Other inputs include the forward and reverse discharge coefficient, set at 1.0 and 0.8, respectively, and the detonation lateral relief parameter, which was set at 1.0; that is, there was no area change within the detonation. Notably, the model has also been translated into other languages, such as Matlab. This implementation is around 3-5x faster than the VBA version; however, the Matlab version was less stable on the provided experiment dataset. This model takes the plenum pressure as input and iterates on the channel pressure that results in matched inlet and exit mass flow rates, given the plenum and ambient conditions.

For the RDC Blowdown Model, a VBA script and Matlab implementation were available. The results shown here were captured with the Matlab version, as it provided the short evaluation times. This model was originally developed for rocket-style RDC devices but was evaluated on the hydrogen-air mixture presented in the research. It takes the plenum pressure as input and iterates until convergence is achieved in the blowdown model with the RDC channel. This model also includes an injector pressure loss term, which was used to iteratively determine the injector

pressure losses that resulted in a match in both the plenum pressure and mass flow rate for a given experimental run. Though this value would not be known ahead of time, this is the only model that can be massaged to match both the flow rate and plenum pressure given experimental conditions.

Finally, the 2-D MOC Model features a full method of characteristic solution of the RDC channel flow. This model implements an inlet sub-model, which does not include backflowing product gases, used to initialize the flow path. It also iterates based on the input plenum pressure term, and for the present research, it was limited to 10 iterations before exiting the solution loop. Though this program was written in Python, the model uses the *Numba* just-in-time (JIT) compiler to convert performance-heavy functions to a compiled version of C code. This drastically improved the speed of the model at the expense of requiring additional time to compile the first time a function is called.

As mentioned above, Table 5.8 contains a subset of the experimental Pintle data that best matched the bin points and had the available data for comparison between the models. In cases marked with *, the next closest matching experimental case was used to provide values if needed. The accuracy of each model was evaluated by how well it matched the thrust, pressure gain, and blockage of the experimental data. It also included an evaluation of either the mass flow rate or plenum pressure, depending on which was not specified as an input condition. Finally, at each data point, the loss metrics from Equation 5.1 and Equation 5.2 were also calculated.

Run	$\dot{m}$ [g/s]	ϕ	P_0 [psi]	Thrust [N]	PG	Blockage
P0	143.7	1.0	20.3	165.0	-0.155	*0.386
P6	135.7	0.6	19.3	91.9	-0.233	*0.368
P7	151.3	0.8	20.7	*126.9	*-0.188	*0.390
P20	289.0	1.0	32.5	371.1	-0.264	*0.237
P40	286.3	0.6	29.5	249.6	-0.328	*0.185
P41	303.8	0.8	32.9	*295.9	*-0.306	*0.221
P49	486.8	0.9	54.0	862.2	-0.257	-

Table 5.8: Sample Dataset for Model Comparison Study. *: next closest point estimate

5.2.2.1 Timing

This section will discuss the timing characteristic of each model, as well as some details on what a more apples-to-apples comparison would look like for each. Figure 5.3 presents the evaluation times for each model across all experimental cases. The y-axis is plotted at the cycle evaluation time in seconds and on a logarithmic scale. From this plot, it is clear that the present cycle model provided a drastic speed-up in model evaluation times. For nearly all test cases in this small subset,

the present model achieves convergence within the 100 ms target evaluation time.

Across the board, the RDC Cycle model from Kaemming et al. took the longest to evaluate, which was expected due to the programming language of choice. Even using the Matlab implementation of the code, the times would only fall around those calculated for the 2-D MOC model of 1-2 minutes; however, a brief attempt was conducted to try to improve the performance of the RDC Cycle model by using a compiled language. Although the compiled implementation only worked for a handful of test cases, it reduced the evaluation times to 2-10 seconds. This time falls around that required to evaluate the RDC Blowdown model, which converged in 1-2 seconds across all cases.

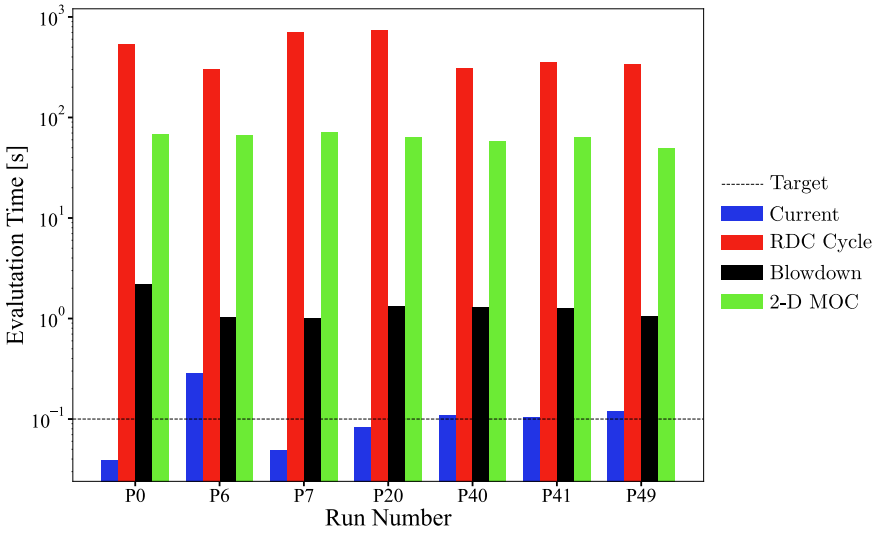


Figure 5.3: Model Evaluation: Times for all Test Points

Although the evaluation times for each model do not compare the same programming language, they present the models as they are currently available. A better comparison would be to have each model developed and optimized in the same programming language across the board; however, this is a tedious task that was not feasible for this research effort. The main takeaway from this analysis is that the present cycle model achieved the target evaluation time and provides a currently available version of a RDC cycle model that can be reasonably used in Monte Carlo based analysis elsewhere

5.2.2.2 Accuracy

The last point of comparison for the presented model is the comparison in accuracy versus the other models. We will first break this down into individual losses in Figure 5.4, which shows the percent errors in the non-specified iteration variable (a), net thrust (b), pressure gain (c), and blockage (d).

From the iteration error perspective, only the RDC Blowdown model does a good job of matching the non-specified value (in this case, mass flow rate). This was discussed previously, but the RDC Blowdown model can be tuned to match both plenum pressure and mass flow by adjusting the injector pressure losses, which was done for these test cases. As the flow rate and plenum pressure increase, all models begin to perform much better (less than 10% error) at predicting the mass flow rate or plenum pressure.

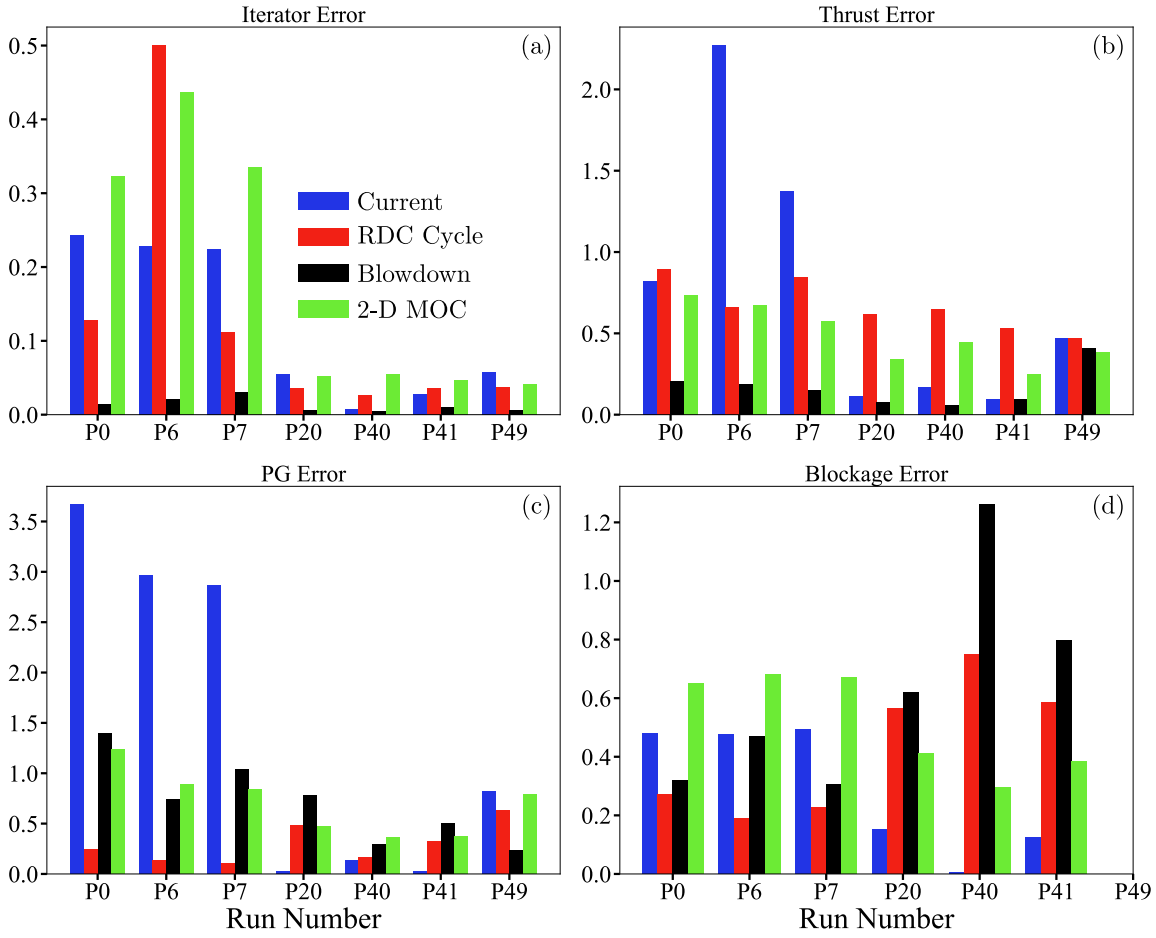


Figure 5.4: Model Evaluation: Percent Errors for all Test Points

For the thrust metric, at the lower flow rates, the present cycle does a much worse job of predicting the RDC thrust; however, at these flow rates only the RDC Cycle model predicts the thrust within the 50% error. This is likely due to the exact matching in the plenum pressure and mass flow rate discussed above. As the flow rates and plenum pressure increase, the present cycle model performs much better and is in line with the RDC Cycle model.

Because the present cycle model predicts the pressure gain based on the thrust value, it again struggles the most at low flow rates, with nearly 370% errors in the worst case. Keep in mind

that the pressure gain metrics are typically small in magnitude, which can create large swings in percent error. Once again, as the flow rates increase, the present model improves significantly and produces the lowest error at moderate flow rates.

Finally, the blockage percent error was calculated for all models. In general, the present model predicts blockage roughly as well as the other models at low flow rates and becomes a much better predictor of blockage at moderate flow rates.

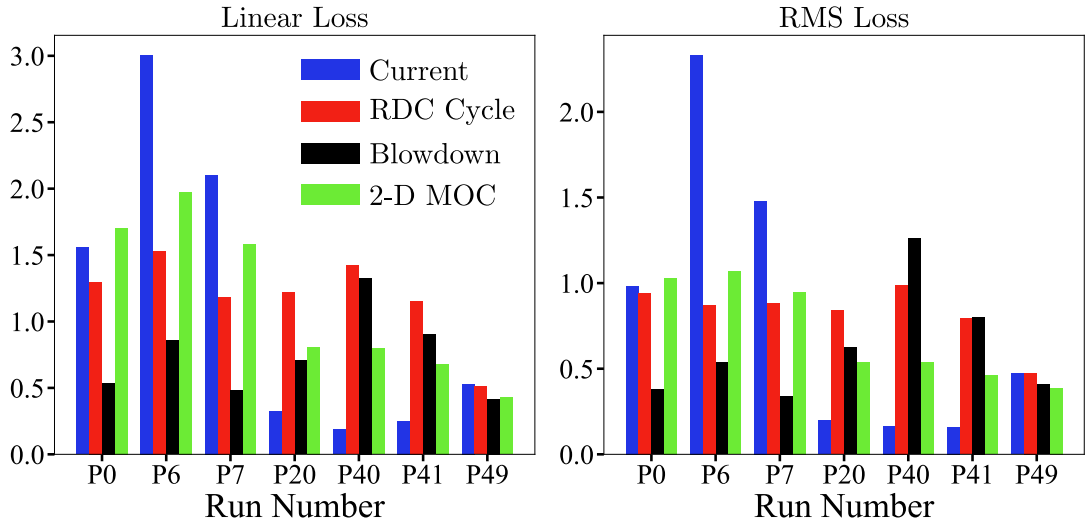


Figure 5.5: Model Evaluation: Loss Metrics for all Test Points

To wrap up the comparison of the accuracy of the model, the loss metrics based on a linear combination of losses, as well as the RMS loss, are presented for each cycle in Figure 5.5. This plot shows the linear loss metric from Equation 5.1 of the left and the RMS loss from Equation 5.2, based on the mass flow rate, plenum pressure, thrust, and blockage. At low mass flow rate conditions, the present mode is clearly worse, but at moderate flow rates, the accuracy improves dramatically. This is the final example showing how much the present model would benefit from improved modeling of the inlet at low mass flow rates. In addition, the potential inclusion of detonation losses, such as parasitic combustion, as a function of the inlet blockage might improve the inlet model, especially under low flow rate conditions.

Finally, Figure 5.6 shows the loss metrics as a function of the cycle evaluation times for each model. The present model has a wide variance in the loss metrics, which is to be expected from the numerous simplifying assumptions and modeling choices that led to the reduction in the evaluation time. It was discussed previously, but the RDC Cycle model from Kaemming et al. was also translated into a compiled programming language. This left the model much less stable but did improve evaluation times. The gray box in Figure 5.6 shows the range of evaluation times that were

achieved with the translated version of the code, which shows the improvements in the evaluation time that can be made by selecting a proper modeling language. It also shows that the presented model is still 20-100x faster than the translated RDC Cycle model, providing credence to the claim that the present model is still providing a much faster model that allows for Monte Carlo analysis.

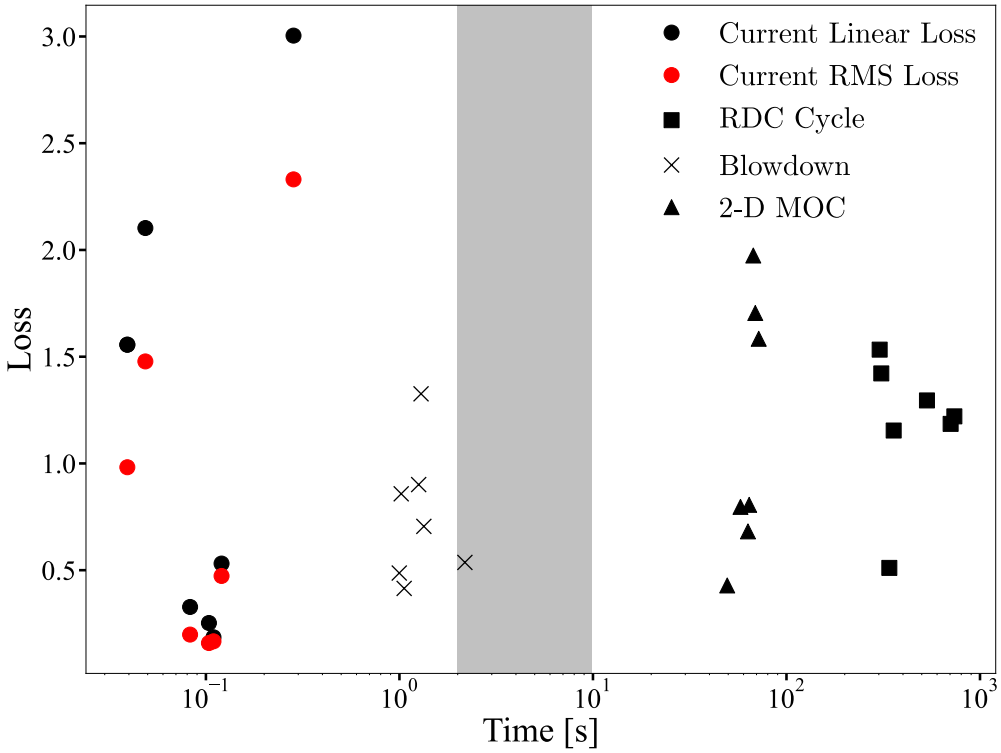


Figure 5.6: Model Evaluation: Times versus Losses for all Models

5.3 Conclusion

This chapter evaluated the performance of the presented cycle model versus an experimental dataset and against similar RDC cycle models. For the experimental comparison, the present cycle model provides an accurate prediction of plenum pressure (less than 10% error) and inlet blockage (below 17% error) for moderate flow rate cases (around 300 g/s). As discussed in the previous chapter, the model provides a low accuracy at low mass flow rates and low plenum pressures, less than 175 g/s and 22 psi, respectively. This was also the case during the comparison with other cycle models at low mass flow rates, where the present model incurred up to an 11x increase in error relative to other models. The model showed low accuracy in predicting the thrust value at the loss mass flow rates, with up to 220% errors. However, we discussed that there may also be issues with the measurement values for thrust as well as issues with the current post-oblique shock processing for the model.

Compared to other models, the present model incurs a 2-4x increase in error predicting performance at lower mass flow rates; however, at moderate flow rates (above 200 g/s), the present model provides a 1-6x improvement over other models in its ability to predict operating conditions and performance. This was also reflected in the loss metrics defined in this chapter.

Finally, the cycle model outperforms all other models significantly in terms of evaluation times. It was between 10-10000 times faster than the other models on average; however, we must take into account the programming languages used to evaluate the other models. If all the models were coded in the same compiled language used for the present model, this drastic improvement in evaluation time would likely decrease.

Overall, this model achieves what it was set out to do, providing a reasonably accurate (10% error or less) cycle model that reduces evaluation times in a manner where the model can be used in Monte Carlo based evaluation tools in the future. For the most part, the model can predict operation conditions accurately, though some additional improvement is required to better predict performance at low mass flow rates and low plenum pressures. The target evaluation time of 100 ms was achieved on average across multiple parametric studies. Additional optimization of the code and improvements on the initial guess could also improve these times.

CHAPTER 6

Is ”Gain” Achievable in a Detonation-Based Cycle?

This chapter is dedicated to the discussion around ”gain” within a detonation-based cycle. In this sense, ”gain” will simply be defined as a performance benefit over conventional cycles. We need to carefully define the ”gain” depending on the application process instead of relying on pressure gain as the sole metric of RDC performance. Despite this last statement, the pressure gain is exactly where we begin with this analysis before moving on to other, potentially more realizable, ”gain” metrics.

6.1 Pressure Gain

When a detonation is analyzed using the CJ or ZND (one-dimensional) framework, a detonation-level pressure gain is demonstrably achieved. Once again, we must be careful in applying this pressure gain definition to applications of detonation combustion as a result of the change in boundary conditions for the detonation wave. We will examine the PDC and RDC applications to discuss reasons why pressure gain may not be a good definition of performance, first focusing on PDCs.

Depending on the time frame used to analyze a PDC cycle, a pressure gain can be demonstrated within the device. For example, measuring the pressure within the PDC chamber starting just after the fresh reactants are injected to the point at which the detonation wave reaches the end of the PDC tube will result in an overall cycle pressure gain. This is similar to looking at a detonation tube or even a CJ/ZND analysis. However, creating an operational PDC device requires additional steps outside of just the detonation wave listed below:

- Fresh reactants require a fill time to reach the end of the tube
- Post-detonation products require an exhaust time to completely exit the PDC, but at an increasingly lower average chamber pressure
- Hot products will initiate deflagrative combustion of the fresh reactant, so a non-reactive purge is required within the cycle

For these reasons, using a cycle average chamber pressure as the numerator, Equation 6.1, will result in a decreased pressure gain and, more likely, a pressure loss relative to the plenum pressure.

$$PG_{\mathrm{PDC}} = \frac{\bar{P}_{chamber}}{P_{plen}} - 1 \tag{6.1}$$

In terms of pressure gain within an RDC, in an air-breathing RDC the inlet plays a critical role in the pressure gain equation. Unlike a typical PDC, the typical RDC device has its plenum exposed directly to the detonation channel. As discussed in Section 3.2.1, the detonation wave directly influences the blockage profile across the inlet, resulting in an increased plenum pressure requirement to drive the same mass flow rate through the inlet. This essentially increases the denominator of the pressure gain equation:

$$PG = \frac{P_{t,8}}{P_{t,3}} - 1 \tag{6.2}$$

It stands to reason that for any increase in detonation performance, specifically the detonation wave pressure ratio, a roughly equal increase in plenum pressure would be required to offset the increase in inlet blockage. In addition to the inlet losses, additional loss mechanisms exist within the RDC device, which would lower the numerator in the pressure gain equation. Appendix A derives pressure gain for RDCs in a more robust manner, tying the processes within an RDC to different region-specific pressure gain or loss.

As for the description of PDCs and RDCs as pressure gain devices, this is technically, but not necessarily correct. From the cycle average pressure gain side, this is likely an incorrect description due to the issues discussed above and the results from the presented RDC cycle model. However, if we look at the detonation wave alone, it does achieve a pressure gain. On the micro scale, at some point within the cycle, a pressure gain is achieved, but on the macro scale, an average pressure gain may not be realized.

Similarly to experimental data, the cycle model presented in this research predicts many of the performance relationships for RDC devices. Figure 6.1 shows the pressure gain metric as a function of the inlet mass flux. We see the same trend: pressure gain is predicted to be negative and to scale inversely to the inlet mass flux. As we have discussed throughout this research, a low inlet flux will result in a less stiff inlet plane, which in turn improves the channel static pressure relative to the plenum pressure. This scaling is troublesome because one of the projected benefits of RDC devices is the high energy density provided by their successful operability at high mass flux conditions.

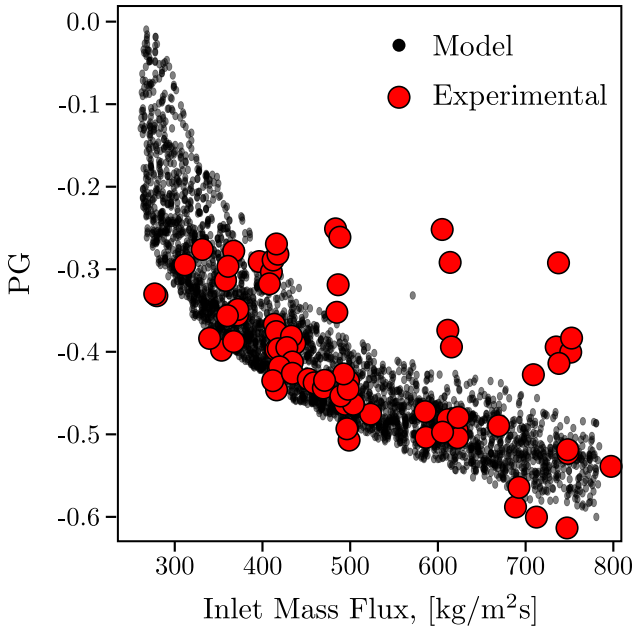


Figure 6.1: Modeled Pressure Gain versus Inlet Mass Flux with Experimental Results.

If an average cycle level pressure gain is not achievable, there are steps that can be taken to at least reduce the pressure losses within the RDC device. This is specific to the inlet of the RDC as it offers a target of opportunity due to the coupling with the detonation wave. Ideally, a valved inlet system would be implemented that tracks the detonation location (actively or passively), reducing the backflow effects from the detonation wave. It would not have as drastic an impact on the inlet blockage, as this device would actively block forward flow in the regions where backflow would exist; however, this could improve the lateral relief aspect of the detonation wave on the furthest upstream side, improving detonation performance without the associated reduction in inlet performance. Essentially, this device would fix the denominator of the pressure gain equation at a slightly higher value while potentially improving the numerator to a greater extent.

Any implementation of this methodology would need to operate at the high frequencies seen within the RDC cycle, be robust against the high-pressure and high-temperature region within the detonation wave, and account for any operation changes within the RDC, specifically changes in wave number and wave speed. This is a great challenge for any valve-based system, so the more likely approach is to improve the backflow resistance of the inlet in a passive manner without significantly reducing the forward flow resistance.

This concept has been termed diodicity and describes inlets that have a different performance, c_d, value depending on the flow direction.[59] These would be fixed, valveless inlet geometries that would mitigate the backflow characteristic on the inlet (see Section 4.3.2.6). This device would likely be designed in some trade-space of diodicity value and machining feasibility, and it will face

similar challenges to a valved system in terms of high pressure and heat loads in the detonation region. The issue with this device and similar designs, in addition to manufacturability, is the reduction in the forward flow performance. Despite a reduction in the backflow from the detonation wave, reducing the forward flow inlet performance will also negatively affect the pressure ratio across the device. The initial results from previous research that considered the effect of diodicity predicted improvements in performance (see Section 4.3.2.6); however, this is still an area of active investigation and more research is required.

Outside of pressure gain, these devices may offer other benefits at the cycle level. The following sections will discuss these metrics and their potential to be achieved in detonation-based applications.

6.2 Additional Thrust Production

The first metric outside pressure gain where RDC may offer a benefit over deflagrative devices is thrust production. The State to State Model from Section 3.3.1 provided a simple model for the thrust, or specific impulse, production of the RDC compared to an ideal deflagrative device operating at the same inlet conditions. In certain cases, the RDC cycle was modeled to produce more thrust, even accounting for some losses. There was one key assumption in the State to State Model that does not align with physics: the lack of azimuthal velocity on the exit plane. It was shown in Section 3.2.3 that the exhaust of the RDC has a high non-zero azimuthal velocity component across the cycle. This effectively reduces the velocity in the thrust producing direction, thereby reducing the thrust production predicted by the State to State Model (see Section 3.4.2.2). This non-zero swirl appears to be a self-excited phenomenon within the RDC cycle due to the periodicity and post-detonation expansion. The cycle model presented in this research captures this effect, showing highly non-uniform flow across the nozzle exit plane. The post-expansion process from the detonation can produce high azimuthal velocity profiles moving opposite of the wave propagation, while the oblique shock will sharply turn the flow in the direction of the wave propagation before the exit plane. These large azimuthal velocities directly reduce the potential thrust.

Chapter 4 also defines a thrust gain metric, which compares the thrust of the RDC to the ideal thrust produced by a deflagrative device operating at the plenum conditions. Though a few configurations allow for a thrust gain, when one includes moderate losses known to exist within the RDC cycle, the model universally predicts a decrease in the thrust gain. These model results are not necessarily indicative of real-world RDC performance, but they do show that there may be challenges in achieving an improved thrust.

6.3 Additional Work Extraction

If direct thrust production does not provide a gain over a similar deflagrative combustion, then utilizing a RDC for work extraction may.[22, 23, 82] This also requires additional consideration with the non-zero azimuthal velocity profile; however, with a stator section, these velocity perturbations may be able to be fully damped out.[82] There are still two large issues with the combination of detonation-based systems and turbo-machinery. The first is the high combustion temperatures present in detonation combustion, in concert with the hope of a pressure gain. If pressure gain is achieved, then film cooling within the first stages of the turbine is not possible without additional pumping of the bleed air before injection. This additional work required for cooling must be overcome with the performance of the RDC device. The other option would be providing a mix-out air stream to reduce stator inlet temperatures, like what was done by Naples et al.[82]

This brings up the second issue: mating RDCs and turbo-machinery due to the mismatch in flux between the two. A proposed benefit of RDCs is the ability to operate at high mass flux, reducing the overall footprint of the device while maintaining the same power output. However, turbo-machinery may have a much lower mass flux processing capability. This means that for a given overall mass flow rate, the RDC flow area could be 2-10x smaller than the turbine flow area. This would require a significant expansion process from the RDC exhaust or operation of the RDC at a reduced mass flow rate and adding a mix-out air stream.

From these two examples, the mix-out air stream may be a requirement to avoid exposing the turbine to high temperature and more closely matching the flux requirements of the two devices. The issue with this setup is the fact that we are expending a tremendous amount of energy to compress the full mass flow, while only combusting a fraction of it, effectively lowering the global equivalence ratio through the combustor. The RDC would then have to provide additional performance benefits to overcome this additional work production.

It is unclear to the author whether or not the challenges with turbo-machinery integration could be overcome, and if RDC could provide a performance upgrade of current gas turbine engine technology. But it could be argued that because of the post-RDC flow processing required, the azimuthal velocities would be damped out. This imply that use of an RDC for power generation would be more preferable than for thrust production.

6.4 Reduced Entropy

Another aspect of detonation combustion is the fact that it theoretically produces less entropy. This is due to the shock providing a much higher combustion pressure, but as we saw in Section 2.4.1, the reduction in entropy across the detonation wave is proportional to the required detonation work

term. This means that the higher performing the detonation is, in terms of wave speed and pressure ratio, the higher the detonation work requirement is. Essentially, any reduction in entropy across the detonation is met with a proportional increase in the detonation work requirement. Based on the simple analysis provided in this research, it would be unwise to ignore this potential benefit; however, one must account for the effects that an improved detonation wave would have on the remainder of the cycle flow path (i.e., inlet blockage).

6.5 Compactness and Combustor Simplicity

This aspect was discussed earlier, but because of the high flux capability of the RDC, the overall size of the device can be reduced compared to a convention deflagration-based combustor given the same heat output. So long as the device can sustain operation, the size of a RDC would be significantly smaller than an equivalent deflagrative device.

However, there are still issues with shortening the RDC and the overall smaller footprint. First, based on the model results seen in Section 4.3.2.3, the RDC length can directly impact the azimuthal velocity profile across the exit plane, where there may be an optimal length that reduces the fraction of the energy that is used to generating the azimuthal velocities.

The second issue is the cooling requirement. The detonation wave provides a local pressure gain, which lowers the effectiveness of film cooling within the RDC channel. The detonation also produces extremely high gas temperatures within the detonation wave, leading to high heat transfer values.[49, 50] These conditions make the use of a metal inner and outer body of the detonation impractical without significant water or other fluid cooling to maintain appropriate metal temperatures for structural soundness. However, Chapter 2 showed how the additional heat transfer within the detonation region would affect the detonation performance, which may reduce the RDC performance downstream.

Finally, a short combustor length means a reduction in the cycle time, in this case, the amount of time that the fuel is present within the combustor. Section 2.4.1 showed that there is likely some fuel that leaks through the detonation without combusting. Provided a long enough residence time, this fuel could be combusted within the channel, just at a lower pressure than if it were consumed in the detonation wave (also see Section 3.3.1). If the RDC is too short, this fuel may exit the device fully before the heat can be released, decreasing the combustion efficiency of the device and reducing the overall performance.

6.6 Application that may Benefit from Detonation Combustion

With the discussion of the potential benefit, and their issues complete, the author wanted to provide a few potential application that would be most likely to benefit from a transition to a detonation-based cycle. These are the opinion of the author, based on the presented cycle model results and prior literature, and are presented in order of which appears ”most achievable”.

The first application that would be suited for the use of RDC-based systems would be their use in rocket motor applications. Current rocket motors already operate at high injector pressure losses; therefore, the RDC inlet can be run at high stiffness, reducing the negative impacts of the detonation wave on the inlet plane. Rocket motors also have to provide significant cooling to the combustion chamber, nozzle, and especially the nozzle throat. So, the cooling requirement for the RDC-based system would likely be on par with what is already required. Also, rocket-style RDC would use highly reactive oxidizer/fuel mixtures, which would reduce the concerns about combustion efficiency due to the reduced cycle time. The reduction in motor size is also of greater benefit to rocket motors, as the dry weight of the rocket directly affects the payload and/or orbital velocities.

The next application where RDCs could potentially be beneficial is when used in a flame-holding application. This could be any base system one could imagine, but using the RDC as a flame-holder would mean many of the performance benefits proposed by RDCs would not be required. This system would only need to produce an energy-dense exhaust flow in a compact profile, and the unsteadiness (high swirl) of the exhaust flow would likely be of benefit to mixing purposes.

6.7 Final Thoughts on the Feasibility of Detonation-Based Systems

This research has presented many aspects of detonation combustion and its extension to devices like RDCs, both positive and less positive. It discussed the loss mechanisms present in a detonation-based system, specifically focusing on the RDC flowfield. It also discussed in depth the limitations of defining performance metrics that are suitable for RDCs, like the pressure gain metric. Outside of system-level outputs, like thrust, there may not be a suitable metric to measure the benefits of RDC at a laboratory scale. This conclusion is purely based on a review of prior literature and the cycle model results presented in this research; therefore, it should not be seen as an indictment on RDC devices or if the proposed benefits, such as pressure gain, are achievable. In fact, as discussed, RDCs have a number of potential benefits that emerge from specific applications.

This raises the point that to ascertain the benefits of detonation combustion; one may need to shift away from simple laboratory-scale performance metrics and begin analyzing RDC performance as it relates to the system in which the RDC, or other detonation-based systems, is applied. In this sense, the benefits of detonation combustion may be less concerned with whether or not the device produces pressure gain and whether the device provides a system-level benefit. This aspect aligns well with the author's goal of providing an efficient reduced order model with the intention of being used in higher level system analysis. To conclude, it is the author's opinion, based on the work presented, that the detonation propulsion community may benefit from moving away from measuring the success of detonation-based systems at the device level, and instead move to a system-level trade-space, where the detonation-based combustor is one component of a system.

CHAPTER 7

Future Work

The following chapter provides some additional future work required to improve the cycle model and examples of potential applications of the cycle model outside of predicting RDC performance directly. The model improvements are broken down into methodologies that will potentially improve the model evaluation time and then the accuracy of the model. Each modification of the model ranges in complexity, and it is currently unknown if adding the feature provides the intended benefit and measurable impact. However, the main benefit of the physics-based modular design of the sub-model framework is that it allows for easy implementation of each change, as well as a simple path forward for future sub-model integration.

7.1 Model Evaluation Time Improvements

We will start by examining potential improvements in the cycle evaluation time. As it stands now, the fastest the cycle will converge with the default configuration setting is just under 100 ms. This is already relatively quick and allows for the application Monte Carlo based analysis methods as is, but improving the evaluation time is still beneficial due to the $1/x$ scaling with the number of function calls per second.

The first, most basic cycle speed-up comes from the fact that little time was dedicated to the optimization of the code base, which was done for two main reasons. The first is that it is the author's judgment that pre-mature code optimization takes time away from more valuable code and model fixes, which will be discussed throughout this chapter. For example, it appears that the post-shock process will require an update, so any code optimizations around this region would potentially be voided with the updated functionality. The next reason the code-base was not manually optimized is that the Rust compiler already does a significant amount of optimizations on the code, with zero additional effort required by the user.

With all of that said, the first area where evaluation times can be improved is the chemical equilibrium solver. Currently, no package within the Rust ecosystem that solves chemical equilibrium

exists, which is required by the CJ solver. This means that the Python implementation of Cantera's Solution object was required, and the model must interact with the Python object, requiring additional overhead in the communication. Ideally, the entire project would be compiled and run directly in the Rust ecosystem, allowing for maximum performance; however, this requires a custom chemical equilibrium solver. As the number of detonation sub-model evaluations is the main scaling factor in the speed of the code, this improvement likely has a high return on investment but at the expense of requiring much more effort to implement. Also, if one is testing a small range of parameters, a lookup table can be constructed in place of the detonation solver.

Another strategy around this method is to provide a better estimate of the initial conditions, specifically the plenum and channel pressure. For example, across all test cases, the modeled channel static pressure, P_{ch}, always converges to the specified ambient pressure. This means that the model can directly initialize the static channel pressure, requiring only one call to the detonation solver. As for the plenum pressure, calibration on a configuration may allow for a better initial guess, reducing the number of iterations required to reach convergence to the target mass flow rate.

The next most obvious path to improve the execution speed is simply to reduce the tolerances required for the model mass flow rate convergence. This is trading off model accuracy for speed, but as was shown in Section 4.3.1.3, this may be tolerable when studying model outputs such as thrust. The speed-up potential for this change is also shown in Section 4.3.1.3 and is already implemented in the current version of the code.

Another similar option, involves tuning the model configuration parameters depending on the application of the model. For example, certain output parameters maintain high accuracy at lower resolutions. Reducing the tolerances/grid resolution for these specific outputs will produce a much faster convergence time while minimally sacrificing accuracy. If the user was only targeting these specific outputs of the model, then the overall execution time would be reduced.

Finally, the Channel Flow solution solver currently implements a one-dimensional integration solver that accepts loss inputs such as friction and heat transfer. It was discussed in Section 4.3.1.2, but the polytropic compression process mimics these loss mechanisms without requiring a complete integration of the flowpath. This allows for the removal of any integration within the model and the use of a simpler one-step jump process.

7.2 Improvements to Model Accuracy

During the model evaluation process, numerous areas of improvement in model accuracy were revealed. The following examples present the areas of opportunity broken down by elements that will improve fidelity in the modeling of the physical processes.

The current CJ detonation solver does not account for any losses other than those specified by

the deflagration loss parameters. Section 2.3.2 discussed a CJ solve that also accounts for the momentum and energy losses within the detonation wave itself. The inclusion of this CJ solver would require additional sub-model inputs but may provide a better estimation of the predicted performance. These inputs, area change, heat transfer, and momentum losses could also be captured in additional model closures to maintain a minimal level of input parameters.

In a similar vein, the addition of a ZND-based detonation solver may improve the model accuracy by capturing the flowfield processes at a higher fidelity. For example, the current model uses a CJ based solver assumes an infinitely thin detonation wave, where a ZND based solver will account for the induction length, and overall length of the detonation wave. This change should provide feedback to the inlet blockage and better predict the results shown by experimental data. This would also update the location and size of the expansion fan complex.

As currently implemented, the model does not account for any process in which the fuel is introduced into the flow field. This includes fuel injector blockage, air injector blockage caused by fuel injection, and mixing. Additional sub-models could capture these effects in an effort to allow the model to better predict operability instead of just performance.

On the topic of inlet improvements and blockage, the injector sub-model contains assumptions that are likely negatively impacting the predictive capability of the model at low flow rates. Aside from fuel-related issues, an improvement in the inlet model would include the need for a time dependency within the injector fill model. Currently, the model assumes that each individual differential area across the inlet plane is a fully developed, steady flow. In reality, the flow in either direction has not reached a steady flow equivalent condition, regardless of how small of a differential area is examined.

Next, across most of the test cases presented in this research, the fill height calculated by the inlet model and the detonation height are not predicted to be the same value. The detonation relocation algorithm simply places the upper portion of the detonation wave at the fill height location without taking into account situations where the wave is much smaller than the provided fill. This was implemented to improve model stability but could be a limiting factor as far as the operability prediction capability of the model. A future implementation of the model could include a fill and detonation height match iteration process. With this implementation, the other input values like $\xi_{\mathrm{P}}$and ξ_{L}can be estimated such that these two heights are equal.

Another option on this front would be for the inclusion of pre-shocked reactant fill. For example, if the fill height is larger than the detonation height, then the oblique shock nearest the inlet plane will shock a portion of the incoming fresh reactants. This would mean that a fraction of the fresh fill would be at a higher temperature and pressure before entering the detonation wave. This model improvement would also allow for better matching of the physic through the inlet plane caused by the oblique shock.

We discussed in Section 4.3.2.3 and Section 4.3.2.7 that the overall exit swirl was not conserved across a wide range of operating conditions. This can be attributed mostly to the post-shock flow, which produces a larger swirl component that the remainder of the non-shocked flow cannot cancel out. Therefore, a potential solution involves the implementation of Channel Flow objects in the post-shock region. An example of this process is shown in Figure 7.1, where the additional post-shock Channel Flow object would account for area changes along the flowpath after the fluid passes through the shock. It would also include a second exit plane calculation of polytropic losses at the end of each flowpath specified by the pressure matching scheme. This may also provide a reduction in the predicted thrust, which could also better align with experimental results.

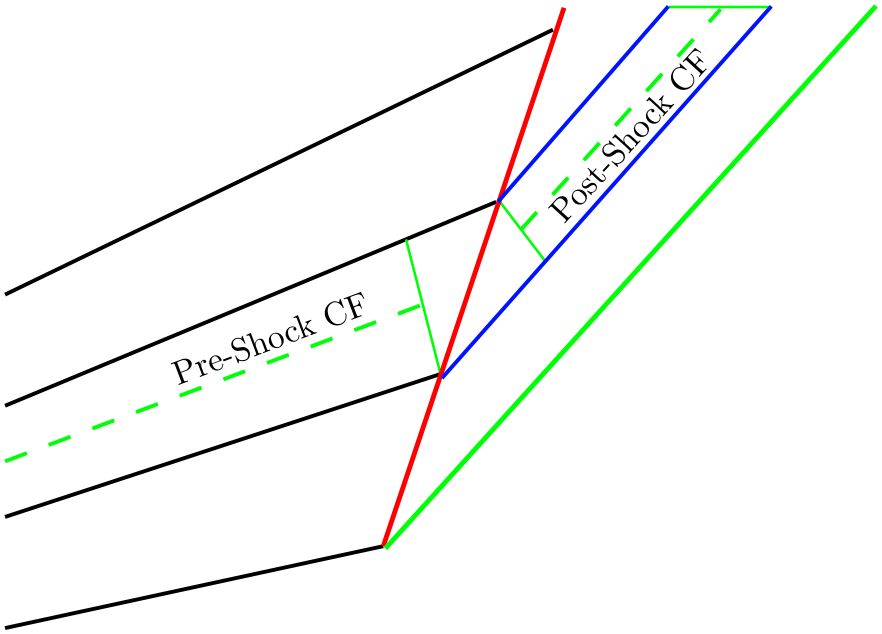


Figure 7.1: Example of the Post-Shock Channel Flow Modification

Next, the current model does not include a variable area nozzle sub-model. This would likely be the most optimal sub-model to add as it provides a much larger set of data for calibration, and most applications of an RDC based system would include some nozzle. This could be done by either directly calculating the nozzle flow in a similar manner to the inlet mass flow calculation or through a methodology to back-propagate the nozzle effects to the inner RDC channel.

Finally, the model provides a physics-based methodology for propagating the effects of the detonation region to the inlet plane. However, the current implementation does not provide a robust framework for relaying the inlet performance to the detonation wave. For example, as the inlet stiffness decreases, it would be rational to assume that the lateral relief the detonation wave experiences would increase. Another example is that at high levels of inlet blockage, it would likely be more probable that a higher level of backflow would occur. This is picked up

by the inlet model; however, the downstream effects, such as parasitic combustion and product re-circulation, are not. An improvement to the model that relates the inlet performance back to the detonation performance is required and should help improve the accuracy of the model with respect to experimental datasets.

7.3 Additional Model Closures

The following model updates, if implemented, would help reduce the number of required input parameters by providing sub-model closures. Currently, the model requires the deflagration loss parameters to be provided as inputs; however, the inclusion of various sub-models could allow for these values to be estimated directly. A few examples include a finite-rate chemistry solver for each Channel Flow object. This would account for any post-detonation combustion process, including the geometry, in a manner that may predict combustion efficiency directly. Next, a mixing model or a stratified detonation model could be implemented to predict the amount of leaked fuel. Additionally, a dwell time/blockage-based sub-model could be implemented to calculate the parasitic combustion fraction, including both parasitic combustion and product gas re-circulation. The latter improvement was also discussed in the previous section.

The inclusion of these updates, or similar closures, for the input parameter reduction, would fully close the model. It would be hoped that these closures also improve the model accuracy and provide a more realistic coupling of the detonation level metrics and the RDC level metrics.

7.4 Additional Model Validation

Another key point of future work involves the continued validation of the model with external data points. This includes the addition of more experimental test points that feature a wider variation in geometric configurations. However, even additional experimental data could not provide validation for many of the sub-models.

In these instances, validation with higher fidelity CFD results would be optimal. For example, although the virtual origin methodology draws from computational particle paths in other reduced order models and 2-D CFD, the validation of the particle paths on a full 3-D configuration might better solidify this assumption. Notably, we should also be careful to use CFD results that were themselves validated with experiment measurements.

7.5 Future Model Applications

The final section of this chapter is dedicated to the future use cases for the cycle model, starting with the inclusion of the cycle model into a larger framework. An example of this application would be in cases where the RDC is used as a combustor within a larger flight system. This would simply require that the RDC cycle model be provided with the appropriate input conditions for an external model, which may require some additional iteration scheme outside of the cycle model. The most basic application of the methodology would be to include a simple inlet model for the RDC and then use the RDC cycle model to predict performance metrics, such as thrust, which leads to the second future use case for the model.

Were one to take this simple inlet for the RDC and use the RDC solely to produce thrust, then a flight trajectory model could be implemented. This would track the vehicle-level flight performance across an entire modeled flight path, which is another example showing the requirement for fast model evaluation. This example can then be extended to optimization of the flight path on some metric of interest.

Another area where optimization would be applied is to the RDC device itself. This could include optimizing the RDC geometry to maximize a given performance metric or to minimize a key loss parameter. An example of this would be to design a geometric configuration and bulk flow condition that would minimize the amount of parasitic deflagration. In order to provide a more realistic optimal geometry, many of the above-mentioned model improvements would be required first.

The final example application revolves around the continued estimation of unknown quantities. Chapter 2 showed examples of using the deflagration loss model to predict losses for a given dataset. Then, this chapter showed how improvements in the model can provide a more accurate estimation of these loss parameters with respect to measured quantities. The final step would be to use the full cycle model, with additional output, to provide an even better estimation of the losses. In this scenario, the loss estimation will be improved by both the increased fidelity of the model and an additional set of output values that can be compared to experimental results.

7.6 Conclusion

Although this section captured many additional future tasks surrounding the cycle model, it should not detract from the current model implementation. We showed in Chapter 4 and Chapter 5 that the model captures many of the expected trends associated with RDC performance and provides an accurate estimation of these metrics within a certain operating range. This chapter exists to show areas of improvement and to display the flexibility allowed by the structure of the model, where

the physics-based sub-models allow for a simple, streamlined path for future improvements.

CHAPTER 8

Conclusions

This research aimed to characterize and quantify different loss mechanisms inherent to detonation waves and applications of detonation combustion, such as Rotating Detonation Combustors. Care was taken when discussing the relationships between loss mechanisms specific to the detonation wave and loss mechanisms specific to the RDC device; however, these mechanisms are often intertwined. Then, with the new understanding of these loss mechanisms, this research developed a new, computationally efficient, non-ideal RDC Cycle model. The model was then compared with experimental data to gauge overall accuracy across performance metrics, including thrust, pressure gain, and inlet blockage. Finally, the model was compared to other state-of-the-art cycle models, showing a 10-10000x improvement in evaluation time across all test points and up to a 6x improvement in predictive capability at mass flow rates greater than 200 g/s.

8.1 Detonation Specific Loss Mechanisms

The loss mechanisms for the detonation wave are all based upon the boundary conditions provided to the detonation wave, specifically those seen in the RDC device. These include heat transfer, friction, and lateral relief, allowing area change through the detonation wave. Other losses include pre-detonation deflagration and leaked fuel, captured by the Deflagration Loss model from Chapter 2. When these loss mechanisms were included, the detonation performance was evaluated to determine the most impactful metrics. The performance metrics of interest were the detonation wave speed, the detonation pressure ratio, and an energy gain metric.

It was shown that parasitic pre-detonation deflagration was the leading loss term across three different performance metrics: detonation wave speed, detonation pressure ratio, and a gain metric based on the energy equation. Parasitic combustion accounted for between 40-80% of the total impact across these performance metrics, where the highest total impact was in the detonation pressure ratio. Other impactful loss mechanisms included leaked fuel through the detonation wave and area expansion across the wave. Not only do these three loss mechanisms have a downstream

impact on the performance of the RDC device, but all three are also modulated by aspects of the RDC device and operation characteristics. An example of these interactions is the change in the inlet blockage with changes in the detonation pressure ratio. The inlet blockage and other downstream effects like exhaust gas re-circulation then provide conditions that may modulate the detonation-specific loss mechanisms, such as the magnitude of the parasitic combustion fraction.

Using the presented cycle model, the detonation-specific loss mechanisms could be studied with respect to the overall RDC performance. A key trend observed was the relationship between the parasitic deflagration fraction and the specific thrust of the RDC. As the parasitic fraction varied from 0.0 to 0.4, the specific thrust decreased between 1.2 and 40x. This was across a wide parametric study with additional losses, flow conditions, and RDC geometries, suggesting that RDC performance could be improved by reducing the deflagration loss fraction.

8.2 RDC Specific Losses

This research relied on three performance metrics for RDC performance to compare the numerous loss mechanisms: thrust, pressure gain, and inlet blockage. Chapter 3 shows the key loss mechanisms for RDC performance were linked to the inlet pressure losses, inlet blockages, and the non-zero azimuthal velocity profile at the inlet and exit planes. These simple sub-model studies showed the impacts on the inlet blockage provided by the detonation wave, where increases in the strength of the detonation wave (pressure ratio) would increase the inlet blockage. This inlet blockage could be overcome with a stiffer inlet but at the expense of pressure recovery through the injection process. However, prior experimental results and reduced order modeling showed that the pressure recovery directly correlates with the pressure gain metric.

Using the presented RDC cycle model, it was also observed that the pressure gain across the device was nearly perfectly correlated with the inlet pressure losses. Across a broad parametric study, it was shown that as the inlet pressure loss went from 30% to 70% of the plenum pressure, the pressure gain decreased from near 0 to a value of -60%. This result suggests a less stiff inlet is preferable; however, the model also showed that as the inlet pressure losses improved, the propensity and magnitude of inlet blockage increased. This suggests that the trade-off in the inlet blockage and pressure recovery is critical when designing an optimal RDC, especially if the target performance metric is pressure gain.

8.3 Detonation and RDC Coupling

The final aspect for evaluating the performance impacts from the multiple loss mechanisms was to study the coupling of the detonation wave and the RDC device. Discussion of examples of

this coupling were provided throughout this research, but the most apparent area involved the inlet and detonation wave interactions. It was shown that the boundary conditions provided by the RDC could excite or enhance detonation-specific loss mechanisms such as lateral relief or parasitic deflagration. It was also revealed that the performance of the detonation wave, specifically the pressure ratio, drastically impacts the RDC inlet plane.

Take a high-performance detonation wave propagating through the RDC flowpath for a thought experiment. In this example, high performance refers to the pressure ratio across the detonation wave. As the post-detonation pressure is significantly higher than the RDC plenum pressure, the inlet blockage increases. An increase in inlet blockage also stands to reason that the likelihood of exhaust gas re-circulation would also increase. This might lead to an increase in the likelihood of parasitic combustion before the next wave. However, parasitic deflagration drastically decreased the detonation pressure ratio, impacting the inlet to a lesser extent. One can see how this process by which the inlet and detonation performance are linked will result in some equilibrium condition, showing the vast complexity within the RDC device despite its simple design.

On the other end of the spectrum, if one cares only about the RDC's performance, would the detonation's performance be a good aspect to target? In general, the answer would be it depends. If the RDC performance metric was pressure gain, the answer might be no due to the lack of correlation between detonation performance and RDC performance predicted by the cycle model. Suppose the performance metric was the thrust production. In that case, the answer is maybe, as shown by the moderate correlation between the detonation performance and the RDC performance predicted from the cycle model. Though not definitive, these results suggest examples where one must be careful not to target the detonation performance (wave speed and/or pressure ratio) to determine how well the RDC is performing, as multiple competing factors could render the detonation performance values mute.

8.4 Non-Ideal RDC Cycle Model

The non-ideal reduced order RDC cycle model developed in the research provides an accurate, modular, and efficient model framework used to predict the performance of RDC devices with included loss mechanisms. Two novel sub-models were developed based on known physics and prior observations. These include the Channel Flow object, which links the detonation region to the remainder of the downstream flowpath of the RDC. Using the Channel Flow objects methodology, additional losses can be captured as the post-detonation products exit the RDC without needing more complex, costly solutions like a complete two-dimensional method of characteristics. This methodology provided expected results, specifically the overall cycle thrust and the highly non-uniform exit plane azimuthal velocity distribution.

The second novel addition to this model was the connection of the detonation and expansion fan regions to the RDC inlet. This included generating an inlet pressure profile solely defined by the detonation wave and subsequent expansion fan. The inlet model also used an inlet that allows for back-flowing product gases, providing a more accurate representation of the physics involved with the RDC inlet. With this implementation, the cycle model could predict broad trends, such as the effects of the detonation pressure ratio on the inlet blockage and the scaling of the blockage as the inlet stiffness was changed.

With these novel coupling methods and the overall incorporation of physics-based sub-models, the RDC cycle model could accurately predict performance metrics such as thrust and inlet blockage with respect to experimental measurements. The model was less accurate at low mass flow rates and plenum pressures, less than 200 g/s and 20 psi, respectively. This is likely due to the inlet model lacking a time dependency; however, because of the overall structure of the model, it would be a more straightforward fix to implement in future iterations. At moderate to high mass flow rates, the model was able to better match RDC performance measurements to within 15% on average, while providing an average evaluation time of 100 ms, allowing the model to be effectively employed in Monte Carlo based analysis and future use as a sub-model for a larger system. Compared to current state-of-the-art cycle models, the presented model provided up to a 6x improvement in accuracy with respect to experimental results above a mass flow rate of 200 g/s. This improved accuracy also came with a 10-10000x improvement in the overall model evaluation time.

Although many aspects of the model should be improved in future iterations, this should not detract from the tremendous benefits the model can provide currently implemented and the usefulness of the philosophy behind the model architecture. As each sub-model was based on experimental and computational observations, one can quickly adapt each sub-model to better match experimentation. Another key benefit of this methodology was removing any curve fit within the cycle that is frequently implemented in other cycles due to their simplicity. This allows for a much simpler path forward for future updates and moves the model into a fully closed, physics-based representation of the process within the RDC device.

On the topic of closing the cycle model, three unknown parameters must be specified before the model evaluation. These include the deflagration loss parameters that capture parasitic combustion, leaked fuel, and combustion efficiency. All other parameters within this model are captured through a sub-model closure, reducing the number of unknown variables and providing a physics-based representation for each. Future work will also focus on implementing closure models for the last three deflagration loss parameters, eventually fully closing the model. Optimization techniques could easily be applied with this closure, such as reducing the parasitic combustion fraction with changes to the RDC geometry.

8.5 Path Forward for RDCs

The high level of coupling between the detonation wave and RDC inlet will likely reduce potential application to either those that are less concerned with inlet losses and pressure gain as we currently define it and those that are not concerned with reduced detonation performance (driven by parasitic combustion). Chapter 6 outlined these issues, but based on the results of the present model, the author would also like to mention that pressure gain may not be the most appropriate metric to capture a performance benefit for the RDC cycle. Other aspects, such as an improved operability map, compactness, and potential thrust improvements, may be better suited but are system-level metrics that are not easily measured at the laboratory scale.

Although the results presented in this research do not show the expected performance benefits proposed by detonation combustion, especially when all loss mechanisms are considered, this should not be considered an indictment of detonation-based combustion cycles. However, this research opens the conversation for improving the metrics one uses when discussing the potential benefits of detonation combustion. The most notable instance was the pressure gain metric, which has been experimentally and somewhat computationally shown to be inadequate to capture all potential benefits of detonation combustion.

APPENDIX A

Pressure Gain

A.1 Introduction

This appendix will discuss some additional derivation of the pressure gain metric, based on some of the sub-models discussed throughout this research effort. We will break down the pressure gain equation into components for which we have known relationships of models. These will be color-coded for convenience.

A.2 Pressure Gain Relationship

We start with the definition of total pressure gain:

$$PG = \frac{P_{t,8}}{P_{t,3}} - 1 \tag{A.1}$$

where $P_{t,8}$ is the total pressure at the RDC exit and $P_{t,3}$ is the total plenum pressure. We can break the leading term down a little further as a function of a few key pressure ratios:

$$\frac{P_{t,8}}{P_{t,3}} = \frac{P_{t,8}}{P_8}\frac{P_8}{P_{3.4}}\frac{P_{3.4}}{P_{3.2}}\frac{P_{3.2}}{P_{3'}}\frac{P_{3'}}{P_{t,3}} \tag{A.2}$$

The first term, in red, is essentially accounting for an average Mach number at the exit of the RDC. The second, shown in blue, represents any process from the work extraction state, (3.4), to the exit plane. The third, shown in green, represents the detonation work expansion process. The fourth term, shown in cyan, is the gain across the detonation wave. Finally, the last term, shown in magenta, represents the inlet static to plenum total pressure ratio (also known as the inlet stiffness).

A.2.1 Exit Total to Static Pressure Ratio

We will now examine each term we have defined above, starting with the total to static pressure ratio at the RDC exit (station 8).

$$\frac{P_{t,8}}{P_8} = f(M_8, \gamma_8) \tag{A.3}$$

Assuming $M_8 = 1.0$:

$$\frac{P_{t,8}}{P_8} = \left(\frac{\gamma_8 + 1}{2}\right)^{\frac{\gamma_8}{\gamma_8 - 1}} \tag{A.4}$$

Otherwise this is also a function of the Mach number at the exit (which we can define as averaged quantity, typically area averaged). This term is bounded between one and the critical pressure ratio. So we know this term contributes positively to the overall pressure gain.

A.2.2 Static Pressure Ratio (8) to (3.4)

The next term is less apparent but make the relationship elsewhere much more simple. This term relates the static pressure at the exit (8) to the static pressure at the work extraction state (3.4). It is likely something we will need to calculate, or at least bound, instead of deriving a more physical relationship. This term will be less than or equal to one, and likely less than one due to any additional processes occurring between (3.4) and (8).

$$\frac{P_8}{P_{3.4}} = f(geom, mdot, Pamb) \tag{A.5}$$

A.2.3 Static Pressure Ratio (3.4) to (3.2)

Next we have the static pressure ratio between the work extraction state (3.4) and the CJ state (3.2). This term is a function of the detonation work term and is modeled as an isentropic expansion.

$$\frac{P_{3.4}}{P_{3.2}} = f(Du_{3.2})|_{s_{3.2}} \tag{A.6}$$

We will relate the pressure ratio to a temperature ratio with the entropy equation:

$$\Delta s = c_p \ln\left(\frac{T_2}{T_1}\right) - R \ln\left(\frac{P_2}{P_1}\right) \tag{A.7}$$

where for an isentropic expansion:

$$c_p \ln\left(\frac{T_{3.4}}{T_{3.2}}\right) = R \ln\left(\frac{P_{3.4}}{P_{3.2}}\right) \tag{A.8}$$

The relationship of c_p, R and γ is:

$$\frac{c_p}{R} = \frac{\gamma}{\gamma - 1} \tag{A.9}$$

Simplifying we have the familiar isentropic relationship:

$$\frac{P_{3.4}}{P_{3.2}} = \frac{T_{3.4}}{T_{3.2}}^{\frac{\gamma}{\gamma-1}} \tag{A.10}$$

We will now bring in the energy equation relating (3.4) to (3.2), where we assume the axial velocity is constant between the two states and the azimuthal velocity (wave direction) is zero at (3.4), matching the azimuthal velocity ahead of the wave $u_{3'}$:

$$h_{3.2} + \frac{u_{3.2}^2}{2} - D u_{3.2} = h_{3.4} \tag{A.11}$$

Assuming calorically perfect gas and constant c_p:

$$c_p T_{3.2} + \frac{u_{3.2}^2}{2} - D u_{3.2} = c_p T_{3.4} \tag{A.12}$$

divide by $c_p T_{3.2}$:

$$\frac{T_{3.4}}{T_{3.2}} = 1 + \frac{u_{3.2}^2}{2 c_{p,3.2} T_{3.2}} - \frac{D u_{3.2}}{c_{p,3.2} T_{3.2}} \tag{A.13}$$

therefore:

$$\frac{P_{3.4}}{P_{3.2}} = \left(1 + \frac{u_{3.2}^2}{2 c_{p,3.2} T_{3.2}} - \frac{D u_{3.2}}{c_{p,3.2} T_{3.2}}\right)^{\frac{\gamma}{\gamma-1}} \tag{A.14}$$

Assuming $D > u_{3.2}$ (which is valid for zero initial azimuthal velocity), we will see this term is less than 1.0, which should be the case.

A.2.4 Detonation Wave Static Pressure Ratio

We then define the static pressure ratio across the wave. This is determined from the CJ calculation and we will use static pressure since it is reference frame agnostic. This term is known to be a

function of the ”performance” of the detonation wave.

$$\frac{P_{3.2}}{P_{3'}} = PR_w = f(D_w, a_{3'}) \tag{A.15}$$

$$\frac{P_{3.2}}{P_{3'}} = PR_w \propto M_w^2 \propto \frac{D^2}{a_{3'}^2} \tag{A.16}$$

A.2.5 Channel Static to Plenum Total Pressure Ratio

Finally, we have the channel static to plenum total pressure ratio, which is by definition less than 1. This term is either measured or modeled.

$$\frac{P_{3'}}{P_{t,3}} = PR_{inlet} \tag{A.17}$$

A.2.6 Putting it All Together

Now we can substitute all of these terms back into the pressure gain equation:

$$PG = \left(\frac{\gamma+1}{2}\right)^{\frac{\gamma}{\gamma-1}} \frac{P_8}{P_{3.4}} \left(1 + \frac{u_{3.2}^2}{2c_pT_{3.2}} - \frac{Du_{3.2}}{c_pT_{3.2}}\right)^{\frac{\gamma}{\gamma-1}} PR_w PR_{inlet} - 1 \tag{A.18}$$

As mentioned early, the static pressure ratio from (3.4) to (8) and the channel static to plenum total pressure ratios are bounded to be less than 1.0

$$\frac{P_8}{P_{3.4}} \leq 1.0 \tag{A.19}$$

$$PR_{inlet} \leq 1.0 \tag{A.20}$$

There is an argument to be made about the correlation between these two terms. If the inlet pressure ratio is 1.0, then the channel static pressure equals the plenum total pressure. This is unlikely to ever occur during operation, but acts as an upper bound. Regardless of the processes across the wave (in the manor the State to State model implements) station (3.4) pressure must be greater than or equal to the channel static pressure, $P_{3.4} \geq P_{3'}$. For example, if the parasitic fraction is set to 1.0, then we would have a fully deflagrative combustion process and the pressure

ratio across the wave would be zero, so too would the detonation work required to be extracted from (3.2) to (3.4). Any realistic combinations of deflagration loss parameters result in a pressure at (3.4) being greater than (3.2) and, therefore, greater than (3′).

The argument for the exit to (3.4) pressure ratio is based upon the thrust production process. If these pressures are equal, then no thrust is produced (here I mean the net thrust production versus the thrust from simply flowing the reactants)

With that said we will assume the product of the two is a constant less than one (or potentially one).

$$\frac{P_8}{P_{3.4}} PR_{inlet} = C_1 \leq 1.0 \tag{A.21}$$

Removing constants, we can write pressure gain as a proportion to the different pressure ratio terms:

$$PG \propto \left(\frac{\gamma+1}{2}\right)^{\frac{\gamma}{\gamma-1}} \frac{P_8}{P_{3.4}} \left(1 + \frac{u_{3.2}^2}{2c_p T_{3.2}} - \frac{D u_{3.2}}{c_p T_{3.2}}\right)^{\frac{\gamma}{\gamma-1}} \frac{D^2}{a_{3'}^2} PR_{inlet} - 1 \tag{A.22}$$

Including the assumption about the relationship between the two static pressure terms. This is equivalent to simply examining the pressure ratios across the detonation wave and post-detonation expansion to station (3.4).

$$PG \propto C_1 \left(\frac{\gamma+1}{2}\right)^{\frac{\gamma}{\gamma-1}} \frac{D^2}{a_{3'}^2} \left(1 + \frac{u_{3.2}^2}{2c_p T_{3.2}} - \frac{D u_{3.2}}{c_p T_{3.2}}\right)^{\frac{\gamma}{\gamma-1}} - 1 \tag{A.23}$$

Now we need the relationship between the wavespeed, speed of sound, and the induced velocity and temperature at (3.2). We know that the induced velocity is simply the wavespeed minus the speed of sound at the CJ plane:

$$u_{3.2} = D - a_{3.2} \tag{A.24}$$

Substituting:

$$PG \propto C_1 \left(\frac{\gamma+1}{2}\right)^{\frac{\gamma}{\gamma-1}} \frac{D^2}{a_{3'}^2} \left(1 + \frac{(D - a_{3.2})^2}{2c_{p,3.2} T_{3.2}} - \frac{D(D - a_{3.2})}{c_{p,3.2} T_{3.2}}\right)^{\frac{\gamma}{\gamma-1}} - 1 \tag{A.25}$$

Expanding:

$$PG \propto C_1 \left(\frac{\gamma+1}{2}\right)^{\frac{\gamma}{\gamma-1}} \frac{D^2}{a_{3'}^2} \left(1 + \frac{D^2 - 2Da_{3.2} + a_{3.2}^2}{2c_{p,3.2} T_{3.2}} - \frac{D^2 - Da_{3.2}}{c_{p,3.2} T_{3.2}}\right)^{\frac{\gamma}{\gamma-1}} - 1 \tag{A.26}$$

Rearranging the last teal term and then multiplying by 2/2:

$$PG \propto C_1 \left(\frac{\gamma+1}{2}\right)^{\frac{\gamma}{\gamma-1}} \frac{D^2}{a_{3'}^2} \left(1 + \frac{D^2 - 2Da_{3.2} + a_{3.2}^2}{2c_{p,3.2}T_{3.2}} + \frac{2Da_{3.2} - 2D^2}{2c_{p,3.2}T_{3.2}}\right)^{\frac{\gamma}{\gamma-1}} - 1 \tag{A.27}$$

Reducing:

$$PG \propto C_1 \left(\frac{\gamma+1}{2}\right)^{\frac{\gamma}{\gamma-1}} \frac{D^2}{a_{3'}^2} \left(1 + \frac{a_{3.2}^2 - D^2}{2c_{p,3.2}T_{3.2}}\right)^{\frac{\gamma}{\gamma-1}} - 1 \tag{A.28}$$

The first term should be greater than one; however, the bracketed term should always be less than one, and raised to a power greater than one which necessarily pushes the value further from one. Also, as ξ_{P} *or* $\xi_{\mathrm{L}} \to \approx 1.0$, $D \to a_{3.2}$. This means the first term also approaches one, while the bracketed term approaches zero. $T_{3.2}$ and $a_{3.2}^2$ scale nearly identically based on the sample data-set, which makes since based on: $a_{3.2}^2 = \gamma_{3.2} R_{3.2} T_{3.2}$. If we substitute the definition of the speed of sound:

$$PG \propto C_1 \left(\frac{\gamma+1}{2}\right)^{\frac{\gamma}{\gamma-1}} \frac{D^2}{a_{3'}^2} \left(1 + \frac{\gamma R T_{3.2} - D^2}{2c_{p,3.2}T_{3.2}}\right)^{\frac{\gamma}{\gamma-1}} - 1 \tag{A.29}$$

Expanding:

$$PG \propto C_1 \left(\frac{\gamma+1}{2}\right)^{\frac{\gamma}{\gamma-1}} \frac{D^2}{a_{3'}^2} \left(1 + \frac{\gamma-1}{2} - \frac{D^2}{2c_{p,3.2}T_{3.2}}\right)^{\frac{\gamma}{\gamma-1}} - 1 \tag{A.30}$$

Simplifying:

$$PG \propto C_1 \left(\frac{\gamma+1}{2}\right)^{\frac{\gamma}{\gamma-1}} \frac{D^2}{a_{3'}^2} \left(\frac{\gamma+1}{2} - \frac{D^2}{2c_{p,3.2}T_{3.2}}\right)^{\frac{\gamma}{\gamma-1}} - 1 \tag{A.31}$$

where $C_1 \in [0.0, 1.0]$.

$$C_2 = C_1 * \left(\frac{\gamma+1}{2}\right)^{\frac{\gamma}{\gamma-1}} \tag{A.32}$$

where $C_2 \in \left[0.0, \left(\frac{\gamma+1}{2}\right)^{\frac{\gamma}{\gamma-1}}\right]$

substituting:

$$PG \propto C_2 \frac{D^2}{a_{3'}^2}\left(\frac{\gamma+1}{2} - \frac{D^2}{2c_{p,3.2}T_{3.2}}\right)^{\frac{\gamma}{\gamma-1}} - 1 \tag{A.33}$$

If we assume the constant, C_2, is the maximum value, we are left with:

$$PG = \left(\frac{\gamma+1}{2}\right)^{\frac{\gamma}{\gamma-1}} \frac{D^2}{a_{3'}^2}\left(\frac{\gamma+1}{2} - \frac{D^2}{2c_{p,3.2}T_{3.2}}\right)^{\frac{\gamma}{\gamma-1}} - 1 \tag{A.34}$$

In order to achieve pressure gain, the following must be true:

$$\left(\frac{\gamma+1}{2}\right)^{\frac{\gamma}{\gamma-1}} \frac{D^2}{a_{3'}^2}\left(\frac{\gamma+1}{2} - \frac{D^2}{2c_{p,3.2}T_{3.2}}\right)^{\frac{\gamma}{\gamma-1}} > 1 \tag{A.35}$$

Rearranging, we are left with the required relationship between the detonation properties relative to the input conditions, assuming the nest case scenario with losses elsewhere:

$$D^2\left(\frac{\gamma+1}{2} - \frac{D^2}{2c_{p,3.2}T_{3.2}}\right)^{\frac{\gamma}{\gamma-1}} > a_{3'}^2\left(\frac{\gamma+1}{2}\right)^{\frac{\gamma-1}{\gamma}} \tag{A.36}$$

A.3 Bounding the problem based on pressure ratio breakdown

$$\frac{P_{t,8}}{P_{t,3}} = \frac{P_{t,8}}{P_8}\frac{P_8}{P_{3.4}}\frac{P_{3.4}}{P_{3.2}}\frac{P_{3.2}}{P_{3'}}\frac{P_{3'}}{P_{t,3}} \tag{A.37}$$

$$PG \propto \left[1.0, \left(\frac{\gamma_8 - 1}{2}\right)^{\frac{\gamma_8}{\gamma_8-1}}\right][?, 1.0][?, 1.0][1.0, PR_{w,max}][0.0, 1.0] - 1.0 \tag{A.38}$$

where the ? means some value greater than zero, but likely dependent on other factors I have not derived yet. If we say the ? is zero, we can combine the bounds into a positive contribution (greater than one) and a negative contribution (less than one) to pressure gain:

$$PG \propto \left[1.0, \left(\frac{\gamma_8 + 1}{2}\right)^{\frac{\gamma_8}{\gamma_8-1}} PR_{w,max}\right][0.0, 1.0]^3 - 1 \tag{A.39}$$

From this breakdown, there are only two terms that contribute positively to pressure gain: the Mach number at the exit (total to static pressure ratio) and the pressure ratio across the wave.

Everything else reduces pressure gain: inlet losses, post-detonation expansion (det work), and the final expansion to the exit. This means in order to achieve pressure gain across this simple cycle model:

$$\left(\frac{\gamma_8+1}{2}\right)^{\frac{\gamma_8}{\gamma_8-1}} PR_w > \frac{1}{\frac{P_8}{P_{3.4}}\frac{P_{3.4}}{P_{3.2}} PR_{inlet}} \tag{A.40}$$

A.4 Conclusions

This attempt to derive a relationship between pressure gain and the sub-processes within the RDC could only be cast as inequalities revolving around the detonation state and the input conditions, under the assumption that the best case scenario was achieved. We were also able to cast the pressure gain as a combination of bounded sub-processes, which gave us a similar inequality. In general, we know that the pressure ratio across the wave, and the fact we can assume the exit Mach number is 1, are the only terms that will positively contribute to the pressure gain across the device. These terms must overcome losses from the plenum to channel injection process, the detonation work extraction (see Section 1.1.1.1), and any other losses within the device as the post-detonation flow process through the channel to the exit. Better modeling or capturing of physics through this region are require before we can say with certainty if pressure gain is achievable or not; however, the process presented here allows for a more mathematical analysis of the pressure gain processes, though it is lacking in fidelity.

APPENDIX B

Trials and Tribulations of Developing a RDC Cycle Model

This appendix will provide some lessons learn during the development of the reduced order RDC cycle model. Many of these lessons were the result of poor initial assumptions, which were later removed, or from iteration on the model to provide a more accurate performance prediction. There were four main takeaways that warranted additional discussion: a singular expansion fan model of the detonation wave, an attempt at a one-dimensional unsteady analogy, the dynamic inlet model pressure profile location, and the specification of momentum and heat losses across the RDC channel.

B.1 Singular Expansion Fan

The initial version of the RDC cycle model included a single expansion fan attached to the top portion of the detonation wave in order to calculate the impact of the detonation on the inlet of the RDC. This is similar to the single bounded detonation wave model from Sommers.[11] Figure B.1 shows an example of the singular expansion fan model.

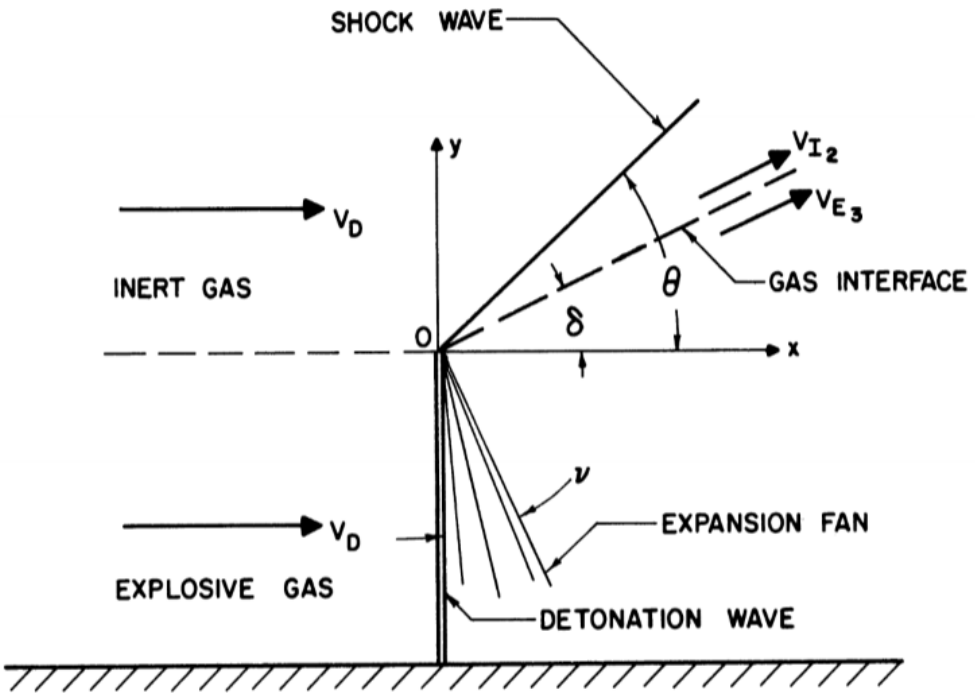


Figure 47. Idealized Flow Model of Detonation Wave-Boundary Interaction.

Figure B.1: Inert Bounded Detonation Model from Sommers.[11]

This model works well for modeling the propagation of a detonation bounded by an inert layer. The basic processes included in this model were adapted for the RDC cycle model. However, one big change was how the RDC cycle model specified the expansion fan angle. This was done based on a required pressure ratio across the expansion fan. The initial pressure was the CJ pressure, P_{CJ}, while the post-expansion pressure was part of the mass flow conservation iterator, P_{ch}.

This downstream pressure represents something akin to the average channel pressure in the RDC channel. With a set of experimental measurements, the pressure ratio specified across the expansion fan was such that the tail end of the expansion fan mach lines would extend towards the exit plane. This would produce the required expansion; however, the information propagated to the inlet presented a much higher than expected block/back-flowing region across the RDC inlet plane. Because of this, the required plenum pressure, P_0, to drive a given mass flow rate through the inlet was 2-10 times higher than experimental measurements. Even when accounting for a non-ideal detonation wave with significant deflagrative combustion, the model still resulted in a higher plenum pressure that experimental data measured.

It was theorized that in the RDC flowpath, there will be a secondary expansion wave emanating from the lower portion of the detonation wave. This secondary expansion fan, along with its interaction with the top fan, will produce a much more condensed expansion process and reduce the plenum pressure requirement to match the given mass flow rate. This meant a redesign of the expansion model to include the second expansion fan and model the interaction of the two.

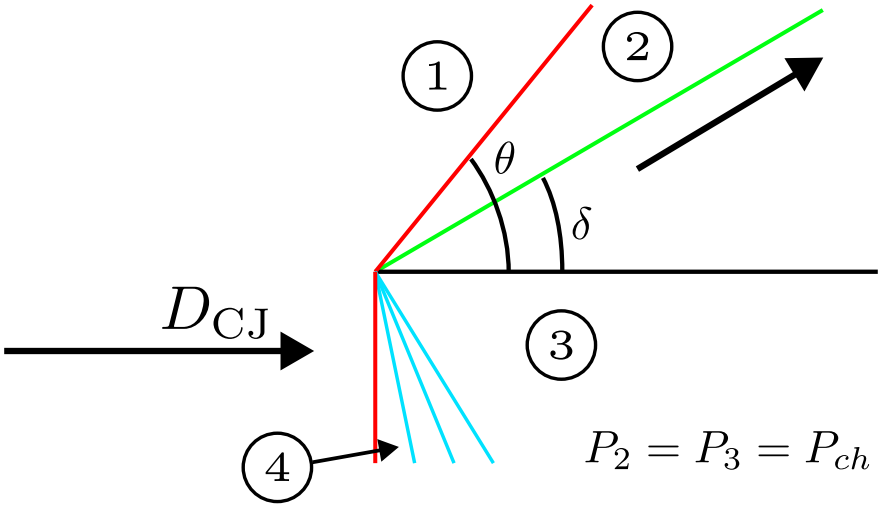


Figure B.2: Expected Behavior of a Singular Expansion Fan Based on Sommers.[11]

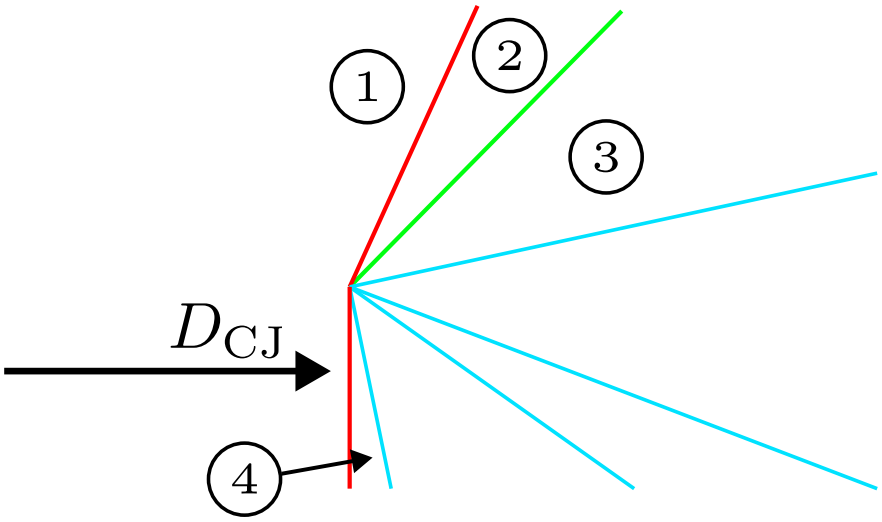


Figure B.3: Actual Behavior of a Singular Expansion at Realistic Channel Pressures, P_{ch}.

B.2 One-Dimensional Shock Tube Analogy

The reason for the development of this model is to capture the effects of the detonation wave on the inlet of the RDC. It is critical to tie the inlet effects to the ”strength” of the detonation wave (detonation pressure ratio specifically). This model employs the method of characteristic for a one-dimensional, unsteady flow with area change and non-constant initial conditions that mimic the inlet region. It was adapted from the methods developed by Zucrow and Hoffman.[83] The main feature of interest in this model is the expansion fan complex that develops due to the expansion process behind the detonation wave. With this expansion fan region fully captured, the inlet flow profile (at some specific plane) can be modeled to understand the flow profile through the inlet, along with the effects of differing strength detonation waves.

The idea for the shock tube analogy springs from a technical report from Dabora.[3] Their model was initially used to predict the propagation of a detonation wave bounded by an inert gas on one side and a solid wall on the other. For reasons described later, this analogy does not properly capture the processes involved in the propagation of a detonation wave with an RDC flowpath, though.

Figure B.4 shows an example of the shock tube analogy for the single inert bounded detonation wave. Because of the wall boundary condition on the bottom of the detonation wave, the combustion process within the wave can be modeled like a shock tube (shown on the right side of Figure B.4). This allows for the calculation of the different regions of interaction between the combustion process and the propagating shock wave and contact surface (labeled Interface).

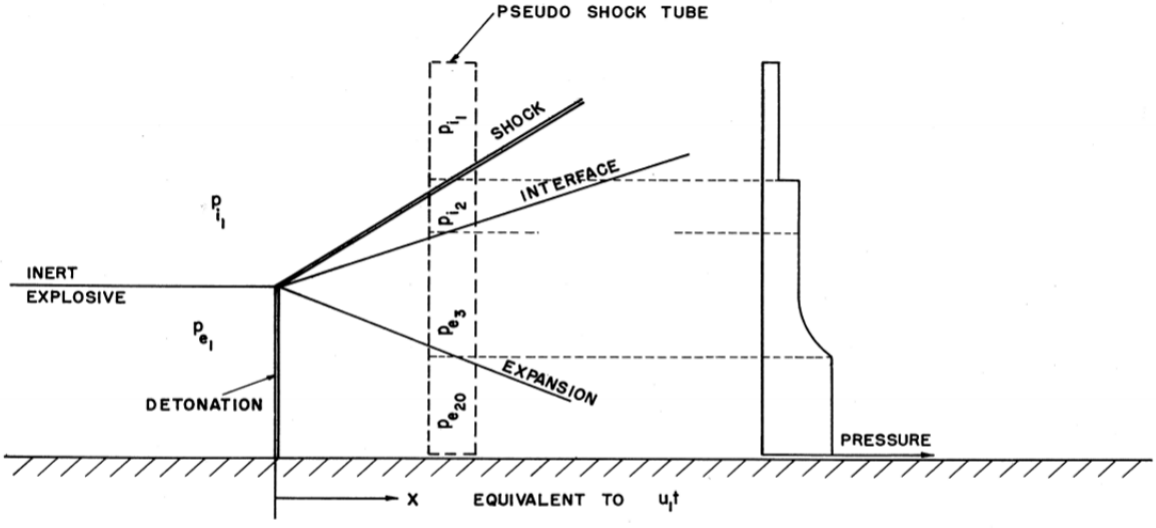


Figure 6. Shock Tube Analogy to the Interaction Process.

Figure B.4: Shock tube analogy for an inert bounded detonation wave.[3]

Essentially, the detonation wave is treated as a infinitesimally thin region that results in an initial pressure profile resembling that of a shock tube before initiation. In a shock tube, the high pressure region produces a leading shock wave, a contact surface between the driver and driven gases, and an expansion wave within the driver section upon initiation. This processes provide a good analogy to the detonation wave, so long as the wave is bounded by a wall at the bottom and moving at a steady rate.

To extend this analogy to the RDC flowpath, a double inert bounded shock tube analogy was developed. Figure B.5 shows the initial pressure conditions for the basic dual shock tube on the left. The inlet and exit plane of the RDC are highlighted on the plot, where the inlet side is initially at a higher pressure compared to the exit plane side. The wave, at the CJ pressure, is the initial driver section. Upon initiation of the dual shock tube, the same shock, interface and expansion complex will emanate from the left and right sides of the CJ pressure region. This produces two expansion fans propagating in the opposite direction of the shock/interface, and these expansion fans eventually intersect to produce the expansion fan complex that is of interest to this model.

Implementation of this simple model did not capture the inlet flow profile that would be expected in the RDC, so it was adapted to include an inlet sub-model. This sub-model used the actual inlet geometry and initial pressure conditions in the plenum and RDC channel. With this information the full flow profile through the inlet can be determined, assuming isentropic flow (unless a shock forms within the diverging region of the inlet) and a steady state flow field. Figure B.5 also shows an example of the inlet flow profile provided by the inlet sub-model. These initial conditions, specified as a function of the axial distance through the inlet, were used to model the flow that the shock structure will see as it propagates into the inlet region.

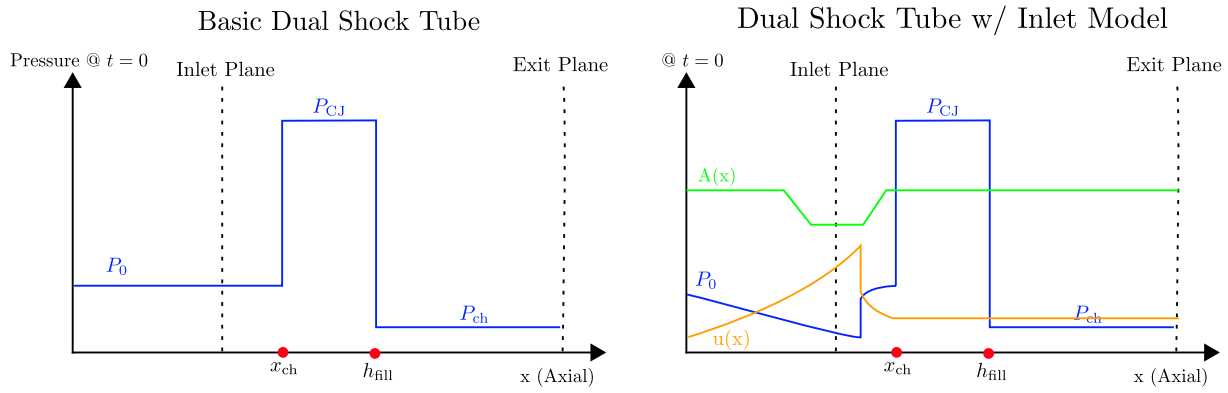


Figure B.5: Example of an one-dimensional dual shock tube configuration (left) and the initial conditions from the inlet sub-model (right).

Figure B.6 shows an example of the one-dimensional method of characteristic solution for the RDC shock/detonation complex. This figure shows the two shock complexes, the contact surfaces,

and the expansion fan complex. With the initial conditions provided in the example, the upstream contact surface begins to curve and eventually move towards the exit of the RDC flowpath. This is caused by the initial inlet profile that provides resistance to backwards flow and the left running expansion fan from the right side of the detonation wave.

The downstream complex propagation is into a constant property flow based on the expanded, post-detonation products. These products were also expanded to the specified channel pressure, P_{ch}.

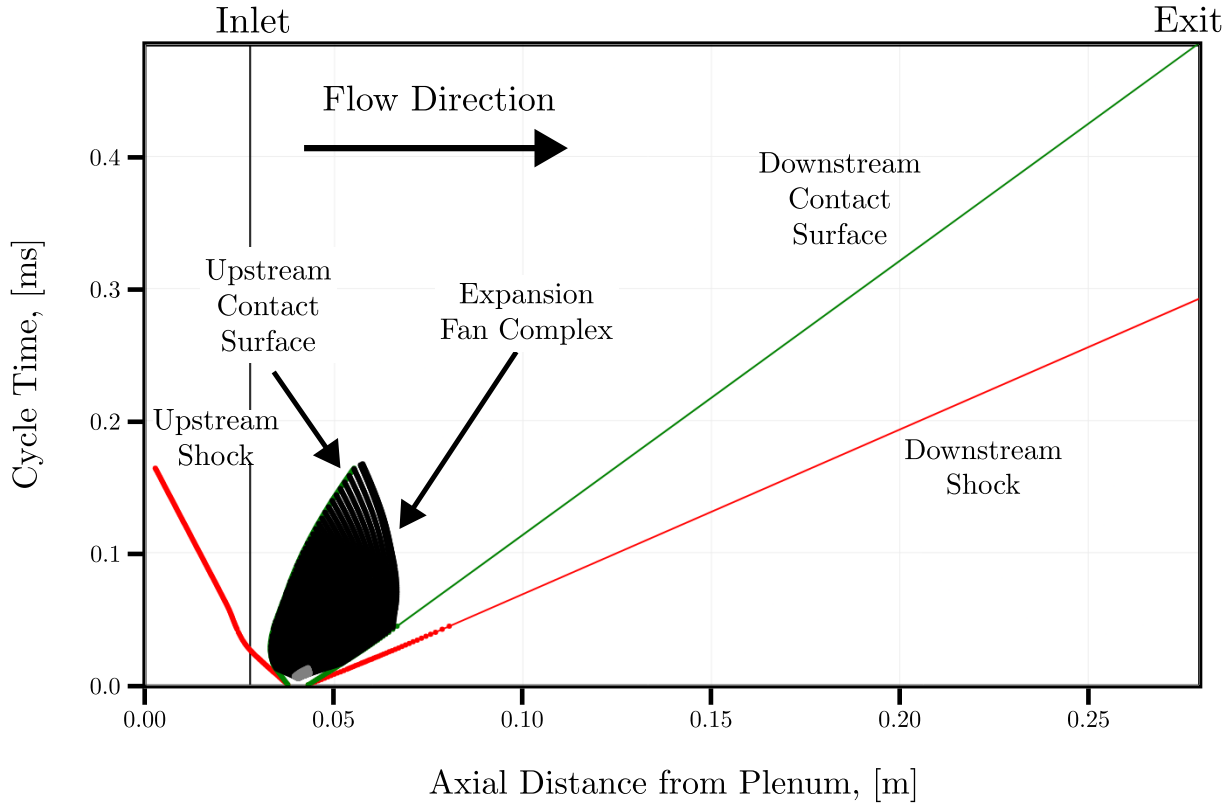


Figure B.6: Example of an isentropic one-dimensional expansion fan complex.

The issues with this method revolve around the fact that the flow field in a RDC has an azimuthal velocity component that differs across the cycle. This means that assuming the reference frame in fixed at the wave speed, D_{CJ}, neglects any of the expansion processes in the azimuthal direction, which forces the expansion to occur solely in the axial direction. First, this is wrong based on our knowledge of the flow-field within the RDC cycle. Second, it makes convergence of the model nearly impossible, as any back flow into the plenum is immediately canceled out by the left running expansion fan from the downstream section of the detonation wave. Because of this, no inlet backflow was observed, even at lower than typical plenum pressures.

These issues lead to the eventual development of the expansion fan complex using 2-D steady

method of characteristic. This update properly captures the azimuthal expansion process; however, the current implementation does not allow for variable area in the inlet region. This resulted in simplifying the expansion fan model significantly.

Because of these results, the question of viability extends to other RDC models that employ a form of one-dimensional shock tube as an analogy for the RDC. One example is modeling the RDC flowpath as a series of one-dimensional shock tubes, all initiated at times corresponding to the lap time of the detonation wave in the RDC. Again, the azimuthal expansion process that occurs within the RDC cycle is neglected in this model.

B.3 Inlet Sub-Model

This section covers some details on the different methods of the inlet model that were attempted for the full cycle model. Initial models of the inlet would make certain assumptions about where the static pressure was location along the inlet profile. Initially, the inlet model would set the static pressure (calculated from the pressure profile) at the injector plane. From this, it would used the isentropic flow relations to calculate a Mach number based on this pressure, and then calculate the mass flow rate through the individual sectors of the inlet.

This is technically not correct because of how we generate the pressure profile in the first place. In the cycle model, and inlet model discussion, the pressure profile, as a function of time/space, was generated using information within the RDC channel region. Through either an exponential decay fit, or by interpolating values from the expansion fan network, the pressure profile was always generated at the channel area, versus the injector area. We can improve fidelity of the inlet model by taking into consideration the geometric flow path from the plenum to the channel, and used these areas when determining the Mach number for a given inlet sector. This was the methodology used for this research effort, which hopefully allows for a more realistic determination of metrics such as inlet blockage.

B.4 Momentum and Heat Loss Capturing

Initially, the cycle model required a specified momentum/friction loss term and a heat transfer loss term as inputs. The inputs would be integrated through the channel flow objects to capture the associated losses, and eventually the reduction in performance. With the inclusion of the polytropic compression algorithm, Algorithm 24, these losses are essentially captured by the a polytropic process at the end of each Channel Flow object. This means we might not need to specify the momentum or heat losses directly, and can instead rely on the polytropic rate terms to estimate

these values, subject to the mass flow conservation at a given pressure at the exit of the channel flow object.

With this new methodology, the one-dimensional flow integration does not need to be included in the model, and the Channel Flow objects can be solved in a much more simple two step process: isentropic jump from the inlet to the exit of the Channel Flow object, followed by the polytropic compression at the exit plane. This could even be further simplified to a single step process by including the area change in the solution of the conservation equations undergoing a polytropic process. In this manor, the area change and additional losses are all accounted for with one iterative sub-model.

BIBLIOGRAPHY

[1] Fabian Chacon and Mirko Gamba. Study of parasitic combustion in an optically accessible continuous wave rotating detonation engine. In *AIAA Scitech 2019 Forum*. Paper No. 2019-0473, 2019.

[2] Alexander Feleo, Jacob France, Logan W. White, and Mirko Gamba. Evaluation of OH emission for determining operation of a rotating detonation engine. In *AIAA Scitech 2019 Forum*. Paper No. AIAA-2019-2252, jan 2019.

[3] E. K. Dabora. The influence of a compressible boundary on the propagation of gaseous detonations. *Technical Report*, 1963.

[4] Thomas A Kaemming, Matthew L Fotia, John L Hoke, and Stephen A Schumacker. Quantification of the loss mechanisms of a ram rotating detonation engine. In *AIAA Scitech 2020 Forum*. Paper No. AIAA-2020-0927, 2020.

[5] Alexander Feleo, Joshua Shepard, and Mirko Gamba. Evaluation of reaction-induced effective inlet blockage of rotating detonation combustors. In preparation, 2024.

[6] Craig A Nordeen, Douglas Schwer, Fredrick Schauer, John Hoke, Th Barber, and B Cetegen. Thermodynamic model of a rotating detonation engine. *Combustion, Explosion, and Shock Waves*, 50(5):568–577, 2014.

[7] Craig A. Nordeen, Douglas Schwer, Andrew T. Corrigan, and Baki Cetegen. Radial effects on rotating detonation engine swirl. In *51st AIAA/SAE/ASEE Joint Propulsion Conference*. Paper No. AIAA-2015-3781, July 2015.

[8] Jonathan Tobias, Robert Miller, and Ajay K Agrawal. Flow measurements inside a rotating detonation combustor. In *AIAA Propulsion and Energy 2020 Forum*, page 3869, 2020.

[9] John A. Grunenwald, James Braun, and Guillermo Paniagua. *Analysis of the Physics of Rotating Detonation with a Method of Characteristics Model*.

[10] Douglas A Schwer and K. Kailasanath. Numerical Investigation of Rotating Detonation Engine. *46th AIAA/ASME/SAE/ASEE Joint propulsion Conference & Exhibit*, (July):1–15, 2010.

[11] William P. Sommers. *The Interaction of a Detonation Wave with an Inert Boundary*. PhD thesis, University of Michigan, 1961.

[12] Stephen R. Turns. *An Introduction to Combustion Concepts and Applications*. McGraw-Hill, New York, 2nd edition, 2000.

[13] Heinz Langweiler. The hydrodynamic theory of detonation. Technical report, 1939.

[14] Geoffrey Ingram Taylor. The dynamics of the combustion products behind plane and spherical detonation fronts in explosives. *Proceedings of the Royal Society of London. Series A. Mathematical and Physical Sciences*, 200(1061):235–247, 1950.

[15] Richard Dyer and Thomas Kaemming. The thermodynamic basis of pulsed detonation engine thrust production. In *38th AIAA/ASME/SAE/ASEE Joint Propulsion Conference*. AIAA, July 2002.

[16] Craig Nordeen, Douglas Schwer, Fred Schauer, John Hoke, Thomas Barber, and Baki Cetegen. Energy transfer in a rotating detonation engine. In *47th AIAA/ASME/SAE/ASEE Joint Propulsion Conference & Exhibit*, page 6045, 2011.

[17] Kenneth K. Kuo. *Principles of Combustion*. John Wiley & Sons, Inc, New Jersey, 2nd edition, 2005.

[18] David G Goodwin, Raymond L Speth, Harry K Moffat, and Bryan W Weber. Cantera: An object-oriented software toolkit for chemical kinetics, thermodynamics, and transport processes. https://www.cantera.org, 2021.

[19] N Hoffman. Reaction Propulsion by Intermittent Detonative Combustion. *German Ministry of Supply*, (Volkenrode Translation), 1940.

[20] J. Nicholls, H. Wilkinson, and R. Morrison. Intermittent detonation as a thrust-producing mechanism. *Journal of Jet Propulsion*, 27(5):534–541, 1957.

[21] Brent A. Rankin, Matthew L. Fotia, Andrew G. Naples, Christopher A. Stevens, John L. Hoke, Thomas A. Kaemming, Scott W. Theuerkauf, and Frederick R. Schauer. Overview of Performance, Application, and Analysis of Rotating Detonation Engine Technologies. *Journal of Propulsion and Power*, 33(1):131–143, jan 2017.

[22] Kurt P Rouser, Paul I King, Frederick R Schauer, Rolf Sondergaard, and John L Hoke. Unsteady Performance of a Turbine Driven by a Pulse Detonation Engine. *48th AIAA Aerospace Sciences Meeting Including the New Horizons Forum and Aerospace Exposition*, (January):1–16, 2010.

[23] Kurt P Rouser, Paul I King, Frederick R Schauer, Rolf Sondergaard, and John L Hoke. Performance Evaluation of an Unsteady Turbine Driven by a Pulsed Detonation Combustor. *Proceedings of ASME Turbo Expo 2011*, (January):GT2011–45396, 2011.

[24] Richard Dyer, Andrew G. Naples, Thomas A. Kaemming, John L. Hoke, and Frederick R. Schauer. Parametric Testing of a Unique Rotating Detonation Engine. *50th AIAA Aerospace Sciences Meeting including the New Horizons Forum and Aerospace Exposition*, (January):1–7, 2012.

[25] Fabian Chacon and Mirko Gamba. OH PLIF visualization of an optically accessible rotating detonation combustor. In *In proceedings AIAA Propulsion and Energy Forum*, 2019.

[26] Alexander Feleo, Fabian Chacon, and Mirko Gamba. Effects of heat release distribution on detonation properties in a H2/air rotating detonation combustor from OH* chemiluminescence. In *AIAA Propulsion and Energy 2019 Forum*. Paper No. AIAA-2019-4045, 2019.

[27] Thomas A. Kaemming and Daniel E. Paxson. Determining the pressure gain of pressure gain combustion. In *2018 Joint Propulsion Conference*. Paper No. AIAA-2018-4567, January 2018.

[28] Thomas A. Kaemming, Matthew L. Fotia, John L. Hoke, and Stephen A. Schumacker. Quantification of the loss mechanisms of a ram rotating detonation engine. *AIAA Scitech 2020 Forum*, 1 PartF, 2020.

[29] Tom Kaemming, Matthew L. Fotia, John Hoke, and Fred Schauer. Thermodynamic modeling of a rotating detonation engine through a reduced-order approach. *Journal of Propulsion and Power*, 33(5):1170–1178, September 2017.

[30] Daniel E. Paxson and Hugh D. Perkins. A simple model for rotating detonation rocket engine sizing and performance estimates. In *AIAA Scitech 2021 Forum*. Paper No. AIAA-2021-0192, January 2021.

[31] Robert T. Fievisohn and Kenneth H. Yu. Steady-state analysis of rotating detonation engine flowfields with the method of characteristics. *Journal of Propulsion and Power*, 33(1):89–99, January 2017.

[32] Petros Dellaportas and Gareth O. Roberts. *An Introduction to MCMC*, pages 1–41. Springer New York, New York, NY, 2003.

[33] N. Metropolis, A. Rosenbluth, M. Rosenbluth, A. Teller, and E. Teller. Equations of state calculations by fast computing machines. *Journal of Chemical Physics*, (6):1087–1091, June 1953.

[34] W. Hastings. Monte carlo sampling methods using markov chains and their applications. *Biometrika*, (1):97–109, April 1970.

[35] Heikki Haario, Eero Saksman, and Johanna Tamminen. An adaptive Metropolis algorithm. *Bernoulli*, 7(2):223–242, 2001.

[36] Heikki Haario, Marko Laine, Antonietta Mira, and Eero Saksman. Dram: Efficient adaptive mcmc. *Statistics and Computing*, pages 339–354, December 2006.

[37] Amir Shahmoradi, Fatemeh Bagheri, and Joshua Alexander Osborne. Fast fully-reproducible serial/parallel monte carlo and mcmc simulations and visualizations via paramonte::python library. *arXiv e-prints*, page arXiv:2010.00724, October 2020.

[38] Peter Strakey, Donald Ferguson, Andrew Sisler, and Andrew Nix. Computationally quantifying loss mechanisms in a rotating detonation engine. In *54th AIAA Aerospace Sciences Meeting*. American Institute of Aeronautics and Astronautics Inc, AIAA, 2016.

[39] Jason R. Burr and Eric Paulson. Thermodynamic performance results for rotating detonation rocket engine with distributed heat addition using cantera. In *AIAA Propulsion and Energy 2021 Forum*. Paper No. AIAA-2021-3682, 2021.

[40] Provence Barnouin, Eric Bach, Ephraim J. Gutmark, Christian O. Paschereit, and Myles Bohon. Low-order model for detonation velocity suppression in rotating detonation combustors. In *AIAA SCITECH 2023 Forum*. American Institute of Aeronautics and Astronautics Inc, AIAA.

[41] Venkat Raman, Supraj Prakash, and Mirko Gamba. Nonidealities in rotating detonation engines. *Annual Review of Fluid Mechanics*, 55(1):639–674, 2023.

[42] David P Stechmann, Swanand Sardeshmukh, Stephen D Heister, and Kota Mikoshiba. Role of ignition delay in rotating detonation engine performance and operability. *Journal of Propulsion and Power*, 35(1):125–140, 2019.

[43] Robert T. Fievisohn, John L. Hoke, and Adam Holley. Thermodynamic and operability implications of product recirculation in rotating detonation engines. *AIAA Propulsion and Energy Forum and Exposition, 2019*, 2019.

[44] Robert T. Fievisohn, John Hoke, and Stephen A. Schumaker. Product recirculation and incipient autoignition in a rotating detonation engine. In *AIAA Scitech 2020 Forum*. Paper No. AIAA-2020-2286, 2020.

[45] M. Sichel. A hydrodynamic theory for the interaction of a gaseous detonation with a compressible boundary. In *2nd Aerospace Sciences Meeting*, 1965.

[46] Sanford Gordon and Bonnie J McBride. Computer program for calculation of complex chemical equilibrium compositions and applications. Part 1: Analysis. *NASA RP 1311*, 1994.

[47] S. T. Browne, J. L. Ziegler, N. P. Bitter, B. E. Schmidt, J. Lawson, and J. E. Shepherd. Sdtoolbox: Numerical solution methods for shock and detonation jump conditions. *GALCIT Report FM2018.001*, 2023.

[48] Arnab Roy, Peter Strakey, Todd Sidwell, and Donald H. Ferguson. *Unsteady Heat Transfer Analysis to Predict Combustor Wall Temperature in Rotating Detonation Engine*.

[49] Scott W. Theuerkauf, Frederick Schauer, Richard J. Anthony, Daniel E. Paxson, Christopher A. Stevens, and John Hoke. Comparison of simulated and measured instantaneous heat flux in a rotating detonation engine. In *54th AIAA Aerospace Sciences Meeting*. Paper No. AIAA-2016-1200, 2016.

[50] Christopher A. Stevens, Matthew Fotia, John Hoke, and Frederick Schauer. *Quasi Steady Heat Transfer Measuments in an RDE*.

[51] Shreyas Ramanagara Sridhara, Umberto Sandri, Pier Carlo Nassini, Marc D. Polanka, Myles Bohon, and Antonio Andreini. *Quantification of Heat Loads for Rotating Detonation Combustors with Gas Turbine Conditions*.

[52] I.M Sobol. Global sensitivity indices for nonlinear mathematical models and their monte carlo estimates. *Mathematics and Computers in Simulation*, 55(1):271–280, 2001. The Second IMACS Seminar on Monte Carlo Methods.

[53] Fedor A. Bykovskii, Sergey A. Zhdan, and Evgenii F. Vedernikov. Continuous spin detonations. *Journal of Propulsion and Power*, 22(6):1204–1216, 2006.

[54] Craig Nordeen, Douglas Schwer, Fredrick Schauer, John Hoke, Baki Cetegen, and Thomas Barber. Thermodynamic modeling of a rotating detonation engine. In *49th AIAA Aerospace Sciences Meeting including the New Horizons Forum and Aerospace Exposition*. Paper No. AIAA-2011-803, January 2011.

[55] Douglas Schwer and Kailas Kailasanath. Effect of inlet on fill region and performance of rotating detonation engines. In *47th AIAA/ASME/SAE/ASEE Joint Propulsion Conference & Exhibit*, 2011.

[56] Andrew Naples, John Hoke, James Karnesky, and Fred Schauer. Flowfield characterization of a rotating detonation engine. In *51st AIAA Aerospace Sciences Meeting including the New Horizons Forum and Aerospace Exposition 2013*. Paper No. AIAA-2013-278, 2013.

[57] Clinton Bedick, Donald H. Ferguson, and Peter Strakey. Validation and application of a reduced-order rotating detonation engine inlet and fill zone model. In *AIAA Scitech 2021 Forum*. Paper No. AIAA-2021-0193, 2021.

[58] Alexander Feleo, Joshua Shepard, and Mirko Gamba. Prediction of detonation-induced disturbances propagating upstream into inlets of rotating detonation combustors. In *AIAA Propulsion and Energy 2021 Forum*. Paper No. AIAA-2021-3687, 2021.

[59] Daniel E. Paxson and Kenji Miki. Computational assessment of inlet backflow effects on rotating detonation engine performance and operability. In *AIAA SCITECH 2022 Forum*. Paper No. AIAA-2022-1263, January 2022.

[60] Li Deng, Hu Ma, Can Xu, Changsheng Zhou, and Xiao Liu. Investigation on the propagation process of rotating detonation wave. *Acta Astronautica*, 139:278–287, 2017.

[61] Ionio Andrus, Marc Polanka, Paul King, Fred Schauer, and John Hoke. Experimentation of premixed rotating detonation engine using variable slot feed plenum. *Journal of Propulsion and Power*, 33(6):1448–1458, 2017.

[62] J. Shepard, Joshua. *Experimental Characterization of Rotating Detonation Engine Loss Mechanisms*. PhD thesis, University of Michigan, 2023.

[63] Daniel Depperschmidt, Robert Miller, Jonathan Tobias, Mruthunjaya Uddi, Ajay K. Agrawal, and Jeffrey B. Stout. Time-resolved PIV diagnostics to measure flow field exiting methane-fueled rotating detonation combustor. In *AIAA Scitech 2019 Forum*. Paper No. AIAA-2019-1514, January 2019.

[64] Ian B. Dunn, Jonathan Sosa, Marc Salvadori, Kareem A. Ahmed, and Suresh Menon. Flowfield velocity measurements of a rotating detonation engine. In *AIAA Scitech 2020 Forum*. Paper No. AIAA-2020-1176, January 2020.

[65] James Duvall, Fabian Chacon, Chadwick Harvey, and Mirko Gamba. Study of the effects of various injection geometries on the operation of a rotating detonation engine. In *2018 AIAA Aerospace Sciences Meeting*. Paper No. AIAA-2018-0631, jan 2018.

[66] Tomohiro Watanabe, Nicolas H. Jourdaine, Nobuyuki Tsuboi, Takayuki Kojima, and Koichi A. Hayashi. *Three-dimensional Numerical Simulation of Disk Rotating Detonation Engine; Unsteady Flow Structure*.

[67] John David Anderson. *Modern compressible flow: with historical perspective*. McGraw-Hill New York, 1990.

[68] Xin Huang, Po-Hsiung Chang, Zhen Wei Teo, Jiun-Ming Li, Chiang Juay Teo, and Boo Cheong Khoo. Particle image velocimetry measurements of unsteady exhaust from a linearized continuous detonation combustor. In *AIAA SCITECH 2023 Forum*. American Institute of Aeronautics and Astronautics, 2023.

[69] Joseph E Shepherd and J Kasahara. Analytical models for the thrust of a rotating detonation engine. *Technical Report FM2017.001*, 2017.

[70] B. K. Hodges. Generalized one-dimensional compressible flow techniques. *Internation Journal of Applied Engineering*, 7(1):56–63, 1991.

[71] Mirko Gamba, Alexander Feleo, Joshua Shepard, and Fabian Chacon. State-to-state model for rotating detonation combustors. In *Proceedings of the 28th International Colloquium on the Dynamics of Explosions and Reactive Systems*, 2022.

[72] Joshua Shepard, Alexander Feleo, and Mirko Gamba. Effects of inlet area ratio on operability of an axial air inlet rotating detonation combustor. In *AIAA Propulsion and Energy 2021 Forum*. Paper No. AIAA 2021-3676, 2021.

[73] Gregory P. Smith, David M. Golden, Michael Frenklach, Nigel W. Moriarty, Boris Eiteneer, Mikhail Goldenberg, C. Thomas Bowman, Ronald K. Hanson, Soonho Song, William C. Gardiner Jr., Vitali V. Lissianski, and Zhiwei Win. Gri-mech 3.0, 2023.

[74] Douglas A. Schwer and Kailas Kailasanath. *Physics of Heat-Release in Rotating Detonation Engines*.

[75] S. She-Ming Lau-Chapdelaine, Matei I. Radulescu, and Zekai Hong. *Quasi-Two-Dimensional Simulation of a Rotating Detonation Engine Combustor and Injector*.

[76] Riley Huff and Mirko Gamba. Effects of non-idealities on gain in a detonation cycle. *Proceedings of the 29th International Colloquium on the Dynamics of Explosions and Reactive Systems*, 29(236), 2023.

[77] Alexander D. Feleo and Mirko Gamba. Evaluation of uncertainties of pressure gain measurements in rotating detonation combustor. *AIAA Journal*, page 1–19, November 2023.

[78] Ral Bielawski, Shivam Barwey, Supraj Prakash, and Venkat Raman. Highly-scalable gpu-accelerated compressible reacting flow solver for modeling high-speed flows. *Computers Fluids*, 265:105972, 2023.

[79] Ethan W. Plaehn, Allyson L. Haynes, Rohan M. Gejji, and Carson D. Slabaugh. Chamber length limits of a continuously variable geometry rotating detonation combustor. *Journal of Propulsion and Power*, 0(0):1–15, 0.

[80] Alexander Feleo, Joshua Shepard, and Mirko Gamba. Experimental study of the invariance of pressure gain with respect to the dynamics of multiple competing waves in a rotating detonation combustor. In *AIAA Scitech 2023 Forum*. Paper No. AIAA 2023-1296, January 2023.

[81] Alexander D. Feleo and Mirko Gamba. Improving base-drag corrections for rotating detonation combustor gross thrust measurements. Submitted to Journal of Propulsion and Power, 2024.

[82] Andrew Naples, John Hoke, Ryan Battelle, and Fred Schauer. T63 turbine response to rotating detonation combustor exhaust flow. *Journal of Engineering for Gas Turbines and Power*, 141(2), October 2018.

[83] M.J. Zucrow and J.D. Hoffman. *Gas Dynamics*. Number v. 2 in Gas Dynamics. Krieger Publishing Company, 1977.